Genetic deletion of *Alox15* is associated with spatial and anxiety phenotypes related to normal ageing.

ANASTASIA GKETSOPOULOU

A THESIS SUBMITTED TO CARDIFF UNIVERSITY IN ACCORDANCE WITH THE REQUIREMENTS FOR THE DEGREE OF DOCTOR OF PHILOSOPHY (PHD)

School of Medicine, Cardiff University

SEPTEMBER 2022

In loving memory of my grandmother,
Anastasia

Acknowledgements

Getting to the end of my PhD has been more rewarding than I could have ever imagined, and I am hugely grateful to so many people for their contribution throughout this whole journey, without whom this thesis would have never been possible. First and foremost, I would like to thank my primary supervisor, Professor Valerie O'Donnell, for her invaluable guidance, advice, feedback and excellent support during my PhD studies. Also, my co-supervisor, Professor Mark Good, for being always available and approachable. I am also grateful for supporting the behavioural and immune chapters, which could not have been achieved without his advice and expertise. I am very thankful to my funding body, the Hodge Foundation, which made my PhD study possible. I genuinely thank Vikki, the lab manager of the Lipidomic Group, for her help and great technical advice for the lipidomic chapters. Also, the rest of the lipidomic group's members and PhD students listened to my rants, helped me refocus when I needed, and shared the ups and downs throughout this journey! Thank you so much, Madj, Daniela and Ali, for being such wonderful and supportive colleagues. I genuinely admire the trustful atmosphere in your research groups. Special acknowledgements go to Dr Thomas Freeman, for helping me with the behavioural tasks. Thank you to every past member of Valerie O'Donnell's research group in the lab. Also, I would like to thank Dr James Burston, who helped me throughout my PhD studies.

Finally, I would like to thank my parents, my grandfather, my brother, sister-in-law and nephew. Their belief in me has kept my motivation high during this journey. I am eternally grateful to my parents and grandparents, who provided me with every opportunity possible to succeed, particularly endless love and support. Without their help, patience and guidance, it would not have been possible to complete this work. It is to them that I owe my eternal gratitude! A special thanks to my best friends who became family this year and were always there for me. Last but not least, my man to whom I dedicate this thesis. You were always patient when I babbled about science and issues in experiments and seemingly endless writing. Without your support, I would not have achieved half of what I have.

Summary

Lipoxygenases are a family of enzymes that generate bioactive inflammatory lipid mediators. Among them, the *Alox15* gene product (15-LOX, 12/15-LOX) has been detected in neurons and glial cells in mice. There is an emerging interest in its potential role in neurodegenerative disease; however, the biological role of this enzyme in the healthy brain has not yet been characterised. This thesis investigates the impact of 12/15-LOX deletion on mouse cognitive function and lipid profiling. Two independent groups of young to middle-aged and old wild type (WT) or *Alox15*$^{-/-}$ mice were studied. A range of behavioural tests, including a novel object recognition task, object location task and elevated plus maze, were used to assess the effects of deletion on cognition and emotional reactivity compared with similarly aged control WT mice. At 10 months of age, both male and female *Alox15*$^{-/-}$ *mice* displayed spatial memory deficits that may be linked to hippocampal impairments.

In contrast, knock-out mice showed normal novel object recognition memory. Also, *Alox15*$^{-/-}$ mice manifested increased anxiety-like behaviour compared to controls. Their increased anxiety phenotype was connected to alterations in the expression levels of various protein markers, including parvalbumin, GABAergic, corticotrophin-releasing factor, and serotonergic receptors. Separately, liquid chromatography with tandem mass spectrometry was used to quantify oxylipins and enzymatically oxidised phospholipids (oxPL) generated via the 12/15-LOX during healthy brain ageing across various brain regions in both groups of mice. Lipidomic analysis of brain regions extracted and revealed elevated levels of selected oxylipins (5-HETE, prostaglandins) but reduced levels of the *Alox15* product, 12-HETE. In eoxPL analysis, the deficiency of *Alox15* did not change the levels of PE 18:0a_12-HETE between genotypes. Taken together, these results suggest a role for 12/15-LOX in regulating normal brain function, and further work is required to determine the biological basis of the anxiety phenotype in mice lacking this enzyme.

Abbreviations

5-LOX	5-lipoxygenase
5-HETE	5-Hydroxyeicosatetraenoic acid
5-oxo-ETE	5-Oxo-eicosatetraenoic acid
6-keto-PGF1α	6-keto-Prostaglandin F1 Alpha
12-LOX	12-lipoxygenase
12-HETrE	12S-hydroxy-5Z,8E,10E-heptadecatrienoic acid
12-HETE	12-Hydroxyeicosatetraenoic acid
13(S)-HODE	13(S)-hydroxy-9Z,11E-octadecadienoic acid
13S-HPODE	13S-hydroperoxyoctadecadienoic acid
13S-HODE	13S-hydroxyoctadecadienoic acid
13-HOTrE	13S-hydroxy-9Z,11E,15Z-octadecatrienoic acid
15-LOX	15-lipoxygenase
15S-HpETE	15S-hydroperoxyeicosatetraenoic acid
15-HETE	15-Hydroxyeicosatetraenoic acid
15-LOX-1	15-lipoxygenase type 1
15-LOX-2	15- lipoxygenase type 2
9-HODE	9-Hydroxyoctadecadienoic acid
9-HOTrE	9-hydroxy-10E,12Z,15Z-octadecatrienoic acid
5-HT_{1A}	Serotonergic receptor 1A
a.m.u.	Atomic mass unit
AA	Arachidonic acid
ALAa	α-linolenic acid
AD	Alzheimer's disease
ANOVA	Analysis of variance
Alox15	15-Lipoxygenase-1
BS	Brainstem
CRF_1	Corticotrophin-releasing factor 1
CREB	cAMP Response Element-Binding Protein
CB	Cerebellum
Ca2+	Calcium ion
COX	Cyclooxygenase
COX-1	Cyclooxygenase-1
COX-2	Cyclooxygenase-2
CYP	Cytochrome P450
CNS	Central nervous system
CoA	Coenzyme A
$cPLA_2$	Cytosolic phospholipase A_2
DR	Discrimination ratio
DHA	Docosahexaenoic Acid
DMSO	Dimethyl sulfoxide
DMPC	1,2-dimyristoyl-sn-glycero-3-phosphocholine
DMPE	1,2-dimyristoyl-sn-glycero-3-phosphoethanolamine

dHPC	Dorsal Hippocampus
DG	Dentate gyrus
EPA	Eicosapentaenoic Acid
EPM	Elevated Plus Maze
EPI	Enhanced Product Ion
EETs	Epoxyeicosatrienoic acids
eoxPLs	Enzymatically oxidized phospholipids
FA	Fatty acid
FLAP	5-lipoxygenase activating protein
$GABA_A$	γ-Aminobutyric acid type A
$GABA_B$	γ-Aminobutyric acid type B
GL	Glycerolipids
GP	Glycoprotein
GPX	Glutathione peroxidase
H.B.	Habituation Phase
HDOHE	Hydroxydocosahexaenoic acid
HETE	Hydroxytetraenoic acid
HPETE	Hydroperoxytetraenoic acid
HPLC	High performance liquid chromatography
HODE	Hydroxyoctadecadienoic acid
IPA	Propan-2-ol
IS	Internal standard
LA	Linoleic acid
FST	Forced swim test
GPCR	G protein-coupled receptor
HPC	Hippocampus
IOC	Input/Output Curve
PLA2β	Phospholipase A2 β
kDa	kilodaltons
LC	Liquid chromatography
LC/MS/MS	Liquid chromatography coupled to tandem mass spectrometry
LPAT	Lysophospholipid acyl transferase
LOXs	Lipoxygenases
LT	Leukotrienes
LTB_4	Leukotriene B4
LTP	Long-term potentiation
LXA_4	Lipoxin A4
LXB_4	Lipoxin B4
MRM	Multiple reaction monitoring
MS	Mass spectrometry
m/z	mass/charge ratio
MW	Molecular weight
NOR	Novel Object recognition task
ng	Nanograms

NSAID	Non-steroidal anti-inflammatory drugs
NMDA	N-methyl-d-aspartic acid
NF-κB	Nuclear factor kappa B
OLT	Object Location task
OB	Olfactory bulb
OxPL	Oxidized phospholipids
PV	Parvalbumin
PPAR-γ	Peroxisome proliferator- activated receptor gamma
PBS	Phosphate-buffered saline
PL	Phospholipids
PC	Phosphatidylcholine
PE	Phosphatidylethanolamine
PG	Prostaglandin
PGH_2	Prostaglandin H2
PGI_2	Prostaglandin I2
PGE_2	Prostaglandin E2
$PGF_{2\alpha}$	Prostaglandin F2α
PLA_1	Phospholipase A1
PLA_2	Phospholipase A2
PUFA	Polyunsaturated fatty acids
PFA	Paraformaldehyde
PFC	Prefrontal cortex
PKC	Protein kinase C
PUFA	Poly-unsaturated fatty acid
PVDF	Polyvinylidinedifluoride
Q6500	Quadrupole 6500
RT-PCR	Real time reverse transcriptase polymerase chain
RT	Retention time
RvD_1	Resolvin D1
RvD_2	Resolvin D2
RvE1	Resolvin E1
RVM	Rostral ventromedial medulla
ROS	Reactive oxygen species
S.P.	Sample Phase
S.E.M.	Standard error of the mean
SDS-PAGE	Sodium Dodecyl Sulphate Polyacrylamide Gel
sn1/sn2	Stereospecific numbering
T.P.	Test Phase
TBS	Tris-buffered saline
TBST	Tris buffered saline - Tween
TLR_4	Toll-like receptor 4
TxA_2	Thromboxane A2
TxB_2	Thromboxane B2
vHPC	Ventral hippocampus

Table of Contents

Chapter 1:

General Introduction

1.1 Chapter overview

Over several decades, improvements in healthcare and clinical practices have led to significant increases worldwide in average life expectancy (Timonin *et al.,* 2016). However, it is widely accepted that as the global population ages, the number of people suffering from age-related diseases will grow. By 2030, it is estimated that the total number of people living with age-related diseases will be approximately 75.6 million, and this figure is projected to triple to 135.5 million people by 2050 according to World Alzheimer's Report 2015. Additionally, with advancing age comes an increased risk of cognitive impairments that often precede the development of dementia later in life (Barrientos *et al.,* 2015; Sharma *et al.,* 2010). There is now a growing interest in identifying novel and accurate brain ageing biomarkers that could indicate cognitive health in ageing populations and identify those at risk of dementia (Franceschi *et al.,* 2018). In recent decades, lipid metabolism in the central nervous system (CNS) has been linked with brain ageing (Yang *et al.,* 2016). Several experimental studies have highlighted the crucial role of lipid metabolites in metabolism and signalling, and they have shown that any alterations associated with ageing affect cognitive function (Jagust, 2013; Dennis *et al.,* 2015; Han X., 2016). Consequently, there is an urgent need for continuous development of novel and accurate lipid biomarkers that could assist in prognoses.

This chapter will introduce the role of the 12/15-lipoxygenase enzyme (12/15-LOX, encoded by the *Alox15* gene) in normal cognitive function and behaviour, followed by the importance of lipid signalling in normal brain ageing. Dementia is a general term to describe the cognitive decline and behavioural deficits (Gorelick *et al.,* 2016). Thus, this baseline in cognitive function needs to be considered in healthy mice lacking the *Alox15* gene in comparison with age-matched control mice throughout this thesis.

1.2 Rodent models in neuroscience research

Understanding the structure and the functional development of the human brain remains a challenging question (Lisman, 2015). A shift to rodent-based research has occurred over the past decades to help elucidate the development of novel and effective treatments to improve human brain health (Mitchell *et al.,* 2015). This area of neurosciences is making rapid progress due to the rodents serving as valuable tools for testing. The mouse brain has become a powerful model for studying how the brain operates, which may be due, in part, to the genes responsible for normal brain function, which have been proven to be 90 % homologous or to have similar

sequences to the human genome (Morrisette *et al.,* 2009; Schmouth *et al.,* 2011; Li et al., 2021). Thus, an increasing number of mouse models have been generated, which produce many aspects of human neurological disorders to truly examine the function of a particular aspect of a human disorder in the context of a mouse (Harper, 2010).

1.2.1 Brain function in health

The mouse brain is an outstanding organ that contains more than 100 million nerve cells, consisting of the CNS and the spinal cord (Hussain *et al.,* 2013; Striedter, 2005). The primary function of the CNS is initiating and coordinating the sensory inputs that the brain receives, followed by the process and regulation of an appropriate motor output response and the integration of most of the nerve messages (Frackowiak, 2004; Hussain *et al.,* 2019). Neurons and glial cells are the main cellular components of the CNS that act synergistically to generate the coordinated response of each cell type to perform its particular functions (Jha *et al.,* 2018). Each neuron linked to many other neurons to communicate information and convey messages via thousands of synaptic connections and changes in the frequency of their firing rate. It controls the function of neural circuits and networks, partly by modulating the synchrony of their components, while the neurons can communicate with effector sites in the periphery via signals over long distances through their axons (Tyler, 2012). The signals are transmitted by neurotransmitters and other extracellular signalling molecules across synapses from one neuron to another and coordinate activity across neuronal networks (Maher, 2000). Axons require a high energy supply to maintain their function and are closely linked with glial cells that support their function and prevent degeneration (Jha *et al.,* 2018). The brain performs a wide range of functions, from the motor to cognitive, demonstrating neurons' vast structural and functional diversity (Shamim *et al.,* 2018). There is growing evidence to suggest that glial cells, including astrocytes and microglia, play critical roles in providing structural and metabolic protection to neurons and brain development and function. Their main functions are regulating homeostasis, forming myelin in the periphery and removing dead neurons (Jha *et al.,* 2018).

1.2.2 The structure of the mouse brain

The brain is composed of three main parts: namely, the cerebrum, the cerebellum, and the brain stem (Rea, 2016).

Cerebrum

The cerebrum is divided into two hemispheres, the right and the left, collectively called the cerebral hemispheres, responsible for cognition and language, memory, emotion and behaviour, respectively. (Ackerman, 1992). The outer surface of the cerebral hemispheres is

composed of a layer of gray matter, namely the cerebral cortex, while the inner deeper layer is termed white matter beneath the cerebral cortex (Murman, 2015; Mercadante *et al.*, 2020). The cerebral cortex is divided into four distinct functionally and spatially defined lobes: frontal, parietal, temporal, and occipital (Abhang *et al.*, 2016; Jawabri *et al.*, 2019).

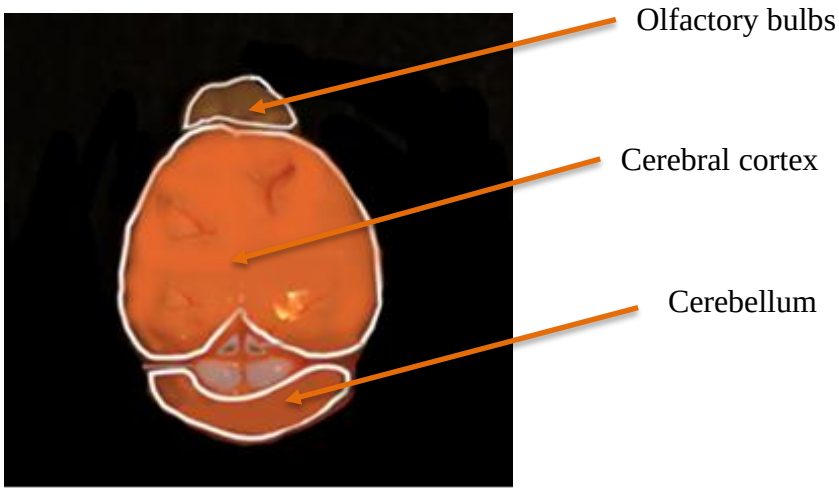

Figure 1. Rodent cerebral cortex and cerebellum structure.

The frontal lobe is at the front of the cerebral hemispheres (Stuss, 2013). This is covered by the frontal cortex, which contains the premotor cortex, motor cortex and olfactory bulbs (Collins *et al.*, 2012). The frontal lobe of the cerebral cortex is associated with cognitive functions, such as maintaining attention, planning, creativity, reasoning, learning and emotions (Felleman, 2009) (Figure 1). The parietal lobe is posterior to the frontal lobe, superior to the temporal lobe and anterior to the occipital lobe (Fogassi *et al.*, 2005). It contains the primary sensory cortex, responsible for integrating simple sensory signals, such as touch, pressure, pain and temperature, that are relayed through the thalamus to this lobe (Jawabri *et al.*, 2019). The temporal lobe is inferior to the parietal and frontal lobes and anterior to the occipital lobe (Squire *et al.*, 2004). This contains several critical brain regions dedicated to processing sensory information and language, such as the primary auditory cortex (Purves *et al.*, 2001; Kiernan, 2012). Additionally, the hippocampus (HPC) is located at the base of the temporal lobe below the cerebral cortex (Anand *et al.*, 2012). The occipital lobe is posterior to the parietal and temporal lobes and it ,consists of the primary visual cortex (Rehman *et al.*, 2019). The HPC is an integral part of the limbic system, which, together with the adjacent amygdala, forms the central axis of this system (Anand *et al.*, 2012). The structure of the HPC resembles a small seahorse (*hippokampos* in Greek) that can also be distinguished externally due to its u-shaped arrangement (de Lanerolle *et al.*, 2009; Hagan *et al.*, 2012). The HPC is composed of three major components, namely the cornu ammonis (CA) subfields (the Latin rendering of

Ammon's horn which is divided into regions CA1 – CA3), the dentate gyrus (DG), and the subiculum (Strange *et al.*, 2014). The hippocampal subfields CA1 and CA3 are subdivided into other major molecular parts: dorsal, dCA1 and dCA3; intermediate, CA1i and CA3i; ventral, vCA1 and vCA3; and ventral tip, CA1vv and CA3vv (Dong *et al.*, 2009; Bienkowski *et al.*, 2018; Lothmann *et al.*, 2021).

The HPC is an extension of the temporal part of the cerebral cortex. It is composed of two hippocampi located on each side of the cerebral hemispheres (Squire *et al.*, 2014). In addition, the HPC is implicated in many functions, including memory consolidation, and is primarily associated with spatial learning, navigation and orientation (Eichenbaum, 2004; Strange *et al.*, 2014; Swanson *et al.*, 2020).

The HPC is divided into the dorsal and ventral regions (Figure 2). Extensive anatomically dissociable research on the dorsal and ventral subregions of the HPC demonstrated distinct roles in cognitive and emotional processing. The dorsal HPC (dHPC), corresponding to a posterior axis in primates, is involved in spatial navigation and memory. In contrast, the ventral HPC, (vHPC), corresponding to the anterior HPC in primates, has been suggested to be involved in processing emotions, such as anxiety and fear-related responses (Bannerman *et al.*, 2004, 2014; Barkus *et al.*, 2010).

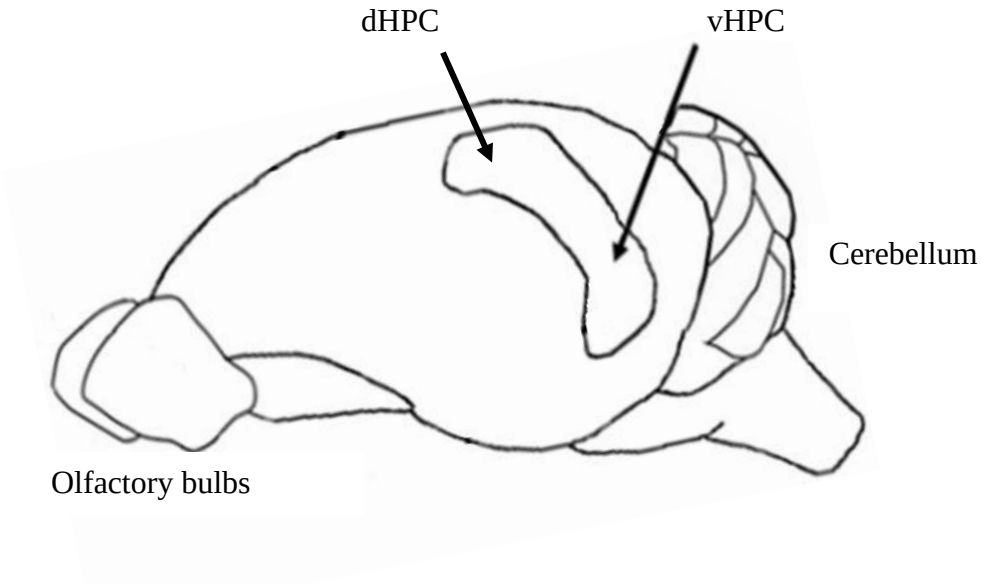

Figure 2. Rodent hippocampal structure and dorsal–ventral (posterior–anterior axis) dichotomy of hippocampal function. Adapted from Lisman, *et al.*, 2017.

Cerebellum

The cerebellum is a central brain region of the hindbrain that is located near the brainstem, underlying the occipital and temporal lobes of the cerebral cortex. It consists of a thin, densely

folded cerebellar cortex surrounding the deep cerebellar nuclei (Ackerman, 1992). Anatomically, the cerebellum is located towards the dorsal surface of the medulla and pons. Traditionally, this structure has been responsible for coordinating motor activity and control, but over many years, several key findings have also emerged that point to other distinct functions in language, cognitive processing and emotional control (Gordon., 2007) (Figure 1). The cerebellum is naturally subdivided into two lateral hemispheres connected by the thin midline vermis (Butts *et al.,* 2014). Each of these hemispheres consists of a central white matter core and a surface outer layer of gray matter (Jimsheleishvili *et al.,* 2020). Next, the cerebellar hemispheres and the vermis are divided into three distinct lobes to elucidate the function of the cerebellum, anterior, posterior and flocculonodular (Van Essen *et al.,* 2018). Functionally, the cerebellar cortex is divided into three layers: an outer molecular layer, an intermediate Purkinje layer, and an inner white matter to the cortical surface layer (the granular layer) (Butts *et al.,* 2014). Any injuries to the cerebellum may cause a lack of muscle control, disruptions or even failure of motor coordination of voluntary movements, known as ataxia (Ferrarin *et al.,* 2005). In addition, the loss of integrated muscular coordination and control may cause muscle tremors and difficulty standing (Hadjivassiliou *et al.,* 2017).

Brain stem

The brain stem is a relay station that connects the cerebrum and cerebellum to the spinal cord. It is composed of two sections in descending order: the midbrain and hindbrain, which involves the pons and medulla oblongata. The latter structure is connected posteriorly with the spinal cord by the pons to the midbrain (Basinger *et al.,* 2019). This structure contains nerve fibres that maintain the proper function of the nervous system and control vital respiratory and cardiac functions such as breathing and heart rate (Rothwell *et al.,* 2012).

1.2.3 Normal brain ageing

Several physical and mental ailments accompany the brain ageing process; thus, it affects the physiological balance between health and disease and reduces lifespan (Peters, 2006). These changes seem to be correlated with morphological alterations within the brain. Within the scope of healthy ageing, the structure of the brain undergoes significant changes, such as a considerable loss of brain volume, a decline in weight and a decrease in brain size in both humans and rodents that accompanies the decline in cognitive function, which will be discussed in the next section (Rapp *et al.,* 2009; Driscoll *et al.,* 2003; Driscoll *et al.,* 2006; Deary *et al.,* 2009). MRI studies have shown that the decline in volume and the loss of gray and white matter

occur predominantly in the HPC and prefrontal cortex (Driscoll *et al.*, 2013; Mattson *et al.*, 2018).

Age is associated with cognitive decline and behavioural heterogeneity

Ageing is associated with an increased risk of multiple health conditions and a greater possibility of a decline in learning and memory in humans, as in rodents (Giusto *et al.*, 2002; Alexander *et al.*, 2012; Mota *et al.*, 2019). Behaviourally, this age-related reduction of cognitive capacities affects specific cognitive domains, including information processing speed, reasoning, executive function and learning and memory (Crook *et al.*, 1986; Erickson *et al.*, 2003; Deary *et al.*, 2009).

The age-related changes in cognitive function that occur with normal ageing are correlated with cellular, neuronal structural, morphological and functional changes in cortical synapses occurring over time in the brain (Cole *et al.*, 2019; Mota *et al.*, 2019). The gradual accumulation of these deleterious biological changes, accompanying a progressive dysfunction of neuronal networks and neuronal loss, leads to the consequent acceleration in the rate of cognitive decline (Blinkouskaya *et al.*, 2021). To this end, these alterations can significantly contribute to the increased risk of dementia, which is probably the most common endpoint of various age-related diseases (DeTure *et al.*, 2019). It has been reported that the development of brain atrophy in brain regions implicated in cognitive function accelerates in advancing age and could increase the risk of developing cognitive deficits and also be the central measure of disease progression in neurodegenerative conditions (De Brabander *et al.*, 1998; Peters, 2006).

The role of lipid metabolism in normal brain ageing

Lipids are an important class of organic molecules influenced by genetic and environmental factors, such as ageing, diet and physical activity (Kirkwood *et al.*, 2007; Johnson *et al.*, 2019). The brain is the second highest lipid content in the human body after adipocytes and comprises approximately 60% of the brain's dry weight in adults (Jové *et al.*, 2018). Due to their wide range of biological functions and biochemical structure, brain lipids play a critical role in maintaining the normal physiological function of neurons, cell survival, cerebral plasticity, signalling by membrane-bound networks, and controlling the regulation of ion channels and receptors (Wenk, 2005; Van Meer *et al.*, 2008; Naudí *et al.*, 2015; Fantini *et al.*, 2015; Adibhatla *et al.*, 2007).

Aging is also associated with a decline in brain tissue levels of omega-3 (ω-3) fatty acids such as docosahexaenoic acid (DHA), the main ω-3 PUFA in cell membranes, as will be discussed

in 1.3.2 section (Fedorova *et al.,* 2013). Many human and animal studies showed that a high ω-3 PUFA intake could protect cognitive performance or slow the physiological disturbances of the brain that are associated with ageing (Kotani *et al.,* 2006; Little *et al.,* 2007; Fotuhi *et al.,* 2009; Kelly *et al.,* 2011). These experimental studies have confirmed that a decrease in brain DHA may have an impact on the decline of physiological regulations that are associated with brain ageing (Cardoso, *et al*., 2016; Sidhu, *et al.,* 2016; Laugero, *et al.,* 2017)

Within the brain, lipid metabolism and distribution are altered during ageing, which may affect the composition of neuronal membranes and myelin sheaths, resulting in a wide range of pathophysiological conditions (Franceschi *et al.,* 2018). Lipid peroxides which are synthesized inevitably from fatty acids, which will be described in section 1.3.2, may damage cell membranes' biophysical properties, leading to the acceleration of cellular ageing. Consequently, the membrane structure could be a key to linking the disease with the lipids in brain health; mainly, the lipids are characterised as the targets of free radicals' action (Skowronska-Krawczyk *et al.,* 2020).

During brain ageing, neurons tend to accumulate dysfunctional and aggregated proteins due to the impaired control of the oxidative imbalance between oxidants and antioxidants. Oxidative stress is defined as a disruption in homeostasis and increased production and accumulation of reactive oxygen species (ROS**)** (Hameister *et al.,* 2020). The ROS compounds are the by-products of the oxygen metabolism and during pathological conditions resulting in the damage of cell membranes (Halliwell, 2001; Zhao, 2009; Denis *et al*., 2015; Cutuli *et al*., 2017; Cheignon *et al*., 2018).

1.3 The molecular biology of lipids

Lipids are essential hydrophobic or amphipathic small molecules soluble in non-polar organic solvents but insoluble in water. They exhibit structural diversity and are found in all cell types (Campbell *et al.,* 1999). Lipids originate entirely, or in part, from key biochemical 'building blocks': ketoacyl and isoprene groups (Lydic *et al.,* 2018; Mesa-Herrera *et al.,* 2019). These biological substances are formed independently of genes and must be produced and metabolized by enzymes or derived from many dietary sources such as vegetable oils, nuts and fish (Wong *et al.,* 2017).

Given the high abundance of lipid species, their structural diversity and function, lipids can act as signalling molecules. Based on their chemical structure, lipids can be classified into two broad groups: simple and complex lipids (Fahy, et al., 2011; Blanco *et al*., 2017).

Fahy and their colleagues have proposed a system for lipids based on the LIPID MAPS consortium system. They have classified them into eight different groups: fatty acids, glycerolipids, glycerophospholipids, sphingolipids, sterol lipids, prenol lipids, saccharolipids, and polyketides (Fahy *et al*., 2005; Fahy *et al.*, 2008). Each of these categories can also be classified into different lipid main classes and subclasses, leading to a total of 43,811 unique lipid structures held within the LIPID MAPS Structure Database (LMSD), the world's largest lipid-only database with distinct structures and properties. The lipids discussed throughout this thesis are polyunsaturated fatty acids (PUFAs) and glycerophospholipids (PL).

1.3.1 Glycerophospholipids in the brain

The brain contains relatively high concentrations of glycerophospholipids (PL), mainly accounting for roughly 25% of the total brain's dry weight (Blanco *et al.*, 2017). PLs synthesised from glycerol-3-phosphate (G3P) are critical in mammalian cell biology serving as essential components of lipoproteins and crucial mediators of cell function and signalling (Ridgway, 2021).

Phospholipids are molecules of three parts: a glycerol backbone that typically contains two long-chain fatty acids, forming a hydrophobic tail (Berg *et al*., 2002). These two fatty acid chains form the non-polar tails (Vance *et al*., 1988). A third part contains a phosphate group attached to a head group, forming a hydrophilic head (Alberts *et al.*, 2016) (Figure 3).

Due to their amphipathic properties, phospholipids form bilayers in the surrounding environments where the polar head region faces outwards and interacts with water, whereas the non-polar tail is buried within the inner leaflet.

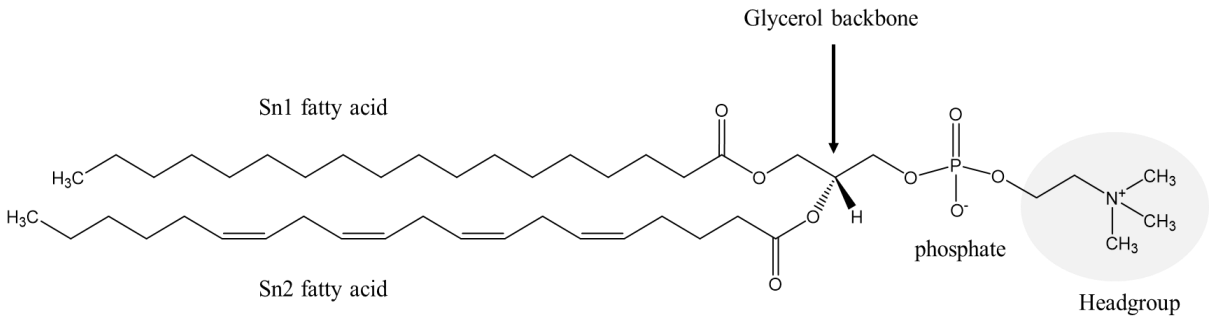

Figure 3. The general structure of phospholipid molecules demonstrating the sn1, sn2 and headgroup positions on the glycerol backbone.

The most abundant PL species in eukaryotic cell membranes are the five primary classes of PL according to the polar head group, namely phosphatidylethanolamine (PE),

phosphatidylcholine (PC), phosphatidylglycerol (PG), phosphatidylinositol (PI) and phosphatidylserine (PS). Among them, PE and PC constitute the primary building blocks of the cell membrane and account for almost two-thirds of total PLs in innate immune cells (Murphy, 2002; Van Meer *et al.*, 2008; Farine *et al.*, 2015). These amphipathic lipids form the cell membranes with the hydrophobic fatty acids positioned to the core and the phosphate head groups facing the aqueous phase (O'Donnell *et al.*, 2018) (Figure 4). The stability, fluidity, and ion permeability of neural membranes can be influenced by glycerophospholipid composition (Alberts *et al.*, 2002; Wallis *et al.*, 2021). Phospholipids are considered to be essential for neurotransmission, synaptic plasticity and memory processing (Garcia-Morales *et al.*, 2015).

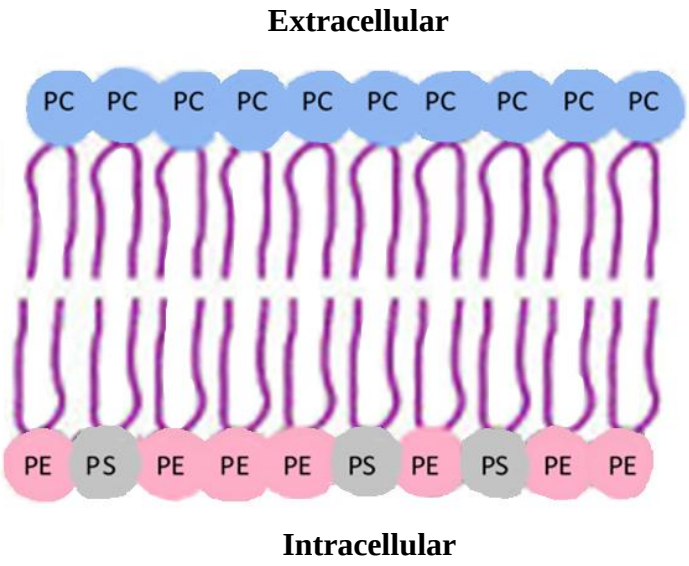

Figure 4. The parts of phospholipid molecule to form bilayers composing of non-polar tails (hydrophobic) and polar heads (hydrophilic).

In particular, glycerol forms the backbone that typically connects the PL head group with the fatty acids, which are attached at the first and second carbons, referred to as the *Sn1* and *Sn2* positions, respectively (Berg *et al.*, 2002) (Figure 4). They also contain a saturated or a monounsaturated fatty acid (MUFA), generally at the *sn1* position, attached through either an acyl chain group, alkyl ether or plasmalogen. Plasmalogens are abundant in innate immune cells (Vance *et al*., 1988; Murphy, 2002; Tvrzicka *et al*., 2011).

The nomenclature that is used for PL is, to begin with, the headgroup for the *Sn1* FA, including 'a' for acyl, 'p' for plasmalogen and 'e' for ether, and the s*n2* FA, which is typically PUFA, is separated by an underscore (_) character, such as PE 18:0a_20:4 (Liebisch *et al.*, 2020; Liebisch *et al.*, 2013). Consequently, all these variations and many FAs can lead to numerous unique PL species.

1.3.2 Fatty acids in the brain

Polyunsaturated fatty acids (PUFAs) contain a long aliphatic chain with a carboxyl group at one end and a methyl group at the other (Patterson *et al*., 2012). The nomenclature of fatty acids is described by the number of carbon atoms and double bonds that the fatty acids contain according to the IUPAC (International Union of Pure and Applied Chemistry, http://www.iupac.org/) (Köfeler, 2016). Thus, their structure is abbreviated by the number of carbon atoms and the number of double bonds, followed by their exact position within the hydrocarbon chain (Patterson *et al*., 2012). PUFAs can be either saturated with zero double bonds between the carbon atoms, such as palmitic acid (C16:0) and stearic acid (C18:0) or monounsaturated such as oleic acid (C18:1) and also polyunsaturated fatty acids such as arachidonic acid (AA) (C20:4), which will be outlined in the following section (Tvrzicka *et al*., 2011).

PUFAs contain two or more double bonds; thus, they can be classified either as omega-3 (ω-3) or omega-6 (ω-6), which are named according to the location of the first double bond in the aliphatic carbon chain, counting from the methyl-end of the molecule (Piomelli *et al*., 2007; Hajeyah *et al*., 2020). Changes in the balance of ω-3/ω-6 PUFAs can alter brain levels and signal pathways implicated in age-related diseases (Joffre, *et al.,* 2016; Horman *et al. 2020*).

Typically, dietary omega3 alpha-linoleic acid ([LA; 18:2(ω-6)]) is metabolised to eicosapentaenoic acid ([EPA; 20:5(ω-3)]) and docosahexaenoic acid ([DHA; 22:6 (ω-3)]). In contrast, omega-6 linoleic acid (LA) may be converted to arachidonic acid ([AA; 20:4 (ω-6)]) (Harauma, *et al*., 2017; Tallima, *et al*., 2018).

In this thesis, most focus has been on the products of AA. Due to its four double bonds in the cis configuration, indicating that all hydrogen groups are on the same side of the double bonds, the compound has a certain degree of flexibility for interaction with proteins (Hanna *et al*., 2018). This mainly helps to maintain the cell membrane fluidity, which is essential for the development and growth of cells in the nervous system (Heller *et al.,* 1998; Fukaya *et al.,* 2007; Tallima *et al*., 2018). AA is predominately present, with its highest concentrations found in human and mammal adipose tissue, liver, brain, and glandular organs (Sonnweber, *et al.,* 2018). These organs cannot really synthesize AA de novo and, therefore, must be obtained from dietary sources of high AA levels, including meat (red and white, including fish), organ meats (e.g. liver, kidney, brain), poultry, eggs and dairy foods. (Forsyth *et al.,* 2016).

Another principal PUFA described in this thesis is DHA, which is more abundant in the brain than in most other tissues, and plays a key role in its development, maintenance and function (Connor, 2000; Orr *et al.,* 2013; Cater *et al.,* 2021). Also, DHA cannot be synthesized *de*

novo in mammals and thus relies on the uptake of dietary consumption primarily through fish oils, the use of supplements or need to be synthesized within the body from α-linolenic acid ([ALA; 18:3 (ω -3)]) (Jenkins *et al.*, 2009).

1.3.3 Overview of oxylipins

Oxylipins are biologically active lipid mediators derived primarily from PUFA (Murphy *et al.*, 2005). The classical pathway of oxylipin formation generally starts with immune cell activation, which leads to the hydrolysis of membrane phospholipids.is Next, the release of fatty acids such as AA occurs at the *Sn-2* position via the action of phospholipase enzymes, particularly the cytosolic phospholipase A_2 ($cPLA_2$) (Dennis *et al.*, 1991; O'Donnell *et al.*, 2009). In particular, this phospholipase catalyses the hydrolysis of phospholipids and cleaves membrane-bound AA, releasing bound AA substrate. Once released, free AA can be metabolized by three separate enzyme families, namely lipoxygenases (LOX), cyclooxygenases (COX) and, to a lesser extent, cytochrome P450 (CYP), resulting in the production of oxylipins (Dennis *et al.*, 2011; O'Donnell *et al.*, 2012; O'Donnell *et al.*, 2014; Ryan *et al.*, 2014). The three families of enzymes will be discussed in the next sections.

Oxylipins can be categorized based on their precursor forming eicosanoids and docosanoids from AA and DHA, respectively (reviewed in Hajeyah *et al.*, 2020). The primary oxidation products of these three separate enzyme families are metabolized into secondary eicosanoids, which act as bioactive lipid metabolites and can also control a wide array of physiological processes, homeostatic functions and inflammatory processes associated with many diseases (Maskrey *et al.*, 2008; Dennis *et al.*, 2015).

Eicosanoids are a subcategory of oxylipins that are biologically active lipid mediators derived primarily from AA or other 20-carbon polyunsaturated fatty acids, differing due to the types of oxygenation (Murphy *et al.*, 2005). They are produced enzymatically by the action of three metabolic pathways, which convert AA to eicosanoids and via non-enzymatic pathways in an uncontrolled manner via free radical mechanisms (Sala *et al.*, 2010). Eicosanoids can signal various cellular immune reactions in brain health and inflammatory responses (Swardfager *et al.*, 2010).

Eicosanoids mediate their signalling actions in their free acid forms via G-protein-coupled receptor (GPCR) to generate bioactive lipid mediators. Eicosanoids regulate multiple brain functions in brain health and disease (Ferdouse *et al.*, 2018). In addition to the free oxylipins, there is also strong evidence that eicosanoids are incorporated into larger functional groups such as phospholipids (Hammond *et al.*, 2012). Thus another family of bioactive lipid

mediators are formed, termed enzymatically oxidized phospholipids (eoxPLs) (O'Donnell *et al.*, 2012).

According to LIPID MAPS, eicosanoids include prostaglandins (PGs), thromboxanes, leukotrienes, lipoxins, and hepoxilins (Hajeyah *et al.*, 2020). The LOX pathway initiates the biosynthesis of hydroxyeicosatetraenoic acids (HETEs), leukotrienes, lipoxins, and hepoxilins, which will be reported in more detail in section 1.4. In contrast, prostanoids are formed from the COX pathway, including prostaglandins and thromboxanes derived from AA, responsible for maintaining physiological or pathophysiologic states, such as neuroinflammation (Smith & Murphy 2002) (Figure 6).

Lipids can be oxidized non-enzymatically in an uncontrolled manner by free radical mechanisms via ROS (Patterson *et al.*, 2012; Uttara *et al.*, 2019). A wide range of eicosanoids, such as isoprostanes, are also generated through non-enzymatic oxidation during chronic inflammation (Czerska *et al.*, 2016; Biringer *et al.*, 2019). These derivatives are considered oxidative stress markers associated with several inflammatory diseases, including AD (Austin Pickens *et al*., 2019; Trostchansky *et al.*, 2021).

1.4 Biochemistry of LOX enzymes

Lipoxygenases (LOX) are non-heme iron-containing dioxygenases in the plant and animal kingdoms (Kuhn *et al*., 2015). LOXs catalyse the stereoselective insertion of molecular oxygen into PUFAs containing a (1Z,4Z)-pentadiene-1,4-dienoic system group forming lipid hydroxyperoxyeicosatetraenoic acids (HPETEs) (Funk *et al*., 2001; Kühn *et al.*, 2006; Hammond *et al*., 2012). These are further reduced to biologically active lipid hydroxy-lipid mediators (Kühn *et al.*, 2015).

The human genome has six functional LOX genes (*ALOXE3, ALOX5, ALOX12, ALOX12B, ALOX15, ALOX15B*), which encode for six different LOX-isoforms and four pseudogenes (*ALOX15*P1, ALOXE3P1, ALOX12P1, ALOX12P2) (Kuhn *et al*., 2005). However, the mouse genome contains six functional orthologs of all human functional LOX genes with tissue-specific patterns (Kuhn *et al*., 2015). In addition, the majority of the genes are located on the orthologous region in chromosome 11, apart from *Alox5* which is on chromosome 6 (Kuhn *et al*., 2015). The currently used nomenclature for LOX is based on the position of molecular oxygen insertion in the substrate, such as AA, which can take place at positions C-5 of the aliphatic chain (5-LOX), C-8 (8-LOX), C-9 (9-LOX), C-11 (11-LOX), C-12 (12-LOX) or C-15 (15-LOX) (Schneider *et al.*, 2007).

ALOX15 gene encodes the leukocyte-type 15-LOX (human monocytes) in humans, while *Alox15* gene encodes 12/15-LOX, which is highly expressed in murine peritoneal macrophages (Kuhn *et al.*, 2018). There are two 15-LOX isoforms: 15-LOX- type 1, which is highly expressed in eosinophils, reticulocytes, human monocytes and epithelial cells and the human 15-LOX- type 2, which is located in the epidermis and exclusively inserts molecular oxygen at carbon atom 15 (Wang *et al.*, 2021*).* 12/15-LOX is highly expressed in reticulocytes, eosinophils, dendritic cells, naïve murine peritoneal macrophages, epithelial cells, and immature dendritic cells (Morgan *et al.*, 2009; Lauder *et al.*, 2017). This particular isoform will be described and investigated throughout this thesis. In the brain, 12/15-LOX is expressed mainly in neurons, and glial cells throughout the cerebrum, HPC, and basal ganglia and interestingly, its increased expression has been linked with the onset of inflammation (Sun *et al.*, 2015). Although emerging work suggests that the 12/15-LOX protein and enzymatic activity are widely expressed in the CNS, and also 12/15-LOX is termed as a "neuronal isoform" however, its exact biological role in the brain is poorly defined (Pratico *et al.*, 2004;

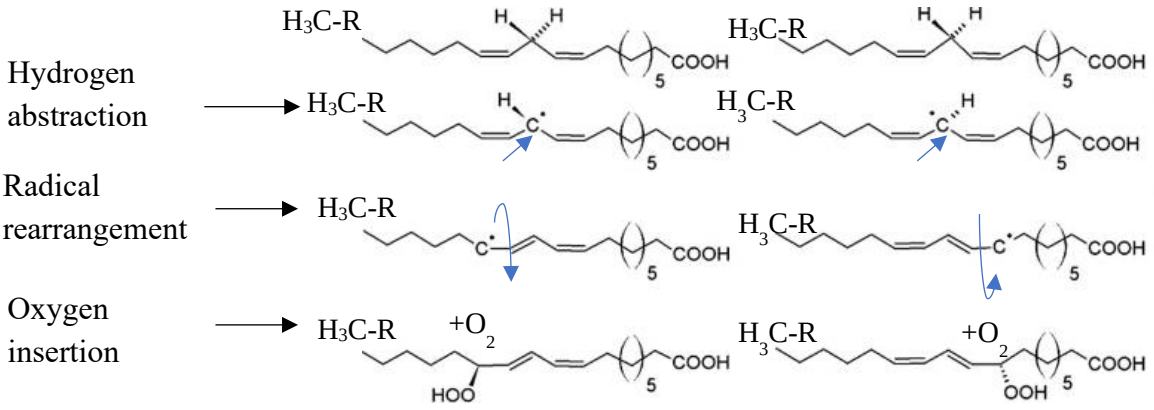

Figure 5. The schematic diagram of radical mechanism of the LOX reaction and the regio-specificity of the reaction mechanism. Adapted from Andreou, *et al.*, 2009.

Chinnici *et al.*, 2005; Fiedorowicz *et al.*, 2013). Notably, a functional role for 12/15-LOX in modulating oxidative reactions in the CNS remains unknown (Chinnici *et al.*, 2005). Also, human neutrophils and monocytes 5-LOX, which ALOX5/Alox5 encodes in both species, generate 5-HETE and several leukotrienes with pro-inflammatory properties (Clark *et al.*, 2011) (Figure 6).

Other than 15-LOX and 5-LOX isoforms, other LOX enzymes are expressed in immune cells. The platelet 12-LOX isoform is encoded by *ALOX12* in humans and is identical to *Alox12* in mice (Kühn *et al.*, 2006). The mouse ortholog of human ALOX12B is expressed in the cortex brain region, but its possible function remains unknown. (Figure 6).

The oxygenation reaction mechanism of LOX is initiated by a stereospecific hydrogen removal from AA, which is based on an eicosanoid-generating isoform, via the mechanism including proton-coupled electron transfer (PCET), with the resulting electron and proton simultaneously. Following the dislocation of the radical electron via direct radical rearrangement, the stereoselective addition of a molecule of oxygen occurs, in the opposite direction of the removed hydrogen to another carbon centre, forming a hydroperoxide radical which GPX can further reduce to their hydroxide analogues (Coffa *et al.*, 2004; Newcomer *et al.*, 2015) (Figure 5). For instance, the hydroperoxides (HPETEs) are reduced to HETEs in AA. For the oxygenation process, LOX products are specific stereoisomeric molecules with defined chirality of the hydroxyl group as either (S) counter-clockwise or (R) clockwise, to describe the configuration of a chirality centre. Notably, the enantiomers that are produced depend on the enzyme, such as the 12-LOX and 15-LOX enzymes form 12(S)-HETE and 15(S)-HETE, along with their chirality centres being inverted (mirroring) (Phillis *et al.*, 2006; Nogradi 2013).

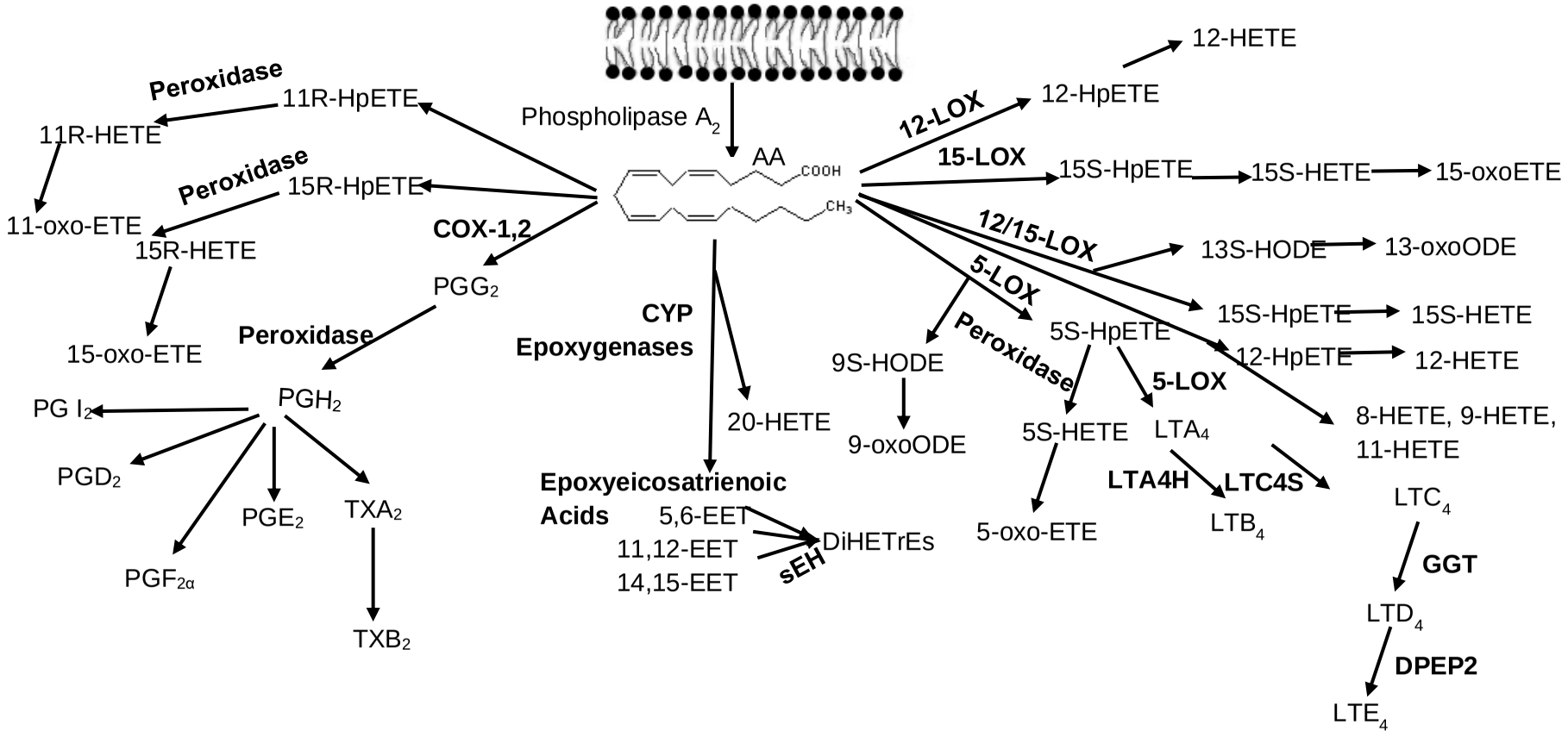

Figure 6. Summary of the metabolites of AA into oxylipins by three primary pathways. Four regioisomeric EETs are primary products of AA metabolism by cytochrome P450 epoxygenases. HETEs are the main primary products initiated by LOXs, whereas the formation of prostaglandins and thromboxanes are derived from the COX pathway.

Table 1. List of the oxylipins detected and analyzed in *Alox15*$^{-/-}$ mouse brain. Adapted from Misheva *et al.*, 2022.

Oxylipin abbreviation	Full name	Fatty acid source	Enzyme	References
5-HETE	5-Hydroxyeicosatetraenoic acid	AA	LOX	(Clark et al., 2011)
5-OxoETE	5-Oxo-eicosatetraenoic acid	AA	LOX	(Powell et al., 1994)
11-HETE	11-Hydroxyeicosatetraenoic acid	AA	LOX, COX	(Austin Pickens, et al., 2019)
12-HETE	12-Hydroxyeicosatetraenoic acid	AA	LOX	(Morgan, et al., 2010)
15-HETE	15-Hydroxyeicosatetraenoic acid	AA	LOX, COX	(Bailey, et al., 1983)
4-HDOHE	4-Hydroxydocosahexaenoic acid	DHA	unknown	(VanRollins, et al., 1984)
13-HDOHE	13-Hydroxydocosahexaenoic acid	DHA	unknown	(Reynaud, et al., 1993)
14-HDOHE	14-Hydroxydocosahexaenoic acid	DHA	LOX	(Su, et al., 2010)
20-HDOHE	20-Hydroxydocosahexaenoic acid	DHA	unknown	(VanRollins, et al., 1984)
9-HODE	9-Hydroxyoctadecadienoic acid	LA	LOX	(Astarita, et al., 2014)
13-HODE	13-Hydroxyoctadecadienoic acid	LA	LOX	(Baer, et al., 1990)
9,10-DiHOME	9,10-Dihydroxyoctadecenoic acid	LA	CYP	(Hayakawa, et al., 1986)
12,13-DiHOME	12,13-Dihydroxyoctadecenoic acid	LA	CYP	(Moran, et al., 1997)
5,6-DiHETrE	5,6-Dihydroxyeicosatrienoic acid	AA	CYP	(Oliw, et al., 1982)

11,12-DiHETrE	11,12-Dihydroxyeicosatrienoic acid	AA	CYP	(Oliw, et al., 1982)
14,15-DiHETrE	14,15-Dihydroxyeicosatrienoic acid	AA	CYP	(Oliw, et al., 1982)
5,6-EET	5(6)-Epoxyeicosatrienoic acid	AA	CYP	(Oliw, et al., 1982)
11(12)-EET	11(12)-Epoxyeicosatrienoic acid	AA	CYP	(Oliw, et al., 1982)
PGD_2	9α,15S-dihydroxy-11-oxo-prosta-5Z,13E-dien-1-oic acid	AA	COX	(Boutaud, et al., 1999)
PGE_1	9-oxo-11α,15S-dihydroxy-prost-13E-en-1-oic acid	LA	COX	(Cawello, et al., 1997)
PGE_2	9-oxo-11α,15S-dihydroxy-prosta-5Z,13E-dien-1-oic acid	AA	COX	(Salomon, et al 1984)
13,14-dihydro-15-keto PGD_2	9α-hydroxy-11,15-dioxo-prost-5Z-en-1-oic acid	AA	COX	(Hirai, et al., 2001)
$PGF_{2\alpha}$	9α,11α,15S-trihydroxy-prosta-5Z,13E-dien-1-oic acid	AA	COX	(Crankshaw, et al., 1995)
TXB_2	9α,11,15S-trihydroxythromba-5Z,13E-dien-1-oic acid	AA	COX	(Lawson, et al., 1986)

1.4.1 Metabolites of 12/15-LOX enzyme

The primary LOX-derived products from AA are hydroperoxyeicosatetraenoic acids (HpETEs), also from DHA hydroperoxydocosahexaenoic acids (HpDOHEs) and LA hydroperoxyoctadecadienoic acids (HpODEs) (Kühn *et al*., 2006). Since these lipid products are unstable, they are further reduced by GPx to their corresponding more stable hydroxy analogues intracellularly, which are hydroxyeicosatetraenoic acids (HETEs), hydroxydocosahexaenoic acids (HDOHEs), and hydroxyoctadecadienoic acids (HODEs), respectively (O'Donnell *et al.*, 2019). Alternatively, further metabolism of HpETEs generates other secondary lipid mediators, including leukotrienes, lipoxins and hepoxilins (Kühn *et al*., 2006) (Figure 6).

12/15-LOX oxygenates AA at C12 and C15 to form two products, 12-HPETE and 15-HPETE, and for this reason, it is referred to as 12/15-LOX (Joshi *et al.*, 2015). More precisely, 12-HPETE and 15-HPETE, which are unstable, are rapidly reduced by GPx to their corresponding hydroxy analogues, 12-HETE and 15-HETE, respectively (Singh *et al.*, 2019) (Figure 7). The mammalian lipoxygenase family is much more complicated than other enzyme families, as they are expressed in different cell types, such as immune cells (Funk *et al*., 2001).

The human leukocyte 15-LOX, which is encoded by *ALOX15* gene, produces predominantly 15(S)-HETE and only small quantities of 12(S)-HETE (ratio of 9:1), while its murine reticulocyte-type 12/15-LOX, which is encoded by *Alox15* gene, produces small quantities of 15(S)-HETE but predominately generates 12-HETE (ratio of 1:3) (Kriska *et al.*, 2012; Fiedorowicz *et al.*, 2013). The physiological substrates for 12/15-LOX enzyme are fatty acids, including AA, DHA and LA, which exhibit high regulated stereospecificity when it comes to oxygenating FA (Kühn *et al.*, 2006).

Lipid metabolites generated from AA can demonstrate pro- and anti-inflammatory properties (Singh *et al*., 2018). For instance, the 12/15-LOX product, 12-HETE, has been suggested to be a potent pro-inflammatory chemoattractant for neutrophils, as hepoxilin A3 is a downstream metabolite of 12-HETE (Stanley, 2005; Sun *et al*., 2015). In contrast, the anti-inflammatory activity of 12/15-LOX metabolites has been shown in several studies, but the mechanisms by which 12/15-LOX exhibits these effects are not fully understood (Sun *et al.*, 2015). The biochemical mechanisms by which 12/15-LOX regulates physiological and pathological immune cell function are still poorly understood.

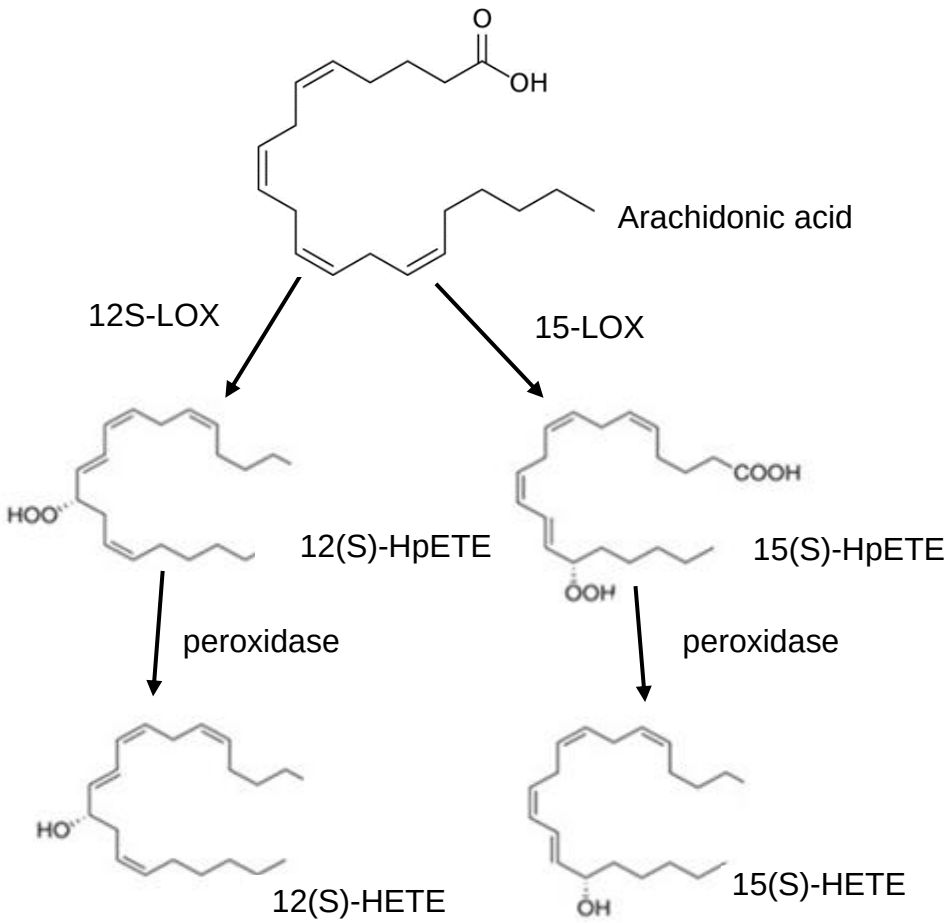

Figure 7. Structural diagram of 12/15-Lipoxygenase which inserts molecular oxygen into AA to form bioactive lipid metabolites. Metabolism of AA by 12/15-LOX pathways with corresponding stereospecific formation of hydro-peroxyeicosatetraenoic acids (HpETEs). Both 15(S)-HpETE and 12(S)-HpETE are converted by cellular glutathione peroxidase to their corresponding hydroxy analogs, 15(S)-HETE) and 12(S)-HETE, respectively.

1.4.2 Pathophysiological role for 12/15-LOX in inflammatory diseases

12/15-Lipoxygenase enzyme has been implicated in numerous inflammatory diseases, such as vascular disease, diabetes, obesity and neurological diseases (Kain *et al.*, 2018). Below I summarise its role in various pathological conditions:

Vascular diseases

Atherosclerosis is a chronic vascular inflammatory disease characterised by an accumulation of predominantly lipid-loaded macrophages as building blocks in the arterial wall. There is growing evidence suggesting a pivotal role of *Alox15* in initiating and developing atherosclerosis in mice. It is characterised mainly by the atherosclerosis-prone genetic background of mice lacking the apolipoprotein E (*ApoE*) and low-density lipoprotein (LDL) receptor. Studies have demonstrated the role of *Alox15* in vascular diseases, such as genetic deletion of *Alox15* in mice crossbred with atherosclerosis-prone ApoE$^{-/-}$ mice generating a

double-KO mouse model of inducible vascular disease (12/15-LOX$^{-/-}$/ApoE$^{-/-}$) displayed reduced atherosclerotic lesions development and lipid peroxidation upon feeding with high-fat diet (Cyrus *et al.*, 2001; Huo *et al.*, 2004). Other complications arising from vascular diseases, such as abdominal aortic aneurysms (AAA) induced via severe atherosclerotic occlusion of the abdominal aorta under high stress and pressure, have also been investigated in relation to *Alox15* deletion. Here, mice lacking *ApoE* and *Alox15* genes were protected against angiotensin-II induced AAA via osmotic mini-pumps over a two-week infusion period (Allen-Redpath *et al.*, 2019). Given the inflammatory nature of the vascular disease, the *Alox15* gene holds unique promise as a future therapeutic target, yet the underlying mechanisms remain unknown.

Diabetes

Diabetes is an autoimmune, metabolic disorder of glucose homeostasis that results from insulin deficiency produced by the *islet* β-cells within the pancreatic islets of Langerhans. Type 1 diabetes is a condition resulting from insulin-producing β-cells, which cannot secrete enough insulin to overwhelm this resistance. Bleich *et al.*, 1999 demonstrated that mice with deficiency of 12/15-LOX showed increased resistance to diabetes in a low-dose streptozotocin-induced immune-mediated animal model (Bleich *et al.*, 1999). A study by McDuffie *et al.*, 2008 using non-obese diabetic mice (NOD) reported that deletion of 12/15-LOX significantly ameliorates autoimmune type 1 diabetes development in NOD mice (McDuffie *et al.*, 2008). Another study showed that 12/15-LOX deficient diabetic mice with baicalein in lipopolysaccharide (LPS)-injection attenuated diabetes-induced kidney histopathological changes by reducing renal oxidative stress and injury (Faulkner *et al.*, 2015).

Obesity

Following type 1 diabetes, obesity is a chronic inflammatory medical condition marked by excess adipose tissue deposition. Several studies have demonstrated the role of 12/15-LOX activity in obesity which is associated with local and systemic insulin resistance by modulating adipocytes in inflammatory pathways (Sears *et al.*, 2009). Deletion of 12/15-LOX in white adipose tissues in mice fed a high-fat diet protects them from local and systemic obesity-induced inflammation (Cole *et al.*, 2012; Kundumani-Sridharan *et al.*, 2013). Furthermore, another study has shown significantly higher expression for 12/15-LOX in omental adipose tissue in obese human patients, which is related to increased production levels of pro-inflammatory cytokines of IL-6, IL-12and chemokine CXCL10 (Dobrian *et al.*, 2010).

Neurological diseases

An increasing number of studies have suggested an involvement of the 12/15-LOX pathway in the pathogenesis of AD. AD is a progressive neurodegenerative disorder characterised by severe dementia with neuropsychiatric symptoms (DeTure *et al.*, 2019). A study by Pratico *et al*., 2004 showed elevated protein levels of 12/15-LOX and its metabolites in the frontal and temporal brain regions of patients with AD or mild cognitive impairments compared to age-matched controls (Pratico *et al*., 2004). Furthermore, other studies have reported that cerebrospinal fluid levels of 12/15-LOX lipid metabolites of AA were increased only in frontal and temporal brain regions of patients with AD compared with age-matched control brains (Yao *et al.,* 2005). In a series of mouse model studies using genetic deletion of 12/15-LOX on the Tg2576 transgenic mice, a widely used transgenic mouse model of AD-like amyloidotic phenotype, it was found that 12/15-LOX regulates AD-linked synaptic pathology and showed a significant reduction in the amyloid-β production and deposition with improvements of cognitive impairments (Yang *et al*., 2010; Joshi *et al*., 2015). Parkinson's disease (PD) is a slow, progressively neurodegenerative disorder characterised by a loss of dopaminergic neurons in the part of the brain called the substantia nigra, as well as the presence of lewly bodies deposition of improperly folded protein. A study by Li *et al*., 1997, has shown that 12/15-LOX activation is related to reduced concentrations of the glutamate-induced antioxidant glutathione (GSH); GSH deficiency was associated with PD as it was the earliest biochemical change in the brain of PD patients, this triggered the activation of neuronal 12-LOX. This leads to the production of 12-LOX-generated products and peroxides and, eventually, neuronal cell death (Li *et al*., 1997).

1.5 The biosynthesis of prostaglandins by COX enzymes

COX enzymes convert AA to prostaglandins PGG_2 and PGH_2, thromboxanes (TXA_2, TXB_2) and prostacyclin (PGI) (Figure 6). In humans, there are two isoforms, COX-1 and COX-2, which differ in their pattern of expression; COX-1 is constitutively found in leukocytes and platelets and almost in all tissues, including the brain, where it mediates physiological functions in the body, whereas the COX-2 is enriched in leukocytes and not in platelets induced by many inflammatory stimuli such as cytokines and elevated under inflammatory conditions (Choi *et al.,* 2009; Gabbs *et al.,* 2015). In addition, COX-2 is expressed in HPC and the cortex; mainly in the postsynaptic dendritic spines, which implies a role in neuronal activity-dependent plasticity (Yamagata *et al.*, 1993; Kaufmann *et al.*, 1996).

The COX enzymes catalyse the key initial reaction that converts the formation of the prostaglandin endoperoxides G to H from AA. The reaction mechanism of COX is known as prostaglandin-endoperoxide synthases, which has two enzymic reactions; firstly, two molecules of oxygen are added to the AA substrate, which has been released from the cellular phospholipids by the action of the enzyme phospholipase A_2 to form PGG_2 (cyclooxygenase activity) (Christie *et al.*, 2020). Followed this, the peroxidase activity reduces PGG_2 to its PGH_2, which is the intermediate product of COX (Thuresson *et al.*, 2000). PGH_2 serves as a precursor for the generation of additional prostanoids, including prostaglandins PGE_2, $PGF_{2\alpha}$, PGD_2, PGI_2 and thromboxane A_2 (Puppolo et al., 2014) (Figure 6). Besides these, thromboxane B_2 (TXB_2), a chemically stable and biologically inactive metabolite, is formed from the non-enzymatic hydrolysis of TXA_2 (Wolfe *et al.*, 1976; Roberts *et al.*, 1982). TXB_2 is further converted enzymatically into 11-dehydro-TXB_2, found in plasma and urine (Westlund *et al.*, 1986) (Figure 6). Notably, the therapeutic anti-inflammatory action of aspirin and ibuprofen, non-steroidal anti-inflammatory medications (NSAIDs) is due to the inhibition of COX-2 (Howard *et al.*, 2004).

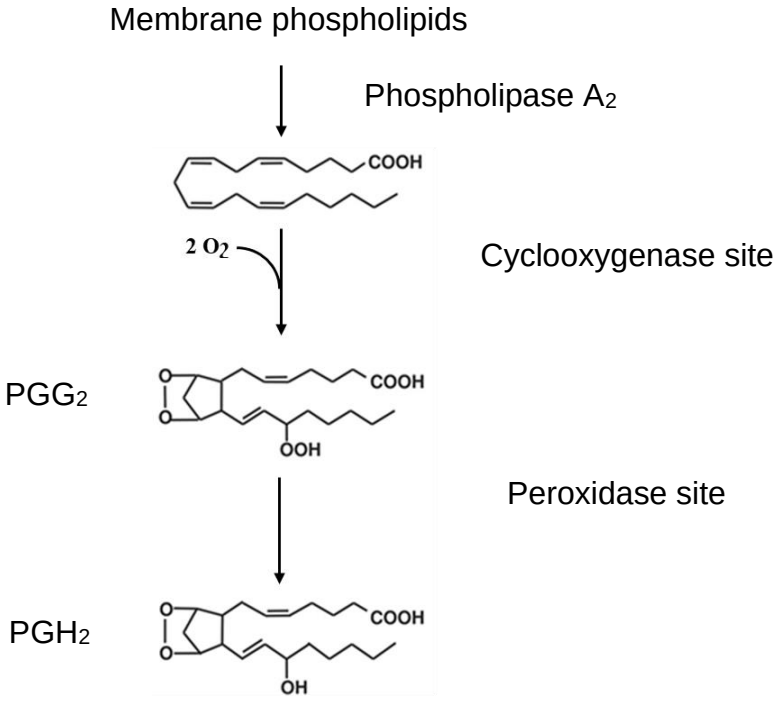

Figure 8. Cyclooxygenase activity occurs via a two-step process. The first stage introduces two molecules of oxygen to AA, which results in the conversion of AA to PGG_2 followed by the reduction of PGG_2 to PGH_2. Adapted from Christie *et al.*, 2020.

1.6 Animal cognition and behaviour

Although understanding the nature of age-related cognitive changes can be captured by studying human participants, including patients with dementia, their use in ageing research is complicated by many factors (Antunes *et al*., 2012; Lange *et al*., 2017). Due to the limited amount of time and also the significant cost required to validate a study using human participants, as well as the ethical limitations and their long natural life span, the bulk of ageing and lifespan data eventually have led to the use of rodents' models (Mogil, 2009). These models share many similarities with humans and are extremely useful for studying healthy brain ageing, resulting in the most commonly used mammalian model in behavioural neuroscience (Carter *et al*., 2015). Understanding the neural underpinning of cognitive changes requires the use of rodents. Establishing an appropriate mouse model for neurological disorders has proven invaluable for researching the effects of neurodegenerative diseases on brain function (Bailey *et al*., 2009).

1.6.1 Testing cognitive function in rodents

Behavioural tests enable researchers to investigate and understand the neurobiological circuitry underpinning behaviour and physiological and molecular cellular mechanisms of memory that are impossible in humans (Cohen *et al*., 2015). Cognitive function has been assessed through various experimental animal models of learning and memory through a wide range of paradigms. These tasks aim to assess the effects of experimental variables on the brain function by measuring behaviours that rely on specific brain regions (Barker *et al.*, 2007). Various behavioural paradigms have been developed to study animal memory mechanisms, and their selection is based on understanding the neural systems that a specific task engages. The following sections outline the rationale for the behavioural tests presented in this thesis.

1.6.2 Learning and memory

Learning is the acquisition of new information to promote survival, while memory is the complex process of encoding, storing and recalling that knowledge over time (Kandel *et al*., 2014).

Traditionally, scientists have widely accepted that there are two distinct memory types; short-term (STM) and long-term memory (LTM), which are based on the length of time during which memory can be recalled (Norris, 2017). The duration of time can last from seconds to minutes in STM, while up to years in LTM. Squire et al. (1996) reported that the classification of LTM includes two major types, which are declarative (explicit) and nondeclarative memory (implicit). The declarative type can be further subdivided into episodic and semantic, whereas priming and procedural memory are the types of nondeclarative memory (Squire, 1992).

Episodic memory refers to memories of past personal experienced events that have taken place at a specific time and place (Baars et al., 2013). This memory is the form of LTM that is more sensitive to brain damage. Episodic memory displays the most dramatic rate of decline during healthy ageing (Nyberg et al., 2012; Harada et al., 2013). By contrast, semantic memory refers to memories about general world knowledge and facts – for example, the names of former politicians in the United Kingdom – that have been explicitly collected and stored throughout the years (Glisky, 2007). It has become increasingly apparent that semantic memory displays a late-life decline in healthy aging (Matthews, 2015). Nondeclarative or procedural memory refers to skills and motor activities performed during an individual's life without conscious awareness of prior experiences (Nyberg et al., 2012). Procedural memory can be maintained over years that later in life are performed automatically (Harada et al., 2013). In addition to the primary distinction associated with STM, working memory is related to keeping and processing information within the mind, often in a task-specific manner (Baddeley, 2001). This type of memory is characterised by a limited capacity when it is being used, and its function is vulnerable to an age-related decline (Reuter-Lorenz et al., 2005; Nyberg et al., 2012).

Recognition memory

Recognition memory is a subcategory of declarative memory, which accurately judges whether an item has been previously encountered, is novel or familiar (Kinnavane et al., 2015). Recognition memory is central to our ability to remember and subsequently requires a capacity for both identification and judgment concerning the prior occurrence of what has been identified (Barker et al., 2011). Typically, it describes the ability to identify an individual object's previous occurrence and decide whether this item is novel or familiar (Brown et al., 2010).

Novel object recognition (NOR) task

At the behavioural level, the ability of a mouse to evaluate the recognition memory exploring a novel object in a controlled environment has received increasing attention in recent years (Baxter 2010). The gold standard recognition method for rodents is the NOR task (Cohen et al., 2015). Ennaceur and Delacour originally developed this task in 1988; this was successfully adapted for use in mice and models of neurodegenerative disorders.

The NOR task comprises three phases: habituation, sample phase or familiarisation and test phase (Antunes et al., 2012). In rodents, recognition memory is tested in an arena. Following habituation to the arena, the animal receives a sample phase involving exploring two identical objects. Following the sample phase, the animals receive a test stage in which one of the familiar objects is replaced with a novel object (usually after a delay between the sample phase

and the test phase) (Warburton *et al*., 2010). Healthy adult mice encode a memory of the sample phase, and during the test phase, they showed a marked increase in exploration because it does not match a memory of any item encountered previously (Ennaceur, 2010). It is important to note that the task relies on a rodent's innate exploratory behaviour and spontaneous drive to explore novel features of its environment (Warburton *et al*., 2015).

Brain regions involved in NOR task

The HPC and the perirhinal cortex (PRH) primarily play crucial roles in object recognition memory (Barker *et al*., 2011; Clark *et al*., 2000). Different types of stimulus information concerning an object size, spatial information and temporal features are encoded to form an integrated memory of the spatio-temporal features of objects, such as what was presented, where and when. Encoding object-based information is required in the HPC, perirhinal cortex, prefrontal and entorhinal cortex (Warburton *et al*., 2010; Barker *et al*., 2011).

Several studies with monkeys and rodents have implicated a crucial role of PRH in the detection of object identity as well as in discrimination between familiar and novel objects (Bussey *et al*., 2000; Brown *et al*., 2001; Brown, 2008). Studies reported that object familiarity–novelty discrimination is severely disrupted after the lesions in the PRH (Bussey *et al*., 1999, Ennaceur *et al*., 1996). Later studies showed that the impairments in the NOR task are delay-dependent between the sample and test phase. For instance, when tested following a 2-min delay, mice with perirhinal impairments displayed no deficits compared to a 10-min delay, where the impairments were more readily identifiable (Warburton *et al*., 2010). Furthermore, lesions of the mPFC did not affect object recognition (Barker *et al*., 2007).

The hippocampal formation plays a vital role in memory for contextual information by encoding information about the spatial location of the objects and novel object preferences, particularly after a long delay between the sample and the test phases (Hammond *et al*. 2004). The spatial and temporal order memory will be discussed in detail in the upcoming sections. The HPC is anatomically linked with the perirhinal cortex, and medial prefrontal cortex (m-PFC) and thus is central to the network to enable recognition memory judgments for temporal order recognition memory (Figure 10) (Barker *et al*., 2011).

Spatial memory

Spatial memory supports storing and retrieving information regarding objects' locations within the environment by navigating previously encountered objects (Turriziani *et al*., 2003; Paul *et al*., 2009). Although humans have maps for their spatial navigation consisting of three elements: what objects are present, the relation to each other, and the room and the experimenter, spatial memory for rodents is crucial to their survival (O'Keefe *et al*., 1978;

Warburton *et al*., 2000). Rodents have to learn and remember the target location that provides them with all the needs, such as food, water, a safe place, and their mates' actual positions (Vorhees *et al*., 2014).

Object location (OLT) task

By altering several critical parameters of the NOR task, it is impossible to study different features of spatial object memory. The OLT can assess the ability of an animal to recognize a change in the spatial location of an object within the arena (Vogel-Ciernia *et al*., 2014). When one object is moved to a new location in the test phase, rodents show a preference to explore the object in the new location relative to the object in the familiar position (Hall *et al*., 2016).

Brain structures involved in OLT task

It is generally accepted that the HPC plays a critical role in acquiring and retrieving spatial information (Barker *et al.,* 2011). Strong evidence suggests that animals with hippocampal dysfunction have impaired spatial memory, and consequently, they demonstrate no preference for the object relocated during the OLT task test phase. (Vogel-Ciernia, *et al*., 2014; Bannerman, *et al*., 2014). This is consistent with a large body of evidence showing impaired spatial memory following hippocampal damage in rodents using several navigation tasks such as T-maze alternation and Morris water-maze (Rawlins *et al.,* 1982; Morris *et al.,* 1990; Moscovitch *et al*., 1995; Gudde *et al*., 2016). Furthermore, lesions of the PRH had no effects on the performance of the OLT task and indicated the critical role of the HPC in processing spatial information (Ennaceur *et al.,* 1996; Barker *et al.,* 2007).

Temporal order recognition memory

In rodents, temporal order recognition memory task is tested in the open field with rodents, which are freely exposed to two identical objects in sample phase 1 and another new set of two identical objects during sample phase 2, with each exposure phase separated by a delay interval of typically one hour. During the test phase, conducted at least four hours later, the animals are shown one object from each sample phase during the test phase. Normal animals show more exploration of the object seen in the first sample phase relative to the object more recently presented in the second sample phase (Hatakeyama *et al.,* 2018; Beldlidia, *et al.,* 2022).

There is growing evidence that temporal order recognition memory is disrupted following lesions, in HPC and PRH and m-PFC lesions impair temporal order discriminations (Dix *et al.,* 1999; Barker *et al.,* 2007; Warburton, et al., 2010; Barker *et al.,* 2011). In addition, disconnection studies have confirmed that the HPC is a vital component of a neural system that operates with the m-PFC and PRH to support the temporal order memory (Barker *et al.,* 2011;

Warburton *et al.,* 2010; Barker *et al*., 2020). The temporal order task examines the animal's ability to differentiate bet ween familiar objects presented at different times previously.

1.7 Anxiety-like behaviour

Anxiety is defined as a persistent and adaptive response to an undetermined situation or a warning to a potentially dangerous and threatening environment or stimulus (Cryan *et al*., 2005; Steimer, 2011). This appropriate response is characterized by physiological symptoms such as sweating, dizziness, increased blood pressure and heart rate, and behavioural changes, including tension, cognitive, emotional, and hormonal reactions (Davis *et al*., 2010). However, anxiety can also become a pathological state/condition when this reaction is extreme, uncontrollable, chronic, excessive and inappropriate for the current environmental situation struggling to deal with challenging events (Sartori *et al.,* 2011). There is no substantial evidence suggesting whether the prevalence rates of anxiety are the highest or not in older age and whether they are different from youth. Anxiety disorders are associated with severe depressive disorders in both age groups, which are highly likely to contribute to cognitive impairments (Joshi *et al.,* 2014). However, clinical data indicate significant differences in the prevalence rates of anxiety disorders between females and males (Kaczkurkin *et al.,* 2019).

1.7.1 Elevated plus maze (EPM) task

Pellow first described EPM as a reliable and straightforward task for evaluating rodent anxiety-like responses (Pellow *et al.,* 1986). The EPM is a well-established behavioural test validated to measure anxiety-like behaviour in rodents (Sakakibara *et al*., 2008). The apparatus consists of four arms raised above the floor, with two opposing arms being open platforms (open arms) while the other two are enclosed with high walls along both sides (closed arms). These four arms are connected by an open central platform (centre square) (Handley *et al*., 1984). The arms are arranged to form a plus-shaped apparatus (Walf *et al*., 2009) (Figure 7).

Anxiety is reflected in the natural tendency of healthy mice to spend more time exploring the closed arms, which are considered the protected environment of the apparatus, versus the opened arms, which are the novel environment (Walf *et al*., 2009). This assay is based on an approach versus avoidance behaviour, with the animal being required to choose whether to explore the open, exposed arms of the maze, which are the unprotected and thus potentially dangerous spaces (avoidance) or to stay in the safe, enclosed spaces (approach) which are considered the safer arms (Holmes *et al.,* 2006). This pattern of approach-avoidance behaviour is characterized by the animal's natural aversion to elevated heights and brightly open areas,

which relies upon an open-arm avoidance which it assumes to be an adaptive response to avoid the risk of the potential threat (Bailey *et al.*, 2009; Bannerman *et al.*, 2014). Hence, the exposed open arms cause a potential danger to the animal compared to the closed arms of the behavioural apparatus. An anxiety phenotype is generated by this approach-avoidance response with regard to excessive avoidance in the exploration of the elevated open arms as a potential danger/risk relative to the closed arms (Barkus *et al.*, 2010).

Behavioural measures in the EPM include the time spent in each arm and the number of entries made into the opened and closed arms (Bailey *et al*., 2009). Additionally, the distance travelled from the centre square is recorded to measure locomotor activity (Walf *et al*., 2007). Normal rodents tend to spend relatively less time in open arms to minimise anxiety caused by exposure to open spaces and increased predation risk. Animals that avoid exploration of the open arms are considered anxious, whereas those that explore the open arm freely are thought to be less anxious relative to normal rodents (Walf *et al*., 2007; Bailey *et al*., 2009).

1.7.2 Brain structures involved in EPM - Neurochemistry of anxiety disorders

A vast majority of studies have provided evidence that multiple brain regions contribute to anxiety (Martin *et al.*, 2009). Although many studies imply that anxiety's central mechanisms are similar in humans and rodents, the complex neuronal circuits for anxiety states have not been thoroughly established (Tovote *et al.*, 2015). Human imaging technology and neurochemical techniques indicate a vital role in the limbic system, with particular emphasis on the amygdala, the HPC, ventral striatum, and the medial prefrontal cortex (mPFC) (Cannistraro *et al.*, 2003; Tovote *et al.*, 2015; Duval *et al.*, 2015; Seeley., 2019). Although it is widely established that the HPC plays a vital role in processing spatial/contextual information, research also suggests that the vHPC also plays a role in anxiety disorders (Deacon *et al.*, 2002; McHugh *et al*., 2004; Barkus *et al.*, 2010). In contrast, the dHPC is involved in cognitive spatial memory processing (Bannerman *et al.*, 2003; Jimenez *et al.*, 2018). The vHPC is connected to subcortical structures, including regions that contribute to the hypothalamic-pituitary-adrenal (HPA) axis (McHugh *et al.*, 2008). Hence the role of vHPC is well established to be involved in the mechanisms underlying anxiety (Kjelstrup *et al.*, 2002; Bannerman *et al.*, 2014).

The amygdala is an almond-shaped brain structure located in the medial temporal lobe (with the HPC). It is comprised of two extensively studied subdivisions, the basolateral group of the amygdala (BLA) and the central nucleus of the amygdala (CeA) (Ressler., 2010). The BLA is a cortex-like structure that refers to a complex of three amygdala nuclei, namely the lateral amygdala (LA), the basal amygdala (BA), and basal medial or accessory basal nuclei amygdala (BMA) nuclei, while the CeA can be divided into the centrolateral amygdala (CeL) and

centromedial amygdala divisions (CeM) (Krabbe *et al.*, 2018; Babaev *et al.*, 2018). Furthermore, BLA relates to other midbrain regions, the prefrontal cortex, the thalamus and the HPC, which integrates information widely throughout these regions to generate anxiety-like behaviour (Janak *et al*., 2015; Babaev *et al*., 2018).

Furthermore, one of the downstream targets affected by vHPC is the mPFC, a neocortical structure subdivided into four distinct regions: the medial precentral cortex, anterior cingulate cortex, and anterior cingulate cortex prelimbic and infralimbic prefrontal cortex (Quirk *et al*., 2003). Based on pharmacological and electrophysiological studies, vHPC, since it is anatomically connected with other limbic structures such as the amygdala and mPFC, is implicated in the regulation of anxiety responses, which are likely mediated via shared synaptic connections (Likhtik *et al.*, 2005; Adhikari *et al.*, 2010) (Figure 9).

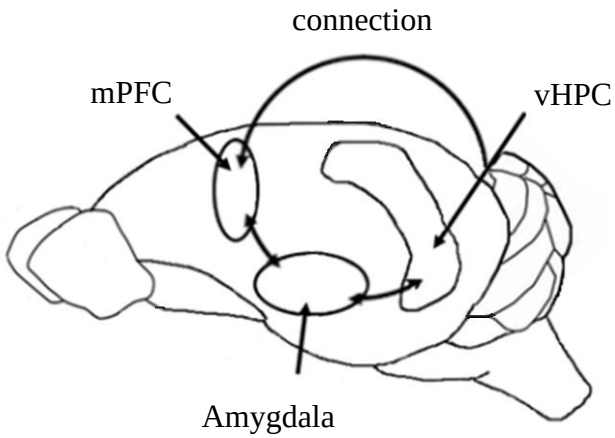

Figure 9. A schematic presentation of the sagittal view of mouse brain including neural circuits implicated in anxiety-like behaviour. The neural activity occurring interactions between the HPC, the prefrontal cortex and the amygdala.

1.8 The emergence of lipidomics

The lipidomic field emerged around 2003, according to LIPID MAPS (www.lipidmaps.org) and has dramatically advanced in recent years using analytical chemistry techniques (O'Donnell *et al*., 2019). Lipidomics is a relatively young sub-discipline of metabolomics which belongs to the 'omics' technologies, including the global characterisation of lipid molecular species (Harkewicz *et al*., 2011). It allows the analysis of many lipid classes, including the identification of complex classes of lipids and quantitation of many lipids in normal physiology (Hartler *et al.*, 2012; Naudí *et al*., 2015). Large-scale lipidomic studies will

also enable the quantitation of lipids with high sensitivity and selectivity (Sethi *et al*., 2017). There is a pressing need for continuous advancement in the field of lipid-based biomarkers signature that could offer new accurate diagnostic tools for standard and pathogenic biological processes (Sethi *et al*., 2017; Zerr *et al*., 2018).

1.8.1 Liquid chromatography with tandem mass spectrometry (LC-MS/MS)

Lipidomics is a subcategory of metabolomics, which belongs to the family of omics technologies, and is the large-scale study of lipid molecules and their biological functions in any biological system (Köfeler *et al.*, 2012). In lipid profiling, mass spectrometry (MS) is primarily used, as it is a state of art analytical detection technique that functions to detect the mass-to-charge ratio *(m/z)* by separating the electrically charged species in the gas phase and accurately measuring their molecular masses generated during the ionisation process of brain lipid extracts (Gross 2006; Han *et al*., 2003; Bienmann *et al*., 2014). Based on the sample introduction method, MS is categorised as a direct infusion (shotgun lipidomics), gas chromatography analytical method mainly for fatty acid analysis, liquid chromatography, or mass spectrometry imaging (Wu *et al.,* 2014; Chiu, *et al.,* 2020). The direct infusion of brain lipid extracts into an electrospray ionisation (ESI) source optimised for separating lipids based on their intrinsic electrical properties has the advantage of a shortened analysis time (Han *et al.,* 2005; Lísa *et al.,* 2017). Another technique is the desorption ionisation techniques MS approach (mass spectrometry imaging, MSI) along with matrix-assisted laser desorption/ionisation (MALDI) ionisation technique to visualise the spatial distribution of metabolites across the brain tissue (Aichler, *et al.*, 2015). In addition, most researchers have favoured the third approach, known as high-performance liquid chromatography (HPLC) in combination with electrospray ionisation (ESI) and tandem mass spectrometry (MS/MS) on triple quadrupole (Q) instruments (LC-MS/MS) (Yang *et al*., 2009; Sethi *et al*., 2017; Yuan *et al*., 2018). The combination of chromatography and mass spectrometry LC-MS/MS has proven to be a powerful analytical technique that aims to separate complex molecules of the samples of interest by providing increased sensitivity and specificity, accuracy, and precision in the measurement of the abundance of each analyte generated during ionization of brain lipid extracts (Han *et al*., 2003; Li *et al*., 2014).

Lipidomics starts with the extraction of lipids from a biological sample. This can be achieved via a commonly used separation method developed by Blight and Dyer (1959). Here the lipids are dissolved in a mixture of organic solvents such as methanol and chloroform (Bligh *et al*., 1959). Phase separation between the hydrophobic and hydrophilic lipid molecules is achieved (Brügger, 2014). This process is accomplished either by solid-phase or liquid-liquid extraction

(LLE) (Canbay, 2017). In this thesis, the samples were injected into the liquid mobile phase, a solution in which the brain lipid extracts were injected at high pressure and passed through a column packed with a solid chromatographic stationary phase at a specific flow rate (Nie *et al*., 2019). The analytes passed through the electrospray needle using high electrical energy, and as a result, they were converted from the liquid form into ionised molecules in the gas phase (Ho *et al*., 2003; Teunissen *et al*., 2017). More specifically, a high voltage source produced an electric field (positive or negative) in which the analytes were ejected and passed from the capillary tube to form charged droplets (Murphy *et al*., 2011). In particular, ESI, a soft ionisation, generated charged state droplets in the spray chamber, where the ions were rapidly evaporated by the heated flowing nitrogen gas phase (Banerjee *et al.,* 2012). In the negative-ion mode, the deprotonated $[M-H]^-$ ion can be generated by losing a proton H^+ and a strong negative signal. In contrast, it is generated by adding hydrogen $[M+H]^+$ in the positive mode. In this thesis, the ionization process was achieved in negative ion mode.

Following the ionization process, the ionized compounds were then transferred into the high vacuum quadrupole system of the mass spectrometer through the mass analysers and reached the mass detector at different parts according to their *m/z* ratio (Köfeler *et al.,* 2012; Köfeler, *et al.,* 2021).

In this thesis, reverse phase LC was used prior to MS/MS, in which the mobile phase is polar while the stationary phase is nonpolar. The MS/MS instrument utilised within this thesis was the triple quadrupole Sciex 6500 QTrap, to detect the precursor ion to the product fragmented ions transitions. In particular, this instrument uses two filtering quadrupoles that serve as mass analysers quadrupole chambers, Q1 and Q3, separated by the q2 that acts as a collision cell where a neutral gas fragments the molecules for the MS/MS analysis (Figure 10) (Hopfgartner *et al*., 2004). The precursor ion, the analyte ion of interest, was selected in Q1 by selecting ions with the *m/z* of interest. These ions were then accelerated into the collision gas cell in q2, as a collision chamber in which fragments of the precursor ion were formed by colliding with nitrogen resulting in fragmentation before passing into Q3. Collision-induced dissociation (CID) is a process in which a gas (nitrogen) chemical reaction produces structure-specific fragment ions. Collision energy (CE) refers to the voltage applied in q2 where precursor ions are fragmented into their characteristic product ions (Fang *et al.,* 2021). Then, these ions were transmitted to mass analyser Q3 to scan the masses of the fragmented product ions resulting from CID. The scan was based on the *m/z* ratio, identifying a specific *m/z* through the detector (Hinterwirth *et al*., 2014). The values for quantification were measured and processed by a computer, which provided data for calculating the measurement levels of each ion in

histograms indicating the relative abundance of the signals of ions according to their *m*/*z* values (Han *et al.*, 2003; Urban, 2016). It is noteworthy to mention that the individual molecular species were separated in a liquid mixture based on their polarity; the polar elutes first and then the least polar ones (Luan *et al*., 2019).

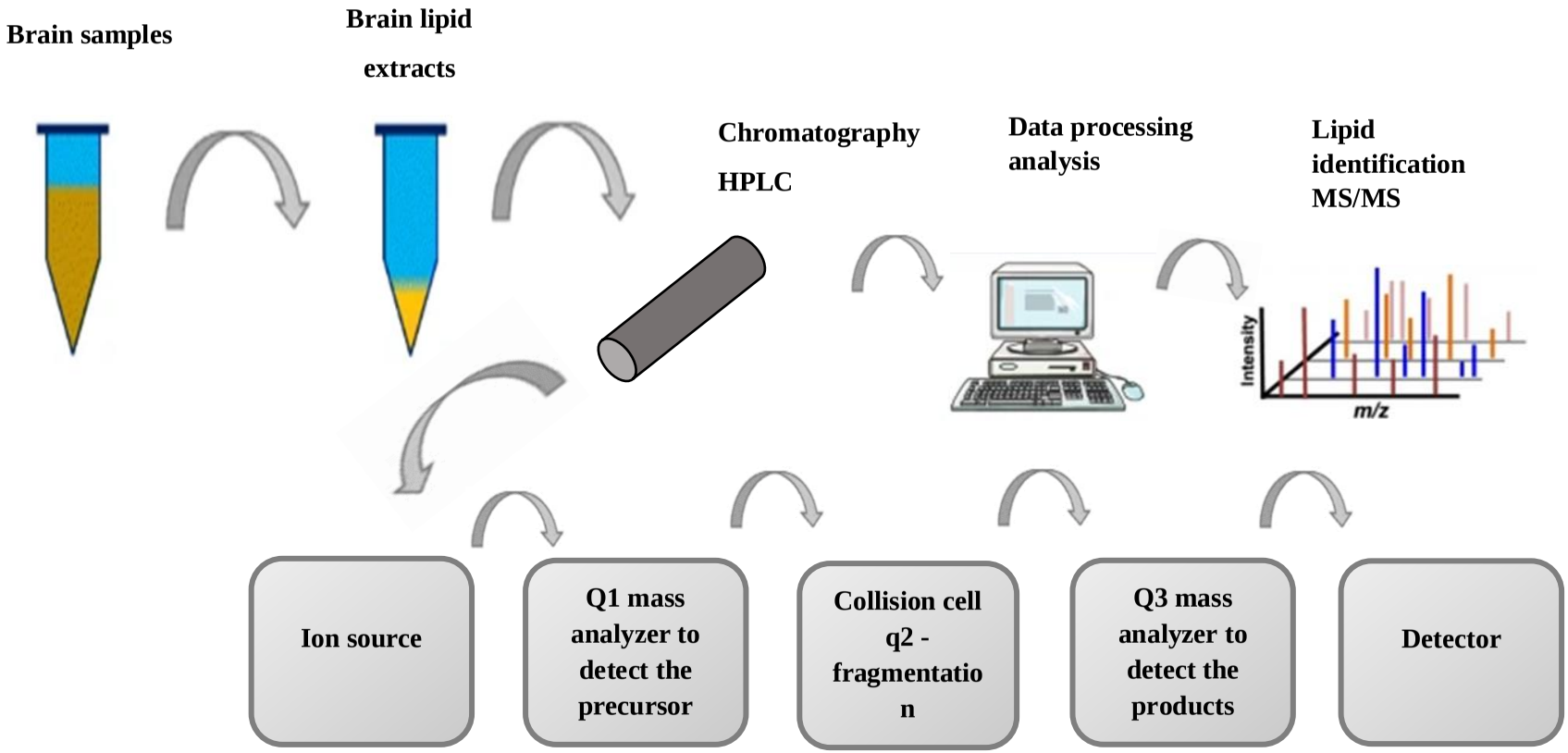

Figure 10. The typical configuration of a liquid chromatography with tandem mass spectrometry (LC-MS/MS) device. System components of the Triple Quadrupole mass spectrometer. Introduction of lipid samples in the ion source. Conversion to gaseous ions. Introduction to the mass spectrometer through direct injection. The precursor ion m/z is detected in Q1 and undergo CID (collisionally induced decomposition) in Q2 using inert gas and fragmented ions are detected in Q3. The signal is communicated to the data processing system and it is displayed in mass spectrum.

1.8.2 Targeted lipidomic approach with LC-MS/MS

LC-MS/MS is a promising tool to enhance the effectiveness of targeted and untargeted global profiling of lipids. The targeted lipid analysis emphasises predefined lipids of interest and measures only a single lipid category, while the non-targeted lipidomic method aims to provide a broad overview of novel or unexpected lipid metabolites simultaneously in a biological system (O'Donnell *et al*., 2014; Lam *et al*., 2013). Also, the latter approach is well suited to discover the lipid composition of a sample (Reisz, *et al.*, 2019).

In targeted LC-MS/MS, the elution order of brain lipids is achieved at varying times from the LC, defined as retention time (RT). Other RTs correspond to different lipid classes. For instance, more polar molecules elute at the beginning of the chromatogram. Then, they are passed to the MS/MS using scheduled multiple reaction monitoring scan mode (MRM), by which product ions are selected in Q3, resulting in the detection of selective and specific transitions (precursor to product ion) (Sorgi *et al*., 2018).

Subsequently, the defined precursor to product ion transitions can be monitored to quantify interest lipids. The first mass analyzer Q1 passes a particular precursor *m/z* and the second mass analyzer only detects the product *m/z*. The instrument is programmed according to the cycle among a prespecified set of ions and collects the data from the molecules of interest (Dettmer *et al*., 2007).

1.9 Chapter Summary

In summary, it is becoming increasingly clear that *Alox15* is expressed in various cells, and a close link exists between *Alox15* and its metabolic products in the pathophysiology of inflammatory diseases. Although the critical role of *Alox15* is highlighted in inflammatory conditions, the role of this enzyme in regulating normal brain function remains poorly defined. There are important questions and areas of contention, particularly regarding the role of the *Alox15* pathway in brain health, that will be described in more detail throughout this thesis.

1.10 Hypothesis

The deficiency of the *Alox15* gene may result in improved cortical and hippocampal-dependent memory in mice.

1.11 Overall Aims

1. To investigate the role of *Alox15* in normal brain function, using a range of behavioural tests to measure different properties of memory and anxiety.
2. To discover functional insights regarding the impact of *Alox15* deletion in male and female mice on cognition and behaviour during normal ageing.
3. To evaluate the effects of *Alox15* deletion on the expression levels of protein markers in the vHPC and dHPC linked with changes in behaviour.
4. To structurally characterise the lipid compounds generated during healthy brain ageing via the *Alox15* pathway. To determine the oxylipin formation as well as eoxPL composition associated with cognitive decline.

Chapter 2:

Materials and methods

2.1 Chapter Overview

This chapter covers the materials and methods that have been used through multiple experiments in the whole thesis. The methodology includes the subjects and the behavioural testing of mouse colony, immunofluorescence in combination with confocal microscopy, and describes the dissection of multiple brain regions and the biochemical protocols used to quantify lipid levels generated via the *Alox15* pathway in the brain.

2.2 Materials

2.2.1 Materials for behavioural testing

1. A large square arena 60 × 60 cm, constructed from laminated plywood, with a white floor and 40 cm high bright white walls, used for all the behavioural experiments
2. An opaque, white paper was used to cover all the inside areas of the arena.
3. Everyday household items, usually made of wood, plastic, and glass, such as vases, coffee containers, and Lego, are used for objects for behavioural testing (Figure 11).

Figure 11. Examples of object sets of various colours and shapes used for behavioural tasks.

2.2.2 Materials for Immunofluorescence

Chemicals and solvents

All chemicals were purchased from Sigma Aldrich / MilliporeSigma (Dorset, UK) unless otherwise stated.

1. Superfrost Plus slides (ThermoFisher, J1800AMNZ).
2. Optimal cutting temperature (OCT) compound (M32631)
3. Isopentane Solution (2-Methylbutane) (PHR1661).
4. Flat white boar bristle brushes with an angle cut suitable for frozen sections (ThermoFisher, 50-364-874)
5. Embedding Stainless-Steel Base Molds (ThermoFisher, 11655960)

Buffers and solutions

Except for those supplied as part of commercial kits used for immunohistochemistry, all buffers are listed below.

1. 0.1 M phosphate-buffered saline (PBS)
   Ten phosphate-buffered saline tablets (Thermo Fisher, MA, USA) dissolved in 1000 mL of distilled H20.
2. Antigen retrieval buffer
   0.05 M sodium citrate solution; add 14.7 g of sodium citrate-2 hydrate to 1 litre of distilled H_2O, and adjust to pH 6.0
3. 10 % normal donkey serum (NDS, Abcam, Cat. ab7475)
4. Blocking buffer
   0.5 % Triton X-100 + 0.3 M Glycine (to reduce background and autofluorescence) + 10 % normal donkey serum pH 7.4 (secondary antibody host species) in 200 ml PBS.
5. 30 % sucrose solution
   Dissolve 30 g sucrose in 70 ml PBS solution.
6. 4 % Formaldehyde solution in PBS.
   Add 40 g paraformaldehyde powder to 960 ml PBS solution in a glass beaker on a stir plate, warmed to approximately 60 ^{o}C in a fume hood. Then add 1N NaOH dropwise from a pipette until the solution clears. Let the solution cool down and adjust the pH to 7.4 with dilute HCl.
7. Washing buffer PBST.
   1 ml Triton-X100 in 0.1 M phosphate buffer.
8. 4′,6-diamidino-2-phenylindole (DAPI, a nuclear counterstain for blue-fluorescence, Vector Laboratories; 1:1000)

9. ProLong® Gold Antifade mountant reagent (P36930, ThermoFisher Scientific).

Antibodies and isotype controls

The following antibodies were used for immunofluorescence.

Table 1. List of the isotype controls used for immunofluorescence throughout this thesis

Isotype Control	Host Species	Dilution	Source / Catalogue number
IgG polyclonal	rabbit	1:100	Abcam, ab171870
IgG polyclonal	goat	1:100	Abcam, ab37373
recombinant IgG, monoclonal	rabbit	1:100	Abcam, ab172730

Table 2. List of the primary antibodies used for immunofluorescence throughout this thesis

Primary Antibody	Host Species	Dilution	Source / Catalogue number
$5HT_{1A}$ Receptor	rabbit	1:100	Abcam, ab85615
$GABA_B$ Receptor 1	rabbit	1:100	Abcam, ab238130
CRF_1 Receptor	goat	1:100	Abcam, ab59023
Parvalbumin (recombinant)	rabbit	1:100	Abcam, ab181086

Table 3. List of the secondary antibodies used for immunofluorescence throughout this thesis

Secondary Antibody	Host	Target species	Dilution	Source / Catalogue number
IgG Alexa Fluor 568	Donkey	Anti-rabbit	1:300	Invitrogen, Cat. A10042
IgG Alexa Fluor 594	Donkey	Anti-goat	1:500	Invitrogen, Cat. A32754

2.2.3 Materials for LC/MS/MS

Chemicals and solvents

All chemicals were purchased from Sigma Aldrich / MilliporeSigma (Dorset, UK) unless otherwise stated. Lipid standards were purchased from Cayman Chemical (Michigan, USA) and Avanti Polar Lipids (Alabama, USA). All solvents were HPLC-grade and were purchased from Thermo Fisher Scientific Ltd. Also, reagents were purchased from Thermo Fisher (MA, USA), including glacial acetic acid, chloroform, methanol (MeOH), and PBS tablets.

Solutions

1. 0.1 M Na acetate – (MW 82.03) (S2889-250G) – 4.102 g in 500 mL HPLC-Grade Water
2. Acidified methanol (AcMeOH) solution

   2 % acetic acid in MeOH (4 mL/ brain tissue prep). Calculations for the volume of AcMeOH using the table below:

ITEMS	VARIABLE & EQUATION
NUMBER OF SAMPLES	n
VOLUME NEEDED (ML)	Vn = n x 4
VOLUME WILL MAKE (ML)	V1 = Vn + 12
VOLUME OF ACETIC ACID	Va = 0.02 x V
VOLUME OF MEOH NEEDED	Vm = V1 - Va

Lipid standards

The phospholipid standards were purchased from Avanti Polar Lipids (Alabama, USA): 1,2-dimyristoyl-sn-glycero-3-phosphoethanolamine (DMPE), 1,2-dimyristoyl-sn-glycero-3-phosphocholine (DMPC). Also, the following deuterated eicosanoid standards were purchased from Cayman Chemical (Cambridge, UK): prostaglandin E2-d4 (PGE2-d4), thromboxane B2-d4 (TxB_2-d4), 11-dehydro thromboxane B2-d4 (11-dehydro TxB2-d4), 13-hydroxyoctadecadienoic acid-d4 (13-HODE-d4), 12(S)- and 15(S)-hydroxyleicosatetraenoic-d8 acid (12(S)- and 15(S)-HETE-d8), arachidonic acid-d8, 1,2-di-O-phytanyl-sn-glycero-3-phosphoethanolamine (4ME 16:0 Diether PE).

2.3 Equipment

2.3.1 Equipment for Behavioural testing

Equipment and software

1. ELP megapixel USB camera (720P/60FPS) was used to record behavioural videos (Ailipu Technology Co Ltd, Guangdong, China) and saved onto a hard drive.
2. Hard driver Crucial MX500 (CT250MX500SSD1) was used.
3. EthoVision XT 13 software (Noldus, Nottingham, UK) for video tracking and analysis
4. iSpy (version 7.2.1.0), WA, Australia)
5. GraphPad (version 9.0; Graph Pad Software Inc., San Diego, CA, USA; www.graphpad.com).

2.3.2 Equipment for Immunofluorescence

Equipment and software

1. CryoStar NX50 Cryostat (Thermofisher, UK)
2. Zeiss confocal LSM800 laser microscope (Carl Zeiss, Germany).
3. Zen software programme, Blue edition.
4. ImageJ Cell Counter plugin, ImageJ software (version 3.1.9; National Institutes of Health)

2.3.3 Equipment for LC/MS/MS

Equipment and software

1. OMNI Bead Ruptor Elite was purchased from Omni-Inc (Cambridgeshire, UK).
2. HPLC (Shimadzu, Japan) coupled 6500 Q-Trap mass spectrometer instrument (AB Sciex, Darmstadt, Germany)
3. Software used for lipidomic analyses were as follows; Analyst 1.7 (AB Sciex, Canada), Endnote Desktop (Clarivate Analytics, PA, USA), Microsoft Office (Microsoft, WA, USA), MultiQuant 3.0.2 (AB Sciex, Canada), LipidFinder (Cardiff Lipidomics Group, Wales)
4. GraphPad (version 9.0; Graph Pad Software Inc., San Diego, CA, USA; www.graphpad.com).

2.4 Methodology for mouse breeding and maintenance

Alox15$^{-/-}$ male and female mice on a C56BL/6 background were bred in-house under the Home Office Animals (Scientific Procedures) Act of 1986, under License (PPL 30/3150). *Alox15*$^{-/-}$ mice were generated around 1993 (129S2) by Collin Funk, as described previously (Sun, &

Funk, 1996). These mice were a kind and generous gift from Dr. Colin D. Funk (University of Pennsylvania). Briefly, Funk *et al.*, 1996 harvested mouse primary macrophages from euthanized mice by peritoneal lavage using sterile PBS followed by in situ hybridization analysis to localise the *Alox15* gene during embryogenesis. Then this gene was cloned from a strain 129 Sv genomic library followed by southern blot analysis of genomic DNA to detect homologous recombination in mouse embryonic stem cell line D3H (a subline of D3 derived from 129), as well as the targeted embryonic stem cell line A36. Also, germline transmission was tested by mating the male chimera offspring with C57BL/6 females (Sun, & Funk, 1996). Hartmut Kühn backcrossed them against C57BL/6 mice for seven generations, but then, Prof Phil Taylor *et al.* backcrossed further from the N7 colony to N11 on the C57BL/6 background at Cardiff university (Funk., 1996; Talor, *et al.* 2012). *Alox15*$^{-/-}$ mouse breeders were housed in isolators and moved to scantainers for maintenance. Gender and age-matched wild-type C57BL/*6J* (WT) mice were purchased from Charles River UK at 12 weeks old. Animals were housed in groups of 2 - 4 per cage and kept in a temperature and humidity-controlled environment (20 – 22 °C). They were maintained on *ad libitum* access to standard chow and water. Also, all mice had access to wood chew sticks and were on a 12-hour light/dark cycle. Each cage was provided with environmental enrichment in cardboard nesting tubes.

2.5 General methodological considerations before behavioural testing

Animal handling is a crucial parameter for all behavioural studies. Environmental factors can influence the performance of animals, and as a result, anxiety levels may be increased and worsen cognitive behaviour (Costa *et al*., 2012).

During normal ageing, animals are tested behaviourally repeatedly during a specific period, which may increase task familiarity. In my study, the overall behavioural approach has been designed to utilise the same groups of animals and test them over different time points repeatedly. There are various ways to reduce the practice effects and eliminate a significant source of errors, thus reducing the likelihood of misinterpreting outcomes when repeated behavioural testing is conducted. The order of the objects involved in behavioural tests (A1 and A2) needs to be counterbalanced to control the effects of variables. Mice frequently interact more with the object they are first introduced to. Another important consideration is that genetically modified and wild-type mice need to be tested randomly to avoid bias. This can be achieved by alternating the order in which each genotype is tested to minimise the risk of errors. Another critical parameter is the blinded manner of assessing behavioural tests. Specifically, it

is suggested that the person who performs the analysis should be blinded to the genotype until after the behavioural experiments are complete (Hånell *et al.*, 2014).

Of interest, animal health should also be considered, such as body weight, heart rate, and signs of wounds, to ensure that the animals do not perform abnormally due to any illness (Carter *et al*., 2015). In addition, a handling cardboard tube should be used to pick up the mouse from its cage to improve the testing performance of mice by minimising any handling-induced anxiety (Gouveia *et al*., 2017). Many studies suggest that using several behavioural paradigms compared to only one for a particular memory assessment may be highly advantageous in confirming findings (Sharma *et al*., 2010). Since many aspects can influence the testing performance, it is urgent to consider all the above parameters and eventually, the validity of the results will be increased.

2.6 Behavioural testing

This section includes the experimental studies and protocols used throughout this thesis to assess mouse recognition, spatial memory, working memory and anxiety-like behaviour. All behavioural tests were conducted using a main cohort of 58 male mice at 4 months of age and onwards (29 WT and 29 *Alox15*$^{-/-}$). In particular, I set up two cohorts of male mice for the behavioural tasks; Cohort 1 included 15 male mice of each strain, and in Cohort 2, they were 14 male mice per genotype. Both cohorts 1 and 2 were combined as they had been very tightly matched designs. Also, the average weight of the male mice was 27-29 g. In addition, tests were conducted using only one cohort of 30 female mice (15 WT and 15 *Alox15*$^{-/-}$ mice) at 4 months and onwards. Their average weight was 27-28 g when they aged 4 months. More details on the experimental design throughout this thesis are presented in section 2.9.

2.6.1 Apparatus and objects

The apparatus was set up in a quiet and brightly lit behavioural testing procedure room, placed on a square table which was elevated 50 cm off the floor. The cues around the arena and the square were consistent throughout the behavioural tests unless otherwise stated. An overhead varifocal USB camera was suspended from the ceiling 90 cm above the centre point of the arena. This was used to monitor mouse activity in the arena and connected to a laptop. Each session was recorded using a free downloaded software recorder, iSpy, and saved onto a USB hard drive. The mice in the arena were live tracked, the data were analysed using EthoVision XT 13 software, and the contact time/interaction with the objects was scored manually along with the EthoVision software data (described in detail the section 2.6.4). The duration of each

trial/ experiment (10 minutes) for object exploration of each mouse was recorded manually with a stopwatch.

During the test, the objects were selected to ensure minimal anxiety based on their size, shape, colour, and texture. Additionally, they were around 15 cm in height and quite heavy to prevent the animals from climbing on them. The objects were placed in the arena roughly 25 cm apart. The floor, objects and walls were cleansed with 70 % ethanol (in distilled water) before every session and between each trial to eliminate any possible odour cues. Also, urine and excrement were cleaned straight after each trial to avoid discrimination issues.

2.6.2 Experimental design - Habituation Phase (HP)

One week prior to experiments, mice were transferred to the behavioural test room in their home cages for 1-2 hours to start the habituation to the new environment along with the animal handling for 5 mins a day. Two days before testing, mice were given two habituation sessions for free exploration of the empty arena without objects for 10 mins. Mice were always transported from their home cages to the arena within cardboard tubes. Each mouse was placed in the centre of the arena facing the same wall throughout all tasks and allowed to explore for 10 mins freely. During this phase, their exploratory behaviour in novel areas, the locomotor activity levels, including the total distance moved and the velocity inside the arena, were measured and assessed.

2.6.3 Experimental design – Sample Phase (SP) and Test scoring

The experiment was consisted of sample phases and test phase. Mainly, the sample stage included two sample phases of 10 mins each, which were separated by a 10-min interval (time spent in a holding cage located in the testing room). Following the second 10-min delay, mice were subjected to a 10-min test phase. *Alox15*$^{-/-}$ and WT mice were tested randomly to avoid bias. This was achieved by alternating the order in which each genotype was tested. The order of the object sets was counterbalanced amongst mice to avoid spatial biases. During the test phase, the duration in the centre of the arena, the distance the mice travelled throughout the arena, their velocity and locomotor activity, in general, were recorded by EthoVision tracking software (Hall *et al.*, 2016).

The centre of the arena was 30 x 30 cm and described as 'Inner Zone', while the remaining part, including the four corners, was described as 'Outer Zone'. The total time and distance spent in each zone were recorded by EthoVision software for each animal.

For all experiments, the dependent variable was the time spent by the mice exploring the objects. Object exploration was defined as time spent interacting with an object at a distance

within 2 cm to face the objects to be tracked (Ennaceur & Delacour, 1988). To this end, object exploration time is not scored as contact time interacting with the objects, when the animal tried to climb on the top of objects to look around or also when the animal's head was in the distance greater than 2 cm of the object (Hale *et al*., 2005).

Notably, to ensure that all tasks were sensitive to differences between the groups, independent of differences in individual contact times, exploration time was translated into a Discrimination Ratio (DR) for each test phase. DR measurement was determined as the novel object exploration time divided by the total exploration time of both objects (calculation below). DR reflects the preferential exploration allocated to a novel item compared to a familiar one and thus is a measure of recognition memory sensitivity (Hall *et al*., 2016). Chance performance is represented by a preference ratio of 0.5, which implies no systematic bias for the target object and translates into an equal exploration of both novel and familiar objects. A value above 0.5 represents a strong preference for the novel target object, while a value below 0.5 indicates a familiar object preference (Hall *et al.*, 2016). Thus, the ratio ranges from −1 to +1, with negative scores indicating a preference for the familiar object and positive scores showing a preference for the novel object.

2.6.4 Video tracking and analysis with EthoVision XT

EthoVision tracking software was used to automate the score of mouse exploratory behaviour with objects. Throughout this thesis, the scoring of the interaction time with the objects was manually operated in conjunction with EthoVision data to provide an objective judgement. The mice were tracked live, but also video files were saved for future use retrospectively for analysis within the EthoVision software. The software enables tracking of the animals' noses, body centre, and tail base point and automatic detection of mobility and elongation of their body.

The arena settings were first used to draw the arena's square shape and create the zone group (areas) labelled as an outer or inner zone. A second zone group was added for the objects to define the shape of each one separately, such as square or round (e.g. Object A). Another object zone was drawn much wider, which extended by 2 cm around the original object zone circumference and added to readjust the previous shape sizes of the objects, such as their width and height (e.g. Object A+2 cm) (Figure 12). The test scoring was determined by the total object exploration time, which was determined as the contact time spent interacting with the object at a distance of 2 cm (Ennaceur *et al*., 1988). Natural behaviours in mice, such as exploratory behaviour, locomotor activity, rearing, and grooming, can be important considerations and measured with EthoVision XT.

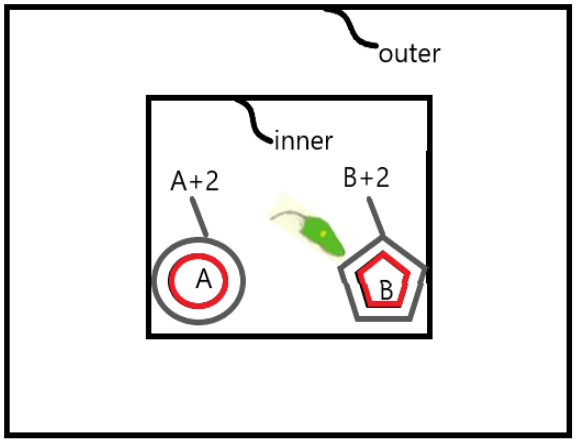

Figure 12. The schematic diagram for the arena settings, including the selection of the shapes, drawing arena, defining the zones.

2.6.5 Novel object recognition task (NOR)

Each animal was placed in the centre of the arena and exposed to two identical familiar objects, A and B, placed in different arena locations within the inner zone. The animals were allowed to explore the arena with the objects for 10 mins during Sample Phase 1. After a 10-min delay (spent in their home cage to rest), mice were returned to the arena to explore the same objects during Sample Phase 2, in which the rest cycle was repeated. However, after the second 10-min delay, either one of the two familiar objects from the Sample phase was replaced with the novel object. The animal was returned to the arena for the test phase to explore the objects for 10 mins. (Figure 13). The objects' position and identity, either familiar or novel, were fully counterbalanced within and between groups (Benice *et al.*, 2008). The time interacting with the objects was measured as described previously using the EthoVision software. Between the sample phases, in both stages, objects and the arena were wiped down with 70 % ethanol prior to returning the mouse to the apparatus for the test stage. The DR was calculated as the amount of time spent by each animal during the test phase exploring the novel object divided by the total time spent exploring both objects. A DR above 0.5 indicates that the mouse has spent more time with the novel object than the familiar one and thus is a measure of recognition memory sensitivity (Hall *et al.*, 2016).

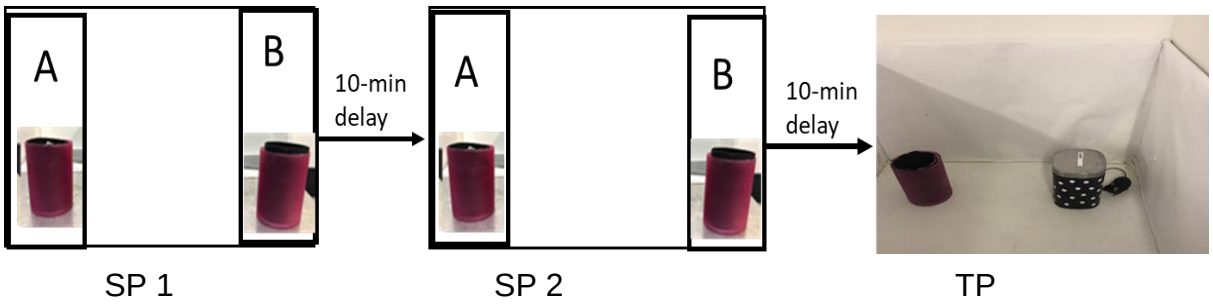

$$\frac{\text{Total time spent exploring ''Novel'' object}}{\text{Total time spent exploring both objects (Novel \& Familiar)}} = \text{DR}$$

Figure 13. The schematic diagram of NOR comprises Sample phases 1 and 2 and the Test phase.

2.6.6 Object location task (OLT)

This task used the same sample phase protocol as previously reported in the NOR task. Specifically, the animals were allowed to explore the arena and object A and B for 10 mins during Sample Phase 1. After a 10-min delay (spent in their holding cage), mice were returned to the arena to explore the same objects during Sample Phase 2. After a second 10-min delay, the mice were ready for the test phase, during which one of the objects from the same location was moved to a new location, and the animal was allowed to explore once more (a location in which the object has not been previously encountered) (Figure 14). The mice' order and the moving object's position in the test phase were fully counterbalanced between the mice. If the animal's memory functions normally, it will spend more time exploring the object that changed position rather than the one that remained in the same position. If the exploration of all objects is the same, this behaviour can be interpreted as a memory deficit. DR was calculated as the time spent by each animal exploring the object that changed position divided by the total time spent exploring all objects.

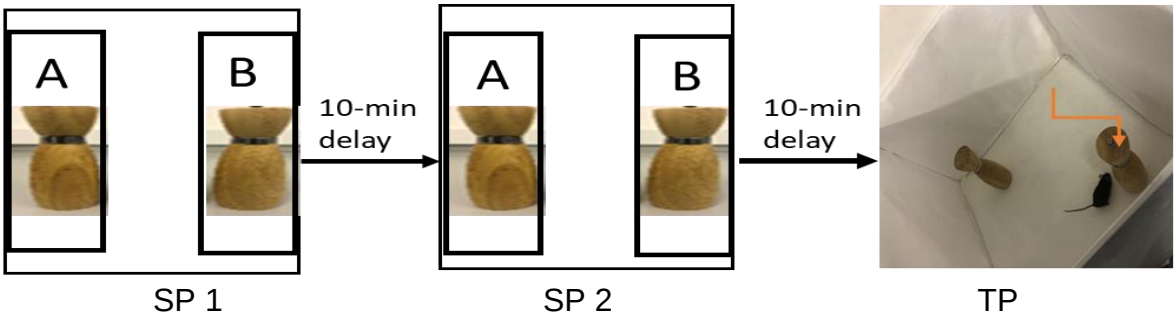

$$\frac{\text{Total time spent exploring the object that changed position}}{\text{Total time spent exploring both objects (changed \& unchanged)}} = \text{DR}$$

Figure 14. The schematic diagram of OLT comprises Sample phases 1 and 2 and the Test phase.

2.6.7 Elevated plus-maze (EPM)

The EPM apparatus is constructed from Plexiglas (black floor, bright walls) and elevated to 75 cm from the floor via a vertical black frame. A 1 cm high lip surrounds the edges of the open arms allowing the mice to see over them to the room and floor, whereas the closed arms are surrounded by 15 cm high black walls restricting any view (Figure 15).

The EPM maze was cleaned with 70% ethanol before each test session, with sufficient time for the ethanol odour to dissipate before the next test session. Mice were picked up in a cardboard tube from their home cage and placed at the junction of the four arms of the maze, on the centre square of the EPM, facing the same open arm each time. They were allowed to freely explore the maze for a single 10-min test session. After the test session, the mouse was removed from the maze and placed back into its home cage. A camera was mounted on the ceiling, directly above the EPM and connected to the laptop, allowing sessions to be video recorded. This software saved on the computer was utilized to collect all the recorded videos of each mouse's activity and calculate the scoring. The plus shape of the arena was drawn, defining the closed and open arms as distinct zones in the arena. Entry into the closed arms was defined as all three body points of the centre, nose and tail base being in the closed arms. An exploration ratio was calculated for each mouse as the time spent in the closed arms divided by the total time in the maze (600s).

The EPM test arena consists of 4 arms raised approximately two feet off the ground. Two arms are enclosed by walls to prevent the mouse from falling. The other two arms are open, with no walls to prevent a mouse from jumping or falling. Mice are averse to open arms because they may fall off, so they prefer to stay in the enclosed arms. Therefore, by measuring how much time mice spent in the open versus closed arms, we can determine their level of anxiety. The less anxious a mouse is, the more time it will spend in open arms than closed arms.

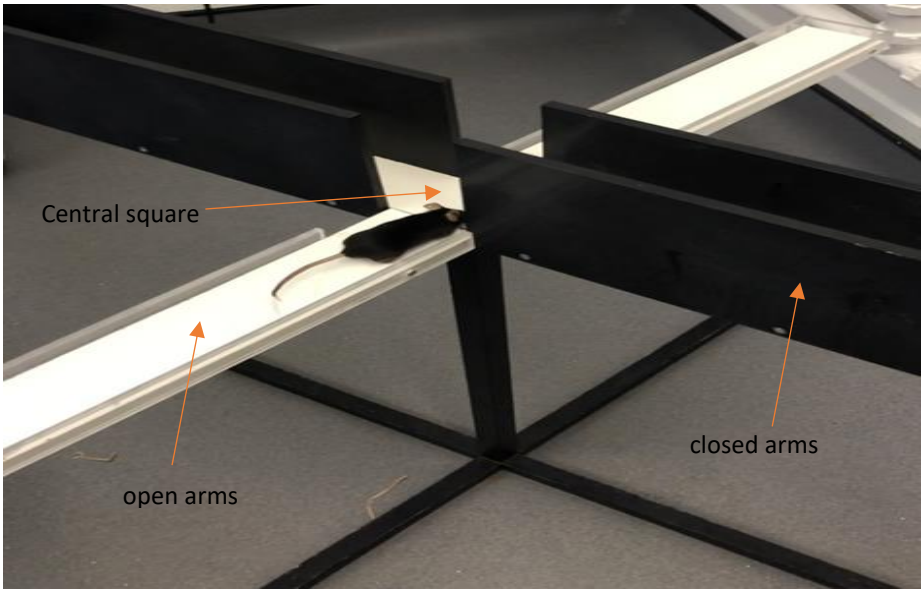

Figure 15. The elevated plus-maze for the assessment of anxiety-like behaviour in mice

2.6.8 Spontaneous Alternation in the T-maze

The T-maze apparatus consists of a melamine floor with clear Perspex walls. The goal arms are 20 cm long and 12 cm wide to form the T-shape. The T-maze was placed on a steel table in the centre of the behavioural testing room, which remained consistent throughout the experiment. Each trial consisted of two consecutive runs; a trial run and a choice run. During the trial run, each mouse was placed in the start arm of the apparatus, which was confined for 15 secs and then the sliding door block was removed. Upon leaving the start arm, the mouse could freely choose the left or the right goal arm by entering with four paws inside. After selecting one of the remaining maze arms during the first trial run, the arm divider was placed on that goal arm, and the animal was kept in it for 30 secs to explore this goal arm. During the choice run, the animal was transferred to the start arm again, and the door blocking divider was

raised after a 60-sec delay period. The mouse had a choice of either entering the previously unvisited arm as a correct choice or repeating the visit on the same arm as a failure.

When the mouse entered either goal arm, it was confined there for 15 secs during the choice run, then removed to its holding cage. Following this, the subsequent mice were used for Day 1 to allow a 5 min inter-trial interval. The series of arm entries was recorded using an overhead camera. The percentage of alternation rate and the total trial duration was measured.

Because spontaneous alternation requires no habituation to the maze as well as no food or water deprivation, and thus it is particularly suitable for testing aged animals. The sliding doors were also placed 10 cm from the end of each lateral arm to create a goal box. Each mouse was then subjected to 10 trials per morning and evening session. Spontaneous alternation was measured by counting the average percentages (%) of correct trials (Figure 16).

2.6.9 Statistical analysis

The data from object interaction were collected and analysed with the EthoVision XT 13 software and exported to Microsoft Excel to calculate separate scoring on both groups of mice. The data were presented using mean scores for each mouse and the standard error of the mean (SEM). All statistical analyses were performed using GraphPad Prism 9. The normality of data was examined using the Shapiro-Wilk W test. Between-group differences were evaluated using a *t*-test, if needed for different group variance, with Mann–Whitney U test in cases where data were not normally distributed. A repeated-measures ANOVA (analysis of variance) with object type/ object location (within-subjects) and genotype (between subjects) was used, for

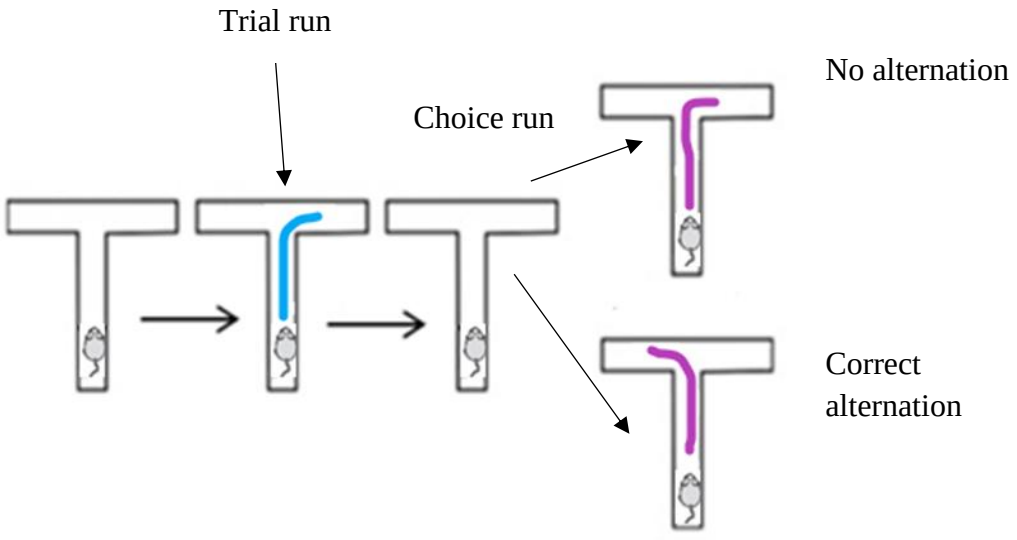

Figure 16. Schematic diagram of the T-maze spontaneous alternation task, consisting of trial run and the choice run. The successful alternation performance is confirmed by entering to the previously unvisited arm.

any experiment, to identify significant differences of groups between samples. Bonferroni adjustment was used on all significant interactions and main effects (F values), adjusting for multiple genotype comparisons. The statistical significance was set at *= $p \leq 0.05$, **=$p<0.01$, ***=$p<0.001$ for genotype comparisons. Data were displayed as Box and Whiskers plots (Tukey plots), line graphs and column charts with mean ± S.E.M.

2.7 Protein markers associated with increased anxiety

This section describes how brain tissue was dissected for immunohistochemical analysis and the analysis used afterwards.

2.7.1 Brain tissue preparation

Animals were culled using an approved Schedule 1 method at 15 months, specifically by placing them in a chamber with a rising concentration of CO_2 followed by confirmation of death using palpation. The mice were pinned to a polystyrene cutting board, and the chest cavity opened using dissecting forceps and scissors. A needle was then inserted into the left ventricle; the right atrium was cut. Mice were perfused with ice-cold phosphate-buffered saline (PBS) followed by 4 % paraformaldehyde (PFA) in 0.1 M PBS. Brains were harvested and postfixed in 4 % PFA overnight at 4 °C, followed by a sucrose solution (30 % sucrose) in PBS until submerged for cryoprotection for three days at 4 °C. Next, the brains were embedded in OCT compound and flash-frozen using pre-cooled isopentane by burying the blocks in dry ice and then kept at -80 °C until sectioning. The embedded tissue blocks were then cut into 20 µm-thick coronary slices using a cryostat set at -20 °C and collected onto Superfrost Plus slides (Figure 17).

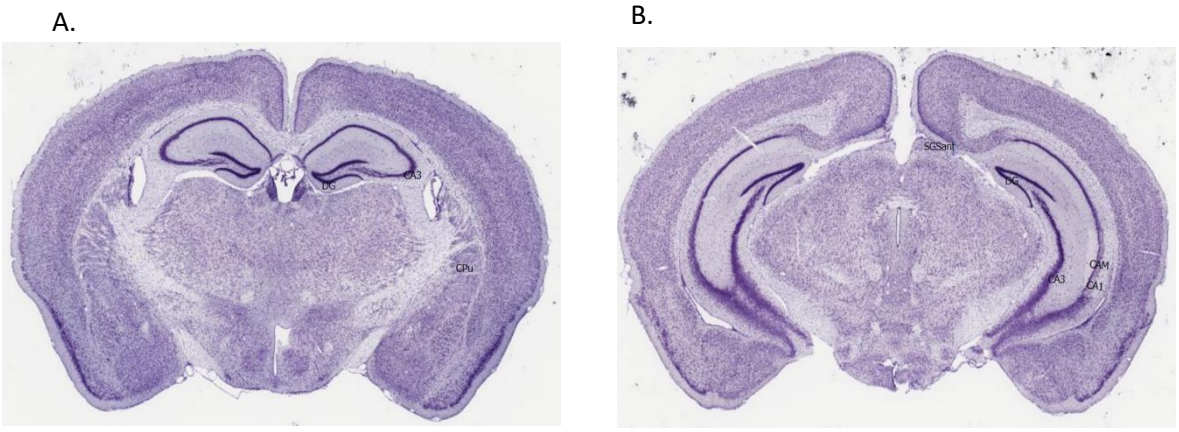

Figure 17. Schematic mouse coronal sections, from a. dorsal HPC and b. ventral HPC cryosections. The brain images were obtained from **http://brainmaps.org**.

2.7.2 Immunofluorescence

Antigen epitopes shielded by 0.05 M sodium citrate buffer were retrieved in a heat-mediated process water bath for 30 mins at 88 °C, adjusted to pH 6.0. Following the incubation, the sections were placed in glass jars with PBS in a fresh 0.05 M sodium citrate buffer to cool down at room temperature for 30 mins. After rinsing three times with PBS, sections were incubated in a blocking solution; 10 % normal donkey serum in PBS-Triton X-100 for 60 min at room temperature (60 mins; 10 % normal goat serum, 0.5 % Triton X-100 and 0.3 M glycine). Cryosections were incubated in primary antibodies overnight at 4 °C in a humidified chamber. Following this, the sections were washed three times in phosphate buffer containing 0.1 % Triton X-100 (PBS-T), incubated in appropriate secondary antibodies for 60 min at room temperature, and kept in the dark to enable fluorescent detection. The secondary antibodies were selected depending on the host species of the primary antibodies. After the secondary antibody was washed out, the sections were washed three times with PBS-T and then were counterstained with DAPI for 5 mins at room temperature for nuclear staining. After rinsing three times with PBS, sections were dried before being coverslipped using the mounting medium on microscope slides in ProLong mountant.

2.7.3 Image acquisition and analysis – Cell counting/signal intensity

Images were acquired using a Zeiss confocal LSM800 laser microscope. The region of interest was outlined, and the HPC was subdivided into subregions (DG, CA1, CA2 and CA3). The channels used were Alexa Fluor 568, an orange/red-fluorescent dye with an excitation wavelength suited to 568 nm and Alexa Fluor 594, a red-fluorescent dye with an excitation wavelength suited to 594 nm. These channels were configured to obtain the best signal during image acquisition of the brain samples to eliminate bleed-through from other fluorophores. The counting of positive cells was determined on images obtained at low magnification objective lenses (20x) to provide an overall unbiased assessment of the proportion of positive cells. The images were taken at the same excitation light intensity and master gain setting for isotype and positive controls to compare signal intensity between genotypes. All immunostained sections were analyzed using the 2.6 Zen software programme. All acquisition parameters were consistent among different conditions in my study between isotype controls and positives (Table 4 A, B).

Table 5 A. Image acquisition was kept consistent between isotypes and positive controls on dorsal HPC

	405 nm laser	568 nm laser	master gain
Isotype control / PV	0.30 %	0.57 %	557 V
Isotype control / $GABA_B^+$	0.29 %	0.55 %	570 V
Isotype control / CRF_1^+	0.29 %	0.60 %	575 V
Isotype control / $5HT_{1A}^+$	0.30 %	0.65 %	580 V

Table 5 B. Image acquisition was kept consistent between isotypes and positive controls on ventral HPC

	405 nm laser	568 nm laser	master gain
Isotype control / PV	0.29 %	0.65 %	560 V
Isotype control / $GABA_B^+$	0.30 %	0.55 %	575 V
Isotype control / CRF_1^+	0.30 %	0.65 %	580 V
Isotype control / $5HT_{1A}^+$	0.30 %	0.65 %	580 V

The stained sections were imaged on the ZEN programme to quantify the labelled positive neurons in the HPC area CA1, CA2, CA3 subregions and DG. Images were acquired using a 20× objective with a final image dimension of 2,048 × 2,048 and analyzed using the open-source ImageJ software blind to genotype. The results were shown as the percentage of the total number of positive $5HT_{1A}^+$, CRF_1^+, $GABA_B^+$ and PV^+ cells. The cell counting was scored manually to ensure accuracy using the ImageJ Cell Counter plugin by outlining the individual nuclei identified by DAPI staining. Next, the counting was performed by the well visible cells with DAPI-stained nucleus and the other staining surrounding with DAPI for PV^+, $5HT_{1A}^+$, CRF_1^+ and $GABA_B^+$ cells. The cells in the granular cell layer of the DG and the pyramidal cell layers of CA1 and CA3 subfields of HPC were counted.

In contrast, those that appeared in the outer layer were excluded. Labelled positive cells were marked by a click of the mouse on their image. A total of four tissue sections per animal were taken and analyzed, and for each animal, a single value was calculated per hippocampal area by averaging all values for that subregion across all four sections. The reference number was

determined by the cells estimated by DAPI nuclear staining used as negative cells. Thus, the counted immuno-positive cells were then calculated by dividing the number of positive cells by the negative reference cells.

In addition to counting positive cells, the fluorescence intensity was determined for each marker per DAPI counted nuclei, and the background signal was subtracted for each channel. Specifically, consistent regions of interest were drawn around the hippocampal areas using the polygon selection tool to measure the mean value of the signal intensity, and the 'analyze particle' function was used to count cells. Mainly, area, integrated density, and mean gray value measurements were considered, together with a background reading. The background fluorescence intensity of the hippocampal images was measured by delineating exactly another area within the same examined image that contained no cellular signals. Then, the values of density were averaged across four sections per animal. We used the signal intensity value of PV, $5HT_{1A}$, CRF_1 and $GABA_B$ after the tissue background subtraction intensity value. More specifically, the corrected total cell fluorescence for a region of interest was calculated as follows:

CTCFl = integrated density – (area region of interest × background fluorescence)

More details on the specific hippocampal subregion are given in the captions of the representative images.

2.7.4 Statistical analysis of immunofluorescence data.

For quantitative comparison, immunofluorescence data from four sections per mouse were used in each group, with a single value per mouse generated. Experimental data were analyzed blinded to the genotype of animals. Statistical analyses, as well as the plotting graphs, were performed using GraphPad Prism 9. Data were presented as the mean ± SEM unless stated in the relevant results or figure legends. The normality of data was examined using the Shapiro-Wilk W test. Between-group differences were evaluated using *t-test*, if needed for different group variance, with Mann–Whitney U test in cases where data were not normally distributed.

2.8 Lipidomic analysis

This section describes how various mouse brain regions were dissected for lipidomic analysis and the protocol for brain lipid extraction and analysis.

2.8.1 Culling, perfusion, and dissection

Animals were culled using a Schedule 1 method at 15 months. The culling and the perfusion were outlined above in Section 2.7.1. Once perfusion was complete, the animal was decapitated using dissection scissors, and the brain was removed. The brain was dissected into specific

regions comprising the prefrontal cortex, cerebellum, and HPC. These regions were snap-frozen in liquid nitrogen and stored at -80℃ until lipid extraction. The weights of all brain regions between 12 WT and 11 *Alox15*$^{-/-}$ mice are presented in Table 10.

2.8.2 Brain Lipid Extraction

Lipids were extracted from brain tissue using liquid-liquid phase separation, which is the gold standard in lipidomic sample preparation. The extraction was based on an acidified and modified Bligh and Dyer method, using chloroform and acidified methanol as solvents and relying on biphasic chloroform-methanol-water mixtures (Bligh, & Dyer, 1959). Each brain region (prefrontal cortex, cerebellum and HPC, approximately 24 mg, was placed into a 2 ml Eppendorf tube. Twelve 1.4 mm ceramic beads and 1.9 mL acidified methanol was added gradually using a pipette (0.95 ml x 2). Then, tissue was homogenized using an OMNI Bead Ruptor Elite for 20 secs at 4 ℃ and a speed of 4 m/sec until well-homogenized. The sample was transferred into a 10 ml glass extraction vial (chromacol) and placed inside a polystyrene box with the lid closed. Next, 10 µl of the oxylipin internal standard solution and 10 µl of the oxidised phospholipid internal standard solution were added to each sample. Then, 1.5 mL sodium acetate was gradually added to each sample using a pipette. 1.8 ml chloroform was then added, and the caps were fastened securely. The samples were placed on ice for 15 mins in the dark. Next, samples were vortexed for 30 secs every three mins (5 times in total), followed by a centrifugation step of five mins at 600 x g at 4 ℃. The lipids were recovered in the bottom layer, which was collected with a glass Pasteur pipette, applying gentle, positive pressure whilst moving through the upper aqueous phase and crossing the interphase. Lipids were recovered into a clean glass vial. The remaining lipids in the bottom layer were re-extracted by the addition of 0.95 mL chloroform to the aqueous upper layer, which was vortexed and centrifuged again as follows: 0.95 ml chloroform was added, the sample was vortexed for 1 min and then centrifuged for 5 mins at 600 x g, and 4 ℃ and the bottom organic layer was collected. Then this step was repeated twice. All these chloroform extracts were combined with the previous layer. The samples were dried under a vacuum at 30 °C. Once dried, samples were resuspended in 143 µL MeOH. The samples were incubated for 5 mins in a water bath at 30 °C, vortexed for 15 secs, and repeated the last step. The samples were transferred to HPLC vials with inserts, centrifuged for one min at 600 x g and 4 ℃. Finally, the samples were transferred to new HPLC vials and were kept at -80 °C prior to analysis for free eicosanoids by LC/MS/MS.

2.8.3 Quantification of enzymatically oxPLs.

Lipid extracts were separated using reverse-phase HPLC on a C_{18} Luna, 3 µm, 2 mm × 150 mm column (Phenomenex, Torrance, CA) with a gradient of 50 %–100 % solvent B over 10 mins, followed by 30 mins at 100 % B (Solvent A: methanol, acetonitrile, water, 1 mM ammonium acetate) at a ratio 60:20:20; B: 100 % methanol, 1 mM ammonium acetate] with a flow rate of 0.2 ml/min. Data were acquired and analysed in MRM mode on a Q-Trap 6500 mass spectrometer, monitoring and quantifying the relative abundance of the oxidized phospholipids by monitoring transitions from Q1 to Q3 in negative ion mode.

The accurate signal of lipids was determined in the below transitions, as shown in Table 6. The native phospholipids are listed as original MRM transitions taken from the collaborator Professor Steffany Bennett at the University of Ottawa. Her methods were used along with the list of retention times made by a former postdoc in the Lipidomics Group at Cardiff University and calculated the oxidised masses. More details will be explained in Chapter 7, such as the *m/z* values that I measured and their oxPLs analysis.

The source conditions were as follows: ion spray (IS) value was set at -4500 V, ion source temperature was set at 500°C, the source gas 1(GS1) was 40 psi, and the source gas 2 (GS2) was 30 psi, the dwell time for each lipid was 100 msec. The declustering potential, entrance potential, collision energy and cell exit potential (CXP) were set at various values as defined in the Table below. The integrations of the peaks were performed manually using the Multiquant 3.0.2 software.

Table 6. MRM transitions were detected and analysed for oxPLs in five WT mice.

ID Analytes - oxidised	Precursor m/z (Q1)	Product m/z (Q3)	Declustering Potential (DP)	Entrance Potential (EP)	Collison Energy (CE)	Collision Cell Exit Potential (CXP)
PE 18:0a_HETE	782.600	319.20	-55	-10	-45	-7
PE 18:1p_HDOHE	789.600	343.20	-50	-5	-38	-9
PE 18:0p_HDOHE	790.600	343.20	-50	-5	-38	-9

PE 18:0a_HETE	795.600	319.20	-55	-10	-38	-7
PE 16:0a_HEPE	780.600	317.20	-50	-10	-45	-11
PE 18:1a_HDOHE	804.700	343.20	-50	-5	-38	-9
PC 18:1p_HDOHE	762.600	343.20	-50	-5	-38	-9
PE 18:0a_HDOHE	806.700	343.20	-50	-5	-38	-9
PE 16:0a_HDOHE	778.600	343.20	-50	-5	-38	-9
PE 16:0p_HETE	754.600	319.20	-55	-10	-38	-7
PE 18:1p_HETE	766.600	319.20	-55	-10	-38	-7
PE 18:0p_HETE	778.600	319.20	-55	-10	-38	-7
PE 16:0a_HEPE	752.600	317.20	-50	-10	-45	-11
PE 16:0p_HDOHE	776.600	343.20	-50	-5	-38	-9
PC 16:0a_HETE	806.700	319.20	-55	-10	-38	-7
PC 16:0a_HETE	798.600	319.20	-55	-10	-38	-7
PC 18:1a_HETE	806.700	319.20	-55	-10	-38	-7
PC 18:0a_HETE	810.600	319.20	-55	-10	-38	-7
PC 18:1a_HETE	826.700	319.20	-55	-10	-38	-7
PC 16:0a_HDOHE	830.700	343.20	-50	-5	-38	-9

PC 18:1a_HETE	826.700	319.20	-55	-10	-38	-7

Internal standards for oxidized phospholipids

1,2-dimyristoyl-sn-glycero-3-phosphocholine (DMPC) and 1,2-dimyristoyl-sn-glycero-3-phosphoethanolamine (DMPE) were diluted in MeOH and were prepared in serial dilutions from concentrations of 1 mg/mL to 0.5 µg/mL Each brain sample spiked with 10 µL (5 ng) of each internal standard mix prior to lipid extraction for determining the relative abundance of oxPLs

LC/MS/MS (MRM and EPI) analysis

LC tandem mass spectrometry (LC/MS/MS) technique with the triple quadrupole mass spectrometers have been operated in MRM scan mode to detect selective and specific transitions and in Enhanced Product Ion (EPI) mode to identify the acquired MS/MS ion spectra at a fixed area threshold setting. In the following sections, they will be introduced in greater detail.

Multiple Reaction Monitoring analysis

The relative abundance of oxidized phospholipids was determined using MRM method on the 6500 Q-Trap mass spectrometer, detecting the selective and specific initial transitions in WT mice, based on the precursor to product ions arising from collision-induced dissociation to form distinct negatively charged ions. The gradient was 50 - 100 % mobile phase B in mobile phase A. [A: methanol, acetonitrile, water,1 mM ammonium acetate) at a ratio 60:20:20; B: 100% methanol, 1 mM ammonium acetate]. The flow rate was 0.2 mL\min. The following conditions of detection were the same as above in Section 2.8.3.

Enhanced product ion (EPI) analysis

The most abundant previous MRM transition was selected for each analyte, and the corresponding MS/MS spectrum was acquired via EPI scan mode. The ions were trapped and accumulated in Q3 for a limited time; they were fragmented in the trap and then scanned out simultaneously for mass determination. The ion trap settings were as follows: the Linear Ion Trap (LIT) fill time set to dynamic fill time and the Q3 entry barrier set at 8.00 V, declustering potential -50 V, entrance potential -10 V, and the collision energy set at -38V. All MS/MS data were acquired using 6500 Q-Trap and were analyzed manually by Multiquant 3.0.2 software. From MS/MS analysis, the list of MRM transitions detected in the brain of WT mice is described in Table 6.

Table 7. A list of MRM transitions from MS/MS analysis was detected in WT mice's brains. All internal product ions have been demonstrated for each precursor ions

ID Analyte	Precursor m/z (Q1)	Product m/z (Q3)	Declustering Potential (V)	Entrance Potential (V)	Collison Energy (V)	Collision Cell Exit Potential (V)
PE 18:0a_HETE	782.600	319.200	-55	-10	-38	-7
PE 18:0a_12-HETE	782.600	179.100	-55	-10	-38	-7
PE 18:0a_5-HETE	782.600	115.100	-55	-10	-38	-7
PE 18:0a_15-HETE	782.600	219.100	-55	-10	-38	-7
PE 18:0a_11-HETE	782.600	167.100	-55	-10	-38	-7
PE 18:0a_8-HETE	782.600	155.100	-55	-10	-38	-7
PE 18:0a_HEPE	780.600	317.200	-50	-10	-45	-11
PE 18:0a_15-HEPE	780.600	219.100	-50	-10	-45	-11
PE 18:0a_12-HEPE	780.600	179.100	-50	-10	-45	-11
PE 18:0a_11-HEPE	780.600	167.100	-50	-10	-45	-11
PE 18:1a_HDOHE	804.700	343.200	-50	-5	-38	-9
PE 18:1a_10-HDOHE	804.700	153.200	-50	-5	-38	-9
PE 18:1a_11-HDOHE	804.700	149.200	-50	-5	-38	-9
PE 18:1p_HDOHE	762.600	343.200	-50	-5	-38	-9
PE 18:1p_10-HDOHE	762.600	153.200	-50	-5	-38	-9
PE 18:1p_11-HDOHE	762.600	149.200	-50	-5	-38	-9
PE 18:1p_14-HDOHE	762.600	205.200	-50	-5	-38	-9
PE 18:0a_HDOHE	806.700	343.200	-50	-5	-38	-9

PE 18:0a_10-HDOHE	806.700	153.200	-50	-5	-38	-9
PE 18:0a_14-HDOHE	806.700	205.200	-50	-5	-38	-9

2.8.4 Quantification of oxylipins

Oxylipin analytes were quantified by LC-MS/MS analysis on the Sciex Q-Trap 6500 and monitored using a scheduled MRM method in negative ion mode. The relative abundance of the oxylipins was quantified using the specific precursor to product ion transitions. These have predetermined collision energy and declustering potential values, as shown in Table 8 below.

Lipid extracts were separated using reverse phase HPLC on an Agilent Eclipse Plus 1.8µm C18 column, 2.1 mm x 150 mm, (Phenomenex, Torrance, CA) held under 45 ^{o}C at a flow rate of 0.5 ml/min. Gradient elution of 30-100 % solvent B over 20 mins, followed by a decrease at 30 % solvent B for 30 mins, which is held until the end of the run at 22.5 mins. (Mobile phase B: 840 ml acetonitrile: 159 ml methanol: 1 ml glacial acetic acid; mobile phase A: 949 ml water: 50 ml of solvent B: 1 ml glacial acetic acid).

The ion source conditions were as follows: ion spray (IS) value -4500 V, ion source temperature 475 ^{o}C, the source gas 1(GS1) 60 psi, source gas 2 (GS2) 60 psi. Dwell time was 100 msec and entrance potential -10 V. Also, declustering potential, collision energy and collision cell exit potential were different for each analyte (Table 8). Chromatographic peaks were integrated manually using Muliquant 3.0.2 software.

Internal standards for oxylipins

The internal standard compounds are used to correct losses during extraction. This standard mix contained the standards 13(S)-HODE-d4, 5(S)-HETE-d8, 12(S)-HETE-d8, 15(S)-HETE-d8, 20-HETE-d6, leukotriene B4-d4, resolvinD1-d5, prostaglandin E2-d4, prostaglandin D2-d4, prostaglandin F2α-d4, thromboxane B2-d4, 11-dehydro thromboxane B2-d4, 11(12)-EET-d11 at various final concentrations in a range of 701-766 nM . Each brain sample was spiked with 10 µL of standard mix prior to lipid extraction to determine oxylipins' relative abundance.

Standard curve

Standard curves were generated to facilitate the accurate quantification of each analyte in the brain samples. The concentration values of the standards were in the range for detection and followed a linear regression. Their generation using authentic standards and matching stable isotope labelled IS is useful for targeted analysis of a few analytes.

Table 8. **Lipid internal standards for oxylipins**

Internal Standard	Formal Name	Precursor m/z (Q1)	Product m/z (Q3)
PGE2-d4	Prostaglandin E2-d4	373.2	173.1
PGD2-d4	Prostaglandin D2-d4	371.2	309.2
PGF2α-d4	ProstaglandinF2α-d4	331.2	167.1
TxB2-d4	Thromboxane B2-d4	319.2	115.1
11-dehydro-TxB2-d4	11-dehydro-Thromboxane B2-d4	319.2	155.1
13(S)-HODE-d4	13S-hydroxy-9Z,11E-octadecadienoic-9,10,12,13-d4 acid	327.2	226.1
5(S)-HETE-d8	S- hydroxy- 5Z, 8Z, 10E, 14Z-eicosatetraenoic- 5, 6, 8, 9, 11, 12, 14, 15- d8 acid	325.2	281.1
12(S)-HETE-d8	12S- hydroxy- 5Z, 8Z, 10E, 14Z-eicosatetraenoic- 5, 6, 8, 9, 11, 12, 14, 15- d8 acid	339.2	197.1
15(S)-HETE-d8	15S- hydroxy- 5Z, 8Z, 11Z, 13E-eicosatetraenoic- 5, 6, 8, 9, 11, 12, 14, 15- d8 acid	380.2	141.1
20-HETE-d6	20-hydroxy-5Z,8Z,11Z,14Z-eicosatetraenoic-16,16,17,17,18,18-d6 acid	355.2	275.1
Leukotriene B4-d4	Leukotriene B4-d4	355.2	275.1
RvD1-d5	Resolvin D1-d5	357.2	313.2
11(12)-EET-d11	11(12)-epoxy-5Z,8Z,14Z-eicosatrienoic-16,16,17,17,18,18,19,19,20,20,20 acid	319.2	167.1

Table 9. **List of MRM transitions for oxylipins analysis using precursor/ product ion transitions**

Eicosanoid	Precursor m/z (Q1)	Product m/z (Q3)	Declustering Potential (V)	Collision Energy (V)	Collision Cell Exit Potential (V)
5-HETE	319.2	115.1	-55	-19	-7
8-HETE	319.2	155.1	-65	-18	-8
9-HETE	319.2	167.1	-50	-20	-9
11-HETE	319.2	167.1	-60	-19	-9
12-HETE	319.2	179.1	-65	-18	-12
15-HETE	319.2	219.1	-55	-18	-14
20-HETE	319.2	275.1	-85	-21	-11
5-HEPE	317.2	115.1	-60	-20	-10
8-HEPE	317.2	155.1	-65	-19	-8
9-HEPE	317.2	167.1	-50	-18	-12
11-HEPE	317.2	167.1	-50	-20	-13
12-HEPE	317.2	179.1	-65	-18	-8
15-HEPE	317.2	219.1	-65	-16	-10
18-HEPE	317.2	259.1	-50	-15	-11
4-HDOHE	343.2	101.1	-50	-17	-9
7-HDOHE	343.2	141.1	-50	-21	-9
8-HDOHE	343.2	189.1	-50	-19	-9
10-HDOHE	343.2	153.1	-55	-21	-5
11-HDOHE	343.2	121.1	-60	-18	-10

13-HDOHE	343.2	193.1	-55	-19	-9
14-HDOHE	343.2	205.1	-45	-17	-9
16-HDOHE	343.2	233.1	-55	-17	-10
17-HDOHE	343.2	201.1	-70	-15	-10
20-HDOHE	343.2	241.1	-55	-17	-11
9-HODE	295.2	171.1	-85	-23	-9
13-HODE	295.2	195.1	-85	-23	-7
9-HOTrE	293.2	171.1	-60	-20	-8
13-HOTrE	293.2	195.1	-70	-22	-12
5-HETrE	321.2	115.1	-70	-19	-9
15-HETrE	321.2	221.1	-70	-21	-11
9-OxoODE	293.2	185.1	-85	-23	-13
13-OxoODE	293.2	195.1	-85	-25	-12
5-OxoETE	317.2	273.1	-65	-20	-11
12-OxoETE	317.2	153.1	-75	-20	-10
15-OxoETE	317.2	113.1	-60	-22	-8
9,10-DiHOME	313.2	201.1	-80	-29	-8
12,13-DiHOME	313.2	183.1	-80	-28	-12
5,6-DiHETrE	337.2	145.1	-75	-24	-10
8,9-DiHETrE	337.2	127.1	-70	-25	-8
11,12-DiHETrE	337.2	167.1	-65	-26	-8
14,15-DiHETrE	337.2	207.1	-65	-25	-10
5,6-DiHETE	335.2	115.1	-60	-23	-8

5,15-DiHETE	335.2	115.1	-60	-21	-9
8,15-DiHETE	335.2	235.1	-65	-22	-4
14,15-DiHETE	335.2	207.1	-65	-23	-10
17,18-DiHETE	335.2	247.1	-65	-24	-8
5-HETrE	321.2	115.1	-70	-19	-9
15-HETrE	321.2	221.1	-70	-21	-11
9-OxoODE	293.2	185.1	-85	-23	-13
13-OxoODE	293.2	195.1	-85	-25	-12
5-OxoETE	317.2	273.1	-65	-20	-11
12-OxoETE	317.2	153.1	-75	-20	-10
15-OxoETE	317.2	113.1	-60	-22	-8
9,10-DiHOME	313.2	201.1	-80	-29	-8
12,13-DiHOME	313.2	183.1	-80	-28	-12
5,6-DiHETrE	337.2	145.1	-75	-24	-10
8,9-DiHETrE	337.2	127.1	-70	-25	-8
11,12-DiHETrE	337.2	167.1	-65	-26	-8
14,15-DiHETrE	337.2	207.1	-65	-25	-10
5,6-DiHETE	335.2	115.1	-60	-23	-8
5,15-DiHETE	335.2	115.1	-60	-21	-9
8,15-DiHETE	335.2	235.1	-65	-22	-4
14,15-DiHETE	335.2	207.1	-65	-23	-10
17,18-DiHETE	335.2	247.1	-65	-24	-8
RvE1	349.2	195.1	-65	-22	-10

RvD1	375.2	215.1	-55	-23	-9
RvD2	375.2	141.1	-65	-21	-11
RvD3	375.2	147.1	-65	-24	-12
RvD5	359.2	199.1	-65	-22	-17
LTB3	337.2	195.1	-65	-22	-8
LTB4	335.2	195.1	-70	-23	-11
20-carboxy LTB4	365.2	347.2	-80	-25	-8
20-hydroxy LTB4	351.2	195.1	-80	-25	-8
6-trans LTB4	335.2	195.1	-65	-23	-9
LXA4	351.2	115.1	-55	-19	-10
Mar 1	359.2	250.1	-60	-23	-11
7,17-diHDPA	361.2	263.1	-65	-20	-4
9(10)-EpOME	295.2	171.1	-80	-21	-10
12(13)-EpOME	295.2	195.1	-80	-19	-8
5(6)-EET	319.2	191.1	-60	-16	-7
8(9)-EET	319.2	167.1	-60	-15	-7
11(12)-EpETE	319.2	167.1	-60	-18	-8
8(9)-EET	319.2	167.1	-60	-15	-7
11(12)-EpETE	319.2	167.1	-60	-18	-8
14(15)-EpETE	319.2	219.1	-65	-18	-6

8(9)-EET	319.2	167.1	-60	-15	-7
11(12)-EpETE	319.2	167.1	-60	-18	-8
14(15)-EpETE	319.2	219.1	-65	-18	-6
17(18)-EpETE	317.2	127.1	-70	-18	-8
7(8)-EpDPA	343.2	113.1	-70	-15	-11
10(11)-EpDPA	343.2	153.1	-70	-18	-6
13(14)-EpDPA	343.2	193.1	-75	-16	-10
16(17)-EpDPA	343.2	233.1	-60	-16	-7
19(20)-EpDPA	343.2	241.1	-70	-18	-11
PGD1	353.2	317.2	-55	-16	-8
PGD2	351.2	271.1	-50	-22	-8
PGD3	349.2	269.1	-50	-17	-11
PGE1	353.2	317.2	-60	-18	-10
PGE2	351.2	271.1	-60	-19	-12
PGE3	349.2	269.1	-60	-17	-10
PGB2	333.2	175.1	-60	-24	-10
13,14-dihydro-15-keto PGE2	351.2	235.1	-55	-19	-13
13,14-dihydro-15-keto PGD2	351.2	207.1	-50	-25	-13
13,14-dihydro-15-keto PF2α	353.2	113.1	-55	-23	-11
11β-PGE2	351.2	271.1	-55	-23	-7
6-keto PGE1	367.2	143.1	-55	-23	-9
8-iso PGE2	351.201	271.1	-55	-21	-10

15-deoxy-Δ12,14-PGJ2	315.2	271.1	-65	-18	-8
8-iso-15-keto PGF2α	351.2	289.1	-50	-23	-12
PGF2α	353.2	309.2	-85	-24	-9
6-keto PGF1α	369.201	163.1	-75	-26	-10
Thromboxane B2	369.2	169.1	-60	-22	-12
11-dehydro Thromboxane B2	367.2	305.2	-60	-20	-10
13(S)-HODE-d4	299.5	198.1	-60	-25	-7
5(S)-HETE-d8	327.2	116.1	-55	-19	-8
12(S)-HETE-d8	327.2	184.2	-60	-20	-12
15(S)-HETE-d8	327.2	226.2	-65	-22	-11
20-HETE-d6	325.2	281.2	-70	-21	-8
Leukotriene B4-d4	339.2	197.2	-65	-21	-9
Resolvin D1-d5	380.2	141.1	-75	-18	-11
Prostaglandin E2-d4	355.2	275.3	-60	-23	-12
Prostaglandin D2-d4	357.5	275.3	-55	-23	-10
Prostaglandin F2α-d4	357.5	313.2	-80	-24	-9
Thromboxane B2-d4	373.3	173.2	-55	-22	-10

11-dehydro Thromboxane B2-d4	371.5	309.2	-55	-21	-11
11(12)-EET-d11	331.2	167.1	-65	-18	-11

2.8.5 Heatmap generation

For the generation of heatmaps, samples were averaged within their groups, and values of each analyte were converted into log10 (wet weight of brain). Heatmaps plots were plotted using the pheatmap package in R, based on lipid hierarchical clustering. In particular, a sparse set of clusters is selected given a clustering tree (dendrogram) (Langfelder *et al.*, 2008; Team, 2013). Then each cluster was subdivided into subclusters. Hierarchical clustering is a method of cluster analysis which seeks to build a hierarchy of clusters. Intensity levels were represented by a colour gradient ranging from dark blue (absent/very low levels) to red (high levels).

2.8.6 Data analysis

The raw data was exported from the Analyst software and analyzed using MultiQuant software. The limit of detection used was a signal-to-noise ratio of 5:1. Also, the peaks had at least 5 data points across the peak.

Statistical analysis was performed using Graphpad Prism 9. The normal distribution of data was determined through the Shapiro-Wilk test. The non-parametric Mann-Whitney test was applied to test for differences between variables. Data were presented as Box and Whisker plots (Tukey plots). The top and bottom edges of the whiskers represent the interquartile range (IQR) with the horizontal line inside the box, indicating the data's median. Also, the points beyond the whiskers indicate 1.5*IQR. The values are expressed as mean ± SEM unless otherwise stated. The statistical significance level was set at *= $p \leq 0.05$, **=$p<0.01$, ***=$p<0.001$, ****=$p<0.0001$.

2.9 Experimental design

The timeline for each cohort of mice, showing the order and the length of time of behavioural tasks, is illustrated in Table 9. Two male cohorts and one cohort of female mice were used for the experimental procedures in this thesis, including behavioural testing, brain dissection and lipidomic analysis or immune analysis. The difference in body weight between genotypes is presented in Chapter 3.

Table 10. Experimental design for each cohort of mice used for in vivo studies.

Experiments	**Months of the age of Cohort 1 male mice**															
	1	**2**	**3**	**4**	**5**	**6**	**7**	**8**	**9**	**10**	**11**	**12**	**13**	**14**	**15**	**16**
A. Novel Object Recognition Task				15 WT vs 15 *Alox15*$^{-/-}$			15 WT vs 15 *Alox15*$^{-/-}$			13 WT vs 15 *Alox15*$^{-/-}$			12 WT vs 14 *Alox15*$^{-/-}$		12 WT vs 12 *Alox15*$^{-/-}$	
B. Object Location Task				15 WT vs 15 *Alox15*$^{-/-}$			15 WT vs 15 *Alox15*$^{-/-}$			13 WT vs 15 *Alox15*$^{-/-}$			12 WT vs 14 *Alox15*$^{-/-}$		12 WT vs 12 *Alox15*$^{-/-}$	
C. Elevated Plus maze							15 WT vs 15 *Alox15*$^{-/-}$			13 WT vs 15 *Alox15*$^{-/-}$			12 WT vs 14 *Alox15*$^{-/-}$		12 WT vs 12 *Alox15*$^{-/-}$	
D. Brain dissection into prefrontal cortex, HPC, cerebellum																12 WT vs 11 *Alox15*$^{-/-}$
E. Targeted LC/MS/MS																12 WT vs 11 *Alox15*$^{-/-}$

Experiments	Months of the age of Cohort 2 male mice															
	1	**2**	**3**	**4**	**5**	**6**	**7**	**8**	**9**	**10**	**11**	**12**	**13**	**14**	**15**	**16**
A. Novel Object Recognition Task				14 WT vs 14 *Alox15*$^{-/-}$			14 WT vs 14 *Alox15*$^{-/-}$			14 WT vs 14 *Alox15*$^{-/-}$			14 WT vs 14 *Alox15*$^{-/-}$		14 WT vs 14 *Alox15*$^{-/-}$	
B. Object Location Task				14 WT vs 14 *Alox15*$^{-/-}$			14 WT vs 14 *Alox15*$^{-/-}$			14 WT vs 14 *Alox15*$^{-/-}$			14 WT vs 14 *Alox15*$^{-/-}$		14 WT vs 14 *Alox15*$^{-/-}$	
C. Elevated Plus maze							14 WT vs 14 *Alox15*$^{-/-}$			14 WT vs 14 *Alox15*$^{-/-}$			14 WT vs 14 *Alox15*$^{-/-}$		14 WT vs 14 *Alox15*$^{-/-}$	
D. Spontaneous alternation T maze															14 WT vs 14 *Alox15*$^{-/-}$	
E. Brain dissection																8 WT vs 10 *Alox15*$^{-/-}$
F. Immunofluorescence staining/Imaging																8 WT vs 10 *Alox15*$^{-/-}$

Experiments	**Months of the age of Cohort female mice**															
	1	**2**	**3**	**4**	**5**	**6**	**7**	**8**	**9**	**10**	**11**	**12**	**13**	**14**	**15**	**16**
A. Novel Object Recognition Task				15 WT vs 15 *Alox15*$^{-/-}$			15 WT vs 15 *Alox15*$^{-/-}$			15 WT vs 15 *Alox15*$^{-/-}$			15 WT vs 12 *Alox15*$^{-/-}$		15 WT vs 11 *Alox15*$^{-/-}$	
B. Object Location Task				15 WT vs 15 *Alox15*$^{-/-}$			15 WT vs 15 *Alox15*$^{-/-}$			15 WT vs 15 *Alox15*$^{-/-}$			15 WT vs 12 *Alox15*$^{-/-}$		15 WT vs 11 *Alox15*$^{-/-}$	
C. Elevated Plus maze							15 WT vs 15 *Alox15*$^{-/-}$			15 WT vs 15 *Alox15*$^{-/-}$			15 WT vs 12 *Alox15*$^{-/-}$		15 WT vs 11 *Alox15*$^{-/-}$	

Table 11. Brain regions weight between 12 WT and 11 *Alox15*$^{-/-}$ mice for lipidomic analysis

Mouse brain region	Weight (mg)
WT1 CORTEX	27
WT2 CORTEX	26
WT3 CORTEX	31
WT4 CORTEX	34
WT5 CORTEX	32
WT6 CORTEX	34
WT7 CORTEX	30
WT8 CORTEX	28
WT9 CORTEX	34
WT10 CORTEX	33
WT11 CORTEX	35
WT12 CORTEX	34
Alox15$^{-/-}$ 1 CORTEX	35
Alox15$^{-/-}$ 2 CORTEX	31
Alox15$^{-/-}$ 3 CORTEX	34
Alox15$^{-/-}$ 4 CORTEX	31
Alox15$^{-/-}$ 5 CORTEX	33
Alox15$^{-/-}$ 6 CORTEX	34
Alox15$^{-/-}$ 7 CORTEX	35
Alox15$^{-/-}$ 8 CORTEX	28
Alox15$^{-/-}$ 9 CORTEX	30
Alox15$^{-/-}$ 10 CORTEX	29
Alox15$^{-/-}$ 11 CORTEX	28
WT1 CEREBELLUM	31

WT2 CEREBELLUM	30
WT3 CEREBELLUM	34
WT4 CEREBELLUM	32
WT5 CEREBELLUM	33
WT6 CEREBELLUM	35
WT7 CEREBELLUM	31
WT8 CEREBELLUM	35
WT9 CEREBELLUM	34
WT10 CEREBELLUM	32
WT11 CEREBELLUM	31
WT12 CEREBELLUM	30
Alox15$^{-/-}$ 1 CEREBELLUM	34
Alox15$^{-/-}$ 2 CEREBELLUM	34
Alox15$^{-/-}$ 3 CEREBELLUM	35
Alox15$^{-/-}$ 4 CEREBELLUM	29
Alox15$^{-/-}$ 5 CEREBELLUM	31
Alox15$^{-/-}$ 6 CEREBELLUM	33
Alox15$^{-/-}$ 7 CEREBELLUM	35
Alox15$^{-/-}$ 8 CEREBELLUM	31
Alox15$^{-/-}$ 9 CEREBELLUM	35
Alox15$^{-/-}$ 10 CEREBELLUM	30
Alox15$^{-/-}$ 11 CEREBELLUM	31
WT1 HPC	31
WT2 HPC	30
WT3 HPC	33
WT4 HPC	32
WT5 HPC	30

WT6 HPC	33
WT7 HPC	30
WT8 HPC	30
WT9 HPC	31
WT10 HPC	34
WT11 HPC	30
WT12 HPC	31
Alox15$^{-/-}$ 1 HPC	29
Alox15$^{-/-}$ 2 HPC	30
Alox15$^{-/-}$ 3 HPC	33
Alox15$^{-/-}$ 4 HPC	30
Alox15$^{-/-}$ 5 HPC	32
Alox15$^{-/-}$ 6 HPC	31
Alox15$^{-/-}$ 7 HPC	32
Alox15$^{-/-}$ 8 HPC	29
Alox15$^{-/-}$ 9 HPC	28
Alox15$^{-/-}$ 10 HPC	35
Alox15$^{-/-}$ 11 HPC	34

Chapter 3:

General *Alox15*$^{-/-}$ mouse phenotype and physical characteristics

INTRODUCTION

3.1 Chapter overview

The brain naturally changes with increasing chronological age, affecting physiological, cognitive and behavioural performance over a lifetime (Peters, 2006). The purpose of this chapter is to record the general phenotype of *Alox15*$^{-/-}$mice. However, less clear is the rate of the change.

3.2 Aims and objectives

The overall aim of the chapter is to report the physical characteristics of the animal model that I will utilize throughout this thesis. I will assess the general health status of the *Alox15*$^{-/-}$ global knock-out mouse model with a particular emphasis on their phenotypic analysis:

1. Determine the biological and physiological aspects of ageing from young mice aged (4 months) to middle-aged (7-13 months) and old (15 months) *Alox15*$^{-/-}$ compared to age-matched WT mice aged 16 months, including the long-term body weight development as the food intake measurement.
2. Investigate any gender-related changes from 4 to 16 months of age.

RESULTS

i. *Alox15*$^{-/-}$ mice demonstrated significant age-dependent weight gain but no difference in total food consumption.

Body weights at 4, 7, 10, 13 and 15 months of age were analysed by a repeated measures ANOVA with age as a within subjects' factor and genotype as the between subjects' factor. The average body weight of male *Alox15*$^{-/-}$ and WT mice aged 4 months was approximately 27 g. There was no marked difference in body weight at 4 months of age (27.491 ±0.4757 vs. 27.134 ± 0.209, $P = 0.9242$) (Figure 18 A). However, *Alox15*$^{-/-}$ mice gained significantly more weight over time than age-matched WT mice aged 7 months (35.948 ±0.798 vs. 29.817 ± 0.253, $P = 0.0462$). The striking increase in body weight of *Alox15*$^{-/-}$ male mice peaked at 10 months of age relative to WT mice (44.628 ±1.176 vs. 32.703 ± 1.745, P=0.0002). A similar pattern was shown at 13 months (48.517 ±1.187 vs. 33.569 ± 2.203, P=0.0001). By 15 months, the maximum weight for a WT male mouse was 44.5 g, whereas for the *Alox15*$^{-/-}$ male mouse was 65 g (54.321 ±1.148 vs. 34.321 ± 2.321, P=0.0001). A further analysis was carried out to examine age-point differences. Significant effects of age were found on the bodyweight of male

mice (age*genotype interaction F (4, 212) = 19.4, P<0.0001). Table 11 A represents the mean body weights of male mice of both genotypes at five different time points.

Similarly, the mean weight of female *Alox15*$^{-/-}$ and WT mice aged 4 months was approximately 29 g. Although there was no difference in body weight at 4 months of age (29.980 ±0.236 vs. 28.227 ± 0.146, $P = 0.3898$), as they aged from 7 months and onwards, the significant body weight gain of *Alox15*$^{-/-}$ female mice was noticeable compared to WT (34.627 ±0.356 vs. 29.587 ± 0.240, $P = 0.0002$) (Figure 18 B). Similarly to male mice, the middle-aged and the old-aged *Alox15*$^{-/-}$ female mice were significantly heavier than the young *Alox15*$^{-/-}$ female mice (> 4 months, all $P < 0.0001$; two-way ANOVA). Specifically, they reached the peak at 10 months of age (47.807 ±0.962 vs. 33.973 ± 0.501, P=0.0001) and had increased adipocyte size compared to WT mice (Figure 18 B). Similarly, *Alox15*$^{-/-}$ female mice were significantly heavier than WT mice (56.760 ±1.041 vs. 38.087 ± 0.410, P=0.0001). By 15 months, the heaviest *Alox15*$^{-/-}$ female mouse was 68 g, compared to the WT female mouse, which was 43.2 g (59.873 ±1.762 vs. 37.727 ± 0.521, P=0.0001). Similar to the analysis in male mice, data were analysed by a two-way ANOVA with Bonferroni's multiple comparison tests revealing that there was an age*genotype interaction (F (4, 112) = 97.11, P<0.0001). As displayed in Table 11 B, the average body weights of female mice of both genotypes were reported over the five-time points.

Further examination revealed that the *Alox15*$^{-/-}$ female mice had extensive hair loss, severe bald patches, and skin lesions at 15 months of age (Figure 19 B). This excessive grooming behaviour was also observed in *Alox15*$^{-/-}$ male mice and was more pronounced.

To determine whether the body weight gain in *Alox15*$^{-/-}$ mice was due to hyperphagia, food intake was measured between groups of mice aged 15 months. There was no significant difference in the amount of food consumed over five days (120 h) between genotypes (Figure 20). Interestingly, *Alox15*$^{-/-}$ mice and WT mice ate $2.589\,g \pm 0.038\,g$ vs 2.746 ± 0.033, P=0.0824 in Day 1, respectively. A similar pattern was demonstrated for the rest days, however this did not reach significance.

A.

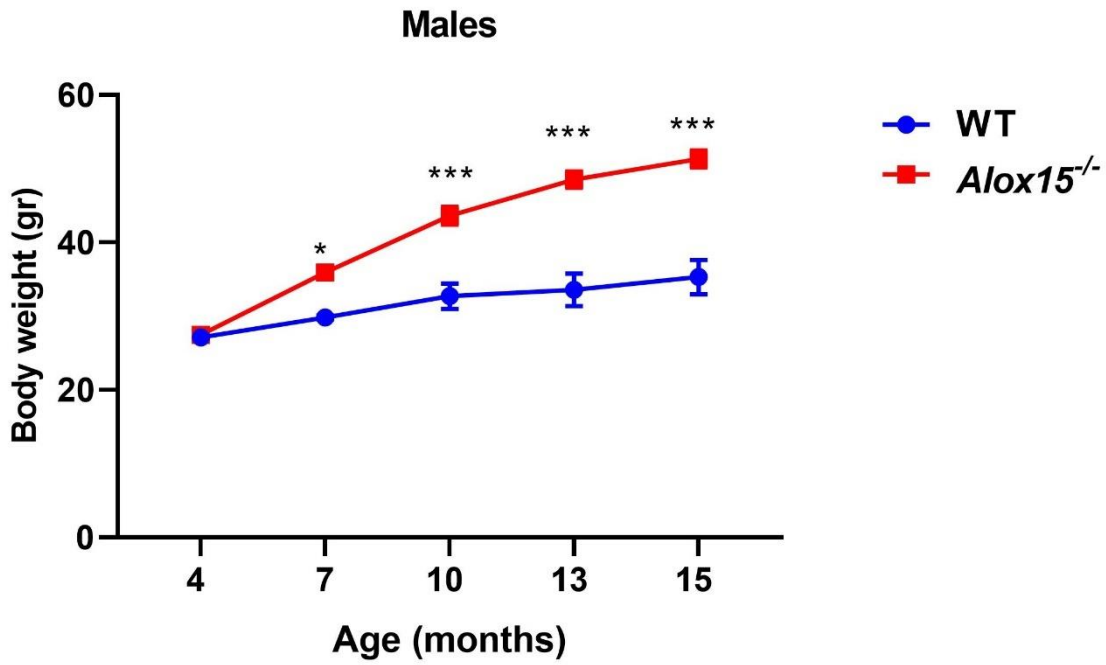

B.

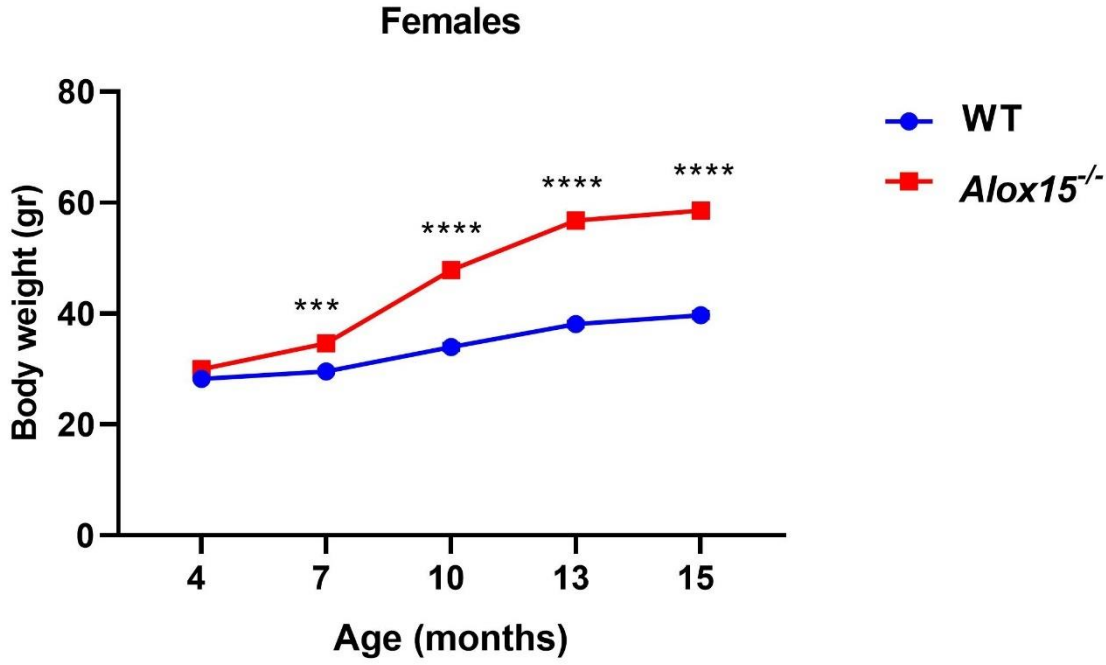

Figure 18. *Alox15*$^{-/-}$ male and female mice displayed an increased age-dependent body weight. A. Mean average weight (g) for WT and *Alox15*$^{-/-}$ male mice. B. Mean average weight (g) for WT and *Alox15*$^{-/-}$ female mice. Data were analysed by a repeated measures ANOVA with the five different age points as a within subjects' factor and genotype as the between subjects' factor and displayed as line graphs with mean ± SEM. n=29 males per genotype, n=15 females per genotype *, **, *** and **** represent $p \leq 0.05$, $p \leq 0.01$, $p \leq 0.001$ and $p \leq 0.0001$ for genotype comparisons, respectively.

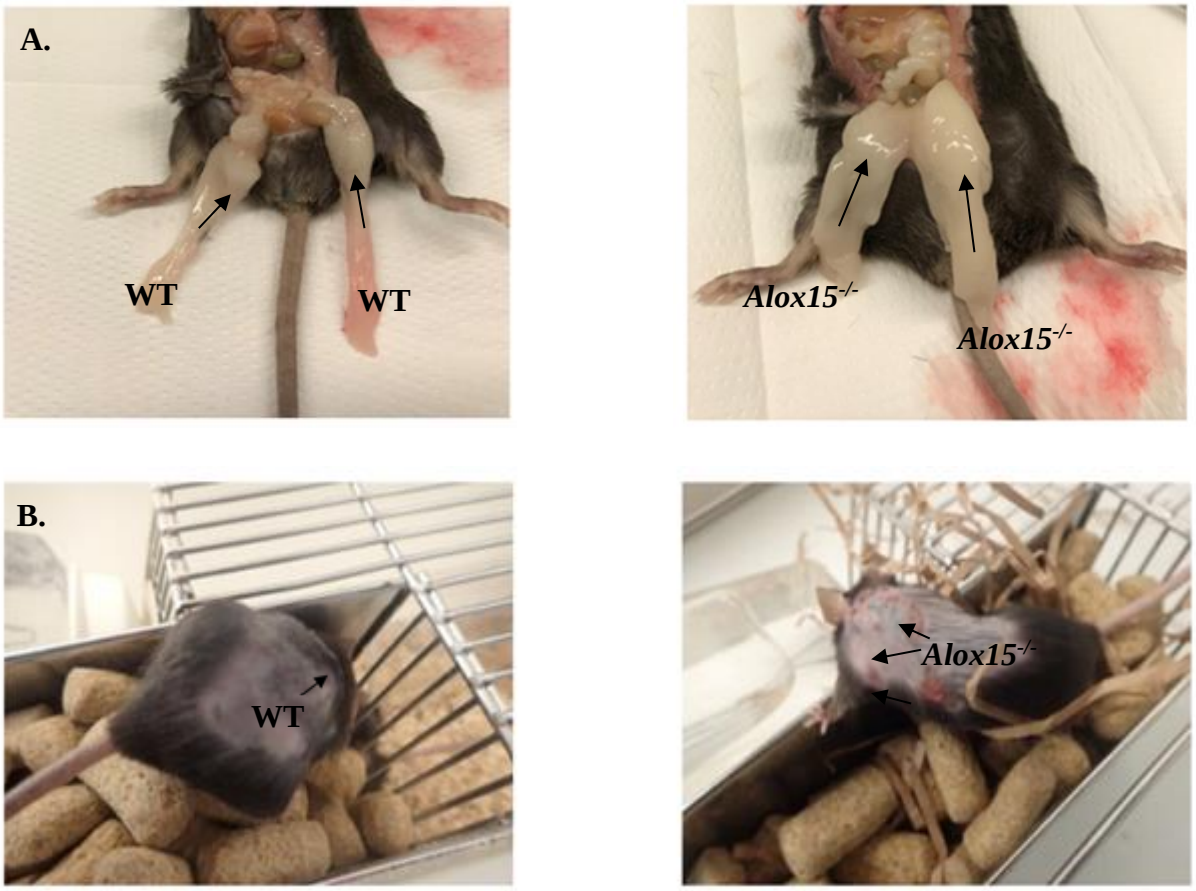

Figure 19. A. Representative pictures of WT mouse and *Alox15*$^{-/-}$ mouse at the age of 15 months, showing differences in the white adipose tissue as indicated by arrows, respectively. B. Representative pictures of WT mouse and *Alox15*$^{-/-}$ female mouse at the age of 15 months, recapitulating hair loss and excessive grooming phenotype, as indicated by arrows, respectively**.**

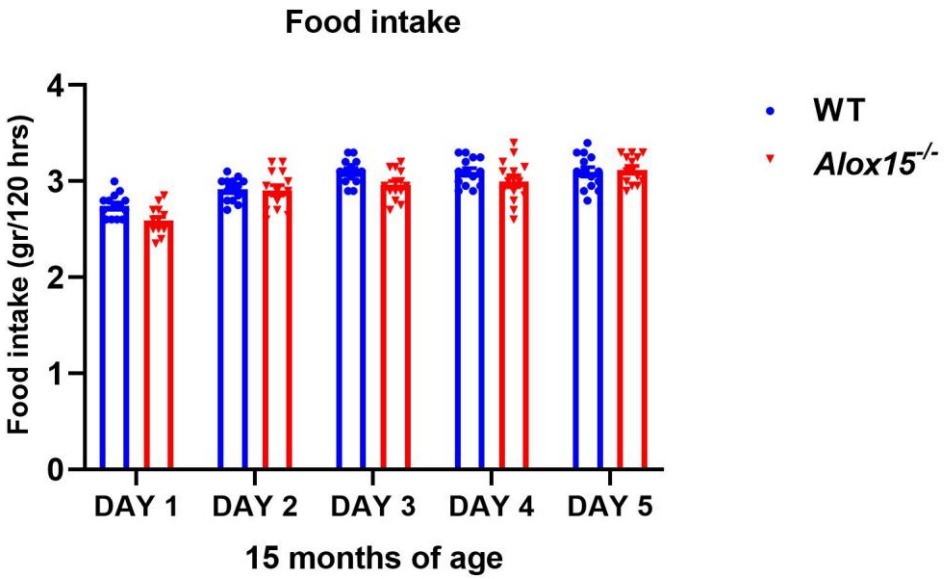

Figure 20. *Alox15*$^{-/-}$ mice displayed no significant differences in daily food intake. The amount of food was measured for a period of five days, as described in Materials and Methods. Data were analysed by a repeated measures ANOVA with the five different days points as a within subjects' factor and displayed as bar graphs with mean ± SEM. n=14 per genotype.

MALES IDs	*4 MONTHS*	*7 MONTHS*	*10 MONTHS*	*13 MONTHS*	*15 MONTHS*
WT GROUP 1 LR	26.4	31.8	34.9	38	36
WT GROUP 1 L	26.5	30.6	36.8	39	40.4
WT GROUP 1 R	26.8	30	36.7	39.8	41.4
WT GROUP 1 BLANK	28.2	30.8	32.3	40	37
WT GROUP 2 R	29	30.6	32.4	34	35
WT GROUP 2 BLANK	26.3	31.2	37.3	36	40.5
WT GROUP 2 L	26.4	29	32.9	34.7	35.8
WT GROUP 2 LR	25	30.8	35.4	33	40.7
WT GROUP 3 R	27.5	30.2	38.6	43	44.5
WT GROUP 3 BLANK	29.2	33	30.9	38	43.6
WT GROUP 3 L	26.5	30.6	41	38.4	39
WT GROUP 3 LR	27.2	30.8	37.8	38	43
WT GROUP 4 R	27.3	30.2	39.8	0	0
WT GROUP 4 L	28.7	30.5	0	0	0
WT GROUP 4 LR	28.4	30	0	0	0
WT GROUP 4 BLANK	28.7	30.4	34	35.2	38
WT GROUP 5 R	27.1	28	37.2	40.6	42
WT GROUP 5 BLANK	28.3	29.3	31.3	34.8	37.6
WT GROUP 5 L	26.2	28.8	35	41.3	42
WT GROUP 5 LR	28.9	32	36	37.9	43.1
WT GROUP 6 BLANK	26.3	29	31	35.2	38.2
WT GROUP 6 L	25.8	27.2	34.3	36.1	37.4
WT GROUP 6 R	27	28.5	35.2	38.7	38.9
WT GROUP 6 LR	25.7	29	36.5	40.8	43.2
WT GROUP 6 LL	27.4	28.9	33.3	35.8	37.6
WT GROUP 7 BLANK	26.5	28.7	35	37	37.2
WT GROUP 7 L	25.7	28	34	35	36.5

Table 12 A. Mean body weights in male WT and *Alox15*$^{-/-}$ mice.

WT GROUP 7 LR	26.9	29	32.8	35	35.3
WT GROUP 7 R	27	27.8	36	38.2	40.4

MALES IDs	4 MONTHS	7 MONTHS	10 MONTHS	13 MONTHS	15 MONTHS
Alox15$^{-/-}$ GROUP 1 LR	29.5	42	50.9	51.7	56
Alox15$^{-/-}$ GROUP 1 L	30.1	41.6	48.9	63.7	65
Alox15$^{-/-}$ GROUP 1 R	29	41.2	58.4	52.5	54
Alox15$^{-/-}$ GROUP 1 BLANK	31.2	41.4	51.5	52.8	53
Alox15$^{-/-}$ GROUP 2 R	29.6	36.4	45	51.5	51.7
Alox15$^{-/-}$ GROUP 2 BLANK	30.2	37.2	49.3	0	0
Alox15$^{-/-}$ GROUP 2 L	28.7	39.6	51	53.5	58
Alox15$^{-/-}$ GROUP 2 LR	27.3	37.2	49.8	50.1	56
Alox15$^{-/-}$ GROUP 3 R	26.9	40.2	45	50	48.9
Alox15$^{-/-}$ GROUP 3 BLANK	27.3	36	49.5	45	61.8
Alox15$^{-/-}$ GROUP 3 L	30.45	40	37	54.5	53
Alox15$^{-/-}$ GROUP 3 LR	29.4	42	48.4	50	51.9
Alox15$^{-/-}$ GROUP 4 R	29.8	36.5	39.8	52.5	49.7
Alox15$^{-/-}$ GROUP 4 L	30.3	39	46.8	54	0
Alox15$^{-/-}$ GROUP 4 LR	27.2	37.9	49.7	53.3	57
Alox15$^{-/-}$ GROUP 4 BLANK	25.3	32.3	35.8	39	0
Alox15$^{-/-}$ GROUP 5 R	23.5	29.1	37.5	41	41.3
Alox15$^{-/-}$ GROUP 5 BLANK	26.5	31	33.4	39.9	41.1
Alox15$^{-/-}$ GROUP 5 L	27.6	30.8	38.5	41.8	42.5
Alox15$^{-/-}$ GROUP 5 LR	26.5	29.5	36.7	45.9	46.7
Alox15$^{-/-}$ GROUP 6 BLANK	23	32.4	39.3	49.9	53.1
Alox15$^{-/-}$ GROUP 6 L	25.3	27.3	36.7	40	49.1
Alox15$^{-/-}$ GROUP 6 R	25.8	33.5	37.2	46	47.5
Alox15$^{-/-}$ GROUP 6 LR	20.5	31	38.4	40	60.2
Alox15$^{-/-}$ GROUP 6 LL	27.1	32.6	40.1	48.8	49.9
Alox15$^{-/-}$ GROUP 7 BLANK	24.9	34.3	41.6	49.8	51.6

Alox15$^{-/-}$ GROUP 7 L	26.4	37.1	39.8	42.6	44.9
Alox15$^{-/-}$ GROUP 7 LR	30.6	37.8	50.1	55	56.8
Alox15$^{-/-}$ GROUP 7 R	27.3	35.6	38.9	48.4	49.5

Table 12 B. Mean body weight values in female 15 WT and 15 *Alox15*$^{-/-}$ mice.

FEMALES IDs	*4 MONTHS*	*7 MONTHS*	*10 MONTHS*	*13 MONTHS*	*15 MONTHS*
Alox15$^{-/-}$ *GROUP 1 LR*	29.4	31.7	39.9	0	0
Alox15$^{-/-}$ *GROUP 1 L*	31	34.8	47.6	59.8	64.5
Alox15$^{-/-}$ *GROUP 1 R*	28.8	33.2	53	58.7	62.3
Alox15$^{-/-}$ *GROUP 1 BLANK*	31.3	36	52.4	62.3	65.4
Alox15$^{-/-}$ *GROUP 2 R*	30.6	34.4	48.4	54.5	0
Alox15$^{-/-}$ *GROUP 2 BLANK*	30.5	36.7	49.6	0	0
Alox15$^{-/-}$ *GROUP 2 L*	29.2	31	51.3	57.2	59.6
Alox15$^{-/-}$ *GROUP 2 LR*	30.3	35	49.6	53.2	54.2
Alox15$^{-/-}$ *GROUP 3 R*	29.2	33.5	46.3	54.5	56.4
Alox15$^{-/-}$ *GROUP 3 BLANK*	28.4	33.2	49.5	66.8	68
Alox15$^{-/-}$ *GROUP 3 L*	29.4	34.5	44.3	57.8	59
Alox15$^{-/-}$ *GROUP 3 LR*	30.2	33.5	47.5	55.9	57.6
Alox15$^{-/-}$ *GROUP 4 R*	31.5	33.5	41.3	0	0
Alox15$^{-/-}$ *GROUP 4 L*	30.1	35.4	46.7	54.3	55.2
Alox15$^{-/-}$ *GROUP 4 LR*	29.8	33.9	49.7	57.5	58.2

FEMALES IDs	*4 MONTHS*	*7 MONTHS*	*10 MONTHS*	*13 MONTHS*	*15 MONTHS*
WT GROUP 1 LR	29	29.8	32.5	37.7	38
WT GROUP 1 L	27.6	28.8	33	39.2	40.5
WT GROUP 1 R	28.6	31	32.7	38.2	42
WT GROUP 1 BLANK	29	31.3	34.4	40.5	40
WT GROUP 2 R	27.5	28.2	35.6	39.6	40.2
WT GROUP 2 BLANK	28.3	29	36.8	40.2	42.2
WT GROUP 2 L	27.4	29.2	33.5	35.5	37
WT GROUP 2 LR	28.3	29	35.1	38	39.7
WT GROUP 3 R	27.9	29	37.2	39.6	43.2
WT GROUP 3 BLANK	28.2	30.4	31.8	37.5	41.5
WT GROUP 3 L	27.7	28.6	36.4	39	40
WT GROUP 3 LR	29.1	30.7	33.8	37.3	39.6
WT GROUP 4 R	28.6	32.4	34.2	37	38.4
WT GROUP 4 L	27.8	29	30.9	36.6	37
WT GROUP 4 LR	28.4	29.8	31.7	35.4	36.6

ii. *Alox15*$^{-/-}$ mice showed markedly age-dependent locomotor activity.

Next locomotor activity concerning the distance that the mice travelled at 4, 7, 10, 13 and 15 months of age was analysed by a repeated measures ANOVA with age as a within subjects' factor and genotype as the between subjects' factor when tested in the open field. The average distance moved of *Alox15*$^{-/-}$ and WT mice aged 4 months was approximately 3800 cm and the difference reached statistical significance (4235.91 ±192.4 vs. 3695.63± 307.34, P = 0.0112) (Figure 21). Furthermore, *Alox15*$^{-/-}$ mice travelled significantly shorter distances than the youngest to middle-aged group. In particular, a two-way ANOVA analysed the overall locomotor activity from the five different time stages with Bonferroni's multiple comparison tests revealing that *Alox15*$^{-/-}$ male mice demonstrated a significant effect of age on distance travelled ($F(4, 224) = 11.61$, $P=0.0016$).

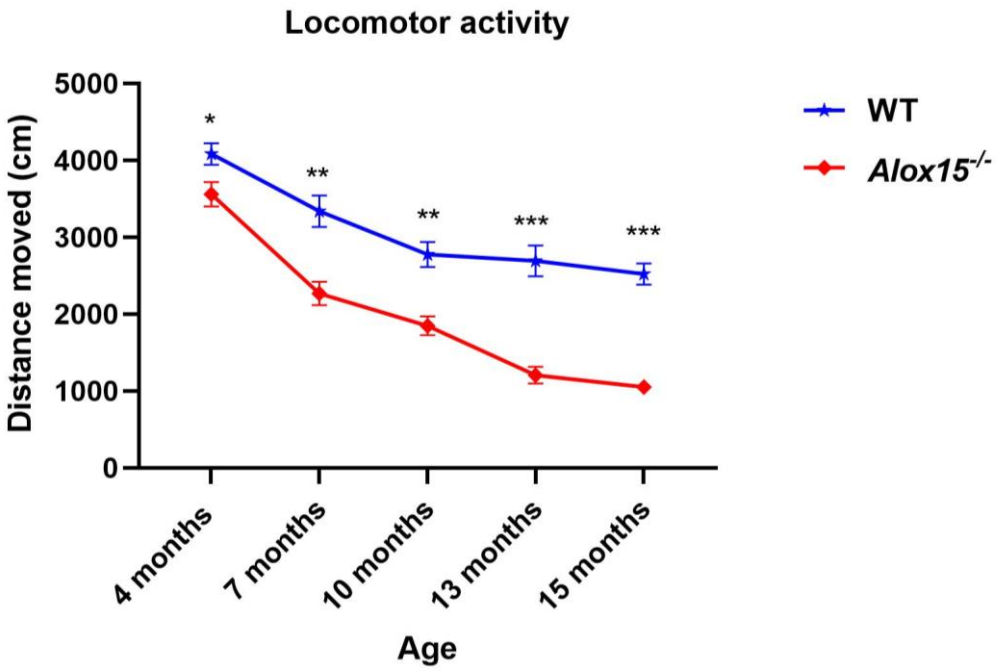

Figure 21. Locomotor activity *Alox15*$^{-/-}$ mice displayed a significant effect of age on the distance travelled when tested in the open field. Mean average distance moved (cm) for WT and *Alox15*$^{-/-}$ mice. Data were analysed by a repeated measures ANOVA with the five different age points as a within subjects' factor and genotype as the between subjects' factor and displayed as line graphs with mean ± SEM. n=29 males per genotype, n=15 females per genotype *, **, *** and **** represent $p\leq0.05$, $p\leq0.01$, $p\leq0.001$ and $p\leq0.0001$ for genotype comparisons, respectively

iii. A significant proportion of *Alox15*$^{-/-}$ female mice developed splenomegaly with ageing.

Furthermore, female *Alox15*$^{-/-}$ mice observed a distinct mortality rate. At 15 months of age, *Alox15*$^{-/-}$ mice examination revealed the development of mild splenomegaly with ageing compared to age-matched WT mice. Consequently, the spleens of both groups were harvested, and distinct changes such as the weight and the size of the *Alox15*$^{-/-}$ female mice spleen compared to WT female mice were observed. The results showed a significant increase in spleen weight in *Alox15*$^{-/-}$ female mice compared to WT mice, as displayed in Figure 22 (85.70 ±4.527 vs. 181.7 ± 3.513, P=0.0079).

A.

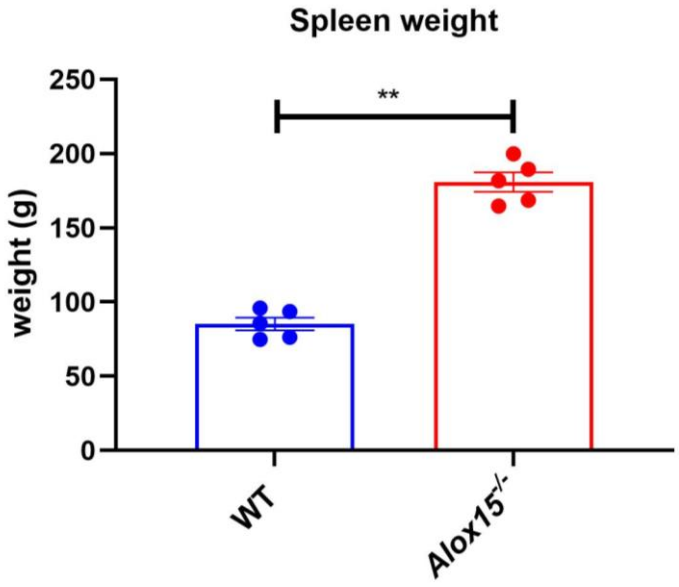

B.

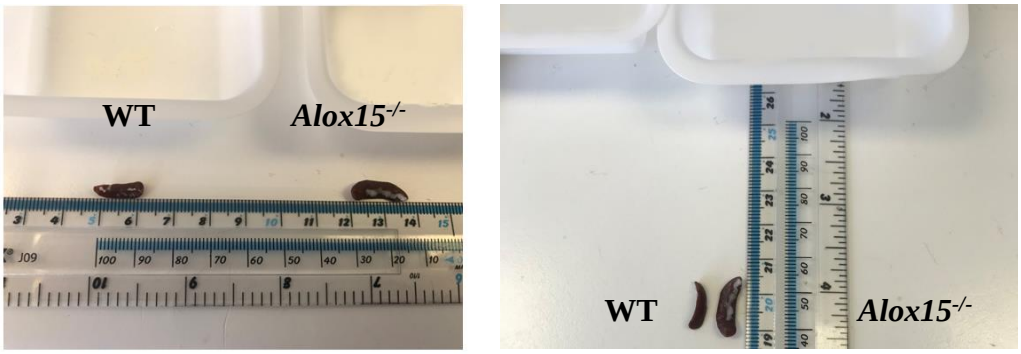

Figure 22. A. *Alox15*$^{-/-}$ female mice displayed an increased spleen weight. A. Mean average spleen weight (g) for WT and *Alox15*$^{-/-}$ female mice. Each dot represents an individual mouse. Data were analysed using Mann- the Whitney non-parametric U test and shown on Tukey box plots with mean ± S.E.M. WT (n=5) and *Alox15*$^{-/-}$ (n=5) female mice, 15 months of age *, **, *** and **** represent p≤0.05, p≤0.01, p≤0.001 and p≤0.0001 for genotype comparisons, respectively. **B. Representative spleens of 15-month-old *Alox15*$^{-/-}$ and WT female mice, respectively.**

DISCUSSION

This chapter recorded the general health of young and middle-aged to old *Alox15*$^{-/-}$ mice relative to age-matched control WT mice. The *Alox15* mouse model revealed age-related physiological changes throughout this thesis.

An important physical characteristic reported in this chapter was the age-related increase in body weight. It was observed that there was a significant effect of age on the bodyweight of both *Alox15*$^{-/-}$ male and female mice compared to age and gender-matched WT mice. Notably, *Alox15*$^{-/-}$ mice displayed a gradual increase in weight gain over time than WT mice. The current findings for WT (C57BL6) mice generally support the previous results and report that ageing from young to middle and old age induces increased body weight (Halloran *et al.*, 2002; Shoji *et al.*, 2016). Although this metabolic phenotype has not been reported previously, this chapter proposes that the genetic deletion of the *Alox15* may be involved in metabolic pathways, attributable to the role of *Alox15* in regulating fat metabolism in the brain. In addition, no hyperphagia was observed between the two groups of mice at 15 months. Although an examination of single food consumption at 15 months of age was measured, conclusions about other contributing factors related to this phenotype cannot be drawn. These mice over-ate and gained weight when aged 7 months when this phenotype initially had a profound effect. This suggests that the source of fat storage in *Alox15*$^{-/-}$ mice may also be due to overeating over their lifetime.

Studies have shown that significant differences in body weight over time are positively associated with decreased survival rates (Reis *et al.*, 2009). This study reported a slight increase in the death rate in aged *Alox15*$^{-/-}$ female mice, but the reason remains unclear. However, previously published works by Middleton *et al.*, 2006, and Taylor *et al., 2012* noted a distinct increase in the mortality rate of *Alox15*$^{-/-}$ mice as they aged compared to WT mice. After a proper examination of *Alox15*$^{-/-}$ mice, the scientists investigated varying degrees of splenomegaly with 100% penetrance compared to WT mice, and they concluded that mortality was associated with increasingly severe splenomegaly. Similarly, these findings were generally consistent with this present study; mild splenomegaly in the absence of *Alox15* was confirmed. It is suggested that the early mortality in *Alox15*$^{-/-}$ mice might be linked to mild splenomegaly. Another striking phenotype of the *Alox15* mouse was the gradual increase in grooming behaviour which was noticeable at 10 months of age and onwards. Mainly at 15 months of age, the *Alox15*$^{-/-}$ female mice displayed excessive grooming behaviour such as extensive hair loss, skin inflammation, and lesion formation resulting in a pathological grooming phenotype.

Collectively, the findings in this study are consistent with a study led by Kim *et al*, which demonstrates the role of *Alox15* in skin inflammation. Mice with *Alox15* deficiency resulted in dorsal skin defects and hair follicle-derived cell loss in adult mice at 16 weeks old. Histopathological analysis of these mice showed increased indices of inflammation, and the dermal adipocytes were abnormally differentiated into myofibroblasts. These data suggest that proinflammatory signals from *Alox15*-deficient dermal adipocytes resulted in abnormal cell types of differentiation and hair follicle cycle defects (Kim *et al.*, 2018).

The next chapter will focus on the role of the *Alox15* mouse model in normal brain function by utilizing well-validated behavioural tasks.

Chapter 4:

Alox15$^{-/-}$ mice manifested spatial memory deficits along with increased anxiety-like behaviour

INTRODUCTION

4.1 Chapter Overview

The ageing brain is associated with a progressive decline of structural, cognitive and physiological functions leading to increased susceptibility to neuronal network changes and the development of neurodegenerative diseases (Peters, 2006; Lopez-Otin *et al.*, 2013). As described in Chapter 1, it is characterized by an acceleration of behavioural and cognitive deficits, including changes in locomotor activity, memory consolidation and anxiety-like behaviour, which are evident even without overt neurodegeneration (Puigoriol-Illamola *et al.*, 2020).

Here, this chapter will focus on the effects of the *Alox15*$^{-/-}$ mice on normal cognition and behaviour, including recognition, spatial memory and working memory performances. However, relatively little is known about the role of the *Alox15* enzyme in normal cognitive function and anxiety-like behaviour and whether normal ageing may interact with its gene deletion. An *Alox15*$^{-/-}$ global knock-out mouse model will be used to address this issue. The following sections will demonstrate the age-related behavioural differences and gender changes resulting from the comparisons between young adult mice (4 months of age) and middle-aged (7-13 months of age) to old mice (15 months of age). This study's experimental strategy will use highly validated behavioural assays such as NOR, OLT, EPM to assess cognitive and emotional behaviours compared with age and gender-matched WT mice.

This behavioural approach will be used to characterize the phenotypes of this knock-out mouse model, allowing significant results from a combined cohort of male mice (Cohort 1,2) as well as another cohort of female mice tested through the interpretation of behavioural outcomes that are assessed with various paradigms (Crawley, 2008).

4.2 Aims and objectives

The goal of this study is to investigate the role of the *Alox15* pathway through gradually cognitive changes that occur during the normal ageing process in mice:

1. A selected set of behavioural assays and phenotypes will facilitate understanding the effects of age and gender on mouse behaviour.

2. The memory will be assessed from 4 to 15 months, but the anxiety-related phenotype will be evaluated from 7 to 15 months relative to age-matched WT mice.

RESULTS

4.3 EXPERIMENT 1: NOR

i. *Alox15*$^{-/-}$ mice displayed a trend toward decreased discrimination ratio compared to WT mice aged 15 months

WT and *Alox15*$^{-/-}$ mice were examined at five different time points to examine any age-related recognition memory changes. In the following sections, the analysis focuses on data generated from the 4, 7, 10, 13 and 15 months of age, between 26 WT and 29 *Alox15*$^{-/-}$ male mice. Starting from the last time point, the findings were as follows:

Habituation Phase – 15 months of age: The mice were individually habituated to the apparatus two consecutive days before performing the experiment. Mainly the mice were placed in the centre of the maze to explore the arena for 10 mins freely. Thus, graphs have been generated using the distance moved from the centre point of the arena and the velocity of each mouse during Day 1 and repeated for Day 2 of the Habituation Phase (HP). Analysis by one-way repeated measures ANOVA indicated that *Alox15*$^{-/-}$ mice aged 15 months had a statistically significant decrease in locomotor activity concerning the distance they moved and their speed compared to WT control mice (P= <0.0001, Figure 22). In addition, the arena can be subdivided into two spatial zones, the inner zone, which is the centre of the arena and the outer zone, which includes the four corners. The analysis of these data showed that the aged *Alox15*$^{-/-}$ mice spent significantly less time in the centre of the arena than WT mice during both days of the HP (P= <0.0001). These data regarding 'the two zones transition', inner and outer zone for Day 1 and 2 of HP are shown in Figure 23.

Recognition memory – Sample Phase - 15 months of age: Following the HP process, mice were placed in the centre of the apparatus and exposed to two identical copies of sample object A (familiar objects) during the Sample Phase (SP). Specifically, mice were allowed to explore the identical objects for 10 mins during SP 1 before being removed from the maze for a 10-min delay spent in their holding cages. During SP 2, mice were replaced in the maze to explore the same objects for 10 mins before being returned to their holding cages. As demonstrated in Figure 24 A, *Alox15*$^{-/-}$ mice spent significantly less time in the center of the arena than WT mice during SP (P=0.0001) and also, *Alox15*$^{-/-}$ mice interacted markedly less with the identical objects compared to WT mice during the two sequential sample exposures, as illustrated in Figure 24 B (P=0.0002, P=0.0008).

Recognition memory – Test Phase - 15 months of age: During the test phase (TP), one of the familiar objects from SP was replaced with a novel item. Figure 25 A, D demonstrated that *Alox15*$^{-/-}$ male mice spent significantly less time in the centre of the arena and the distance they moved compared to WT mice (P=0.0001). Inspection of these data showed that *Alox15*$^{-/-}$ mice appeared hypoactive, as demonstrated by a significantly decreased locomotor activity.

Next, *Alox15*$^{-/-}$ mice spent significantly less contact time with the novel object, indicating a lack of novel object preference during TP (P=0.0091, Figure 25 B). The DR was calculated to ensure that the experiment was sensitive to differences between the genotypes. DR reflects the preferential exploration allocated to a novel item compared to the total time spent on both objects by measuring the recognition memory sensitivity. Inspection of Figure 25 C shows that *Alox15*$^{-/-}$ male mice could discriminate between the novel and familiar objects as WT male mice. Additionally, one sample non-parametric U-test confirmed that the novelty preference of *Alox15*$^{-/-}$ and WT mice were significantly above chance (DR data, 0.582±0.035 vs 0.655±0.018, P=0.0433 vs, P=0.0039, respectively).

Recognition memory – Test Phase – 4-15 months of age: The above results were presented at the last time stage, which was 15 months; however, more tests were conducted on the previous age-points. The parameters analysed were the locomotor activity, the contact time with the novel object and DR. The middle-aged *Alox15*$^{-/-}$ male mice behaved similarly to old mice and could discriminate significantly above chance. Also, *Alox15*$^{-/-}$ mice showed a lower preference for the novel object than WT mice, as shown in Figures 26 - 28. Conversely, young *Alox15*$^{-/-}$ mice demonstrated no significant difference in the contact time with the novel object compared to WT mice (Figure 29).

Collectively DR data – 4-15 months of age: Taken together the interaction with the familiar and novel objects converted into the analyses of the DR data from the five different time points, it was noticeable that *Alox15*$^{-/-}$ male mice did not display any statistically significant difference in the DR compared to age-matched WT male mice. The interaction between age and genotype was not significant as analysed by mixed-effects repeated measures ANOVA with Bonferroni's multiple comparison tests in *Alox15*$^{-/-}$ and WT male mice (13 months: 0.53±0.033 vs 0.64±0.019, 10 months: 0.55 ±0.046 vs 0.64±0.022, 7 months: 0.61±0.044 vs 0.71±0.016, 4 months: 0.67±0.024 vs 0.752± 0.019, respectively). Overall, there was no main effect of age [F (4, 212) = 0.1246, P=0.9735 (Figure 30 A)].

Similarly, a summary of the data analyses of the DR measurements from the same five age-points illustrated that *Alox15*$^{-/-}$ female mice showed a trend towards a decline in recognition memory compared to age-matched WT female mice, but these differences did not reach

statistical significance (Figure 30 B). A further analysis was also performed by two-way ANOVA, revealing that there was no main effect of age [F (4, 110) = 0.6487, P= 0.6284] in female mice.

- **Habituation Phase: Time point – 15 months of age**

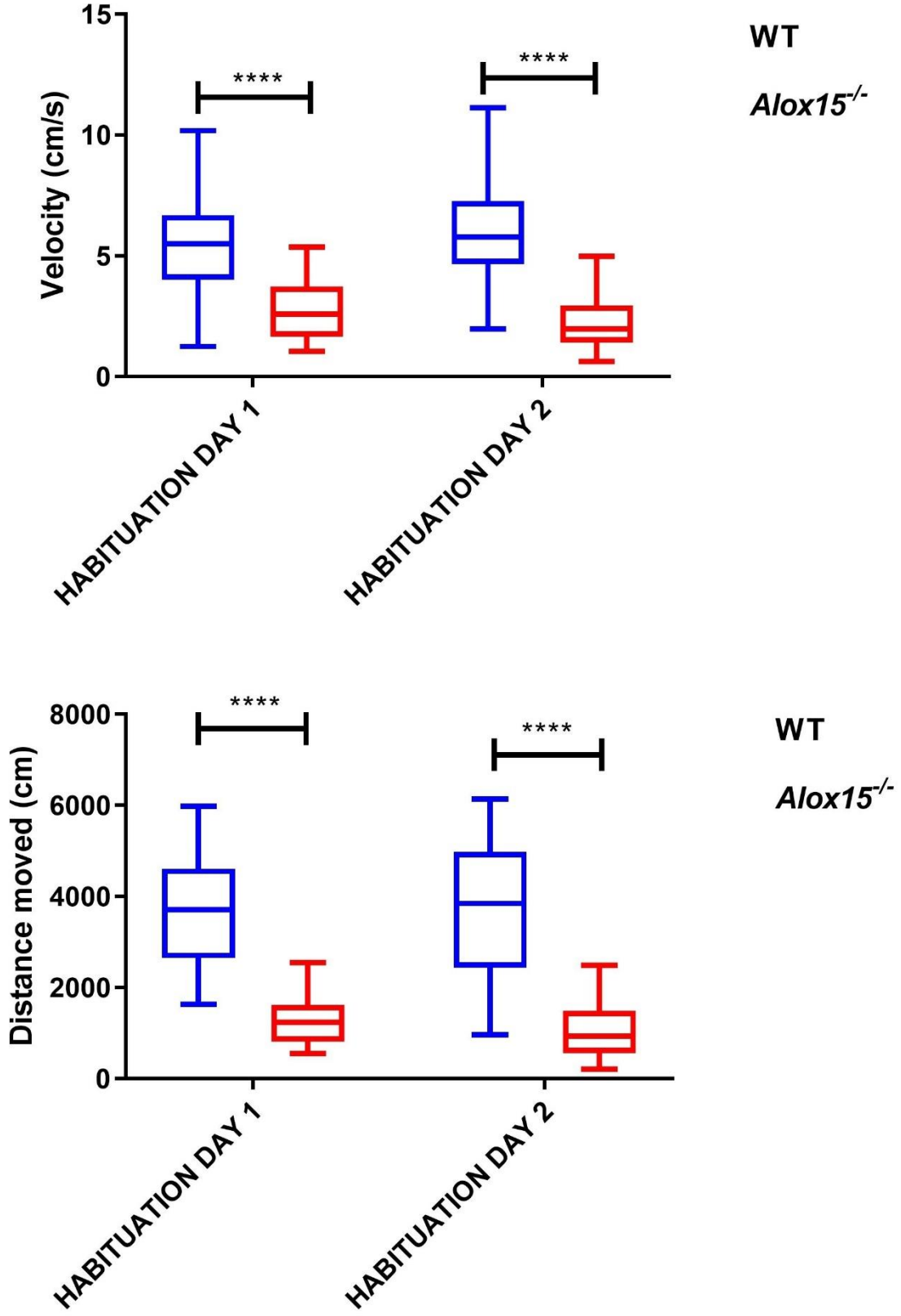

Figure 22. *Alox15*$^{-/-}$ male mice displayed significant decrease in the mean velocity and mean distance (cm) travelled from the centre of the arena during Day 1 and Day 2 of HP. Data were analysed by a repeated measures ANOVA with the habituation days as a within subjects' factor and genotype as the between subjects' factor and displayed as Tukey box plots with mean ± S.E.M. n=26 per genotype *, **, *** and **** represent $p \leq 0.05$, $p \leq 0.01$, $p \leq 0.001$ and $p \leq 0.0001$ for genotype comparisons, respectively.

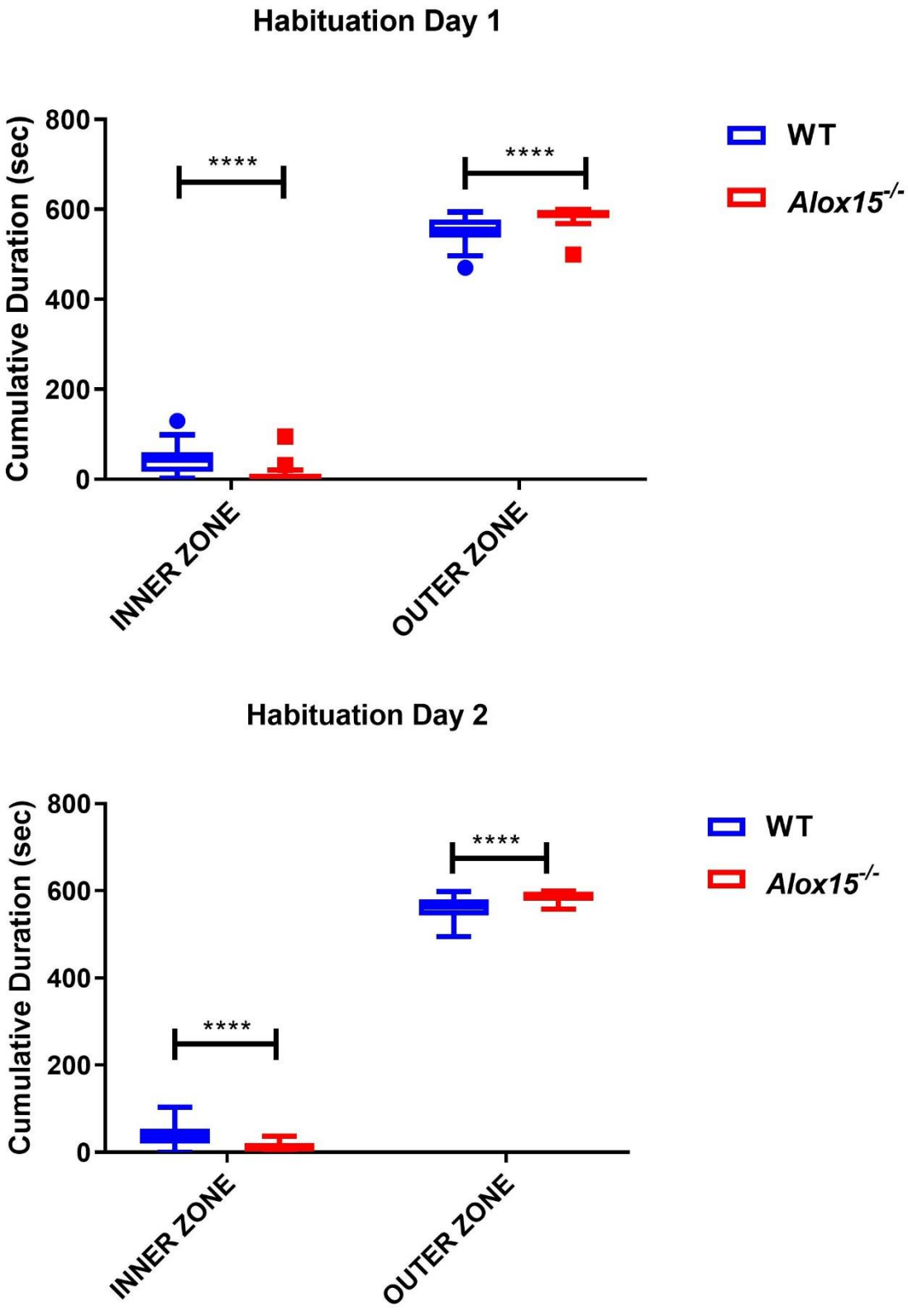

Figure 23. *Alox15*$^{-/-}$ male mice spent significantly less time in the center of the arena during Day 1 and Day 2 of HP. Data were analysed by a repeated measures ANOVA with the zones as a within subjects' factor and genotype as the between subjects' factor and displayed as Tukey box plots with mean ± S.E.M. n=26 per genotype *, **, *** and **** represent $p \leq 0.05$, $p \leq 0.01$, $p \leq 0.001$ and $p \leq 0.0001$ for genotype comparisons, respectively.

- **Sample Phase: Time point – 15 months of age**

A.

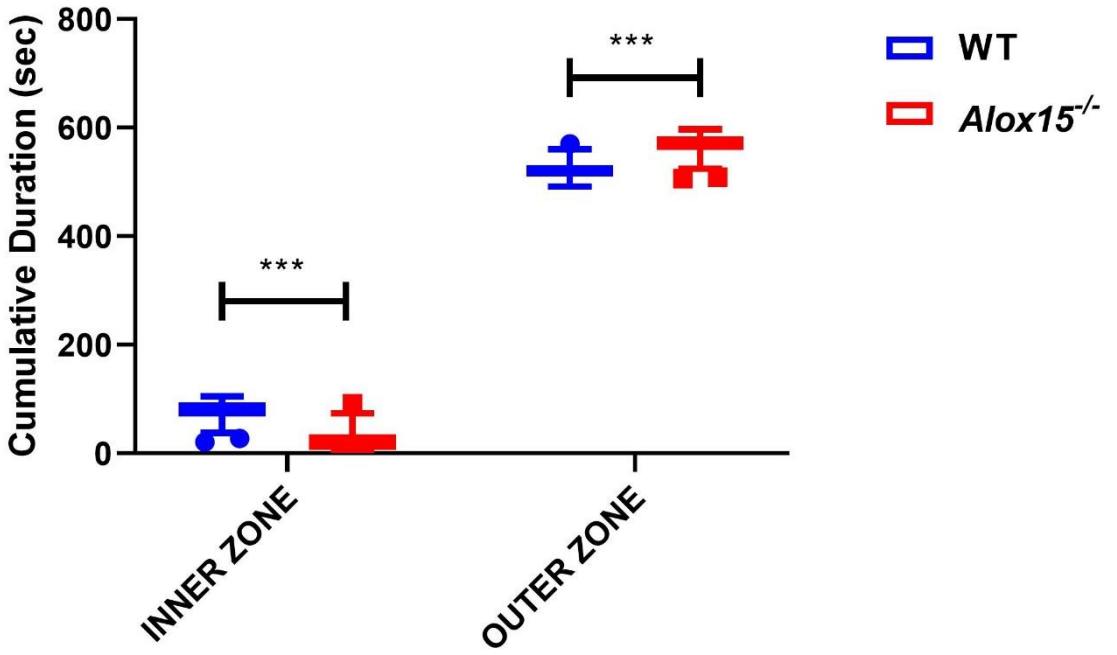

B.

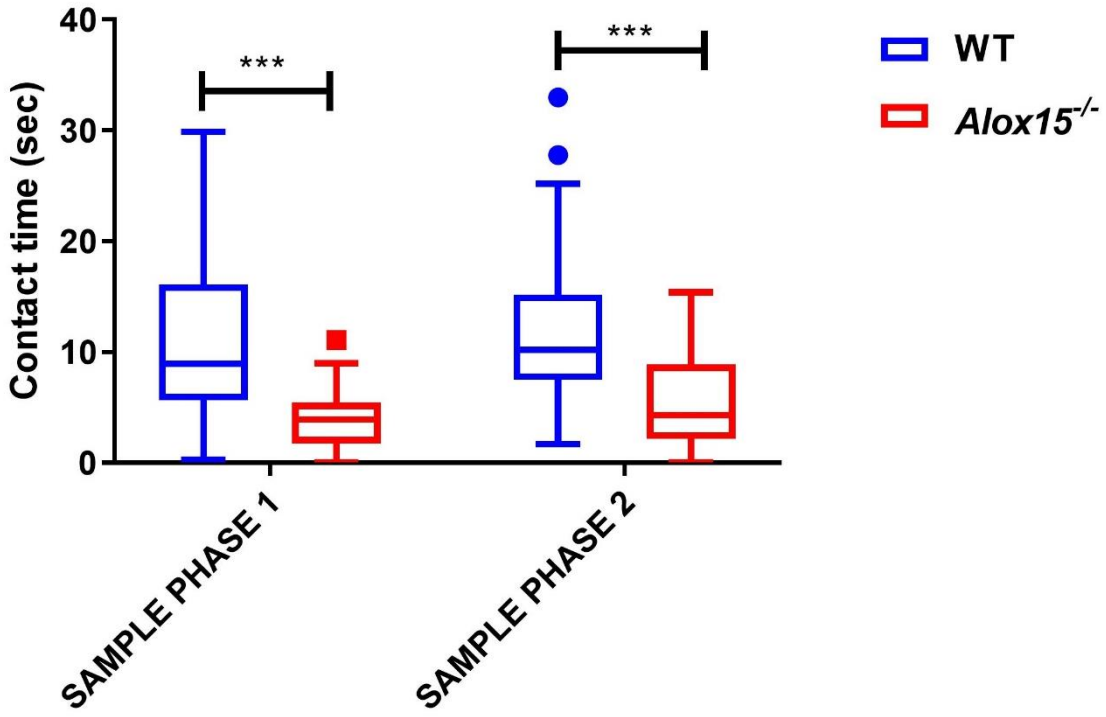

Figure 24. A. *Alox15*$^{-/-}$ male mice spent significantly less time in the center of the arena during Sample Phase. B. *Alox15*$^{-/-}$ male mice displayed significantly less mean contact time (sec) during the two Sample Phases. *Alox15*$^{-/-}$ male mice interacted with the objects significantly less compared to WT mice. The interaction between object and genotype reached statistical significance in both S.P. Data were analysed by a repeated measures ANOVA with the sample phases as a within subjects' factor and genotype as the between subjects' factor and displayed as Tukey box plots with mean ± S.E.M. n=26 per genotype *, **, *** and **** represent $p \leq 0.05$, $p \leq 0.01$, $p \leq 0.001$ and $p \leq 0.0001$ for genotype comparisons, respectively.

- **Test Phase: Time point – 15 months of age**

A.

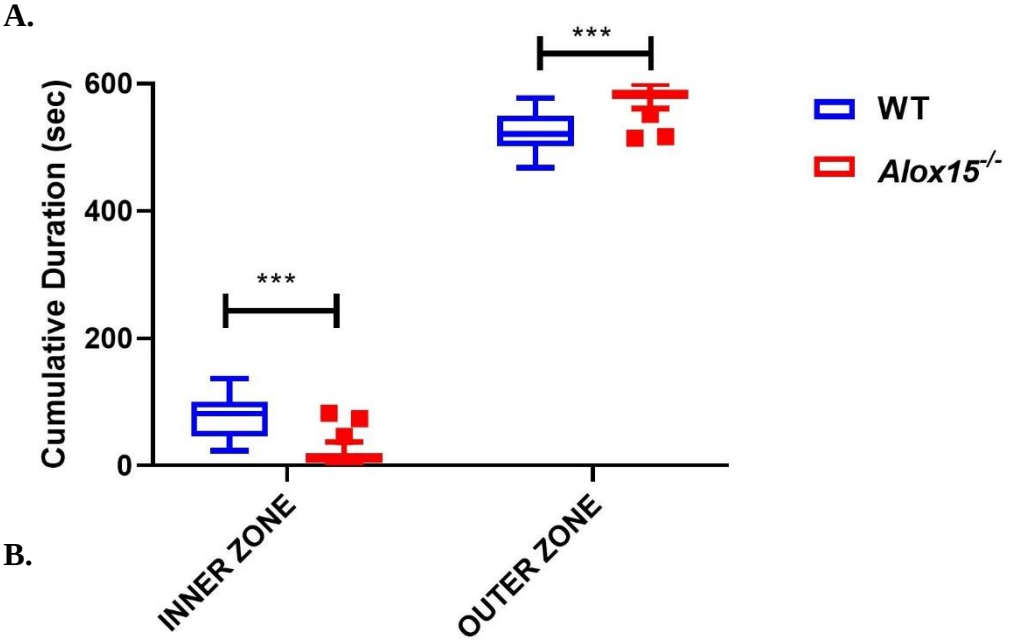

B.

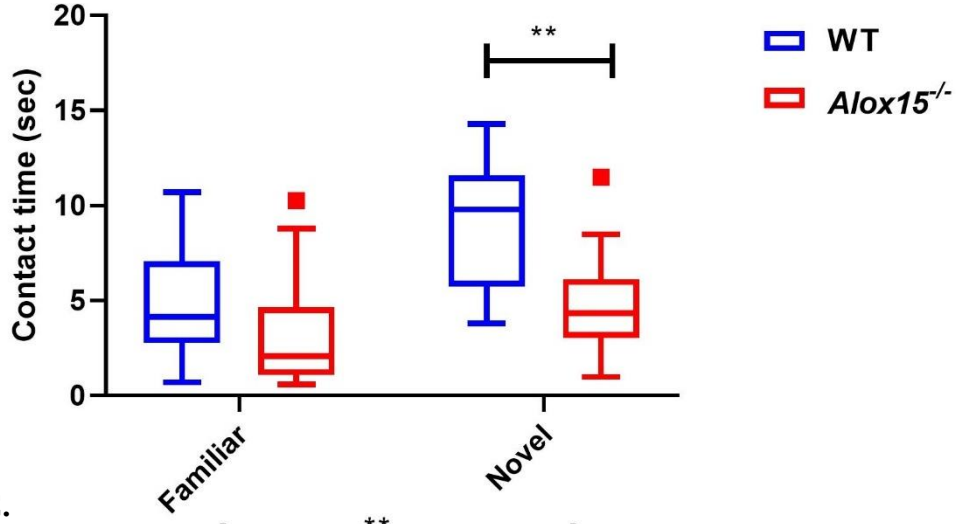

C.

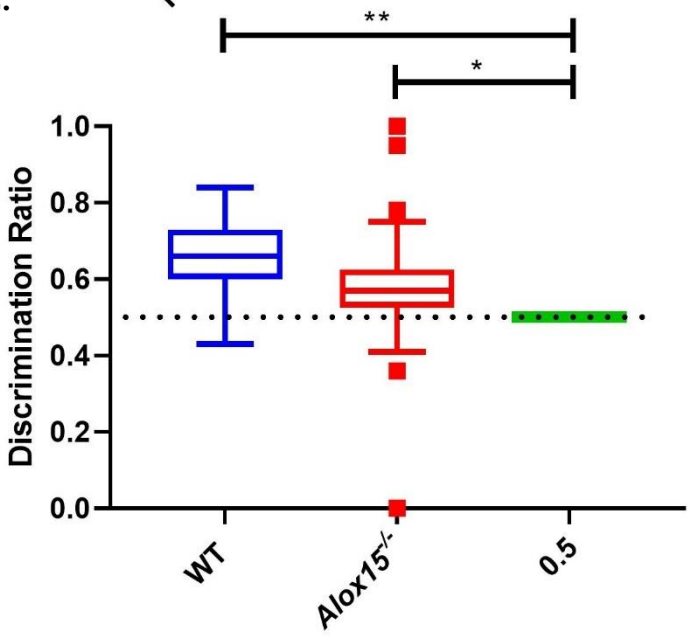

D.

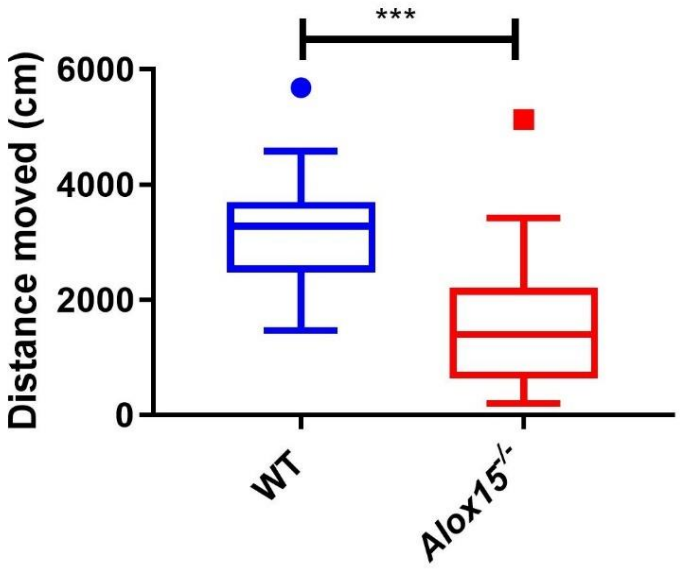

Figure 25. A. *Alox15*$^{-/-}$ male mice, aged 15 months of age, spent significantly less time in the center of the arena during TP. B. *Alox15*$^{-/-}$ male mice spent significantly less contact time (sec) with the novel object. C. *Alox15*$^{-/-}$ male mice were able to discriminate between the novel and familiar objects. Also the performance of both WT and *Alox15*$^{-/-}$ mice was significantly above chance 0.5. D. *Alox15*$^{-/-}$ male mice displayed significantly decreased mean distance (cm) travelled from the centre of the arena. Data were analysed by a repeated measures ANOVA with the zones as a within subjects' factor and genotype as the between subjects' factor and displayed as Tukey box plots with mean ± S.E.M. n=26 per genotype *, **, *** and **** represent $p \leq 0.05$, $p \leq 0.01$, $p \leq 0.001$ and $p \leq 0.0001$ for genotype comparisons, respectively.

- **Test Phase: Time point – 13 months of age**

A.

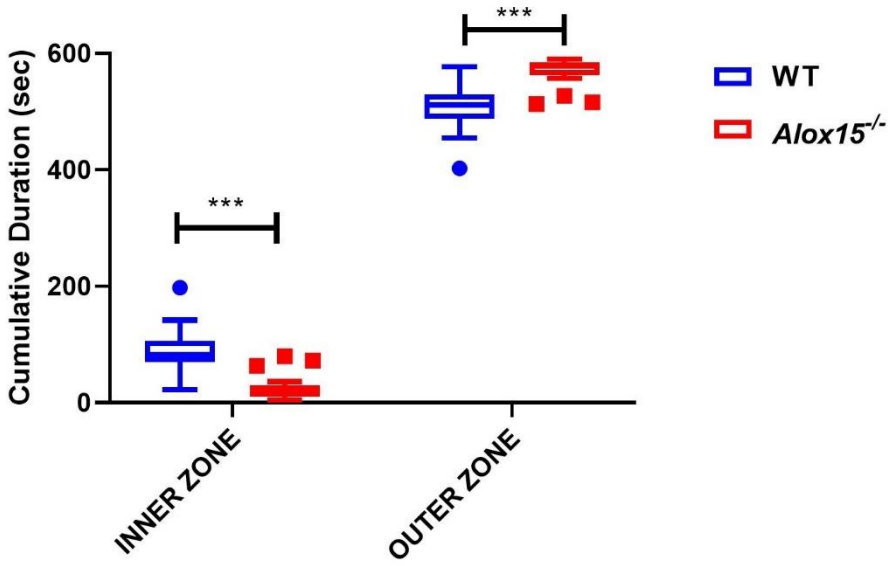

B.

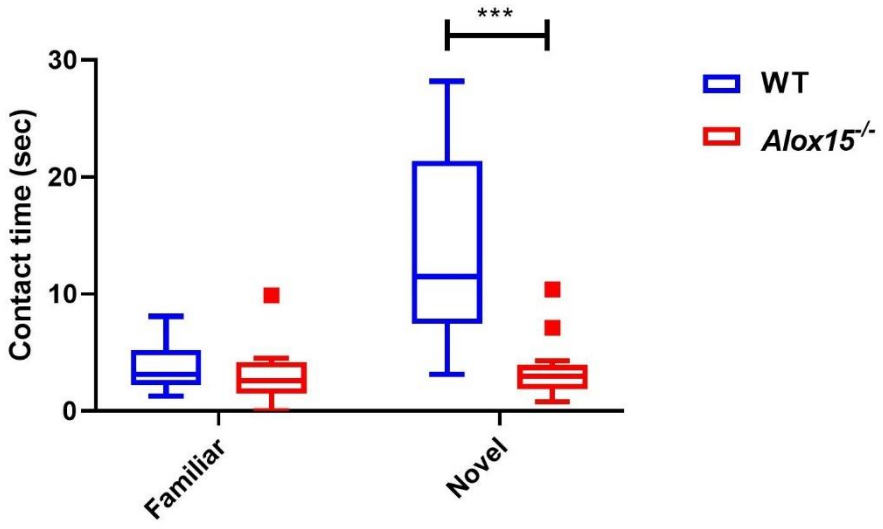

C.

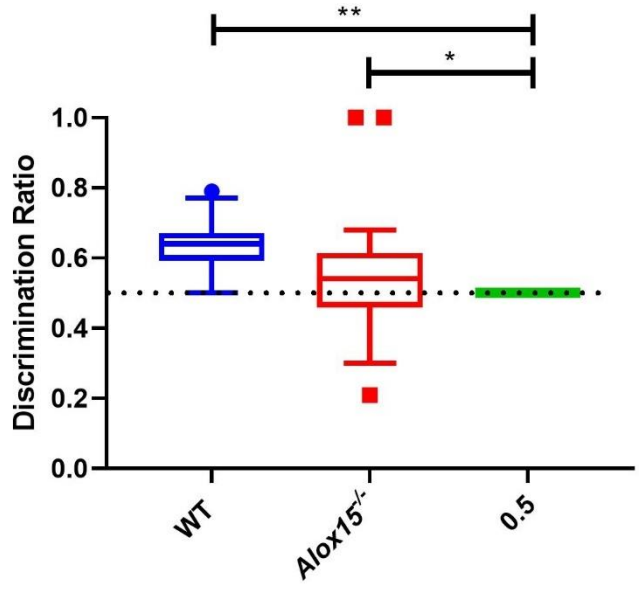

D.

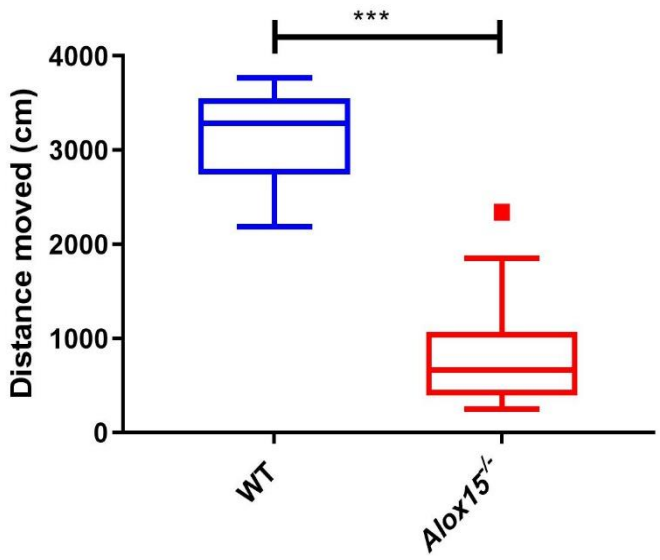

Figure 26. A. *Alox15*$^{-/-}$ male mice, aged 13 months of age, spent significantly less time in the center of the arena during TP. B. *Alox15*$^{-/-}$ male mice spent significantly less contact time (sec) with the novel object compared to WT mice. C. *Alox15*$^{-/-}$ male mice were able to discriminate between the novel and familiar objects. D. *Alox15*$^{-/-}$ male mice displayed significantly decreased mean distance (cm) travelled from the centre of the arena. Data were analysed by a repeated measures ANOVA with the zones as a within subjects' factor and genotype as the between subjects' factor and displayed as Tukey box plots with mean ± S.E.M. WT (n=26) and *Alox15*$^{-/-}$ (n=28) *, **, *** and **** represent $p \leq 0.05$, $p \leq 0.01$, $p \leq 0.001$ and $p \leq 0.0001$ for genotype comparisons, respectively.

- **Test Phase: Time point – 10 months of age**

A.

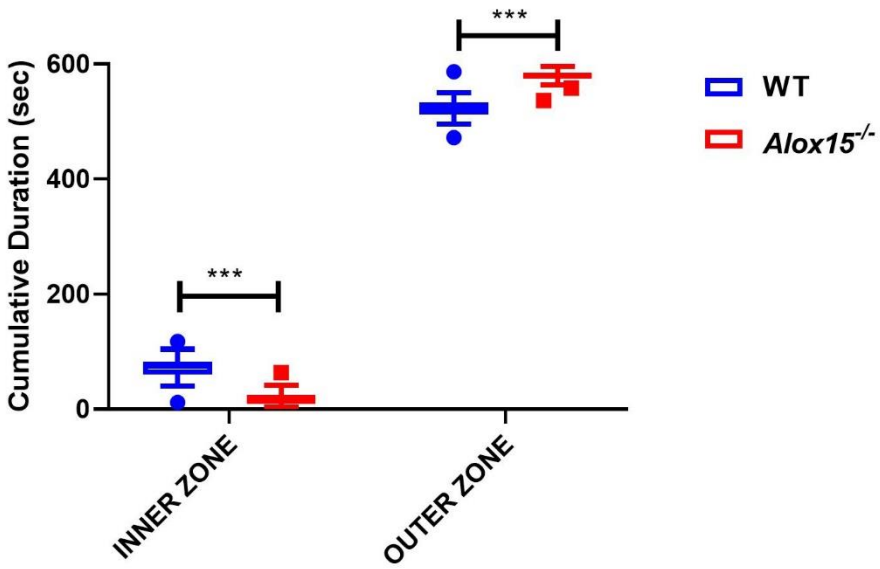

B.

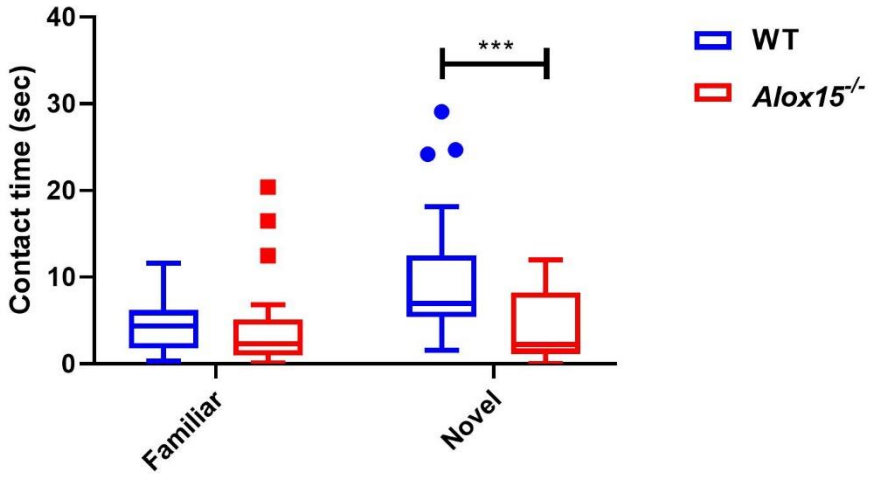

C.

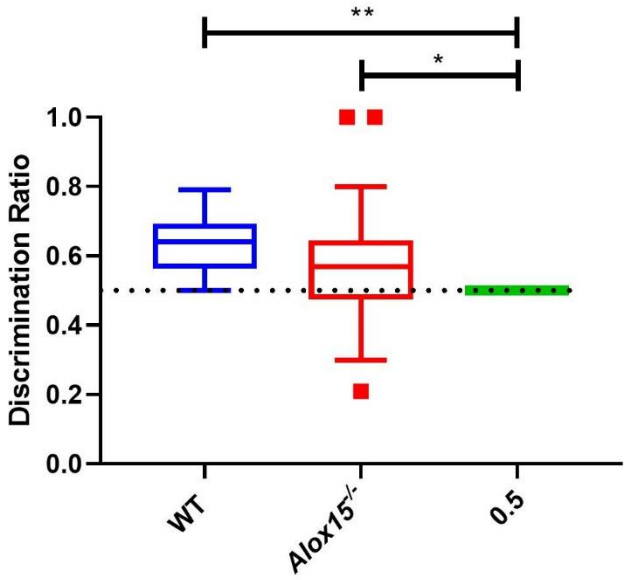

D.

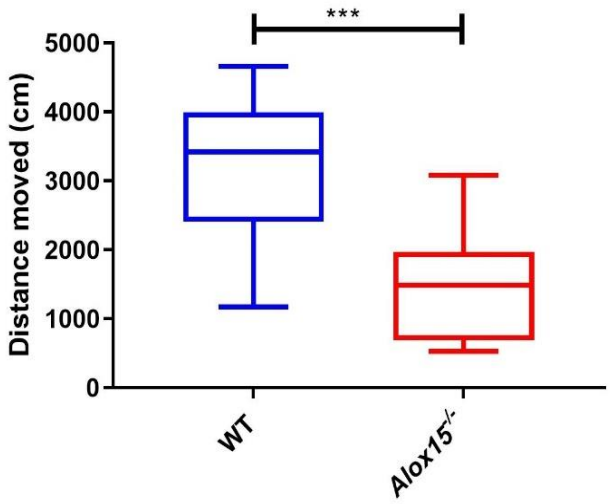

Figure 27. A. *Alox15*$^{-/-}$ male mice, aged 10 months of age, spent significantly less time in the center of the arena during TP. B. *Alox15*$^{-/-}$ male mice spent significantly less contact time (sec) with the novel object. C. *Alox15*$^{-/-}$ male mice were able to discriminate between the novel and familiar objects. D. *Alox15*$^{-/-}$ male mice displayed significantly decreased mean distance (cm) travelled from the centre of the arena. Data were analysed by a repeated measures ANOVA with the zones as a within subjects' factor and genotype as the between subjects' factor and displayed as Tukey box plots with mean ± S.E.M. n=27 per genotype *, **, *** and **** represent p≤0.05, p≤0.01, p≤0.001 and p≤0.0001 for genotype comparisons, respectively.

- **Test Phase: Time point – 7 months of age**

A.

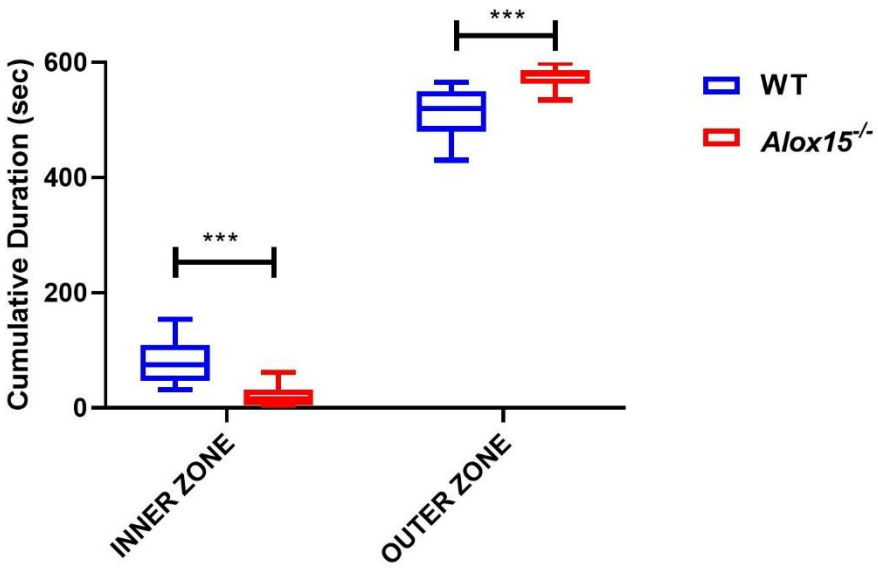

B.

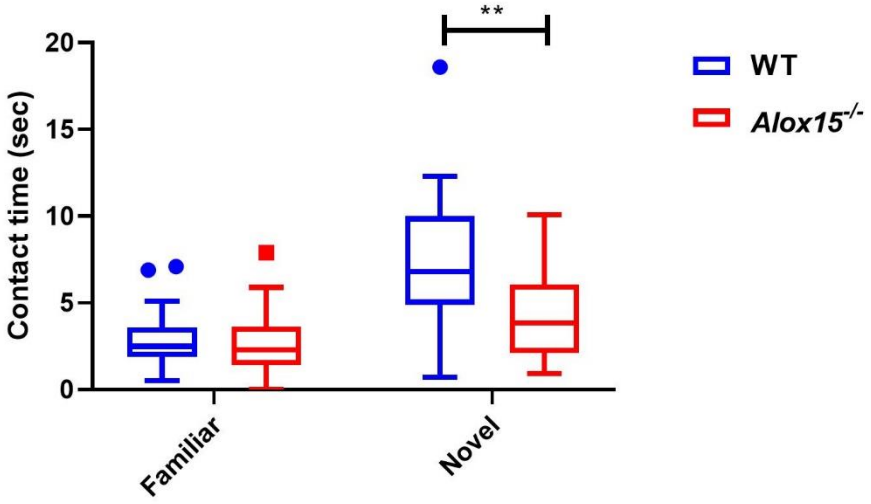

C.

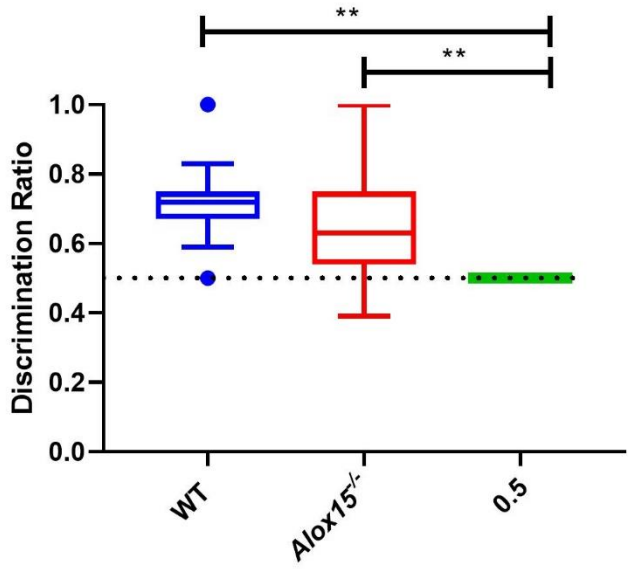

D.

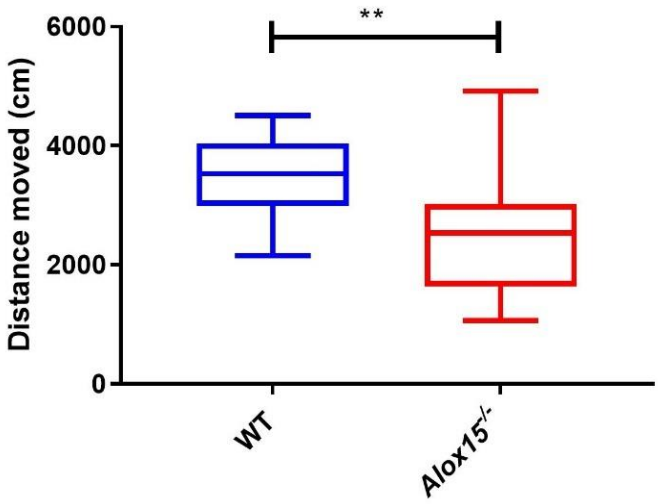

Figure 28. A. *Alox15*$^{-/-}$ male mice, aged 7 months of age, spent significantly less time in the center of the arena during TP. B. *Alox15*$^{-/-}$ male mice spent significantly less contact time (sec) with the novel object. C. *Alox15*$^{-/-}$ male mice were able to discriminate between the novel and familiar objects. D. *Alox15*$^{-/-}$ male mice displayed significantly decreased mean distance (cm) travelled from the centre of the arena. Data were analysed by a repeated measures ANOVA with the zones as a within subjects' factor and genotype as the between subjects' factor and displayed as Tukey box plots with mean ± S.E.M. n=29 per genotype *, **, *** and **** represent p≤0.05, p≤0.01, p≤0.001 and p≤0.0001 for genotype comparisons, respectively.

- **Test Phase: Time point – 4 months of age**

A.

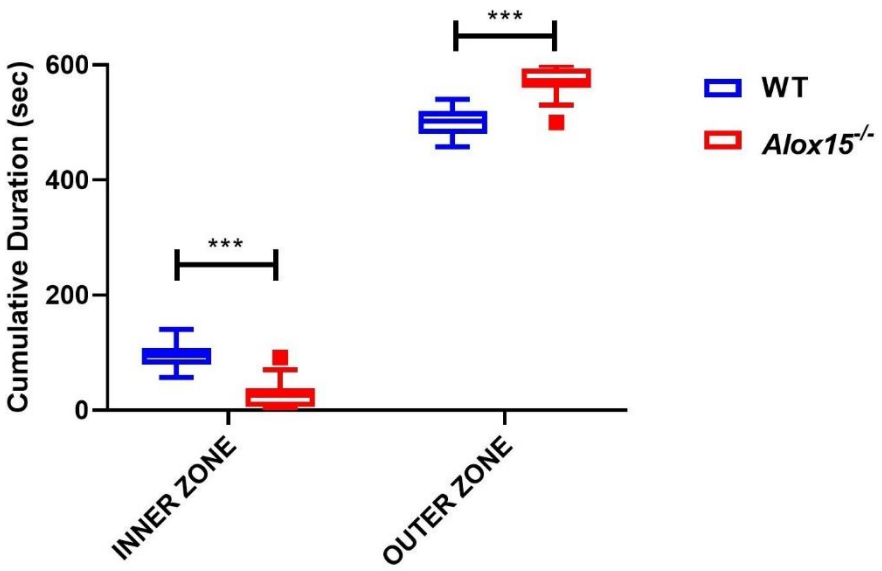

B.

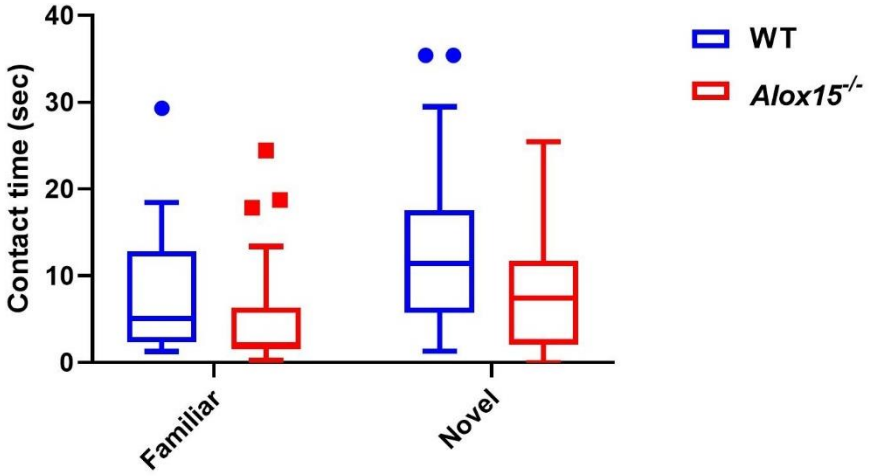

C.

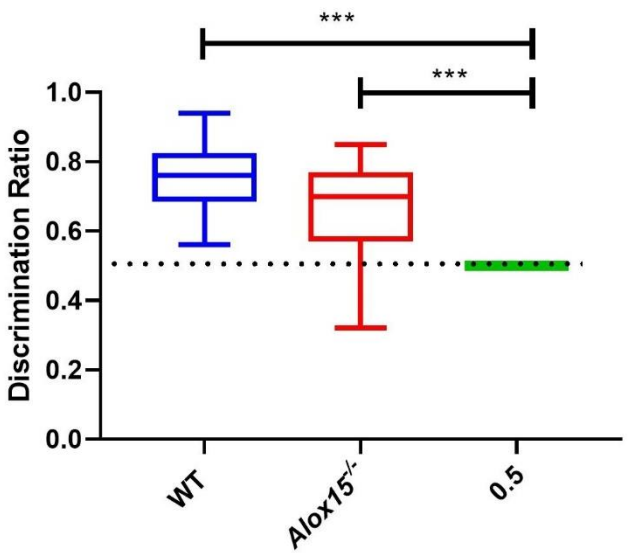

D.

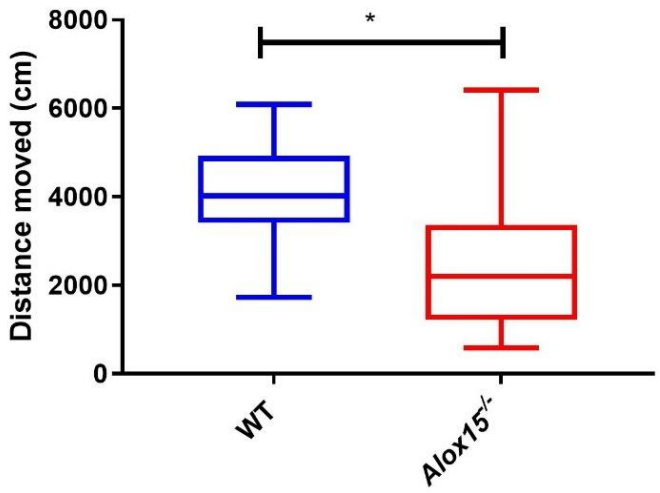

Figure 29. A. *Alox15*$^{-/-}$ male mice, aged 4 months of age, spent significantly less time in the center of the arena during TP. B. *Alox15*$^{-/-}$ male mice spent similar contact time (sec) with the novel object. C. *Alox15*$^{-/-}$ male mice were able to discriminate between the novel and familiar objects. D. *Alox15*$^{-/-}$ male mice displayed significantly decreased mean distance (cm) travelled from the centre of the arena. Data were analysed by a repeated measures ANOVA with the zones as a within subjects' factor and genotype as the between subjects' factor and displayed as Tukey box plots with mean ± S.E.M. n=29 per genotype *, **, *** and **** represent $p \leq 0.05$, $p \leq 0.01$, $p \leq 0.001$ and $p \leq 0.0001$ for genotype comparisons, respectively.

- **Test Phase: Time points 4-15**

A.

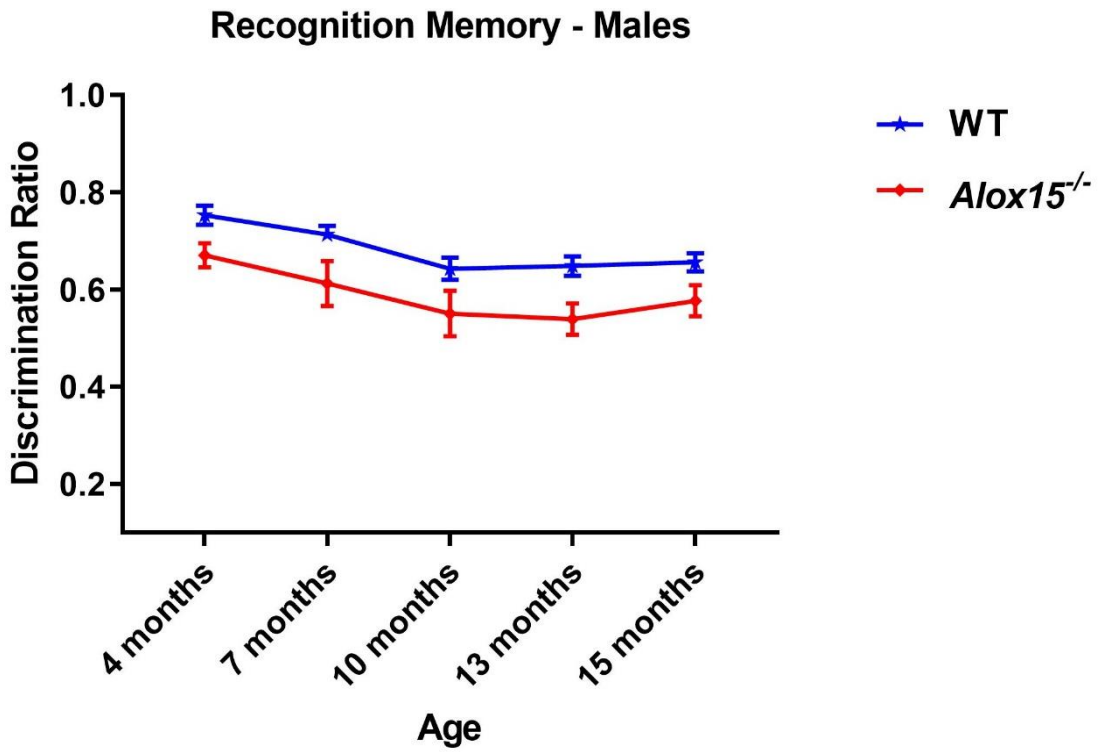

B.

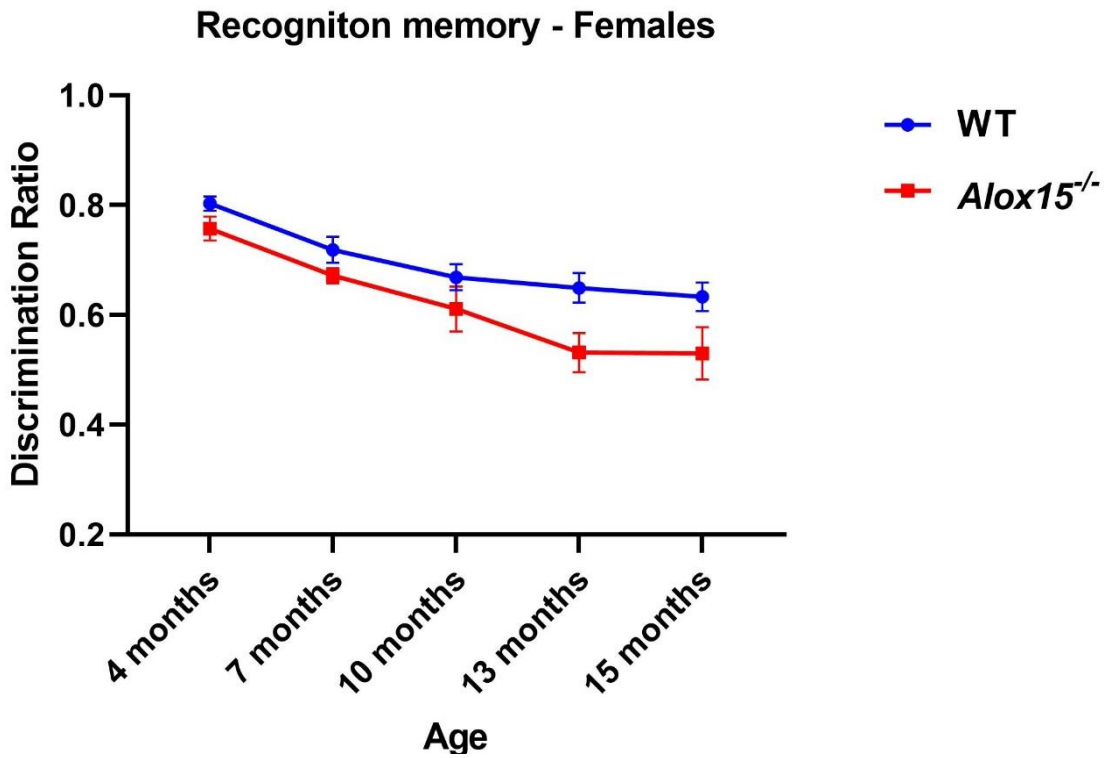

Figure 30. ***Alox15*$^{-/-}$ male and female mice displayed a trend toward decreased DR over five different time points, 4 months, 7 months, 10 months, 13 months and 15 months of age.** Data were analysed by a repeated measures ANOVA with the five different age points as a within subjects' factor and genotype as the between subjects' factor and displayed as line graph with mean ± S.E.M. n=29 per genotype.

4.4 EXPERIMENT 2: OLT

ii. Alox15$^{-/-}$ mice demonstrated spatial memory deficits compared to WT aged 15 months

The main aim of this experiment was to investigate whether the deficiency of *Alox15* is associated with differences in spatial memory between genotypes. To examine the age-dependent memory changes, both WT and *Alox15*$^{-/-}$ mice were tested again at five different time stages between 4 months and 15 months of age. Beginning the analysis from the last time point, 15 months of age, the following graphs were generated:

Spatial memory - Sample phase -15 months of age: As described in Experiment 1,following to HP, there were two sample phases which were identical to those used for the NOR. Analysis by one-way repeated measures ANOVA with the sample phases as a within subjects' factor and genotype as the between subjects' factor revealed that *Alox15*$^{-/-}$ male mice spent significantly less time in the inner zone of the maze than WT mice (P= <0.0001, Figure 31 A). Also, inspection in Figure 31 B shows that *Alox15*$^{-/-}$ mice displayed significantly reduced contact times with the two identical objects than WT mice during the S.P. 1 and S.P. 2 (P=0.0009, P=0.0007, respectively).

Spatial memory - Test Phase - 15 months of age: During the TP, one of the two objects was moved to a new location. Figure 32 A illustrates that *Alox15*$^{-/-}$ mice spent markedly less time in the inner zone than WT mice (P= <0.0001). A visual inspection of these data demonstrates that *Alox15*$^{-/-}$ mice were hypoactive, with decreased locomotor activity concerning the distance they moved compared to WT mice, as indicated in Figure 32 A. Next, *Alox15*$^{-/-}$ mice spent significantly less contact time with the object that moved in the new location than WT mice; however, no statistical differences were observed in the familiar object (P= 0.0002).

The DR measurement was also calculated, demonstrating that *Alox15*$^{-/-}$ mice could not discriminate between the object that has remained in the exact location and the object that has moved to a new location, compared to WT mice as shown in Figure 32 C (0.475±0.028 vs 0.73±0.025, P= 0.0006). Additionally, one sample non-parametric U-test confirmed that their preference for the object in the new location was just below chance 0.5. Furthermore, *Alox15*$^{-/-}$ male mice displayed significantly decreased mean distance travelled from the centre of the arena than WT mice, as shown in Figure 32 D (P= <0.0001).

Spatial memory - Test Phase – 4-15 months of age: Similar behavioural domains, including the cumulative duration in the inner and outer zone, locomotor and exploratory activity, the

contact time with the object that moved to the new place, the DR measurement, and the locomotor activity, were assessed in the previous time points 4-13. In particular, the middle-aged *Alox15*$^{-/-}$ male mice displayed similar spatial memory deficits as the old *Alox15*$^{-/-}$ mice, as shown in Figures 33 - 35. The DR measurement at 13, 10, and 7 months showed that *Alox15*$^{-/-}$ male mice could not discriminate between the object that stayed in the same location and the object that was placed in a new location, as illustrated in Figure 33 C [(13 months: 0.49±0.025 vs 0.67±0.021, P= 0.0002) (10 months: 0.54±0.031 vs 0.71±0.019, P=0.0048) (7 months: 0.62±0.021 vs 0.73±0.022, P=0.0433) (4 months: 0.70±0.039 vs 0.757±0.033), respectively]. In contrast, the young *Alox15*$^{-/-}$ mice were able to discriminate between the object in the same location and the other object that moved to the new place compared to WT mice, as demonstrated in Figure 36.

Collectively DR data – 4-15 months of age: Taken together, a two-way ANOVA analysed the DR data from the five different time stages with Bonferroni's multiple comparison tests revealing that *Alox15*$^{-/-}$ male mice demonstrated a significant effect of age in spatial memory decline (F (4, 212) = 4.131, P=0.003) (Figure 37 A). Conversely, the age-related interaction in spatial memory decline was not significant in female mice [(F (4, 110) = 1.807 , P= 0.1326)] and also separately the DR data [15 months: 0.43±0.023 vs 0.63±0.022, 13 months: 0.47±0.038 vs 0.63±0.029, 10 months: 0.50±0.042 vs 0.65±0.031, 7 months: 0.62±0.031 vs 0.68±0.031, 4 months: 0.71±0.057 vs 0.76±0.047] (Figure 37 B).

- **Sample Phase: Time point – 15 months of age**

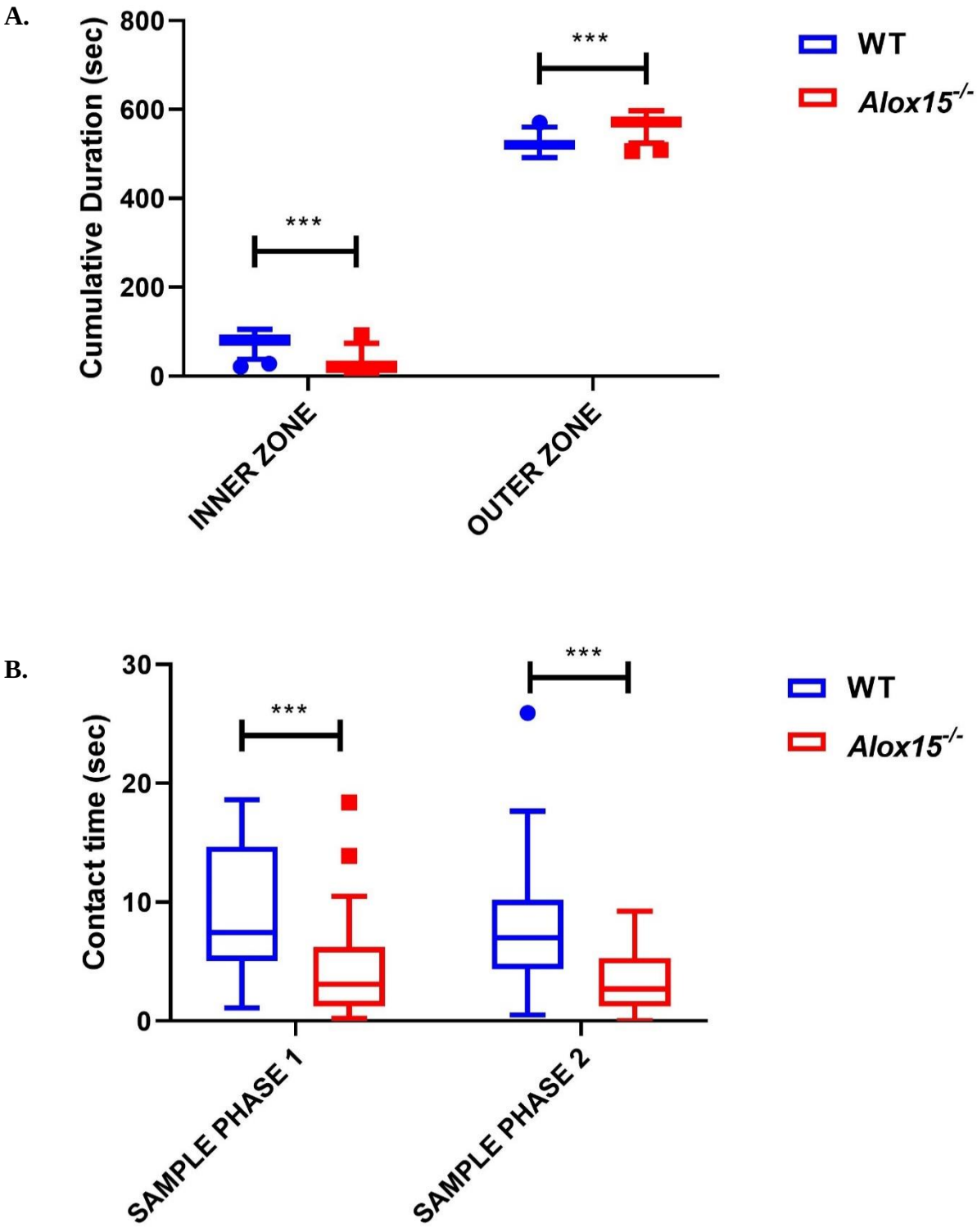

Figure 31. *Alox15*$^{-/-}$ male mice displayed significantly less mean contact times (sec) during the two Sample Phases. Data were analysed by repeated measures ANOVA with the sample phases as a within subjects' factor and genotype as the between subjects' factor and displayed as Tukey box plots with mean ± S.E.M. n=29 per genotype *, **, *** and **** represent $p \leq 0.05$, $p \leq 0.01$, $p \leq 0.001$ and $p \leq 0.0001$ for genotype comparisons, respectively.

- *Test Phase:* **Time point – 15 months of age**

A.

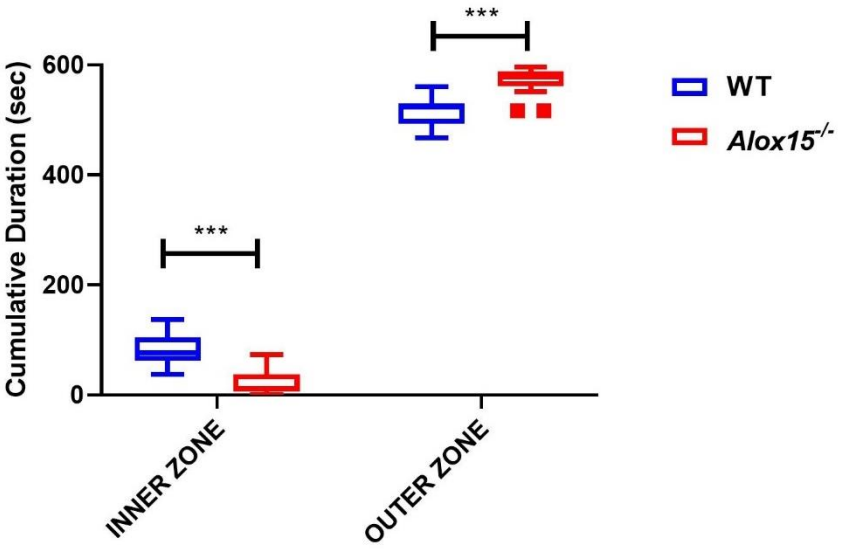

B.

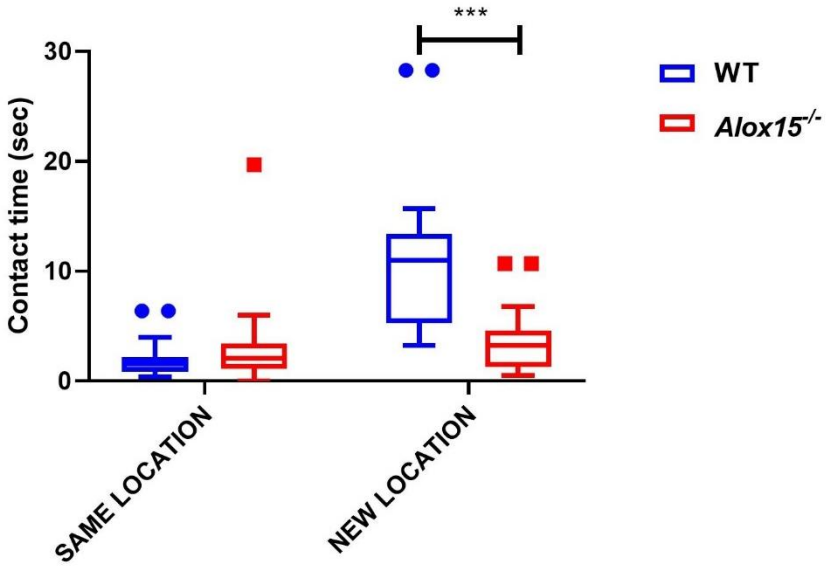

C.

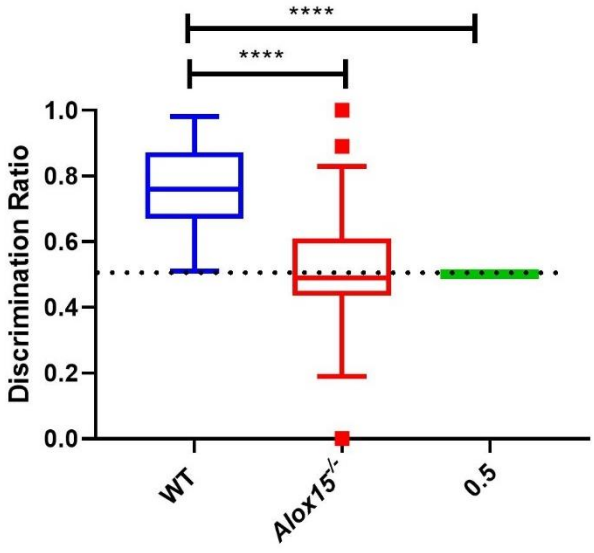

D.

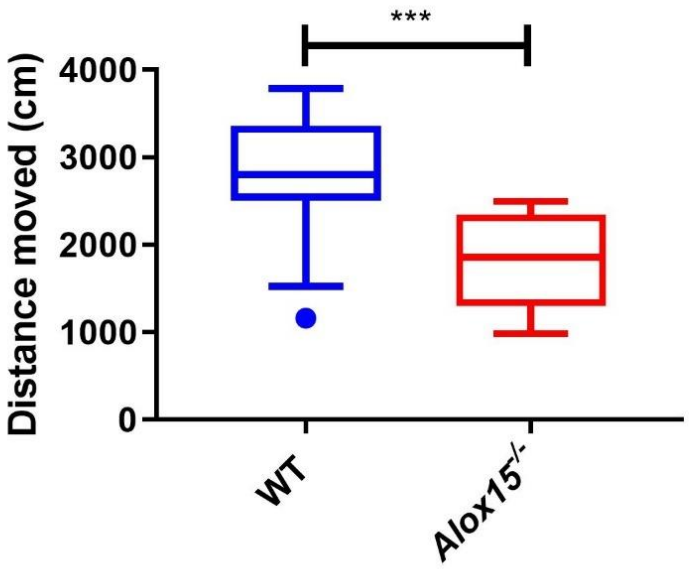

Figure 32. A. *Alox15*$^{-/-}$ male mice, aged 15 months, spent markedly less time in the center of the arena than WT mice during TP. B. *Alox15*$^{-/-}$ male mice interacted markedly less with the object in the new location compared to WT mice. C. *Alox15*$^{-/-}$ male mice were not able to discriminate between the object in the same location and another object in the new location. D. *Alox15*$^{-/-}$ male mice displayed significantly decreased mean distance (cm) travelled from the centre of the arena. Data were analysed by a repeated measures ANOVA with the zones and object location as a within subjects' factor and genotype as the between subjects' factor and displayed as Tukey box plots with mean ± S.E.M. n=29 per genotype *, **, *** and **** represent $p \leq 0.05$, $p \leq 0.01$, $p \leq 0.001$ and $p \leq 0.0001$ for genotype comparisons, respectively.

- **Test Phase: Time point – 13 months of age**

A.

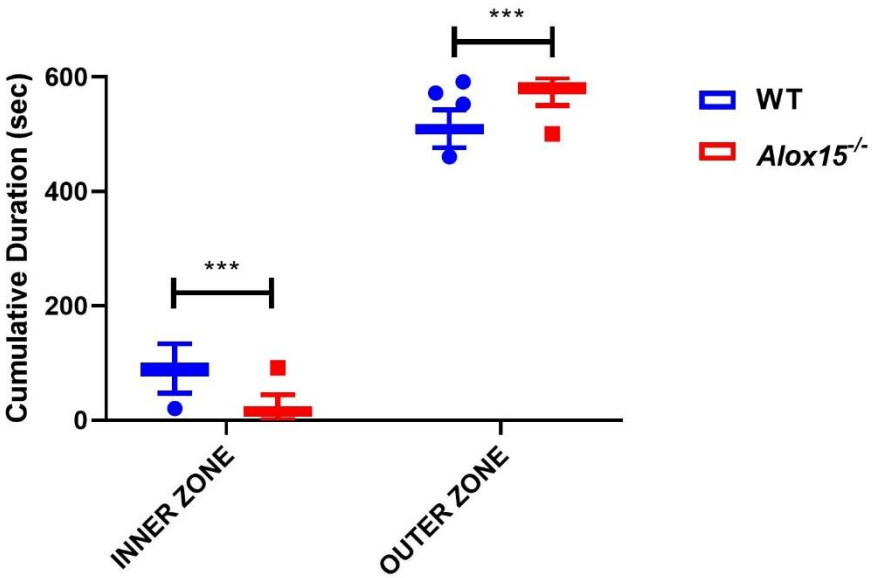

B.

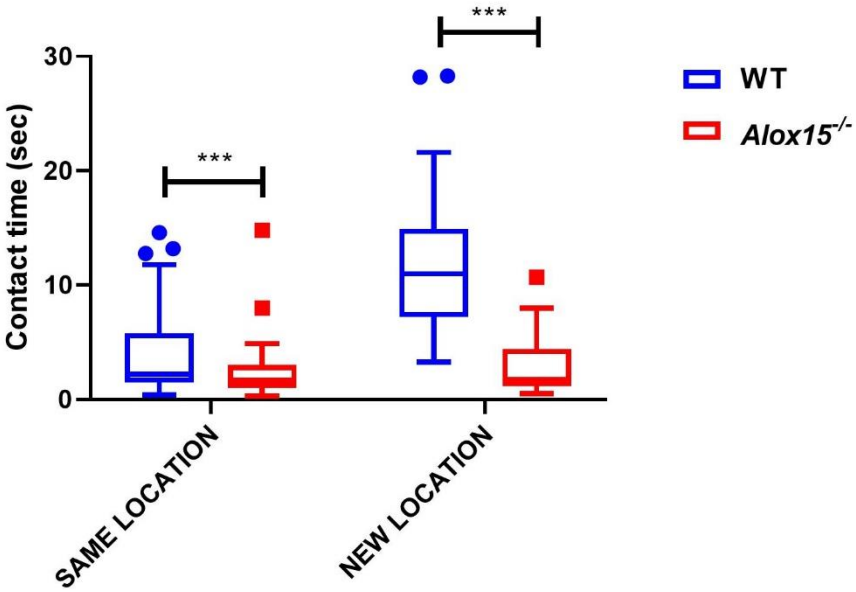

C.

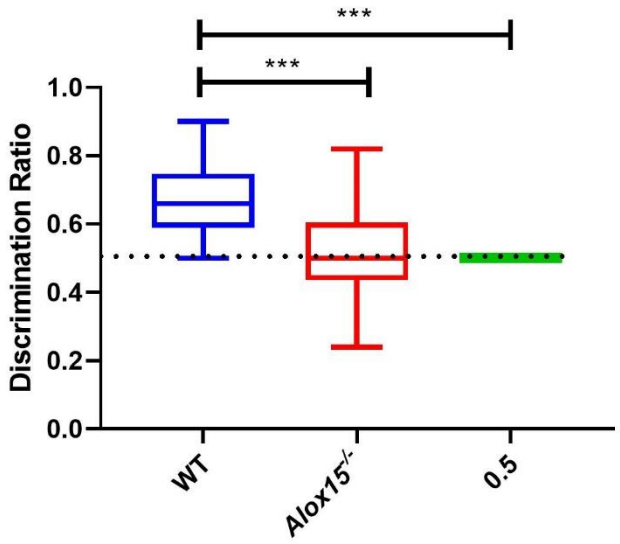

D.

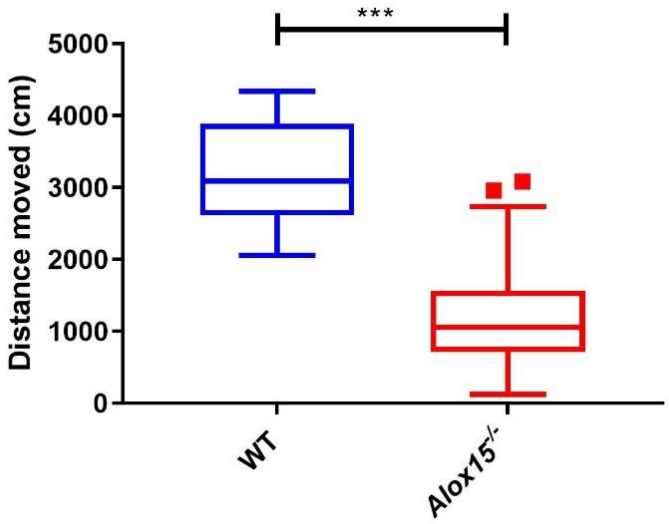

Figure 33. ***A. Alox15*$^{-/-}$ male mice, aged 13 months, spent markedly less time in the center of the arena during TP. B. *Alox15*$^{-/-}$ male mice interacted significantly less with the object in the new location. C. *Alox15*$^{-/-}$ male mice were not able to discriminate between the object in the same location and another object in the new location. D. *Alox15*$^{-/-}$ male mice displayed significant*ly decreased* mean distance (cm) travelled from the centre of the arena.** Data were analysed by a repeated measures ANOVA with the zones and object location as a within subjects' factor and genotype as the between subjects' factor and displayed as Tukey box plots with mean ± S.E.M. WT (n=26) and *Alox15*$^{-/-}$ (n=28) *, **, *** and **** represent p≤0.05, p≤0.01, p≤0.001 and p≤0.0001 for genotype comparisons, respectively.

- **Test Phase: Time point – 10 months of age**

A.

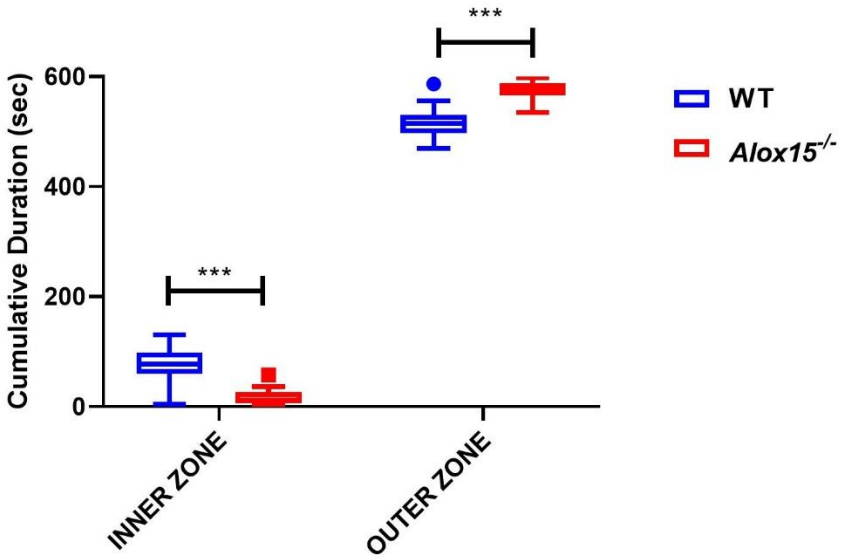

B.

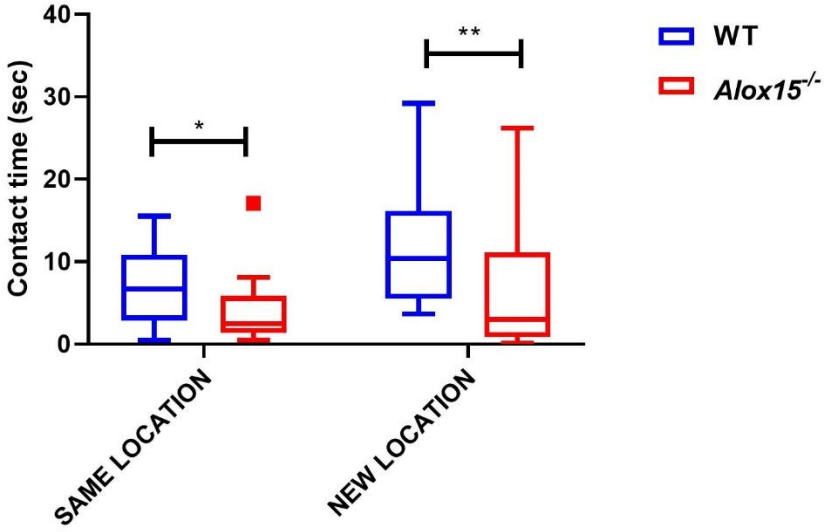

C.

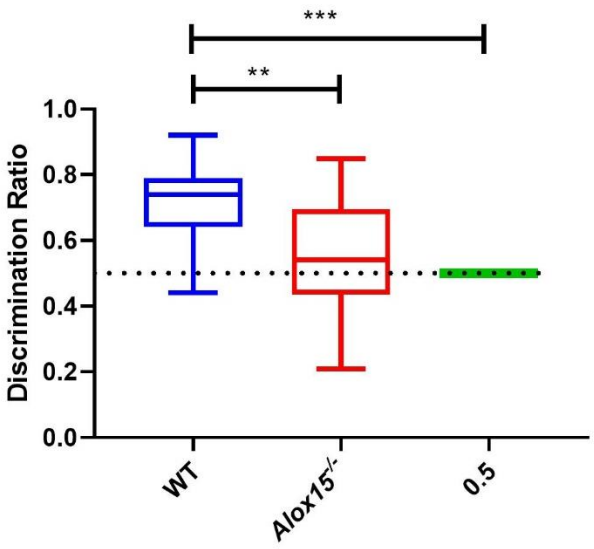

D.

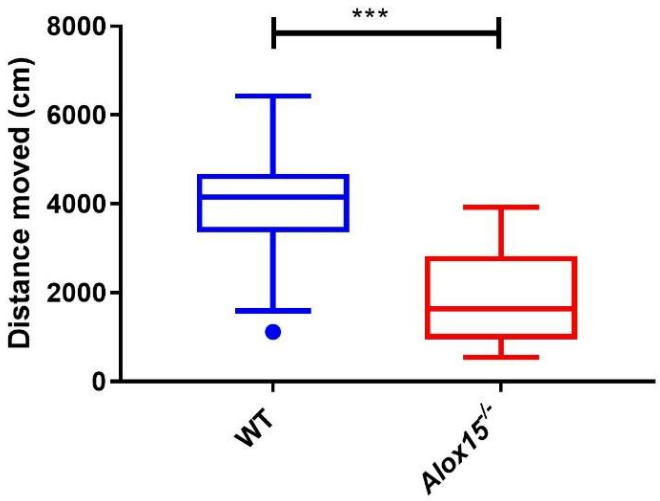

Figure 34. ***A. Alox15*$^{-/-}$ male mice, aged 10 months, spent *markedly* less time in the center of the arena during *TP*. B. *Alox15*$^{-/-}$ male mice interacted markedly less with the object in the new location. *C. Alox15*$^{-/-}$ male mice were *not* able to discriminate between the object in the same location and another object in the new location. *D. Alox15*$^{-/-}$ male mice displayed significant*ly decreased* mean distance (cm) travelled from the centre of the arena.** Data were analysed by a repeated measures ANOVA with the zones and object location as a within subjects' factor and genotype as the between subjects' factor and displayed as Tukey box plots with mean ± S.E.M. n=27 per genotype *, **, *** and **** represent $p \leq 0.05$, $p \leq 0.01$, $p \leq 0.001$ and $p \leq 0.0001$ for genotype comparisons, respectively.

- **Test Phase: Time point – 7 months of age**

A.

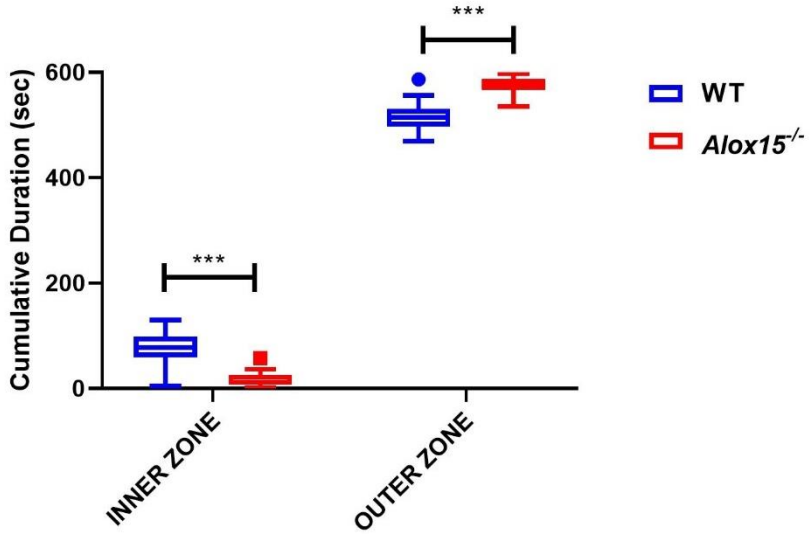

B.

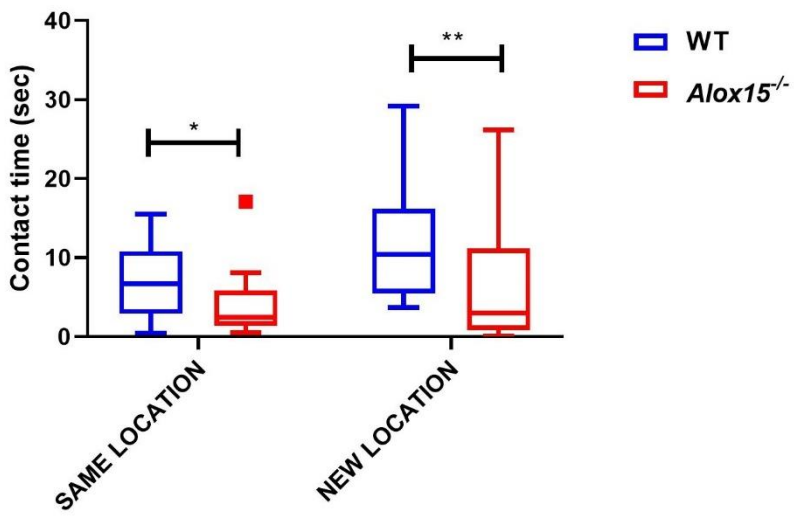

C.

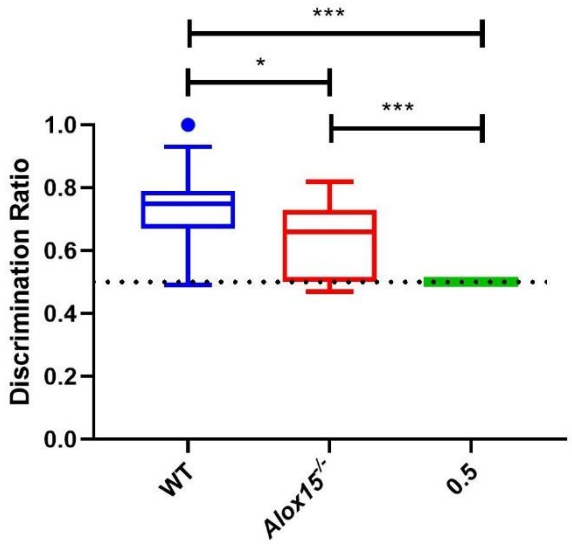

D.

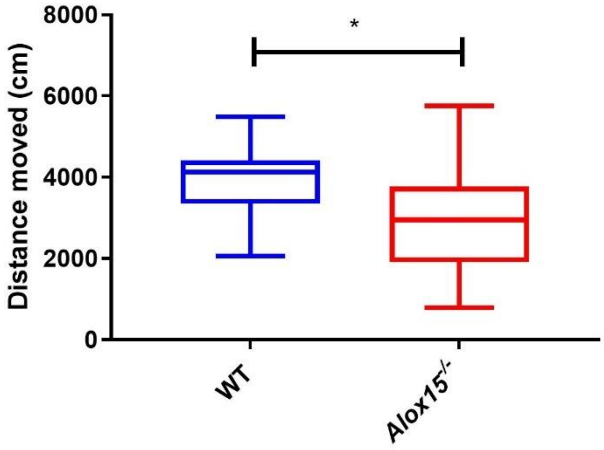

Figure 35. A. *Alox15*$^{-/-}$ male mice, aged 7 months, spent markedly less time in the inner zone of the arena during TP. B. *Alox15*$^{-/-}$ male interacted markedly less time with the object in the new location. C. *Alox15*$^{-/-}$ male mice were able to discriminate between the object in the same location and another object in the new location. D. *Alox15*$^{-/-}$ male mice displayed significantly decreased mean distance (cm) travelled from the centre of the arena. Data were analysed by a repeated measures ANOVA with the zones and object location as a within subjects' factor and genotype as the between subjects' factor and displayed as Tukey box plots with mean ± S.E.M. n=29 per genotype *, **, *** and **** represent $p \leq 0.05$, $p \leq 0.01$, $p \leq 0.001$ and $p \leq 0.0001$ for genotype comparisons, respectively.

- **Test Phase: Time point – 4 months of age**

A.

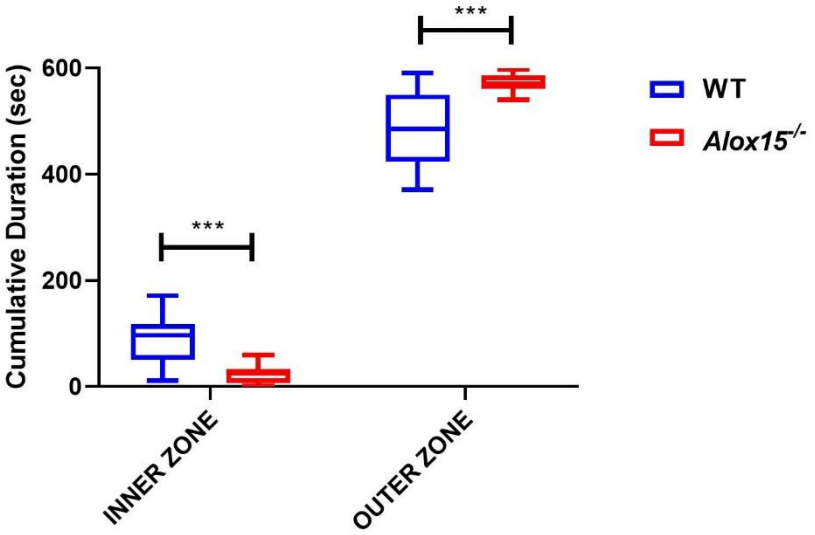

B.

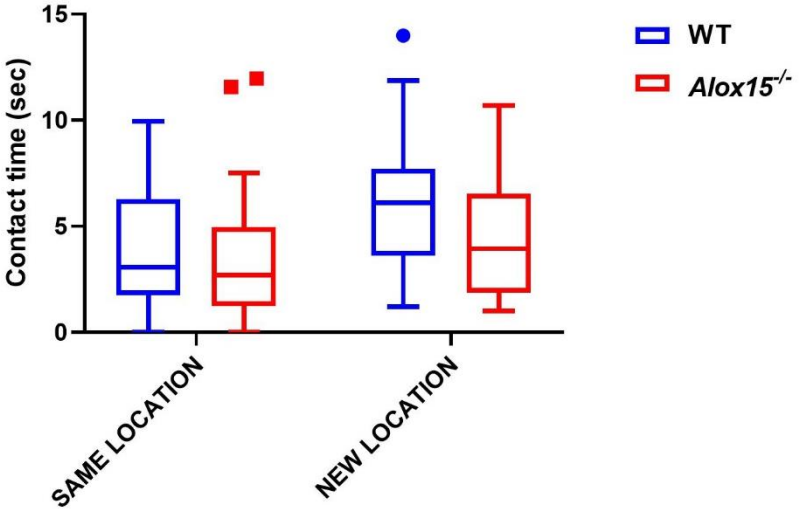

C.

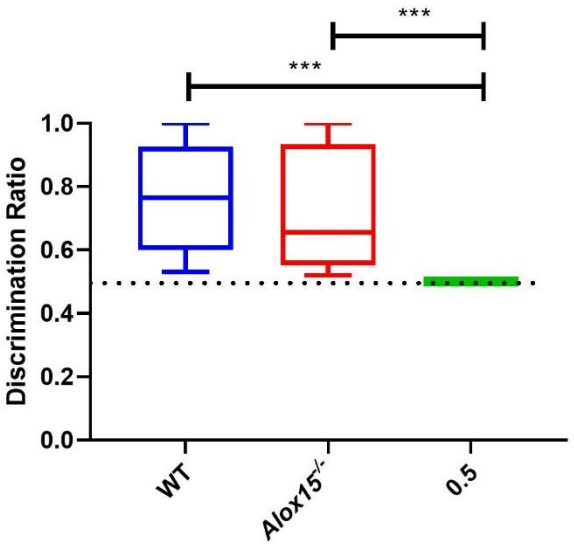

D.

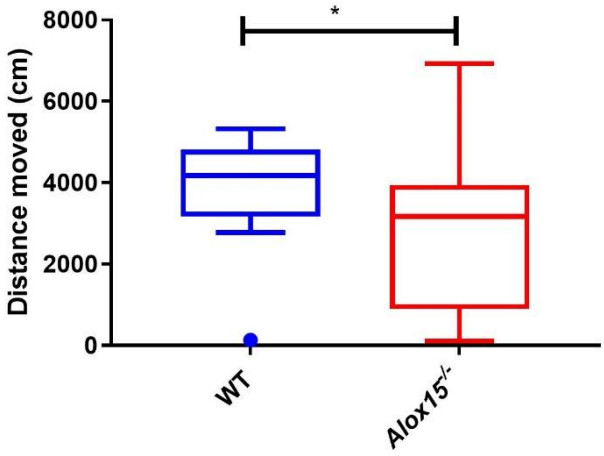

Figure 36. ***A. Alox15*$^{-/-}$ male mice, aged 4 months, spent *markedly* less time in the inner zone of the arena during *TP*. B. *Alox15*$^{-/-}$ male spent less contact time with the object in the new location, but this was not significant. *C. Alox15*$^{-/-}$ male mice were able to discriminate between the object in the same location and another object in the new location. *D. Alox15*$^{-/-}$ male mice displayed significantly decreased mean distance (cm) travelled from the centre of the arena.** Data were analysed by a repeated measures ANOVA with the zones and object location as a within subjects' factor and genotype as the between subjects' factor and displayed as Tukey box plots with mean ± S.E.M. n=29 per genotype *, **, *** and **** represent p≤0.05, p≤0.01, p≤0.001 and p≤0.0001 for genotype comparisons, respectively.

- **Test Phase: Time points 4-15**

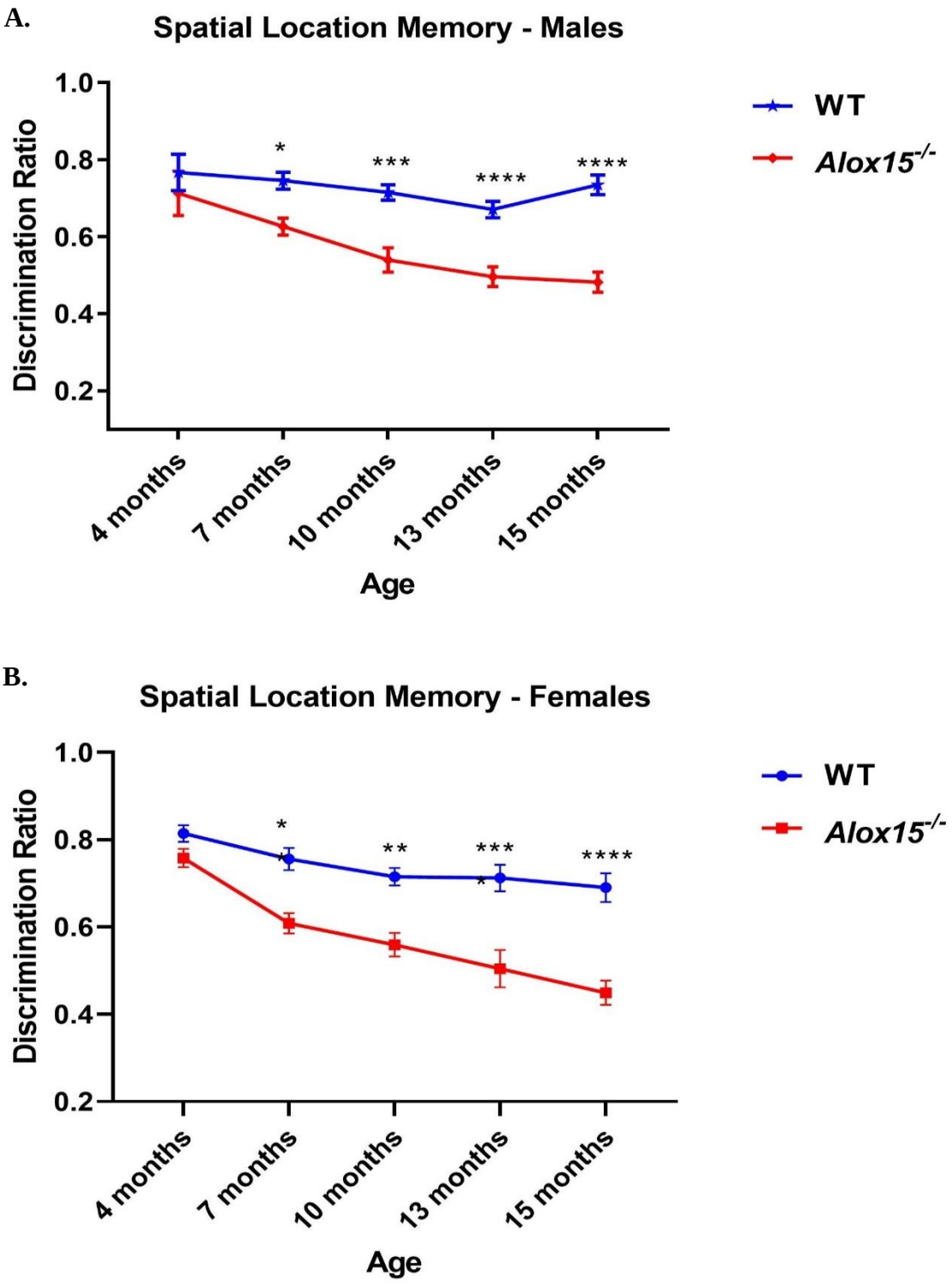

Figure 37. *Alox15*$^{-/-}$ male and female mice displayed markedly decreased DR in spatial memory over five different time points, 4 months, 7 months, 10 months, 13 months and 15 months of age. Data were analysed by a repeated measures ANOVA with the five different age points as a within subjects' factor and genotype as the between subjects' factor and displayed as line graph with mean ± S.E.M. n=29 per genotype *, **, *** and **** represent $p \leq 0.05$, $p \leq 0.01$, $p \leq 0.001$ and $p \leq 0.0001$ for genotype comparisons, respectively.

4.5 EXPERIMENT 3: SPONTANEOUS ALTERNATION IN T-MAZE

iii. Alox15$^{-/-}$ male mice showed spatial working memory deficits compared to WT aged 15 months

To further investigate whether the cognitive deficits in hippocampal-dependent processing spatial information extended to other behavioural tests, *Alox15*$^{-/-}$ mice were also subjected to a spontaneous alternation T-maze paradigm. To evaluate their spontaneous alternation, a measure of spatial working memory and their exploratory activity, *Alox15*$^{-/-}$ and WT mice, aged 15 months, were allowed to freely explore the T-maze apparatus and choose one of the two-goal arms during the trial run. In the choice run, the mice decide whether they alternate and visit a new goal arm. Herein, only the morning sessions were included in this section; thus, the spontaneous alternation of only the morning sessions was calculated.

Working memory – 15 months of age: Results from this task can be seen in Figure 38 A, indicating that *Alox15*$^{-/-}$ mice performed poorly across the training sessions and had significantly lower spontaneous alternation scores compared to age-matched WT control mice (48.929 ±1.303 vs 65.285 ± 1.344, P=0.0012). Furthermore, the time taken to complete the total number of 10 trials during the morning session was recorded to measure gross exploratory behaviour, as shown in Figure 38 B. *Alox15*$^{-/-}$ mice completed the 10 trials on average 280 secs in the morning sessions, significantly slower than the 130 secs by the wild-type group of mice (289.286 ±6.668 vs 133.214 ± 4.245, P=0.0001).

- **Time point – 15 months of age**

A.

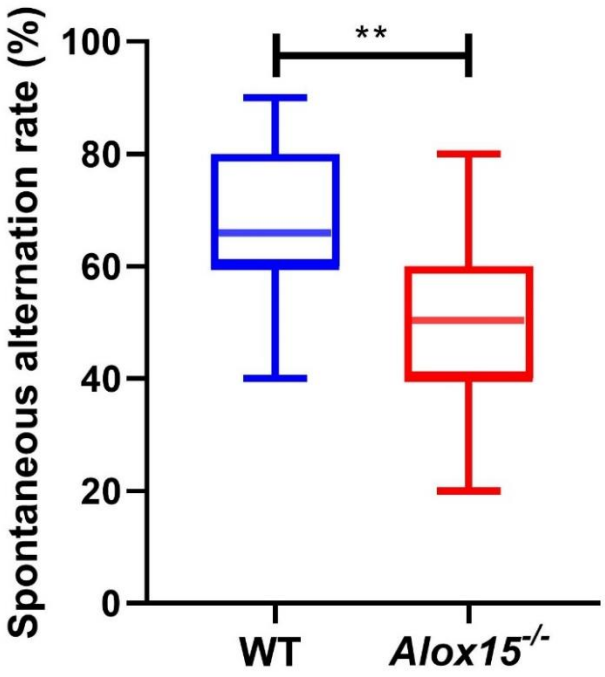

B.

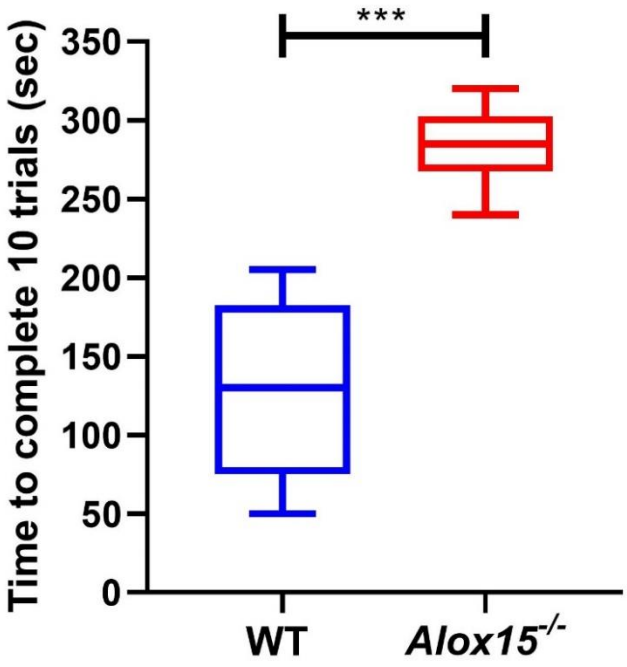

Figure 38. *Alox15*$^{-/-}$ male mice displayed markedly impaired spatial working memory A. The percentage of spontaneous alternation rate in the T-maze was significantly reduced in *Alox15*$^{-/-}$ mice B. Significant differences in the total time to complete 10 trials in the morning sessions in the spontaneous alternation task. Data were analysed using Mann-Whitney non-parametric U test and displayed as Tukey box plots with mean ± S.E.M. n=14 per genotype *, **, *** and **** represent $p \leq 0.05$, $p \leq 0.01$, $p \leq 0.001$ and $p \leq 0.0001$ for genotype comparisons, respectively..

4.6 EXPERIMENT 4: EPM

iv. Alox15$^{-/-}$ male mice manifested increased anxiety-like behaviour compared to WT aged 15 months

The EPM has been widely used to assess anxiety-like behaviour. Further to the previous memory tests, *Alox15*$^{-/-}$ mice were examined in the EPM to evaluate their anxiety status and age effects. Both groups of mice, WT and *Alox15*$^{-/-}$ mice, were tested at four different age points starting from 7 months and onwards. The cut-off time point was 15 months of age. The below graphs have been produced from these time points, between 29 WT and 29 *Alox15*$^{-/-}$ mice and were displayed starting from 15 months of age. Data on the number of entries, distance travelled and cumulative duration were analysed by the Mann-Whitney U test to compare the two genotypes.

Anxiety-like behaviour – 15 months of age: Visual inspection suggested that aged *Alox15*$^{-/-}$ mice made significantly fewer entries to the open areas than controls. The analysis on the number of entries by the Mann-Whitney U test revealed statistical significance (P=0.0002) (Figure 39 A). Also, the mean distance travelled by each group of mice was calculated to measure the general locomotive activity in the apparatus. A simple comparison showed that *Alox15*$^{-/-}$ mice travelled significantly less than WT mice in the maze (P<0.0001) (Figure 39 B). WT mice showed more open arms exploration than *Alox15*$^{-/-}$ mice, leading to an increased overall duration percentage in the open arms during the 10-minute EPM test. In particular, *Alox15*$^{-/-}$ mice displayed significantly less exploration of the open arms compared to the closed arms, generally avoiding the open platforms of the maze to a much greater extent than the age-matched WT mice. There were significant differences in the cumulative duration in open arms between *Alox15*$^{-/-}$ mice and WT mice (82.36±1.84 vs 49.93±7.88, P<0.0001, respectively) (Figure 39 C). Furthermore, *Alox15*$^{-/-}$ mice appeared to take longer to enter the open arms and spent less time per entry, resulting in decreased duration in the open arms compared to age-matched WT male mice. Heatmaps conducting overall exploration in open and closed arms indicated significant differences in open arm exploration between genotypes (Figure 39 D).

Anxiety-like behaviour – 13-7 months of age: The middle-aged *Alox15*$^{-/-}$ mice exhibited similar anxiety-like behaviour patterns as the old mice, as shown in Figures 40 and 41. Similarly, young *Alox15*$^{-/-}$ mice spent significantly less time in the open arms than age-matched male controls (% duration open arms in 13 months: 81.72±2.01 vs 52.79±7.31, 10 months: 76.62±2.041 vs 59.38±26.85, 7 months: 68.23±2.23 vs 36.43±23.20, respectively) (Figure 42).

Collectively Anxiety-like behaviour – 15-7 months of age: The data regarding the time spent in open and closed arms, from four different time points, were analysed revealing that *Alox15*$^{-/-}$ male mice spent significantly less time in open arms, which deteriorated with age (Figure 43 A). There was a significant effect of age for *Alox15*$^{-/-}$ male mice on time spent in open arms, further exacerbated at 13 months of age and onwards in a two-way ANOVA ($F(3, 156) = 9.683$, $P<0.0001$) Figure 43 A). Similarly, the percentages of time spent on open arms in *Alox15*$^{-/-}$ female mice suggested increased anxiety-like behaviour than WT mice; demonstrated also a significant effect of age in female mice [(% duration open arms: (15 months: 88.36±1.84 vs 59.93±1.39), (13 months: 85.51±2.01 vs 67.18±1.69), (10 months: 83.62±2.04 vs 68.38±1.60), (7 months: 70.23±2.23 vs 52.93±2.18)] ($F(3, 112) = 30.99$, $P<0.0001$) (Figure 43 B).

- **Time point – 15 months of age**

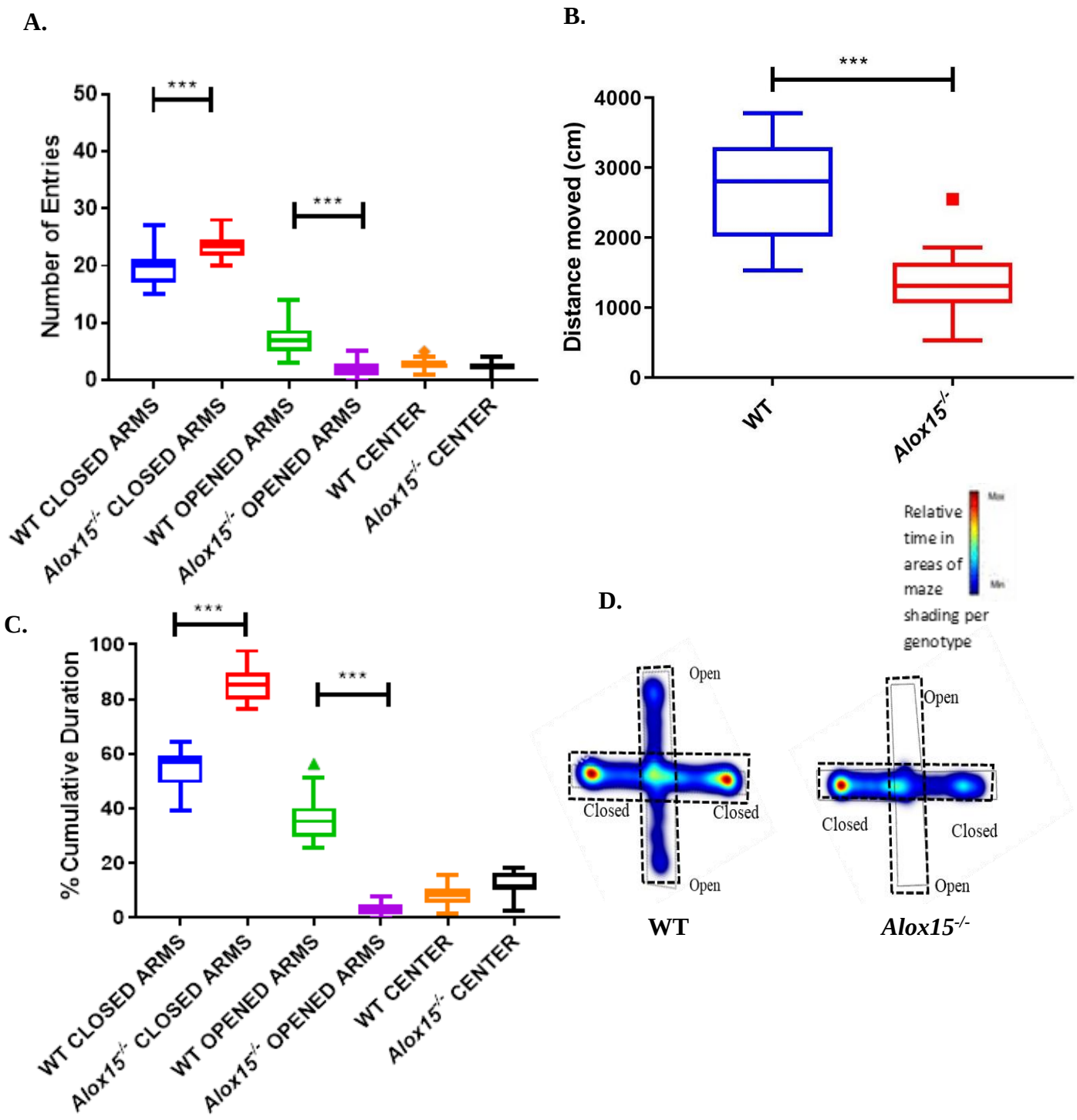

Figure 39. *Alox15*$^{-/-}$ male mice, aged 15 months, showed greater anxiety-like behaviour in EPM. A. *Alox15*$^{-/-}$ mice made significantly fewer entries in the opened areas. B. Mean distance travelled of the *Alox15*$^{-/-}$ mice throughout exploration of the EPM C. *Alox15*$^{-/-}$ mice spent significantly less duration time in the open arms. D. Heatmaps displayed relative exploration of the open and closed arms across genotypes. Data were analysed using Mann- Whitney non-parametric U test and shown on Tukey box plots with mean ± S.E.M. n=26 per genotype. *, **, *** and **** represent p≤0.05, p≤0.01, p≤0.001 and p≤0.0001 for genotype comparisons, respectively.

- **Time point – 13 months of age**

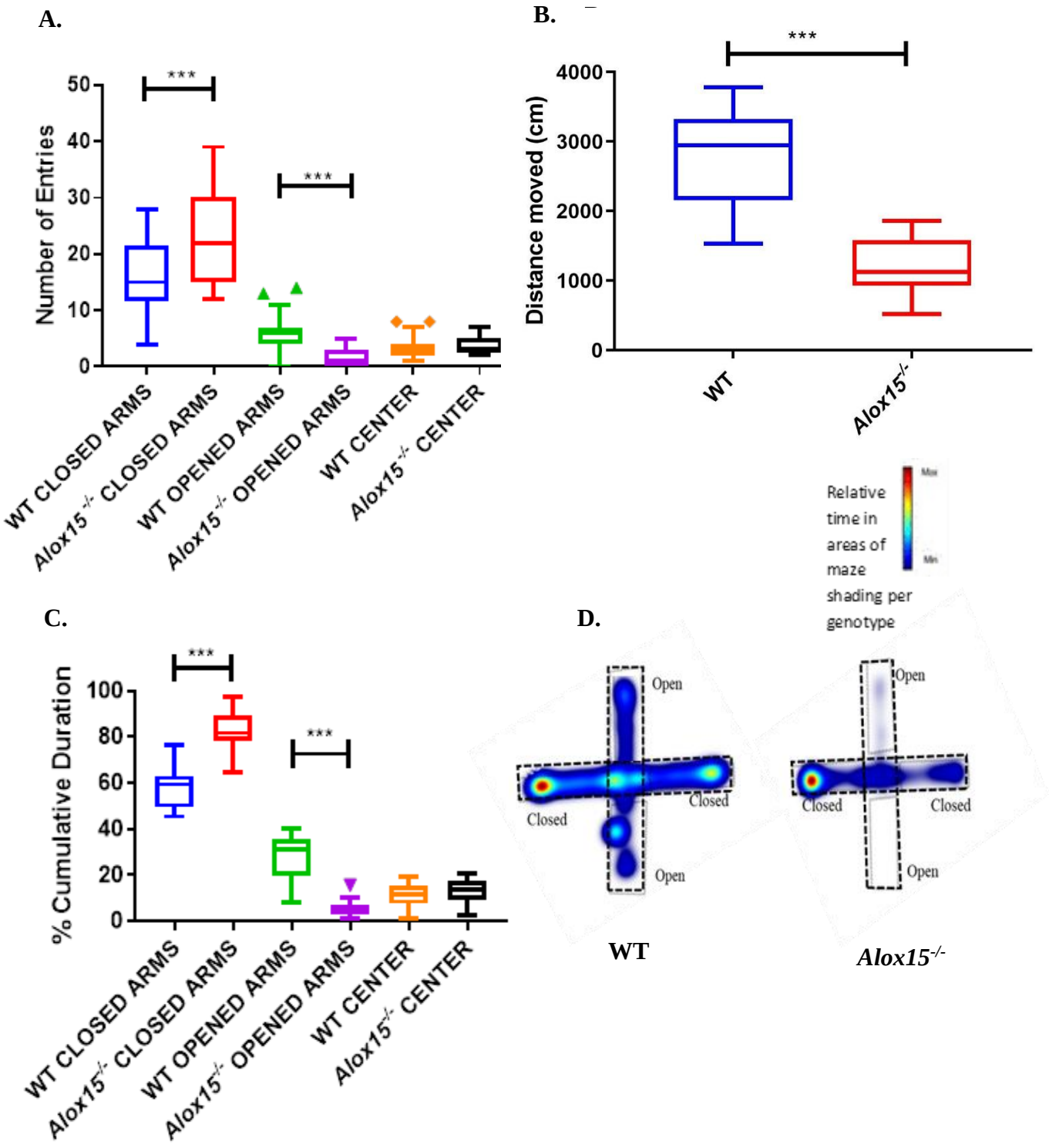

Figure 40. *Alox15*$^{-/-}$ male mice, aged 13 months, displayed markedly increased anxiety-like behaviour in EPM. A. *Alox15*$^{-/-}$ mice made markedly more entries in the closed areas B. Mean distance moved by *Alox15*$^{-/-}$ mice C. *Alox15*$^{-/-}$ mice spent significantly more duration time in the closed arms. D. Heatmaps displayed relative exploration of the open and closed arms across genotypes. Data were analysed using Mann- Whitney non-parametric U test and shown on Tukey box plots with mean ± S.E.M. WT (n=26) and *Alox15*$^{-/-}$ (n=28) *, **, *** and **** represent p≤0.05, p≤0.01, p≤0.001 and p≤0.0001 for genotype comparisons, respectively.

- **Time point – 10 months of age**

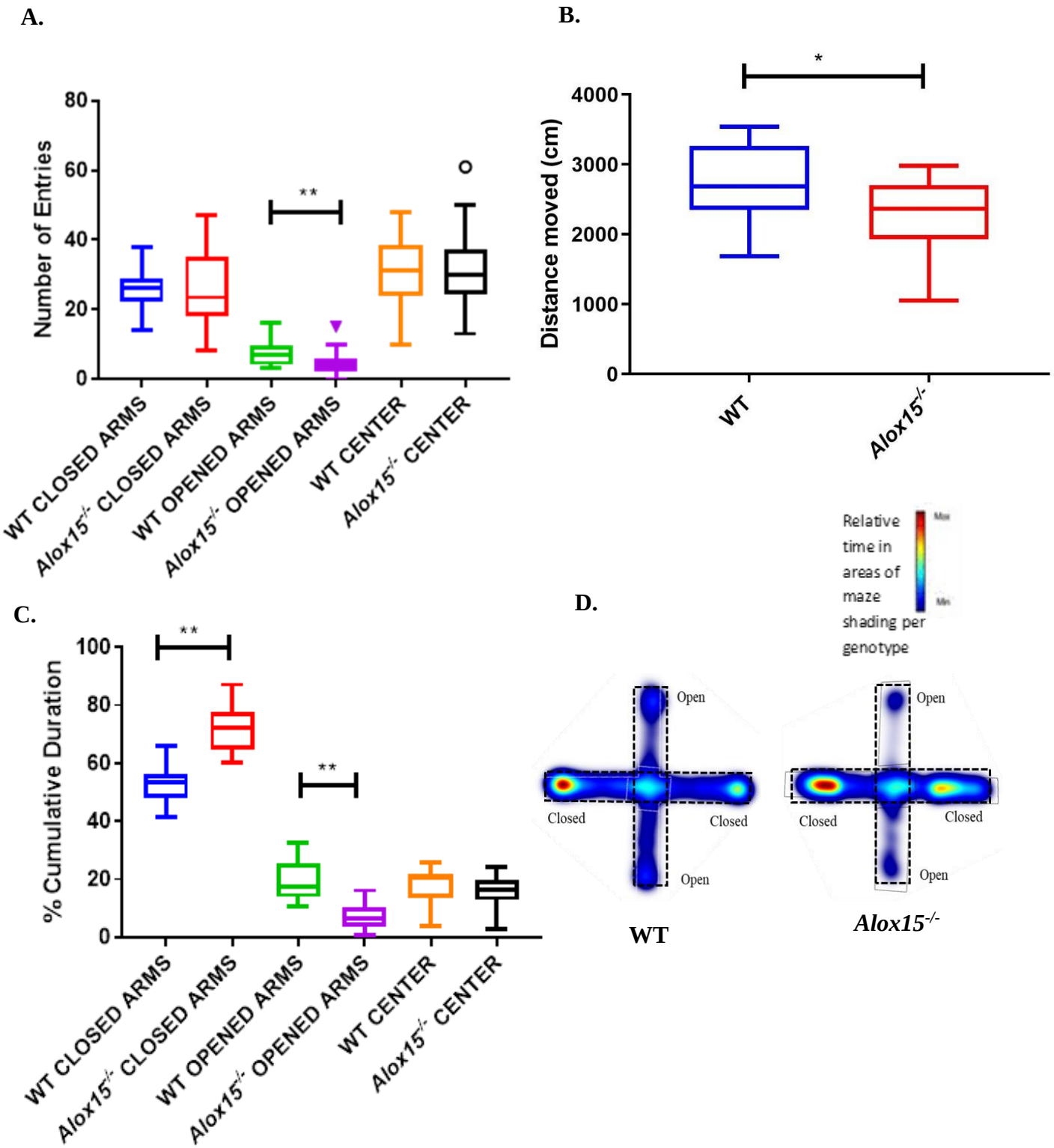

Figure 41. *Alox15*$^{-/-}$ male mice, aged 10 months, showed increased anxiety-like behaviour in EPM compared to WT mice. A. *Alox15*$^{-/-}$ mice made significantly fewer entries in open arms. B. Mean distance travelled by *Alox15*$^{-/-}$ mice in the apparatus C. *Alox15*$^{-/-}$ mice spent significantly less duration time in the open arms. D. Heatmaps displayed relative exploration of the open and closed arms across genotypes. Data were analysed using Mann- Whitney non-parametric U test and shown on Tukey box plots with mean ± S.E.M. n=27 per genotype *, **, *** and **** represent p≤0.05, p≤0.01, p≤0.001 and p≤0.0001 for genotype comparisons, respectively.

- **Time point – 7 months of age**

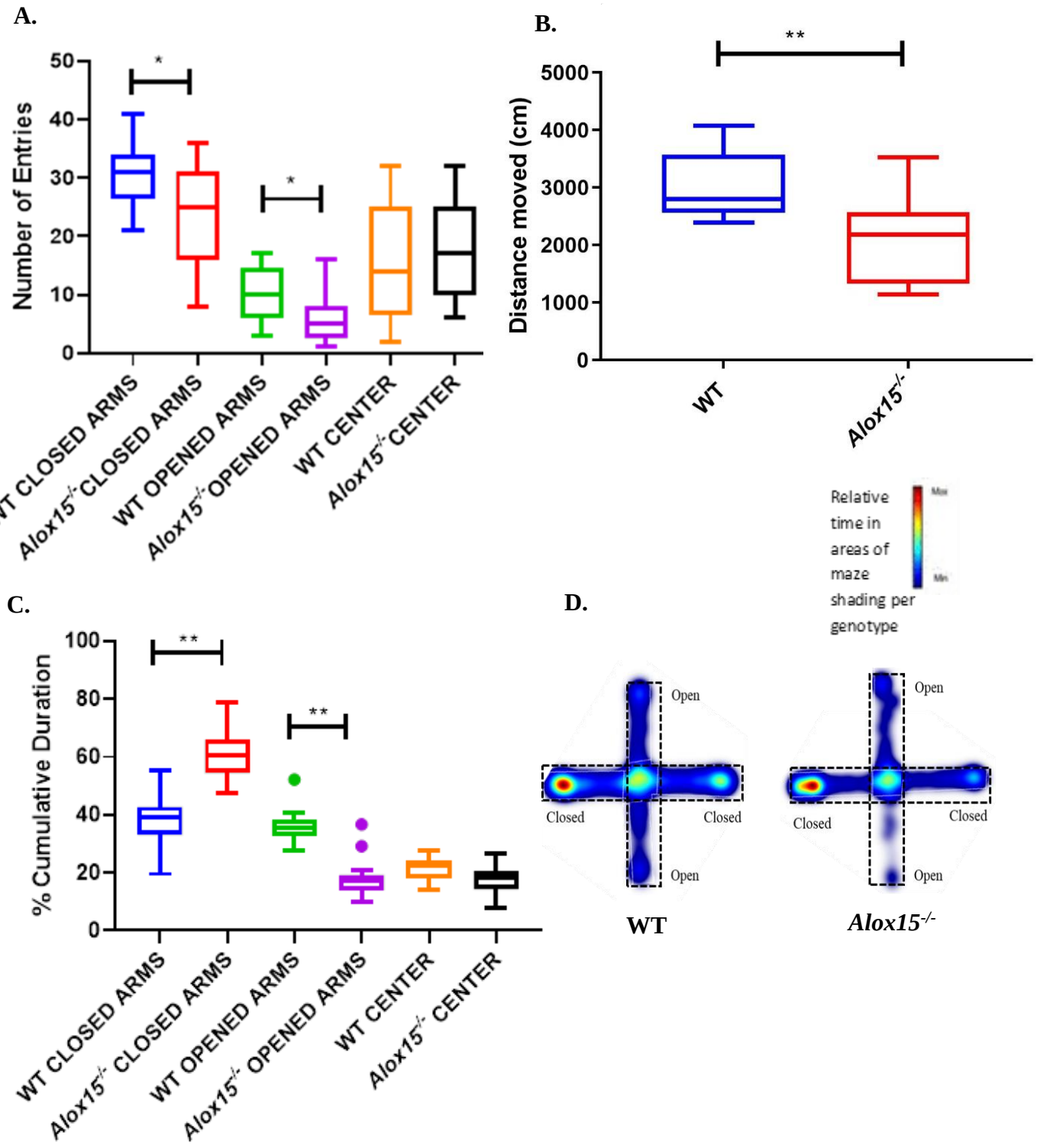

Figure 42. *Alox15*$^{-/-}$ male mice, aged 7 months, exhibited higher anxiety-related behaviour in EPM. A. *Alox15*$^{-/-}$ mice made significantly fewer entries in the open areas. B. Mean distance moved by *Alox15*$^{-/-}$ mice in the apparatus C. *Alox15*$^{-/-}$ mice spent markedly less duration time in the open arms. D. Heatmaps demonstrated relative exploratory activity between open and closed arms across both groups. Data were analysed using Mann- Whitney non-parametric U test and shown on Tukey box plots with mean ± S.E.M. n=29 per genotype *, **, *** and **** represent p≤0.05, p≤0.01, p≤0.001 and p≤0.0001 for genotype comparisons, respectively.

A. Anxiety-like behaviour - Males

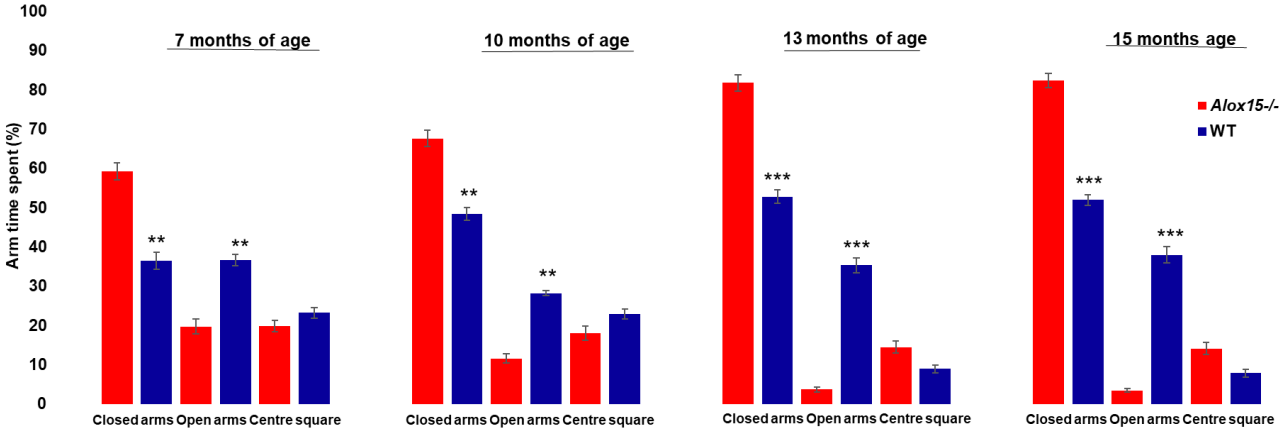

B. Anxiety-like behaviour - Females

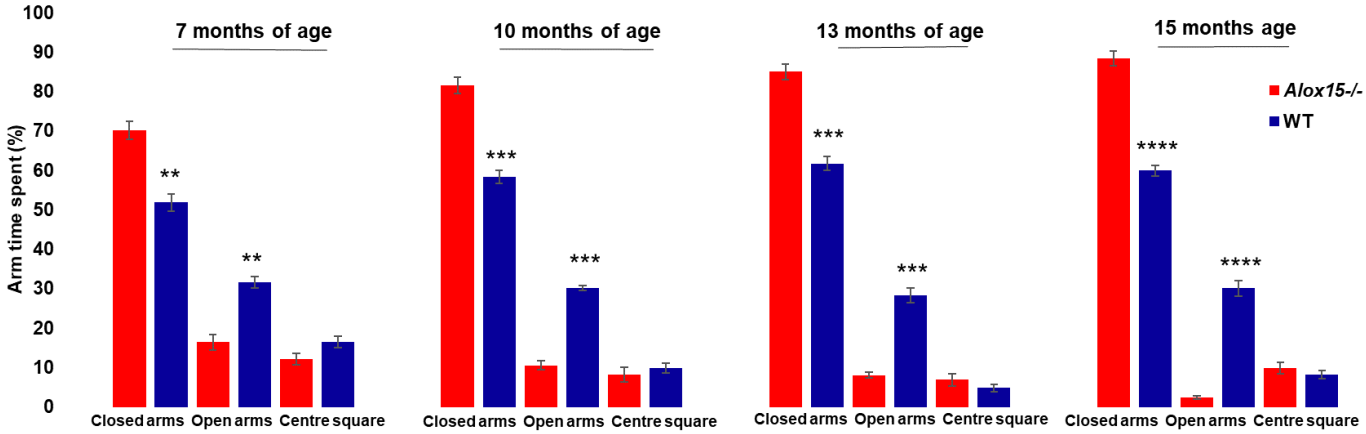

Figure 43. *Alox15*$^{-/-}$ male and female mice showed markedly increased anxiety-like behaviour in EPM at four different time points 7 months, 10 months 13 months and 15 months of age. Data were analysed by a repeated measures ANOVA with the five different age points as a within subjects' factor and genotype as the between subjects' factor and displayed as 2-D columns with mean ± S.E.M. n=26 per genotype *, **, *** and **** represent p≤0.05, p≤0.01, p≤0.001 and p≤0.0001 for genotype comparisons, respectively.

DISCUSSION

Summary table of the behavioural effects resulting from Alox15 genetic deletion:

Body weight:	A significant age-dependent increased weight gain.
Locomotor activity:	A markedly age-dependent reduced locomotor activity, concerning the distance that they moved and the speed at which they travelled during HP and TP of various tasks.
Recognition memory:	A trend towards a decline in recognition memory, but did not reach statistical significance, as illustrated in NOR test.
Spatial memory:	A significant effect of age in spatial memory decline as performed in OLT task
Working memory:	Significantly lower spontaneous alternation scores at 15 months of age, as showed in spontaneous alternation T-maze task.
Anxiety-like behaviour:	An age-dependent anxiety phenotype, which further exacerbated at 13 months of age and onwards, as demonstrated in EPM

This study was conducted to understand the effects of normal ageing on the brain and behaviour in the deficiency of *Alox15* gene. These effects were determined at 4 (young), 7-13 (middle-aged), and 15 (old) months of age in *Alox15*$^{-/-}$ mice relative to control mice. The *Alox15* mouse model was used to reveal dissociable effects on cognitive and emotional behaviours compared to age-matched control WT mice. A unique finding in this chapter is that deficiency of *Alox15* leads to a reproducible anxiety phenotype in mice that appears to worsen with age. A second main finding suggests that a significant component of spatial memory deficits that *Alox15*$^{-/-}$ mice displayed during normal aging may be associated with the failure of the hippocampus to store differences in contextual information compared to WT mice. The HPC is the brain structure related to processing spatial representations, which has been linked with the dHPC and the vHPC with anxiety (Bannerman *et al.*, 2003). These results suggest that age is also a controlling factor for the onset of anxiety and memory impairment. These findings support my hypothesis that the genetic deletion of *Alox15* has an impact in the cognitive function in young or aged healthy mice.

The main result of this chapter is that genetic deletion of *Alox15* exhibits an anxiety-related behaviour in mice as measured by EPM, and there is an age-dependent effect. The EPM task

is used to characterize animals' natural exploratory activity and drive between open arms, represented as unprotected arms of the apparatus, versus closed arms, considered safer. Thus, an increased length of time and a higher number of entries in the open arms are an objective index of low anxiety-related behaviour of mice. In contrast, a higher number of entries and time duration in closed arms indicate an increased anxiety phenotype. The results of this chapter showed that *Alox15*$^{-/-}$ mice spent more time in the closed arms and less time in the open arms than WT mice, reflecting the development of an anxiety-like phenotype. Furthermore, visual inspection of the heatmaps in EPM task indicates marked differences in the overall exploration in the open arms between genotypes. Indeed, *Alox15*$^{-/-}$ mice manifested an increased anxiety-like behaviour more severely with age than age-matched WT mice.

This is the first evidence of anxiety behavioural phenotype development being linked to the genetic deletion of *Alox15*. The specificity of the anxiety phenotype exhibited by *Alox15*$^{-/-}$ mice at the behavioural level was consistent with the significantly less time that *Alox15*$^{-/-}$ mice spent in the inner zone during the HP and TP than WT mice. As might be expected from the data regarding the time spent in the inner zone, *Alox15*$^{-/-}$ mice demonstrated a reduced cumulative duration in open arms as well as an overall reduced locomotor activity around the mazes. Based on the findings, *Alox15*$^{-/-}$ mice spent significantly less time in the inner zone than WT mice, showing overall decreased locomotor activity around the T-maze, the EPM apparatus. That has confirmed the validity of the third behavioural task, EPM, as an index of anxiety-like behaviour.

The anxiety phenotype is broadly consistent with published work by *Joshi et al.*, which demonstrated that the manipulation of *Alox15* causes significant changes in anxiety-like behaviour and deteriorates with age (Joshi *et al*., 2014). More specifically, the effect of age-associated anxiety-like behaviour is similar to genetically deleting or over-expressing this enzyme. Based on this finding, it is implied that age-associated anxiety behaviour may be influenced by an equilibrium of the downstream *Alox15* pathway, lipid metabolites, and mechanisms that might change the brain system. Another published work from the same group has shown that the genetic deletion of 5-lipoxygenase, a related enzyme that converts arachidonic acid to leukotriene metabolites, which are fatty acid signalling molecules, results in a similar anxiety phenotype. In their study, *Alox5*$^{-/-}$ mice did not manifest any anxiety-like behaviour at 3 months of age as measured by EPM; however, at 6 months of age and onwards, they exhibited increased anxiety-like behaviour compared to WT controls (Joshi, *et al*., 2011; Joshi, *et al*., 2013). However, last year, an article published in "For Better Science" stated that Pratico, Yoshi, and their colleagues' studies on AD appeared to be controversial*:*

https://forbetterscience.com/2020/10/22/the-pratfalls-of-domenico-pratico/. The controversy was about identical WB results between different mice across 4 different papers, as they were not in the same blot. Thus, his previous work may need re-evaluation.

Various behavioural tasks, including the NOR and OLT, were designed to evaluate memory function. The measurement of memory in both tasks was based on the exploration time with the objects during TP, which relies on a rodent's spontaneous preference for novel features of objects or an object array (Warburton *et al*., 2015). Multiple brain regions play an essential role in memory function, and when an area is damaged, the performance in recognition or spatial memory tasks is impaired too. The second finding is that the genetic deletion of *Alox15* is associated with hippocampal deficits as measured by the OLT task. Specifically, *Alox15*$^{-/-}$ mice spent significantly less time interacting with the object that moved into a new location than WT mice. Disruption of object-position information is associated with impaired hippocampal function (Warburton *et al*., 2010; Barker *et al.,* 2011). The data suggests an age-related decline, occurring mainly between 7 to 15 months of age. Similarly, female *Alox15*$^{-/-}$ mice showed a significant age-related decrease which is more severely with age in spatial learning and memory compared with age-matched WT females. In general, these findings support the conclusion that the impairment in spatial memory tests is not a result of sensory deficits.

As a measure of spatial learning and memory function, another test was used to evaluate the spatial working memory, the spontaneous alternation in a T-maze (Lalonde, 2002). In this chapter, it is suggested that the performance of *Alox15*$^{-/-}$ male mice was worse in the spontaneous alternation test, a test that has been widely used to study spatial working memory and is known to be dependent on hippocampal function. Olton *et al.* 1979, suggested that the ability of animals to display this trial-specific memory demonstrates a form of working memory. Typically, this task probes the decision-making and cognitive function based on the natural tendency of mice to explore a new environment and they prefer to investigate a new arm rather than returning to the familiar one, showing an alteration behaviour (Deacon *et al.,* 2006). This paradigm was chosen because it combines the evaluation of both spatial working memory and motor function while retaining a relatively less non-stressful environment (Wu *et al.,* 2018). The results of the T-maze task showed that *Alox15*$^{-/-}$ mice displayed a significantly lower spontaneous alternation rate between arms, as opposed to the revisiting of the recently explored arm, compared to WT mice. Also, the behavioural patterns exhibited significant differences in the locomotion activities between the genotypes. *Alox15*$^{-/-}$ mice were mainly characterized by physical immobility and some signs of stress observed during their performance. Therefore, the significantly reduced alternation performance on the T-maze task

might be correlated with the hippocampal deficits, confirming that the HPC plays a crucial role in exploratory behaviour (Gerlai, 1998). However, the pattern of spatial deficits across two tasks strongly suggests that the genetic deletion of *Alox15* has detrimental effects on spatial learning and memory.

Conversely, the findings from the NOR task reveal that the *Alox15*$^{-/-}$ mice could discriminate between the familiar and the novel object during TP, as these mice have encoded information taken from the SP. Interestingly, Figure 13 illustrates that *Alox15*$^{-/-}$ mice showed a trend towards reduced DR as they did not learn the information of the objects during SP to the same extent as the WT mice. Collectively, the data from DR ranging from 7 to 15 months of age showed that both *Alox15*$^{-/-}$ male and female mice demonstrated an age-related decline in recognition memory compared to age-matched WT mice, but it was not significant. The lack of statistical power in the NOR behavioural data may be due to the sample size. However, it is noteworthy to mention that increasing the sample size, may not necessarily result in significant results. Notably, *Alox15*$^{-/-}$ mice were able to discriminate between the two objects (familiar and novel) at a rate significantly above chance 0.5, indicating that there was no impact on their processing of recognition memory associations.

Furthermore, the findings from Chapter 3, stating that *Alox15*$^{-/-}$ mice demonstrated significant weight gain compared to controls, suggest that this significant difference in body weight may have contributed to the markedly reduced locomotor during the SP and TP. A visual inspection of the weight data indicates that an *Alox15*$^{-/-}$ mouse, which weighed 65 g, was more anxious when aged 15 months compared to when this mouse was 7 months. These data suggest that *Alox15*$^{-/-}$ mice, with the most prominent weight difference, were more anxious at 15 months; however, when these mice aged 7 months, they weighed less and were less anxious.

The findings of the EPM test implied that decreased overall locomotor activity and increased anxiety-like behaviour were found in aged *Alox15*$^{-/-}$ mice compared to middle-aged and young mice (15, 13, and 10 months of age < 7 months, $p < 0.0001$, $p < 0.001$ and, $p = 0.0044$ respectively). In particular aged *Alox15*$^{-/-}$ mice travelled significantly shorter distances across the maze and were more anxious than the youngest to middle-aged group, as there was an age-dependent increase in the percentage time spent in the open arms in the EPM, which further exacerbated at 13 months of age and onwards (Figure 43). The mean distance of aged *Alox15*$^{-/-}$ mice moved throughout exploration of EPM was 1150 cm; however it was 2200 cm at 4 months of age. Similarly, the results from Chapter 3, demonstrating an age-dependent decrease in locomotor activity, which was observed in the open field test.

To the best of my knowledge, the work presented in this chapter provides the first evidence for selective memory deficits following *Alox15* deletion. It is important to note that no other published study has investigated the role of the *Alox15* gene in normal cognition and anxiety as a function of age. Consequently, significant questions remain regarding any possible involvement of *Alox15*$^{-/-}$ mice in brain health. These results suggest a novel role for the *Alox15* gene in normal brain function.

There are no relevant clinical studies regarding the role of 12/15-LOX lipid products in neuropsychiatric disorders, except for a study conducted in an *Alox12*$^{-/-}$ Korean cohort, in which polymorphisms in the *Alox12* were associated with schizophrenia risk such as rc1042357 in the recessive model (Kim *et al*., 2010). The ageing brain is a lipid-rich organ and is susceptible to oxidative stress as it contains high concentrations of fatty acids that are vulnerable to lipid peroxidation. Of importance, bioactive lipids can contribute to the deterioration of neuronal functioning, which is involved in various neuropsychiatric disorders (Gemma *et al*., 2007).

In summary, the present study reveals a novel role for the *Alox15* pathway in the pathogenesis of anxiety-like behaviour, which could be helpful for later life in dissecting the pathophysiology of anxiety disorders. Ultimately, this study demonstrates that genetic deletion of *Alox15* increases anxiety-like behaviour in mice leading to an age-dependent effect. These findings indicate that ageing is associated with gradual changes in behaviours related to locomotor activity, anxiety-like behaviour, and spatial memory deficits from young to old age. The following chapter will investigate whether the changes in anxiety-like behaviour noted in *Alox15*$^{-/-}$ mice were associated with changes in the expression levels of various protein markers in the hippocampal area.

Chapter 5:

Altered anxiety-related proteins in *Alox15*$^{-/-}$ mice

INTRODUCTION

5.1 Chapter overview

In Chapter 4, behavioural tests were used to evaluate the cognitive function and anxiety-like behaviour utilizing *Alox15*$^{-/-}$ male compared with age-matched control WT mice at five different developmental stages (4, 7, 10, 13 and 15 months of age). The main finding was that *Alox15*$^{-/-}$ mice displayed an anxiety-like behavioural phenotype that appeared to worsen with age.

Next, in this chapter *Alox15*$^{-/-}$ and WT male mice, from the last time-point at 15 months, will be used to investigate the expression levels of four protein markers proposed to associate with increased anxiety-related behaviour, as shown in Chapter 4. Mainly, this study will elucidate the validation and localization of these proteins of interest in the ventral and dorsal subregions of the HPC of aged mice. The goal is to examine any possible neurobiological correlations of anxiety-related behavioural changes.

In Chapter 1, an overview of the role of several neurotransmitter systems in regulating anxiety-related behaviour in mice, including parvalbumin (PV), GABAergic, corticotrophin-releasing factor and serotonergic receptors, was introduced with emphasis on the hippocampal area. Although the HPC is a medial temporal lobe structure implicated in spatial memory processing, it is among the most highly susceptible brain regions to stress stimulation and the target of stress hormones (Kim *et al.*, 2002; Moodley *et al.*, 2004; Hill *et al.*, 2015). Hippocampal brain imaging and behavioural data in stress-induced rodents with anxiety disorders indicated a significant reduction in the region volume and impaired memory task performance (van Tol *et al.*, 2010; Bannerman *et al.*, 2014).

5.2 Anxiety and the HPC

Several neurotransmitter systems have been implicated in regulating anxiety-related behaviour in mice, including PV, GABAergic, corticotrophin-releasing factor and serotonergic receptors (Andrews *et al.*, 1994; File *et al.*, 1996; Zou *et al.*, 2016; Page *et al.*, 2019; Sloviter *et al.*, 1999; Schuler *et al.*, 2001; Pilc *et al.*, 2005; Booker *et al.*, 2013; Giachino *et al.*, 2014). The following sections will review the putative role of these pathways in anxiety. The HPC has been extensively studied regarding its function in declarative and spatial memory formation and its implication in emotional information relevant to anxiety-like behaviour (McEwen., 1999; Deacon *et al.*, 2002). The HPC is severely affected by age-related disorders and shows many molecular and cellular changes in normal ageing. Coronal brain sections will be used to investigate multiple protein expression levels and localizations of $GABA_B$, PV, $5HT_{1A}$, and

CRF_1 in the ventral and dorsal subregions of the HPC immunohistochemical analysis in conjunction with confocal microscopy between aged male *Alox15*$^{-/-}$ and WT mice.

- **Gamma-aminobutyric acid receptors (GABA)**

Gamma-Aminobutyric acid (GABA) functions as the chief inhibitory neurotransmitter in the brain accounting for 15% of the total neuronal function, playing a critical role in the regulation of many physiological and neurodevelopmental processes (Charles *et al.,* 2003; Bettler *et al.,* 2014). GABA is synthesized from the amino acid glutamate enzyme as a substrate by the action of glutamic acid decarboxylase (GAD) enzyme that catalyzes the decarboxylation of glutamate to GABA (Klausberger *et al*., 2008; Bhat *et al.,* 2010). GAD is expressed in cells that use GABA as an inhibitory neurotransmitter. In mammals, two isoforms of different molecular weights have been reported: GAD_{67}, located in neuronal soma, and GAD65 on the axons (Zhao *et al.*, 2013; Grone *et al*., 2016). GABA receptors release GABA into the synaptic nerve terminals, the primary inhibitory receptors belonging to the CNS's largest class of inhibitory neurons.

Once synthesized, neuronal inhibition by GABA is mediated via fast-acting ionotropic $GABA_A$ receptors, which are ligand-gated ion channels and open chloride channels, and also via slower-acting metabotropic $GABA_B$ receptors, which are broadly expressed in the brain with the ability to modulate synaptic transmission throughout the CNS (Bowery., 1989; Millan., 2003; Emson., 2007).

Presynaptically, $GABA_B$ receptors are present at inhibitory terminals and coupled to Gi or G0 protein through the family of GPCR, which inhibit voltage-gated calcium (Ca^{+2}) channels (acting as autoreceptors) (Padgett *et al.,* 2010; Chalifoux *et al.,* 2011) (Figure 44). Postsynaptically, $GABA_B$ receptors are present at excitatory terminals to activate other receptors that inhibit the release of other neurotransmitters, such as glutamatergic interneurons (acting as heteroreceptors) (Kerr *et al*., 1995; Brambilla *et al*., 2004). Activation of $GABA_B$ receptors is mediated via potassium channels, which function as a heterodimer of two subunits, R1 and R2, necessary for G protein signalling, that inhibits neuronal activity resulting in membrane hyperpolarization (Cryan *et al.,* 2004; Kotak *et al.,* 2013; Booker *et al.,* 2013; Li *et al.,* 2017). This may lead to an imbalance between the inhibitory and excitatory neurotransmitter system activity on pyramidal neurons, as well as to altered expression levels of crucial proteins for neurotransmission at the presynaptic site resulting in the onset of anxiety disorders (Caillard *et al.,* 2000; Schwaller *et al., 2*004; Bebarroch *et al.,* 2012; Volman *et al*., 2011).

Although GABAergic inhibitory interneurons account for roughly 15% of the total CNS neuronal population, they serve significant functions in neural networks, such as the regulation of the synchronization of the neural networks (Klausberger *et al.,* 2008; Lehmann *et al.,* 2012; Pelkey *et al.,* 2017). Their distinct morphology defines hippocampal GABAergic systems, synaptic connectivity and contribution to the processing of anxiety-like information (Klausberger *et al.,* 2008). Disruption of these important regulators of neural activity has significant consequences for brain function and, thus, behaviour. Several studies suggest that any interruption to GABAergic signalling is closely associated with emotional disorders, including anxiety (Gonzalez-Burgos *et al.,* 2011).

Roughly all neurons and glial cells express the $GABA_B$ receptors; thus, their activity affects many systems in the CNS and behavioural states. Recent functional studies have highlighted the role of $GABA_B$ receptors in modulating anxiety (Giachino *et al*., 2014; Degro *et al.,* 2015; Jurado-Parras *et al.,* 2016; Booker *et al.,* 2020). Several studies investigated its role by utilizing KO mice for $GABA_B$ receptors which displayed prominent anxiety-related behaviour assessed by various anxiety paradigms (Felice *et al.,* 2016). Anxiety-like behaviour was evaluated in mice by investigating the approach-avoidance conflict, such as the EPM, open field, and light-dark box, as they are the most validated tests (Bailey., 2009). A preclinical study by Mombereau *et al*., 2005 demonstrated that mice lacking $GABA_B$ receptors manifested an anxiety-like behaviour, as assessed in several paradigms, including the light-dark box and EPM.

Benzodiazepines, which act through $GABA_A$ receptors, have been extensively prescribed as anxiolytic drugs for depression, epilepsy, insomnia, anxiety, and they may not be the most effective and safe treatment of anxiety disorders due to side effects associated with sedation, ataxia, cognitive impairment due to non-selective binding. Conversely, in 1980's baclofen, a $GABA_B$ receptor agonist, has been discovered and its anxiolytic-like effects in several tests was found to be a promising therapeutic strategy, with fewer side effects than benzodiazepines (Cryan *et al.,* 2004; Cryan *et al.,* 2005). Notably, baclofen has been reported to reverse the anxiogenic response induced by withdrawal from chronic diazepam and alcohol treatment in rodents (File *et al.,* 1991; File *et al.,* 1992). Moreover, clinically baclofen reversed the anxiety associated with post-traumatic stress and panic disorder (Drake *et al.,* 2003; Breslow *et al.,* 1989; Jacobson *et al.,* 2005). Nevertheless, the role of $GABA_B$ receptors and the underlying mechanisms in modulating anxiety are not fully understood (Krystal *et al.,* 2002; Brambilla *et al.,* 2003; Lydiard., 2003).

A study by Mombereau *et a.l.,* in 2004 showed that $GABA_B^{-/-}$ mice, lacking functional $GABA_B$ receptors, were more anxious than WT in widely used anxiety paradigms, such as in the light-dark box and staircase tests (Mombereau *et al.*, 2004). Specifically, in this study, $GABA_B^{-/-}$ mice showed a significant decrease in the time spent in the light; demonstrated a significantly reduced number of light-dark transitions compared to WT mice, as well as a reduction in the number of steps climbed compared to WT mice (Mombereau *et al.,* 2004; Mombereau *et al.*, 2005). In addition to this behavioural approach, another approach targeting chronic and acute administration of GS39783 in $GABA_B^{-/-}$ mice, a novel $GABA_B$ receptor-positive modulator, demonstrated a decreased anxiety in the light-dark box test for anxiety-related behaviours (Mombereau *et al.,* 2004). These results showed that deletion of $GABA_B$ receptors resulted in a more anxious phenotype in mice, suggesting that activation of $GABA_B$ receptors decreased anxiety-like behaviour. Another study by Cryan *et al*., 2004 demonstrated that acute administration of GS39783 displayed an anxiolytic profile in mice in the elevated zero maze and stress-induced hyperthermia tests (Cryan *et al*., 2004; Jacobson and Cryan, 2008). Supporting these findings, this positive modulator of $GABA_B$ receptors may serve as a novel therapeutic strategy for developing anxiolytic effects. In summary, these observations will direct the hypothesis that activation of $GABA_B$ receptor leads to reduced anxiety-related behaviour in mice.

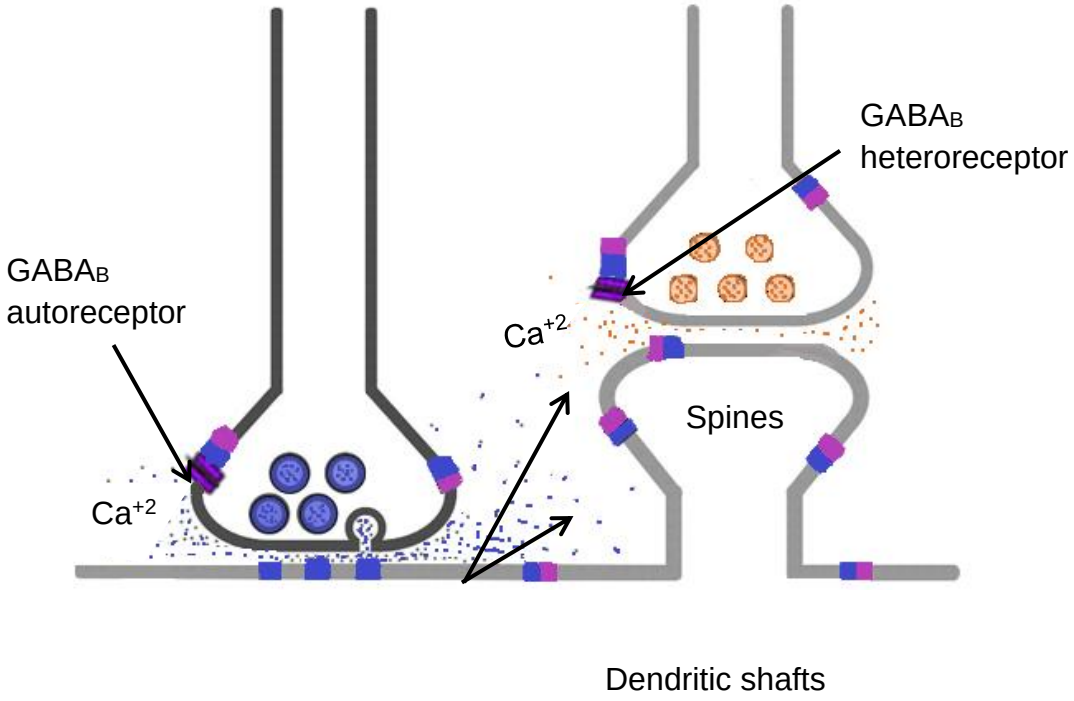

Figure 44. The underlying mechanism of $GABA_B$ receptor activation in the HPC. $GABA_B$ receptors are heterodimers of two subunits, $GABA_B$(1) (blue) and $GABA_B$(2) (violet). Presynaptic $GABA_B$ autoreceptors modulate neurotransmitter release via voltage activated Ca^{2+} channels, whereas $GABA_B$ heteroreceptors inhibit the release of several other neurotransmitters (e.g. glutamate). Metabotropic $GABA_B$ receptors are activated by spilled-over GABA (dots). Adapted from Kulik, *et al*., 2003.

- **Parvalbumin (PV)**

Parvalbumin (PV) is a protein that belongs to the category of intracellular free calcium (Ca^{2+})-binding proteins, along with calbindin D-28k (CB) and calretinin (CR) (Schwaller *et al.*, 2002). Undoubtedly, PV was found to be a marker for the most well-known subpopulation of GABAergic interneurons (Urakawa *et al*., 2013).

The parvalbumin-expressing interneurons (PV-INs) account for 40% of the total GABAergic inhibitory population (Xu *et al*., 2010). PV-INs form inhibitory synapses onto cell bodies or the axonal terminals of pyramidal cells (thick myelinated sheets around axon neurons) (Caillard *et al.*, 2000). Any reduced levels or absence of calcium in the soma and dendrites of the pyramidal cell layer could alter the properties of PV-containing GABAergic interneurons resulting in significant changes in calcium homeostasis (Zaletel *et al.*, 2016).

According to detailed mapping of the PV+ cells, most PV-positive interneurons are abundantly expressed in multiple brain regions, especially in the cerebral cortex and HPC (Celio, 1990). Specifically, PV-positive cells are widely distributed in the HPC, at granule cells in the DG

and CA3, CA1 pyramidal cells (Godavarthi *et al*., 2012; Bezaire *et al*., 2013; Zaletel *et al*., 2016).

Electrophysiological studies have shown that the properties of PV-INs are characterized by their typical fast-spiking phenotype, mainly at the level of the HPC (Kawaguchi *et al.,* 1987; Fuchs *et al.,* 2007; Hu *et al.,* 2014). The signals of these cells are characterized by a rapid-response profile, as they fire upon stimulation coordinating the neuronal activity at high frequency, and adapting at low spike frequency; PV-Ins can covert an excitatory input signal to inhibitory signal within millisecond (Goldberg *et al.,* 2008; Hu *et al.,* 2014; Bartholome *et al.,* 2020). PV-INs target the body cells and axons of dendrites of their hippocampal target cells and control the output of post-synaptic neurons via feedforward and feedback inhibition along with the high-frequency synchronisation (Hu *et al.,* 2014).

Several studies have highlighted the role of hippocampal PV^+ cells in anxiety. An immunohistochemical study by Czeh *et al* in 2005 in adult male tree shrews, which were subjected to a 5-week session of stress, showed a significant reduction of the number of PV immunoreactive interneurons in the DG, CA2 and CA3, while no changes were detected in CA1 (Czeh *et al.,* 2005). Thus, the authors demonstrated that chronic stress caused anxiety, which was associated with decreased PV^+ interneurons. However, these reductions were prevented by treatment with fluoxetine or SLV-323, antagonists for the novel neurokinin-1 receptor (NK_1R) to correct the dysfunction (Czeh *et al.,* 2005).

Similarly, adult male Wistar rats subjected to 9 weeks of daily chronic stress showed changes in various subtypes of hippocampal GABAergic interneurons by employing immunohistochemistry. Notably, a reduction in the number of PV+ interneurons in all regions of the dHPC was noted, whereas, in the vHPC, a significant decrease was detected only in the CA1 subregion (Czeh *et al.* 2015).

Another interesting study by Godavarthi *et al*., 2014 showed that Ube3a deficient mice showed a dramatic down-regulation of PV+ interneurons in the hippocampal CA3 and DG regions and the basolateral amygdala. Ube3a deficient mice represent a mouse model of Angelman syndrome (AS), primarily caused by the loss of function of the inherited UBE3A gene and reduced synaptic plasticity; AS mice show increased anxiety and reduced hippocampal PV expression compared to WT. The anxiety-like behaviour can be partially reversed by treatment with fluoxetine, a selective serotonin reuptake inhibitor class of antidepressants (Godavarthi *et al.,* 2014). Further evidence of the role of PV immunoreactivity in mice comes from a recent study by Deng *et al*. (2019), who showed reduced PV interneurons in the ventral CA1 hippocampal area after two months of social isolation being single housed for 8 weeks

compared to group-housed mice. Similarly, a study by Murthy *et al.*, (2019) utilized mice with repeated maternal separation with early weaning (MSEW) for 8 hours from P6-P16 and showed increased anxiety in their adulthood confirmed by EPM and reduced intensity of PV in the vHPC compared to controls (Murthy *et al.*, 2019).

In summary, the findings of the previous studies will direct the hypothesis that a decreased number of PV-containing GABAergic interneurons are associated with increased anxiety levels in the HPC.

- **Corticotropin-releasing factors (CRF) receptor**

The corticotropin-releasing factor (CRF) is a hormone and neurotransmitter mainly synthesized in the paraventricular nucleus of the hypothalamus (PVN). CRF receptors are G-coupled receptors that bind to the adrenocorticotropin releasing hormone (ACTH) and play a key role in regulating the neuroendocrine and behavioural response to stress, including emotion and anxiety, via the hypothalamic-pituitary-adrenocortical axis (HPA) (Reul *et al.*, 2002; Wang *et al.*, 2017). Under stressful conditions, CRF is released from the PVN and activates CRF receptors resulting in the secretion of ACTH into the bloodstream (Risbrough *et al.*, 2006). ACTH, in turn, activates ACTH receptors in the adrenal cortex, releasing glucocorticoids via HPA axis; cortisols in human and corticosterone in rodents to inhibit the CRF production (Bale *et al.*, 2000).

There are two main subtypes of CRF receptors: CRF receptor type 1 (CRF_1 receptor) and CRF receptor type 2 (CRF_2 receptor) (Contarino *et al.*, 1999). In rodents, the CRF_1 receptor is widely distributed in the cortex, limbic regions and brain stem and mediates behavioural changes associated with anxiety (Contarino *et al.*, 1999; Risbrough *et al.*, 2006).

Interestingly, animal studies suggested that the overexpression of CRF_1 receptor due to stress responses are particularly implicated in the early onset of significant anxiety disorders. Notably, knockout mice with deletion of the CRF_1 receptor displayed decreased anxiety-like behaviour as revealed by the EPM and reduced anxiety in the Black and White test box (Contarino *et al.*, 1999; Bale *et al.*, 2002; Van Gaalen *et al.*, 2002). Similarly, Smith and his colleagues showed that CRF_1 deficient mice exhibited significantly reduced anxiety-like behaviour with respect to control mice and displayed dysregulation of the HPA axis (Smith *et al.*, 1998). Also, a study utilizing conditional CRF_1 knockout mice showed significantly reduced anxiety where CRF_1 was inactivated in limbic system structures compared to null mutants, while there were no alterations in basal HPA-system activity. The behavioural analysis was deduced from the light-dark box and EPM paradigms, implying that the anxiolytic

effects of CRF_1 receptors can be independent of HPA axis activity and, more importantly, that CRF_1 modulates increased anxiety-related behaviour (Müller *et al.*, 2003). Similarly, Lu *et al.* (2008) used a knock-in mouse model that permits overexpression of CRF in the temporal lobe, resulting in increased active stress-coping behaviour as Open Field test and restraint stress confirmed(Lu *et al.*, 2008).

Another transgenic mouse model overproducing CRF_1 receptor has been generated to evaluate the anxiety-like behaviour in behavioural paradigms relevant to anxiety. The overexpression of the CRF_1 receptor in mice resulted in reduced exploratory activity in novel areas and increased anxiety-like behaviour as a light-dark exploration box (Van Gaalen *et al.*, 2002).

Based on the previous results, the hypothesis is that the increased expression of the CRF_1 receptor is associated with more significant anxiety in the hippocampal subregions.

- **Serotonin receptors (5-HT)**

Serotonin (5-hydroxytryptamine or 5-HT) is a monoamine neurotransmitter widely distributed throughout the CNS, mainly originating from the raphe nuclei in the midbrain (Jacobsen *et al.*, 2011). 5-HT acts as a multifunctional neurotransmitter in the brain with roles in regulating mood, sleep, stress, emotion, sensory processing, cognitive functions and as a hormone in the periphery (Ögren *et al.*, 2008; Berger *et al.*, 2009; Lam *et al.*, 2010; Yadav, 2012).

Among the 14 different 5-HT receptor subtypes, the $5\text{-}HT_{1A}$ receptor has received the most attention because of its association with anxiety and depression (Toth., 2003; Garcia-Garcia *et al.*, 2014). The 5-HT1A receptor, like most of the 5-HT receptors, belongs to the superfamily of G-coupled receptors that control many intracellular cascades, such as inhibition of cAMP formation and in humans encoded by the HTR1A gene (Parks *et al.*, 1998). The structural location of the brain $5\text{-}HT_{1A}$ receptor identifies synaptic proteins and hence is operated both presynaptically and postsynaptically (Hamon., 2000).

Presynaptically, $5\text{-}HT_{1A}$ receptors regulate 5-HT release from axon terminals and act as auto-receptors located on soma and dendrites of serotonergic neurons in the raphe nuclei (Lesch *et al.*, 2005; Hannon *et al.*, 2008). It has been reported that presynaptic $5HT_{1A}$ activation by agonist leads to the reduction of serotonergic neurons, suppression of 5-HT release and consequently release of 5-HT signalling at downstream target receptors in its projection areas (Parks *et al.*, 1998; Palchaudhuri *et al.*, 2005).

At a postsynaptic level, $5\text{-}HT_{1A}$ heteroreceptors are distributed in non-serotonergic neurons, primarily in the limbic structures, including hippocampal pyramidal subregions, DG, prefrontal cortex and amygdala (Zhuang *et al.*, 1999; Sibille *et al.*, 2000). Remarkably, the serotonergic

innervation of the HPC originates from the dorsal and median raphe nuclei; as such, the 5-HT_{1A} is expressed in the early stages of embryonic development in the pyramidal and granular cells of the HPC (Pompeiano *et al.,* 1992; Rojas *et al.,* 2016). The HPC receives an essential serotoninergic projection, resulting in a high expression of 5-HT_{1A} heteroreceptors in the brain (Hensler *et al*., 2007). The activation of postsynaptic 5-HT_{1A} heteroreceptors is associated with regulating their activity through dendrites of glutamatergic projection neurons and axon terminals of GABAergic inhibitory interneurons (Riad *et al.,* 2000; Santana *et al.,* 2004). Thus, this pathway is mediated via several neurotransmitter systems and involved in the regulation of synaptic plasticity, cognitive functions, emotional processing, and the pathophysiology of mood and anxiety disorders (Sibille *et al.,* 2000; Varnas *et al.,* 2004; Christoffel *et al*., 2011) (Figure 45).

Strong evidence suggests that the serotonergic neurotransmitter system is vital in modulating several processes relevant to anxiety (Toth., 2003; Akimova *et al.,* 2009). A mouse model with deficiency or low expression levels of the 5-HT_{1A} receptor was generated independently in 3 labs from different genetic backgrounds and examined under similar conditions. Behaviourally, mice with deficiency of the 5-HT_{1A} receptor demonstrated an increased anxiety phenotype associated with a reduction in the HPC and cortex using behavioural paradigms, such as EPM, zero maze and open field and novelty-suppressed feeding tests (Heisler *et al.,* 1998; Parks *et al.,* 1998; Ramboz *et al.,* 1998). Immunocytochemical studies revealed the localization of 5-HT_{1A} receptors in prefrontal cortical neurons (Goodfellow *et al*., 2009).

Further evidence comes from Jacobsen *et al.* (2011), who used Pet-1 null mice, resulted in deficits in serotonergic system which manifested an anxiety phenotype. They argued that 5-HT1A receptor expression levels were up-regulated in the HPC but down-regulated in the striatum and cortex of Pet-1 knockout compared with WT mice. These findings were assessed *in situ* hybridization and immunofluorescence (Jacobsen *et al.,* 2011). The following year, *in-situ* hybridization and immunofluorescent work carried out by Czesak and colleagues revealed that 5-HT_{1A} mRNA and protein were increased in the dorsal raphe region, and postsynaptic 5-HT_{1A} receptors were down-regulated in the frontal cortex (Czesak *et al.,* 2012). Pharmacological studies showed that acute administration of 5-HT_{1A} receptor agonists, such as 8-OH-DPAT, into the dorsal and median raphe nuclei, resulted in anxiolytic effects in animal studies. Also, the acute stimulation of the postsynaptic 5-HT_{1A} receptors in the dHPC results in an anxiogenic effect in the EPM task (Andrews *et al.,* 1994; File *et al.,* 1996).

In summary, the findings of the previous studies will test the hypothesis that reduced activity of postsynaptic 5-HT_{1A} receptors is responsible for increased anxiety levels, whereas elevated

5-HT_{1A} autoreceptor expression is associated with depression and resistance to chronic SSRI treatment.

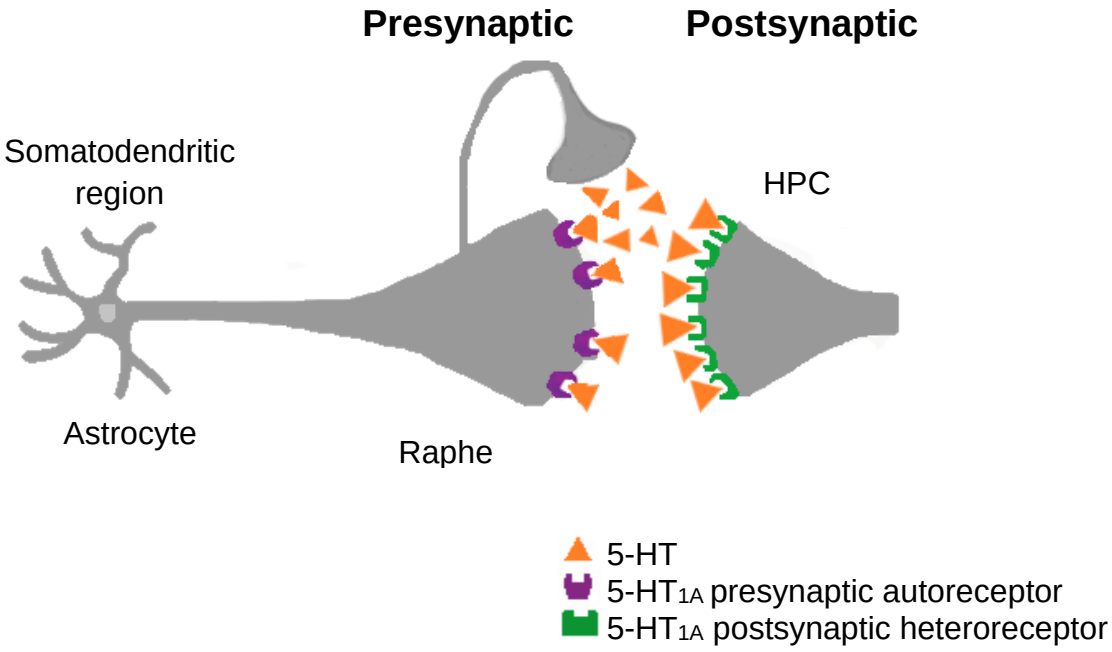

Figure 45. Distribution of 5-HT_{1A} autoreceptors and heteroreceptors in the brain. Activation of 5-HT_{1A} autoreceptors is located at the cell body and dendrites. In the HPC the 5-HT_{1A} postsynaptic receptors. Adapted from de Aguiar, R.P., *et al.*, 2002.

5.3 Aims and objectives

The main aim of this chapter is to determine whether alterations in the expression levels of PV, $GABA_B$ receptor, CRF_1 receptor and $5HT_{1A}$ receptor are present in *Alox15*$^{-/-}$ male mice relative to age-matched WT male mice, 15 months of age. In addition, to examine whether they may contribute to previous behavioural changes from Chapter 4 relevant to anxiety-like behaviour compared to WT mice.

1. To evaluate the expression levels of the above markers by acquiring immunofluorescence signals with confocal microscopy in the mouse hippocampal subregions of aged mice and compare them between genotypes.
2. To investigate differences in the distributional patterns of the above markers among CA1, CA2/3 and DG subfields of the HPC between genotypes regarding signal intensity and the number of positive cells.
3. To examine any notable differences in the expression levels of various proteins in the vHPC compared to the dHPC.

4. To assess the results of the two separate approaches for each specific marker, including the percentage of the DAPI-labelled positive cells and the average mean fluorescent intensity, which may give a different reading to the level of immunofluorescence.

RESULTS

i. Parvalbumin-expressing interneurons (PV-INs) were markedly reduced in the HPC of Alox15$^{-/-}$ mice.

The primary subclass of GABAergic interneurons includes those containing the calcium-binding protein, PV^{+}- expressing interneurons (PV-INs) (Schwaller *et al.*, 2002). Here, a closer examination of the merged images with DAPI counterstaining revealed that the PV expression in WT male mice was widely distributed in the vCA3, CA1 pyramidal cell layers and granule cell layer of the DG (Figure 46 C, G, K), was significantly higher than the vHPC subregions in *Alox15*$^{-/-}$ male mice (Figure 46 O, R, Y). Similarly, the PV immunoreactivity was markedly elevated in the subregions of dHPC in WT mice (Figure 48 C, G, K) relative to *Alox15*$^{-/-}$ male mice (Figure 48 O, R, Y).

The percentage of PV immunoreactivity in the vHPC as well as in dHPC was analysed by Mann- Whitney non-parametric U test for genotype comparisons. *Alox15*$^{-/-}$ mice displayed a 50 % dramatic reduction in the percentage of PV^{+} cells in the vCA3 subregion, a 15 % decrease in the CA1 area, and a 60 % drop in the DG relative to WT, as shown in Figure 47 A, B, C ($P<0.00001$, $P=0.0001$, $P<0.00001$, respectively). Similarly, *Alox15*$^{-/-}$ mice showed a marked 35 % - 40 % reduction in the number of PV-immunoreactive cells in the dCA3 region, 20 % in the dCA1 area and a remarkable decrease to 60 % in the dDG compared to WT mice, as indicated in Figure 49 A, B, C ($P=<0.00001$). Most PV-INs were stained strongly in granule cell somata and the CA3 and CA1 pyramidal cell bodies in WT mice relative to *Alox15*$^{-/-}$mice.

Qualitative analysis was also performed by Mann- Whitney non-parametric U test, revealing that *Alox15*$^{-/-}$ mice showed PV markedly weaker corrected total fluorescent signal intensity (CTCFI) in CA3, CA1 pyramidal cells layers, as well as the granule cell layers of the DG in vHPC and dHPC than WT mice, as illustrated in Figure 47 D, E, F and Figure 49 D, E, F ($P=0.00001$, $P=0.0001$, $P=0.0031$ vs $P<0.00001$, respectively). The lower PV expression levels generally led to significantly weaker intensity of PV fluorescent signals in *Alox15*$^{-/-}$ compared to WT mice.

Strikingly, PV cell clustering was remarkably distributed in the cell soma and dendrites in the CA3 region compared to other hippocampal subregions. These characteristics, including the cell properties with their diverse morphologies and axon terminal distribution, were similar to a previous study by Urakawa and his colleagues about the classification of PV-positive neurons into four major morphological types (Chez *et al.*, 2015; Steullent *et al.*, 2010; Urakawa *et al.*, 2013).

- **PV – vHPC**

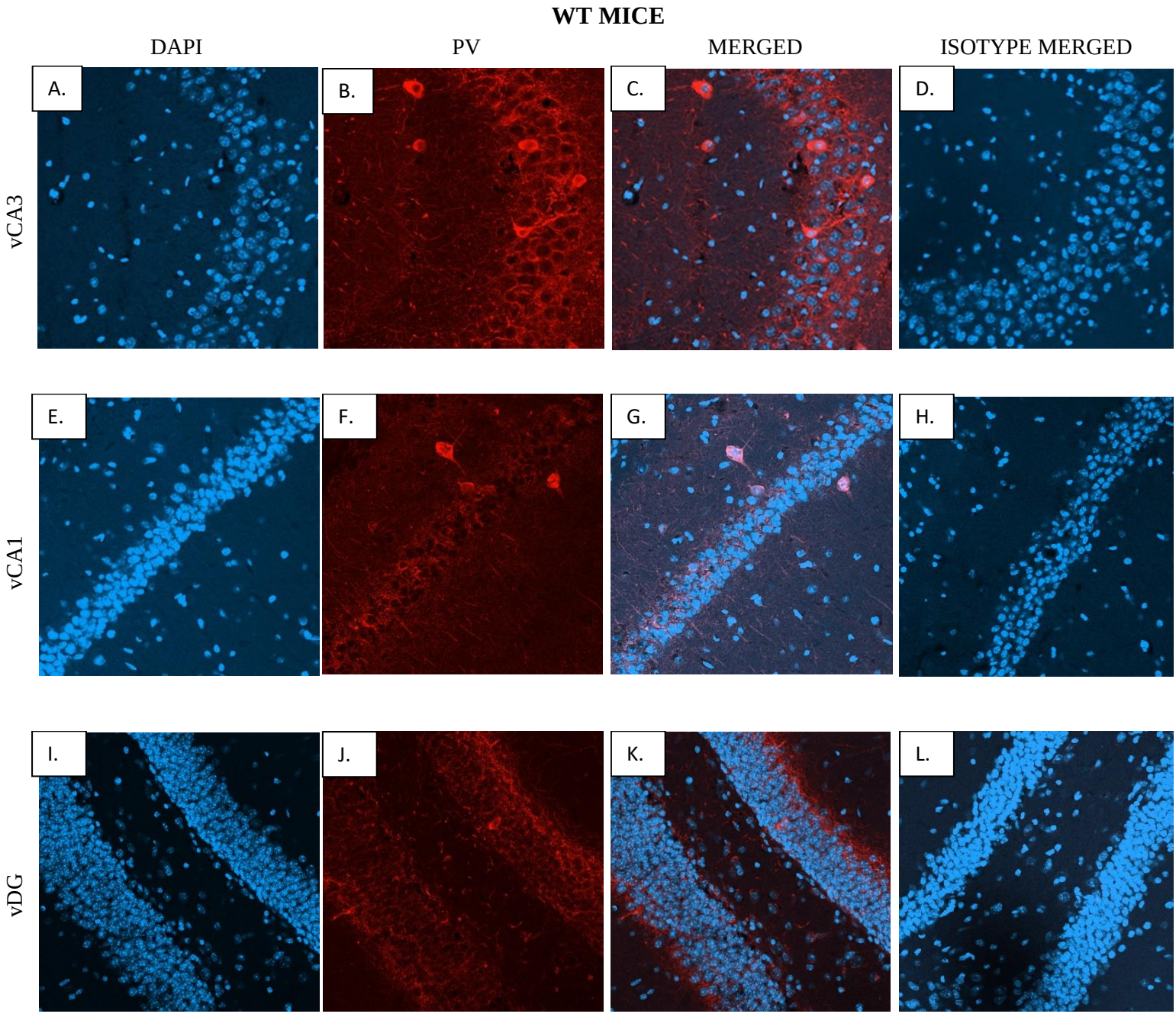
WT MICE
DAPI
PV
MERGED
ISOTYPE MERGED
vCA3
vCA1
vDG
A.
B.
C.
D.
E.
F.
G.
H.
I.
J.
K.
L.

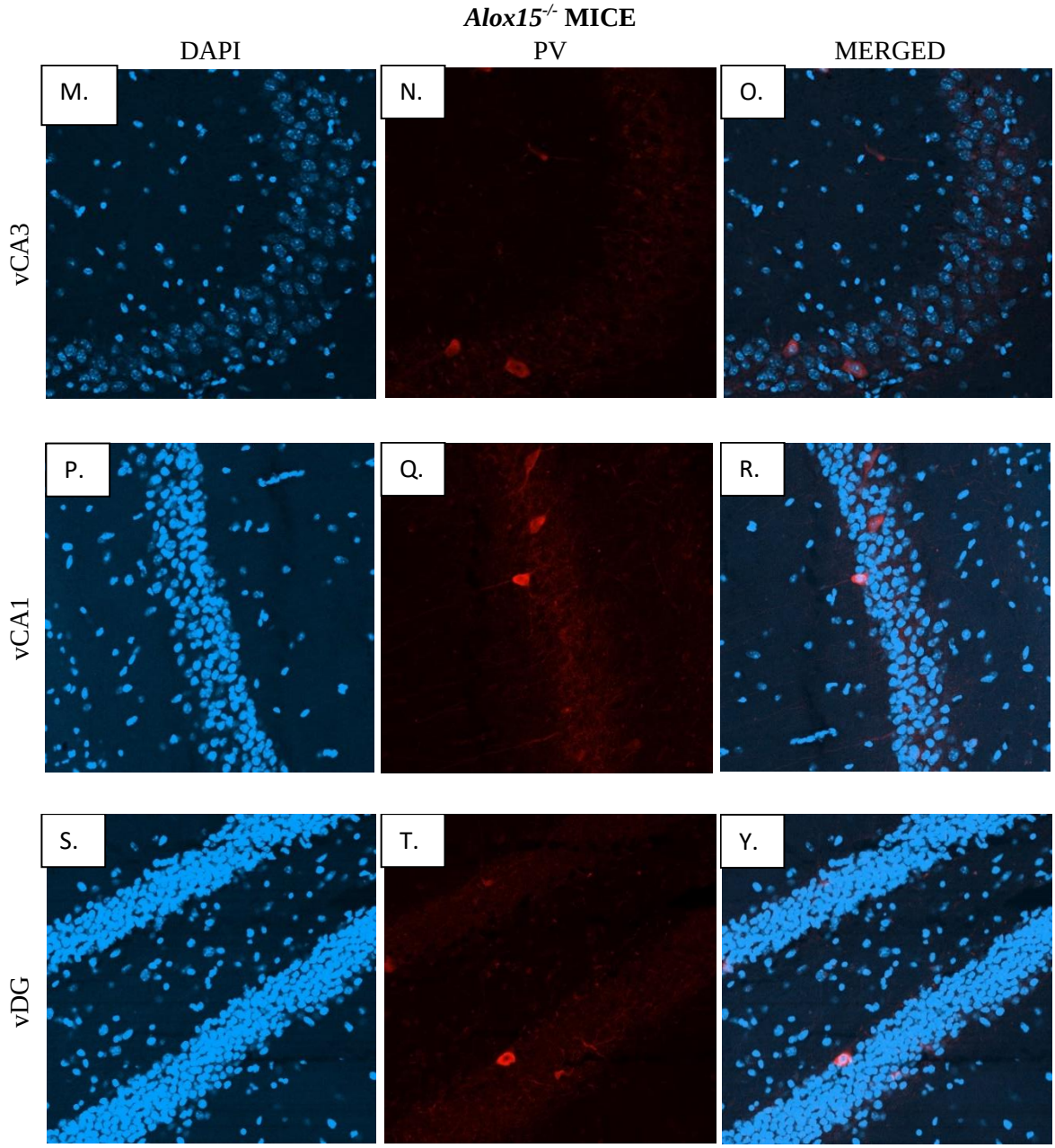

Figure 46. Comparison of immunofluorescent visualization of the coronal brain sections of 20 µm thickness showing detection and localization of PV in vHPC CA1, CA2/3 and DG. The top panel corresponds to CA3 subfield of WT mouse vHPC (A) single channel acquisition of DAPI staining (blue) of cell nuclei (AF405) (B) single channel PV staining AF568 (orange/red) (C) merged image of PV in colocalization with DAPI (D) an overlay imaging on isotype control, rabbit IgG polyclonal, merged with DAPI counterstaining. The middle panel corresponds to CA1 subfield of WT mouse vHPC (E) single channel acquisition of DAPI staining (F) single channel PV staining AF568 (G) merged image of PV with DAPI (H) merged image on isotype control. The bottom panel corresponds to DG subfield of WT mouse vHPC (I) single channel acquisition of DAPI staining (J) single channel PV staining AF568 (K) merged image of PV with DAPI (L) merged image on isotype control. In contrast, the top panel corresponds to CA3 subfield of *Alox15*$^{-/-}$ mouse vHPC (M) single channel acquisition of DAPI staining (N) single channel PV staining AF568 (O) merged image of PV with DAPI. The middle panel corresponds to CA1 subfield of *Alox15*$^{-/-}$ mouse vHPC (P) single channel acquisition of DAPI staining (Q) single channel PV staining AF568 (R) merged image of PV with DAPI. The bottom panel corresponds to DG subfield of *Alox15*$^{-/-}$ mouse vHPC (S) single channel acquisition of DAPI staining (T) single channel PV staining AF568 (Y) merged image of PV with DAPI WT (n=12) and *Alox15*$^{-/-}$ (n=11) male mice, 15 months of age. Scale bars, 100 µm.

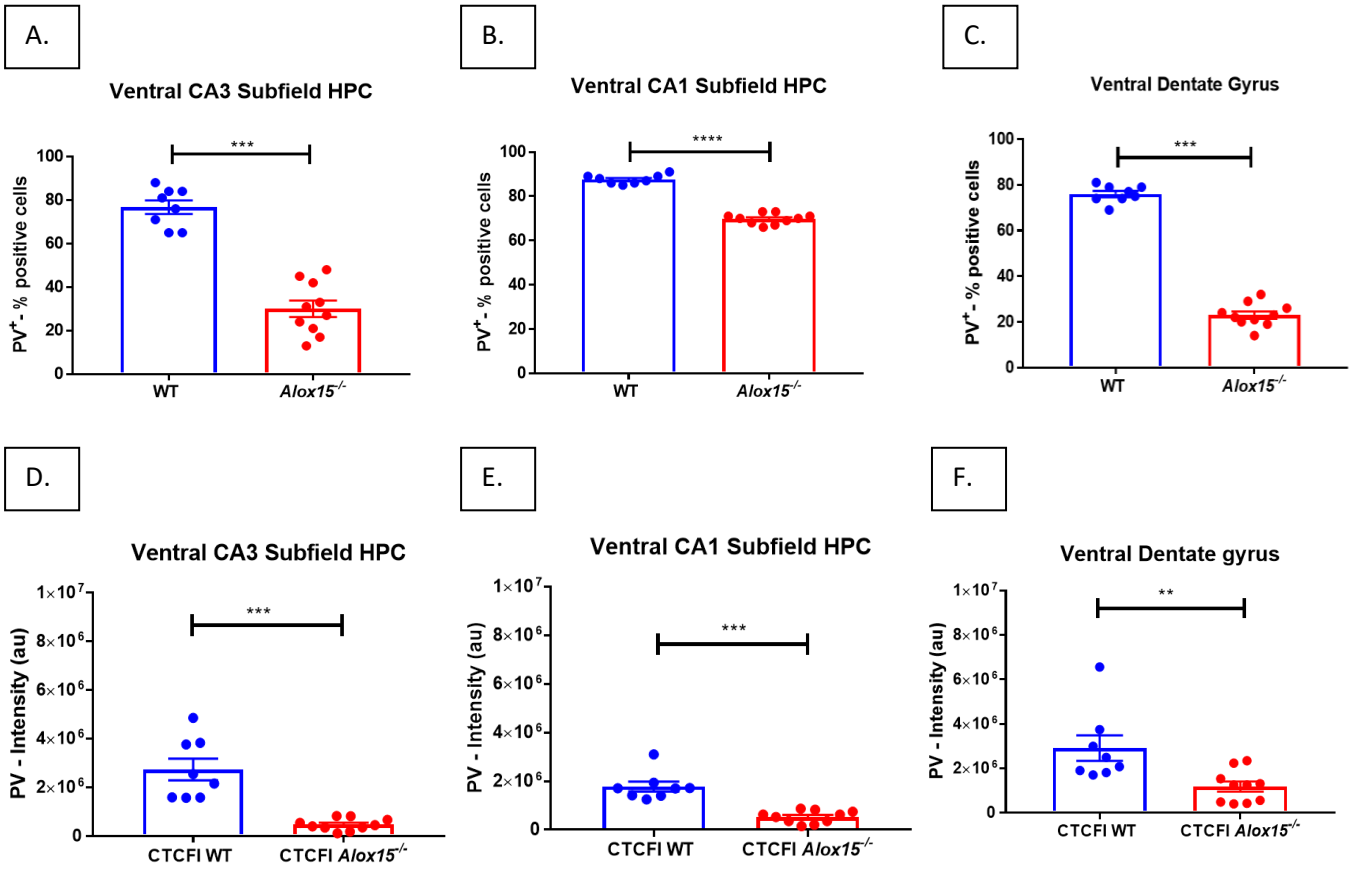

Figure 47. Quantification of the percentage number of PV$^+$ cells and the corrected immunofluorescence PV signal intensity (CTCFl) in all the subregions of vHPC. The formula used to calculate CTCFl was described in Materials and Methods. The top panel corresponds to the percentage of positive cells where all of the cells, including the nucleus evidenced by DAPI staining, was within the thickness of the section surrounding the cell (A) in the CA3 area (B) in the CA1 area (C) in the DG of vHPC. The bottom panel shows scatterplots of signal intensities of PV staining in all subregions of vHPC between WT and *Alox15*$^{-/-}$ mice. (D) in CA3 pyramidal cell layer (E) in CA1 pyramidal cell layer (F) in the granule cell layer of DG. Data were represented as signal intensities in the pyramidal cell layer of CA1, CA3 and granule cell layer of the DG. Each dot represents an individual mouse. Data were analysed using Mann- Whitney non-parametric U test and shown on Tukey box plots with mean ± S.E.M WT (n=12) and *Alox15*$^{-/-}$ (n=11) male mice, 15 months of age *, **, *** and **** representing $p \leq 0.05$, $p \leq 0.01$, $p \leq 0.001$ and $p \leq 0.0001$ for genotype comparisons, respectively.

- **PV – dHPC**

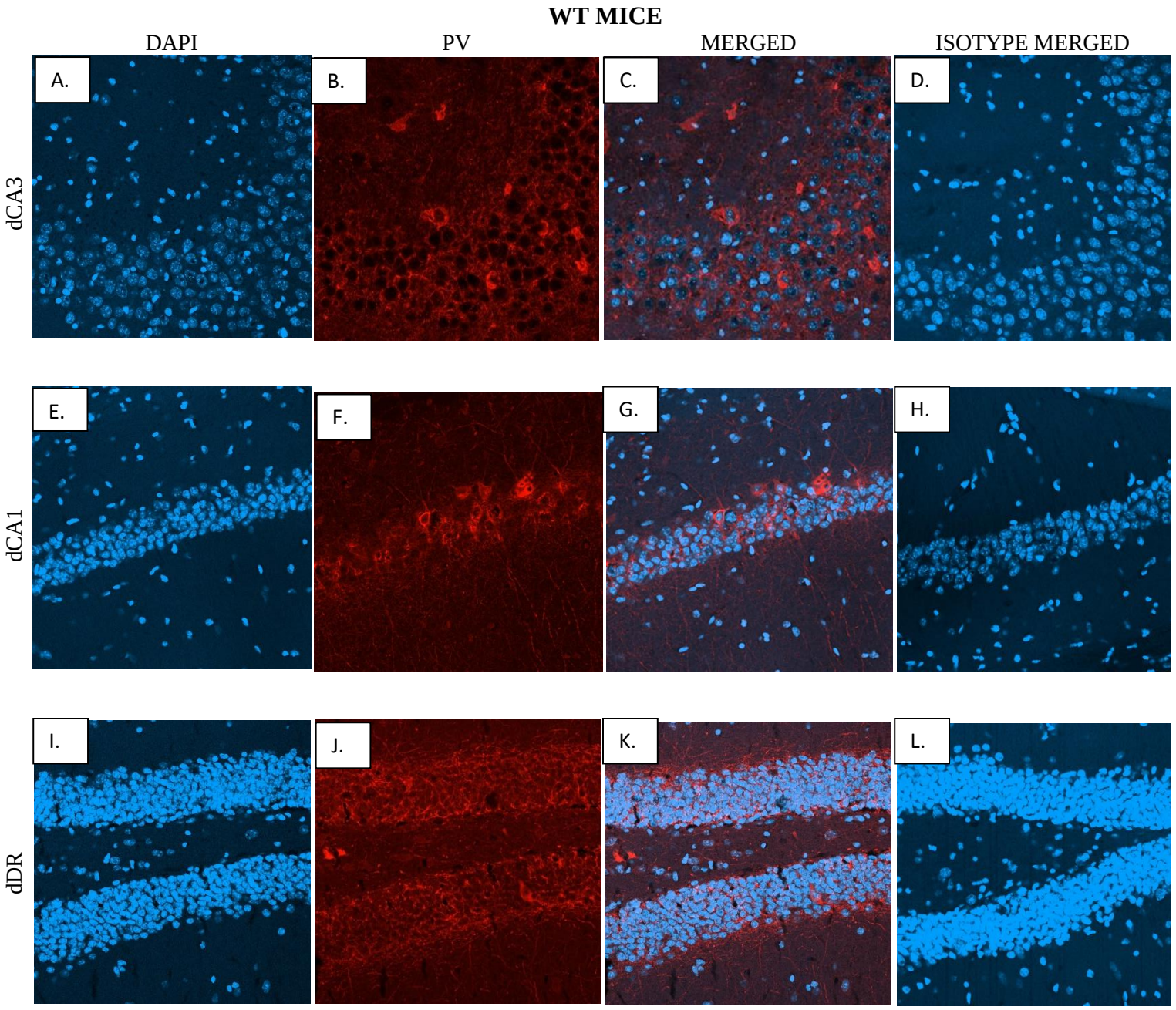
WT MICE
DAPI
PV
MERGED
ISOTYPE MERGED
dCA3
dCA1
dDR
A.
B.
C.
D.
E.
F.
G.
H.
I.
J.
K.
L.

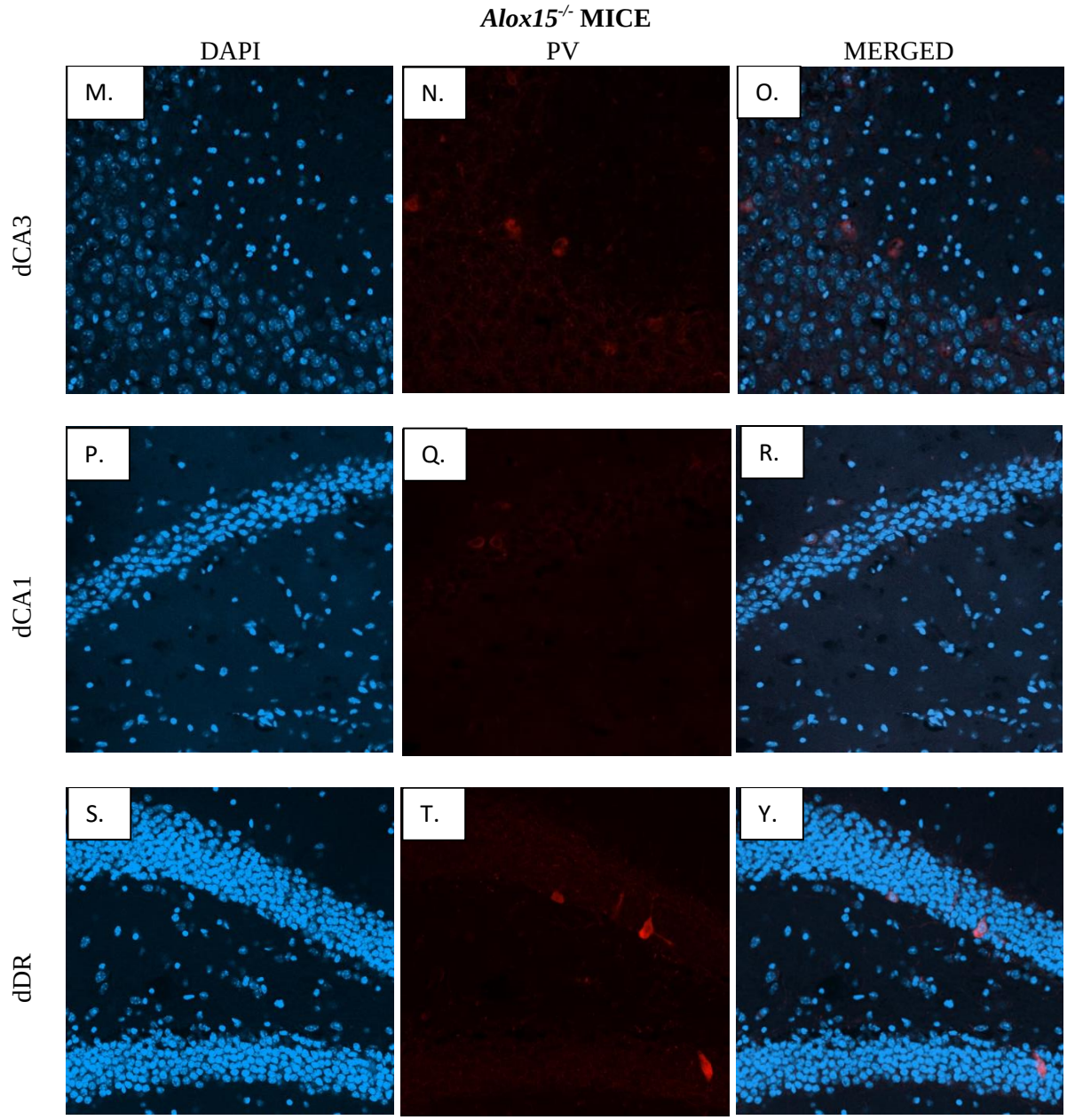

Figure 48. Comparison of immunofluorescent visualization of the coronal brain sections of 20 µm thickness showing detection and localization of PV in dHPC within CA1, CA2/3 and DG. The top panel corresponds to CA3 subfield of WT mouse dHPC (A) single channel acquisition of DAPI staining (blue) of cell nuclei (AF405) (B) single channel PV staining AF568 (orange/red) (C) merged image of PV in colocalization with DAPI (D) an overlay imaging on isotype control, rabbit IgG polyclonal, merged with DAPI counterstaining. The middle panel corresponds to CA1 subfield of WT mouse dHPC (E) single channel acquisition of DAPI staining (F) single channel PV staining AF568 (G) merged image of PV with DAPI (H) merged image on isotype control. The bottom panel corresponds to DG subfield of WT mouse dHPC (I) single channel acquisition of DAPI staining (J) single channel PV staining AF568 (K) merged image of PV with DAPI (L) merged image on isotype control. In contrast, the top panel corresponds to CA3 subfield of *Alox15*$^{-/-}$ mouse dHPC (M) single channel acquisition of DAPI staining (N) single channel PV staining AF568 (O) merged image of PV with DAPI. The middle panel corresponds to CA1 subfield of *Alox15*$^{-/-}$ mouse dHPC (P) single channel acquisition of DAPI staining (Q) single channel PV staining AF568 (R) merged image of PV with DAPI. The bottom panel corresponds to DG subfield of *Alox15*$^{-/-}$ mouse dHPC (S) single channel acquisition of DAPI staining (T) single channel PV staining AF568 (Y) merged image of PV with DAPI WT (n=12) and *Alox15*$^{-/-}$ (n=11) male mice, 15 months of age. Scale bars, 100 µm.

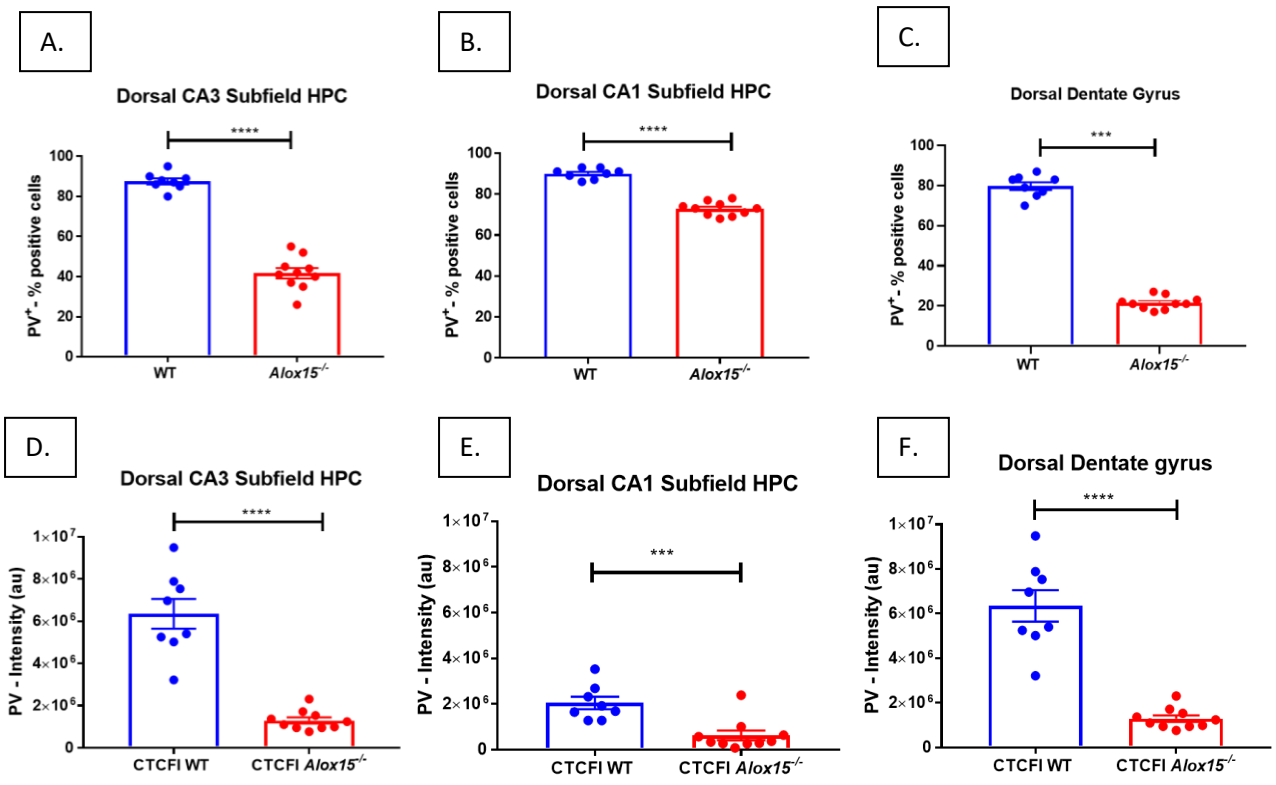

Figure 49. Quantification of the percentage number of PV$^+$ cells and the immunofluorescence PV signal intensity (CTCFl) in the studied subregions of dHPC. The formula used to calculate CTCFl was described in Materials and Methods. The top panel corresponds to the percentage of positive cells where all of the cells, including the nucleus evidenced by DAPI staining, was, within the thickness of the section surrounding the cell (A) in the CA3 area (B) in the CA1 area (C) in the DG of dHPC. The bottom panel shows scatterplots of signal intensities of PV staining in all subregions of dHPC between WT and *Alox15*$^{-/-}$ mice. (D) in CA3 pyramidal cell layer (E) in CA1 pyramidal cell layer (F) in the granule cell layer of DG. Data were represented as signal intensities in the pyramidal cell layer of CA1, CA3 and granule cell layer of the DG. Each dot represents an individual mouse. Data were analyzed using Mann- the Whitney non-parametric U test and shown on Tukey box plots with mean ± S.E.M. WT (n=12) and *Alox15*$^{-/-}$ (n=11) male mice, 15 months of age *, **, *** and **** represent p≤0.05, p≤0.01, p≤0.001 and p≤0.0001 for genotype comparisons, respectively.

ii. $GABA_B$ receptor immunoreactivity is present at low levels in the HPC of $Alox15^{-/-}$ mice

Furthermore, I investigated the hippocampal pattern of detection and localization of $GABA_B$ receptors between the two groups. The $GABA_B$ receptor expression on the merged images with DAPI counterstaining was significantly decreased in all the vHPC subregions in *Alox15*$^{-/-}$ mice (Figure 50 O, R, Y) than in WT (Figure 50 C, G, K). Similarly, its expression was dramatically lower in the dHPC of *Alox15*$^{-/-}$ (Figure 52 O, R, Y) relative to WT mice (Figure 52 C, G, K).

Qualitative data were analysed using the Mann-Whitney non-parametric U test, demonstrating that *Alox15*$^{-/-}$ mice showed a 40 % dramatic reduction in the percentage of $GABA_B$ receptor-positive cells in the vCA3, 13 % in the vCA1, and 15 % in the vDG (P=0.001, P=0.0285, P=0.0014, respectively) (Figure 51 A, B, C). A similar pattern of markedly lower $GABA_B$ receptor-positive cells was unveiled in the dHPC in *Alox15*$^{-/-}$ mice. In particular, *Alox15*$^{-/-}$ mice displayed an approximate 35 % significant decrease in the dCA3, 15 % in the dCA1 positive pyramidal cells and 25 % in the granule cells in the dDG relative to WT mice (P=0.001, P=0.0062, P=0.0085, respectively) (Figure 53 A, B, C).

Quantitative analysis of the fluorescent signal in the vHPC was performed by Mann-Whitney non-parametric U test, revealing that WT mice displayed markedly strong signal intensity of $GABA_B$ receptors in the vCA3 and vCA1 pyramidal cells layers and the granule cell layer of the DG in comparison with *Alox15*$^{-/-}$ mice (P<0.001, P=0.0014, P=0.0285, respectively) (Figure 51 D, E, F). Also, the quantification of the fluorescent signal on the dHPC was similar; the $GABA_B$ receptor displayed lower cell surface clusters of fluorescence on the granule cell layer of the DG and CA3, CA1 pyramidal cell layers in *Alox15*$^{-/-}$ dHPC relative to WT mice (P<0.001, P=0.001, P=0.0031, respectively) (Figure 53 D, E, F).

- **$GABA_B$ receptor – vHPC**

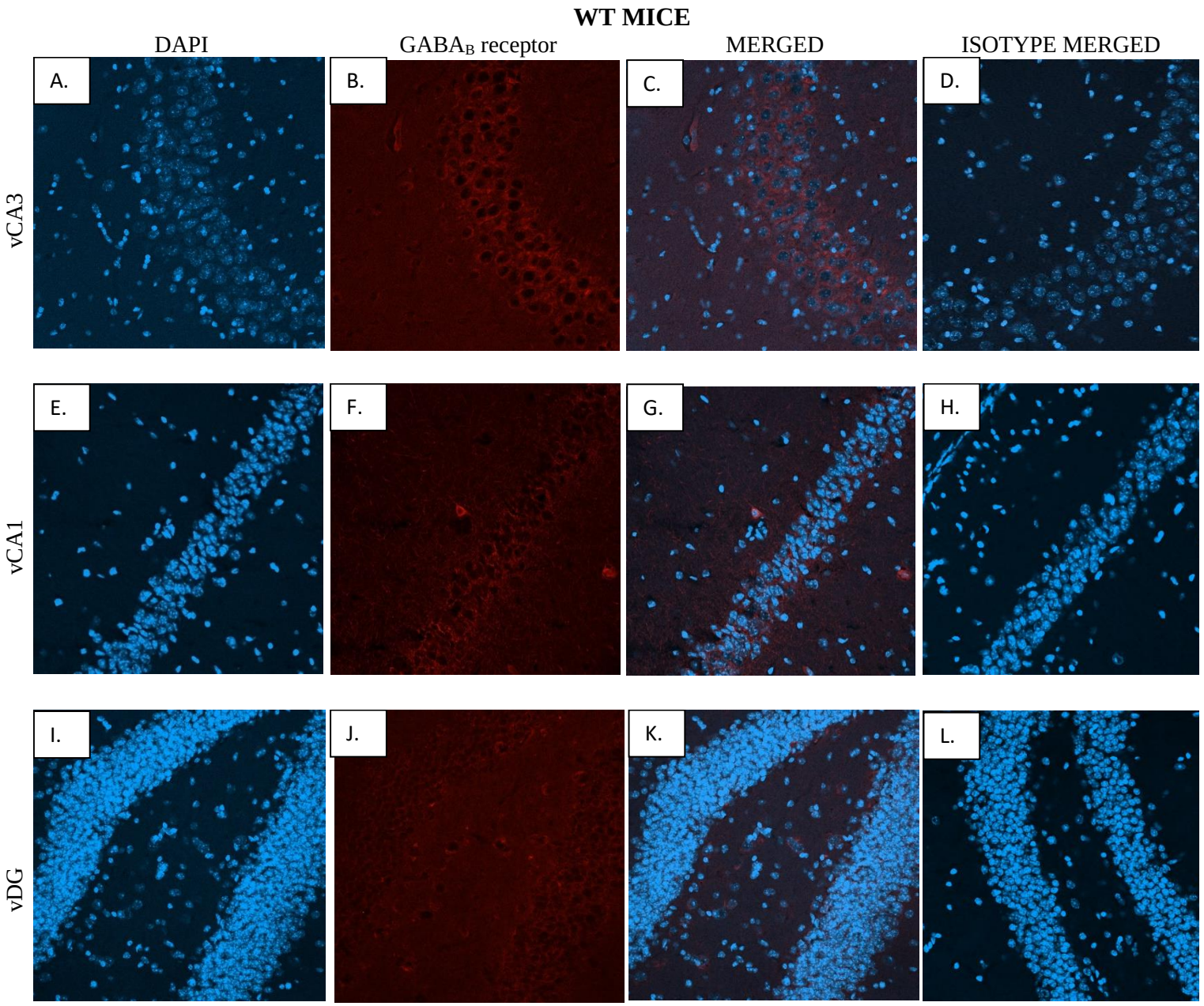

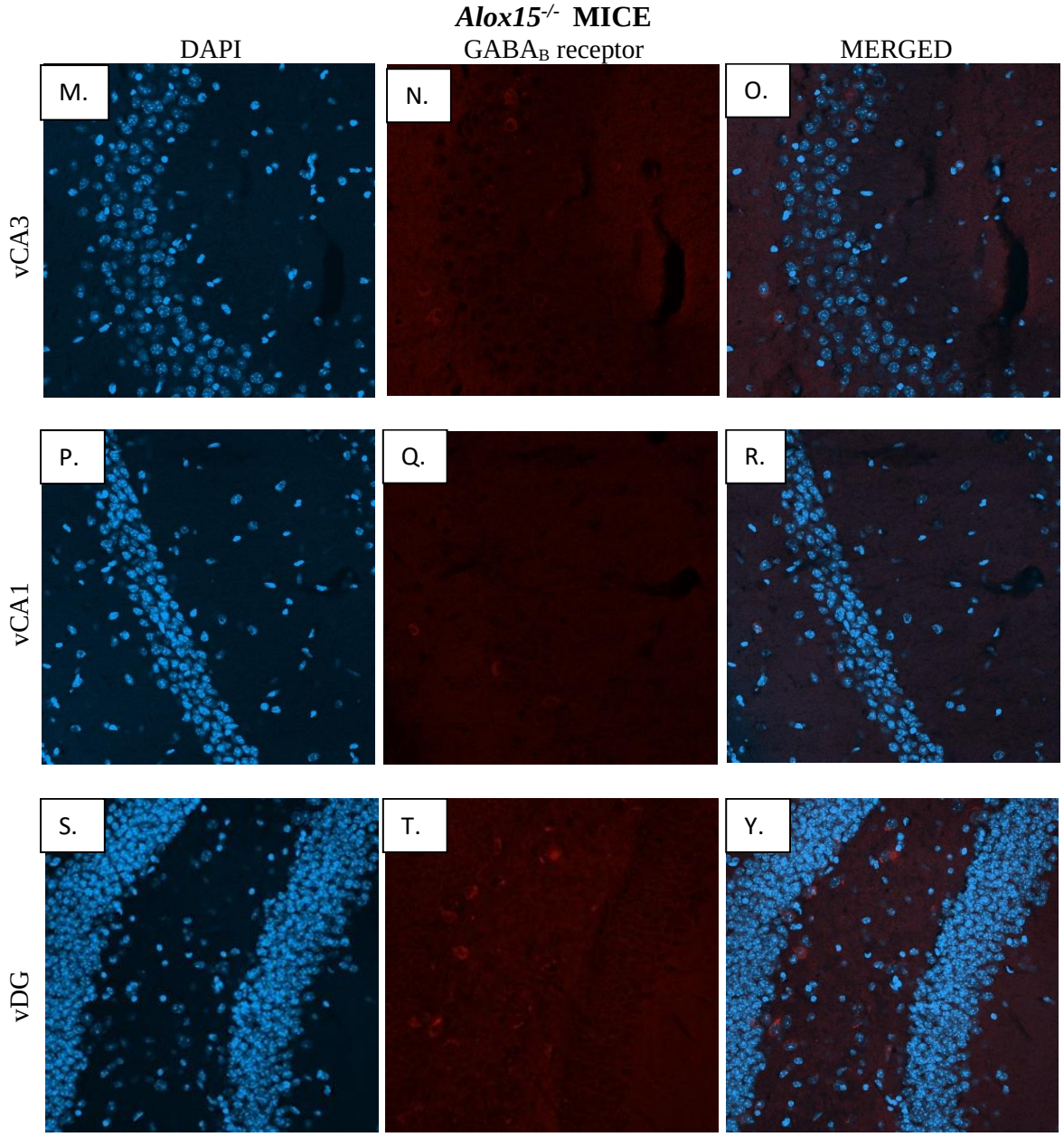

Figure 50. Representative immunofluorescent images show the detection and localization of GABA$_B$ receptor in the CA3, CA1, and DG subregions of vHPC coronal cryosections 20 µm. The top panel corresponds to CA3 subfield of WT mouse vHPC (a) single channel acquisition of DAPI staining (blue) of cell nuclei (AF405) (b) single channel GABA$_B$ staining AF568 (orange/red) (c) merged image of GABA$_B$ in colocalization with DAPI (d) an overlay imaging on isotype control, rabbit IgG polyclonal, merged with DAPI counterstaining. The middle panel corresponds to CA1 subfield of WT mouse vHPC (e) single channel acquisition of DAPI staining (f) single channel GABA$_B$ staining AF568 (g) merged image of GABA$_B$ with DAPI (h) merged image on isotype control. The bottom panel corresponds to DG subfield of WT mouse vHPC (i) single channel acquisition of DAPI staining (j) single channel GABA$_B$ staining AF568 (k) merged image of GABA$_B$ with DAPI (l) merged image on isotype control. In contrast, the top panel corresponds to CA3 subfield of *Alox15*$^{-/-}$ mouse vHPC (m) single channel acquisition of DAPI staining (n) single channel GABA$_B$ staining AF568 (o) merged image of GABA$_B$ with DAPI. The middle panel corresponds to CA1 subfield of *Alox15*$^{-/-}$ mouse vHPC (p) single channel acquisition of DAPI staining (q) single channel GABA$_B$ staining AF568 (r) merged image of GABA$_B$ with DAPI. The bottom panel corresponds to DG subfield of *Alox15*$^{-/-}$ mouse vHPC (s) single channel acquisition of DAPI staining (t) single channel GABA$_B$ staining AF568 (y) merged image of GABA$_B$ with DAPI WT (n=12) and *Alox15*$^{-/-}$ (n=11) male mice, 15 months of age. Scale bars, 100 µm.

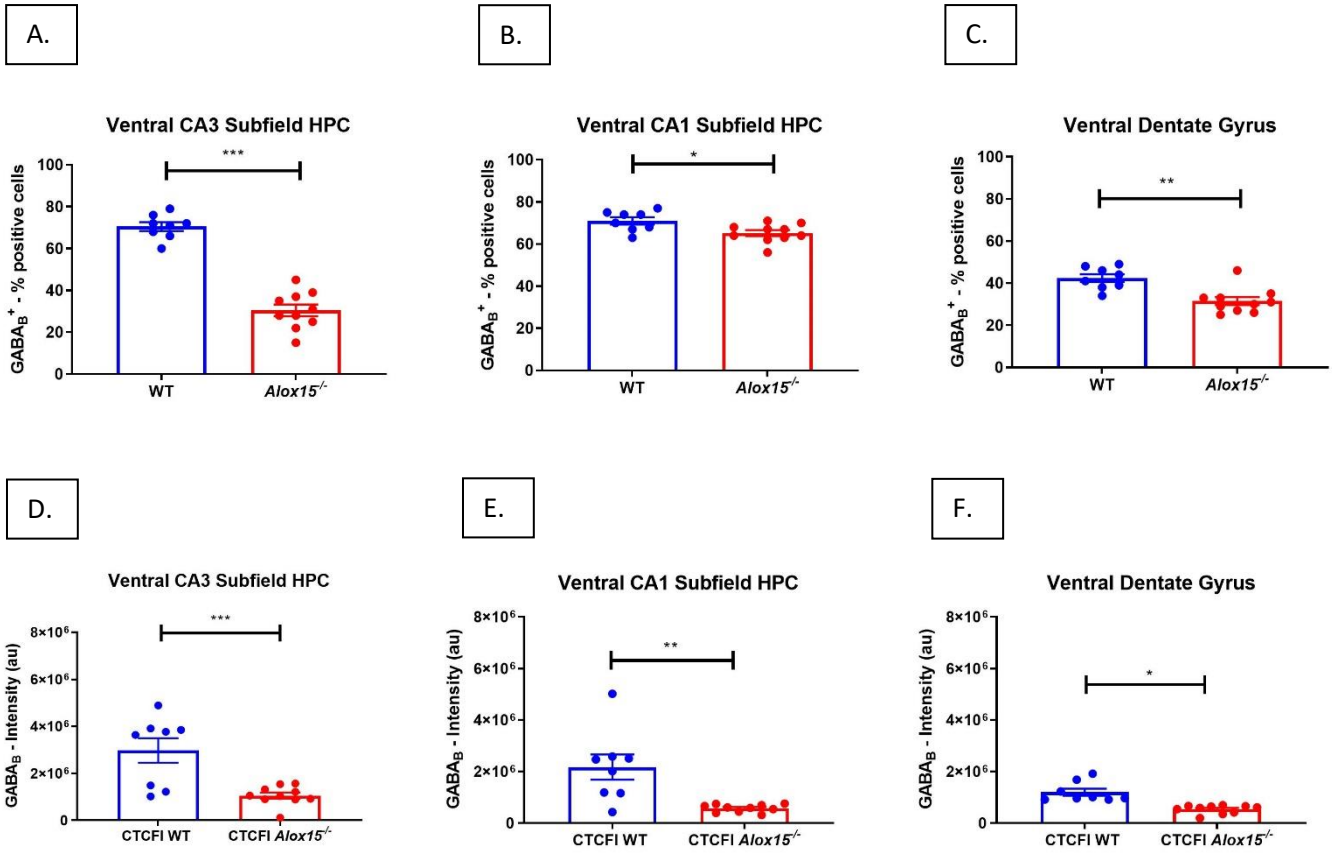

Figure 51. Quantification of the percentage number of $GABA_B^+$ receptor cells and the immunofluorescence $GABA_B$ (CTCFl) signal intensity in the studied subregion of vHPC. The formula used to calculate CTCFl was described in Materials and Methods. The top panel corresponds to the percentage of positive cells where all of the cells, including the nucleus evidenced by DAPI staining, were within the thickness of the section surrounding the cell (A) in the CA3 area (B) in the CA1 area (C) in the DG of vHPC. The bottom panel shows scatterplots of signal intensities of $GABA_B$ staining in all subregions of vHPC between WT and *Alox15*$^{-/-}$ mice. (D) in CA3 pyramidal cell layer (E) in CA1 pyramidal cell layer (F) in the granule cell layer of DG. Data were represented as signal intensities in the pyramidal cell layer of CA1, CA3 and granule cell layer of the DG. Each dot represents an individual mouse. Data were analysed using Mann- Whitney non-parametric U test and shown on Tukey box plots with mean ± S.E.M WT (n=12) and *Alox15*$^{-/-}$ (n=11) male mice, 15 months of age *, **, *** and **** represent $p \leq 0.05$, $p \leq 0.01$, $p \leq 0.001$ and $p \leq 0.0001$ for genotype comparisons, respectively.

- **$GABA_B$ receptor – dHPC**

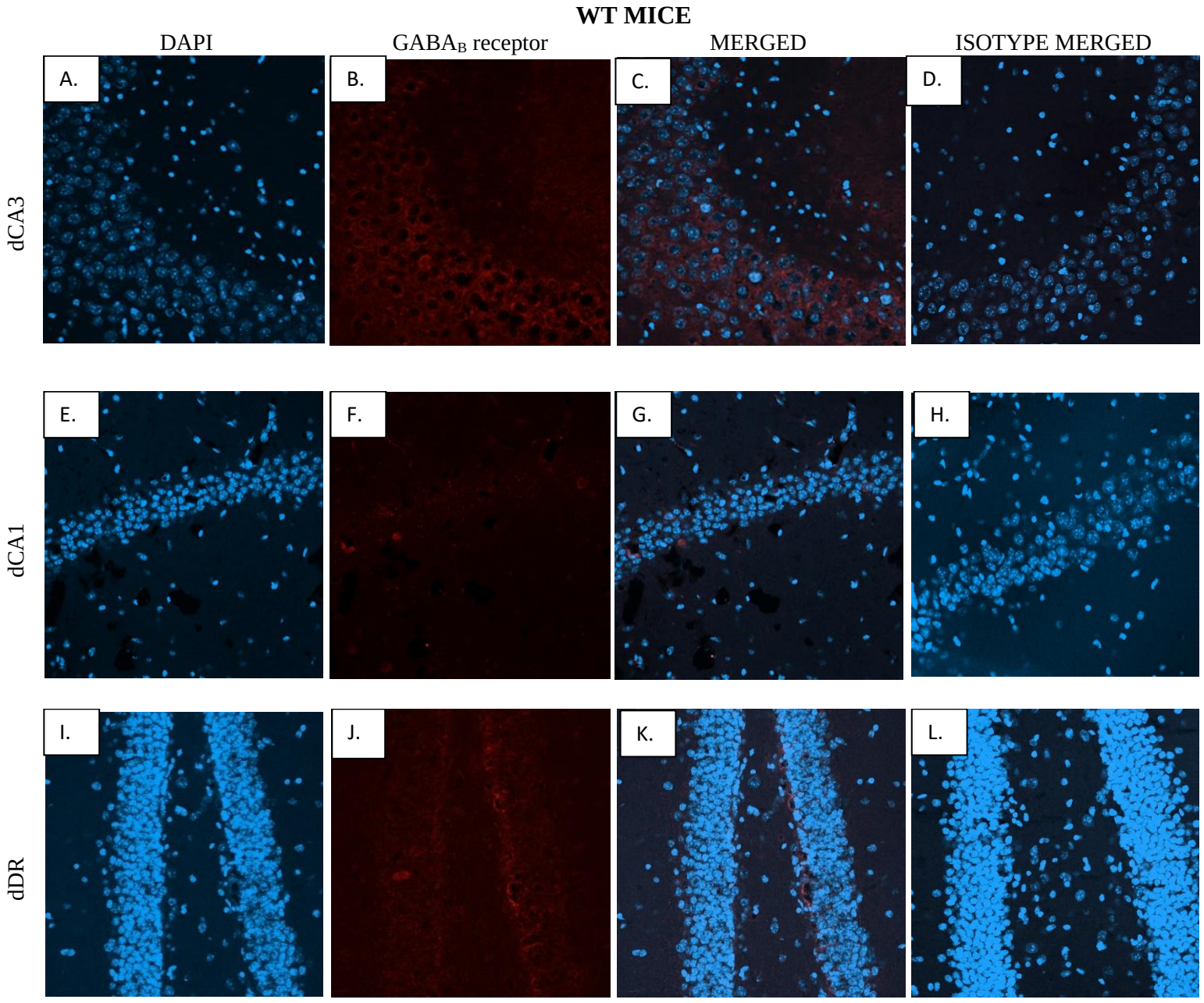

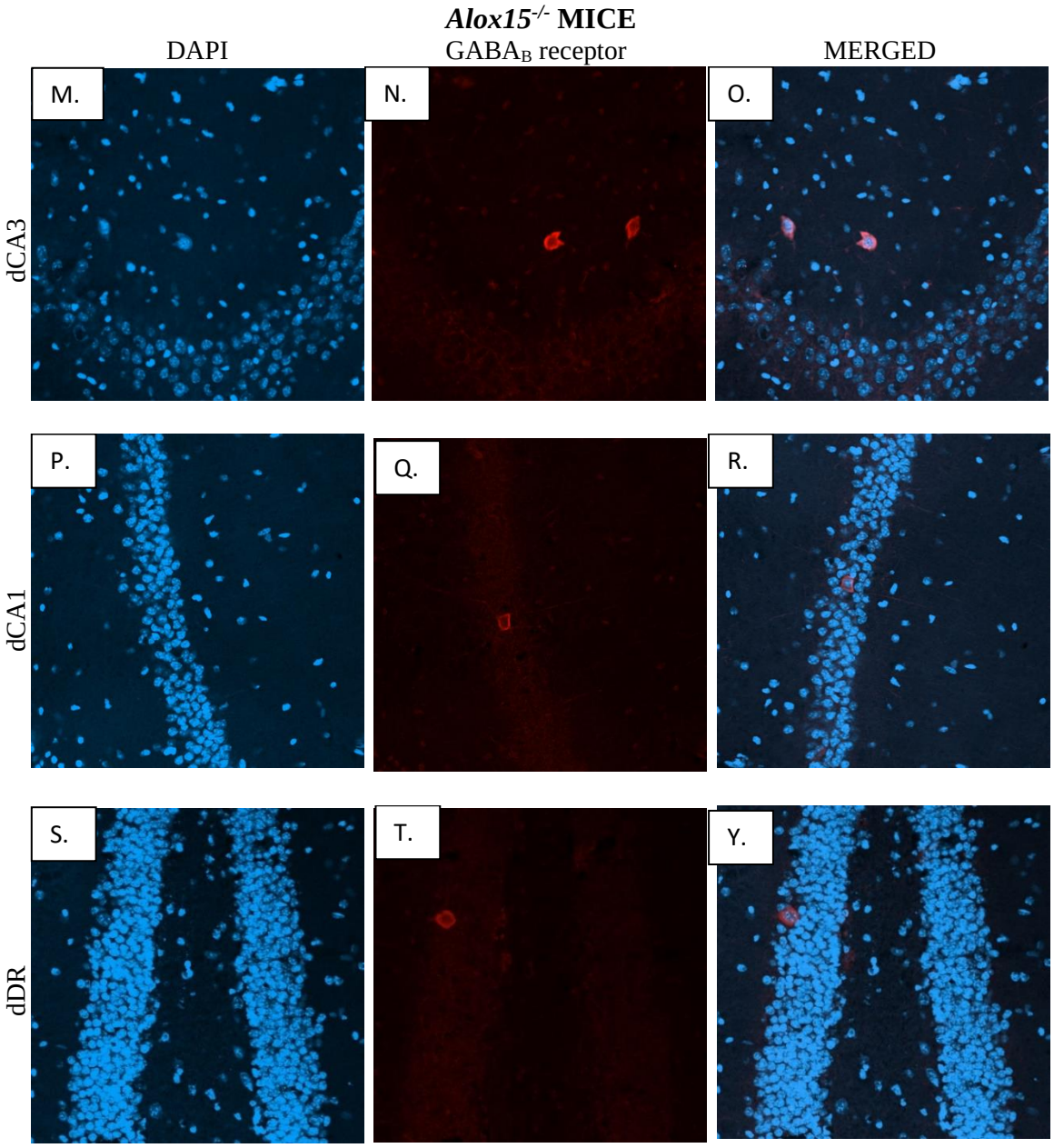

Figure 52. Representative immunofluorescent imaging showing detection and localization of GABA$_B$ receptor in the CA1, CA2/3, and DG subregions of dHPC coronal cryosections 20 µm thickness. The top panel corresponds to CA3 subfield of WT mouse dHPC (a) single channel acquisition of DAPI staining (blue) of cell nuclei (AF405) (b) single channel PV staining AF568 (orange/red) (c) merged image of GABA$_B$ in colocalization with DAPI (d) an overlay imaging on isotype control, rabbit IgG polyclonal, merged with DAPI counterstaining. The middle panel corresponds to CA1 subfield of WT mouse dHPC (e) single channel acquisition of DAPI staining (f) single channel GABA$_B$ staining AF568 (g) merged image of GABA$_B$ with DAPI (h) merged image on isotype control. The bottom panel corresponds to DG subfield of WT mouse dHPC (i) single channel acquisition of DAPI staining (j) single channel GABA$_B$ staining AF568 (k) merged image of GABA$_B$ with DAPI (l) merged image on isotype control. In contrast, the top panel corresponds to CA3 subfield of *Alox15*$^{-/-}$ mouse dHPC (m) single channel acquisition of DAPI staining (n) single channel GABA$_B$ staining AF568 (o) merged image of GABA$_B$ with DAPI. The middle panel corresponds to CA1 subfield of *Alox15*$^{-/-}$ mouse dHPC (p) single channel acquisition of DAPI staining (q) single channel GABA$_B$ staining AF568 (r) merged image of GABA$_B$ with DAPI. The bottom panel corresponds to DG subfield of *Alox15*$^{-/-}$ mouse dHPC (s) single channel acquisition of DAPI staining (t) single channel GABA$_B$ staining AF568 (y) merged image of GABA$_B$ with DAPI WT (n=12) and *Alox15*$^{-/-}$ (n=11) male mice, 15 months of age. Scale bars, 100 µm.

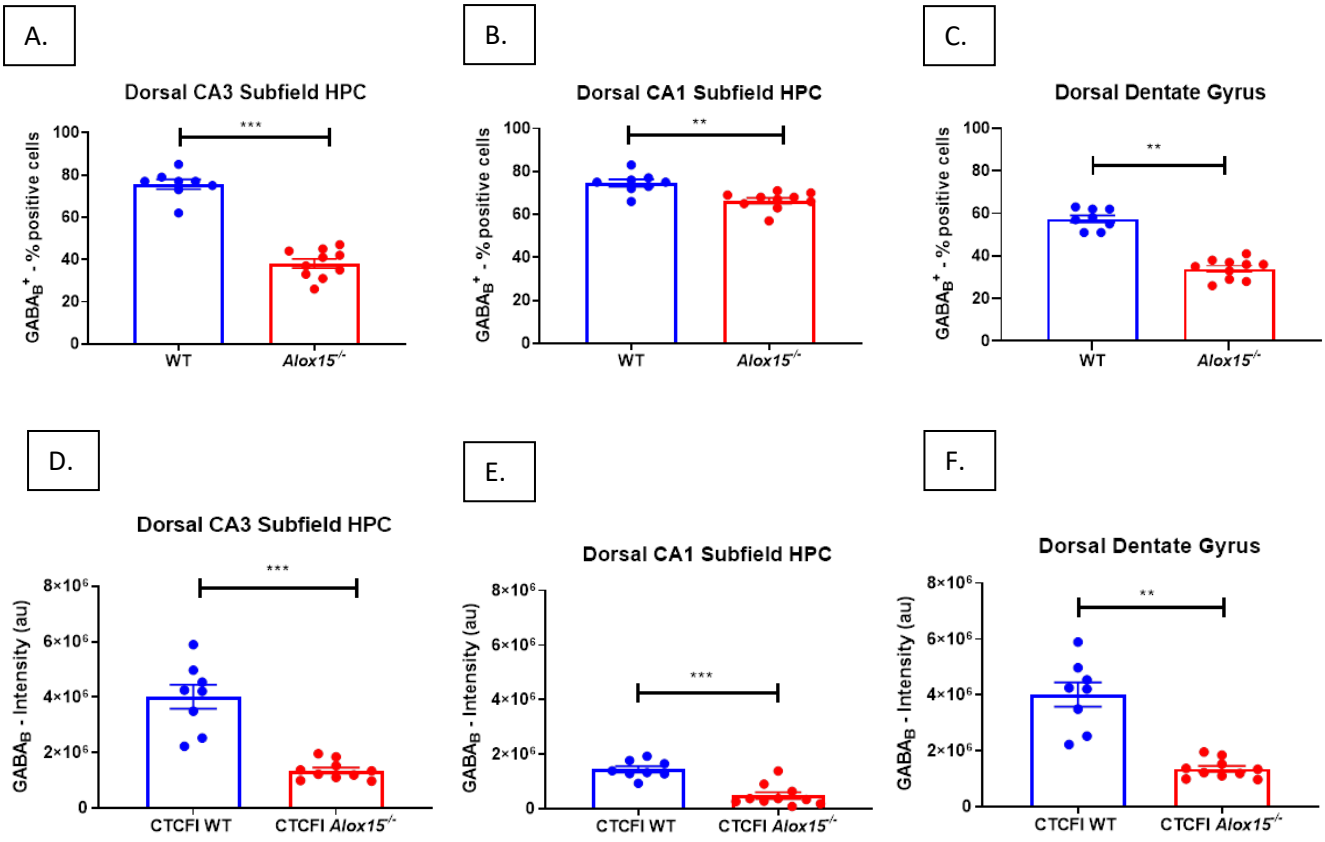

Figure 53. Quantification of the percentage number of $GABA_B^+$ receptor cells and the immunofluorescence $GABA_B$ signal intensity (CTCFl) in the studied subregion of dHPC. The formula used to calculate CTCFl was described in Materials and Methods. The top panel corresponds to the percentage of positive cells where all of the cells, including the nucleus evidenced by DAPI staining, was within the thickness of the section surrounding the cell (A) in the CA3 area (B) in the CA1 area (C) in the DG of dHPC. The bottom panel shows scatterplots of signal intensities of $GABA_B$ staining in all subregions of dHPC between WT and *Alox15*$^{-/-}$ mice. (D) in CA3 pyramidal cell layer (E) in CA1 pyramidal cell layer (F) in the granule cell layer of DG. Data were represented as signal intensities in the pyramidal cell layer of CA1, CA3 and granule cell layer of the DG. Each dot represents an individual mouse. Data were analysed using Mann- Whitney non-parametric U test and shown on Tukey box plots with mean ± S.E.M WT (n=12) and *Alox15*$^{-/-}$ (n=11) male mice, 15 months of age *, **, *** and **** representing $p \leq 0.05$, $p \leq 0.01$, $p \leq 0.001$ and $p \leq 0.0001$ for genotype comparisons, respectively.

iii. CRF_1 receptor is increased within the HPC of Alox15$^{-/-}$ mice.

Immunofluorescence was also performed to determine the localization and distribution of CRF_1 receptors in the HPC of both groups. The representative merged images with DAPI staining showed that the CRF_1 immunoreactivity was significantly higher in the vCA3 and vCA1 subregions in *Alox15*$^{-/-}$ mice (Figure 54 O, R) compared to WT mice (Figure 54 C, G). Conversely, no differences were observed in the DG of the vHPC between genotypes (Figure 54 K, Y).

It was observed a significant rise in the percentage of CRF_1^+ receptor-labelled cells in the vHPC of *Alox15*$^{-/-}$ mice relative to WT mice, as revealed by the analysis using the Mann-Whitney non-parametric U test. Mainly, this increase was roughly 10 % in CA3 (P= 0.0044, Figure 55 A) and 8 % in CA1 subfields (P= 0.0231, Figure 55 B). However, no statistically significant difference was detected in the DG of the vHPC between the groups (Figure 55 C). Similarly, the number of CRF_1^+ receptor cells in the dHPC of *Alox15*$^{-/-}$ mice was significantly higher in the CA3 (approximately 18 % increase) and CA1 (around 8 % increase) subregions, whereas no statistical difference was observed in the DG (P=0.0033, P=0.0079) (Figure 57 A, B, C). Although the CRF_1 receptor-positive cells were most prominent in the CA3 pyramidal cell layer, they were enriched in moderately labelled.

Quantitative analysis of the fluorescent signal indicated a significant increase in the signal intensity of CRF_1 receptor (CTCFl) in the vCA3 and vCA1 in *Alox15*$^{-/-}$ mice (P=0.0266, P=0.014, respectively) (Figure 55 D, E); but no statistically significant changes were detected in the DG between the groups (Figure 55 F). Besides that, the statistically increased fluorescent signal of CRF_1 receptor was also observed in dorsal hippocampal, including dCA3 and dCA1 pyramidal cell layers as well as the granule cell layers of the DG in *Alox15*$^{-/-}$ mice relative to WT mice (P=0.0012, P=0.0015) (Figure 57 D, E, F). Certainly, CRF_1 immunoreactivity was more significant in the dHPC than vHPC in *Alox15*$^{-/-}$ mice compared to WT mice, as revealed in Figures 55 and 57.

- **CRF_1 receptor – vHPC**

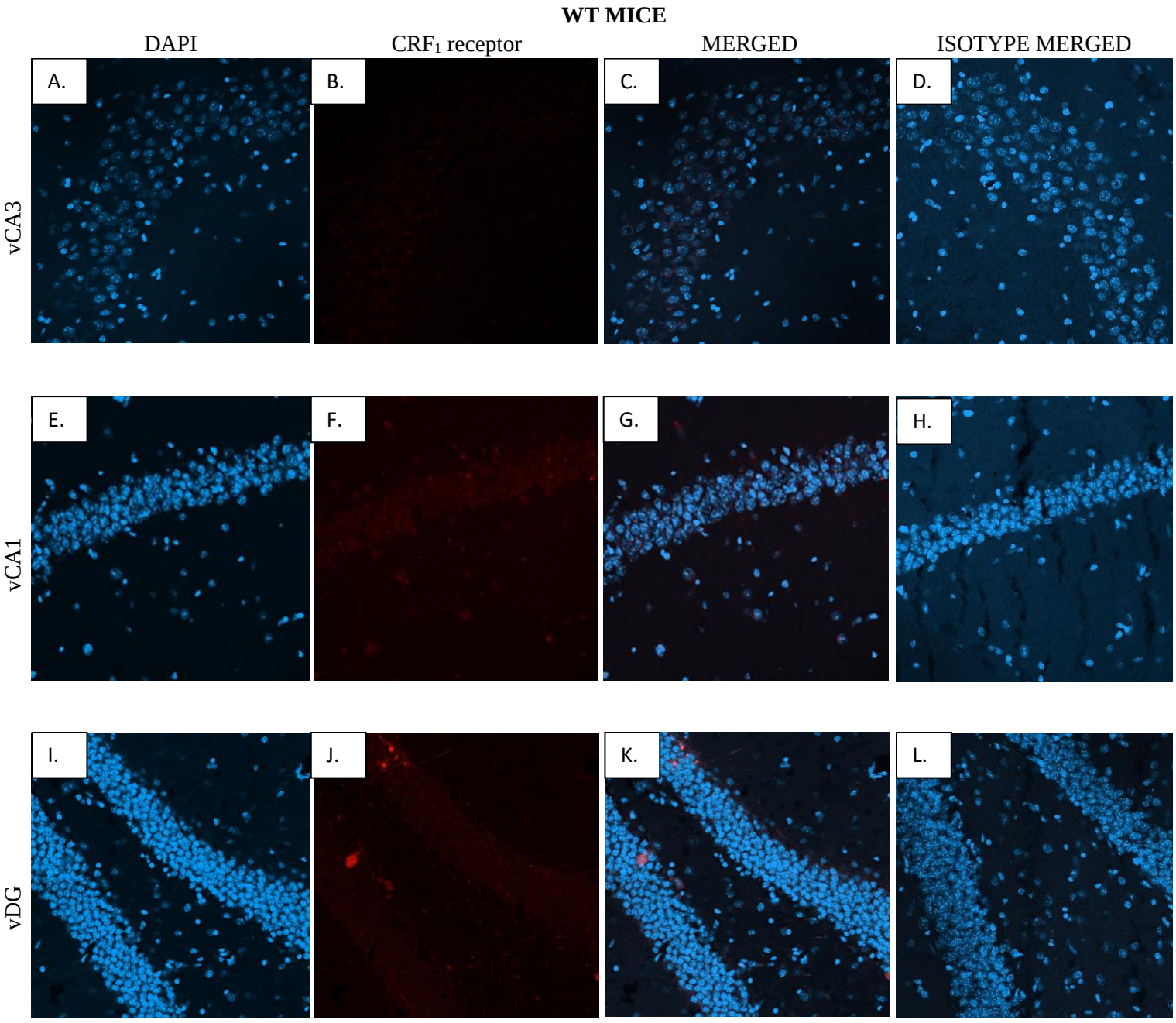

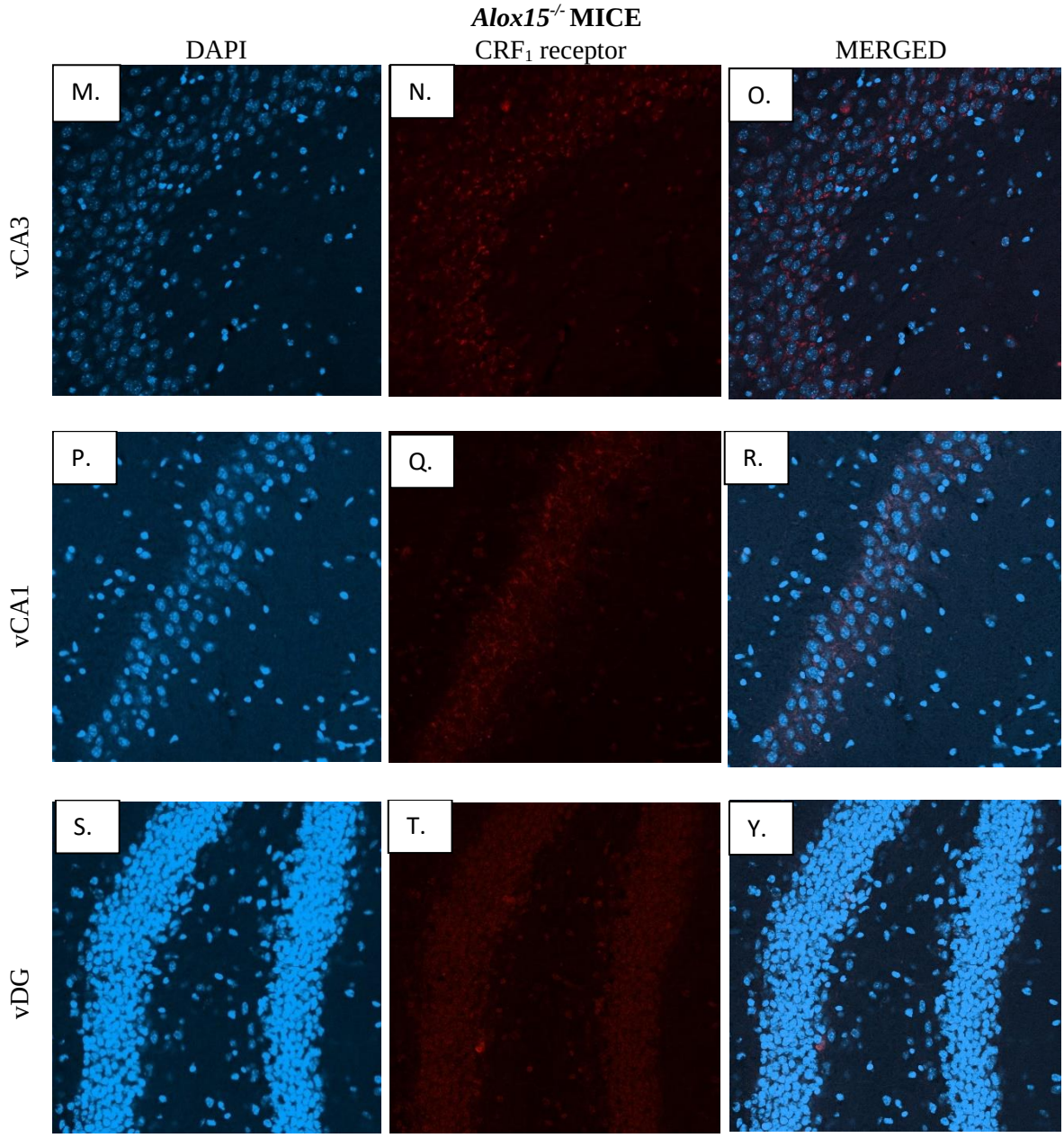

Figure 54. Immunofluorescent labelling for CRF_1 receptor of the coronal brain sections of 20 µm thickness indicates significant vHPC changes. The top panel corresponds to CA3 subfield of WT mouse vHPC (a) single channel acquisition of DAPI staining (blue) of cell nuclei (AF405) (b) single channel CRF_1 staining AF594 (red) (c) merged image of CRF_1 in colocalization with DAPI (d) an overlay imaging on isotype control, goat IgG polyclonal, merged with DAPI counterstaining. The middle panel corresponds to CA1 subfield of WT mouse vHPC (e) single channel acquisition of DAPI staining (f) single channel CRF_1 staining AF594 (g) merged image of CRF_1 with DAPI (h) merged image on isotype control. The bottom panel corresponds to DG subfield of WT mouse vHPC (i) single channel acquisition of DAPI staining (j) single channel CRF_1 staining AF594 (k) merged image of CRF_1 with DAPI (l) merged image on isotype control. In contrast, the top panel corresponds to CA3 subfield of *Alox15*$^{-/-}$ mouse vHPC (m) single channel acquisition of DAPI staining (n) single channel CRF_1 staining AF594 (o) merged image of CRF_1 with DAPI. The middle panel corresponds to CA1 subfield of *Alox15*$^{-/-}$ mouse vHPC (p) single channel acquisition of DAPI staining (q) single channel CRF_1 staining AF594 (r) merged image of CRF_1 with DAPI. The bottom panel corresponds to DG subfield of *Alox15*$^{-/-}$ mouse vHPC (s) single channel acquisition of DAPI staining (t) single channel CRF_1 staining AF594 (y) merged image of CRF_1 with DAPI WT (n=12) and *Alox15*$^{-/-}$ (n=11) male mice, 15 months of age. Scale bars, 100 µm.

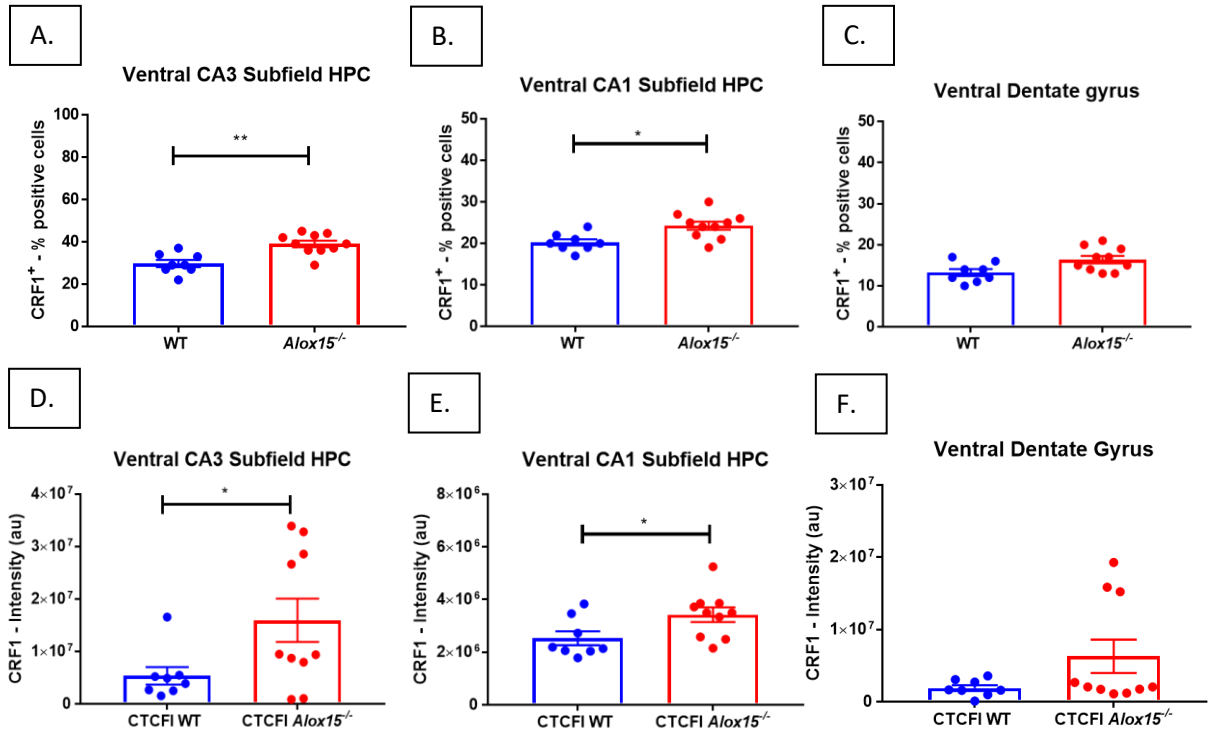

Figure 55. Quantification of the percentage number of CRF_1+ receptor cells and the immunofluorescence CRF_1 signal intensity (CTCFl) in the studied subregions of vHPC. The formula used to calculate CTCFl was described in Materials and Methods**.** The top panel corresponds to the percentage of positive cells where all of the cells including the nucleus evidenced by DAPI staining was within the thickness of the section surrounding the cell (A) in the CA3 area (B) in the CA1 area (C) in the DG of vHPC. The bottom panel shows scatterplots of signal intensities of CRF_1 receptor staining in all subregions of vHPC between WT and *Alox15*$^{-/-}$ mice. (D) in CA3 pyramidal cell layer (E) in CA1 pyramidal cell layer (F) in the granule cell layer of DG. Data were represented as signal intensities in the pyramidal cell layer of CA1, CA3 and granule cell layer of the DG. Each dot represents an individual mouse. Data were analysed using Mann- Whitney non-parametric U test and shown on Tukey box plots with mean ± S.E.M WT (n=12) and *Alox15*$^{-/-}$ (n=11) male mice, 15 months of age. *, **, *** and **** represent $p \leq 0.05$, $p \leq 0.01$, $p \leq 0.001$ and $p \leq 0.0001$ for genotype comparisons, respectively.

- **CRF_1 receptor – dHPC**

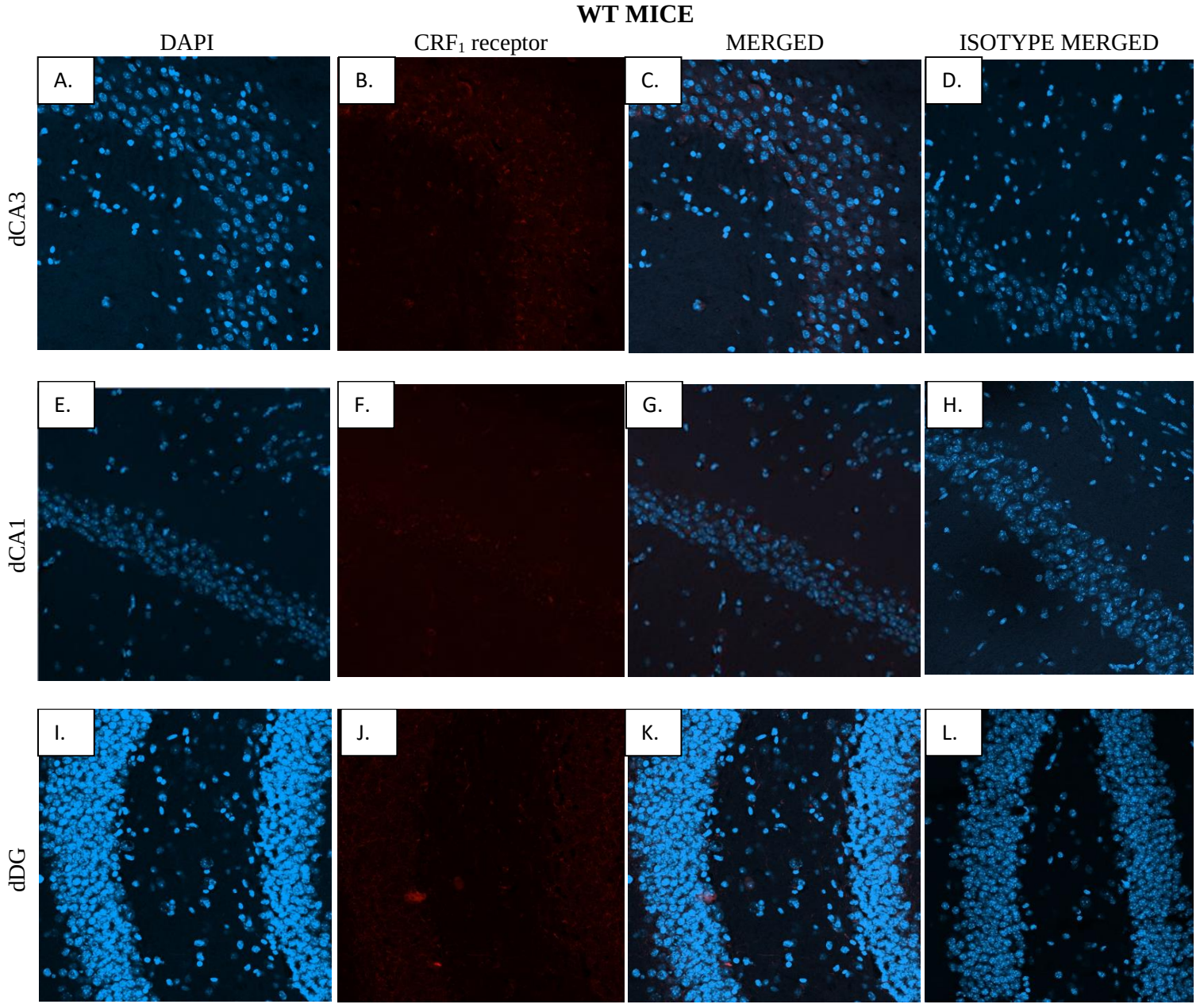

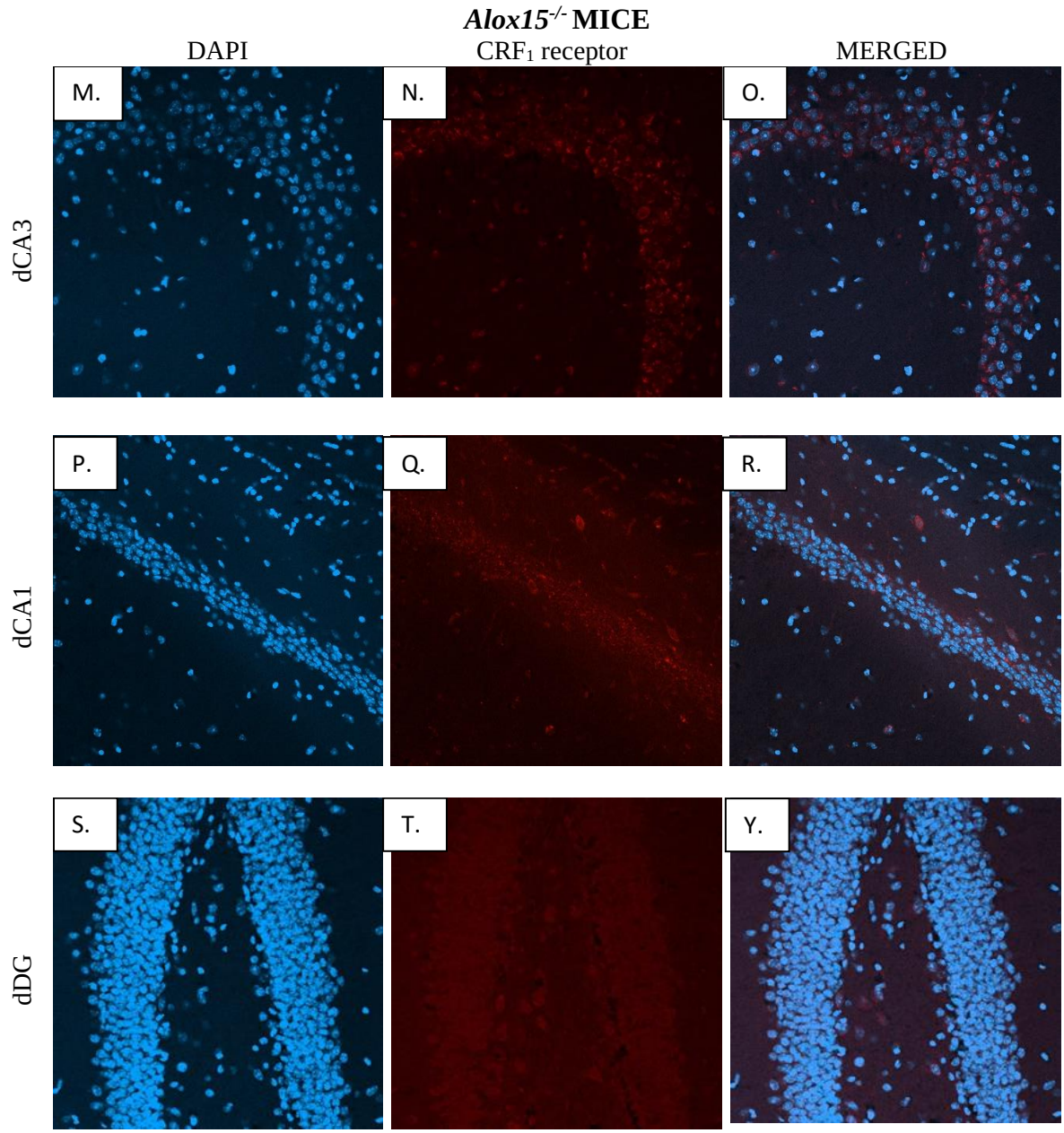

Figure 56. Immunofluorescent labelling for CRF$_1$ receptor of the coronal brain sections of 20 µm thickness indicates significant dHPC changes. The top panel corresponds to CA3 subfield of WT mouse dHPC (a) single channel acquisition of DAPI staining (blue) of cell nuclei (AF405) (b) single channel CRF$_1$ staining AF594 (red) (c) merged image of CRF$_1$ in colocalization with DAPI (d) an overlay imaging on isotype control, goat IgG polyclonal, merged with DAPI counterstaining. The middle panel corresponds to CA1 subfield of WT mouse dHPC (e) single channel acquisition of DAPI staining (f) single channel CRF$_1$ staining AF594 (g) merged image of CRF$_1$ with DAPI (h) merged image on isotype control. The bottom panel corresponds to DG subfield of WT mouse dHPC (i) single channel acquisition of DAPI staining (j) single channel CRF$_1$ staining AF594 (k) merged image of CRF1with DAPI (l) merged image on isotype control. In contrast, the top panel corresponds to CA3 subfield of *Alox15*$^{-/-}$ mouse dHPC (m) single channel acquisition of DAPI staining (n) single channel CRF$_1$ staining AF594 (o) merged image of CRF$_1$ with DAPI. The middle panel corresponds to the CA1 subfield of *Alox15*$^{-/-}$ mouse dHPC (p) single channel acquisition of DAPI staining (q) single channel CRF$_1$ staining AF594 (r) merged image of CRF$_1$ with DAPI. The bottom panel corresponds to the DG subfield of *Alox15*$^{-/-}$ mouse dHPC (s) single channel acquisition of DAPI staining (t) single channel CRF$_1$ staining AF594 (y) merged image of CRF$_1$ with DAPI WT (n=12) and *Alox15*$^{-/-}$ (n=11) male mice, 15 months of age. Scale bars, 100 µm.

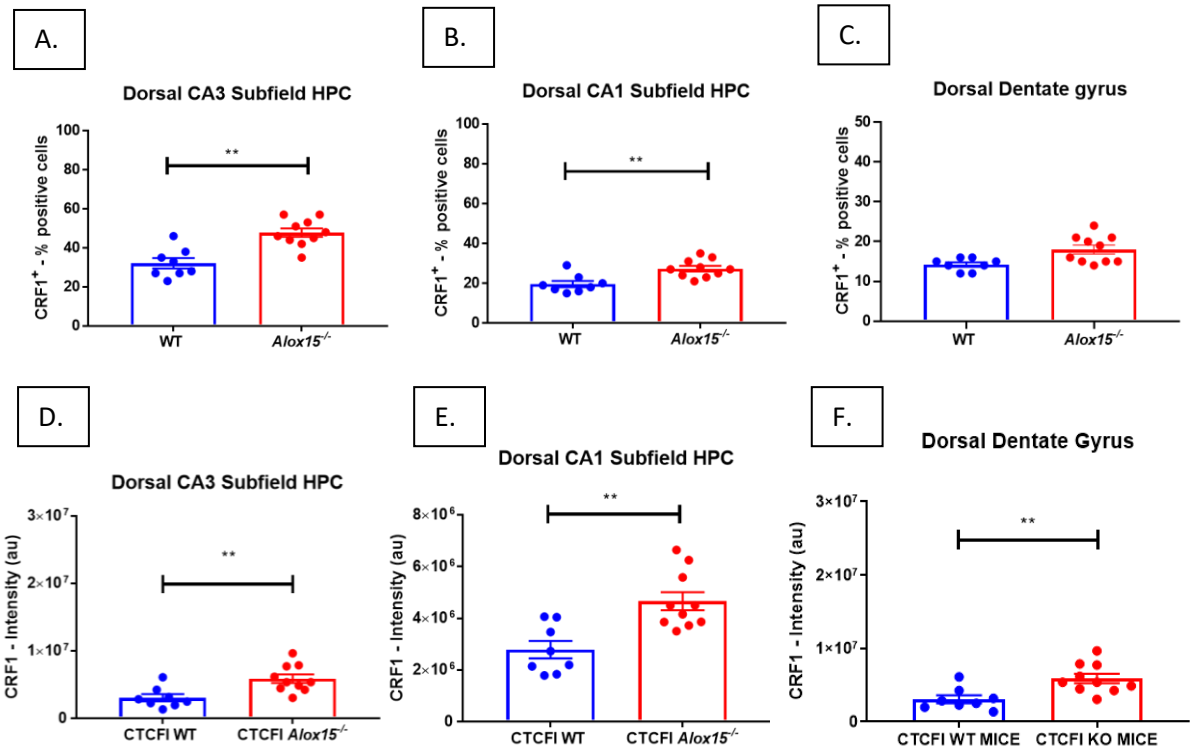

Figure 57. Quantification of the percentage number of CRF_1^+ receptor cells and the immunofluorescence CRF_1 signal intensity (CTCFl) in all the subregion of dHPC. The formula calculated for this analysis was described in Materials and Methods. The top panel corresponds to the percentage of positive cells where all of the cells including the nucleus evidenced by DAPI staining was within the thickness of the section surrounding the cell (A) in the CA3 area (B) in the CA1 area (C) in the DG of dHPC. The bottom panel shows scatterplots of signal intensities of CRF_1 receptor staining in all subregions of dHPC between WT and *Alox15*$^{-/-}$ mice. (D) in CA3 pyramidal cell layer (E) in CA1 pyramidal cell layer (F) in the granule cell layer of DG. Data were represented as signal intensities in the pyramidal cell layer of CA1, CA3 and granule cell layer of the DG. Each dot represents an individual mouse. Data were analysed using Mann- Whitney non-parametric U test and shown on Tukey box plots with mean ± S.E.M WT (n=12) and Alox15$^{-/-}$ (n=11) male mice, 15 months of age. *, **, *** and **** represent $p \leq 0.05$, $p \leq 0.01$, $p \leq 0.001$ and $p \leq 0.0001$ for genotype comparisons, respectively.

iv. 5HT$_{1A}$ receptor is increased in vCA3 and dCA3, but decreased in vCA1 and dCA1 hippocampal subregions in Alox15$^{-/-}$ mice

Next, immunohistochemical analysis was carried out to examine the differential expression of the 5-HT$_{1A}$ receptor in the HPC between *Alox15*$^{-/-}$ and WT male mice aged 15 months. The representative merged images with DAPI counterstain showed that 5HT$_{1A}$ receptor immunoreactivity was significantly higher in the CA3 region as well as the DG and the hilus of the vHPC of *Alox15*$^{-/-}$ (Figure 58 C, K) compared to WT mice (Figure 58 O, Y). Also, the overlay images with DAPI staining indicated that 5HT$_{1A}$ receptor expression was significantly greater in the CA3 subfield of the dHPC of *Alox15*$^{-/-}$ mice (Figure 60 C, K) compared to WT mice (Figure 60 O, Y).

The quantitative data analysis showed that the number of 5-HT$_{1A}$-positive cells was statistically increased in the vCA3 in *Alox15*$^{-/-}$ relative to WT mice; it rose by almost 10 % (P= 0.0306) (Figure 59 A). The number of 5HT$_{1A}$-positive cells within the DG was significantly higher in the vHPC of *Alox15*$^{-/-}$ than in WT mice (P= 0.0237) (Figure 59 C). In contrast, the number of 5-HT1A-positive cells was statistically decreased in vCA1 pyramidal cells (P= 0.0211) (Figure 59 B). Next, the percentage of 5-HT$_{1A}$-positive cells was statistically increased in dCA3 pyramidal cells in *Alox15*$^{-/-}$ compared to WT mice (approximately 10 % increase) (P= 0.0190) (Figure 61 A). Conversely, the dCA1 pyramidal cells were significantly reduced in *Alox15*$^{-/-}$ relative to WT mice (approximately 8 % decrease) (P= 0.0235) (Figure 61 B). However, no differences were detected in the number of 5HT$_{1A}$-positive cells in the DG between groups (Figure 61 C).

Visual inspection of the fluorescent signal revealed that 5-HT$_{1A}$ receptor signal intensity was predominantly detected in the CA3 pyramidal cell layer of the vHPC and dHPC in *Alox15*$^{-/-}$ compared to WT mice. Quantitative analysis of the data demonstrated that there was significantly decreased 5HT$_{1A}$ receptor signal intensity in the CA1 pyramidal cell layer of the vHPC and dHPC in *Alox15*$^{-/-}$ compared to WT mice (P= 0.0112, P=0.0266 , respectively) (Figure 59 E, 61 E). Furthermore, analysis of the signal intensity of the 5HT$_{1A}$ receptor revealed that there are no differences between groups in the dDG (Figure 61 F). In contrast, the analysis showed that the ventral granule cell layers of the DG displayed a moderate, but significantly increased signal intensity in *Alox15*$^{-/-}$ relative to WT mice (P= 0.0073) (Figure 59 F).

- **5HT$_{1A}$ receptor – vHPC**

WT MICE

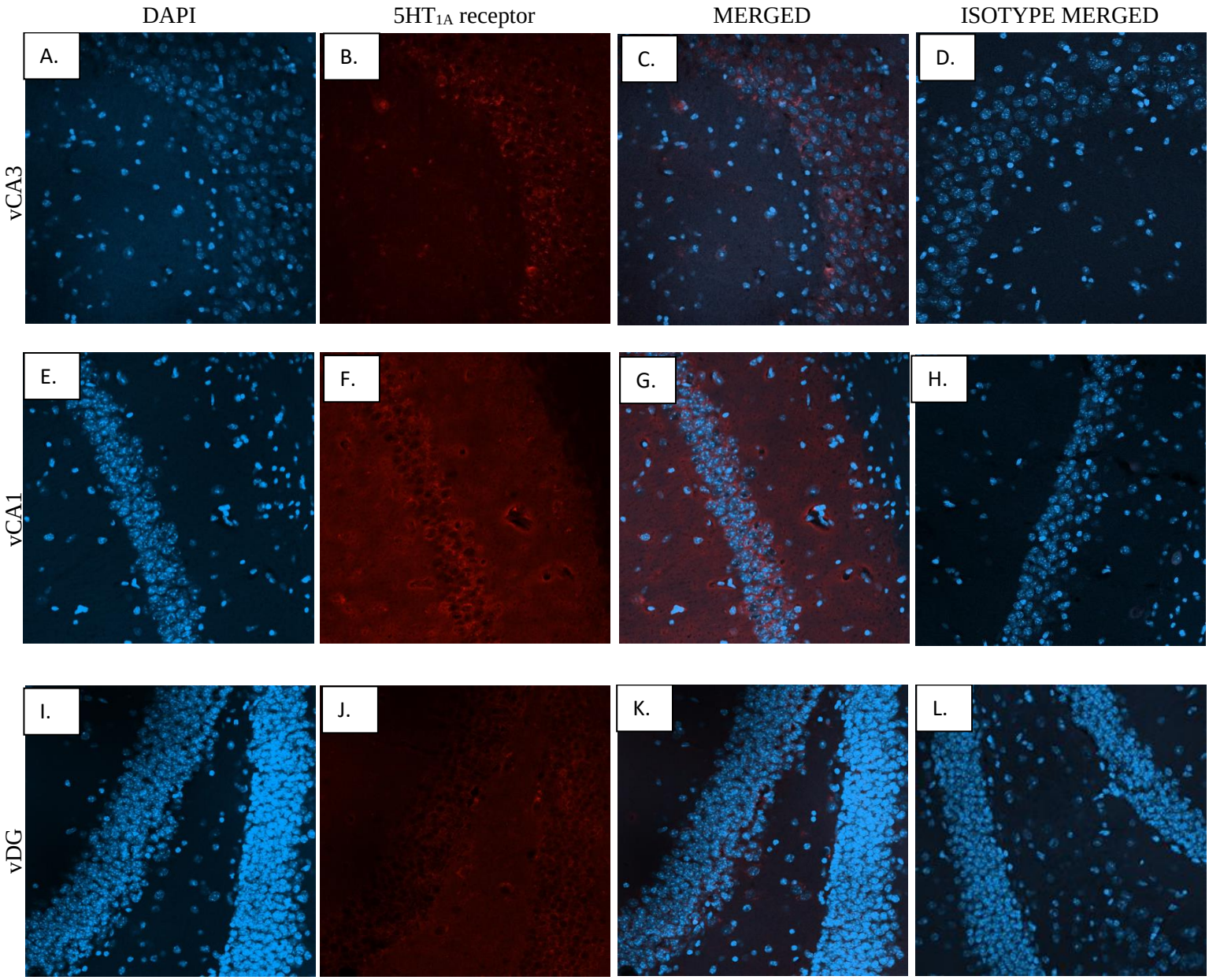

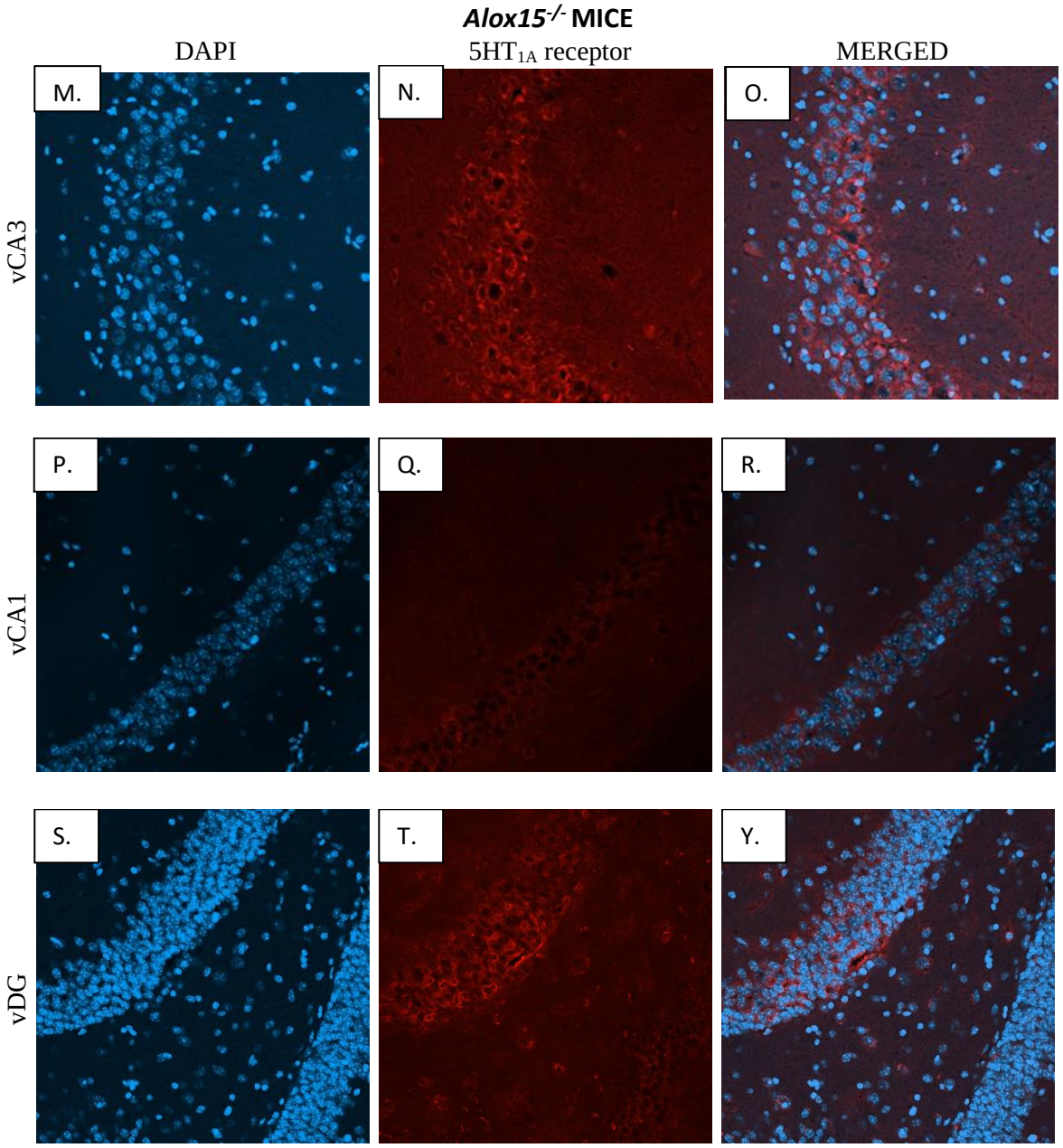

Figure 58. Representative confocal imaging illustrates the detection and localization of 5HT1A receptors in the CA1, CA2/3, and DG subregions of the vHPC coronal cryosections of 20 µm thickness. The top panel corresponds to the CA3 subfield of WT mouse vHPC (a) single channel acquisition of DAPI staining (blue) of cell nuclei (AF405) (b) single channel $5HT_{1A}$ staining AF568 (red) (c) merged image of $5HT_{1A}$ in colocalization with DAPI (d) an overlay imaging on isotype control, rabbit IgG polyclonal, merged with DAPI counterstaining. The middle panel corresponds to the CA1 subfield of WT mouse vHPC (e) single channel acquisition of DAPI staining (f) single channel $5HT_{1A}$ staining AF568 (g) merged image of $5HT_{1A}$ with DAPI (h) merged image on isotype control. The bottom panel corresponds to the DG subfield of WT mouse vHPC (i) single channel acquisition of DAPI staining (j) single channel $5HT_{1A}$ staining AF568 (k) merged image of $5HT_{1A}$ with DAPI (l) merged image on isotype control. In contrast, the top panel corresponds to the CA3 subfield of *Alox15*$^{-/-}$ mouse vHPC (m) single channel acquisition of DAPI staining (n) single channel $5HT_{1A}$ staining AF568 (o) merged image of $5HT_{1A}$ with DAPI. The middle panel corresponds to the CA1 subfield of *Alox15*$^{-/-}$ mouse vHPC (p) single channel acquisition of DAPI staining (q) single channel $5HT_{1A}$ staining AF5968 (r) merged image of $5HT_{1A}$ with DAPI. The bottom panel corresponds to the DG subfield of *Alox15*$^{-/-}$ mouse vHPC (s) single channel acquisition of DAPI staining (t) single channel $5HT_{1A}$ staining AF568 (y) merged image of $5HT_{1A}$ with DAPI WT (n=12) and *Alox15*$^{-/-}$ (n=11) male mice, 15 months of age. Scale bars, 100 µm.

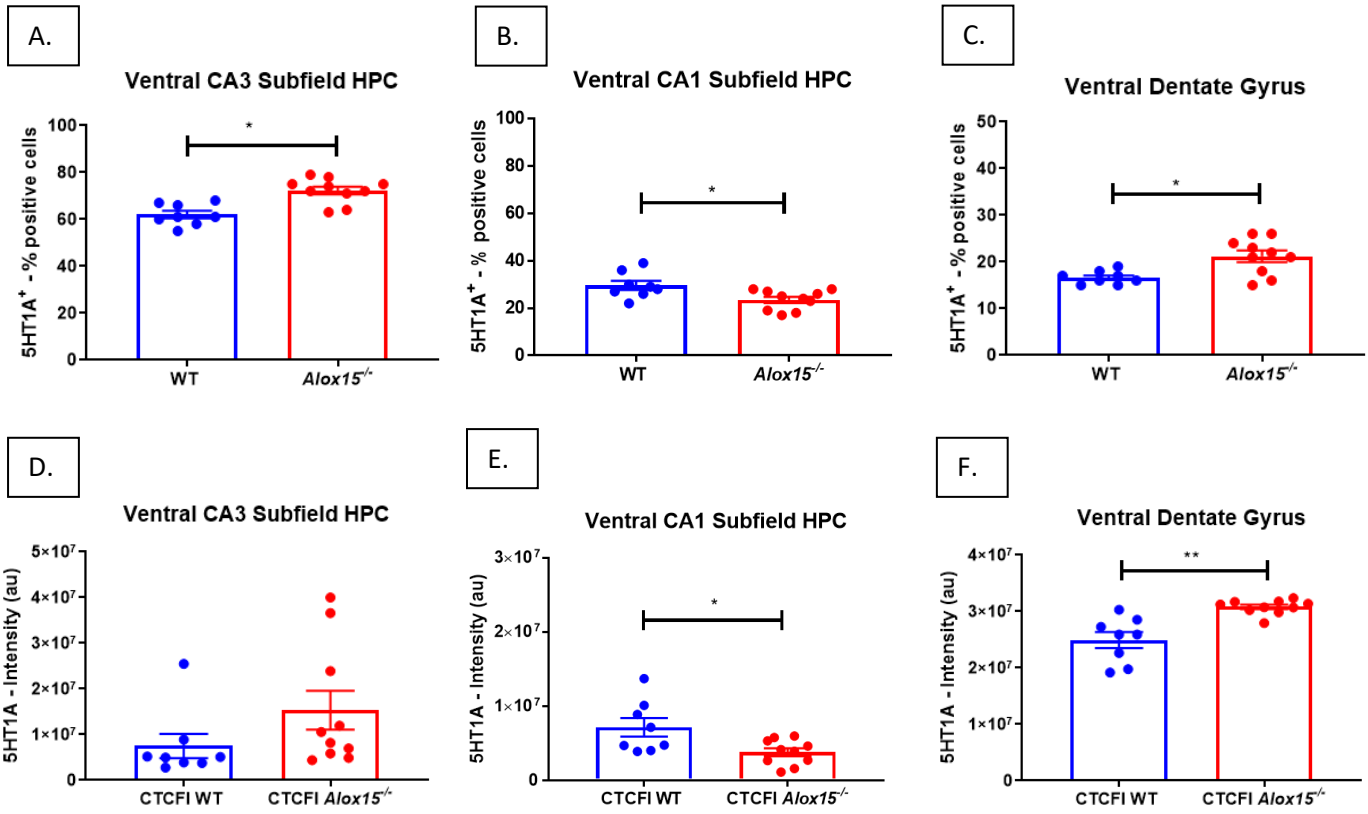

Figure 59. Quantification of the percentage number of $5HT_{1A}$+ receptor cells and the immunofluorescence $5HT_{1A}$ signal intensity (CTCFl) in all the subregions of vHPC. The formula used to calculate CTCFl was described in Materials and Methods. The top panel corresponds to the percentage of positive cells where all of the cells, including the nucleus evidenced by DAPI staining was, within the thickness of the section surrounding the cell (A) in the CA3 area (B) in the CA1 area (C) in the DG of vHPC. The bottom panel shows scatterplots of signal intensities of $5HT_{1A}$ receptor staining in all subregions of the vHPC between WT and *Alox15*$^{-/-}$ mice. (D) in CA3 pyramidal cell layer (E) in CA1 pyramidal cell layer (F) in the granule cell layer of the DG. Data were represented as signal intensities in the pyramidal cell layer of CA1, CA3 and granule cell layer of the DG. Each dot represents an individual mouse. Data were analysed using Mann- Whitney non-parametric U test and shown on Tukey box plots with mean ± S.E.M WT (n=12) and *Alox15*$^{-/-}$ (n=11) male mice, 15 months of age. *, **, *** and **** represent $p \leq 0.05$, $p \leq 0.01$, $p \leq 0.001$ and $p \leq 0.0001$ for genotype comparisons, respectively.

- **5HT$_{1A}$ receptor – dHPC**

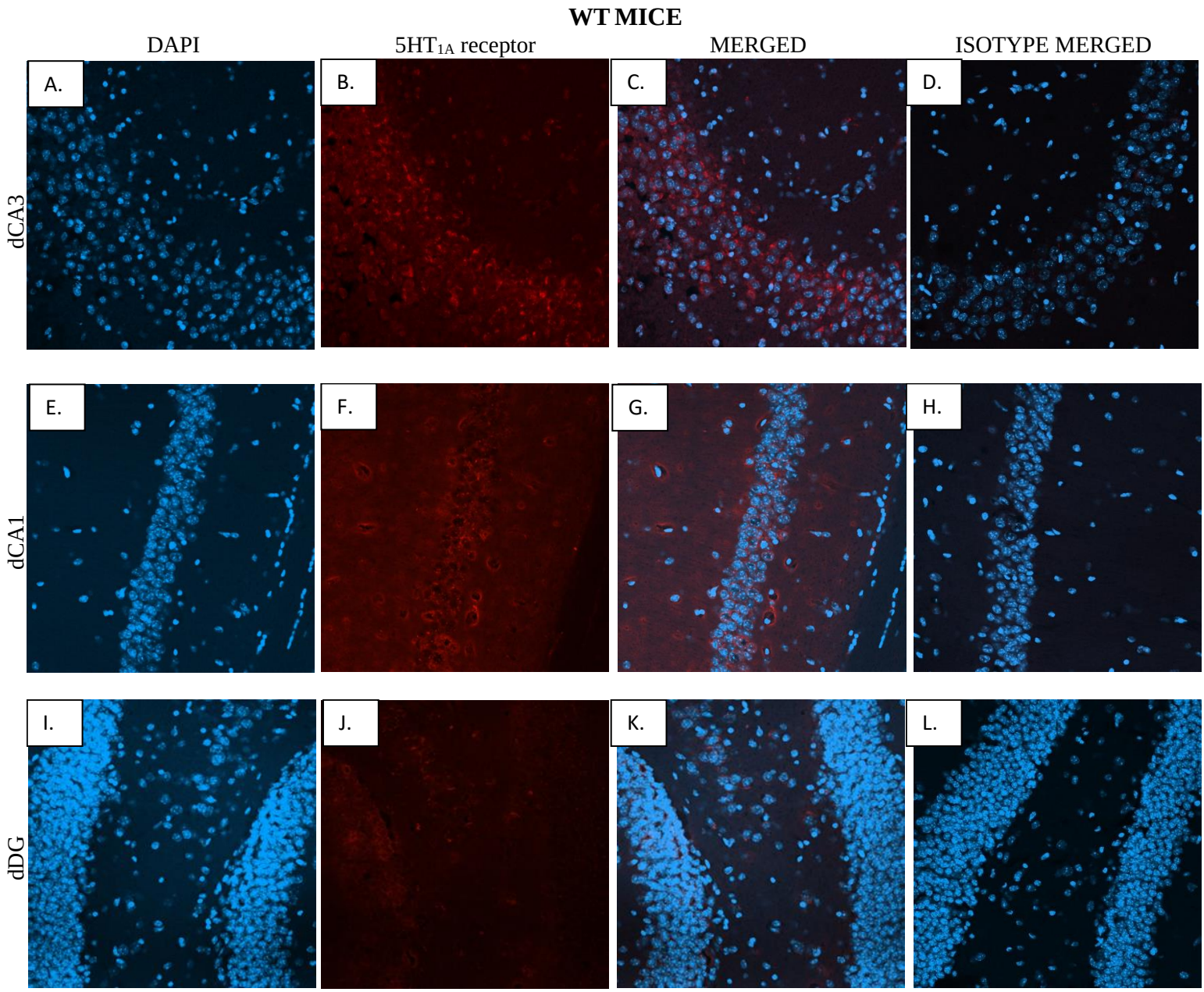

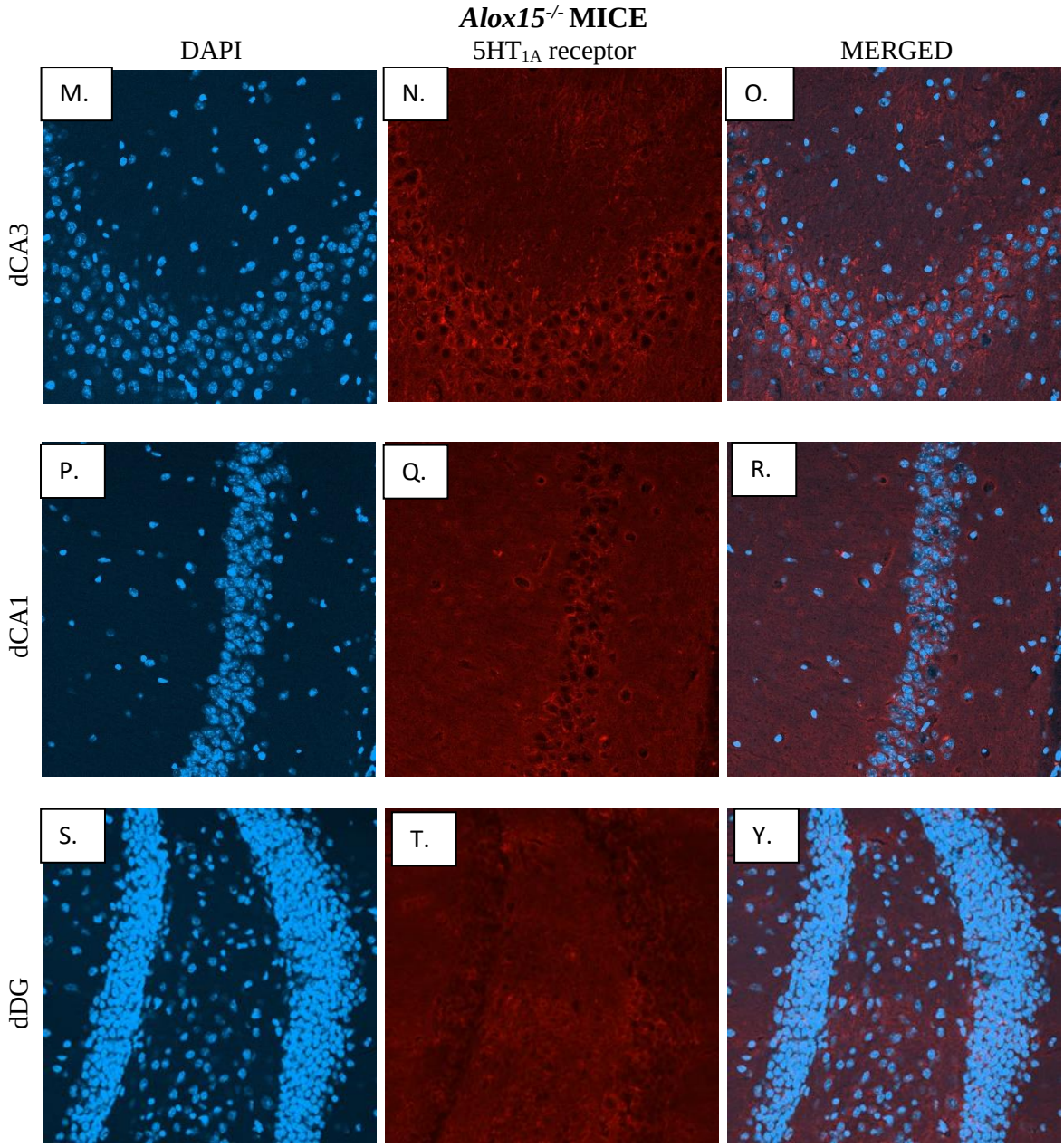

Figure 60. Representative confocal imaging illustrating detection and localization of 5HT$_{1A}$ receptor in the CA1, CA2/3, DG subregions of dHPC of coronal cryosections of 20 µm thickness. The top panel corresponds to CA3 subfield of WT mouse dHPC (a) single channel acquisition of DAPI staining (blue) of cell nuclei (AF405) (b) single channel 5HT$_{1A}$ staining AF568 (orange/red) (c) merged image of 5HT$_{1A}$ in colocalization with DAPI (d) an overlay imaging on isotype control, rabbit IgG polyclonal, merged with DAPI counterstaining. The middle panel corresponds to the CA1 subfield of WT mouse dHPC (e) single channel acquisition of DAPI staining (f) single channel 5HT$_{1A}$ staining AF568 (g) merged image of 5HT$_{1A}$ with DAPI (h) merged image on isotype control. The bottom panel corresponds to the DG subfield of WT mouse dHPC (i) single channel acquisition of DAPI staining (j) single channel 5HT$_{1A}$ staining AF568 (k) merged image of 5HT$_{1A}$ with DAPI (l) merged image on isotype control. In contrast, the top panel corresponds to CA3 subfield of *Alox15*$^{-/-}$ mouse dHPC (m) single channel acquisition of DAPI staining (n) single channel 5HT$_{1A}$ staining AF568 (o) merged image of 5HT$_{1A}$ with DAPI. The middle panel corresponds to the CA1 subfield of *Alox15*$^{-/-}$ mouse dHPC (p) single channel acquisition of DAPI staining (q) single channel 5HT$_{1A}$ staining AF568 (r) merged image of 5HT$_{1A}$ with DAPI. The bottom panel corresponds to the DG subfield of *Alox15*$^{-/-}$ mouse dHPC (s) single channel acquisition of DAPI staining (t) single channel 5HT$_{1A}$ staining AF568 (y) merged image of 5HT$_{1A}$ with DAPI WT (n=12) and *Alox15*$^{-/-}$ (n=11) male mice, 15 months of age. Scale bars, 100 µm.

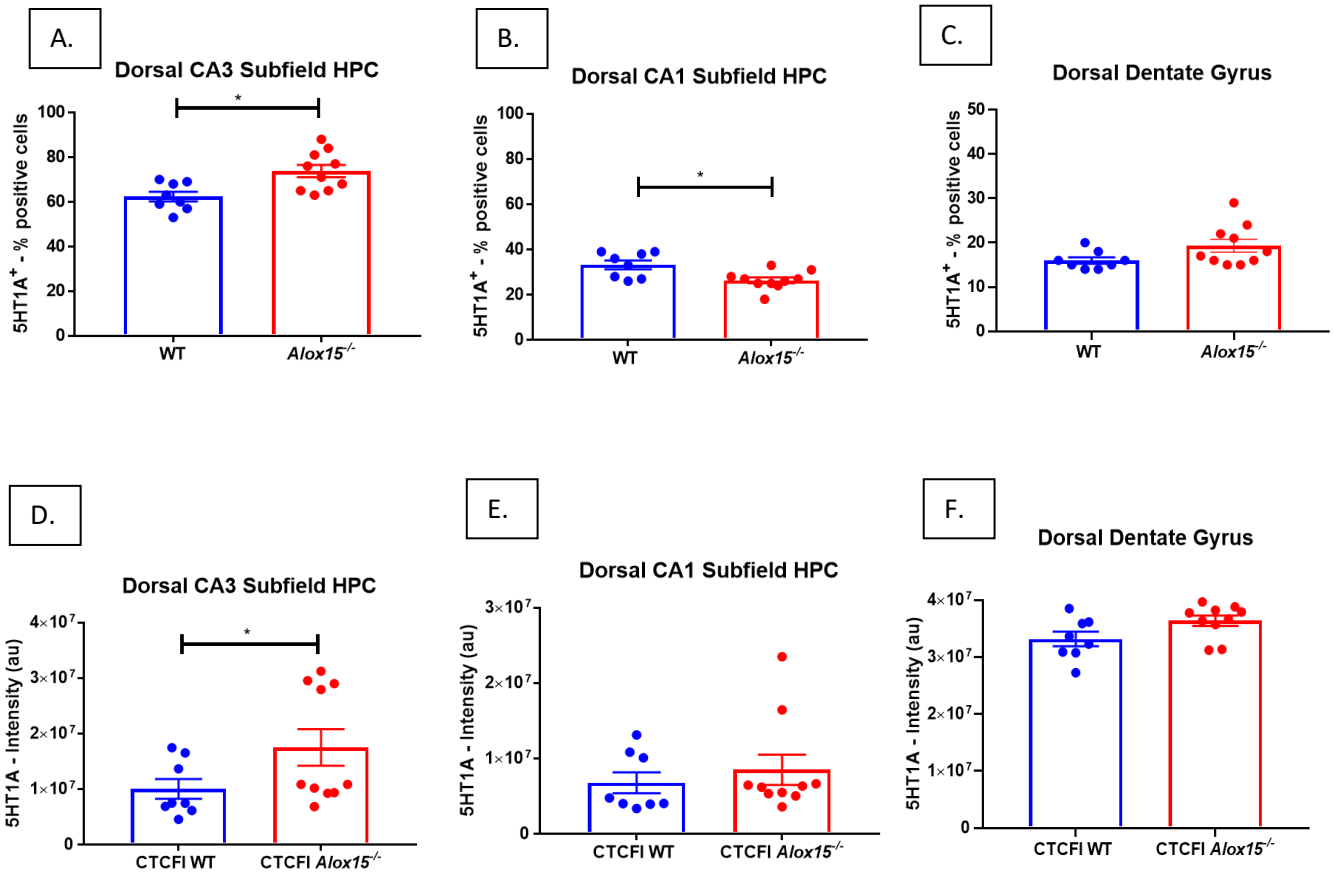

Figure 61. Quantification of the percentage number of $5HT_{1A}$+ receptor cells and the immunofluorescence $5HT_{1A}$ signal intensity (CTCFl) in all the subregion of dHPC. The formula used to calculate CTCFl was described in Materials and Methods. The top panel corresponds to the percentage of positive cells where all of the cells including the nucleus evidenced by DAPI staining was within the thickness of the section surrounding the cell (A) in the CA3 area (B) in the CA1 area (C) in the DG of dHPC. The bottom panel shows scatterplots of signal intensities of $5HT_{1A}$ receptor staining in all subregions of dHPC between WT and *Alox15*$^{-/-}$ mice. (D) in CA3 pyramidal cell layer (E) in CA1 pyramidal cell layer (F) in the granule cell layer of DG. Data were represented as signal intensities in the pyramidal cell layer of CA1, CA3 and granule cell layer of the DG. Each dot represents an individual mouse. Data were analysed using Mann- Whitney non-parametric U test and shown on Tukey box plots with mean ± S.E.M WT (n=12) and *Alox15*$^{-/-}$ (n=11) male mice, 15 months of age. *, **, *** and **** represent $p \leq 0.05$, $p \leq 0.01$, $p \leq 0.001$ and $p \leq 0.0001$ for genotype comparisons, respectively.

DISCUSSION

Summary data of the expression levels of proteins markers aged Alox15$^{-/-}$ male mice

Parvalbumin	*Significant reduction in the percentage of PV-INs in HPC*
GABA$_B$ receptor	*Markedly reduction in the percentage of* GABA$_B$ receptor positive cells in HPC
CRF$_1$ receptor	*Significant increase in* CRF$_1$ receptor positive cells in *vCA3 and dCA3, vCA1 and dCA1*
5HT1$_A$ receptor	*Significant increase in 5HT1$_A$* receptor positive cells in *vCA3 and dCA3, but decrease in vCA1 and dCA1*

In the previous chapter, deficiency of *Alox15* mouse leads to a reproducible anxiety phenotype that appeared to worsen with age. In the current experiment, I assessed several protein markers, including GABA$_B$, PV, CRF$_1$ and 5-HT$_{1A}$ receptors associated with the anxiety phenotype of aged *Alox15$^{-/-}$* male mice. Consistent with the literature, the increased anxiety-related behaviour was associated with the decreased number of PV and GABA$_B$ positive interneurons and the increased number of CRF$_1$ receptor-positive cells in the HPC of *Alox15$^{-/-}$* male mice. However, my findings that the increased hippocampal 5-HT$_{1A}$ receptor-positive cells in increased anxiety-like behaviour did not support previous studies. Collectively, the results in this chapter partially support my hypothesis that deficiency of the *Alox15* pathway is correlated with various expression levels, which may manifest an anxiety-like behaviour, both behaviourally and functionally.

As a calcium-binding protein, PV is a critical component of Ca^{2+} homeostatic mechanisms (Volma *et al*., 2011; Collin, *et al.,* 2005; Marín, 2012). The maintenance of PV is essential for attenuating neuronal loss, suggesting a neuroprotective effect (Van Den Bosch *et al*., 2002; Filice, *et al.,* 2016). Studies have shown that changes in GABAergic function mediated by dysfunction of PV interneurons may lead to impaired learning and synaptic function and plasticity and altered neuropathological disorders such as schizophrenia (Hu *et al.,* 2014; Steullet, *t al.,* 2017). Consequently, thea robust link existtween PV neuronal dysfunction and neuropsychiatric disorders, such as epilepsy, autism, depression, and schizophrenia (Torrey *et al*., 2005; Sohal *et al*., 2009; Rossignol, 2011). *Alox15* is predominantly expressed

in CNS, and this current study demonstrates that deficiency of the *Alox15* pathway is correlated with significantly reduced numbers of PV neuronal cells in hippocampal pyramidal and granule cells. These findings are consistent with previous results showing that chronic anxiety-related responses impact decreased expression (Sloviter, *et al*., 1999; Czeh, *et al.* 2005; Venero, *et al.*, 2005; Hu, *et al.*, 2010; Godavarthi, *et al.*, 2014; Czeh *et al*. 2015; Zou, *et al*., 2016). Steullet and his colleagues suggested that PV interneurons are vulnerable to impaired mitochondrial function and redox dysregulation, which result in higher levels of oxidative stress in the brain due to their fast-spiking electrophysiology (Steullet, *et al.*, 2010; Cabungcal, *et al.*, 2013). Of particular note, elevated oxidative stress is correlated with decreased PV-positive hippocampal interneurons, especially in vCA3 and DG subregions of the vHPC (Steullet, *et al.*, 2010**).** These results are related to previous studies, implying the correlation of *Alox15* with ageing-associated brain oxidative stress and neuronal injury due to their lipid-rich oxidizing properties and ability to damage mitochondria (van Leyen, *et al.*, 2000; Pratico, et al., 2004; Chinnici, *et al*., 2005).

A closer examination of the $GABA_B$ receptor immunoreactivity in this study showed that *Alox15* deficiency is associated with significantly decreased $GABA_B$ receptors in hippocampal pyramidal neurons and granule cells. Previous work indicated that the reduced number of $GABA_B$ receptor cells is associated with reduced neuronal inhibition affecting the downstream signalling of the $GABA_B$ receptor in the HPC of mice (Maier, *et al*., 2014; Mizukami, *et al.*, 2000; Vigot, *et al.*, 2006; Booker, *et al.*, 2013; Giachino, *et al.*, 2014; Maie, *et al*., 2014; Song, *et al.*, 2021). Another study has shown that $GABA_B$ transmission and changes in the expression of hippocampal $GABA_B$ receptors shift the balance between excitatory and inhibitory receptors circuits leading to the dysfunction of hippocampal circuitry (Han, *et al.*, 2012). Anxiety disorders such as depression, anxiety and epilepsy are conditions that are based on a disequilibrium between excitatory and inhibitory neurons in the aged HPC (Zhang, *et al.*, 2002; Marin, 2012; McQuail, *et al.*, 2015; Govindpani, *et al.*, 2017; Rozycka, *et al*., 2017; Wang, *et al*., 2021). Therefore, the decreased number of $GABA_B$ inhibitory neurons, GABA release, would be an attempt to counterbalance the enhanced excitatory neuronal activity caused by increased anxiety (Han, *et al.*, 2012). Hence, the number of hippocampal GABAergic interneurons and the number of PV cells significantly decreased under anxiety-related responses.

This chapter also showed increased CRF_1-receptor immunoreactivity in the dorsal and ventral HPC of *Alox15*$^{-/-}$ compared to WT mice. Although CRH acts as a neuroendocrine corticotropin-releasing factor for ACTH, the CRF_1 receptor is a vital regulator of the actions of CRF

neuropeptide and plays an essential role as a stress regulator in the brain (Chen, *et al*., 2004; Brunson, *et al*., 2011). A study by Chen and his colleagues reports that the CRF_1 receptor-immunoreactive cells are present in a subpopulation of GABAergic interneurons in the mature hippocampal pyramidal cells in CA3 and CA1 areas (Chen, *et al.,* 2004). Under physiological conditions, when they are released from GABAergic terminals, CRF acts as excitatory neuromodulator enhancing the synaptic neurotransmission throughout the CNS. However, under stress related responses CRF needs to travel a lot within the brain to reach CRF_1-receptor causing premature cognitive decline to the insufficient peptides (Yan, *et al*., 1998; Brunson, *et al.,* 2002; Chen, *et al.,* 2004; Chen, *et al.,* 2008). These results are consistent with the current findings that the prominent CRF-immunoreactive cells were located predominantly in the hippocampal CA3 pyramidal layer, and fewer were observed in the CA1 layer in *Alox15*$^{-/-}$ mice compared to WT mice (Brunson, *et al*., 2001; Radulovic, *et al.,* 1998; Chen, *et al*., 2000; Chen, *et al*., 2004; Chen, *et al.,* 2008; Sherrin, *et al* 2009; Wang, *et al.,* 2017). Additionally, CRF_1 receptor cells resided in the granule cell layer and the hilus of the DG, but no changes were detected in the CRF_1 receptor immunoreactivity between genotypes.

It is well-established that serotonin can modulate anxiety, and any disturbances in serotonin transmission, as well as dysregulation of $5HT_{1A}$ receptor levels, are implicated in emotional disorders (Graeff, *et al*., 1996; Ramboz, *et al.,* 1998; Cryan, *et al.,* 2000; Rojas, *et al.,* 2016). This chapter reports that the deficiency of *Alox15* leads to contradictory results in $5HT_{1A}$ receptor expression and the numbers of $5HT_{1A}$ neuronal cells in hippocampal CA3 and CA1 pyramidal neurons and granule cells of the DG. The main inconsistency was observed in the number of $5HT_{1A}$ positive neurons in the ventral and dorsal CA3 subfields in *Alox15*$^{-/-}$ mice relative to WT. However, the $5HT_{1A}$ receptor-positive neurons in the dCA1 and vCA1 subfield were significantly lower in *Alox15*$^{-/-}$ mice than in WT. These findings contrast with some previous studies regarding rodents' decreased expression of the $5HT_{1A}$ receptor (Czesak, *et al.,* 2012). Furthermore, previous studies are implicated in chronic administration of selective serotonin reuptake inhibitors (SSRIs), which are widely used antidepressants, to induce neurogenesis in the HPC, resulting in decreased anxiety (Stockmeier, 1998; Haddjeri, *et al.,* 1998; Santarelli, *et al.,* 2013; Samuels, *et al.,* 2015). Interestingly, a study by File *et. al,* 1996, performed two behavioural tasks to assess the rodent's anxiety-like behaviour, such as social interaction and EPM to compare the presynaptic and postsynaptic $5HT_{1A}$ in the modulation of anxiety. Their results showed that the presynaptic 5-HT_{1A} receptor leads to an anxiolytic action, while the postsynaptic 5-HT1A receptor is stimulated in the dorsal HPC following administration of a $5HT_{1A}$ agonist leading to an anxiogenic effect (File, *et al.,* 1996; Czesak, *et*

al. 2012). Thus, results suggest that stimulating autoreceptors and heteroreceptors of $5HT_{1A}$ may lead to opposing phenotypes in anxiety regulation.

In summary, this chapter suggests that the genetic deletion of *Alox15*, which was shown previously to be associated with the development of the anxiety phenotype, is also linked with altered expression levels of various protein markers. To the best of my knowledge, these findings highlight the first evidence for a novel role of behavioral anxiety phenotype linked to changes in *Alox15* expression levels. Altered hippocampal expression levels of various proteins are correlated with anxiety-like behaviour in the *Alox15* pathway. The retrospective analysis includes RNA sequencing (RNA-seq), which would have been a paramount approach to identifying promising candidate genes related to the *Alox15* pathway, including up-regulated and down-regulated genes between *Alox15*$^{-/-}$ and WT mice; however, this was not performed in the current study. Also, due to low sample size, (n=7) I could not proceed with gender differences analysis for immunohistochemistry data. Hence, a future research with greater sample size is recommended to elucidate the sex differences in the aged brain of healthy *Alox15*$^{-/-}$ mice.

Chapter 6:

Alox15 deficiency is associated with altered brain levels of oxylipins

INTRODUCTION

6.1 Chapter overview

In previous chapters, behavioural and cognitive phenotypes of *Alox15*$^{-/-}$ mice were elucidated. As introduced in Chapter 1, oxygenated PUFA are bioactive lipid mediators that can be formed enzymatically by the action of three metabolic pathways: LOX, COX or CYP450, resulting in the generation of oxylipins. Also, PUFA oxidation can be mediated non-enzymatically through free-radical uncontrolled processes via reactive oxygen/nitrogen species (ROS) during inflammation (Patterson *et al.*, 2012; Uttara *et al.*, 2019; O'Donnell *et al.*, 2009). Herein, I will investigate the impact of *Alox15* deletion on oxylipin levels in the brain. Consequently, I will examine whether these lipid mediators differ in various brain regions such as the prefrontal cortex, cerebellum and HPC.

LC-MS/MS analysis will be used in this chapter. The LOX enzyme being studied in this thesis is 12/15-LOX. This generates the AA lipid products 12-HETE, 12-oxo-ETE, 15-HETE, 15-oxoETE and 5,15-DiHETE. Also, this enzyme can generate LA-derived products, including 13(S)-HODE and 13-oxo-ODE; EPA-derived products 12-hydroxyeicosapentaenoic acid (HEPE), and the DHA metabolite 14-hydroxydocosahexaenoic acid (14-HDoHE). Furthermore, 5-LOX generates 5-HETE and 5-oxo-ETE, as well as the leukotrienes LTA_4, LTB_4, LTC_4, LTD_4, and LTE_4 (Figure 62 A).

The CYP 450 pathway produces epoxyeicosatrienoic acids (EET) from AA metabolism, via epoxygenase activity and epoxyoctadecamonoenoic acids (EpOME) from LA (Harmon *et al.*, 2006). AA undergoes metabolism by CYP450 to generate four regioisomeric epoxyeicosatrienoic acids (EETs) 5,6-, 8,9-, 11,12-, and 14,15-EET, which function as autocrine and paracrine lipid mediators to maintain homeostasis in the body (Spector, 2009; Massey *et al.*, 2013). These epoxides can be further metabolized by soluble epoxide hydrolase (sEH), to more stable corresponding metabolites, into dihydroxyeicosatrienoic acids (DiHETrE), dihydroxyoctadecamonoenoic acids (DiHOME), derived from AA and LA, respectively (Gabbs *et al.*, 2015) The CYP enzymes reduce inflammation by generating or metabolizing bioactive mediators and have potent vasodilation actions (Gilroy *et al.*, 2016) (Figure 62 A).

The COX enzymes catalyse the reaction that converts the prostaglandin endoperoxides G to H from AA (Smith *et al.*, 2002; Barreiro-Iglesias, 2020). PGH_2 which is an unstable intermediate, is further metabolized to other prostaglandin series, including prostaglandin E_2 (PGE_2),

prostacyclin (PGI_2), prostaglandin D_2 (PGD_2) and prostaglandin $F_{2\alpha}$ ($PGF_{2\alpha}$) and thromboxane A_2 (TXA_2), which are termed prostanoids , as part of the oxylipin family (Smith *et al.*, 2000) (Figure 62 B). Prostaglandin production is generally very low under normal conditions, but increases dramatically during an inflammatory response (Ricciotti *et al.*, 2011).

By contrast, these differ from non-enzymatically generated oxylipins through uncontrolled oxidation via free radical mechanisms during cell stress or inflammation (WJ Griffiths *et al.*, 2019). Non-enzymatically formed isoprostanes (isoP), prostaglandin-like molecules, and non-AA products of COX, LOX, and P450 metabolites are prone to free-radical mediated oxidation of AA as they present harmful biological activities (Czerska *et al.*, 2016; Biringer *et al.*, 2019). These derivatives are considered oxidative stress markers associated with several inflammatory diseases, including AD (Austin Pickens *et al*., 2019; Trostchansky *et al.*, 2021).

6.2 Aim and objectives

The overall aim is to study how the genetic deletion of *Alox15* influences oxylipin generation. Here, I will focus on the targeted LC-MS/MS analysis of oxylipins synthesized from AA and DHA, LA and their metabolites, as they are the most well- studied. In addition, this chapter will emphasize the biosynthesis of some oxylipins, formed non-enzymatically by ROS in the *Alox15*$^{-/-}$ compared to the WT brain.

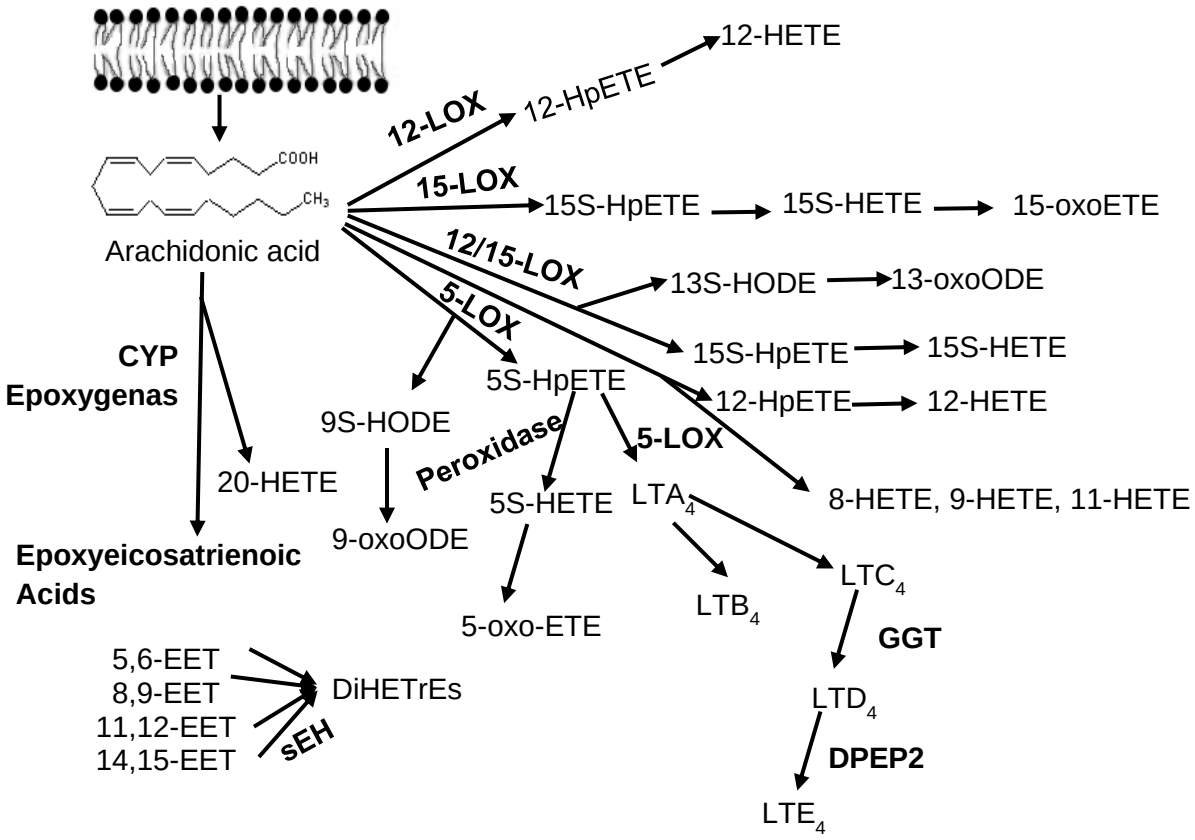

Figure 62 A. Summary of the metabolites of AA into oxylipins by three primary pathways. Four regioisomeric EETs are primary products of AA metabolism by cytochrome P450 epoxygenases. HETEs are the main primary products initiated by LOXs.

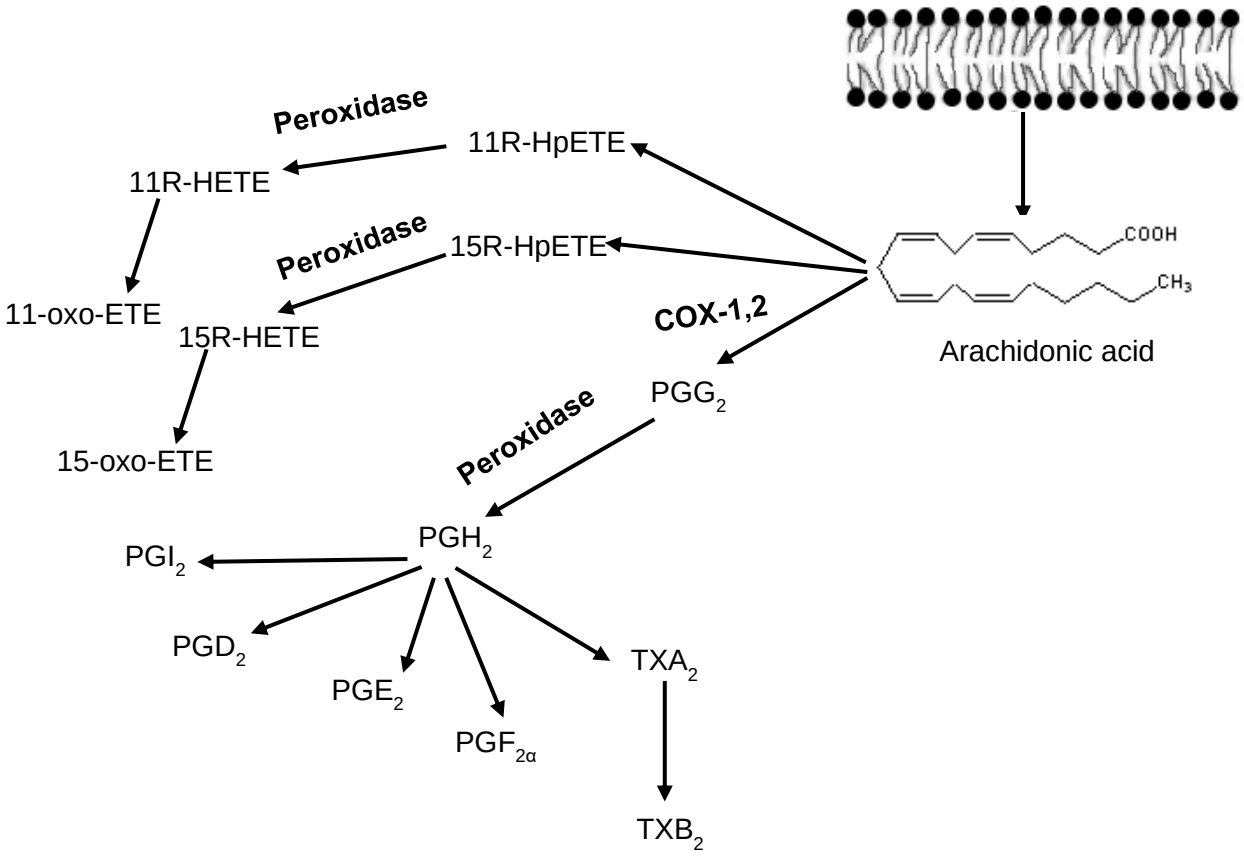

Figure 62 B. Summary of the metabolites of AA into oxylipins by COX pathway. The formation of prostaglandins and thromboxanes are derived from the COX pathway.

Results

6.3 LC/MS/MS analysis reveals the oxylipin profile of *Alox15*$^{-/-}$ mouse brain

Using a targeted lipidomic approach, I measured oxylipins in brain regions in 12 WT and 11 *Alox15*$^{-/-}$ male mice aged 15 months and visualized the data on a heatmap to compare the brain regions that differed between genotypes (Figure 63). Most of the oxylipins analyzed in this chapter were generated from ω-6 AA, ω-6 LA and ω-3 DHA through LOX, COX and CYP-450 pathways. Hierarchical clustering in the heatmap was carried out to cluster oxylipins. This was obtained by analyzing the average values per oxylipin, revealing clusters of lipids with common behaviour. A close inspection revealed that oxylipins abundance was quite different in the cerebellum between genotypes.

The hierarchical clustering showed trends whereby different subclasses of lipids grouped based on lower or higher abundance relative to other groups (Figure 63). For instance, all HETEs demonstrated similar behaviour and were grouped into cluster 4, showing a moderate abundance in the three brain regions for both genotypes. Similarly, the HDOHEs, derived from DHA, grouped into cluster 1 due to their low abundance. Also, a greater abundance of COX metabolites from AA-derived prostaglandins, including PGD_2 and PGF_{2a}, showed the highest quantity and grouped into cluster 3. Conversely, CYP epoxygenase products, such as 11,12-DiHETrE and 14,15-DiHETrE, are grouped into cluster 2 due to their very low abundance.

The representative chromatograms for the oxylipins measured in this chapter are presented in section 6.13.

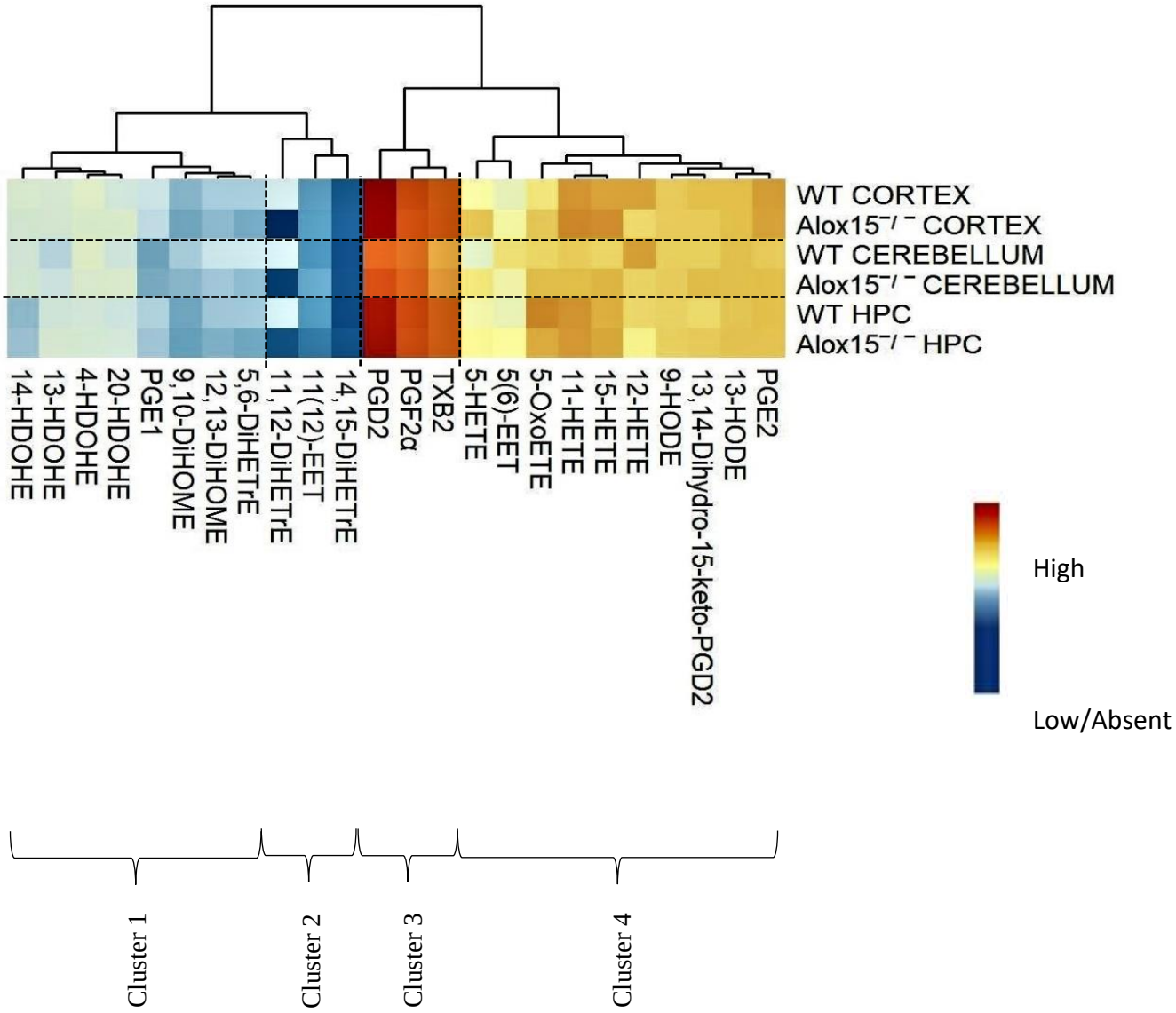

Figure 63. Hierarchical clustering heatmap analysis was performed for oxylipins in the cortex, HPC, and cerebellum. As described in Materials and Methods, lipids were extracted from various brain regions and quantified by LC-MS/MS. The heatmap of the average values (mean) for each genotype was generated using 24 metabolites that differed among the genotype and was shown as log10 values in replicates for each analyte normalized to brain tissue weight (mg). log10 transformed and plotted as a heatmap with hierarchical clustering using the pheatmap R package WT (n=12) and *Alox15*$^{-/-}$ (n=11).

The list of 24 individual oxylipins detected in WT mice is presented below (Table 13). The following sections focus on each particular group of lipids, including HETEs, HDOHEs, PGs, HODEs, DiHETrEs and DiHOMEs, by comparing their levels with age-matched *Alox15*$^{-/-}$ mice using multiple non-parametric tests.

6.4 *Alox15*$^{-/-}$ brain showed significantly elevated 15-HETE and reduced 12-HETE.

The primary 12/15-LOX products are 12S-HETE and 15S-HETE from AA, while COX isoforms can also generate 15R-HETE. Data in each brain region were analysed by multiple Mann- Whitney non-parametric U tests revealing that *Alox15*$^{-/-}$ brain contained significantly higher amounts of 15-HETE in the cortex and cerebellum than WT mice (P= 0.0187, P=0.014) (Figure 64). However, no differences were marked in the HPC between genotypes. 12-HETE was reduced in the brain of *Alox15*$^{-/-}$ mice compared to WT, but this was not significant (Figure 64).

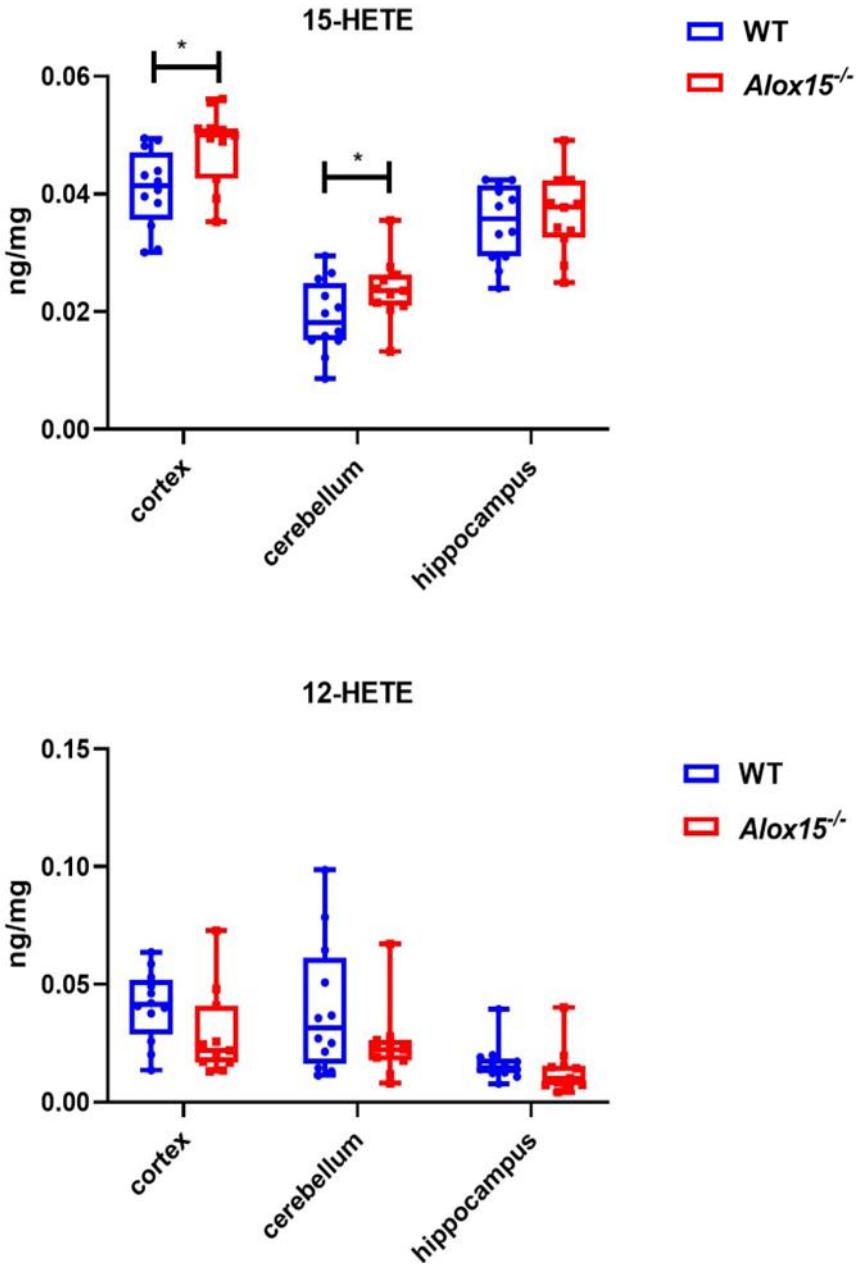

Figure 64. 12-HETE is slightly reduced and 15-HETE are significantly reduced in *Alox15*$^{-/-}$ mice. Lipids were extracted from three brain regions as described in Materials and Methods. Data in each brain region were analysed using Mann- Whitney non-parametric U test and shown on Tukey box plots with mean ± S.E.M. WT (n=12) and *Alox15*$^{-/-}$ (n=11) *, **, *** and **** represent p≤0.05, p≤0.01, p≤0.001 and p≤0.0001 for genotype comparisons, respectively.

6.5 *Alox15*$^{-/-}$ brain demonstrated significantly increased 5-HETE

5-HETE is a LOX-derived AA-metabolite that is produced by mouse neutrophils via 5-LOX. Here 5-LOX inserts molecular oxygen into the carbon at position 5 of free AA to form potent bioactive lipid mediators. 5-LOX first metabolizes AA, forming 5-HpETE, an unstable lipid derivative (Czapski, *et al.,* 2016). Then 5-HpETE is rapidly reduced by the action of glutathione peroxidase to 5-HETE, or it can be oxidized to the electrophilic lipid 5-oxo-eicosatetraenoic acid (5-oxo-ETE) (Rubin, *et al.,* 2007). In addition, leukotrienes are lipid mediators of inflammation, derived downstream of 5-LOX oxidation of AA, but previously were not found in brain regions of WT mice (Salmon, *et al.*, 1987). Here, data in each brain region were analysed using Mann- Whitney non-parametric U test and revealed that 5-HETE was significantly increased in the prefrontal cortex, cerebellum and HPC of *Alox15*$^{-/-}$ mice compared to WT (P= 0.0221, P= 0.0369, P= 0.0433, respectively). Similarly, elevated levels were detected of 5-oxo-ETE of *Alox15*$^{-/-}$, although they did not reach statistical significance (Figure 65).

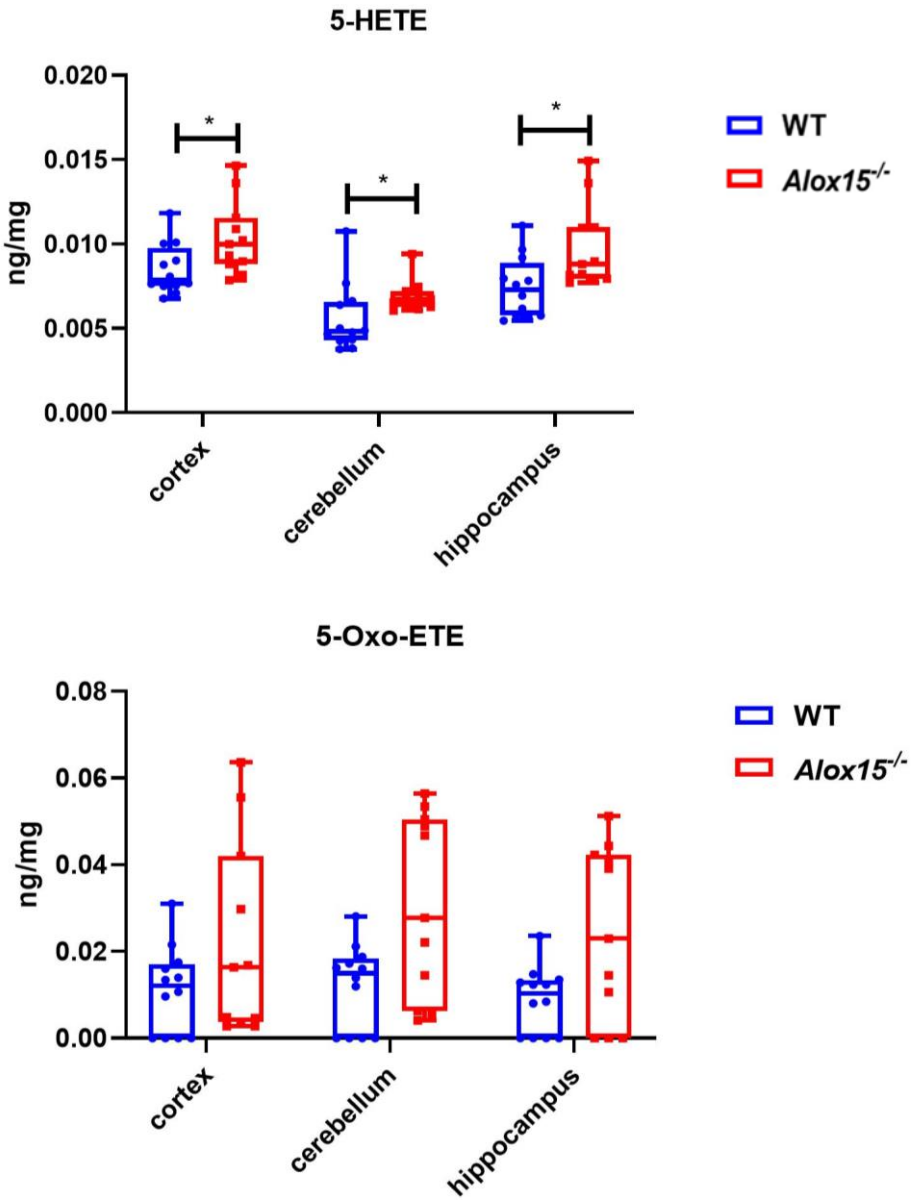

Figure 65. 5-HETE is markedly elevated in *Alox15*$^{-/-}$ mice. Lipids were extracted from three brain regions as described in Materials and Methods. Data in each brain region were analysed using Mann-Whitney non-parametric U test and shown on Tukey box plots with mean ± S.E.M. WT (n=12) and *Alox15*$^{-/-}$ (n=11) *, **, *** and **** represent $p \leq 0.05$, $p \leq 0.01$, $p \leq 0.001$ and $p \leq 0.0001$ for genotype comparisons, respectively.

6.6 *Alox15*$^{-/-}$ brain contained markedly higher 11-HETE than wild type

11-HETE is synthesized through non-enzymatic oxidation from AA and has been described as a marker of lipid peroxidation (Guido, *et al.*, 1993). 11-HETE can also be formed through enzymatic oxidation as a by-product of prostaglandin biosynthesis by COXs (Xiao, *et al.*, 1997). Here, Mann-Whitney non-parametric U test revealed that *Alox15*$^{-/-}$ mice showed significantly increased levels of 11-HETE in the cortex and cerebellum compared to WT mice (P=0.0107). However, no differences were noticed in the HPC between the two groups (Figure 66).

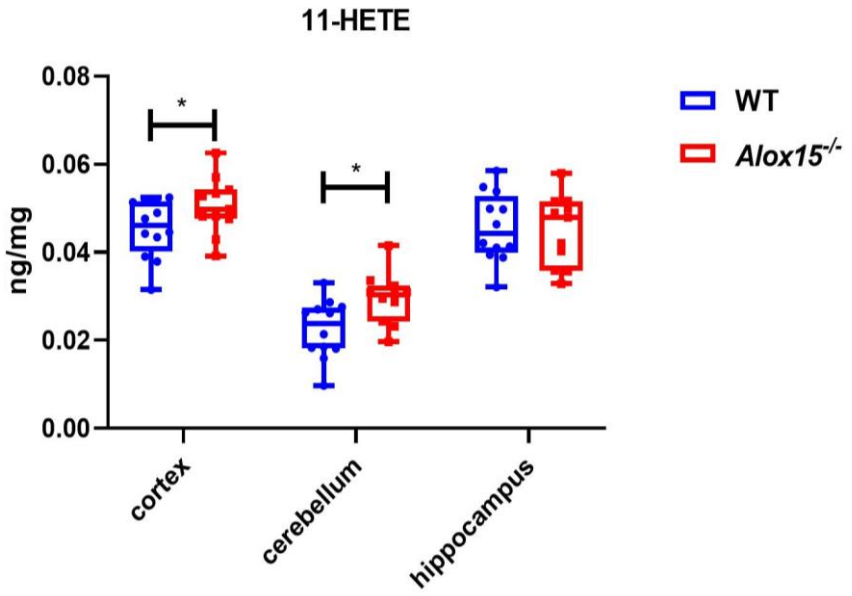

Figure 66. 11-HETE is significantly increased in *Alox15*$^{-/-}$ mice. Lipids were extracted from three brain regions as described in Materials and Methods. Data in each brain region were analysed using Mann- Whitney non-parametric U test and shown on Tukey box plots with mean ± S.E.M. WT (n=12) and *Alox15*$^{-/-}$ (n=11) *, **, *** and **** represent p≤0.05, p≤0.01, p≤0.001 and p≤0.0001 for genotype comparisons, respectively.

6.7 *Alox15*$^{-/-}$ brain demonstrated increased cerebellum levels of 4-HDOHE and 16-HDOHE.

Next, DHA can be metabolized via the LOX pathway, resulting in the production of HDOHE (Miyata, *et al.*, 2021). Mann-Whitney non-parametric U test revealed that the levels in three brain regions of 14-HDOHE were similar between genotypes, as shown in Figure 67. However *Alox15*$^{-/-}$ mice had significantly higher 4-HDOHE levels in the cerebellum compared to WT mice but similar levels in the cortex and cerebellum between the two strains (P=0.0045) (Figure 67).

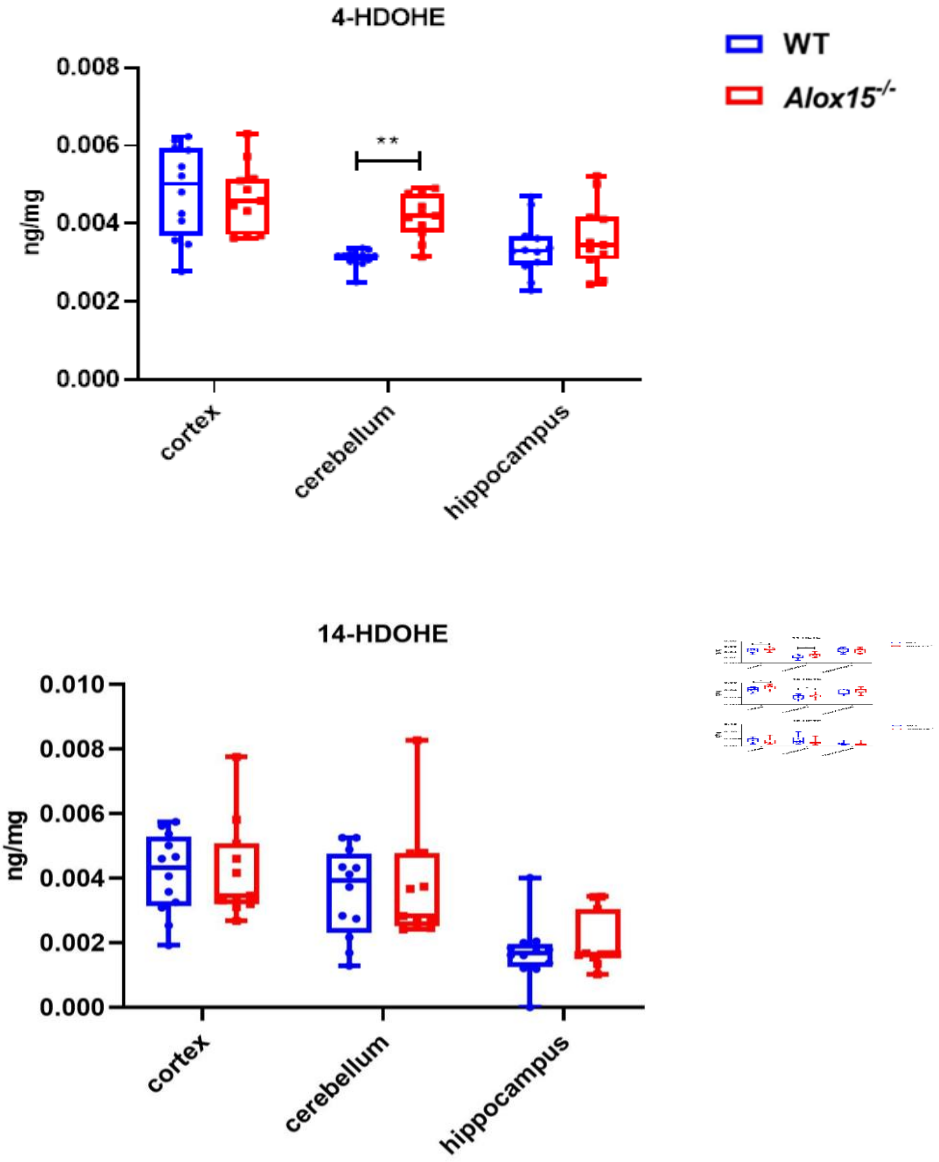

Figure 67. 4-HDOHE significantly vary in the cerebellum and 14-HDOHE remains unchanged between. Lipids were extracted from three brain regions as described in Materials and Methods. Data in each brain region were analysed using Mann-Whitney non-parametric U test and shown on Tukey box plots with mean ± S.E.M. WT (n=12) and *Alox15*$^{-/-}$ (n=11) *, **, *** and **** represent p≤0.05, p≤0.01, p≤0.001 and p≤0.0001 for genotype comparisons, respectively.

6.8 *Alox15*$^{-/-}$ cerebellum demonstrated elevated levels of 13-HDOHE and 20-HDOHE

DHA is metabolized via the COX pathway generating 13-HDOHE (Serhan, *et al.*, 2002). Oxylipins can also be formed from DHA via CYP-450 epoxygenase. For example, CYP via ω-hydroxylase activity produces 20-HDOHE with a hydroxyl group near the methyl end of DHA (VanRollins, *et al.*, 1984). Mann-Whitney non-parametric U test in the cerebellum revealed that 13-HDOHE and 20-HDOHE levels were significantly higher in the cerebellum than in WT mice, but they were similar in the HPC and cortex across both strains (P=0.04820, P=0.0433, respectively) (Figure 68).

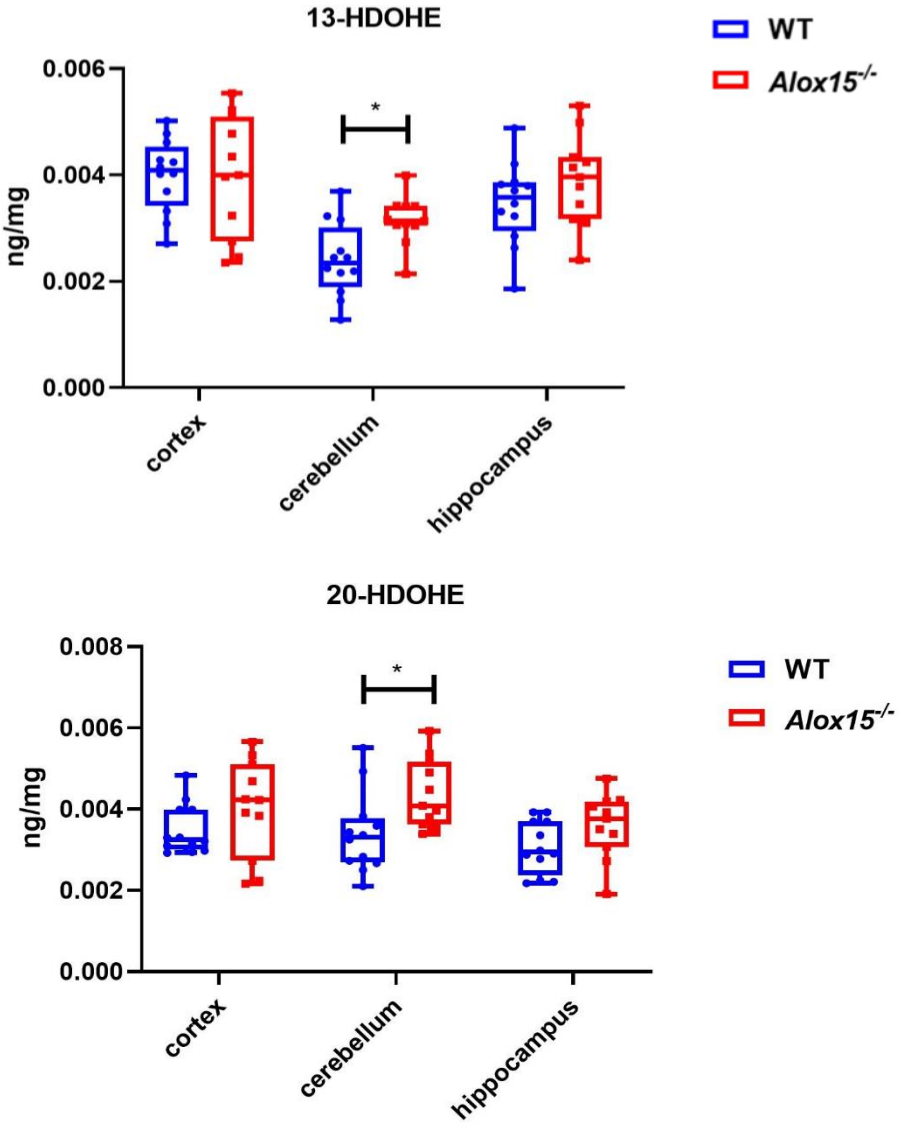

Figure 68. 13-HDOHE and 20-HDOHE are significantly elevated in the cerebellum of *Alox15*$^{-/-}$ mice. Lipids were extracted from three brain regions as described in Materials and Methods. Data in each brain region were analysed using Mann-Whitney non-parametric U test and shown on Tukey box plots with mean ± S.E.M. WT (n=12) and *Alox15*$^{-/-}$ (n=11) *, **, *** and **** represent p≤0.05, p≤0.01, p≤0.001 and p≤0.0001 for genotype comparisons, respectively.

6.9 *Alox15*$^{-/-}$ brain contained similar levels of LA metabolites.

9-HODE is formed via the non-enzymatic oxidation of LA by 5-LOX (Vangaveti *et al.*, 2010). 13-HODE is derived from LA through the activity of 12/15-LOX, which is involved in chemotaxtic activity (Szczuko *et al.*, 2020). First, the enzyme generates 13-HPODE, which is then reduced to 13-HODE by GPx (Zivkovic *et al.*, 2012). Here, 9-HODE and 13- HODE levels did not differ between *Alox15*$^{-/-}$ and WT mice in the three brain regions (Figure 69).

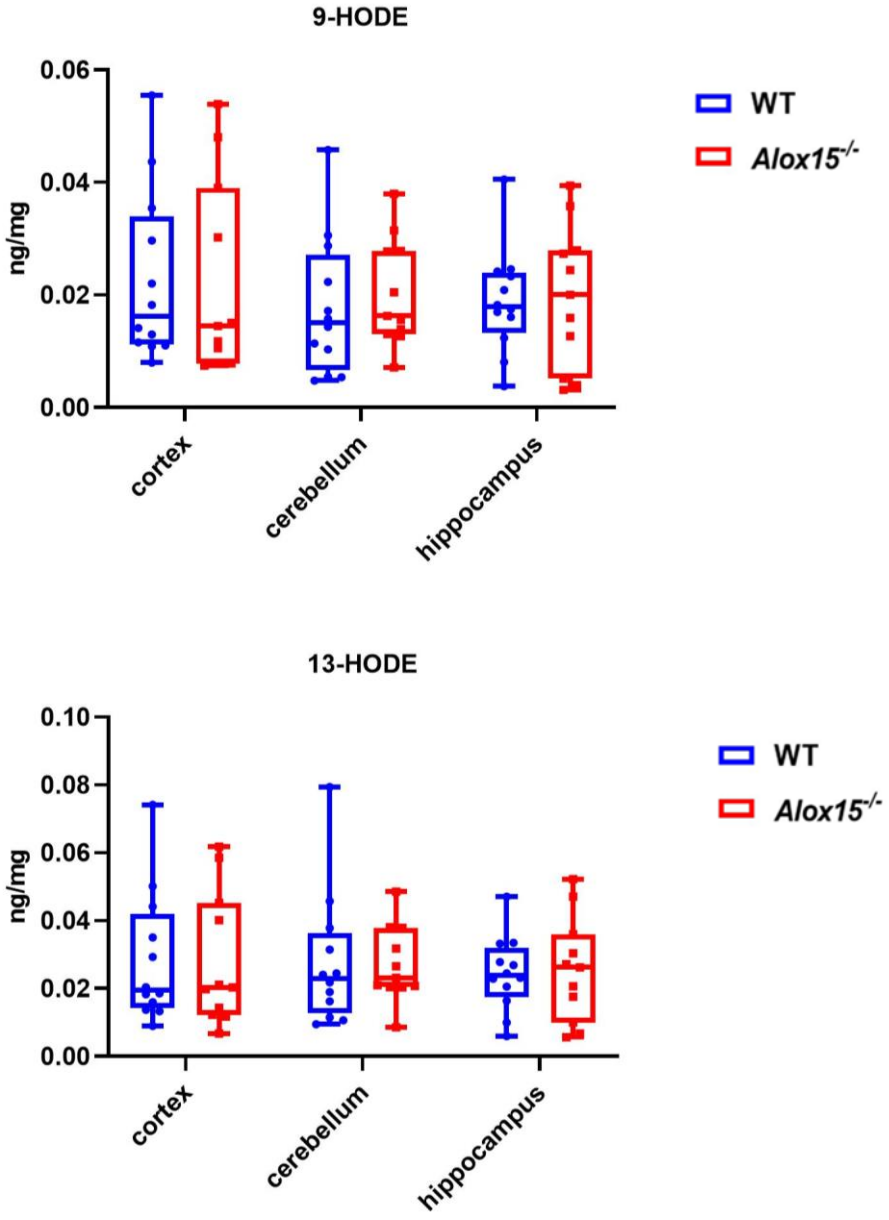

Figure 69. 9-HODE and 13-HODE remain unchanged in *Alox15*$^{-/-}$ mice. Lipids were extracted from three brain regions as described in Materials and Methods. Data in each brain region were analysed using Mann- Whitney non-parametric U test and shown on Tukey box plots with mean ± S.E.M. WT (n=12) and *Alox15*$^{-/-}$ (n=11).

6.10 *Alox15*$^{-/-}$ cerebellum contained significantly increased levels of prostaglandins

AA is metabolized to form oxylipins via the COX pathway, generating PGG_2 and subsequently PGH_2 (Smith, *et al.*, 2011). Additional products made from PGH_2 metabolism include $PGF_{2\alpha}$, thromboxane A_2 (TXA_2), thromboxane B_2 (TXB_2), PGE_2, PGD_2, and prostacyclin (PGI_2) (Zivkovic, *et al.*, 2012). The analysis in each brain region was performed by Mann- Whitney non-parametric U test.

Several prostaglandins, including PGE_1, PGE_2, PGD_2 and 13,14-dihydro-15-keto-PGD_2, were significantly increased in *Alox15*$^{-/-}$ cerebellum compared to WT (P=0.0218, P=0.0351, P=0.0479, P=0.0470, respectively) (Figure 71). With regard to TXB_2, which is the stable metabolite of TXA_2, no differences were detected in the levels in the three brain regions between *Alox15*$^{-/-}$ mice and WT (Figure 70). Conversely, $PGF_{2\alpha}$ levels were not altered between the two strains (Figure 72).

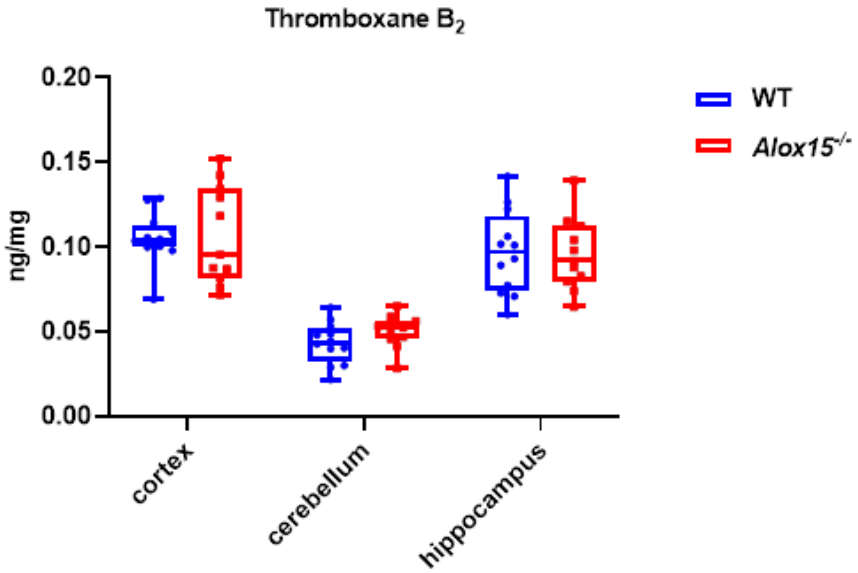

Figure 70. TXB_2 remain unchanged in *Alox15*$^{-/-}$ mice. Lipids were extracted from three brain regions as described in Materials and Methods. Data in each brain region were analysed using Mann- Whitney non-parametric U test and shown on Tukey box plots with mean ± S.E.M. WT (n=12) and *Alox15*$^{-/-}$ (n=11).

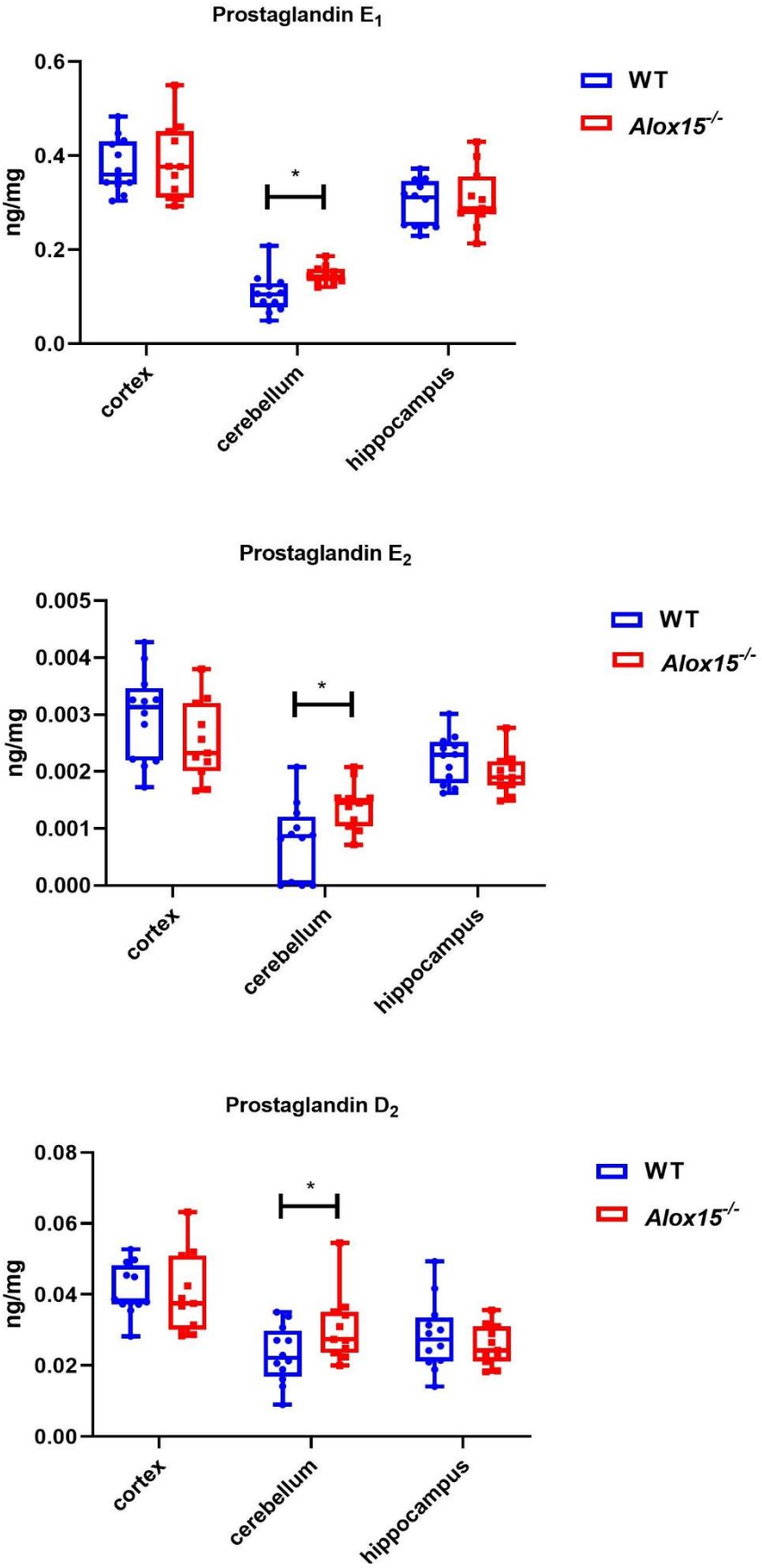

Figure 71. PGE_1, PGE_2, and PGD_2 are significantly elevated in the cerebellum in *Alox15*$^{-/-}$ mice. Lipids were extracted from three brain regions as described in Materials and Methods. Data in each brain region were analysed using Mann- Whitney non-parametric U test and shown on Tukey box plots with mean ± S.E.M. WT (n=12) and *Alox15*$^{-/-}$ (n=11) *, **, *** and **** represent $p \leq 0.05$, $p \leq 0.01$, $p \leq 0.001$ and $p \leq 0.0001$ for genotype comparisons, respectively.

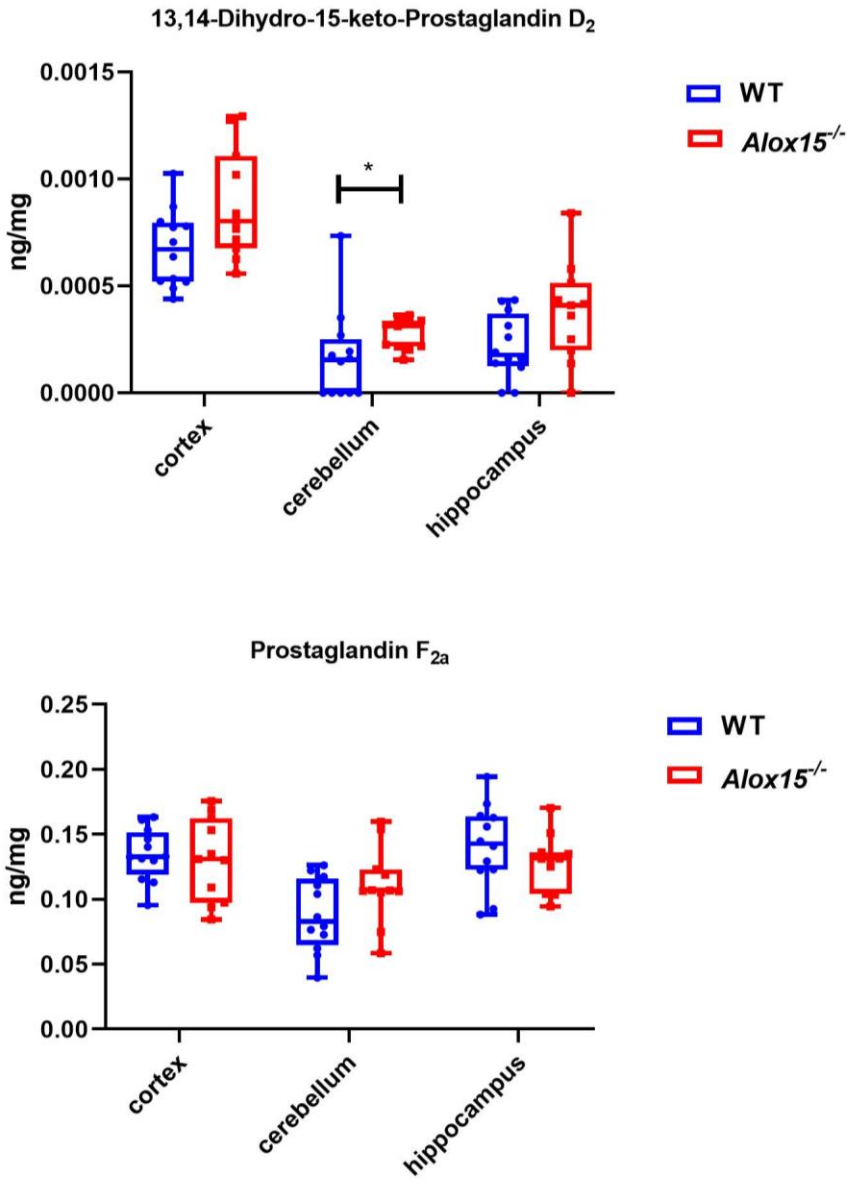

Figure 72. 13,14-Dihydro-15-keto-PGD$_2$ is significantly increased in the cerebellum in *Alox15*$^{-/-}$ mice. Lipids were extracted from three brain regions as described in Materials and Methods. Data in each brain region were analysed using Mann- Whitney non-parametric U test and shown on Tukey box plots with mean ± S.E.M. WT (n=12) and *Alox15*$^{-/-}$ (n=11) *, **, *** and **** represent p≤0.05, p≤0.01, p≤0.001 and p≤0.0001 for genotype comparisons, respectively.

6.11 *Alox15*$^{-/-}$ brain showed no changes in the levels of CYP-derived oxylipins

Epoxides synthesized from AA by CYP enzymes, including 5(6)-EET and 11(12)-EET, were unchanged in brain regions of *Alox15*$^{-/-}$ mice compared to WT (Figure 73). Moreover, a simple comparison on their further metabolite 11,12-DiHETrE, showed significantly lower amounts in *Alox15*$^{-/-}$ cerebellum than in WT (*P=0.0289). In contrast, no changes were detected in 5,6 DiHETrE between genotypes in the three brain regions. 14,15- DiHETrE levels were similar between the two strains (Figure 74).

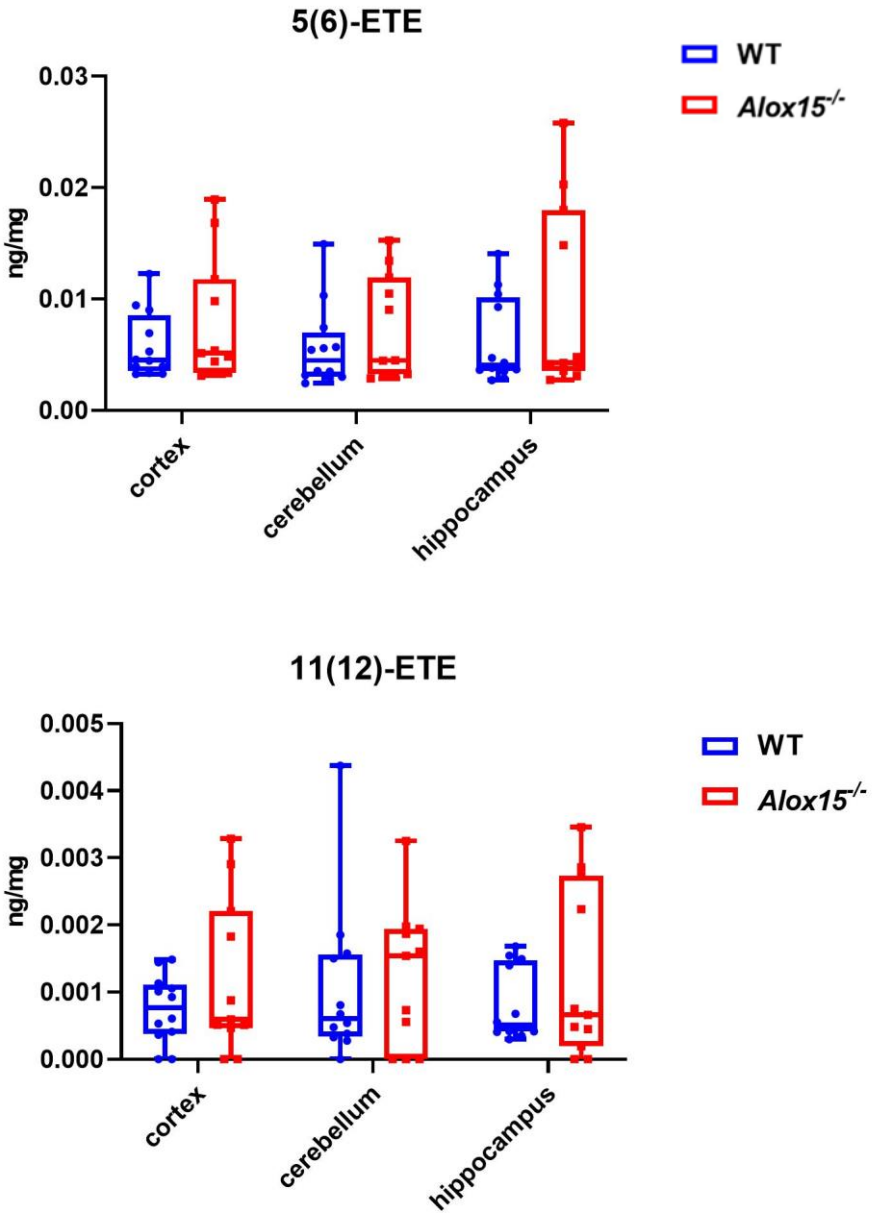

Figure 73. EETs remain unchanged in *Alox15*$^{-/-}$ mice. Lipids were extracted from three brain regions as described in Materials and Methods. Data in each brain region were analysed using Mann- Whitney non-parametric U test and shown on Tukey box plots with mean ± S.E.M. WT (n=12) and *Alox15*$^{-/-}$ (n=11).

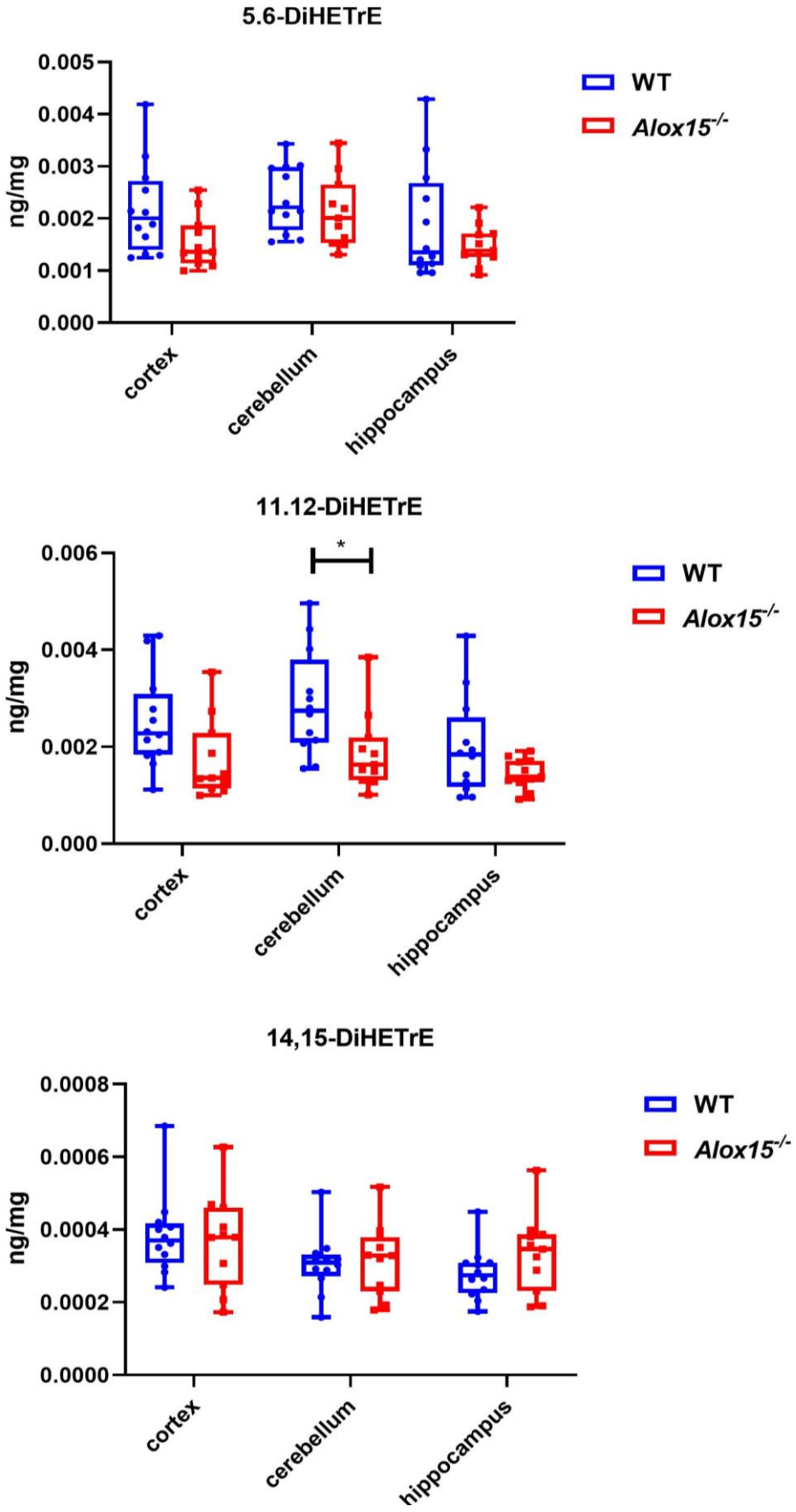

Figure 74. 11,12-DiHETrE is significantly decreased in the cerebellum in *Alox15*$^{-/-}$ mice. Lipids were extracted from three brain regions as described in Materials and Methods. Data in each brain region were analysed using Mann-Whitney non-parametric U test and shown on Tukey box plots with mean ± S.E.M. WT (n=12) and *Alox15*$^{-/-}$ (n=11) *, **, *** and **** represent $p \leq 0.05$, $p \leq 0.01$, $p \leq 0.001$ and $p \leq 0.0001$ for genotype comparisons, respectively.

6.12 *Alox15*$^{-/-}$ cerebellum displayed markedly decreased levels of 12,13-DiHOME.

The levels of LA-derived epoxides formed by CYP enzymes are shown in Figure 75. Data in each brain region were analysed by Mann- Whitney non-parametric U test and revealed that 12,13-DiHOME was significantly lower in *Alox15*$^{-/-}$ cerebellum compared to WT mice (P=0.0248). However, the levels of 12,13-DiHOME in the cortex and HPC were similar between genotypes. 9,10-DiHOME was decreased in *Alox15*$^{-/-}$ cerebellum, but this did not reach statistical significance.

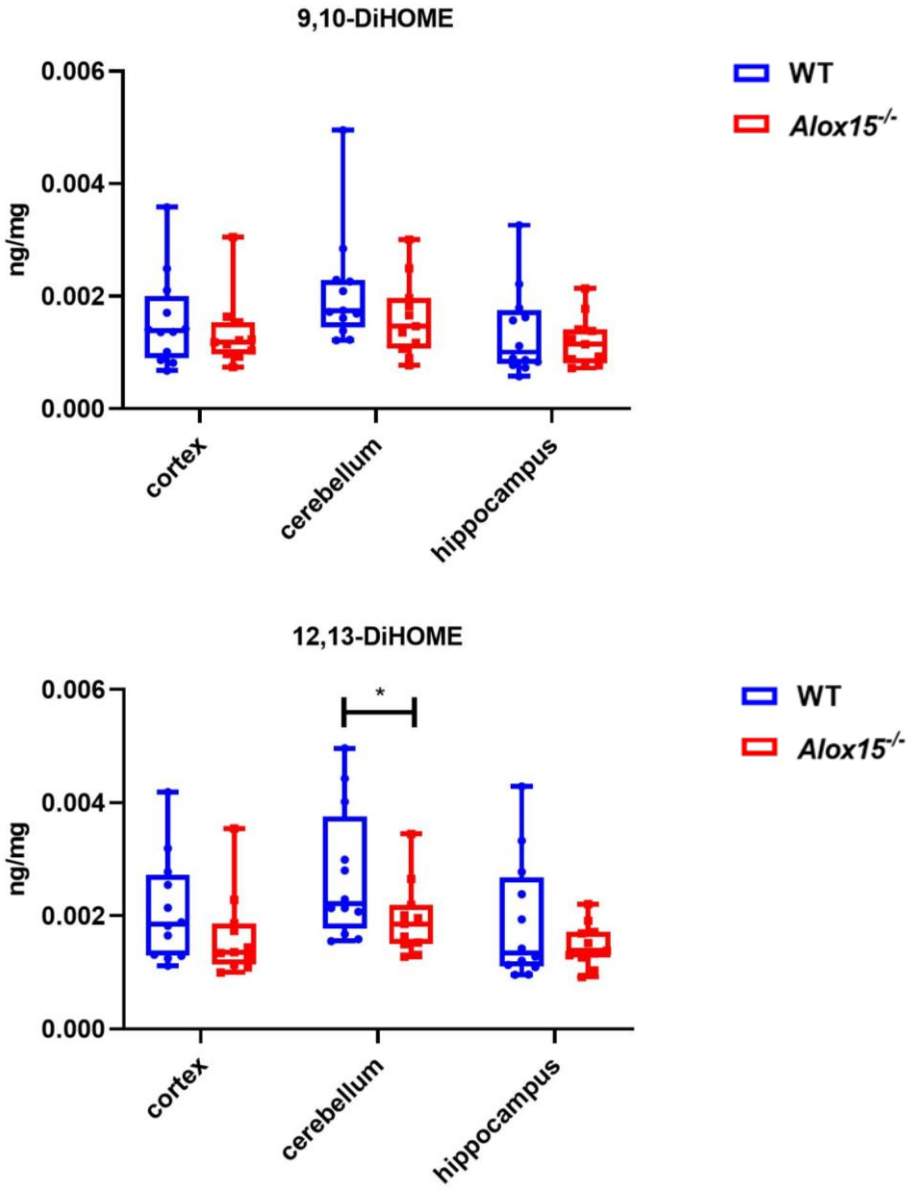

Figure 75. 12,13-DiHOME is significantly reduced in the cerebellum in *Alox15*$^{-/-}$ mice. Lipids were extracted from three brain regions as described in Materials and Methods. Data in each brain region were analysed using Mann- Whitney non-parametric U test and shown on Tukey box plots with mean ± S.E.M. WT (n=12) and *Alox15*$^{-/-}$ (n=11) *, **, *** and **** represent p≤0.05, p≤0.01, p≤0.001 and p≤0.0001 for genotype comparisons, respectively.

6.13 Representative Chromatograms for oxylipins analysis

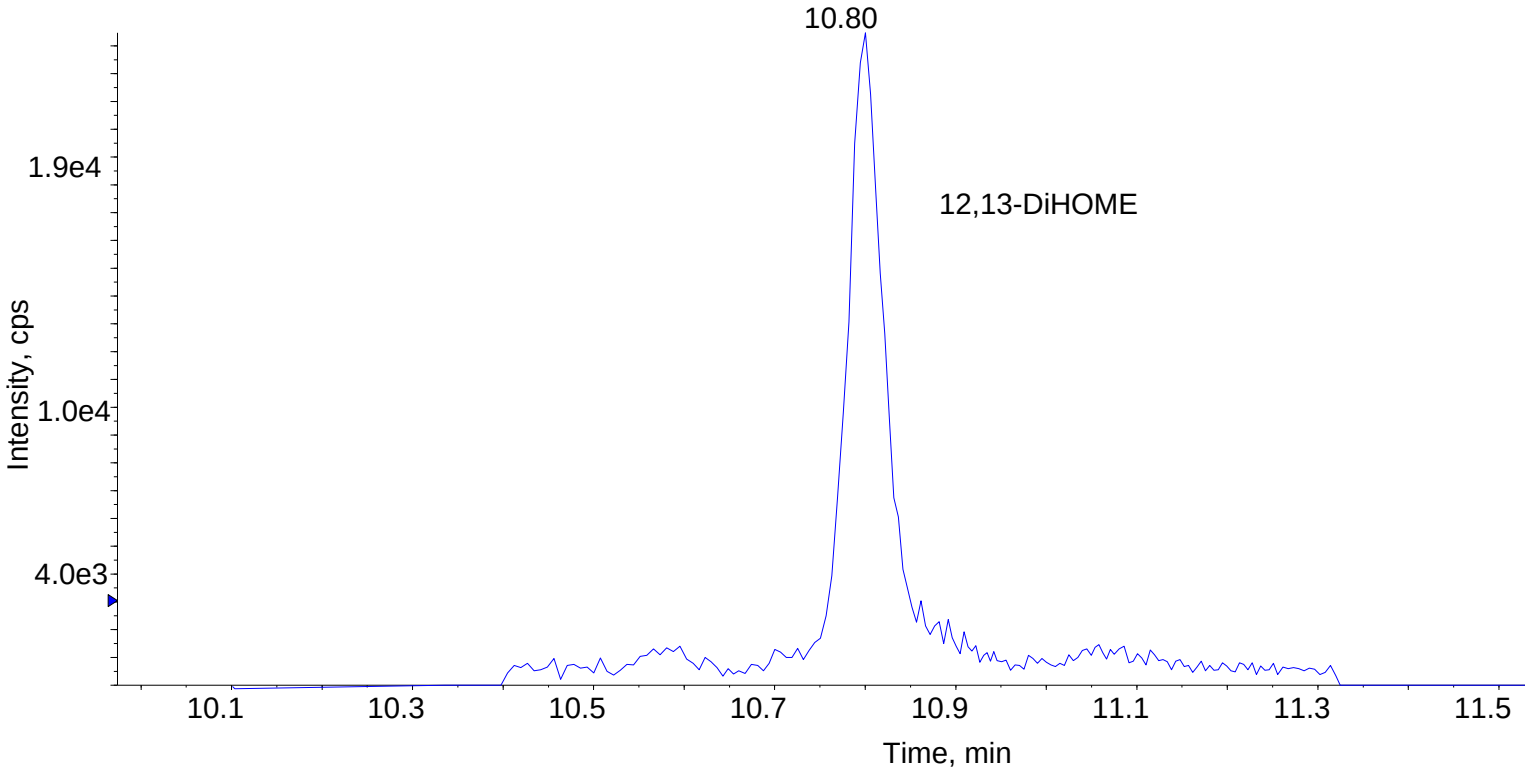

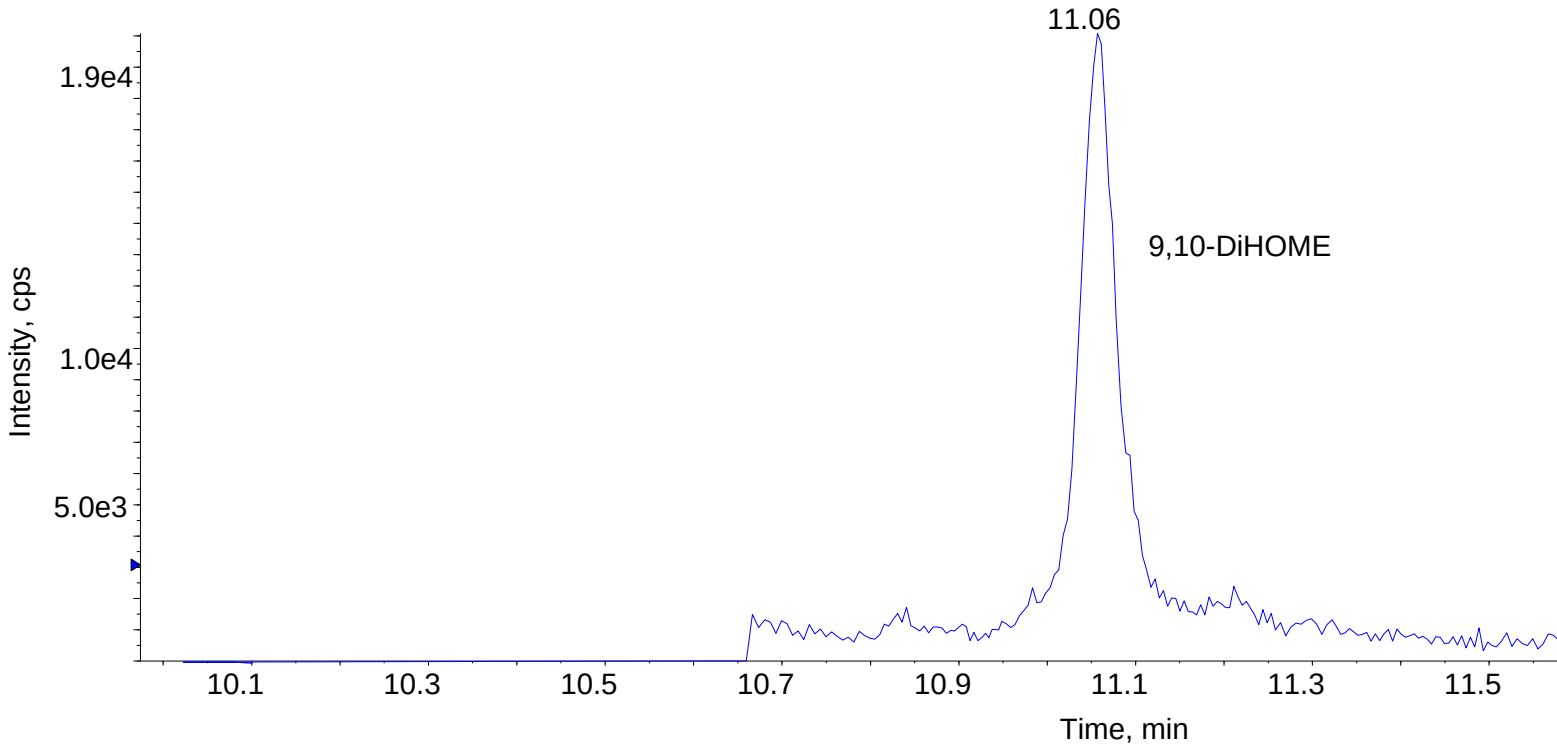

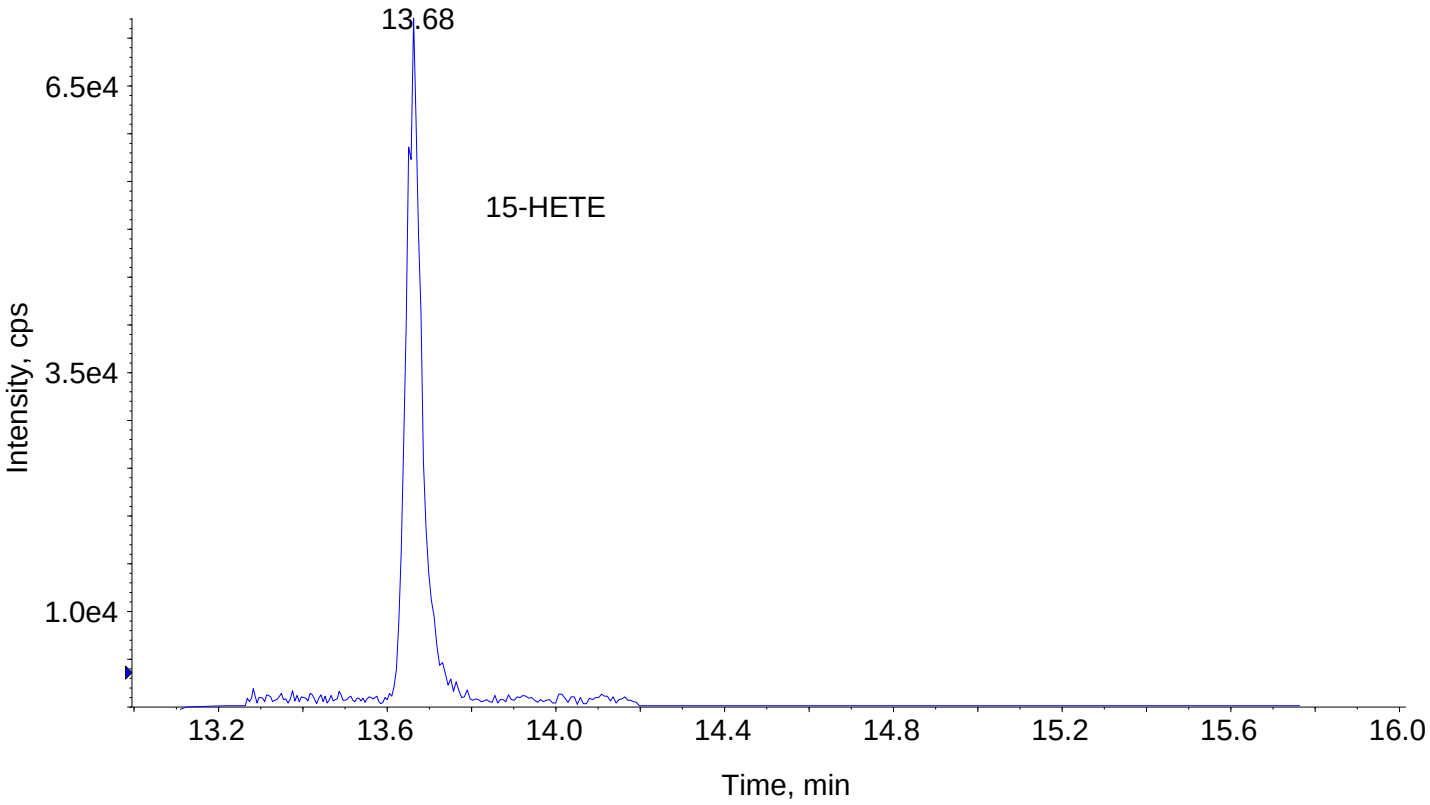
13.68
6.5e4
15-HETE
3.5e4
1.0e4
Intensity, cps
13.2
13.6
14.0
14.4
14.8
15.2
15.6
16.0
Time, min

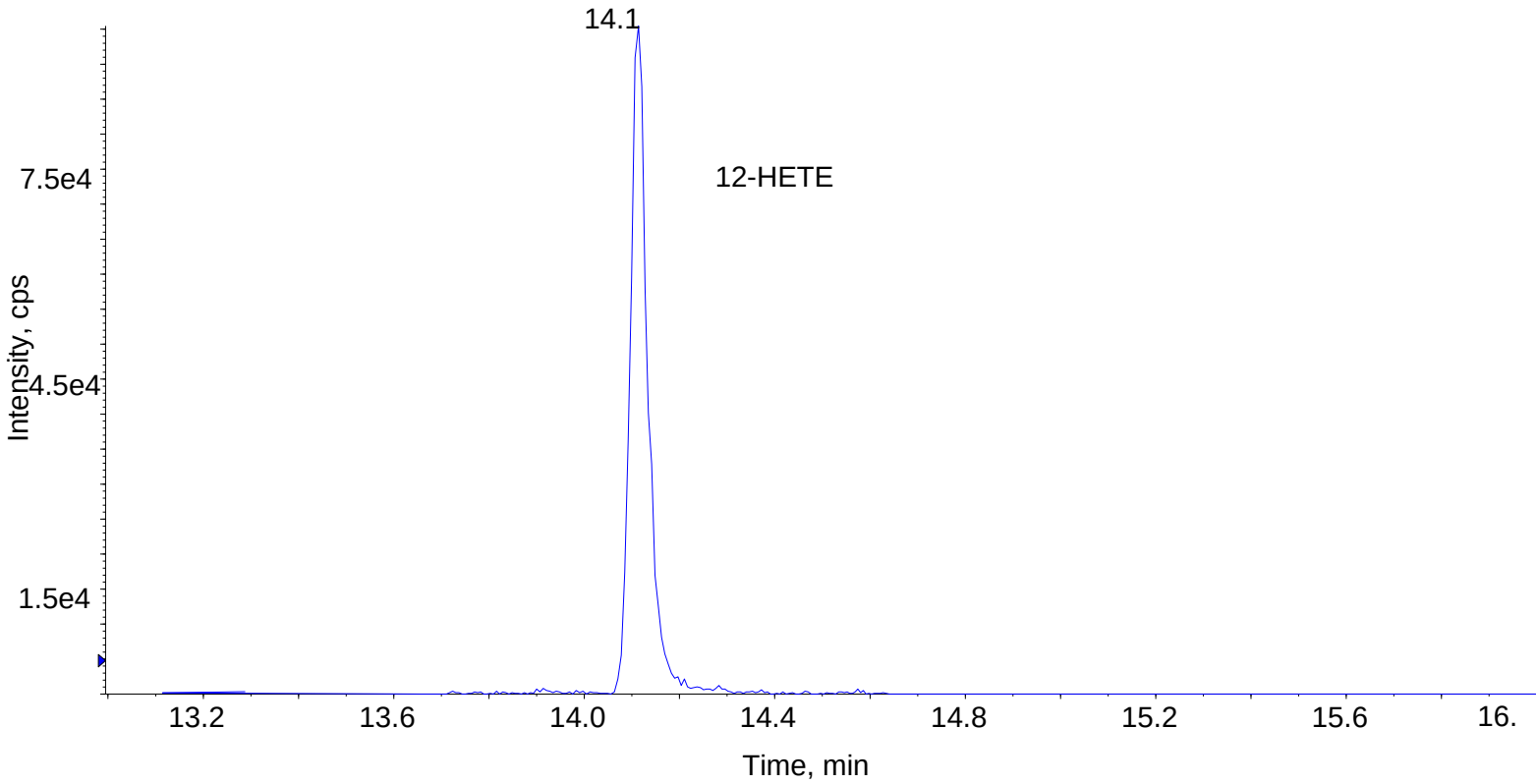
14.1
7.5e4
12-HETE
4.5e4
1.5e4
Intensity, cps
13.2
13.6
14.0
14.4
14.8
15.2
15.6
16.
Time, min

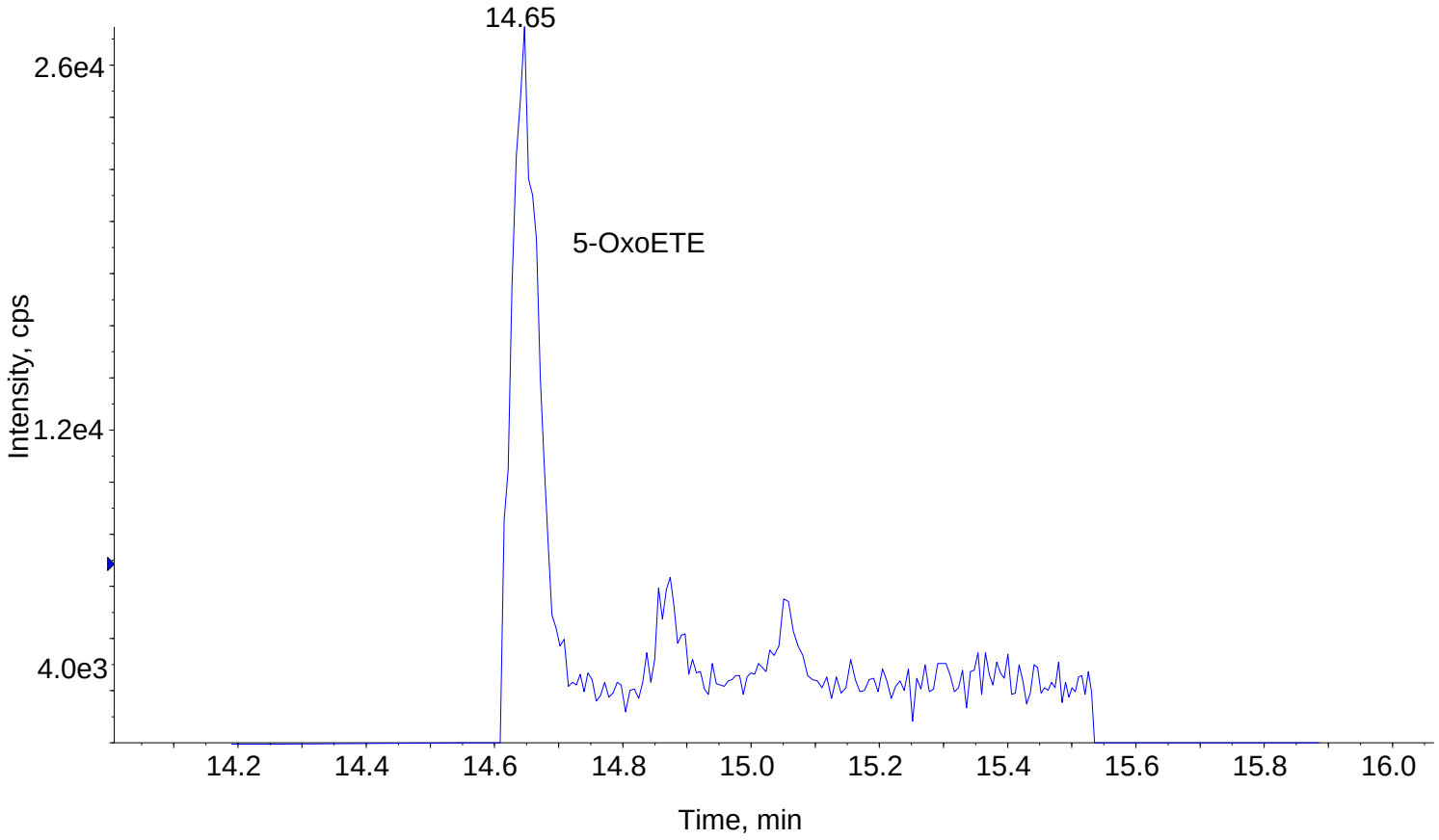
14.65
2.6e4
1.2e4
4.0e3
5-OxoETE
Intensity, cps
14.2
14.4
14.6
14.8
15.0
15.2
15.4
15.6
15.8
16.0
Time, min

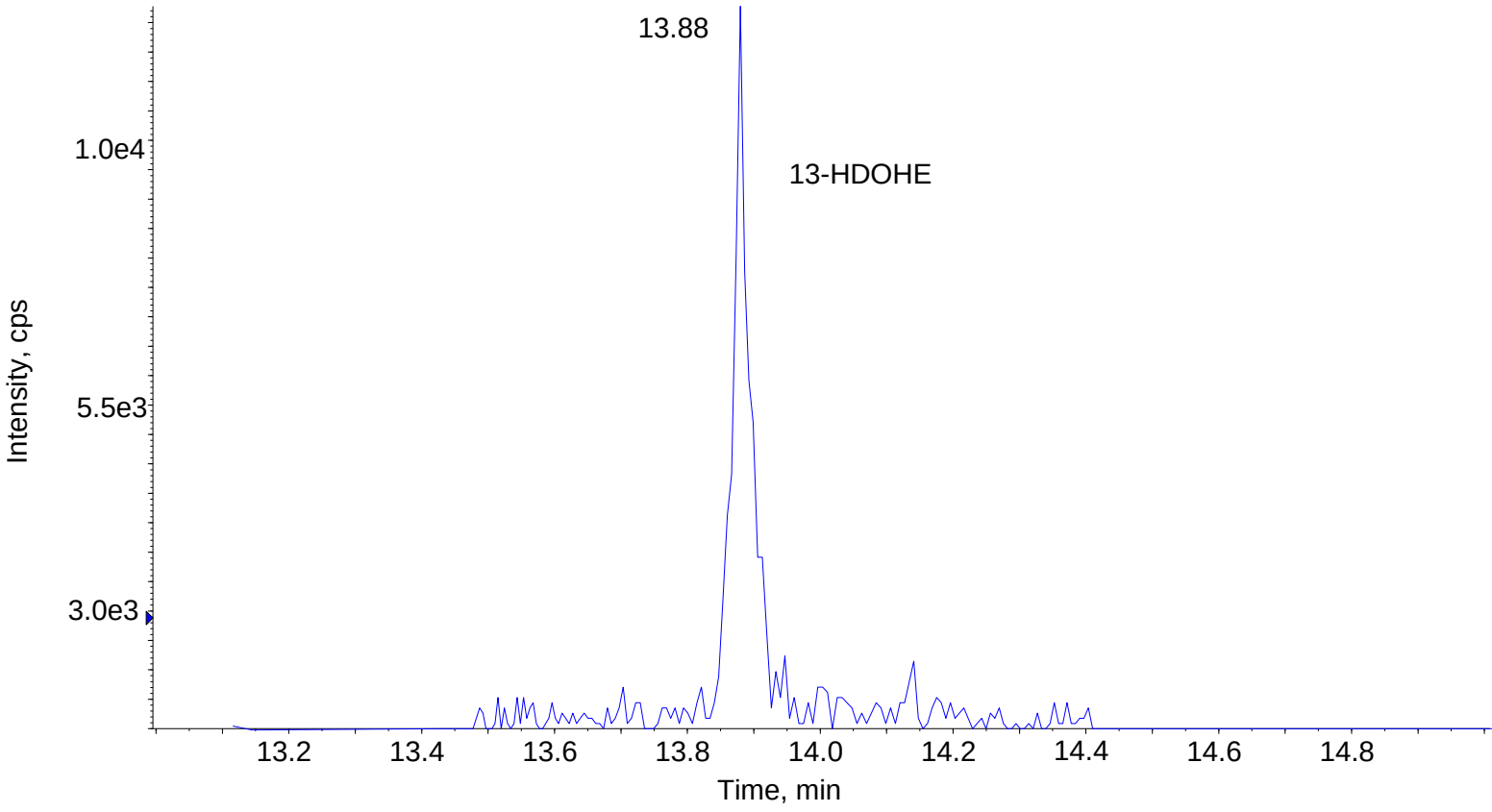
13.88
1.0e4
5.5e3
3.0e3
13-HDOHE
Intensity, cps
13.2
13.4
13.6
13.8
14.0
14.2
14.4
14.6
14.8
Time, min

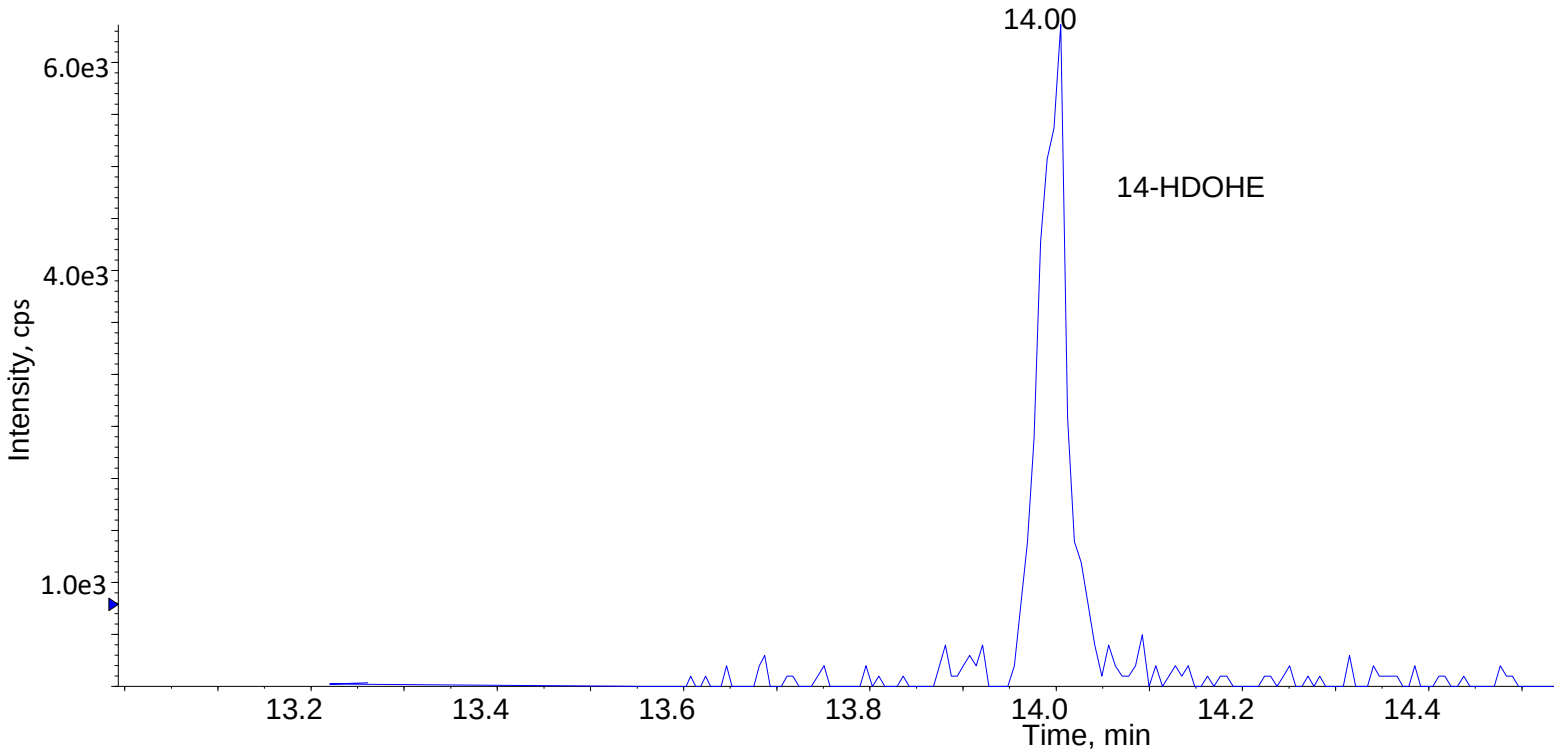
14.00
14-HDOHE
6.0e3
4.0e3
1.0e3
Intensity, cps
13.2
13.4
13.6
13.8
14.0
14.2
14.4
Time, min

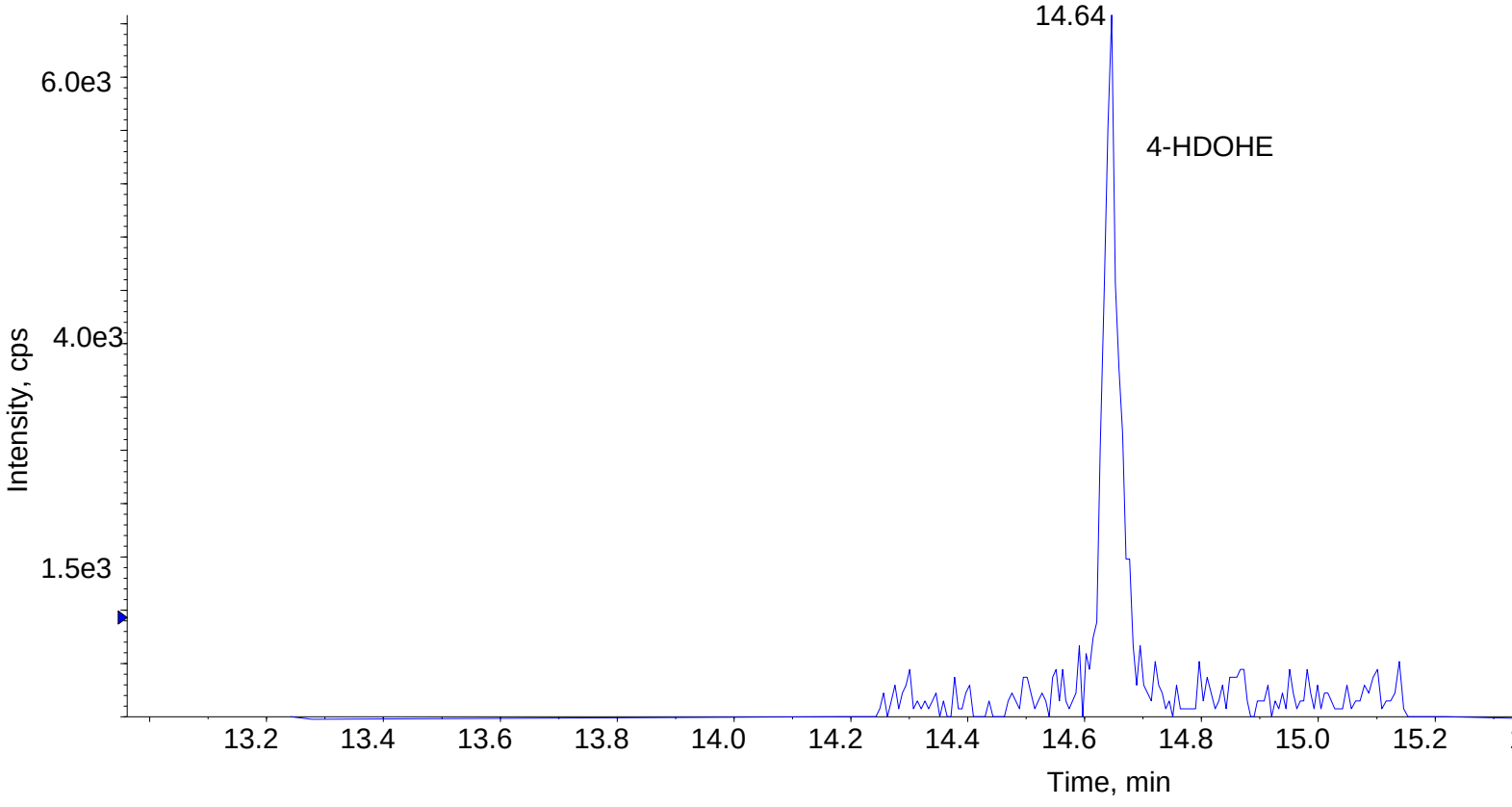
14.64
4-HDOHE
6.0e3
4.0e3
1.5e3
Intensity, cps
13.2
13.4
13.6
13.8
14.0
14.2
14.4
14.6
14.8
15.0
15.2
Time, min

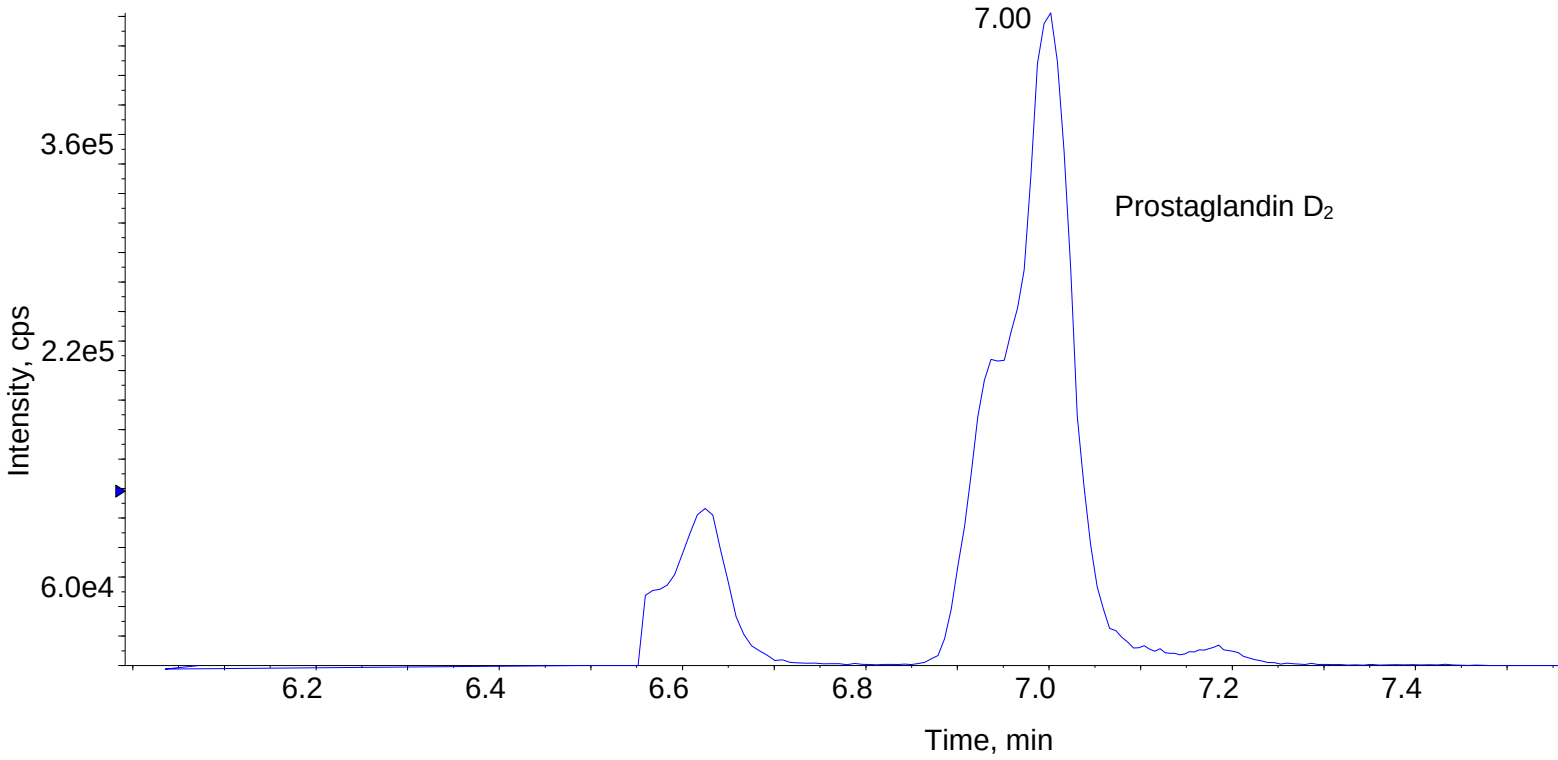
7.00
Prostaglandin D2
3.6e5
2.2e5
6.0e4
Intensity, cps
6.2
6.4
6.6
6.8
7.0
7.2
7.4
Time, min

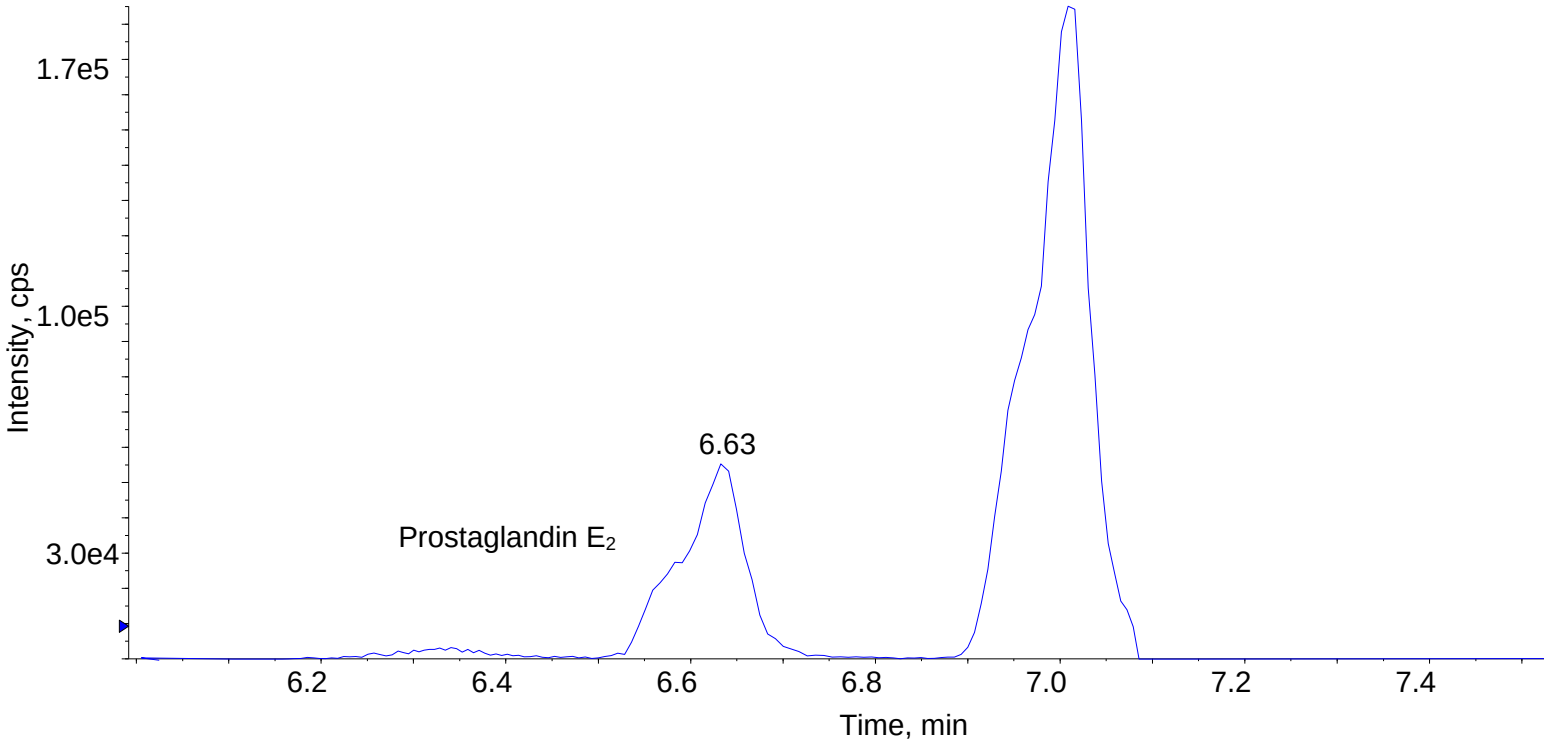
1.7e5
1.0e5
3.0e4
Intensity, cps
6.63
Prostaglandin E2
6.2
6.4
6.6
6.8
7.0
7.2
7.4
Time, min

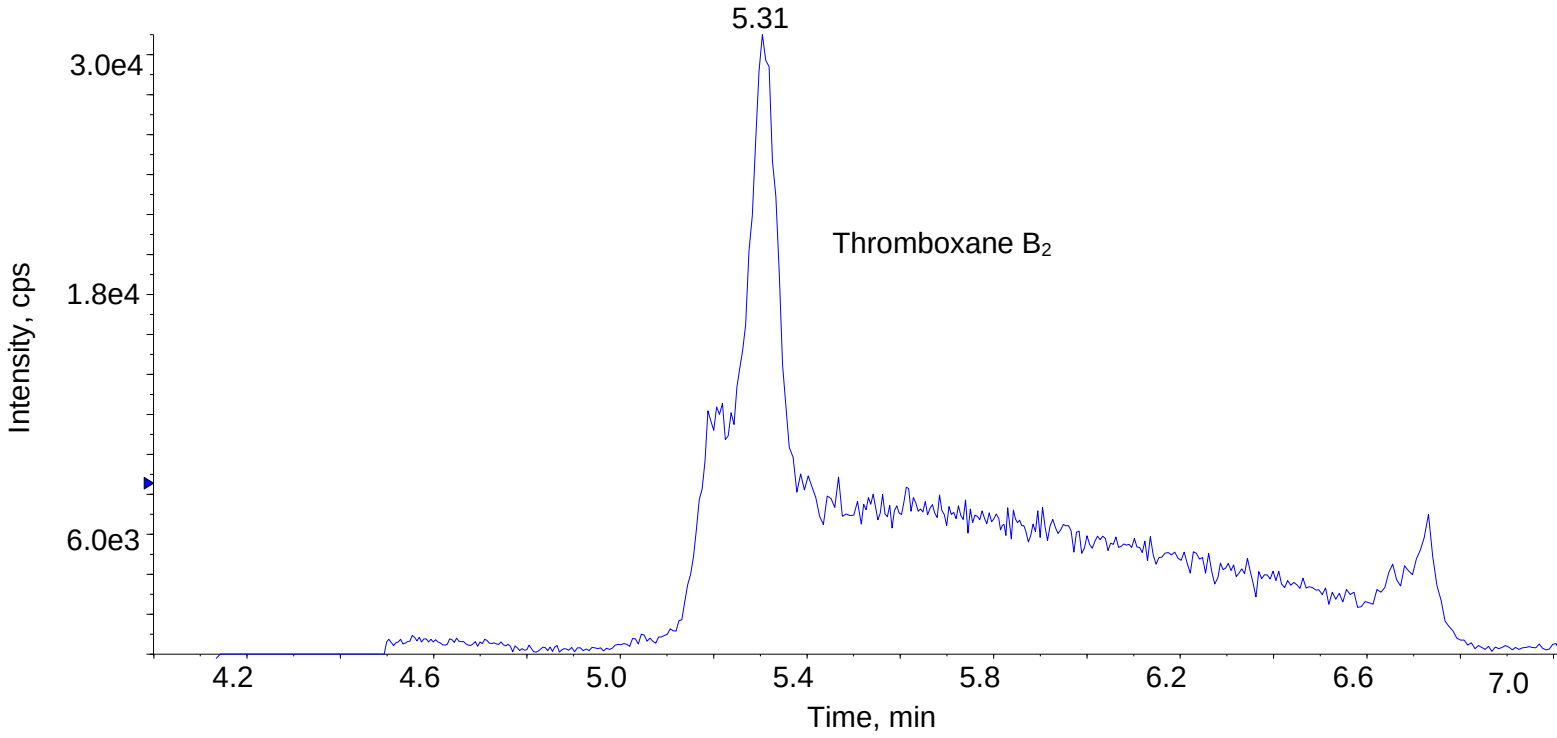
5.31
3.0e4
1.8e4
6.0e3
Intensity, cps
Thromboxane B2
4.2
4.6
5.0
5.4
5.8
6.2
6.6
7.0
Time, min

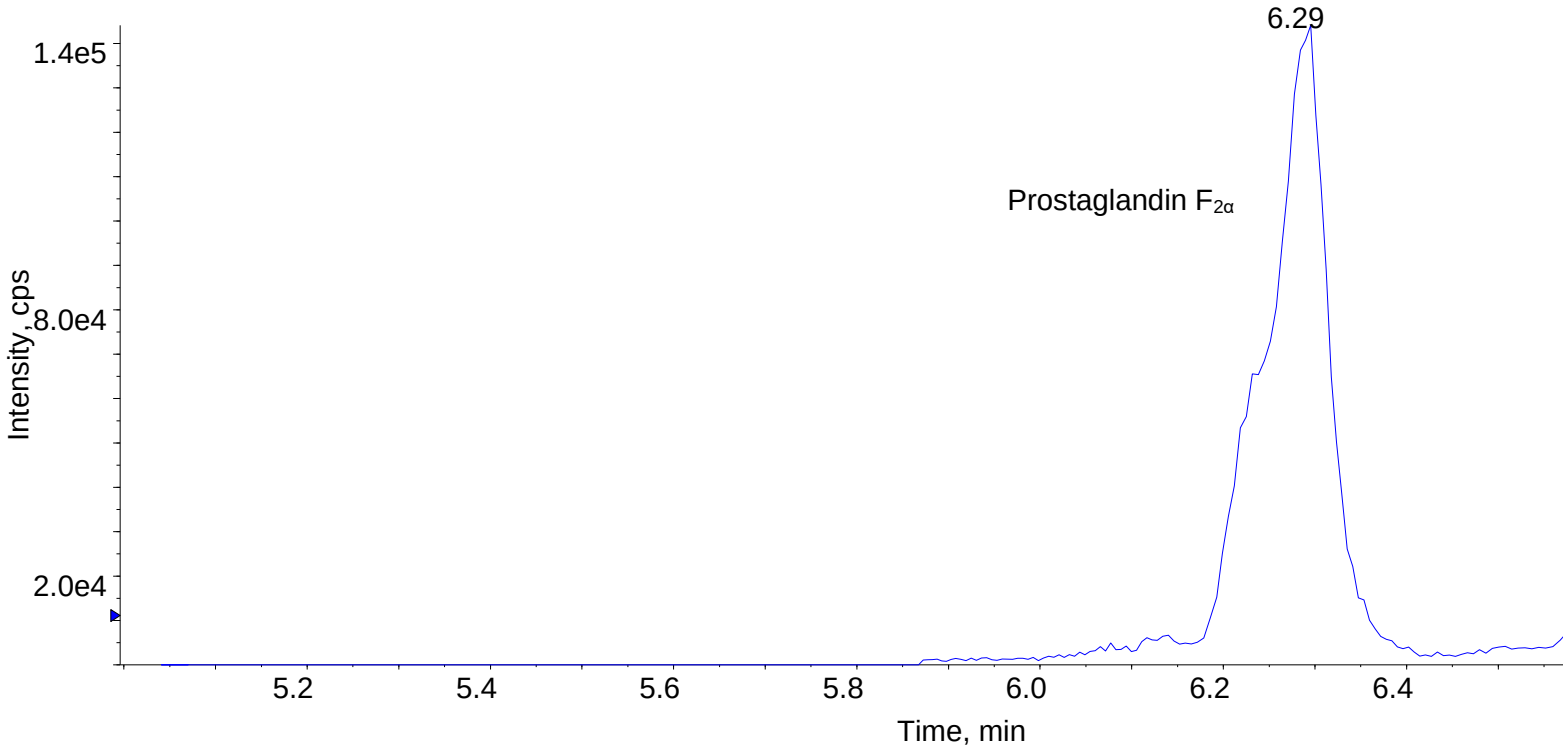
6.29
1.4e5
8.0e4
2.0e4
Intensity, cps
Prostaglandin F2α
5.2
5.4
5.6
5.8
6.0
6.2
6.4
Time, min

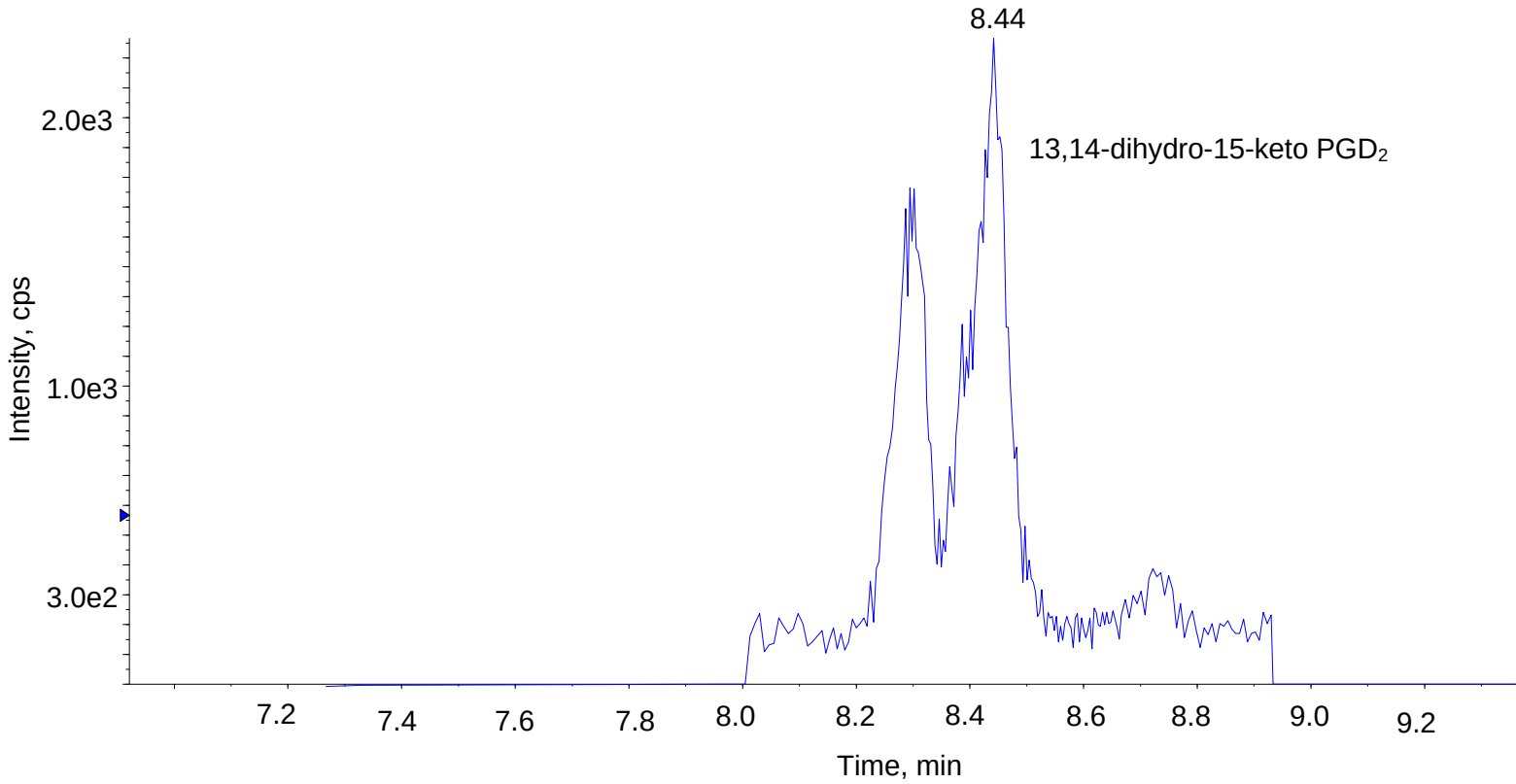
8.44
13,14-dihydro-15-keto PGD2
2.0e3
1.0e3
3.0e2
Intensity, cps
7.2
7.4
7.6
7.8
8.0
8.2
8.4
8.6
8.8
9.0
9.2
Time, min

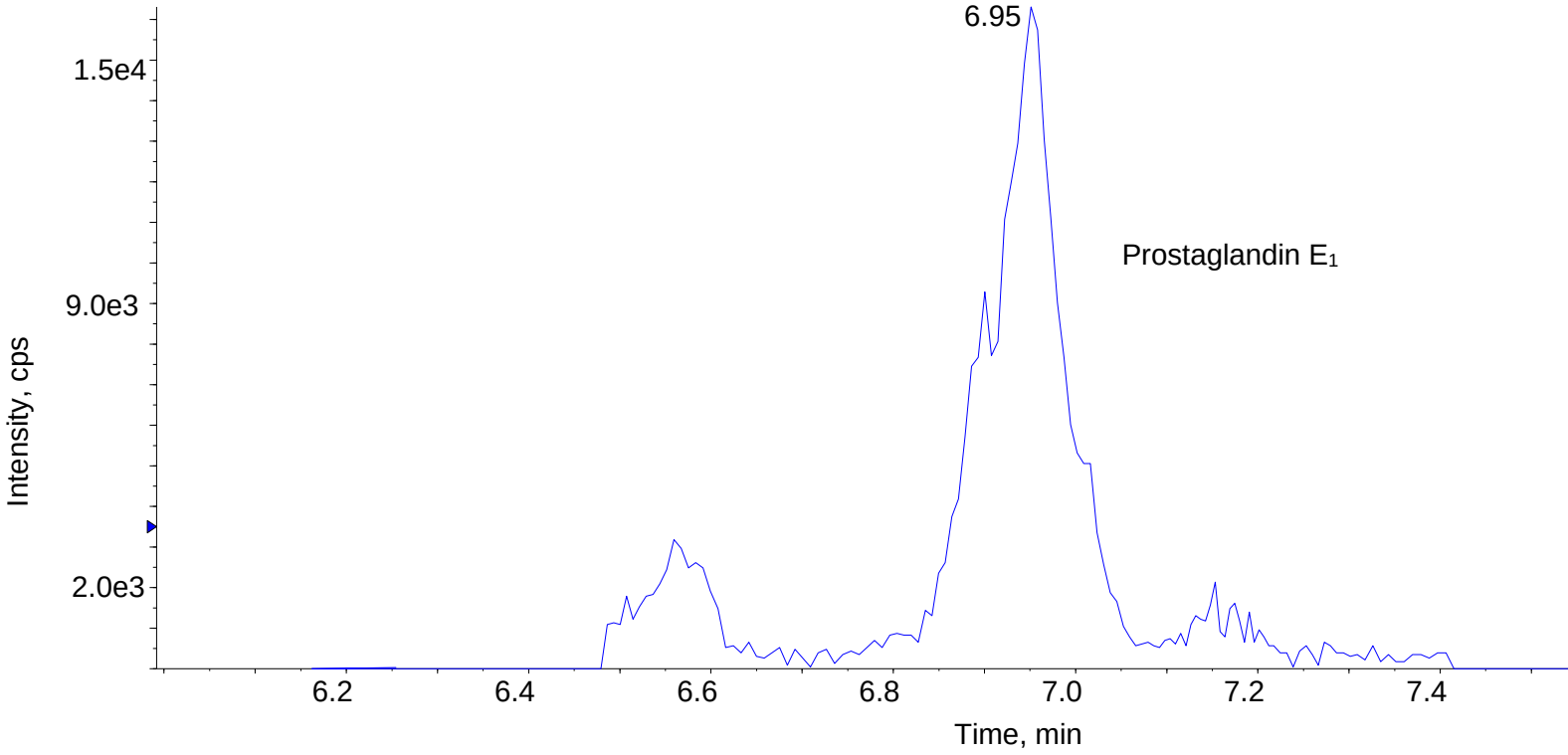
6.95
Prostaglandin E1
1.5e4
9.0e3
2.0e3
Intensity, cps
6.2
6.4
6.6
6.8
7.0
7.2
7.4
Time, min

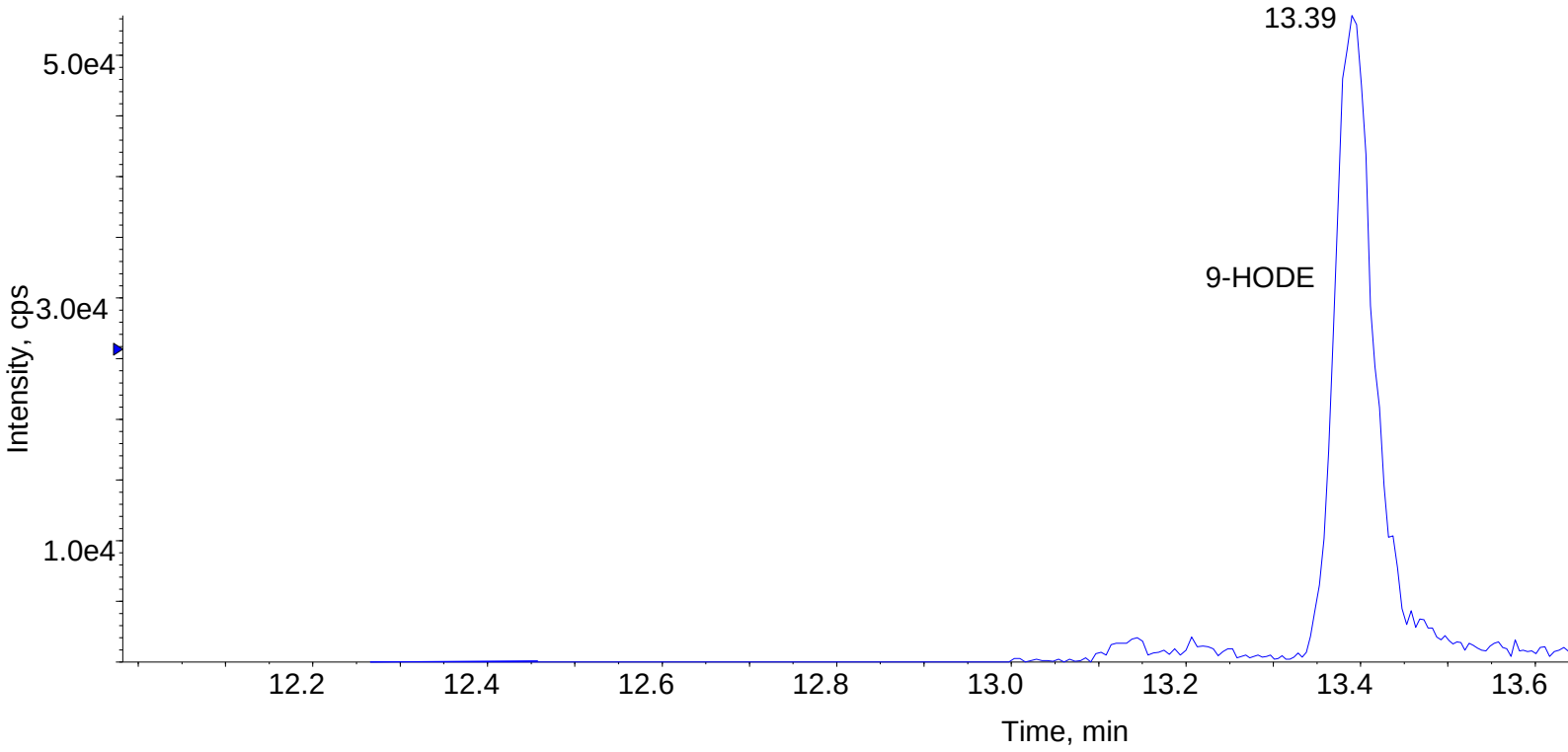
13.39
9-HODE
5.0e4
3.0e4
1.0e4
Intensity, cps
12.2
12.4
12.6
12.8
13.0
13.2
13.4
13.6
Time, min

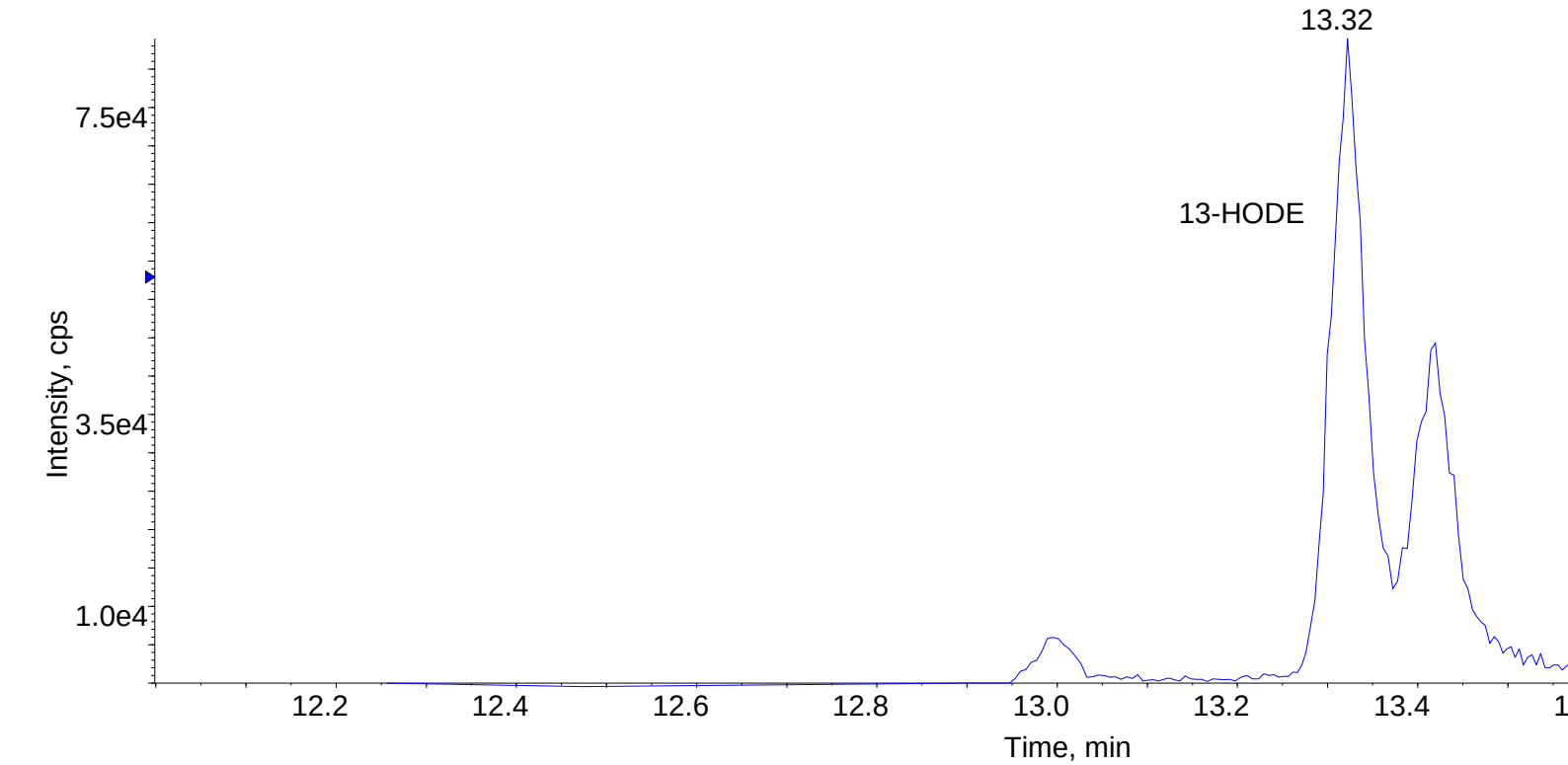
13.32
13-HODE
7.5e4
3.5e4
1.0e4
Intensity, cps
12.2
12.4
12.6
12.8
13.0
13.2
13.4
Time, min

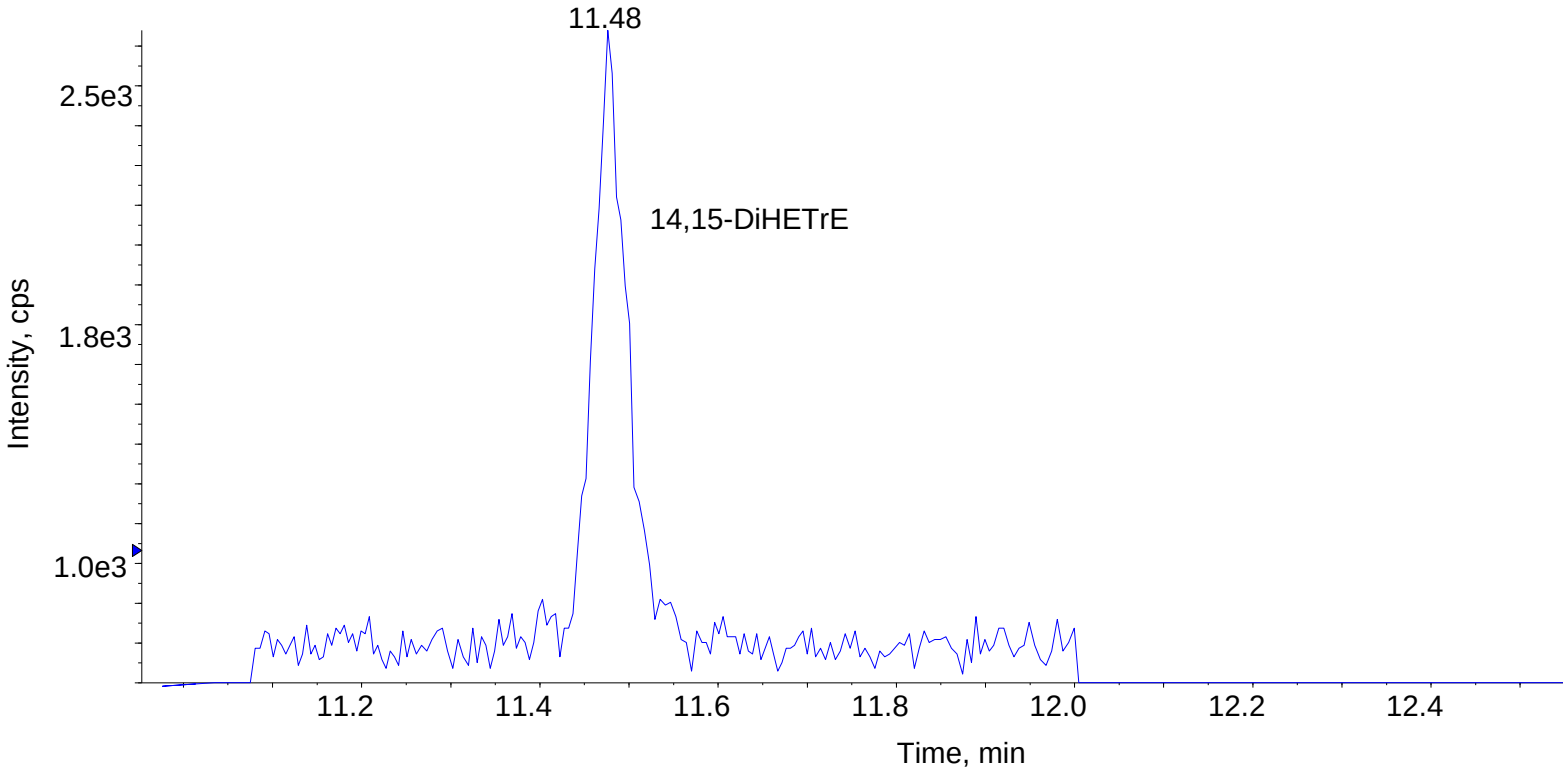
11.48
2.5e3
1.8e3
1.0e3
14,15-DiHETrE
Intensity, cps
11.2
11.4
11.6
11.8
12.0
12.2
12.4
Time, min

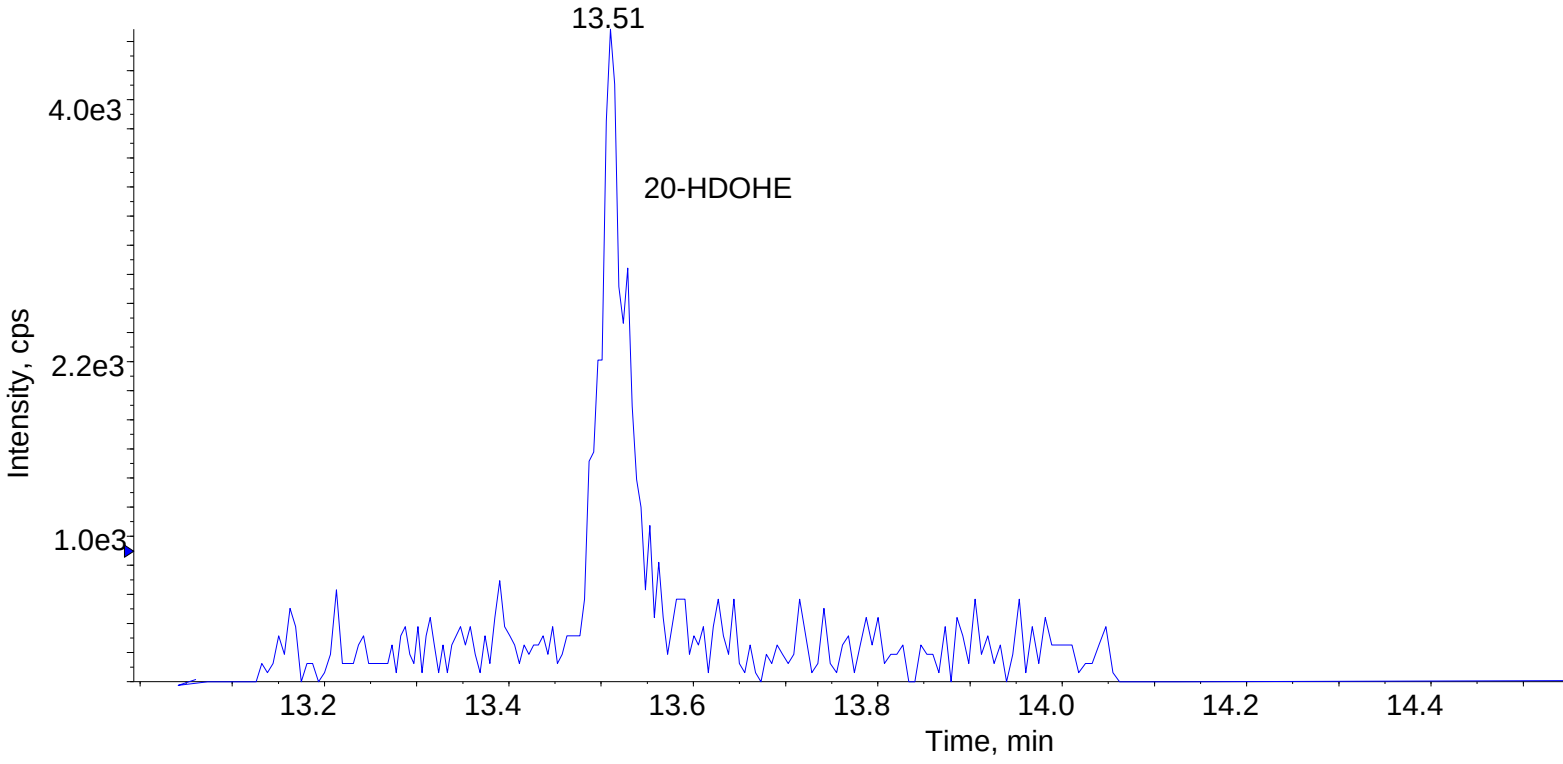
13.51
4.0e3
2.2e3
1.0e3
20-HDOHE
Intensity, cps
13.2
13.4
13.6
13.8
14.0
14.2
14.4
Time, min

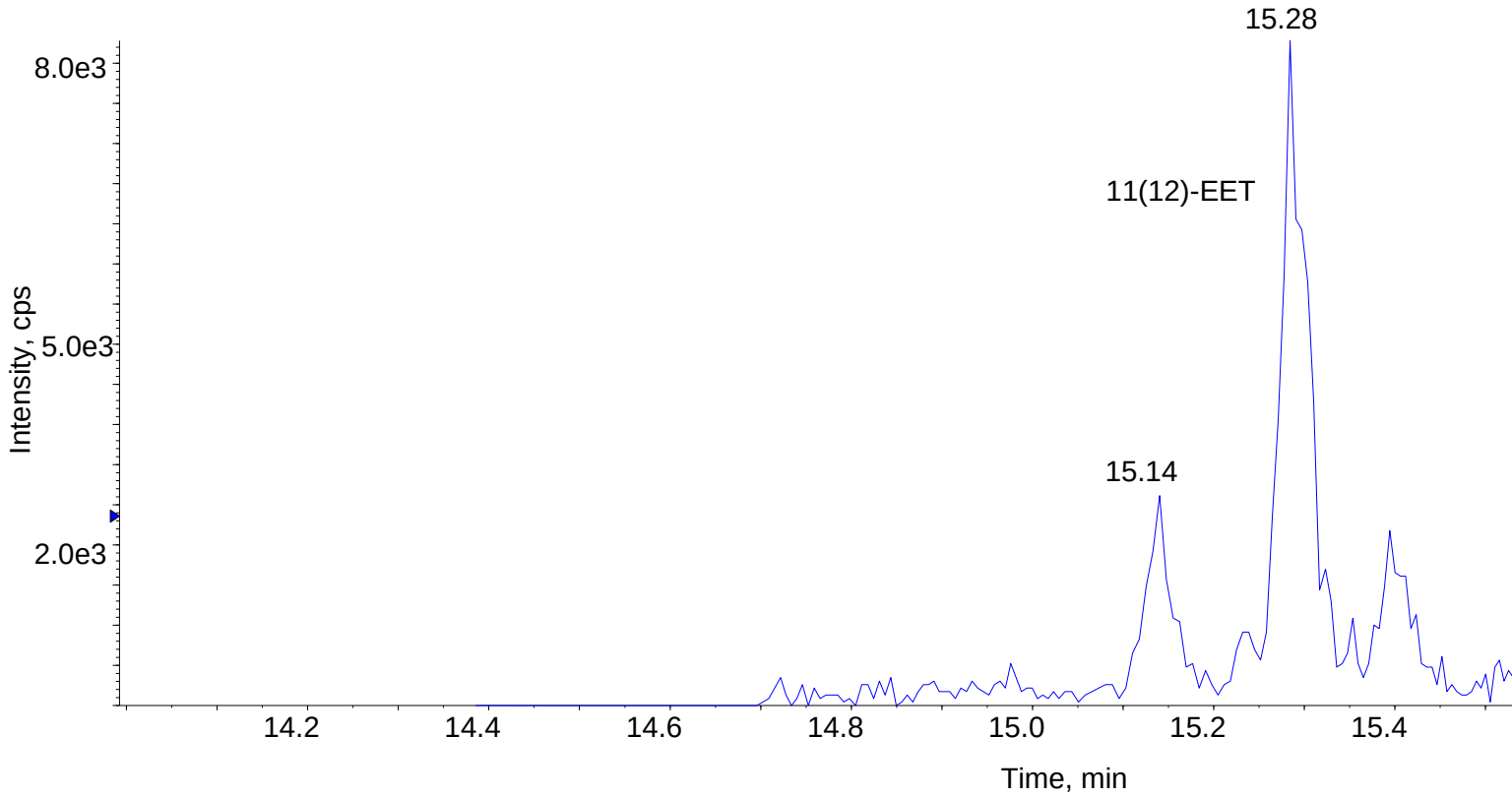
15.28
11(12)-EET
15.14
8.0e3
5.0e3
2.0e3
Intensity, cps
14.2
14.4
14.6
14.8
15.0
15.2
15.4
Time, min

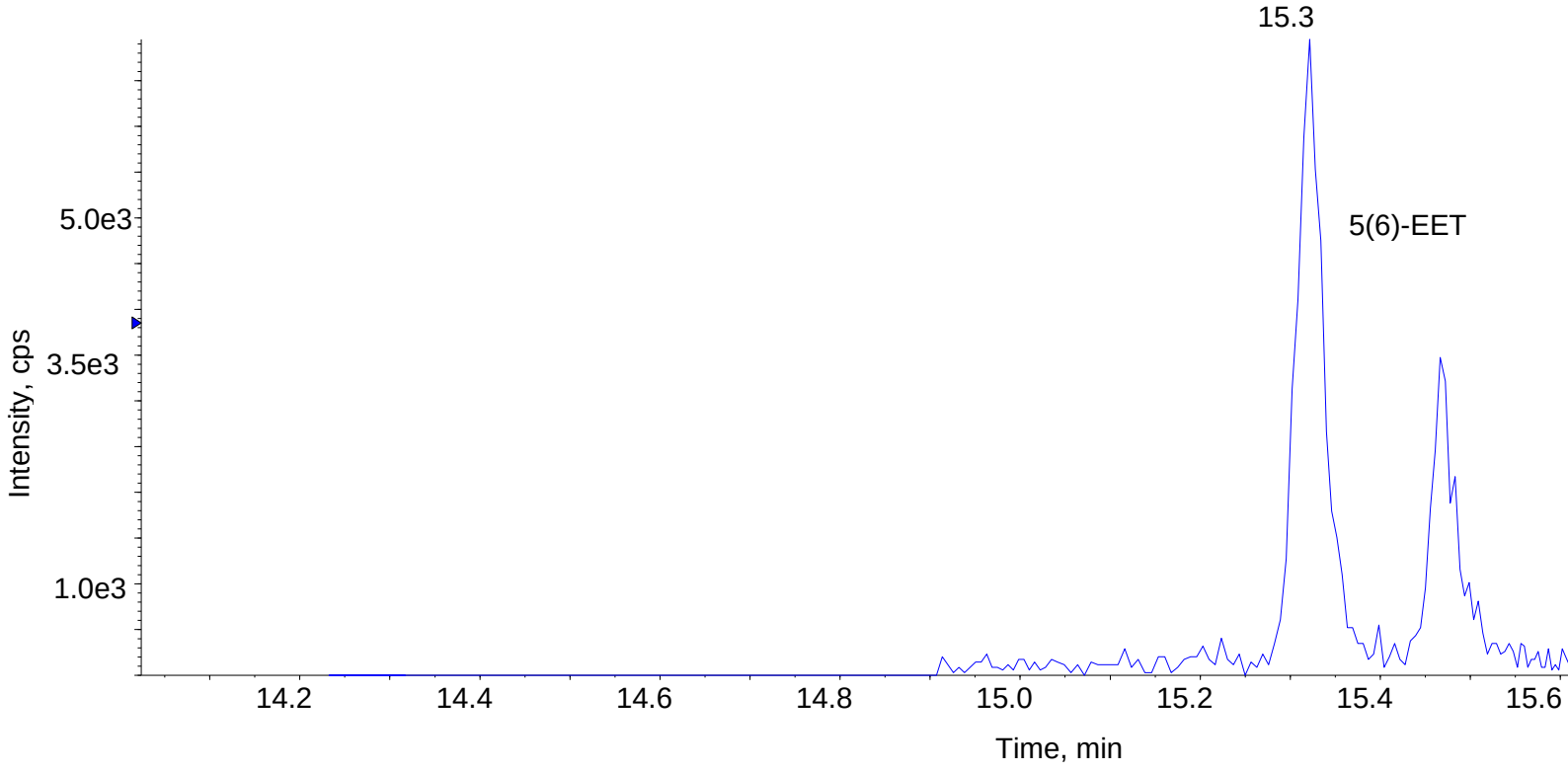
15.3
5(6)-EET
5.0e3
3.5e3
1.0e3
Intensity, cps
14.2
14.4
14.6
14.8
15.0
15.2
15.4
15.6
Time, min

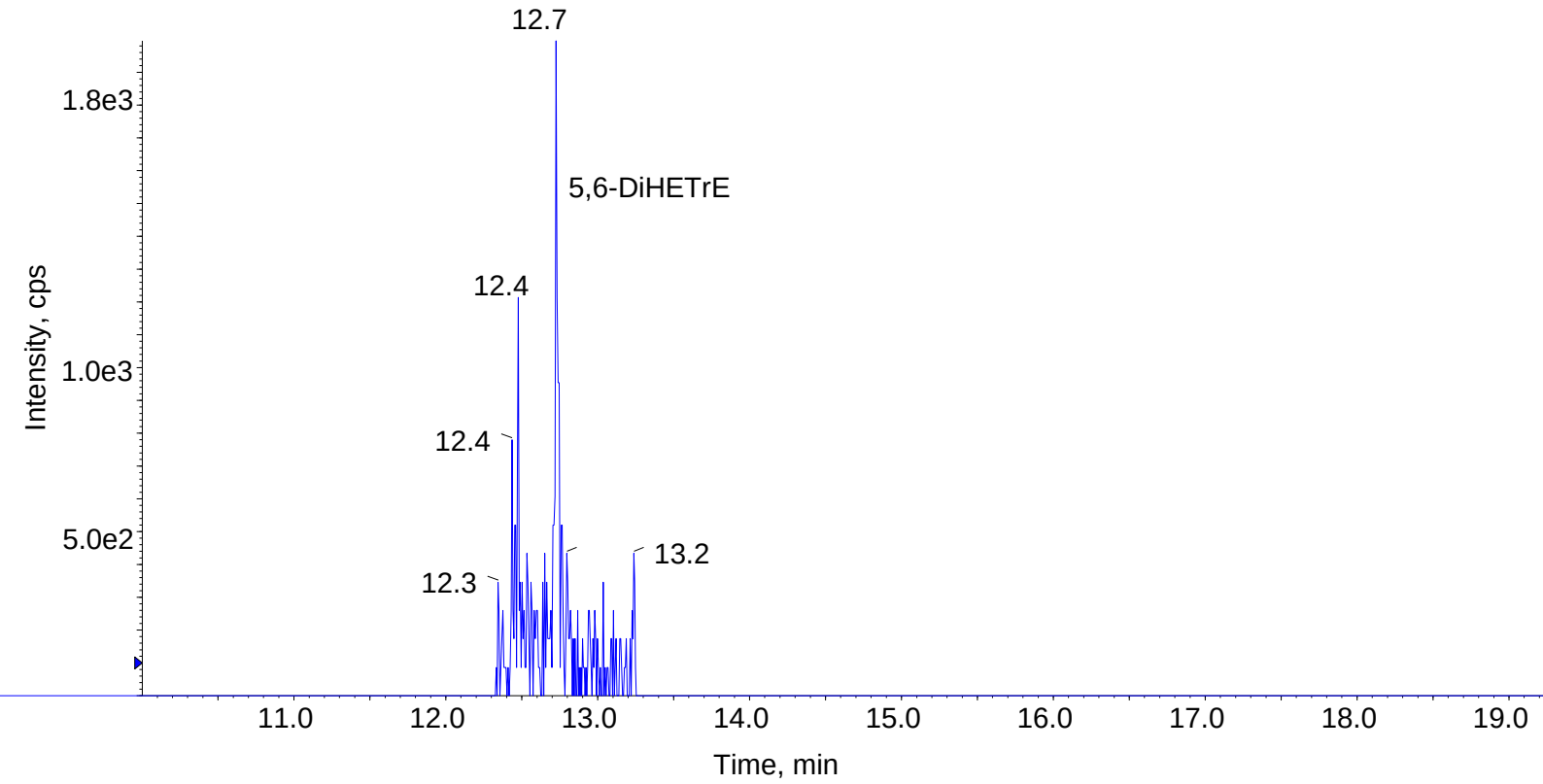
12.7
1.8e3
5,6-DiHETrE
12.4
1.0e3
12.4
5.0e2
13.2
12.3
Intensity, cps
11.0
12.0
13.0
14.0
15.0
16.0
17.0
18.0
19.0
Time, min

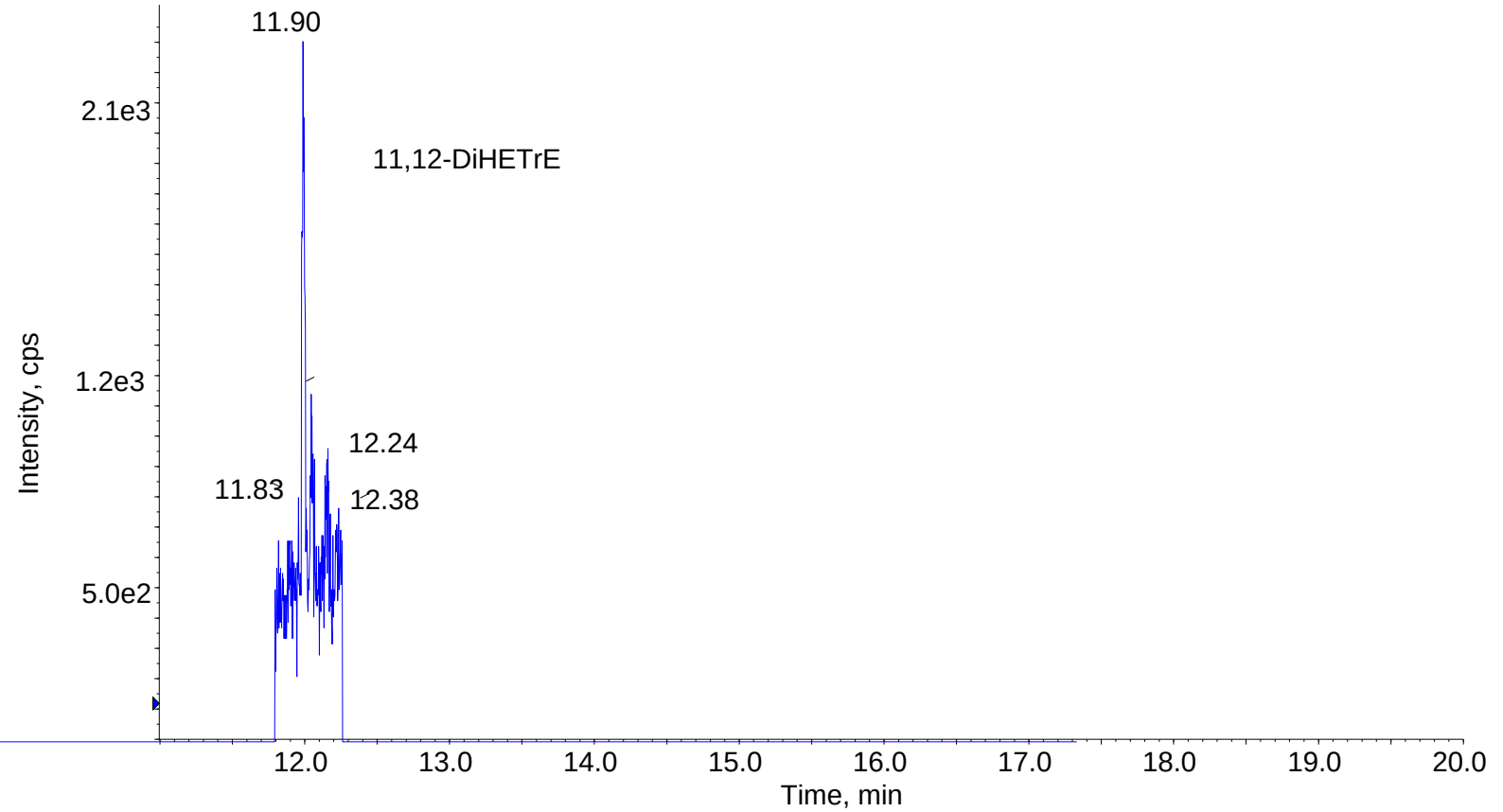
11.90
2.1e3
11,12-DiHETrE
1.2e3
12.24
11.83
12.38
5.0e2
Intensity, cps
12.0
13.0
14.0
15.0
16.0
17.0
18.0
19.0
20.0
Time, min

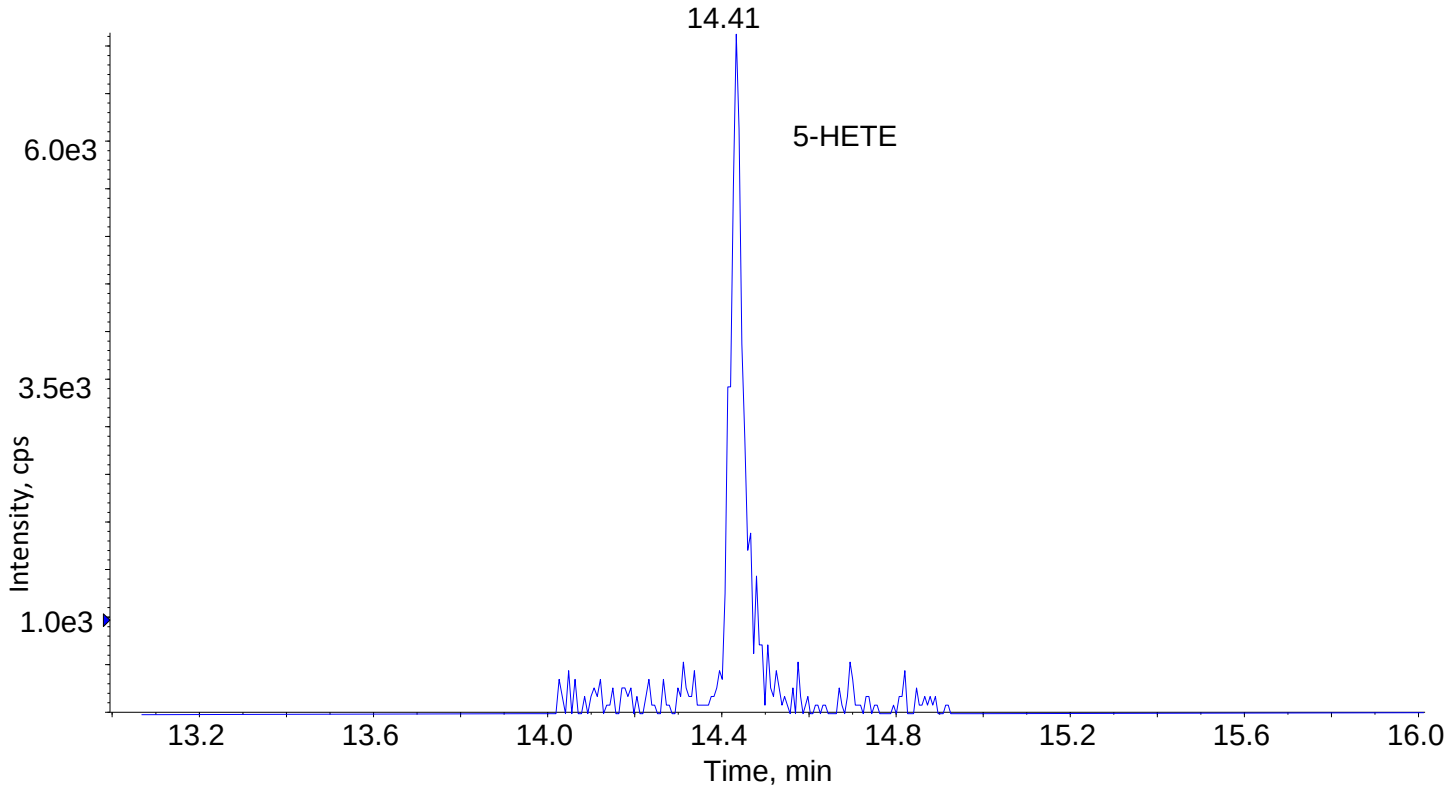
14.41
5-HETE
6.0e3
3.5e3
1.0e3
Intensity, cps
13.2
13.6
14.0
14.4
14.8
15.2
15.6
16.0
Time, min

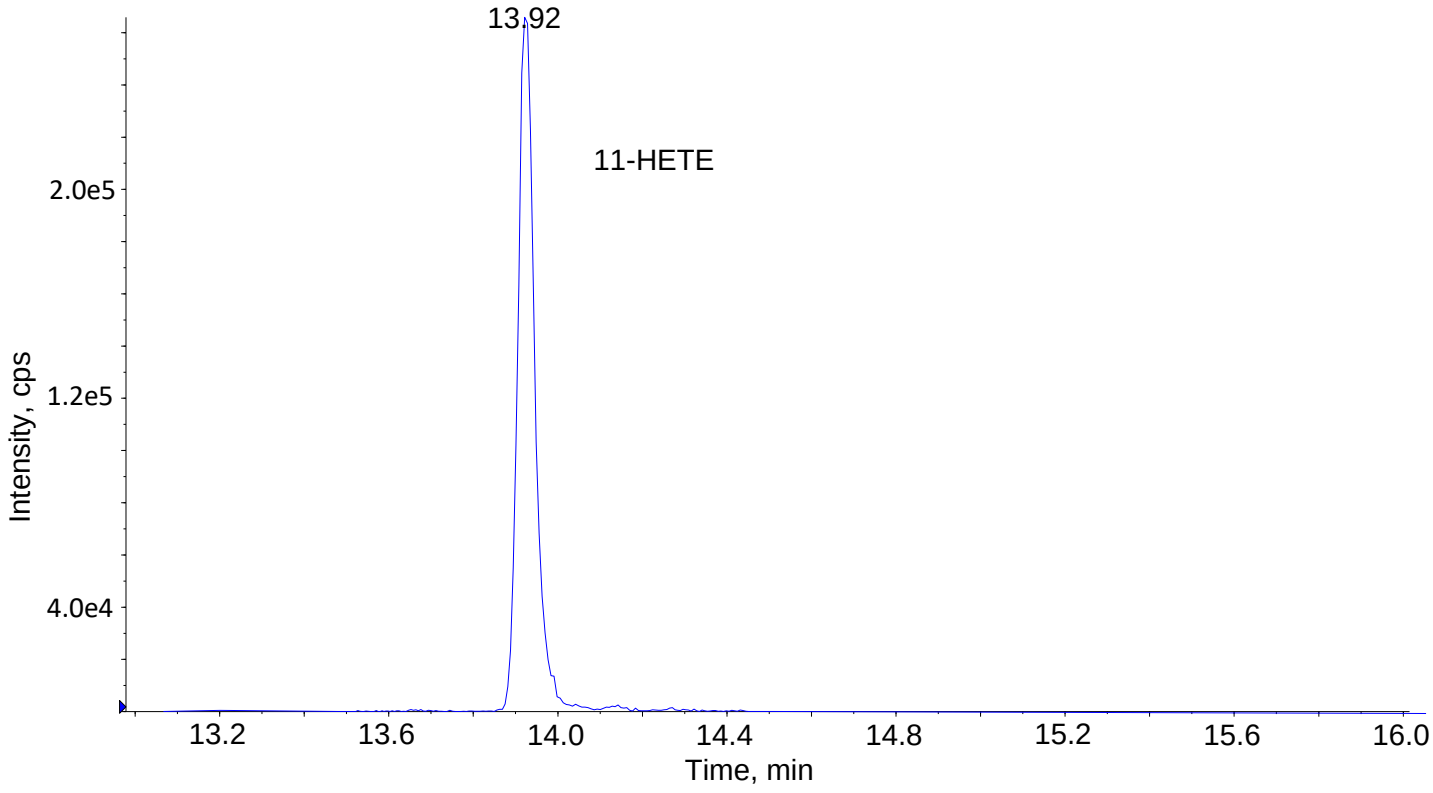
13.92
11-HETE
2.0e5
1.2e5
4.0e4
Intensity, cps
13.2
13.6
14.0
14.4
14.8
15.2
15.6
16.0
Time, min

DISCUSSION

A targeted liquid chromatography-tandem mass spectrometry method was applied to quantify and characterize free oxylipins generated either enzymatically by LOXs, COXs, and CYPs pathways or non-enzymatically by reactive oxygen species in *Alox15*$^{-/-}$ compared with age-matched WT mice. The oxylipins derived from AA were ranked first, followed by the DHA and last, the LA, according to relative abundance.

The critical question was how the *Alox15* deletion impacts oxylipins in the mouse brain. The main finding is that the overall COX activity appears to be upregulated; for example, one of the COX isoforms may be induced, causing higher production of prostaglandins and increased levels of 15-HETE and 11-HETE in *Alox15*$^{-/-}$ mouse brain and potentially mediating inflammation.

In particular, COX enzymes also produce 15*R*- HpETEs as side products, which can be further reduced into their corresponding products by peroxidase activity. Also, 15-HETE can be formed non-enzymatically from *Alox15* (15S-HETE) (routes in Figure 1) (Kuhn *et al.*, 2006). I could address this by using chiral chromatography to determine the relative amounts of 15-HETE S and R enantiomers (Kuhn *et al.*, 1987). That is due to LOX and COX, which exhibit stereospecificity regarding oxygenating PUFA, primarily AA. Interestingly, 11-HETE can be produced enzymatically as a by-product of prostaglandin synthesis by both COX isoforms, and it could have some function involved in inflammation regulation (Xiao *et al.*, 1997).

Furthermore, the most abundant products of AA metabolism were prostaglandins derived from COX enzymes. Here, their significantly elevated levels in the cerebellum in *Alox15*$^{-/-}$ mice suggest higher levels of COX enzymes. Consequently, the similar behaviour of the increased levels of prostaglandins and the abundance of 15-HETE and 11-HETE may imply induction of COX-2, which can be linked with inflammation. COX-2 is an inducible enzyme under stress conditions, including neuroinflammation (Phillis *et al.*, 2006).

The platelet type 12-LOX, an isoform that belongs to the family of lipid-oxidizing enzymes expressed in mammals mainly by immune cells and platelets (thrombocytes), is encoded by *Alox12*, and this enzyme generates 12(S)-HETE (Kuhn *et al.*, 1999; Dobrian *et al.*, 2019). The murine orthologue leukocyte-type 12/15-LOX is encoded by the *Alox15* gene and produces small amounts of 15-HETE and primarily 12-HETE. Subsequently, in mice, 12-HETE can originate from 12/15-LOX and platelet 12-LOX (Kuhn *et al.*, 1999; Dobrian *et al.*, 2019). Thus, 12-HETE detected in *Alox15*$^{-/-}$ mice could be generated by 12-LOX, as platelets might cross the blood-brain barrier during perfusion (Kriska *et al.*, 2012). As described in Methodology,

the animals that used for the lipidomic analysis (both WT and *Alox15*$^{-/-}$ mice) were perfused, indicating that most of the circulating cells and platelets, which might contributed a significant pool of enzyme function were removed. Thus, metabolites identified from the brain tissue could have been present due to diffusion from the blood or endogenous production by enzymes expressed by brain cells. It has been noted that 12-HETE and 15-HETE have both pro-and anti-inflammatory properties (Sun *et al.,* 2015; Singh *et al*., 2018). 12-HETE acts as an inhibitory neuromodulator by decreasing calcium channel content via voltage-activated channels and attenuating glutamate secretion (Sun *et al.,* 2015).

Furthermore, 5-HETE was the least abundant metabolite among all HETEs and is generally produced by neutrophils. The relative higher abundance of 5-HETE in the HPC and cortex in *Alox15*$^{-/-}$ mice suggests more elevated levels of 5-LOX, which is encoded by the *Alox5* gene and is activated by the membrane protein 5-LOX-activating protein (FLAP), resulting in the production of leukotrienes such as leukotriene B_4 (Czapski *et al.,* 2016). The precise role of FLAP in 5-LOX reactions remains unknown; however, it is suggested that FLAP functions as a scaffold for 5-LOX (Dixon *et al.,* 1990). Studies indicate that the 5-LOX level is mainly expressed in the cortex and HPC, which are particularly vulnerable to neurodegeneration (Lammers *et al.,* 1996; Chinnici *et al.,* 2007; Chu *et al.,* 2012). In studies utilizing AD mouse models, Tg2576 and 3xTg mice, 5-LOX knockout was associated with improvements in learning and memory and restoration of hippocampal LTP, whereas overexpression of 5-LOX was correlated with more significant cognitive decline (Chu *et al.,* 2012; Giannopoulos *et al.,* 2013). Another study by Chinnici showed that the highest mRNA levels and FLAP protein levels of 5-LOX were significantly higher in the HPC of aged WT mice versus young WT mice (Chinnici *et al.,* 2006).

Of particular interest, PGE_2 levels have previously been seen to be higher in AD development and to decline with disease progression (Combrinck *et al.,* 2006). PGE_2 plays a critical role in immunity and inflammation (Park *et al.,* 2006). In a study by Choi, the levels of brain PGE_2 were significantly elevated in COX-$1^{-/-}$ mice, whereas the levels of TXB_2 were decreased in COX-$1^{-/-}$ mice compared to WT mice, likely due to the compensation upregulation of COX_2 enzyme (Choi *et al.,* 2006). Another study utilizing the APPSwe-PS1ΔE9 (APPS) transgenic mouse model of familial AD showed that PGE_2 signalling through its receptor E-prostanoid 3 (EP3) which was elevated in the HPC during the early time of onset of neuroinflammation compared to controls, leading to a critical component of neuroinflammatory response that contributes to the AD development (Shi *et al.,* 2012).

Here, 4-HDOHE generated from DHA by LOX was significantly higher in the cerebellum in the *Alox15*$^{-/-}$ mouse brain than in WT. Studies indicate that DHA and its docosanoids have been implicated in having beneficial effects against age-related cognitive decline in normal mice or AD models (Suzuki *et al.*, 1998; Hashimoto *et al.*, 2015; Lim *et al.*, 2005). In a study by Hasmimoto suggested that TAK-085 administration that contains ω-3 DHA and EPA ethyl-ester in aged wistar rats for 17 weeks resulted in recused AA-derived metabolites, compared to increased EPA and DHA derived metabolites, according to plasma n-6/n-3 molar ratio. DHA-derived molecules are proposed to be anti-inflammatory, suggesting a critical role in resolving inflammation and protecting neurones (Maskrey *et al.*, 2013). Recently a study by Shalini *et al.* 2018, reported that the *Alox15* inhibitor, PD146176, which was injected into the prefrontal cortex of rat brains, showed a reduction in resolvin D1 levels in the prefrontal cortex, which is derived from DHA. This lipid was measured by LC/MS/MS analysis. This inhibition blocked LTP induction of HPC-prefrontal cortex pathway displayed impaired performance in the T-maze test by increasing the errors in alternation in this task. This finding suggested that this lipid may play a role in spatial memory (Shalini *et al.*, 2018). These results are consistent with Chapter 4, whereby *Alox15*$^{-/-}$ mice displayed spatial memory deficits but the metabolites from DHA remained unchanged in the prefrontal cortex between genotypes. In line with my results from Chapter 3, a study by Hennebelle *et al.*, 2012, using Wistar rats showed that ω-3 PUFA dietary deprivation was associated with increased grooming and reduced locomotor activity, as it has been measured in the open field test and EPM, but the mechanism remains to be elucidated compared to rats enriched with ω-3 PUFA.

Future work could involve chiral analysis of 15-HETE to determine if elevated levels are due to biosynthesis through enzymatic, non-enzymatic, or a combination of both reactions to better understand the association between 15-HETE and brain function. In particular, to investigate further the pathway produced in this chapter, either from the COX pathway (15R-HETE) or 12/15-LOX (15S-HETE) (Funk *et al.*, 2022). Ultimately, one way to verify all the above suggestions of increased lipid levels, such as 5-LOX and COX-1,2, is by measuring their protein levels and the gene expression of oxylipin-producing enzymes by applying immunohistochemistry along with brain imaging.

Chapter 7:

Alox15 deficiency is associated with reduced hippocampal levels in diverse oxPLs

INTRODUCTION

7.1 Chapter overview

As discussed in Chapter 1, eicosanoids act as free biologically active lipid mediators secreted from cells of origin via specific G-protein-coupled receptors or incorporated into PLs (PLs-esterified eicosanoids). In particular, oxylipins can be re-esterified into the PL membrane to form additional families of oxidised phospholipids (oxPLs) (Morgan *et al*., 2010; O'Donnell *et al.*, 2017; O'Donnell *et al.*, 2019). OxPL play additional functions, such as inflammation mediators beyond their free acid metabolites (Aldrovandi *et al.*, 2013). OxPL can be produced either enzymatically (eoxPL) or non-enzymatically and comprise diverse lipid structures (Morgan *et al*., 2009). EoxPL remain cell-localised, where they have various biological effects on different cell types in health and inflammatory diseases. The enzymatic formation of eoxPLs is mediated by LOX and COX enzymes, and their biosynthesis includes intracellular signalling pathways, whereas non-enzymatic formation is characterised by chronic inflammation and regulated by free radical mechanisms through free radical mechanisms reactive oxygen species (O'Donnell *et al.*, 2012; Aldrovandi *et al.*, 2013).

As mentioned in Chapter 1, the LOX enzymes insert molecular oxygen in AA, and depending on its position in the aliphatic chain, form HpETEs such as 5-, 8-, 12-, and 15-HpETE. Then, the HpETEs are further reduced into HETEs by peroxidases (Wang, *et al.*, 2021). Also, the LOX enzymes oxidise DHA to form HpDOHEs, such as 14- and 17- HpDOHE which can then be reduced to HDOHE (Morgan, *et al.*, 2010). Furthermore, 12-HEPE and 15-HEPE are the LOX metabolite synthesized from EPA via the action of 12-LOX and 15-LOX, respectively (Chiu, *et al.*, 2017).

In this Chapter, LC/MS/MS has been operated in MRM scan mode to detect the selective and specific initial 96 transitions, based on the precursor to product ions. The analysis revealed that the signal of the majority of the lipids, particularly 75 lipids, was very weak. In MRM, these analytes were monitored through the transition of a precursor ion to product ion arising from collision-induced dissociation to form distinct negatively charged ions.

Several lipidomic studies identified and characterised HETE-PL species formed by the LOX pathway via the cellular activation of human platelets (Thomas *et al.*, 2010; O'Donnell *et al.*, 2018). Our group discovered these species, utilising precursor scanning LC/MS/MS to search for product ions corresponding to HETEs (*m/z* 319.2) attached to PL (Maskrey *et al.*, 2007). Among the most abundant PL species in eukaryotic cell membranes are PE and PC, which

constitute the primary building blocks of the cell membrane and include both acyl and plasmalogen forms (Murphy, 2002; Van Meer *et al.,* 2008; Farine *et al.,* 2015).

7.2 Biosynthesis of oxidised phospholipids

The biosynthesis of enzymatically oxidised phospholipids usually begins with the hydrolysis of PUFA from PL by PLA_2, normally the cytosolic isoform (Hammond *et al.,* 2012). PLA_2 hydrolyses acyl from the *sn2* position, and this is then oxygenated through the action of LOX or COX enzymes to form free acid eicosanoids. The next step is the acylation of lysophospholipid (lysoPL) with coenzyme A (FA-CoA) via acyl-CoA synthases (ACSL), followed by their acyl-CoA-dependent esterification into a membrane lysoPL to the *sn2* position by an *sn*-2 acyltransferase activity (lysophospholipid acyltransferase, or LPAT) (Gijón *et al.,* 2008; Yamashita *et al.,* 2014; Liu *et al.,* 2019; O'Donnell *et al.,* 2019). The cycle of PL hydrolysis by PLA_2 into FA/lysoPL, oxygenation, and re-esterification of free eicosanoids to form eoxPL is part of the Lands cycle (Lands, 1958; Lands, 1965) (Figure 76). Platelets, neutrophils, and macrophages generate eoxPL acutely following cell activation (O'Donnell *et al.,* 2019).

Although the eoxPLs formed via 5-LOX and 12-LOX enzymes require a cycle of hydrolysis and re-esterification, those from 12/15-LOX, generated by macrophages, do not need the Lands' cycle, but direct PL oxidation (Thomas, *et al.,* 2010). Maskrey et al. (2007) demonstrated an entirely different process unique to 12/15-LOX, which does not require PLA_2. They described the ability of 15-LOX to directly oxidize PE to form eoxPL without the prior release of AA to form free 15-HETE (Maskrey *et al.,* 2007).

LC-MS/MS analysis has demonstrated a range of positional isomers of eoxPL in human cells, formed in a cell-specific manner by 5-LOX (5-HETE-PL in neutrophils, monocytes) containing three plasmalogen PE species (PE 18:0p_5-HETE, PE 18:1p_5-HETE, PE 16:0p_5-HETE), 15-LOX (15-HETE-PL, 17-HDOHE-PL in human eosinophils), and 12-LOX (12-HETE-PL, 14-HDOHE-PL in platelets) (Maskrey et al., 2007; Clark *et al*., 2011; O'Donnell *et al.,* 2012; Slatter *et al.,* 2018). In mice, 15-LOX is represented by a 12/15-LOX gene product expressed in murine peritoneal macrophages and is strongly induced by Th2 cytokines (Kuhn *et al.,* 2016). This isoform generates 12-HETE-PL and 15-HETE-PL primarily.

Similar to HETE-PL, the formation of HDOHE-PLs in platelets occurs via PLA_2 hydrolysis of DHA, which is then oxygenated and re-esterified into plasmalogen (16:0p, 18:0p) or diacyl (16:0a, 18:0a) PEs at the S*n1* position (Thomas *et al*., 2010; Morgan *et al*., 2010; Hammond *et*

al., 2012; Aldrovandi *et al.*, 2013). HDOHE-PLs are acutely formed by 12-LOX in thrombin-activated platelets (Morgan *et al*., 2010).

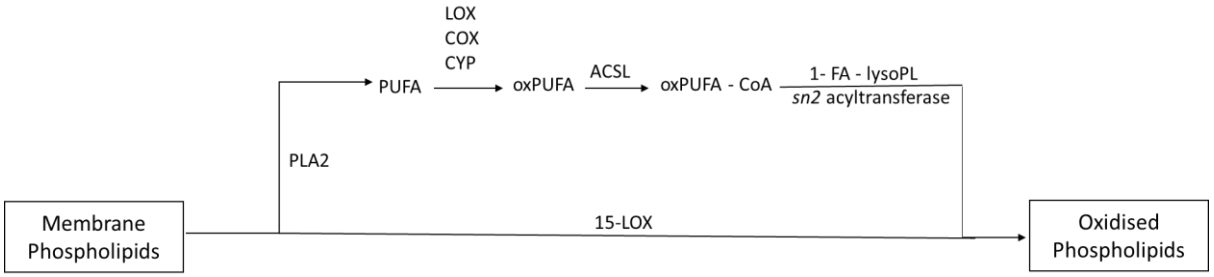

Figure 76. The biosynthesis of oxidised phospholipids. The top pathway involves the action of PLA_2 on membrane phospholipids, the oxidation of the released non-esterified fatty acid at the sn-2 position catalysed by the three enzymes and then re-esterified to lysoPL. **T**he bottom pathway includes the direct oxygenation of membrane phospholipids by 15-LOXs without PLA_2 requirement.

7.3 Aim and objectives

Previously, in Chapter 6 oxylipins were measured in the *Alox15*$^{-/-}$ mouse brain and compared them with age-matched WT mice. Here, a targeted lipidomic approach will detect and identify unknown eoxPLs formed in the WT mouse brain. Initially, I will use LC/MS to profile lipid extracts from the prefrontal cortex, HPC, and cerebellum in WT mice. For each lipid, the precise oxPL structural identification will be determined based on MRM in negative ion mode. Then, MS/MS spectra will be applied for validation. Once the spectra is acquired, a comparison will be performed to investigate how these lipids vary between WT and *Alox15*$^{-/-}$ mice within the specific regions.

7.4 LC/MS/MS defines which eoxPL are present in WT mouse brain

Based on the literature, no studies have yet determined eoxPLs in the WT mouse brain. LC/MS/MS in MRM scan negative mode was first performed on WT brain lipid extracts to identify and characterise which eoxPL are present in the normal brain, as described in Materials and Methods.

For this purpose, I first used MRM transitions obtained from Professor Steffany Bennett's (University of Ottawa) methods, where she analysed post-mortem brain tissue from patients with AD. The Bennet lab published the lipidome of murine brain tissues obtained from commonly used transgenic mouse models of AD, namely the Swedish mutant of $APP_{K670N,M671L}$ (APP), and PS1-APP double transgenic lines (Axelsen *et al.*, 2010; Han *et al.*, 2001; Chan, *et al.*, 2012; Bennett SA et al., 2013). In particular, Bennett *et al.*, previously created and analysed 29 neurolipidomic datasets generated by eight different labs aiming to identify changes in phospholipid metabolism in AD compared to normal elderly (human) or murine samples (Bennett *et al.*, 2013).

To this end, I used *m/z* values of native PL detected in mouse brains and then generated putative MRMs of mono-oxygenated species by adding one oxygen to each, causing a mass shift of +16 mass units (Table 14). The new transitions were used to set up a method, in conjunction with calculations of estimated retention times for each oxPL species using an established LC/MS/MS method in our laboratory.

Initially, LC/MS/MS was operated in MRM scan mode to detect the selective and specific initial 96 transitions based on the precursor to product ions *m/z* 319.2 (HETE, $[M-H]^-$), of *m/z* 317.2 (HEPE, $[M-H]^-$), and *m/z* 343.2 (HDOHE, $[M-H]^-$), with dwell time every 100 ms with a collision energy of −38 V. In particular, these 96 MRM transitions were included in my method, with 16:0, 18:0 or 18:1 carbon chains at the *Sn*-1 position and 20:4(O), 20:5(O) (EPA; ω-3) or 22:6(O) (DHA, ω−3) at the *Sn*-2 position (Table 14). For each MRM transition, I used the precursor *m/z* value, and the fragment ion from the relevant mono-oxygenated *Sn2* fatty acid. I next analysed wild-type brain lipid extracts, revealing that the signal of most lipids, particularly 75 lipids, was very weak. Thus only 21 of the MRM transitions showed detectable and sufficient peaks in MRM negative ion mode, on the 6500 Q-Trap, monitoring precursor *m/z* to oxidised fatty acid as product ions (Table 14). Of the 21 detected, the most abundant were the oxidised species containing acyl PE molecular species 18:0a and the least

abundant were the ones containing plasmalogen, such as 18:1p, 18:0p, and 16:0p at the *Sn1* position.

However, several peaks were detected by LC/MS/MS; thus, it was crucial to find the correct peaks of eoxPLs. Oxidised phospholipids are more polar than native phospholipids; consequently, they elute at earlier retention times on reverse phase HPLC (Morgan *et al.*, 2009; Thomas *et al.*, 2010; O'Donnell, 2011). Based on this literature, I concentrated on analysing the eoxPLs that eluted within the RT 13-15 minutes. Also, the later peaks are not polar enough and thus are not consistent with oxPL (Thomas, *et al.*, 2010). It is noteworthy to mention that further work is needed to work out and verify which peaks on the chromatograms are eoxPLs. The 21 MRM chromatograms for each lipid with visible peaks are shown in Figure 77.

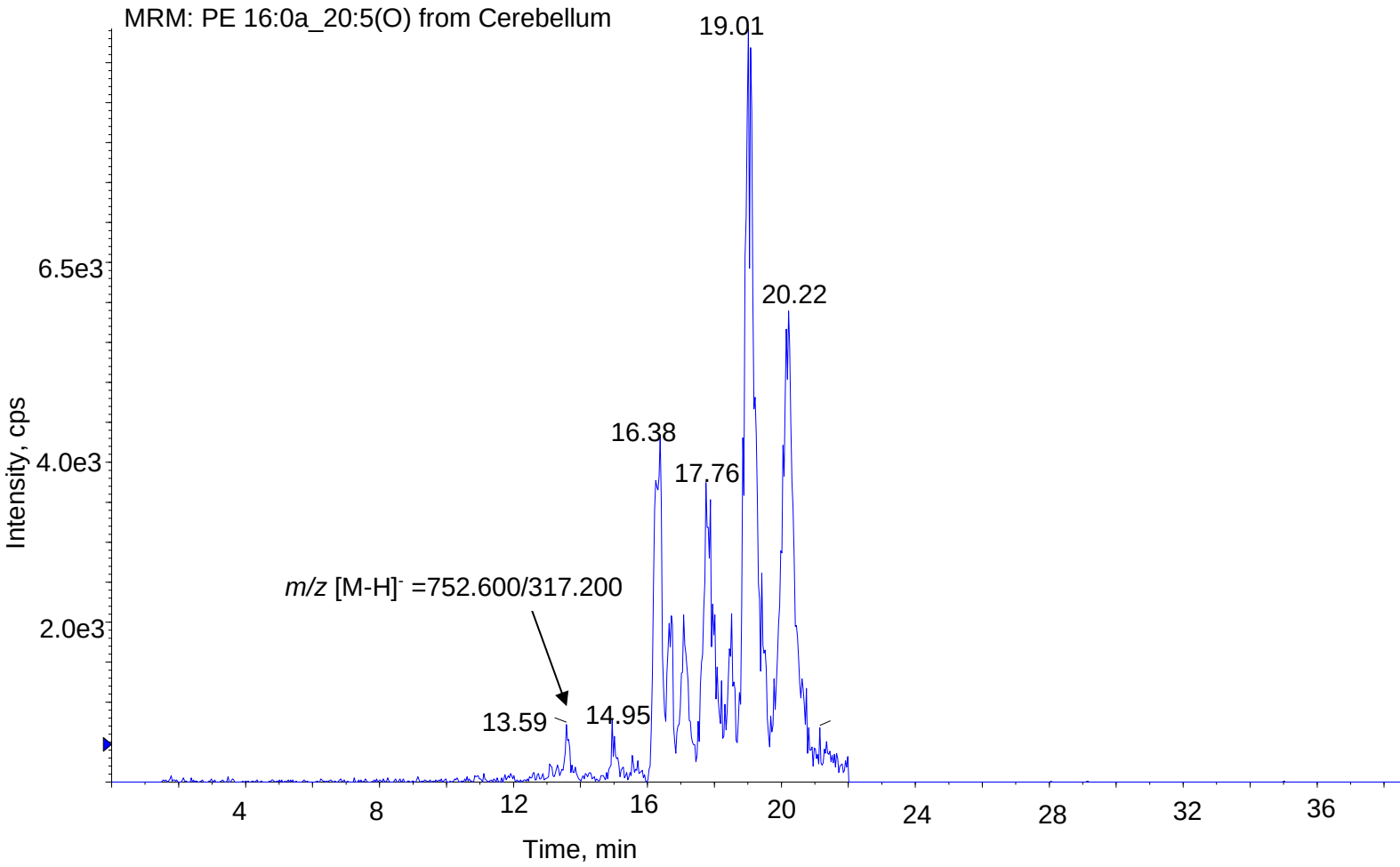
MRM: PE 16:0a_20:5(O) from Cerebellum
19.01
20.22
16.38
17.76
6.5e3
4.0e3
2.0e3
Intensity, cps
m/z [M-H]- =752.600/317.200
13.59
14.95
4
8
12
16
20
24
28
32
36
Time, min

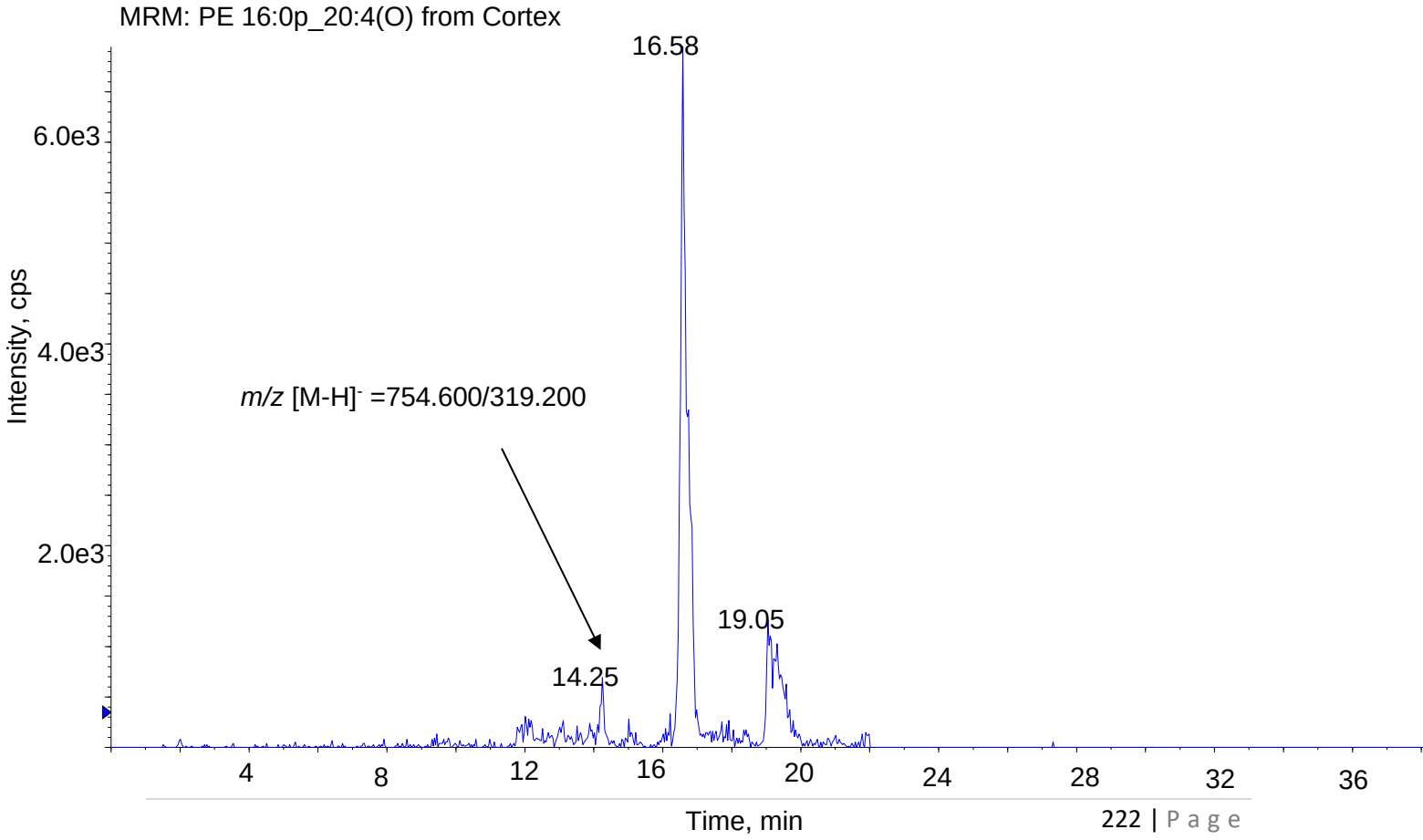
MRM: PE 16:0p_20:4(O) from Cortex
16.58
6.0e3
4.0e3
2.0e3
Intensity, cps
m/z [M-H]- =754.600/319.200
19.05
14.25
4
8
12
16
20
24
28
32
36
Time, min

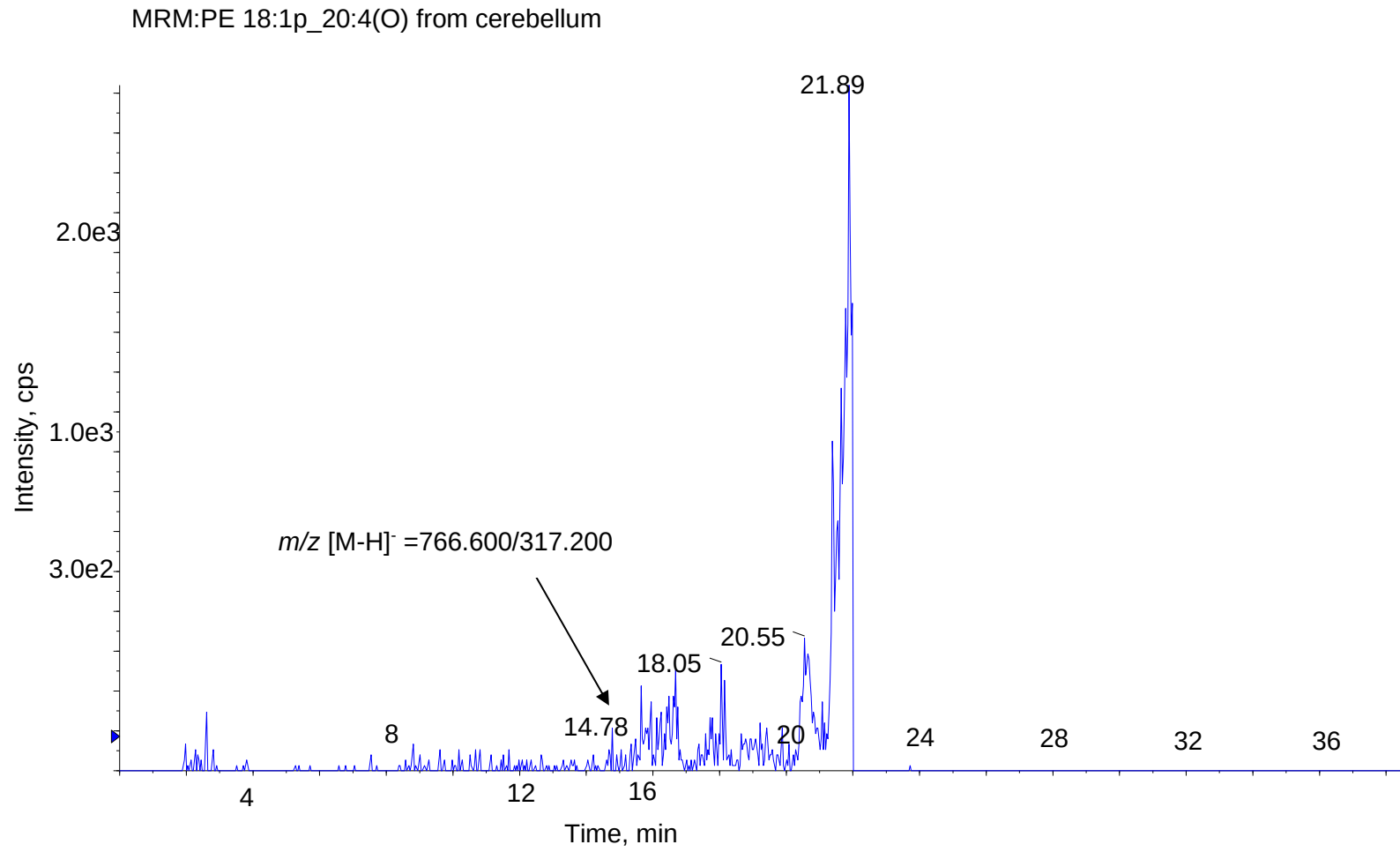
MRM:PE 18:1p_20:4(O) from cerebellum
21.89
2.0e3
1.0e3
3.0e2
Intensity, cps
m/z [M-H]- =766.600/317.200
20.55
18.05
14.78
8
20
24
28
32
36
4
12
16
Time, min

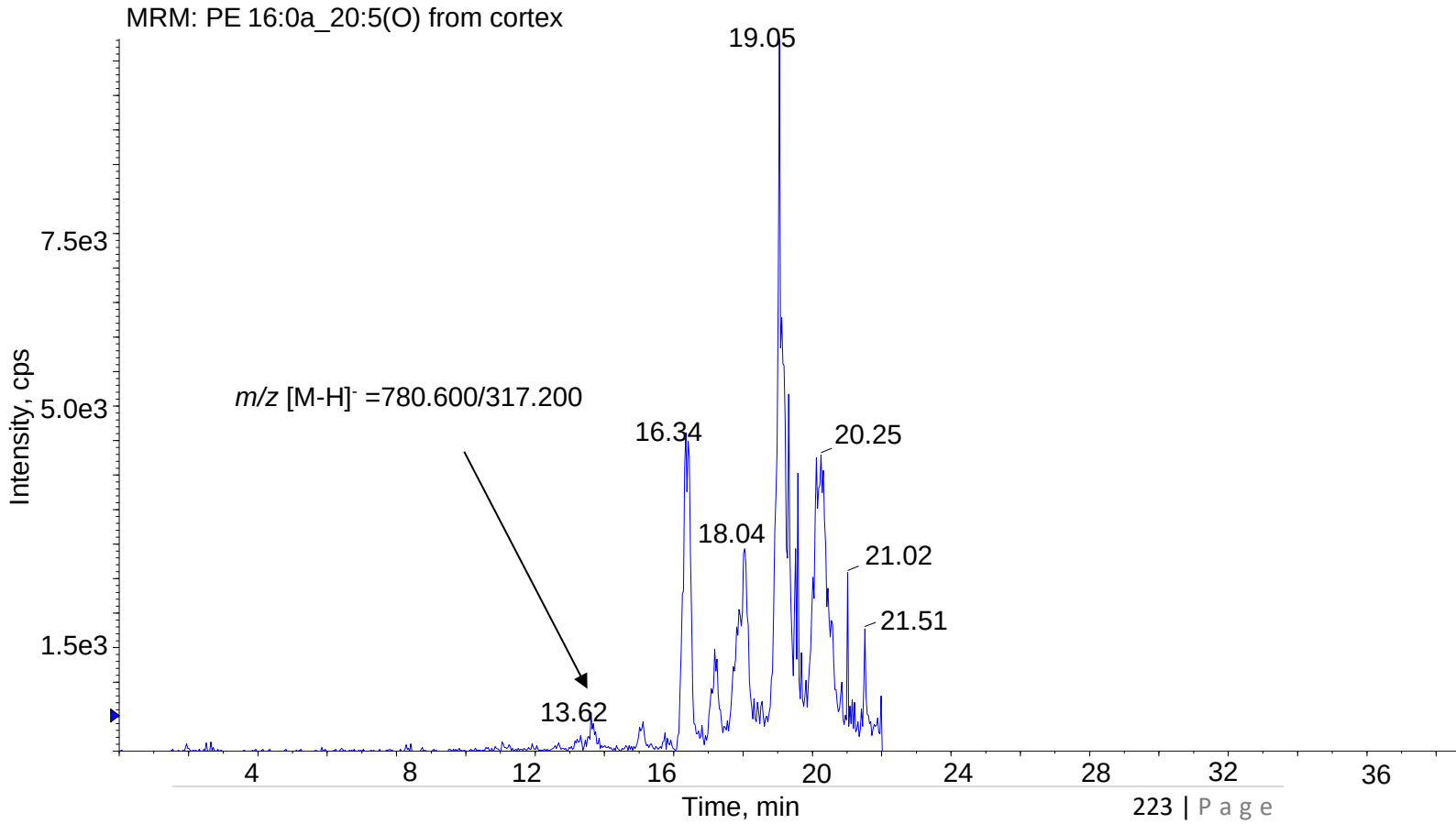
MRM: PE 16:0a_20:5(O) from cortex
19.05
7.5e3
5.0e3
1.5e3
Intensity, cps
m/z [M-H]- =780.600/317.200
16.34
20.25
18.04
21.02
21.51
13.62
4
8
12
16
20
24
28
32
36
Time, min

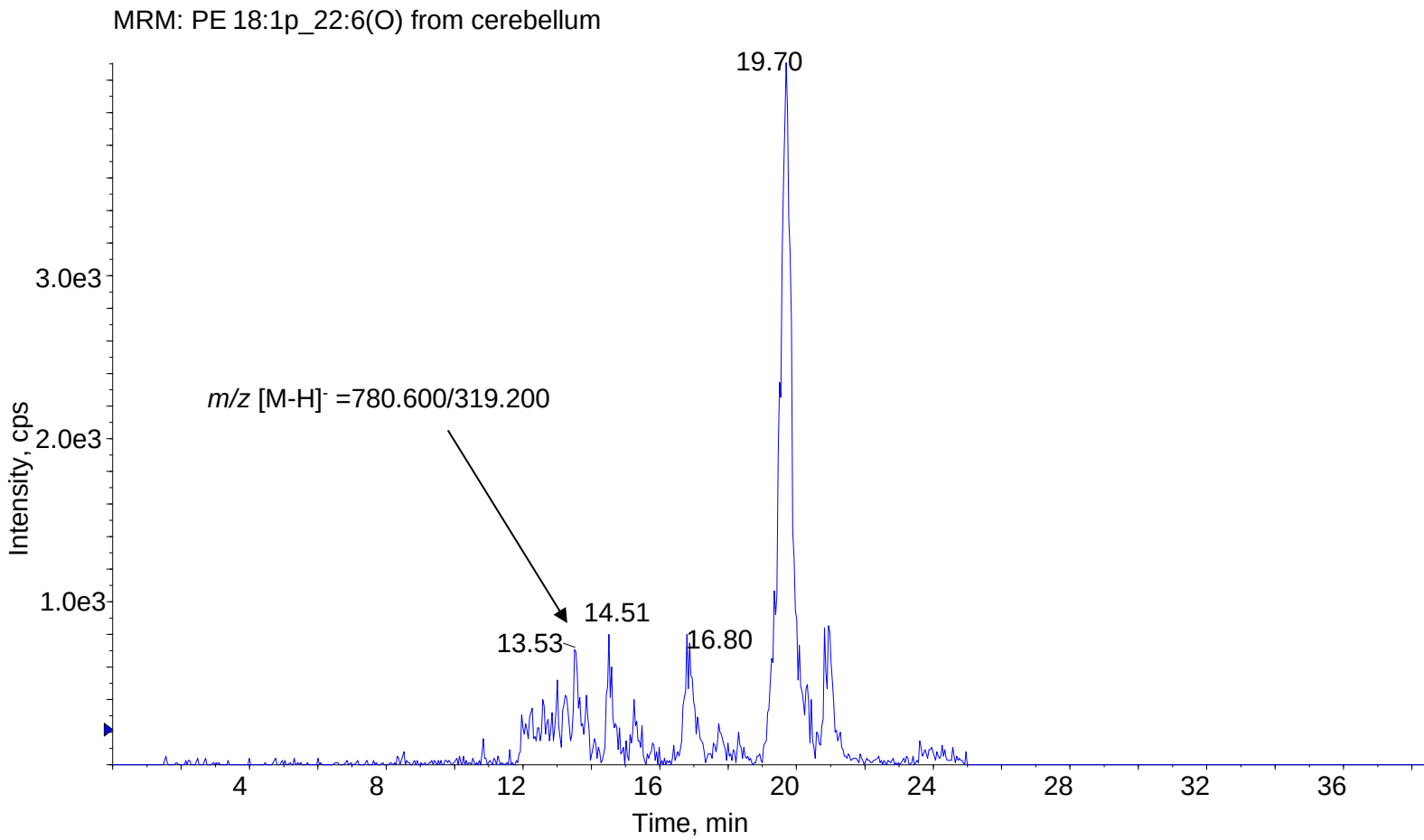
MRM: PE 18:1p_22:6(O) from cerebellum
19.70
3.0e3
m/z [M-H]- =780.600/319.200
2.0e3
Intensity, cps
1.0e3
14.51
13.53
16.80
4
8
12
16
20
24
28
32
36
Time, min

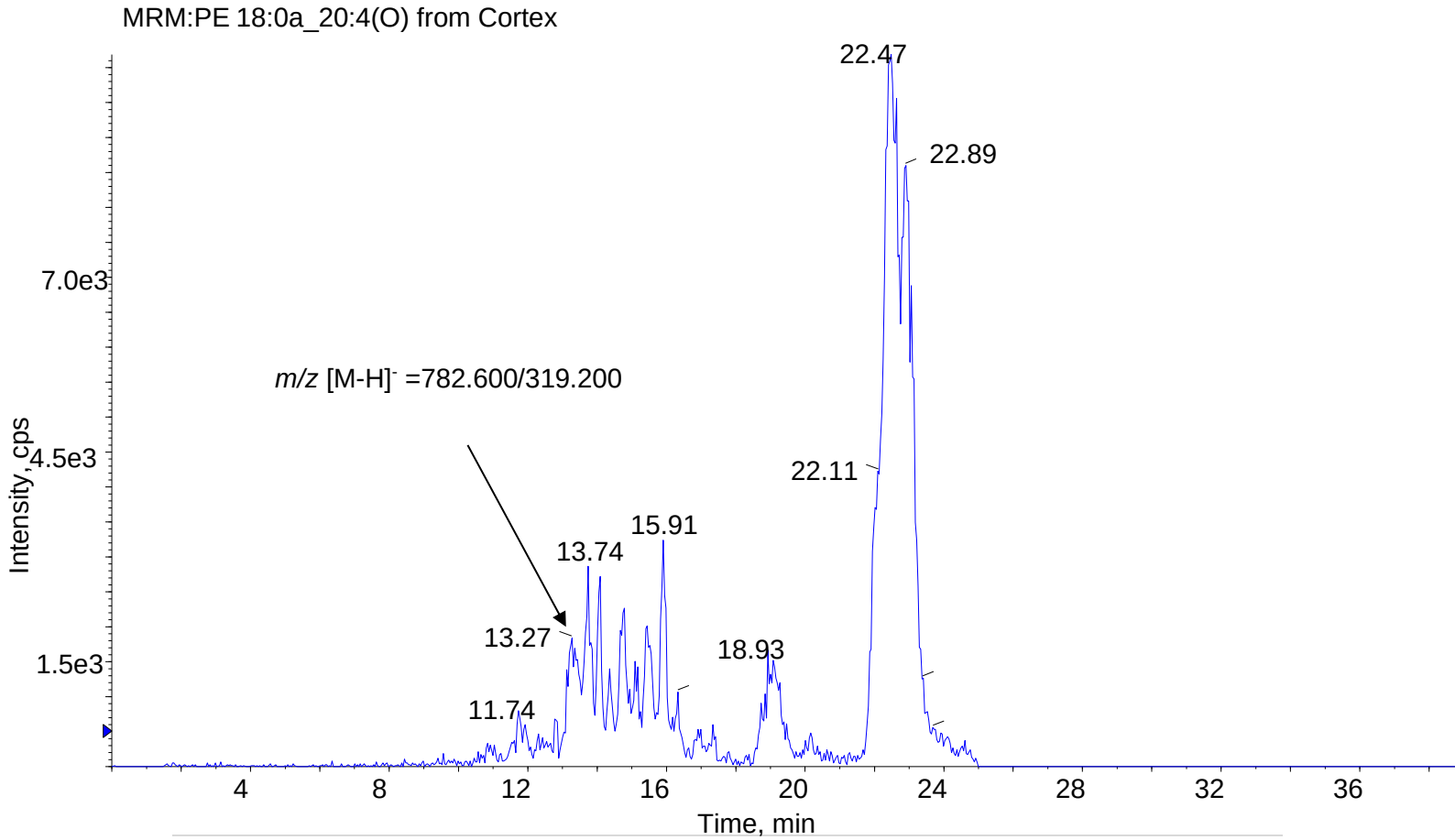
MRM:PE 18:0a_20:4(O) from Cortex
22.47
22.89
7.0e3
m/z [M-H]- =782.600/319.200
4.5e3
Intensity, cps
22.11
15.91
13.74
13.27
18.93
1.5e3
11.74
4
8
12
16
20
24
28
32
36
Time, min

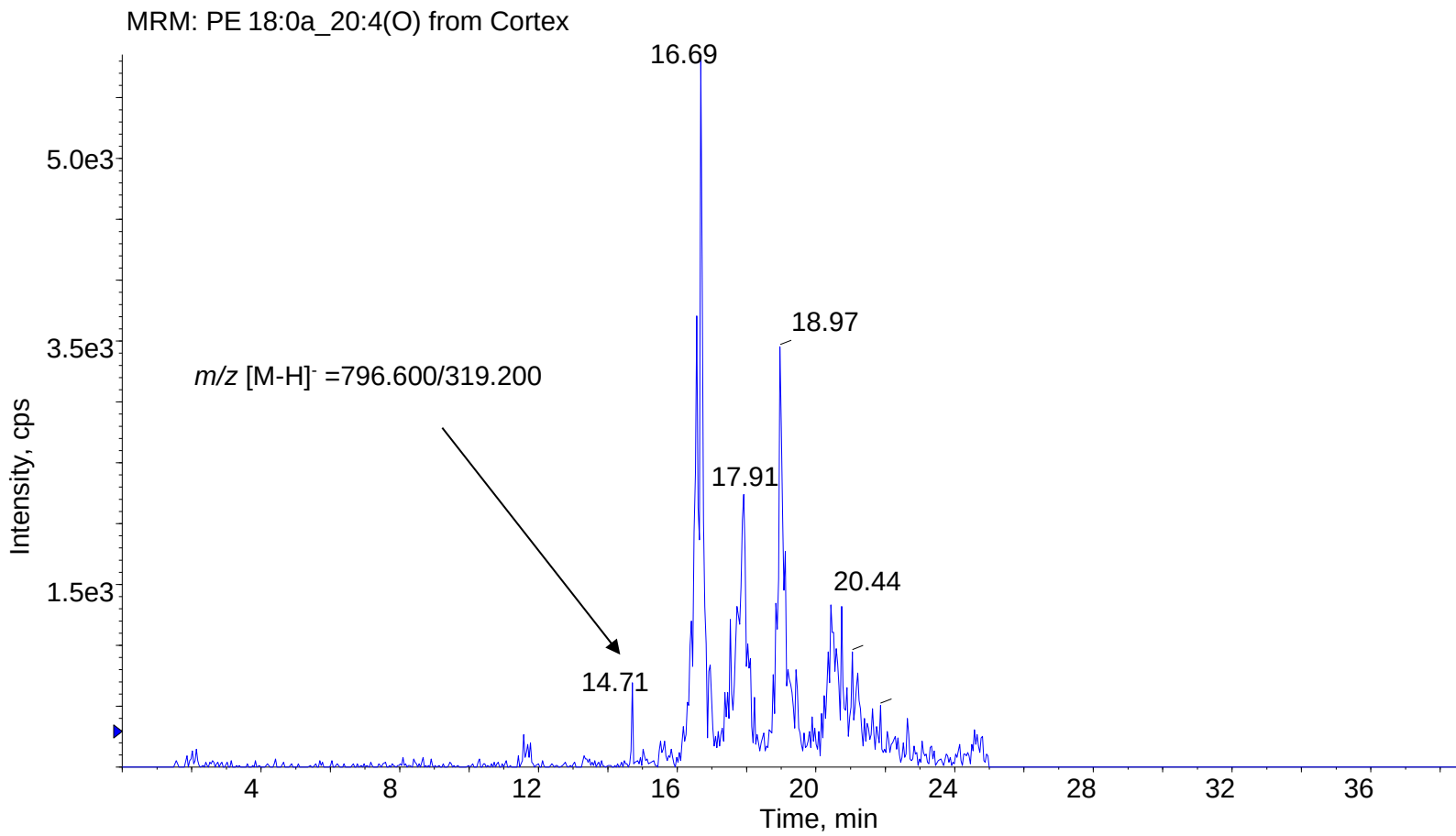
MRM: PE 18:0a_20:4(O) from Cortex
16.69
5.0e3
3.5e3
18.97
m/z [M-H]- =796.600/319.200
17.91
1.5e3
20.44
14.71
Intensity, cps
4
8
12
16
20
24
28
32
36
Time, min

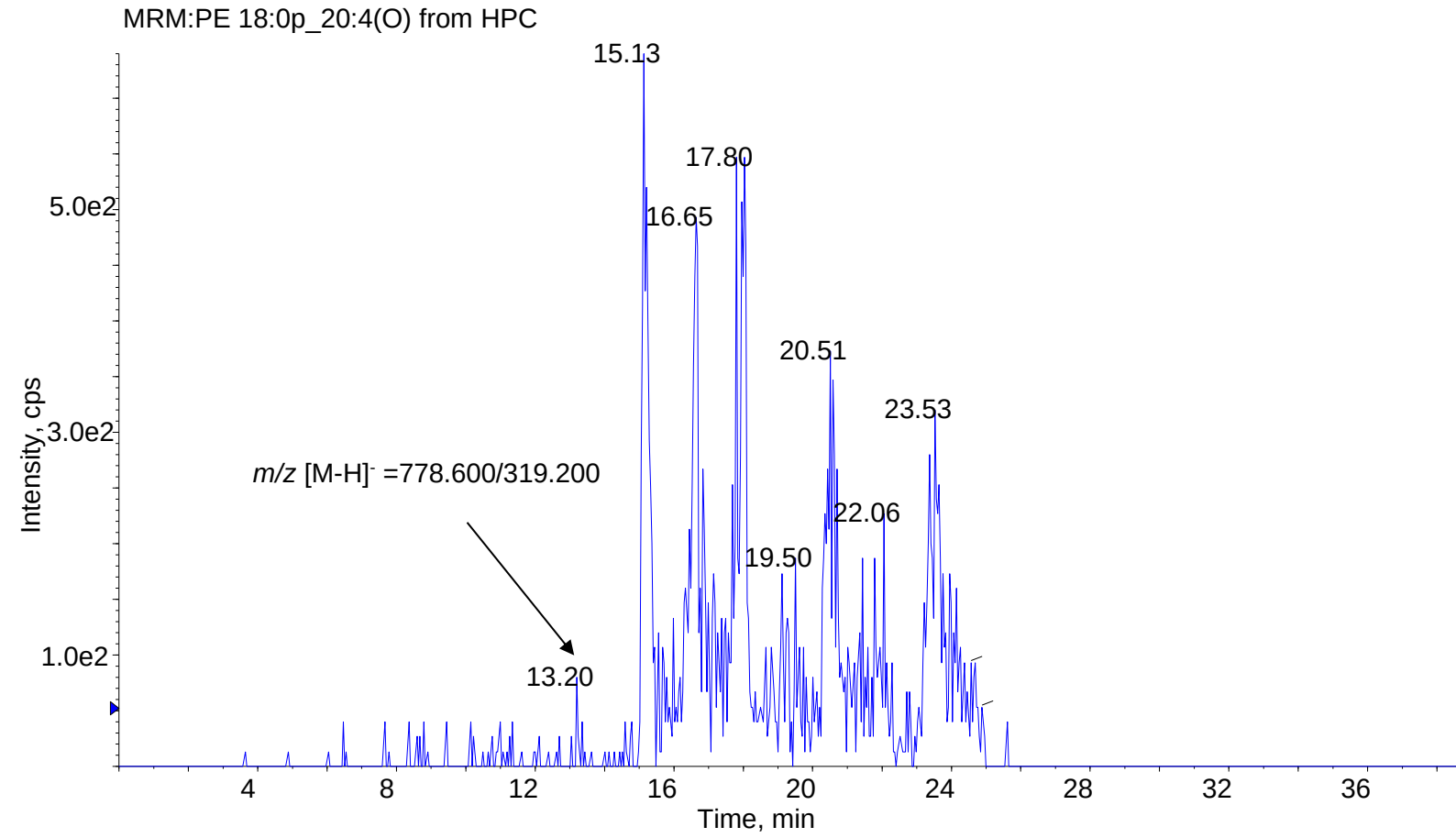
MRM:PE 18:0p_20:4(O) from HPC
15.13
17.80
5.0e2
16.65
20.51
23.53
3.0e2
m/z [M-H]- =778.600/319.200
22.06
19.50
1.0e2
13.20
Intensity, cps
4
8
12
16
20
24
28
32
36
Time, min

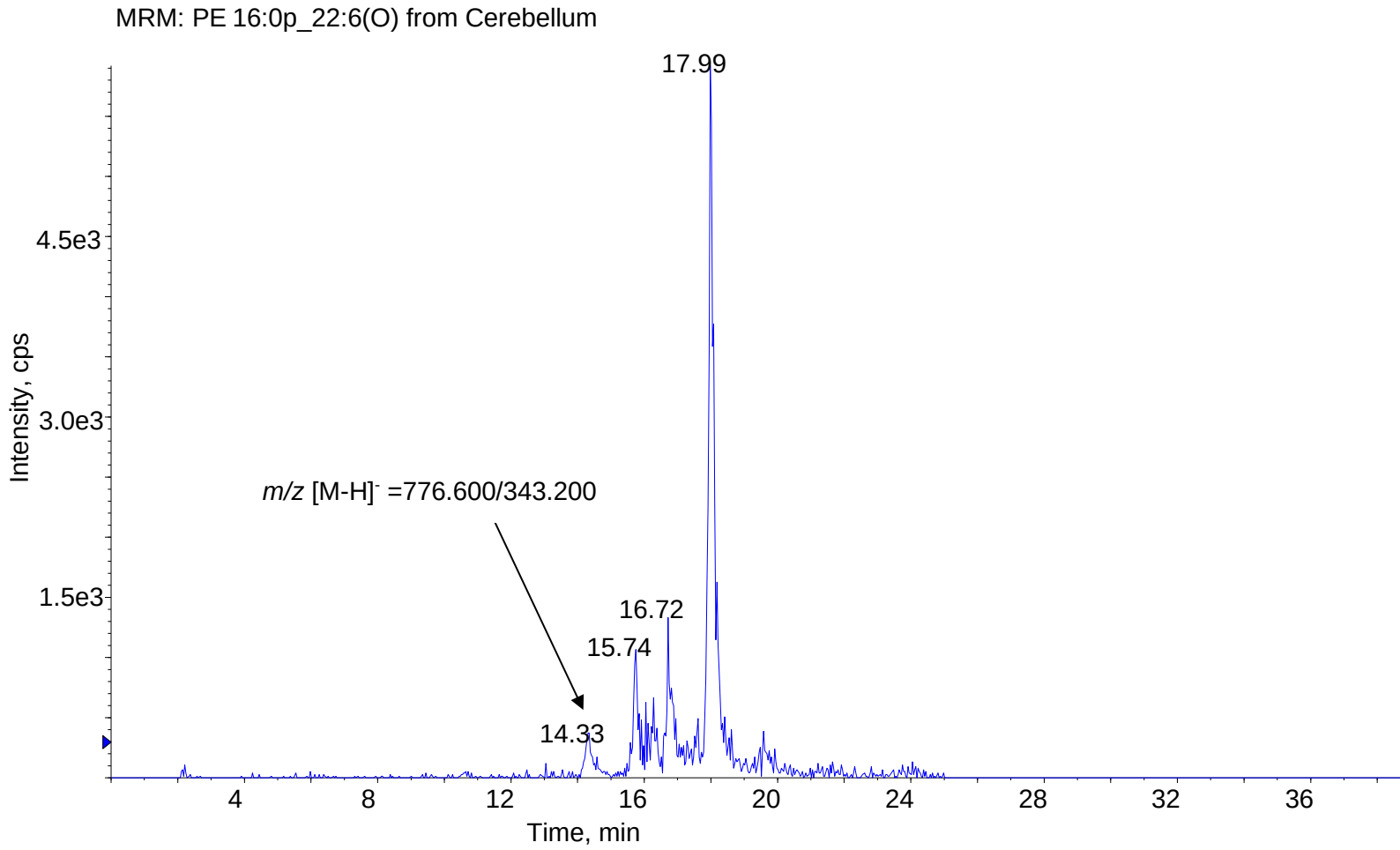
MRM: PE 16:0p_22:6(O) from Cerebellum
17.99
4.5e3
3.0e3
1.5e3
Intensity, cps
m/z [M-H]- =776.600/343.200
16.72
15.74
14.33
4
8
12
16
20
24
28
32
36
Time, min

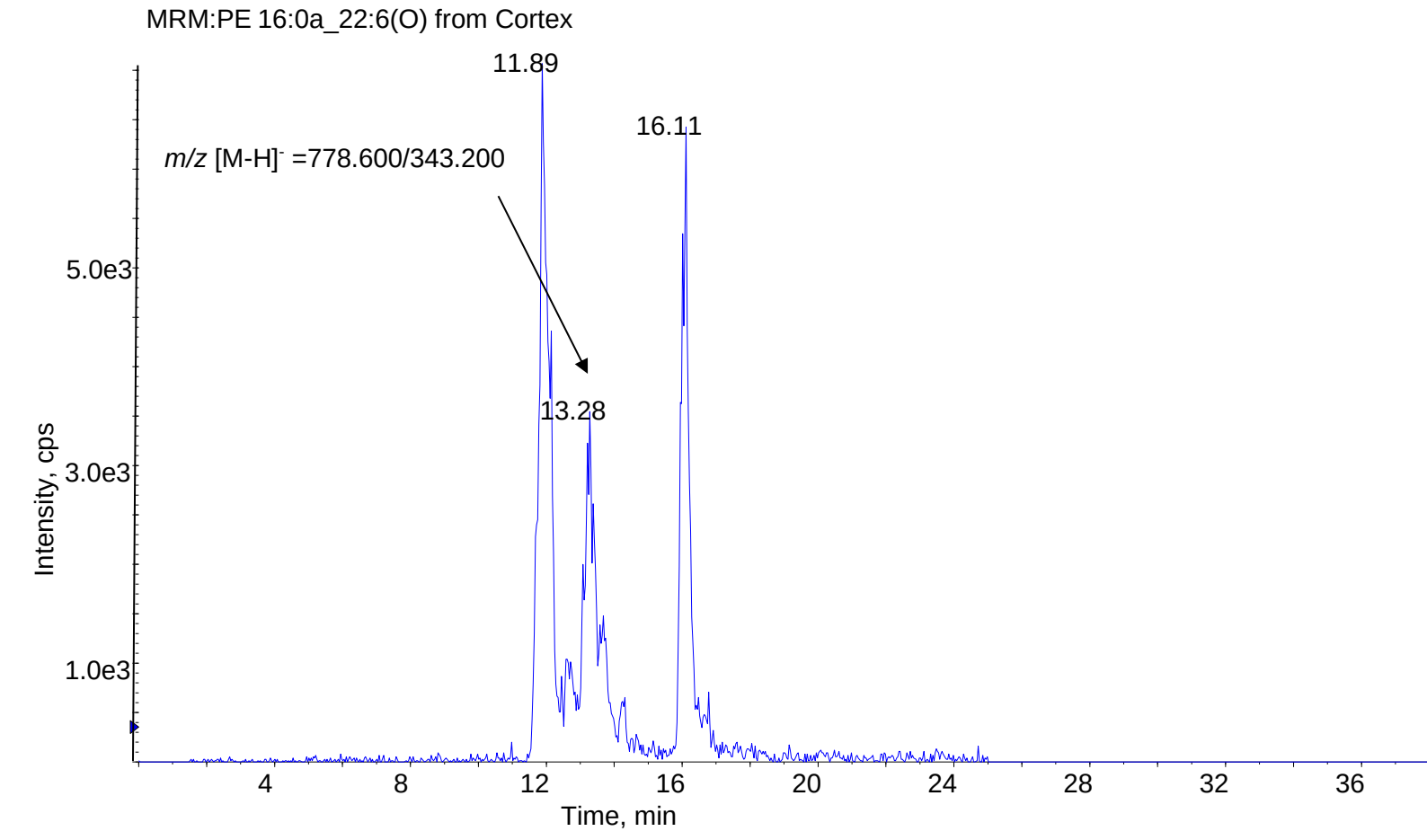
MRM:PE 16:0a_22:6(O) from Cortex
11.89
16.11
m/z [M-H]- =778.600/343.200
5.0e3
3.0e3
1.0e3
Intensity, cps
13.28
4
8
12
16
20
24
28
32
36
Time, min

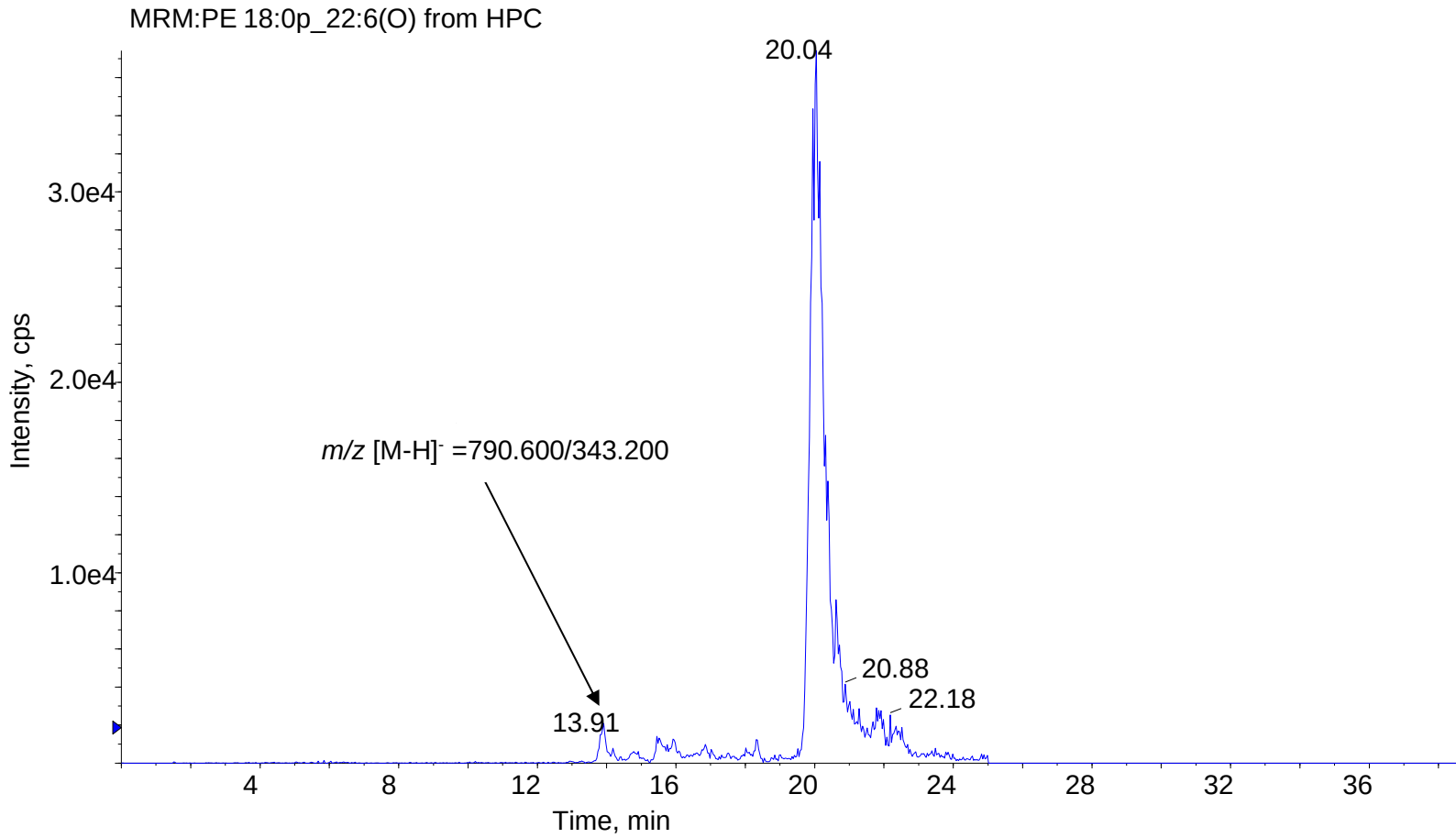
MRM:PE 18:0p_22:6(O) from HPC
20.04
3.0e4
2.0e4
1.0e4
Intensity, cps
m/z [M-H]- =790.600/343.200
13.91
20.88
22.18
4
8
12
16
20
24
28
32
36
Time, min

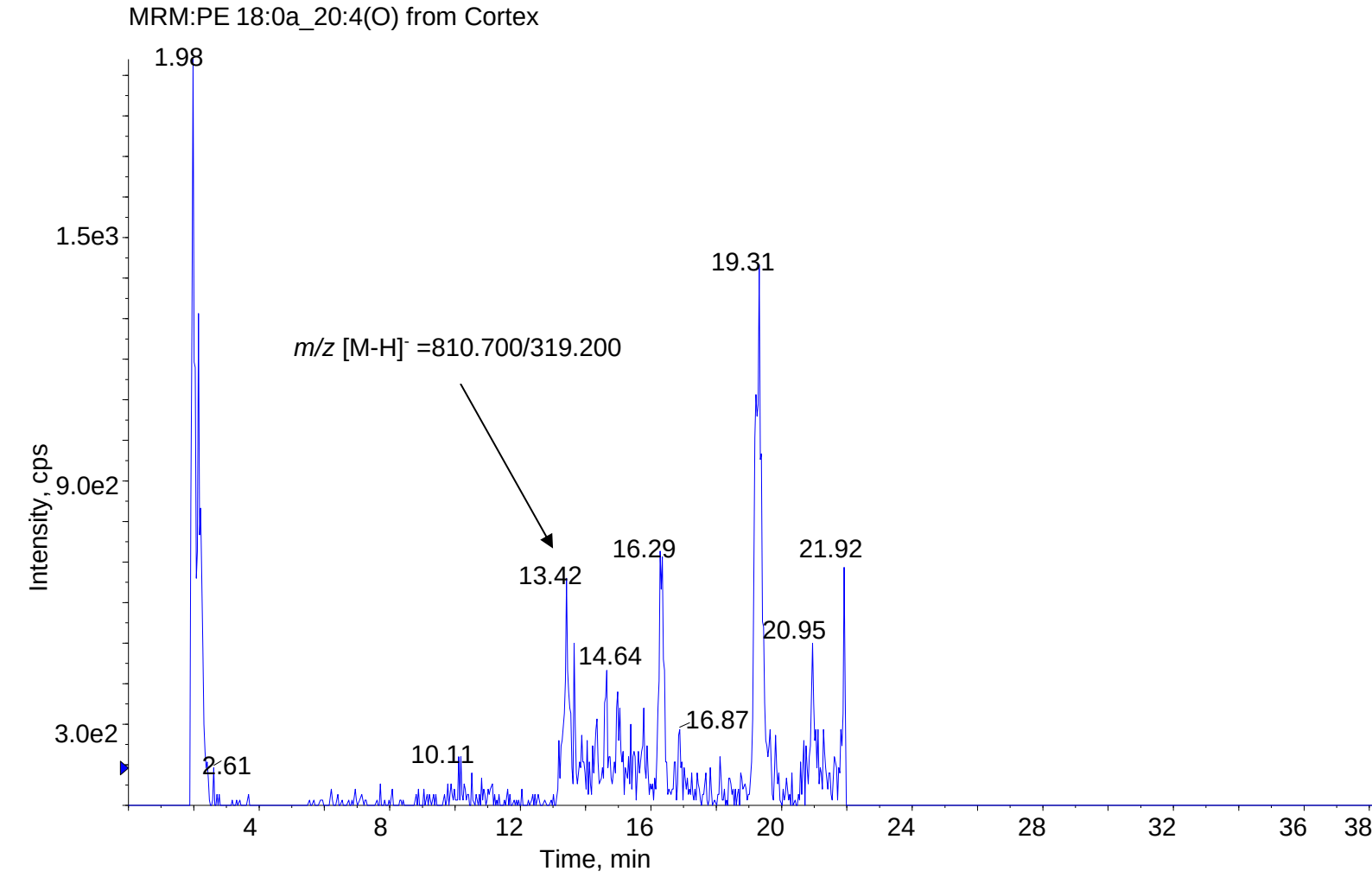
MRM:PE 18:0a_20:4(O) from Cortex
1.98
1.5e3
9.0e2
3.0e2
Intensity, cps
19.31
m/z [M-H]- =810.700/319.200
16.29
13.42
21.92
20.95
14.64
16.87
10.11
2.61
4
8
12
16
20
24
28
32
36
38
Time, min

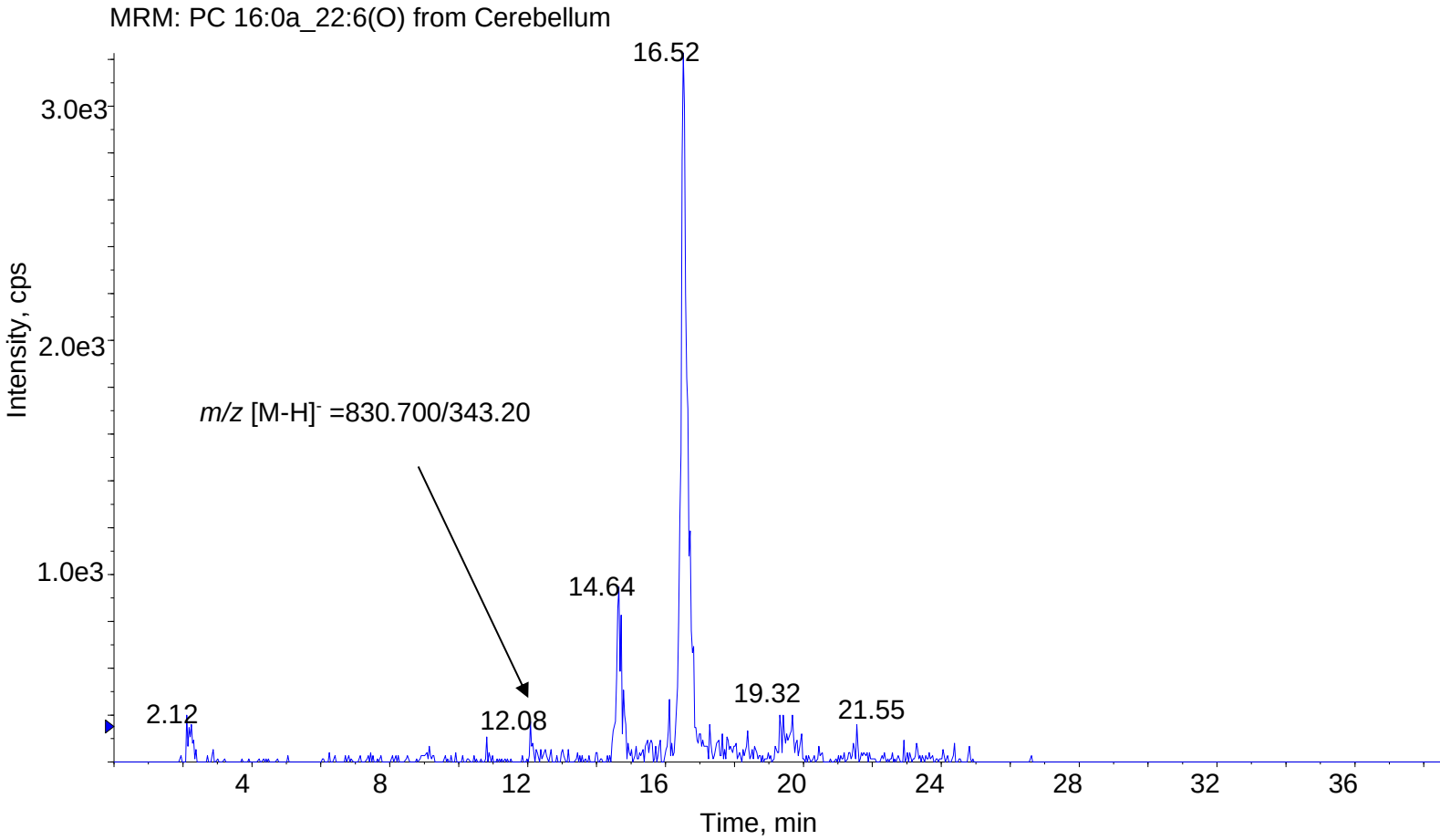
MRM: PC 16:0a_22:6(O) from Cerebellum
16.52
3.0e3
2.0e3
1.0e3
Intensity, cps
m/z [M-H]- =830.700/343.20
14.64
19.32
21.55
2.12
12.08
4
8
12
16
20
24
28
32
36
Time, min

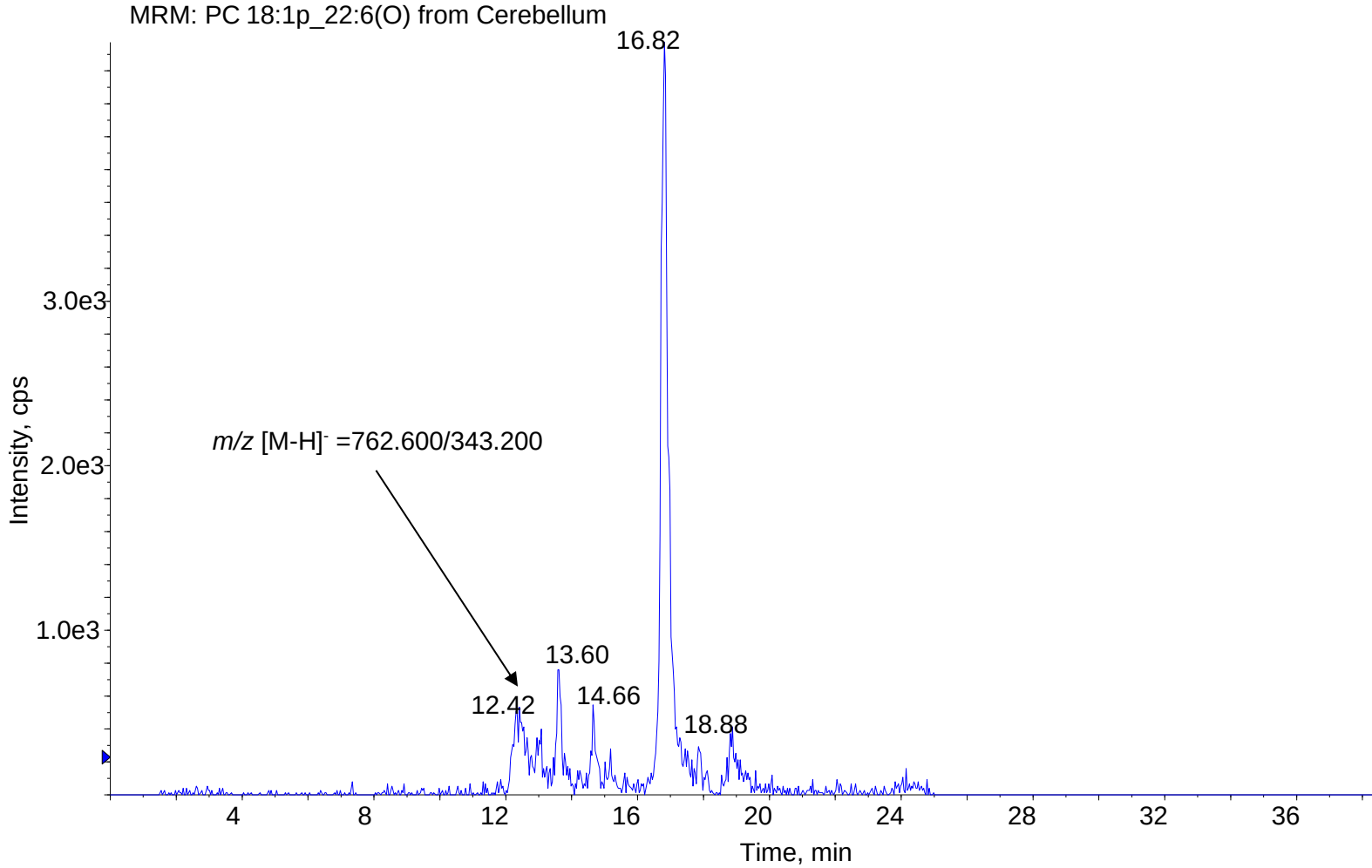
MRM: PC 18:1p_22:6(O) from Cerebellum
16.82
3.0e3
2.0e3
1.0e3
Intensity, cps
m/z [M-H]- =762.600/343.200
13.60
14.66
12.42
18.88
4
8
12
16
20
24
28
32
36
Time, min

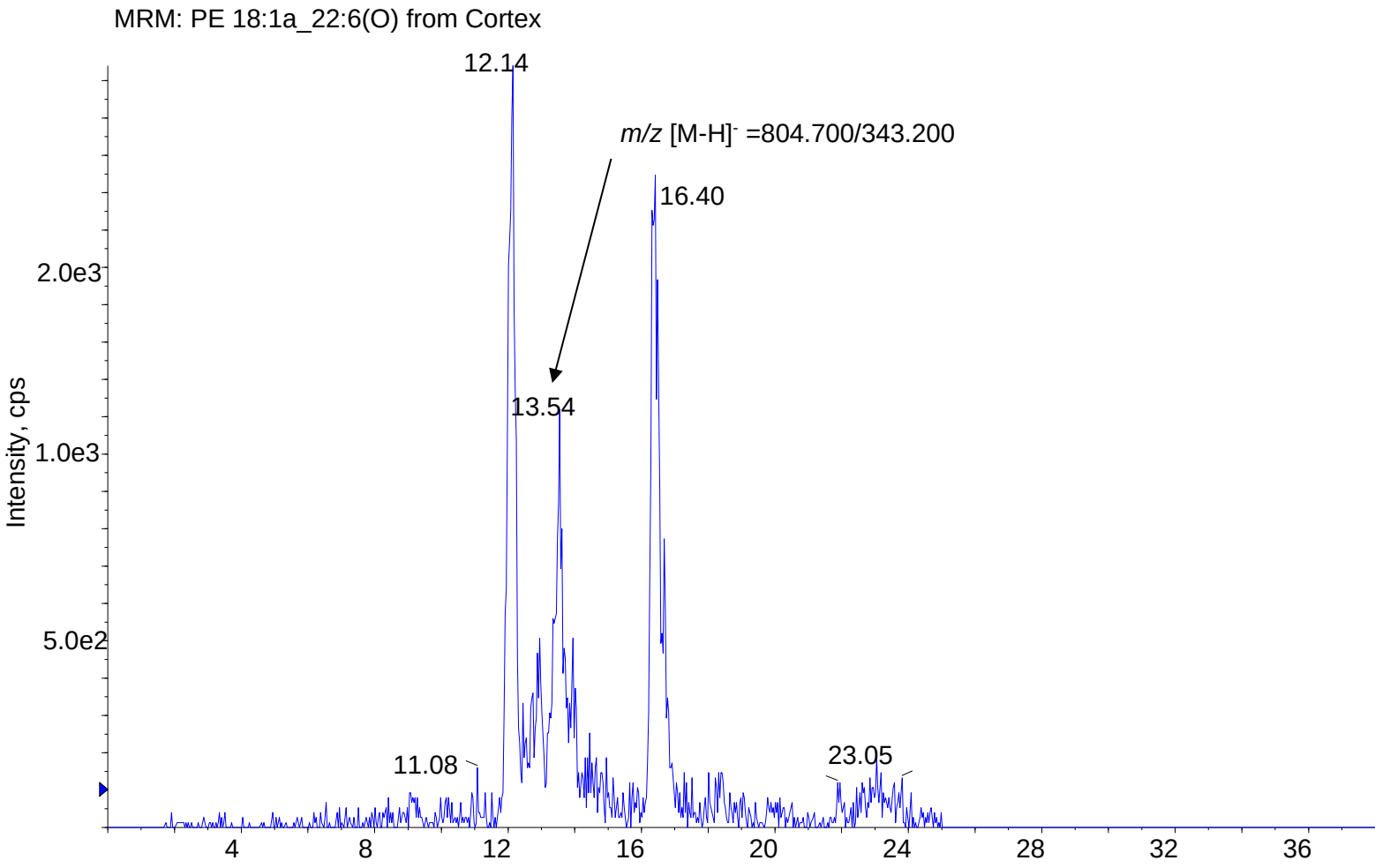
MRM: PE 18:1a_22:6(O) from Cortex
12.14
m/z [M-H]- =804.700/343.200
16.40
13.54
11.08
23.05
2.0e3
1.0e3
5.0e2
Intensity, cps
4
8
12
16
20
24
28
32
36
Time, min

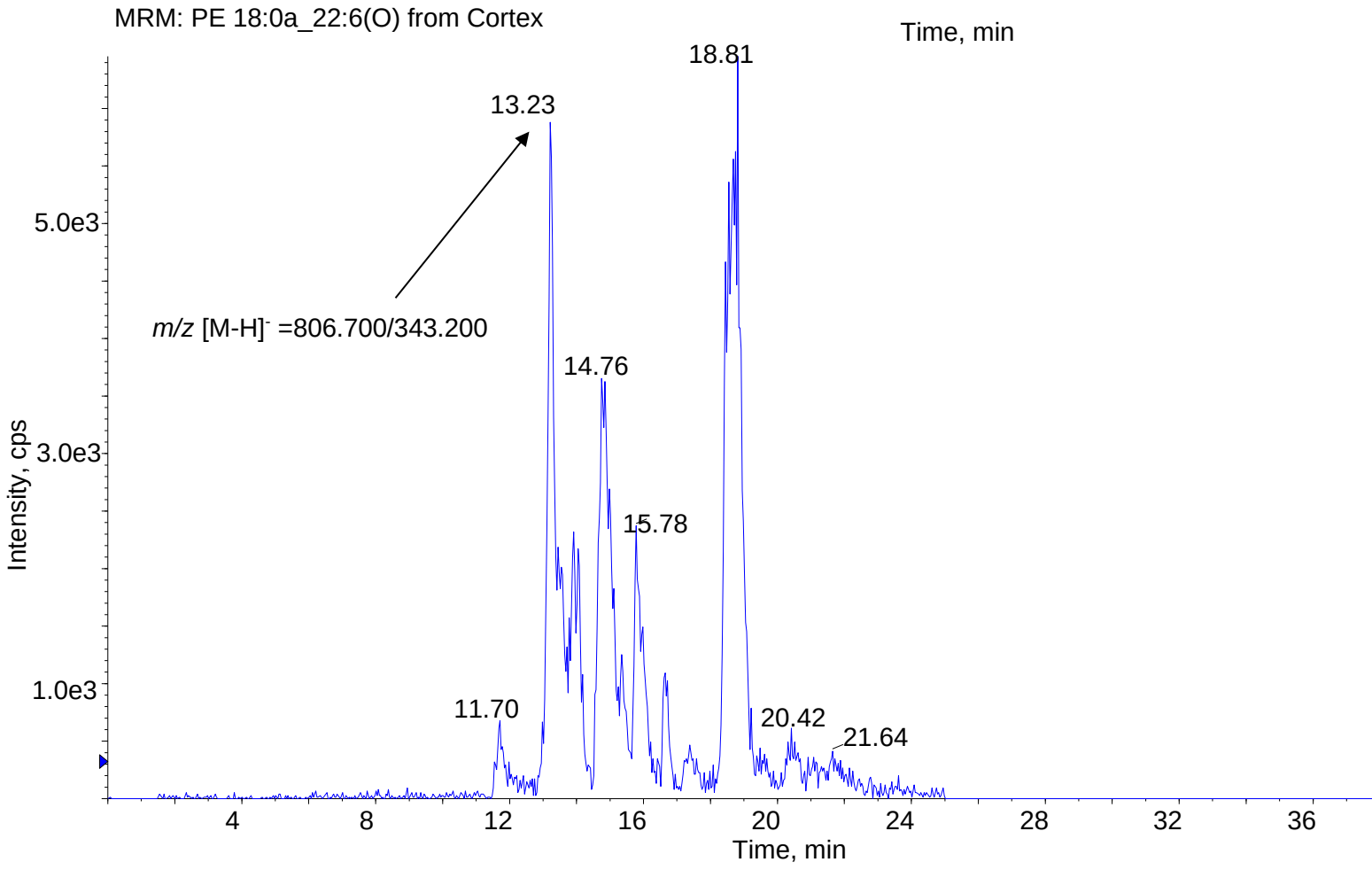
MRM: PE 18:0a_22:6(O) from Cortex
18.81
13.23
m/z [M-H]- =806.700/343.200
14.76
15.78
11.70
20.42
21.64
5.0e3
3.0e3
1.0e3
Intensity, cps
4
8
12
16
20
24
28
32
36
Time, min

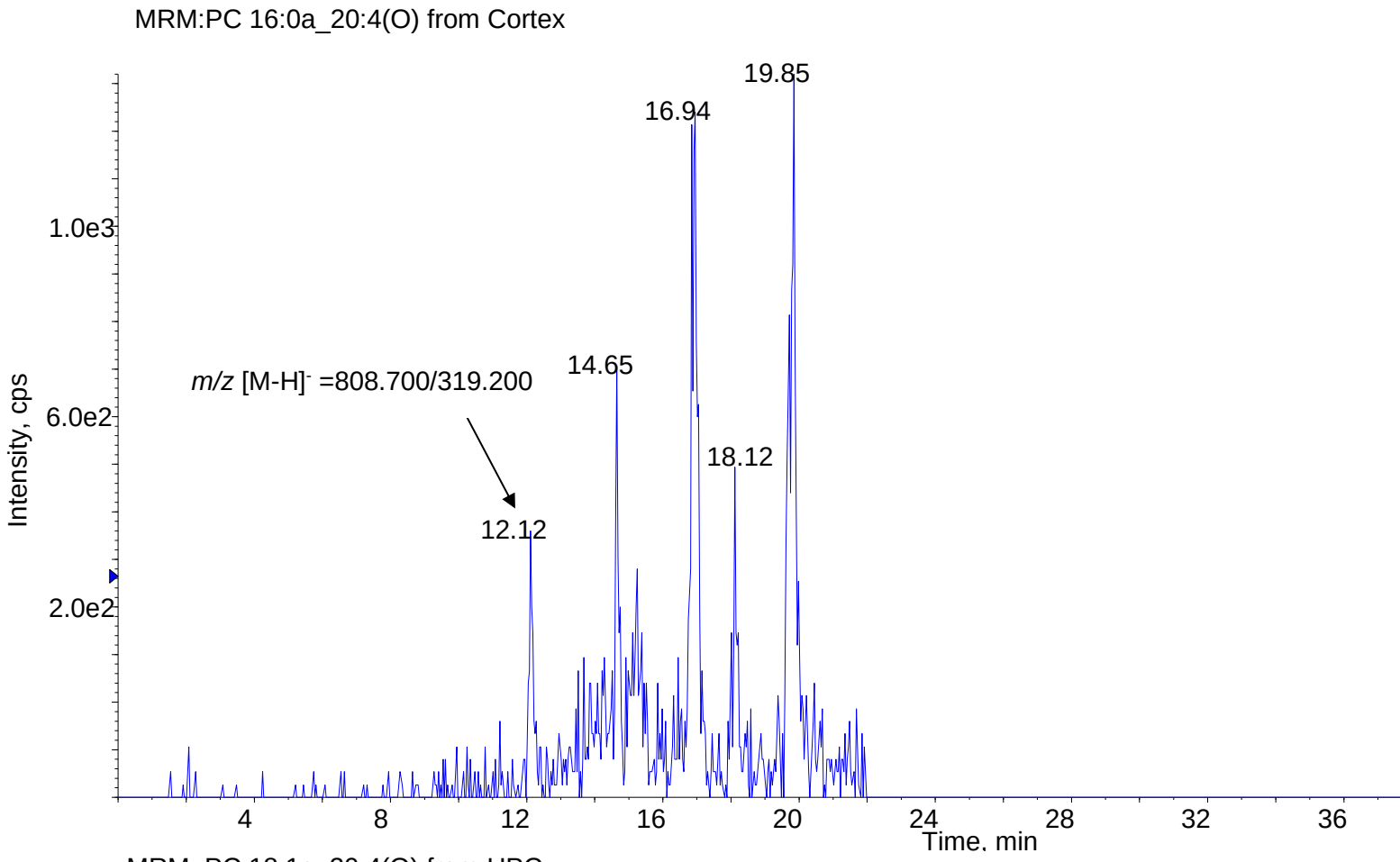
MRM:PC 16:0a_20:4(O) from Cortex
19.85
16.94
1.0e3
14.65
m/z [M-H]- =808.700/319.200
6.0e2
18.12
12.12
2.0e2
Intensity, cps
4
8
12
16
20
24
28
32
36
Time, min

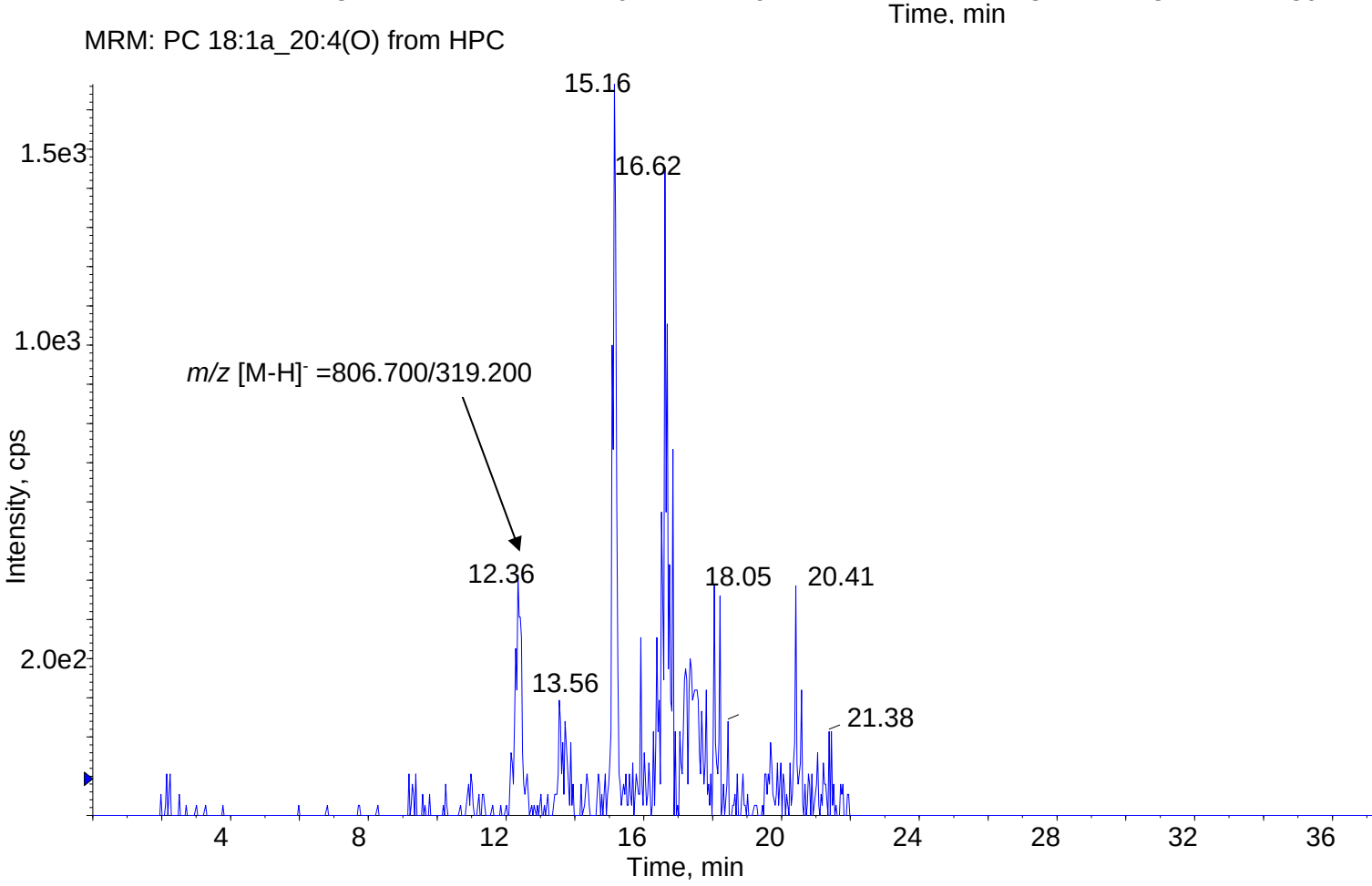
MRM: PC 18:1a_20:4(O) from HPC
15.16
1.5e3
16.62
1.0e3
m/z [M-H]- =806.700/319.200
12.36
18.05
20.41
2.0e2
13.56
21.38
Intensity, cps
4
8
12
16
20
24
28
32
36
Time, min

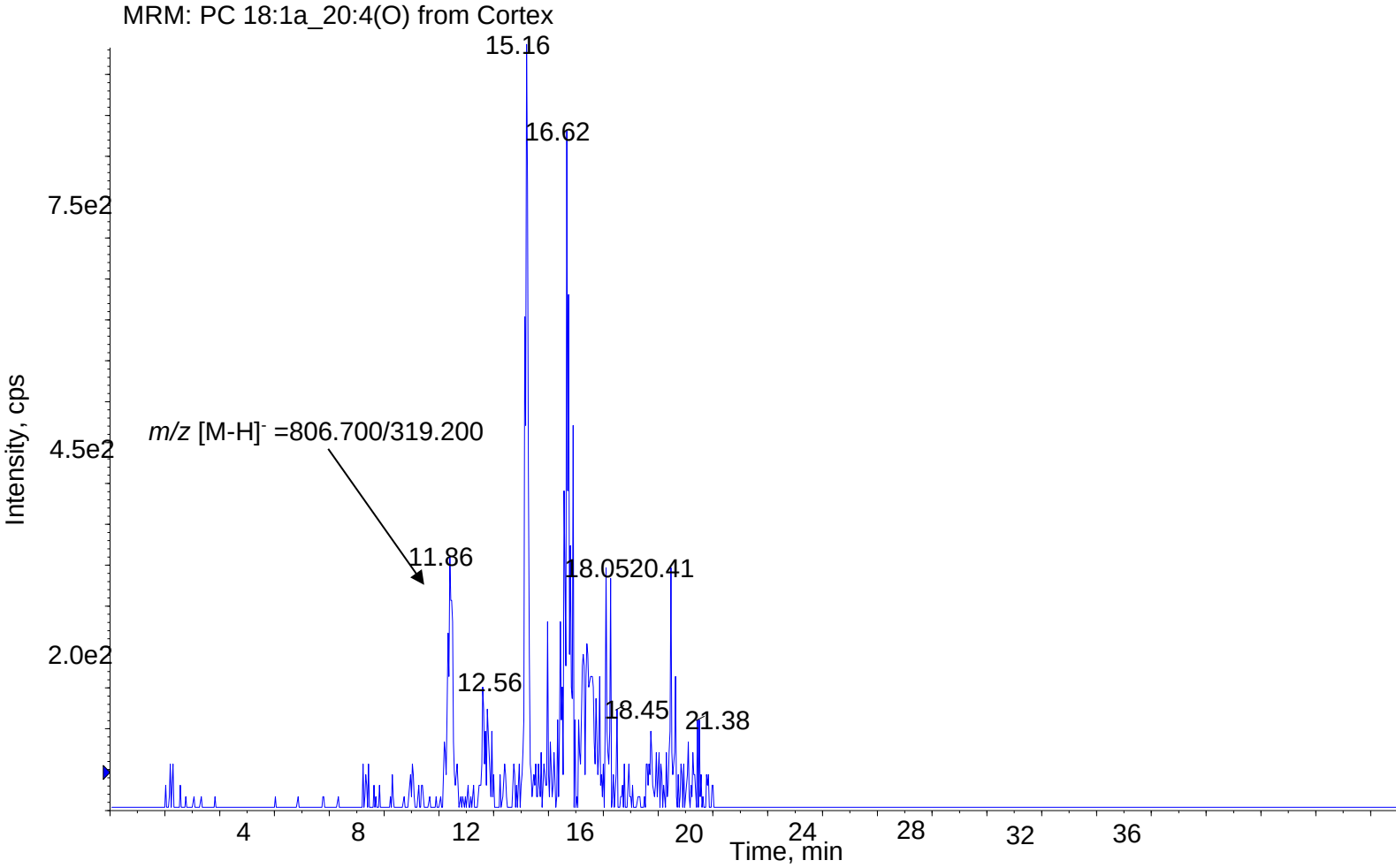
MRM: PC 18:1a_20:4(O) from Cortex
15.16
16.62
7.5e2
4.5e2
2.0e2
Intensity, cps
m/z [M-H]- =806.700/319.200
11.86
18.05
20.41
12.56
18.45
21.38
4
8
12
16
20
24
28
32
36
Time, min

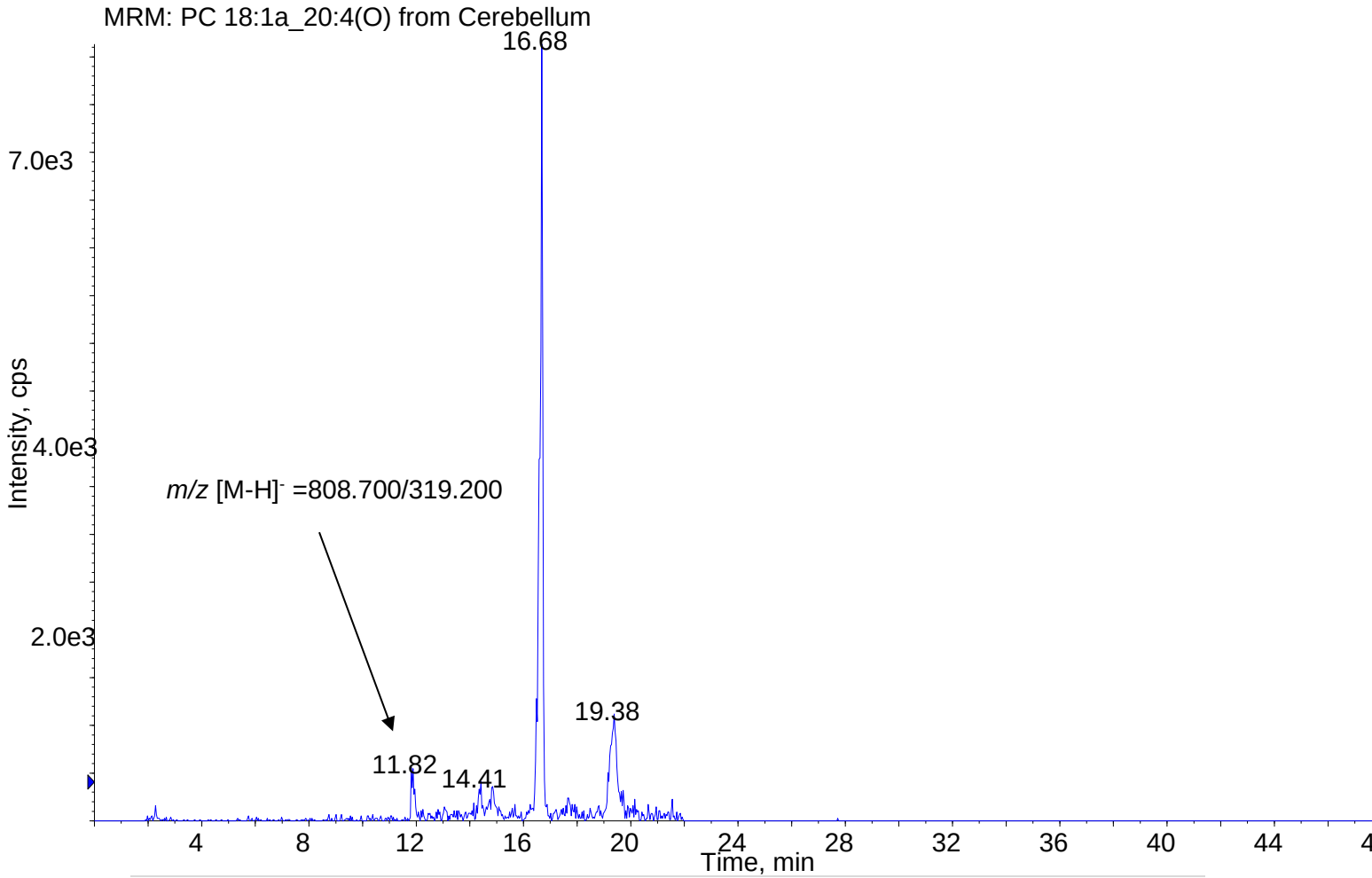
MRM: PC 18:1a_20:4(O) from Cerebellum
16.68
7.0e3
4.0e3
2.0e3
Intensity, cps
m/z [M-H]- =808.700/319.200
19.38
11.82
14.41
4
8
12
16
20
24
28
32
36
40
44
Time, min

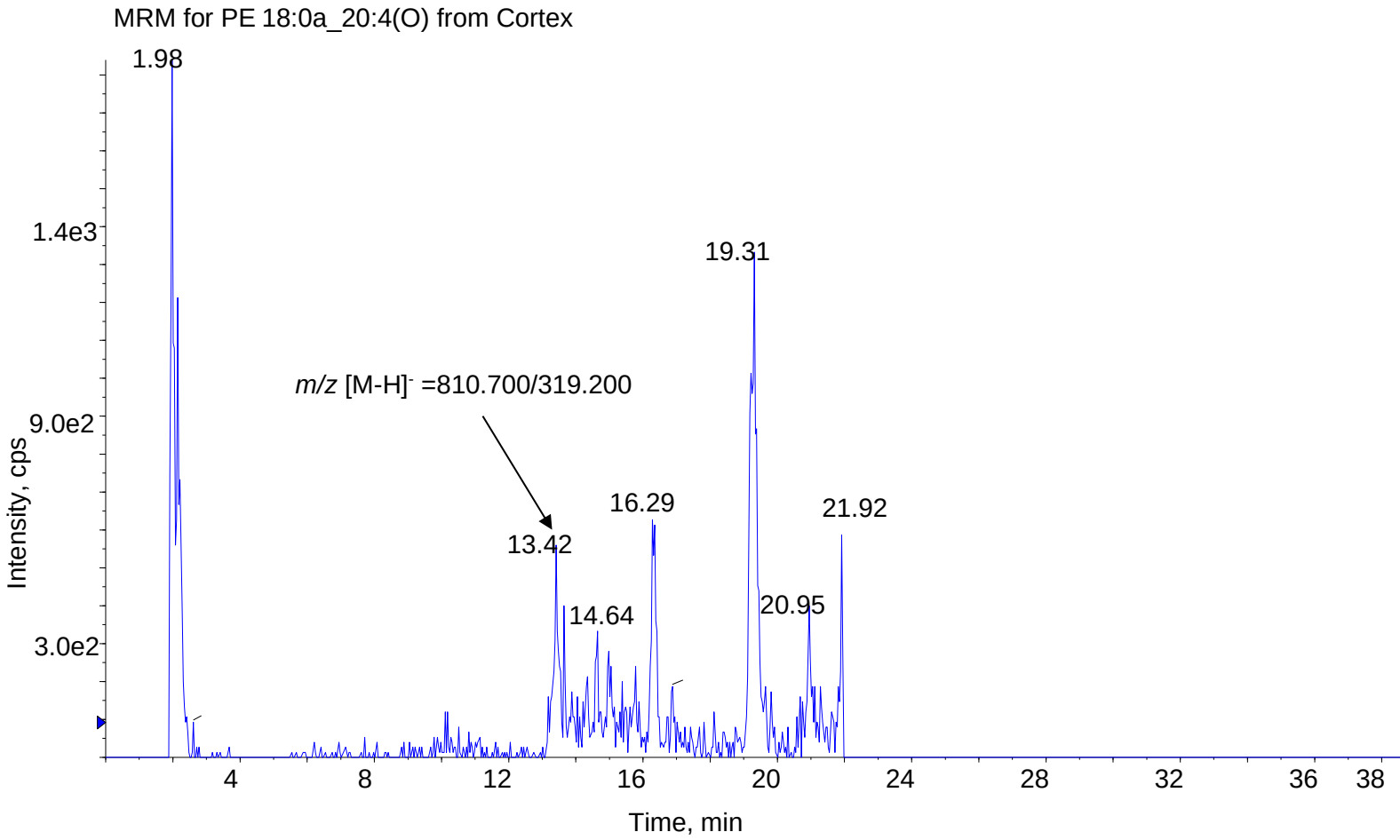

Figure 77. Representative MRM chromatograms for the eoxPL analysis analysed in negative ion mode as part of targeted lipidomic analysis of various brain regions in WT mice, monitoring precursor *m/z* to product ions. The WT brain lipids were extracted as described in Materials and Methods. The arrows show the peaks that were integrated for their analysis.

Table 13. Molecular species and precursor *m/z* of the lipids before and after oxygenation.

Native molecular Species/ Analytes	Precursor m/z (Q1) before oxygenation	Precursor m/z (Q1) after oxygenation	Oxidised molecular species	Product ion m/z (Q3)
PE(18:0/20:4)	766.600	782.600	PE 18:0a_20:4(O)	319.20
PE(P-18:1/22:6)	773.600	789.600	PE 18:1p_22:6(O)	343.20
PE(P-18:0/22:6)	775.600	790.600	PE 18:0p_22:6(O)	343.20
PE(18:0/22:4)	779.600	795.600	PE 18:0a_20:4(O)	319.20
PE(16:0/20:5)	764.600	780.600	PE 16:0a_20:5(O)	317.20
PE(18:1/22:6)	788.700	804.700	PE 18:1a_22:6(O)	343.20
PC(P-18:1/22:6)	746.600	762.600	PC 18:1p_22:6(O)	343.20
PE(18:0/22:6)	790.700	806.700	PE 18:0a_22:6(O)	343.20
PE(16:0/22:6)	762.600	778.600	PE 16:0a_22:6(O)	343.20
PE(P-16:0/20:4)	738.600	754.600	PE 16:0p_20:4(O)	319.20
PE(P-18:1/20:4)	749.000	766.600	PE 18:1p_20:4(O)	319.20
PE(P-18:0/20:4)	762.600	778.600	PE 18:0p_20:4(O)	319.20
PE(16:0/20:5)	736.600	752.600	PE 16:0a_20:5(O)	317.20
PE(P-16:0/22:6)	760.600	776.600	PE 16:0p_22:6(O)	343.20
PC(16:0/20:4)	790.700	806.700	PC 16:0a_20:4(O)	319.20

PC(16:0/20:4)	782.600	798.600	PC 16:0a_20:4(O)	319.20
PC(18:1/20:4)	790.700	806.700	PC 18:1a_20:4(O)	319.20
PC(18:0/20:4)	794.600	810.600	PC 18:0a_20:4(O)	319.20
PC(18:1/20:4)	810.700	826.700	PC 18:1a_20:4(O)	319.20
PC(16:0/22:6)	814.700	830.700	PC 16:0a_22:6(O)	343.20
PC(18:1/20:4)	808.700	826.700	PC 18:1a_20:4(O)	319.20

Next, EPI scan mode was operated for each precursor ion to confirm their proposed structures to obtain MS/MS spectra. Several different MRM transitions were chosen from the MS/MS spectra, as shown in Table 14. EPI scan mode uses the linear ion trap to trap the resulting fragments by operating a mass scan during specific elution time windows to particular ions. The product ion spectra were acquired from each lipid at the elution peak within the retention time for oxPL with precursor *m/z* 782.6, 780.6, 804.7, 762.6 and 806.7, respectively, as described in Materials and Methods.

For identity confirmation, MS/MS spectra were obtained; therefore, only one peak was identified for each positional isomer. Then, they were examined closely to determine whether they matched the proposed structure. Using this method, only the PE molecular species at *m/z* 782.6, *m/z* 780.6, *m/z* 762.6, m/z 804.7, and *m/z* 806.7 had sufficiently strong signals to help with identification, generating visible product ions at *m/z* 319.2 (HETE $[M\text{-}H]^-$), *m/z* 317.2 (HEPE $[M\text{-}H]^-$), and *m/z* 343.2 (HDOHE $[M\text{-}H]^-$) in negative ion mode. In general, the WT mouse brains were identified as PE, as follows PE 18:1p_HDOHE (*m/z* 762.6), PE 18:1a_HDOHE (*m/z* 804.7), PE 18:0a_HETE (*m/z* 782.6), PE 18:0a_HDOHE (*m/z* 806.7), and PE 18:0a_HEPE (*m/z* 780.6). Next, the positional isomers of PE containing HETEs, HEPEs and HDOHEs, respectively, were analysed (Table 15).

Following this, representative chromatograms of MRM transitions from various brain regions were provided in the following figures per individual lipid and chromatograms from MS/MS analysis for validation. Product ion scans were generated at the top of the peak for each precursor transition scanning from *m/z* 700 to 900 amu.

Table 14. Multiple reaction monitoring (MRM) transitions for the oxPL were analysed in negative ion mode as part of the targeted lipidomic analysis of various brain regions in WT mice.

ID Analyte	MRM transition	RT (min)
PE 18:0a_HETE	**782.600 → 319.200**	**13-15**
PE 18:0a_15-HETE	782.600 → 219.100	13.24
PE 18:0a_11-HETE	782.600 → 167.100	13.47
PE 18:0a_12-HETE	782.600 → 179.100	13.69
PE 18:0a_8-HETE	782.600 → 155.100	13.88
PE 18:0a_5-HETE	782.600 → 115.100	14.12
PE 18:0a_HEPE	**780.600 → 317.200**	**13-15**
PE 18:0a_15-HEPE	780.600 → 219.100	13.51
PE 18:0a_11-HEPE	780.600 → 167.100	13.67
PE 18:0a_12-HEPE	780.600 → 179.100	13.89
PE 18:1a_HDOHE	**804.700 → 343.200**	**13-15**
PE 18:1a_11-HDOHE	804.700 → 149.200	13.59
PE 18:1a_10-HDOHE	804.700 → 153.200	13.65
PE 18:1p_HDOHE	**762.600 → 343.200**	**13-15**
PE 18:1p_14-HDOHE	762.600 → 205.200	13.9
PE 18:1p_10-HDOHE	762.600 → 153.200	14.11

PE 18:1p_11-HDOHE	762.600 →149.200	14.24
PE 18:0a_HDOHE	**806.700 →343.200**	**13-15**
PE 18:0a_14-HDOHE	806.700 → 205.200	15.03
PE 18:0a_10-HDOHE	806.700 → 153.200	15.08

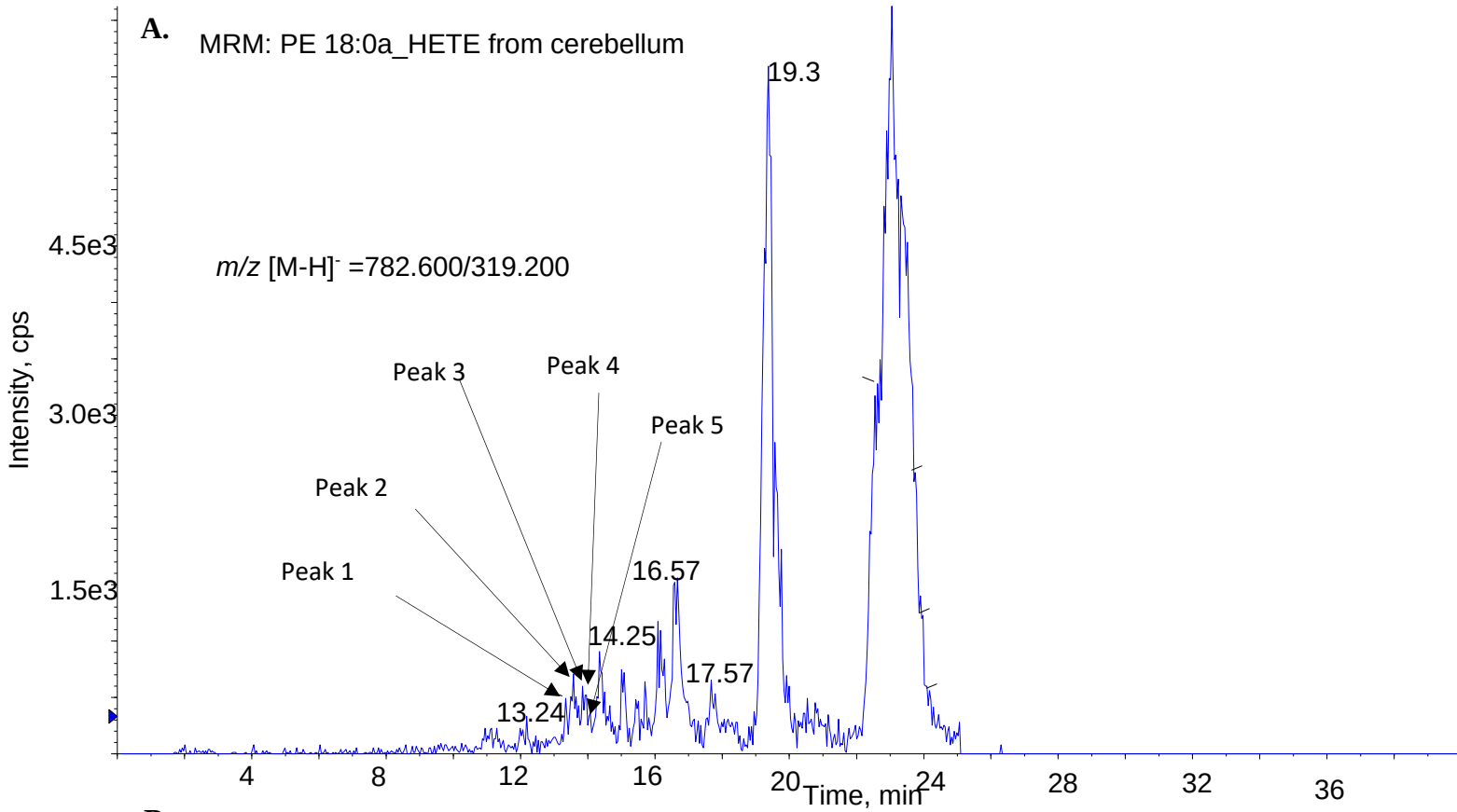
A.
MRM: PE 18:0a_HETE from cerebellum
19.3
4.5e3
m/z [M-H]- =782.600/319.200
Peak 3
Peak 4
Peak 5
Peak 2
3.0e3
Intensity, cps
Peak 1
16.57
1.5e3
14.25
17.57
13.24
4
8
12
16
20
24
28
32
36
Time, min

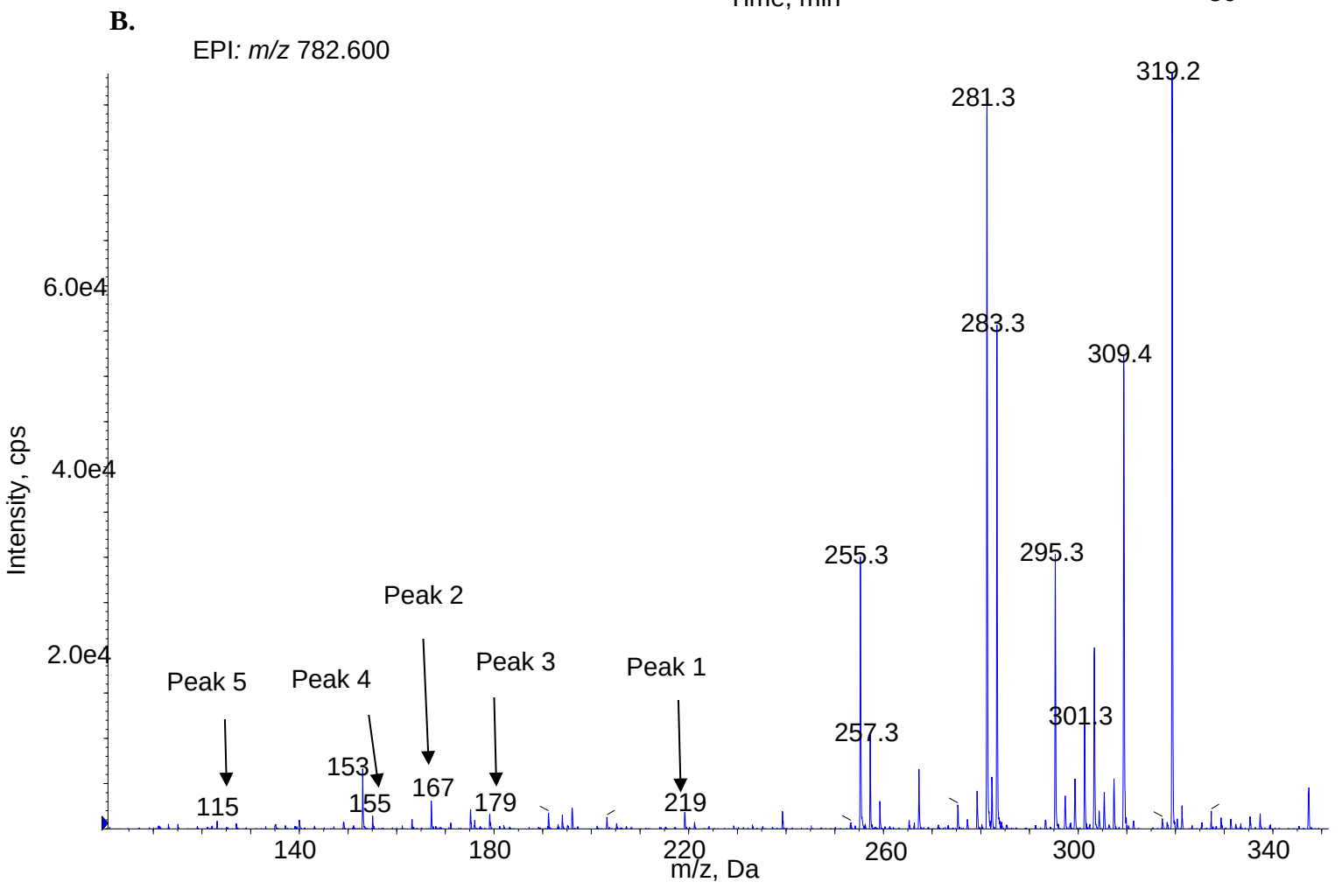
B.
EPI: m/z 782.600
319.2
281.3
6.0e4
283.3
309.4
4.0e4
Intensity, cps
255.3
295.3
Peak 2
2.0e4
Peak 5
Peak 4
Peak 3
Peak 1
301.3
257.3
153
167
115
155
179
219
140
180
220
260
300
340
m/z, Da

Figure 78. **Representative chromatogram showing structural identification of PE 18:0a_HETE at m/z 782.6, using MS/MS spectrum**. Panel A. Negative ion LC/MS/MS analysis using precursor m/z 782 to product m/z 319 MRM transitions. Brain lipid extracts were separated as described in Material and Methods using reverse phase HPLC and analysed using LC/MS/MS. Five prominent ions at m/z 782.6 were identified. Panel B. MS/MS spectrum extracted from chromatograms obtained from lipids eluting at RT 13-15 min.

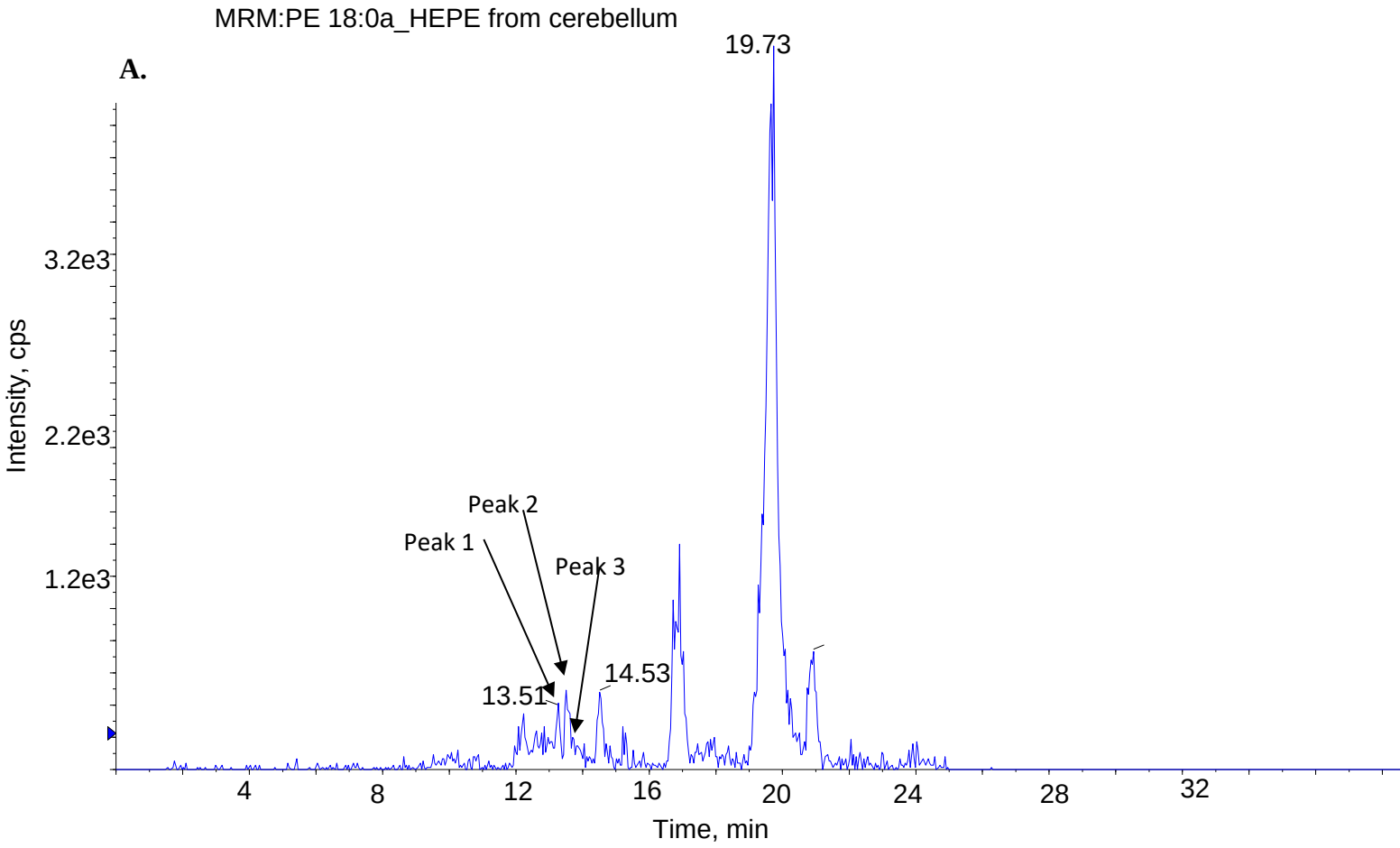
MRM:PE 18:0a_HEPE from cerebellum
A.
19.73
3.2e3
2.2e3
1.2e3
Intensity, cps
Peak 2
Peak 1
Peak 3
14.53
13.51
4
8
12
16
20
24
28
32
Time, min

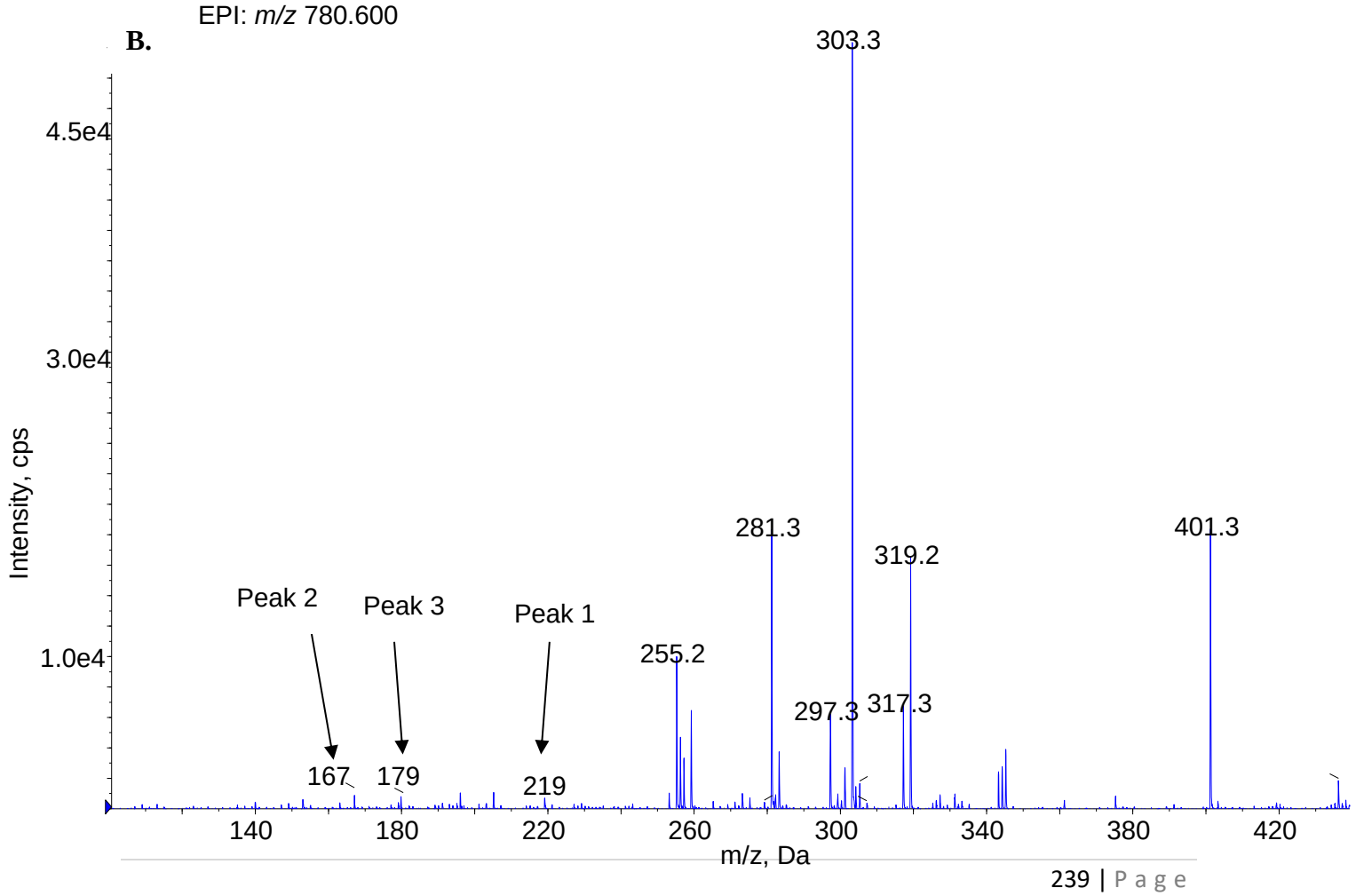
EPI: m/z 780.600
B.
303.3
4.5e4
3.0e4
1.0e4
Intensity, cps
281.3
319.2
401.3
Peak 2
Peak 3
Peak 1
255.2
297.3
317.3
167
179
219
140
180
220
260
300
340
380
420
m/z, Da

Figure 79. **Representative chromatogram showing structural identification of PE 18:0a_HEPE at m/z 780.6, using MS/MS spectrum**. Panel A. Negative ion LC/MS/MS analysis using precursor m/z 780.6 to product m/z 343.2 MRM transitions. Brain lipid extracts were separated as described in Material and Methods using reverse phase HPLC and analysed using LC/MS/MS. Five prominent ions at m/z 780.6 were identified. Panel B. MS/MS spectrum extracted from chromatograms obtained from lipids eluting at RT 13-15 min.

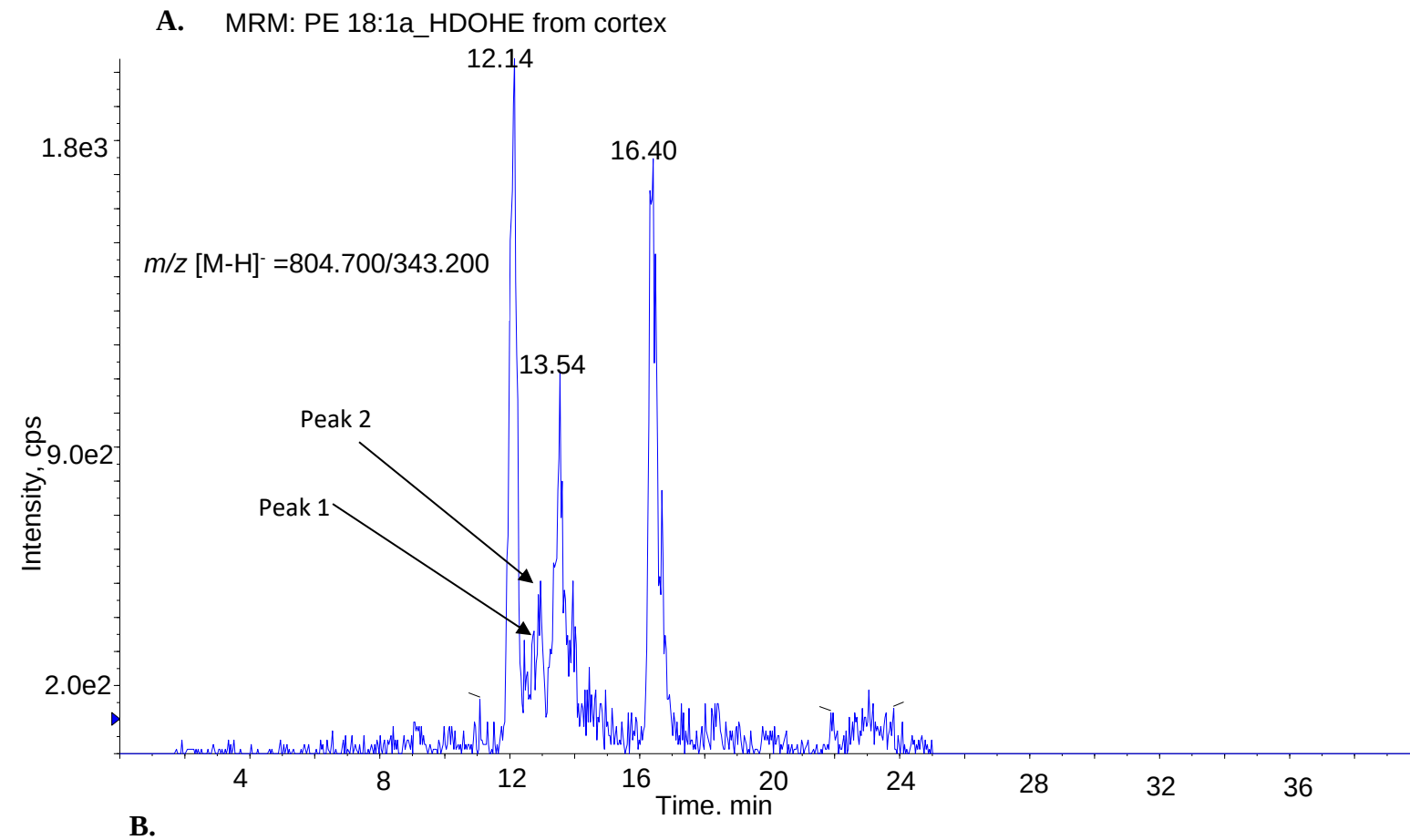
A.
MRM: PE 18:1a_HDOHE from cortex
12.14
16.40
13.54
1.8e3
9.0e2
2.0e2
m/z [M-H]- =804.700/343.200
Peak 2
Peak 1
Intensity, cps
4
8
12
16
20
24
28
32
36
Time. min

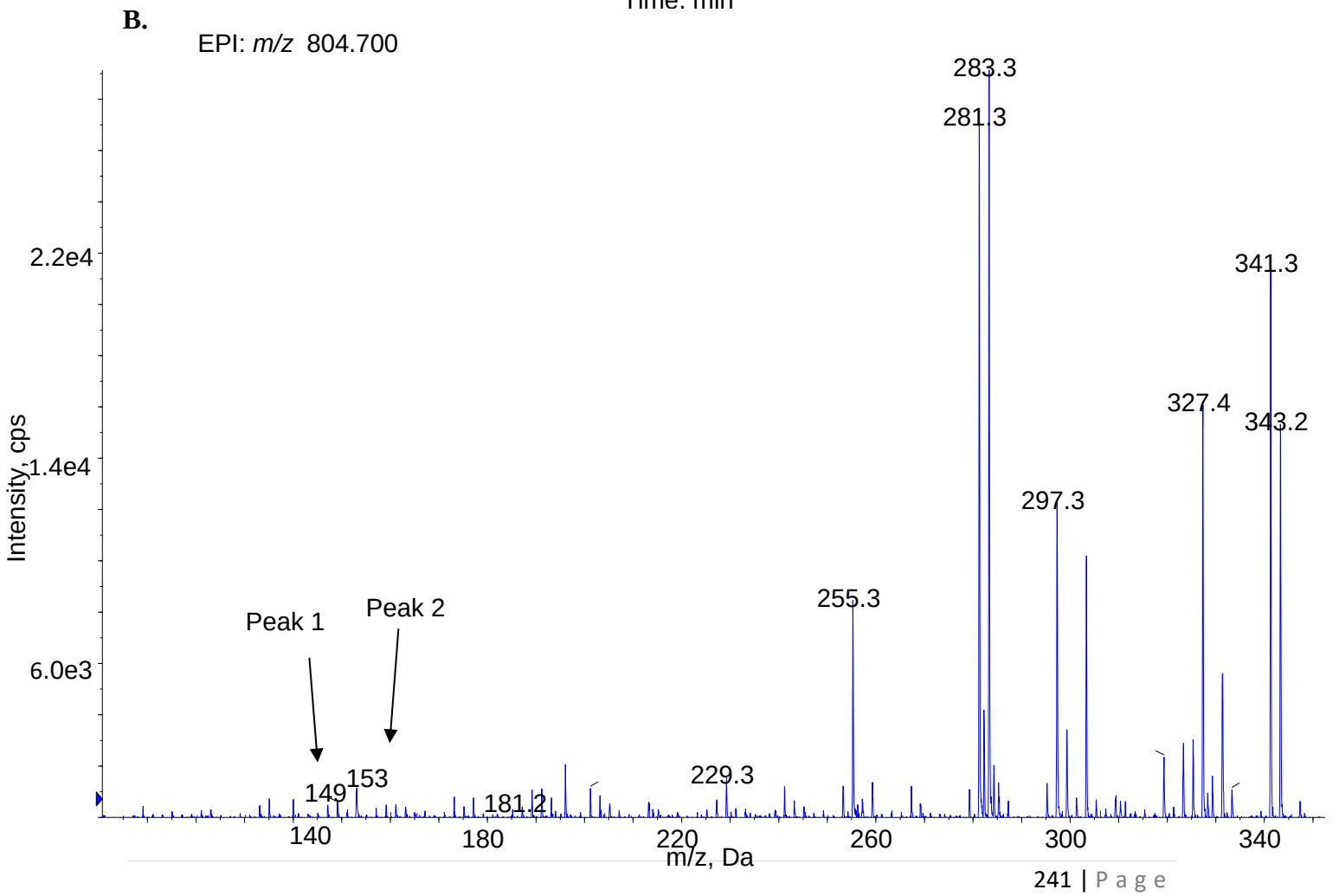
B.
EPI: m/z 804.700
283.3
281.3
341.3
327.4
343.2
297.3
255.3
2.2e4
1.4e4
6.0e3
Peak 1
Peak 2
149
153
181.2
229.3
Intensity, cps
140
180
220
260
300
340
m/z, Da

Figure 80. Representative chromatogram showing structural identification of PE 18:1a_HETE at m/z 804.7, using MS/MS spectrum. Panel A. Negative ion LC/MS/MS analysis using precursor m/z 804.7 to product m/z 343.2 MRM transitions. Brain lipid extracts were separated as described in Material and Methods using reverse phase HPLC and analysed using LC/MS/MS. Five prominent ions at m/z 804.7 were identified. Panel B. MS/MS spectrum extracted from chromatograms obtained from lipids eluting at RT 13-15 min

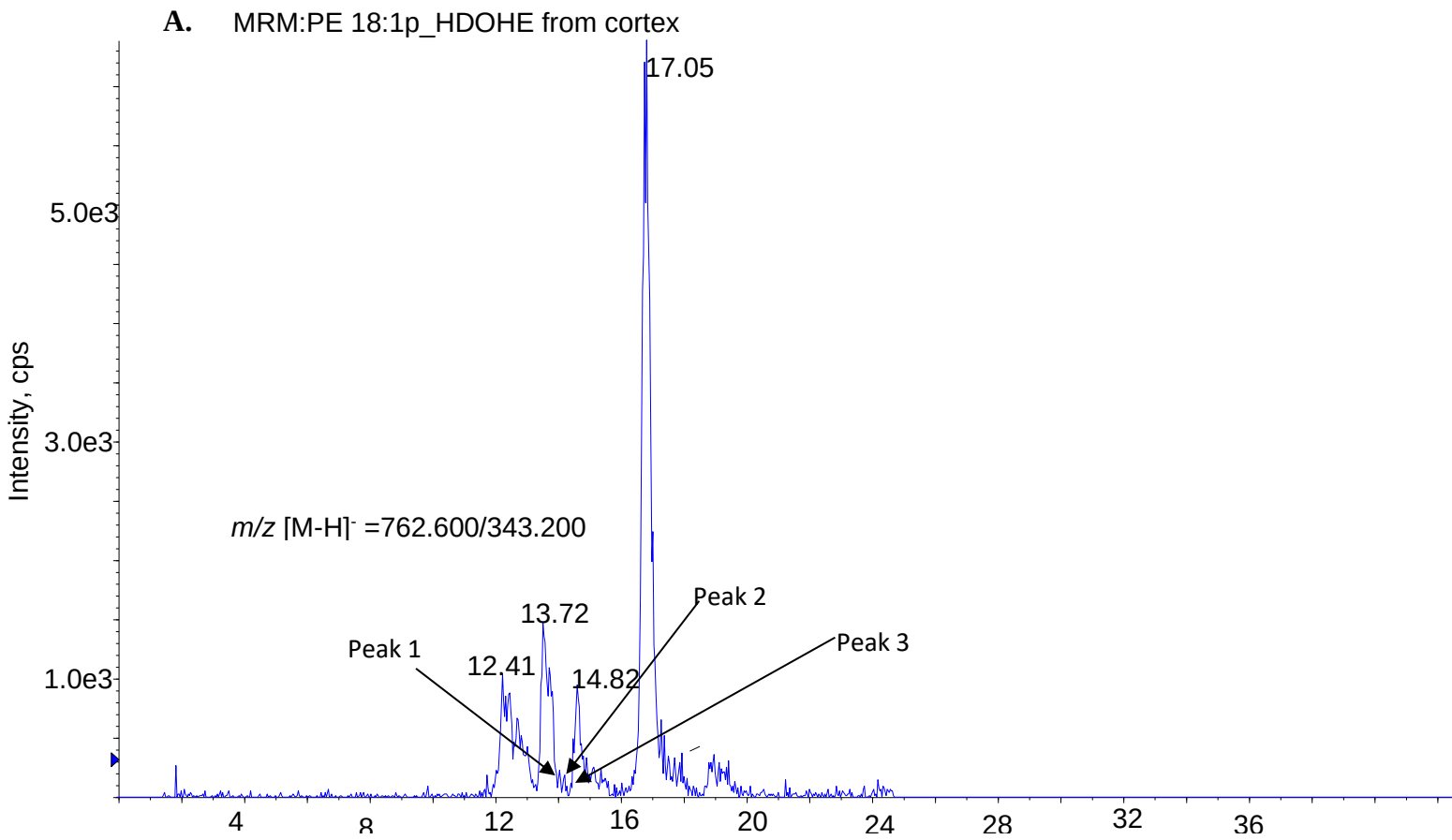
A.
MRM:PE 18:1p_HDOHE from cortex
17.05
5.0e3
3.0e3
1.0e3
Intensity, cps
m/z [M-H]- =762.600/343.200
13.72
Peak 2
Peak 1
Peak 3
12.41
14.82
4
8
12
16
20
24
28
32
36

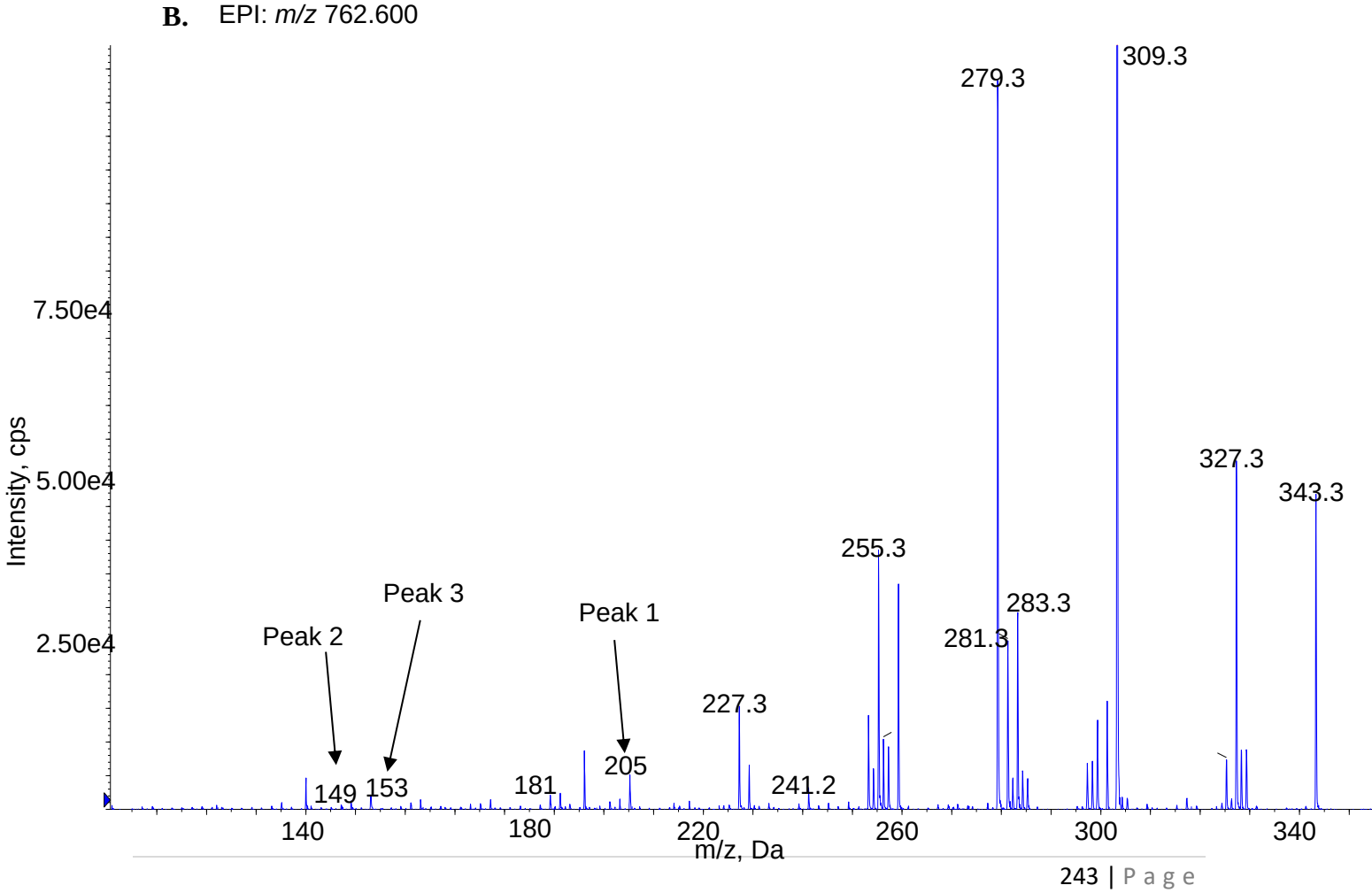
B.
EPI: m/z 762.600
309.3
279.3
7.50e4
5.00e4
2.50e4
Intensity, cps
327.3
343.3
255.3
283.3
Peak 3
Peak 1
281.3
Peak 2
227.3
205
149
153
181
241.2
140
180
220
260
300
340
m/z, Da

Figure 81. **Representative chromatogram showing structural identification of PE 18:1p_HDOHE at m/z 762.6, using MS/MS spectrum**. Panel A. Negative ion LC/MS/MS analysis using precursor m/z 762 to product m/z 343.2 MRM transitions. Brain lipid extracts were separated as described in Material and Methods using reverse phase HPLC and analysed using LC/MS/MS. Five prominent ions at m/z 762.6 were identified. Panel B. MS/MS spectrum extracted from chromatograms obtained from lipids eluting at RT 13-15 min.

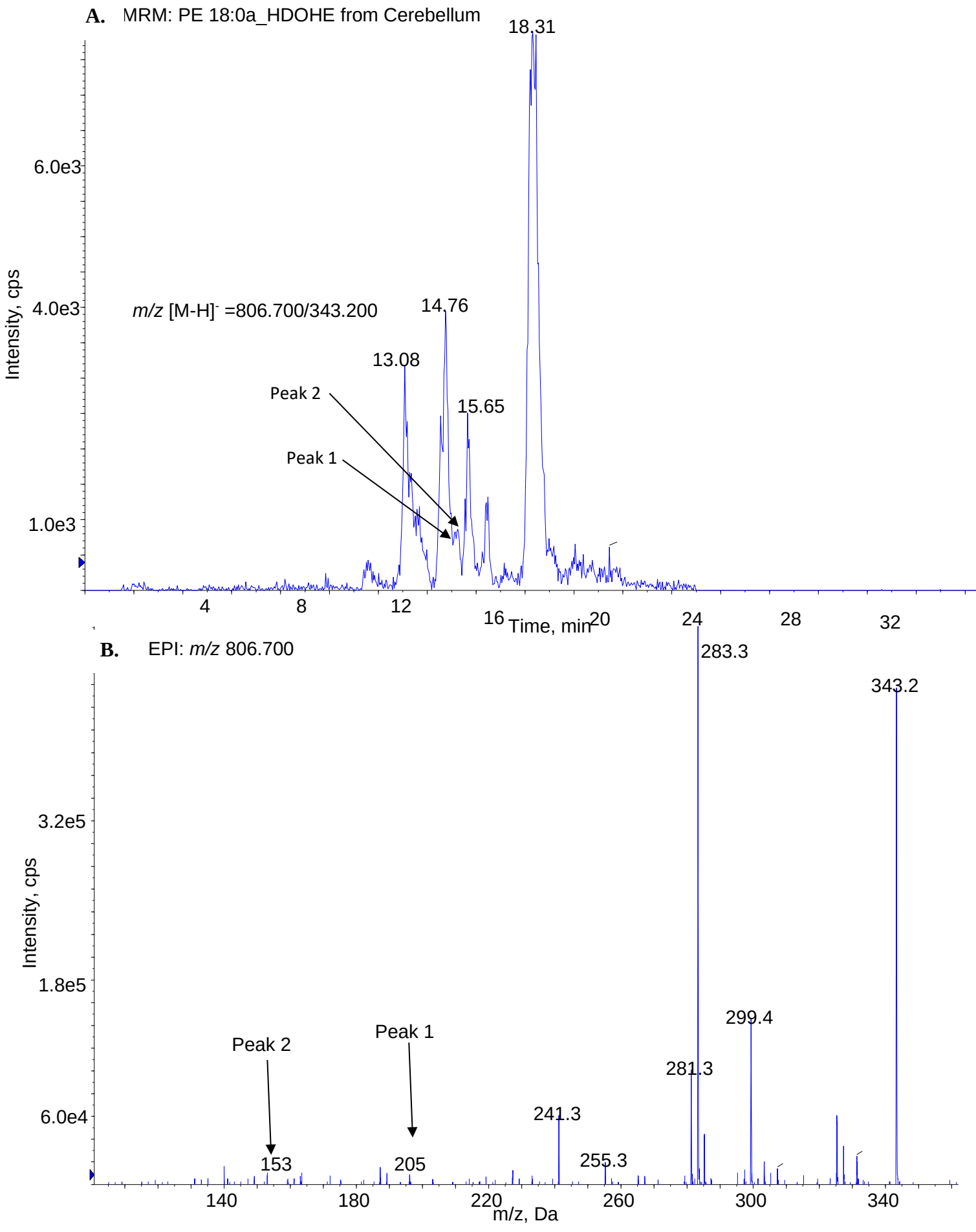
A.
MRM: PE 18:0a_HDOHE from Cerebellum
18.31
6.0e3
4.0e3
1.0e3
Intensity, cps
m/z [M-H]- =806.700/343.200
14.76
13.08
Peak 2
15.65
Peak 1
4
8
12
16
20
24
28
32
Time, min
B.
EPI: m/z 806.700
283.3
343.2
3.2e5
1.8e5
6.0e4
Intensity, cps
299.4
Peak 2
Peak 1
281.3
241.3
153
205
255.3
140
180
220
260
300
340
m/z, Da

Figure 82. Representative chromatogram showing structural identification of PE 18:0a_HDOHE at *m/z* 806.7 using MS/MS spectrum. Panel A. Negative ion LC/MS/MS analysis using precursor m/z 806.7 to product *m/z* 343.2 MRM transitions. Brain lipid extracts were separated as described in Material and Methods using reverse phase HPLC and analysed using LC/MS/MS. Five prominent ions at m/z 806.7 were identified. Panel B. MS/MS spectrum extracted from chromatograms obtained from lipids eluting at RT 13-15 min.

Next, the actual peaks were integrated. That was used to determine relative amounts of different positional isomers of HETEs, HEPEs and HDOHEs by using the same precursor ion with other product ions for each lipid.

The MRM transitions were monitored by the precursor-to-product transition arising from collision-induced dissociation to give a major product ion for HETE-PEs at *m/z* 319.2. Product ion spectra were acquired at the top of each LC elution peak containing all *m/z* 319.2. MS/MS for PE molecules species containing a HETE functional group in Q3 (*m/z* 319.2) showed the presence of multiple ions, particularly five major ions, at *m/z* 782.6, eluting between 13- 15 min. All five coeluted, as a big mixture of isomers, with the same retention time as a oxPE standard in the 13-15 min window (Figure 78 A). In the WT brain, the peak at *m/z* 782 corresponds to 18:0a, confirming the structure as PE 18:0a_HETE. The first peak (Peak 1) that elutes at R.T. 13.24 through the precursor *m/z* 782 to *m/z* 219.1 transition, represents the 15-HETE confirming the positional isomer structure as PE 18:0a_15-HETE, as shown in Figure 78A. The next peaks are 11-HETE-PE eluting at R.T. 13.47, 12-HETE-PE eluting at R.T. 13.69, 8-HETE-PE eluting at R.T. 13.88 and 5-HETE-PE eluting at R.T. 14.12 (Peaks 2-5) (Figure 78 A). In the case of HETE-PEs, elution between 13-15 min was used to identify each isomer containing 18:0a at *sn1* and 20:4(O)/HETE at *sn2* (Figure 78 B). Although the evidence of HETE-positional isomers was challenging, especially since the presence of 12-HETE-PE and 8-HETE-PE were very weak, *m/z* 319.2 exists for the intact oxylipin.

Next, LC/MS/MS analysis for PE containing a HEPE functional group = (*m/z* 317.2) in Q3, using reverse-phase HPLC, is shown in Figure 79. For *m/z* 780.6, product ion spectra were obtained by following a product ion at *m/z* 317.2. With Q3 set at 317.2, three ions were seen to elute between 13 - 15 min (Figure 79 A). All three peaks coeluted within the same retention 13-15 min window. In the WT brain, *m/z* 780.6 corresponds to 18:0a at the *Sn1* position, confirming the structure as PE 18:0a_HEPE and showing the fragmentation for all three HEPE-containing species. The first peak (Peak 1) that elutes at R.T. 13.51 in the precursor *m/z* 780.6 to *m/z* 219.1 transition identifies the 15-HEPE containing PE isomer. The second peak, Peak 2, is the 11-HEPE-PE that elutes in R.T. 13.67 through the precursor *m/z* 780.6 to *m/z* 167.1 transition and the third peak, (Peak 3) represents the 12-HEPE-PE that elutes in R.T. 13.89 through the precursor *m/z* 780.6 to *m/z* 179.1 transition (Figure 79 A). Subsequently, the ions, eluting between 13-15 min, were proposed as HEPE-PEs containing 18:0a at S*n1* and 20:5(O) at the s*n2* position (Figure 79 B).

Following this, the lipids containing a HDOHE functional group (*m/z* 343.2) in Q3 were

analysed in LC/MS/MS, using precursor *m/z* 804.7 to product *m/z* 343.2. For *m/z* 804.7, the product ion spectra were generated, and two distinct ions were eluted between 13 and 15 min. These two peaks were coeluted within the same retention window between 13 and 15 min, demonstrating the fragmentation of two HDOHE-containing PE molecular species (Figure 80 A). Peak 1 elutes in R.T. 13.59 through the precursor *m/z* 804.7 to product *m/z* 149.2 transition, stating the 11-HDOHE-PE, while Peak 2 is subjected to the precursor *m/z* 804.7 to *m/z* 153.2 transition, corresponding to 10-HDOHE-PE eluting in R.T 13.65, as shown in Figure 80 A. Consequently, the ions, eluting between 13-15 min, are suggested as PEs containing 18:1a at *sn1* and 22:6(O) at s*n2* positions (Figure 80 B).

The following lipids containing a HDOHE functional group (*m/z* 343.2) in Q3 were displayed in Figure 81. MS/MS spectra were acquired and assigned the fragmentation for three HDOHE-PEs at *m/z* 762.6, representing plasmalogen species (Figure 81 A). During elution between the 13-15 min window, the specific positional isomers were detected, monitoring from the precursor ion at *m/z* 762.6 to product ion *m/z* 343.2 transitions. The first peak (Peak 1), corresponding to PE 18:1p_14-HDOHE, elutes in the R.T. 13.9 through the precursor *m/z* 762.6 to product *m/z* 205.2 transition. The second peak (Peak 2) is the PE 18:1p_11-HDOHE eluting in R.T. 14.11 through the precursor *m/z* 762.6 to product *m/z* 149.2 transition, while Peak 3 is PE 18:1p_10-HDOHE and elutes in R.T. 14.24 through the precursor *m/z* 762.6 to product *m/z* 153.2 transition, as shown in Figure 81 B. Therefore the ions, eluting between 13-15 min, are demonstrated as PEs containing 18:1p at S*n1* and a 22:6(O) at s*n2* positions (Figure 81 B).

Next, a similar strategy has been followed as previously. MS/MS spectra have obtained the presence of two ions for HDOHE-PEs at *m/z* 343.2 in Q3 and demonstrated two different ions at *m/z* 806.7. The two coeluted, as a big mixture of isomers, within the same retention window between the 13-15 min (Figure 82 A). The WT brain contains two HDOHE-containing PE molecular species, with each comprising two positional isomers containing 14-HDOHE-PE that are subjected to the precursor *m/z* 806.7 to product *m/z* 205.2 transition, eluting in R.T. 15.03 (Peak 1), and also the 10-HDOHE-PE, which elutes in R.T. 15.08 through the precursor *m/z* 806.7 to product *m/z* 153.2 transition (Peak 2), as illustrated in Figure 82. Thus, these are proposed as HDOHE- containing PEs containing 18:0a at *Sn1* and 22:6(O) at *Sn2* positions (Figure 82 B).

7.5 LC/MS/MS analysis suggests diverse eoxPLs in *Alox15*$^{-/-}$ mice

The area under the curve for the precursor ion to product ion was integrated and normalised to the internal standard DMPE and expressed relative to the weight of brain tissue analysed. Since there was no access to primary standards for these eoxPL, the data generated is comparative only. According to their *m/z* values and MS/MS fragmentation patterns, the transitions identified in Table 15 in the WT mouse brain were proposed to compare the relative abundance of each eoxPL between WT and *Alox15*$^{-/-}$ mice.

A close inspection of the chromatograms reveals that the chromatographic peaks were weak and poorly resolved, and thus the quality of the data presented for this comparison is relatively low. Specifically, these lipids are present in low abundance in brain tissue. Representative MRM chromatograms in negative ion mode are shown in Figure 83.

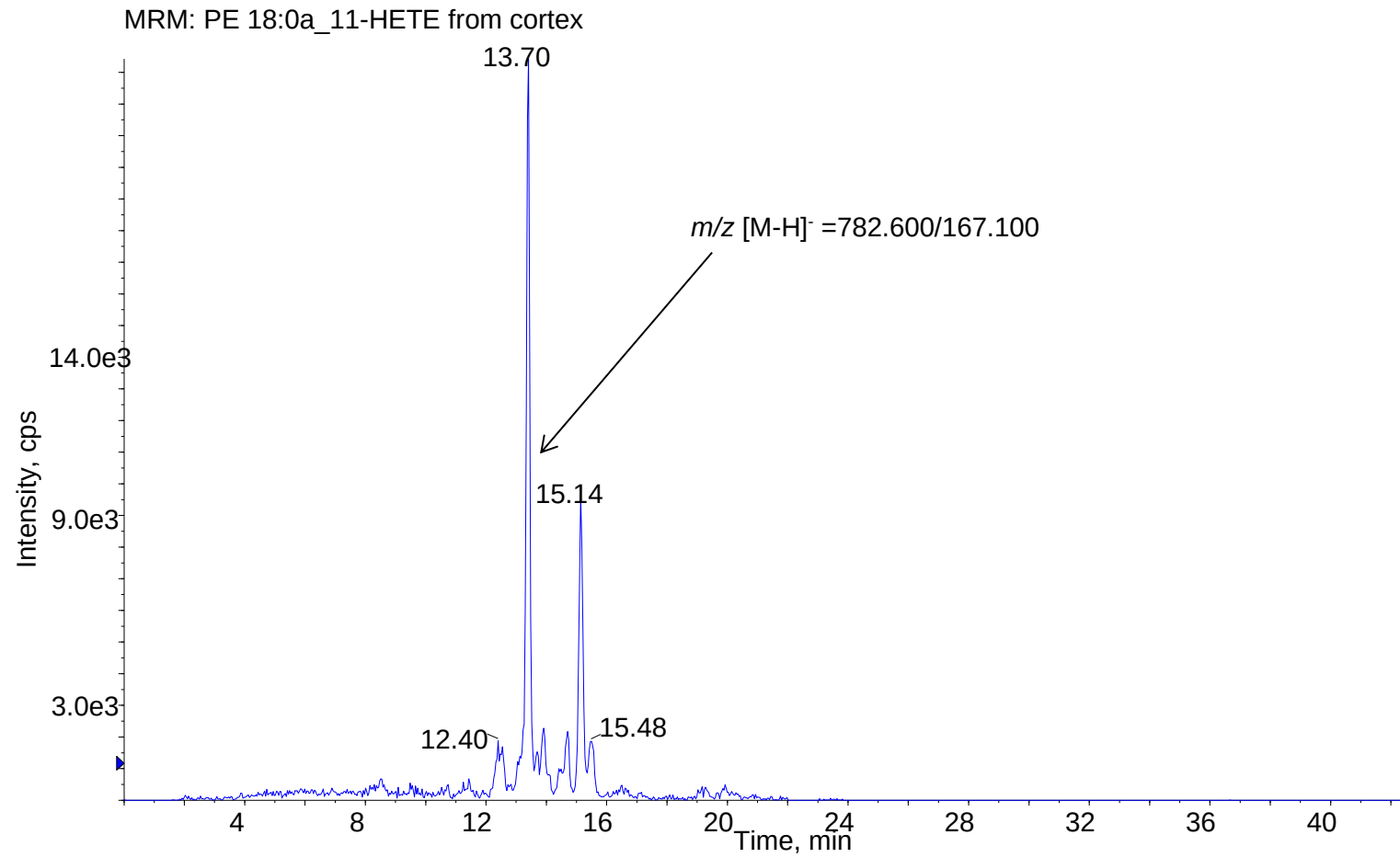
MRM: PE 18:0a_11-HETE from cortex
13.70
m/z [M-H]- =782.600/167.100
14.0e3
9.0e3
3.0e3
Intensity, cps
15.14
12.40
15.48
4
8
12
16
20
24
28
32
36
40
Time, min

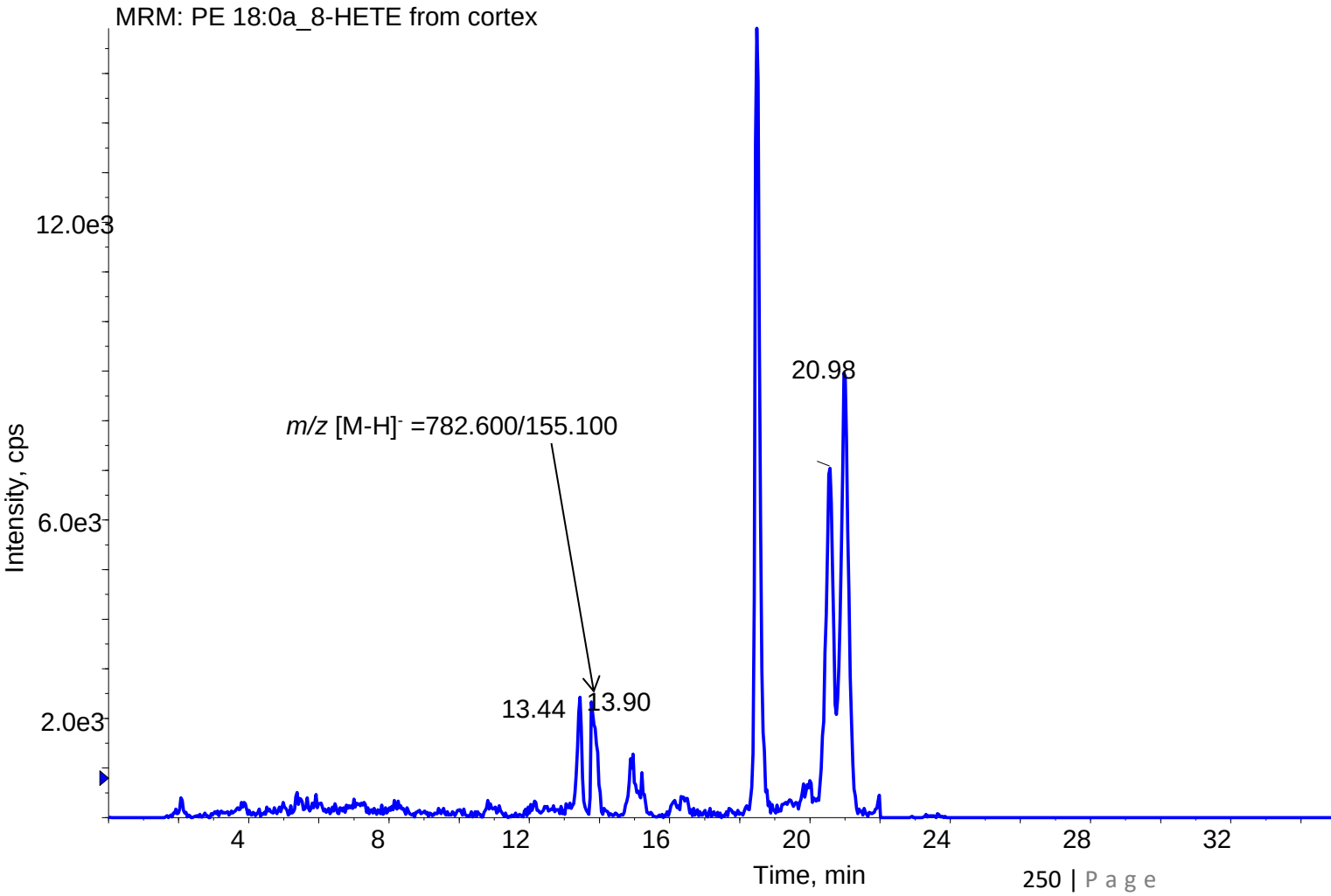
MRM: PE 18:0a_8-HETE from cortex
12.0e3
6.0e3
2.0e3
Intensity, cps
20.98
m/z [M-H]- =782.600/155.100
13.44
13.90
4
8
12
16
20
24
28
32
Time, min

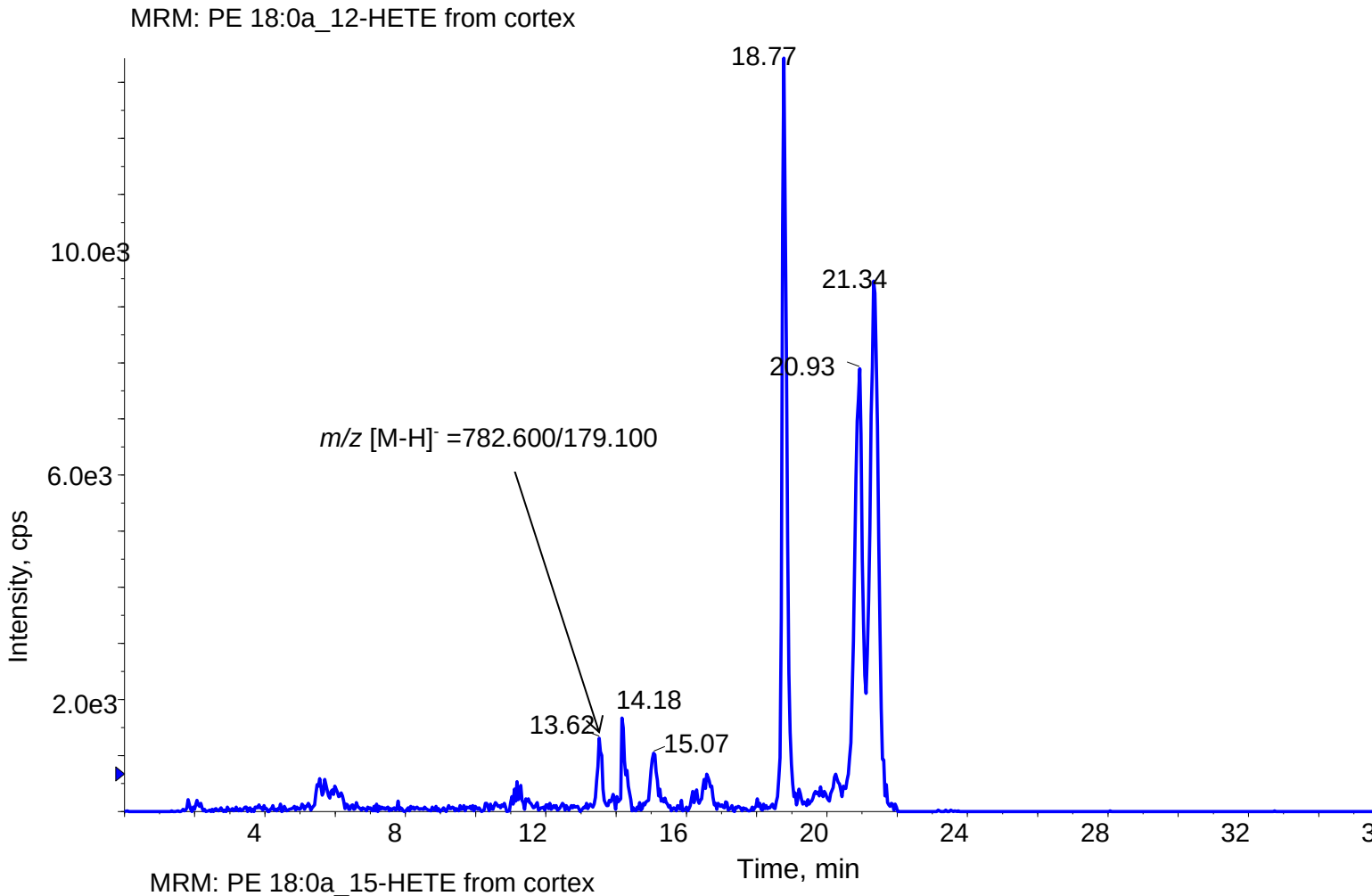
MRM: PE 18:0a_12-HETE from cortex
18.77
10.0e3
21.34
20.93
m/z [M-H]- =782.600/179.100
6.0e3
Intensity, cps
2.0e3
14.18
13.62
15.07
4
8
12
16
20
24
28
32
Time, min

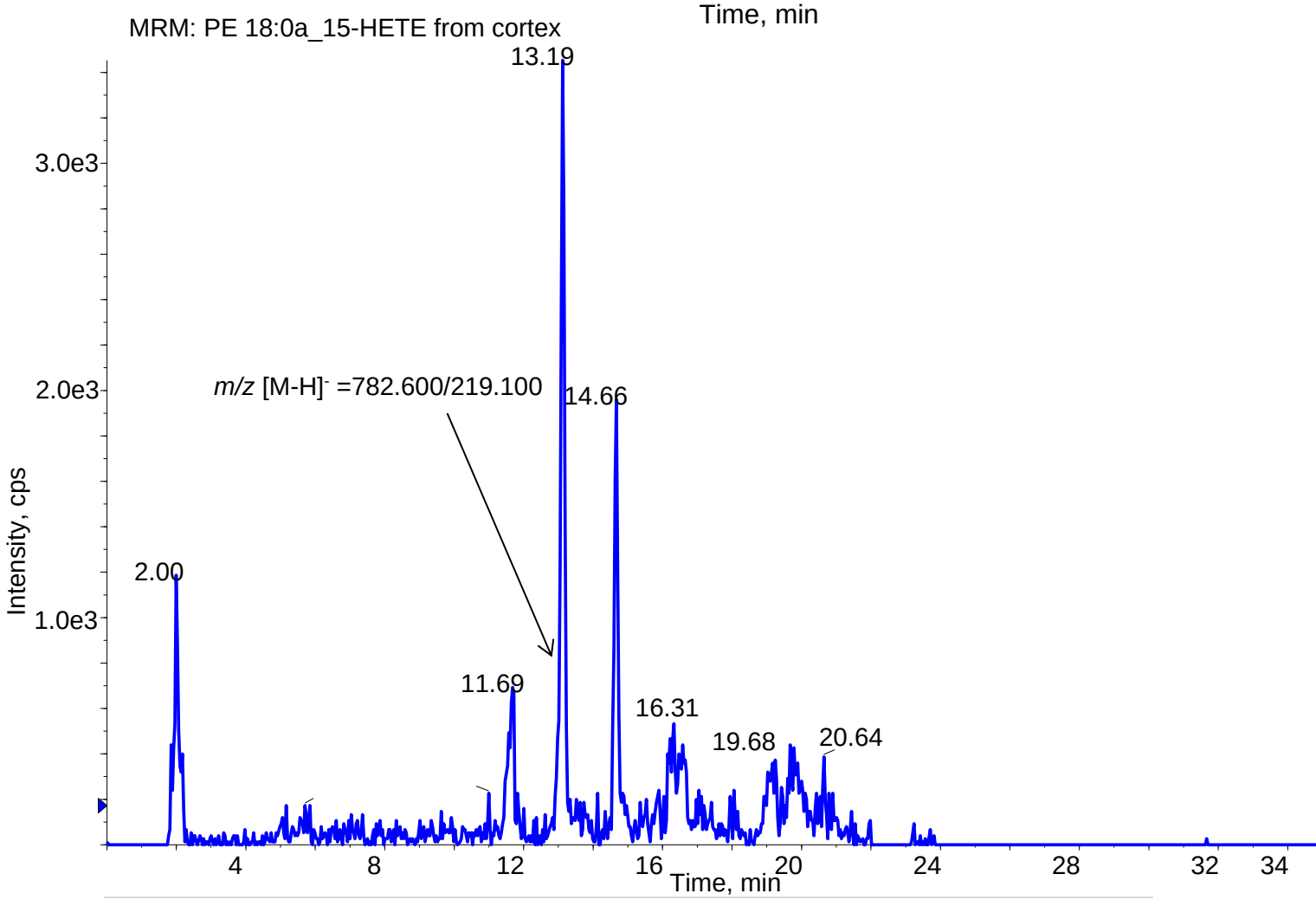
MRM: PE 18:0a_15-HETE from cortex
13.19
3.0e3
m/z [M-H]- =782.600/219.100
14.66
2.0e3
Intensity, cps
2.00
1.0e3
11.69
16.31
19.68
20.64
4
8
12
16
20
24
28
32
34
Time, min

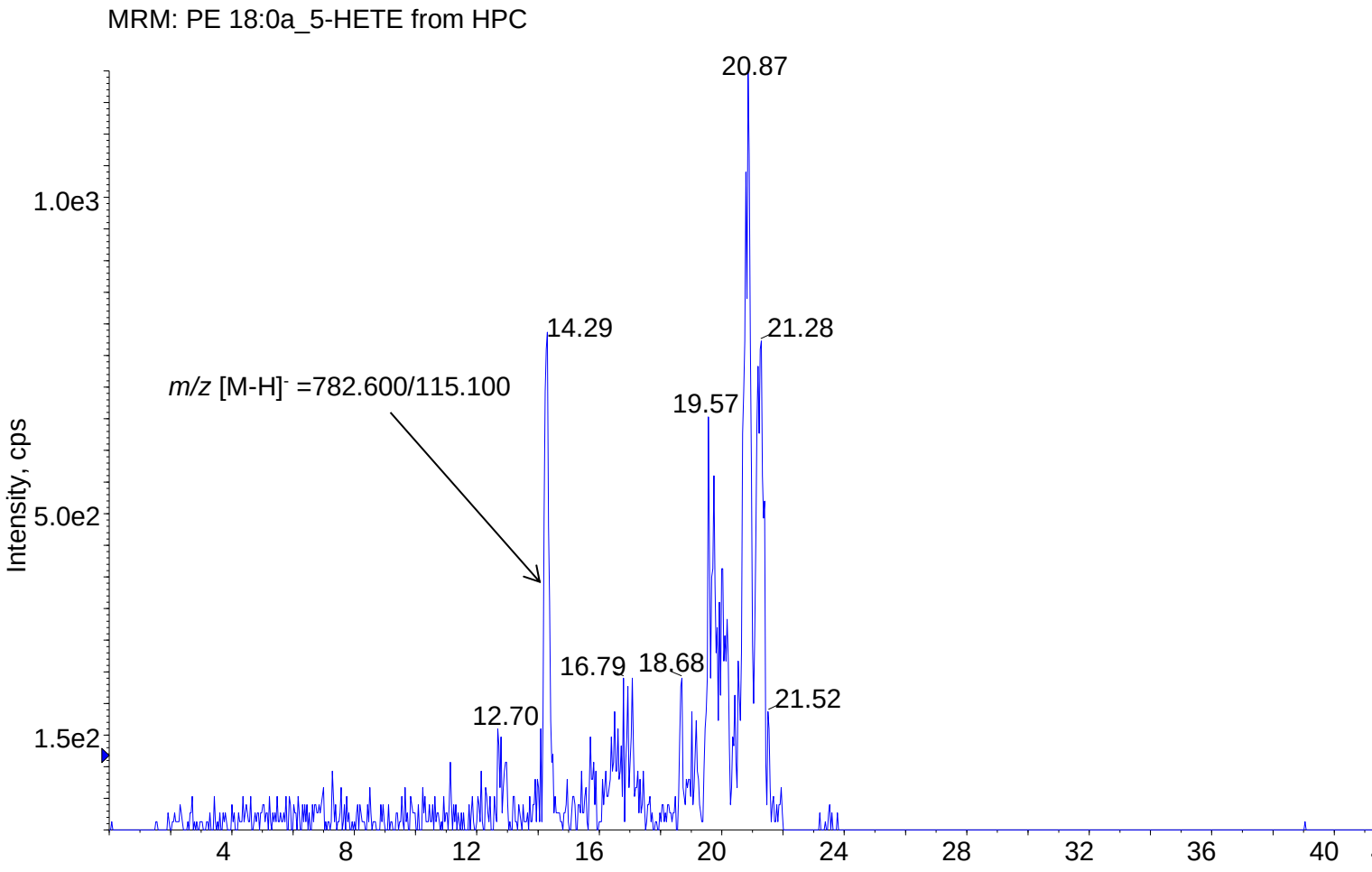
MRM: PE 18:0a_5-HETE from HPC
20.87
1.0e3
14.29
21.28
m/z [M-H]- =782.600/115.100
19.57
Intensity, cps
5.0e2
16.79
18.68
21.52
12.70
1.5e2
4
8
12
16
20
24
28
32
36
40

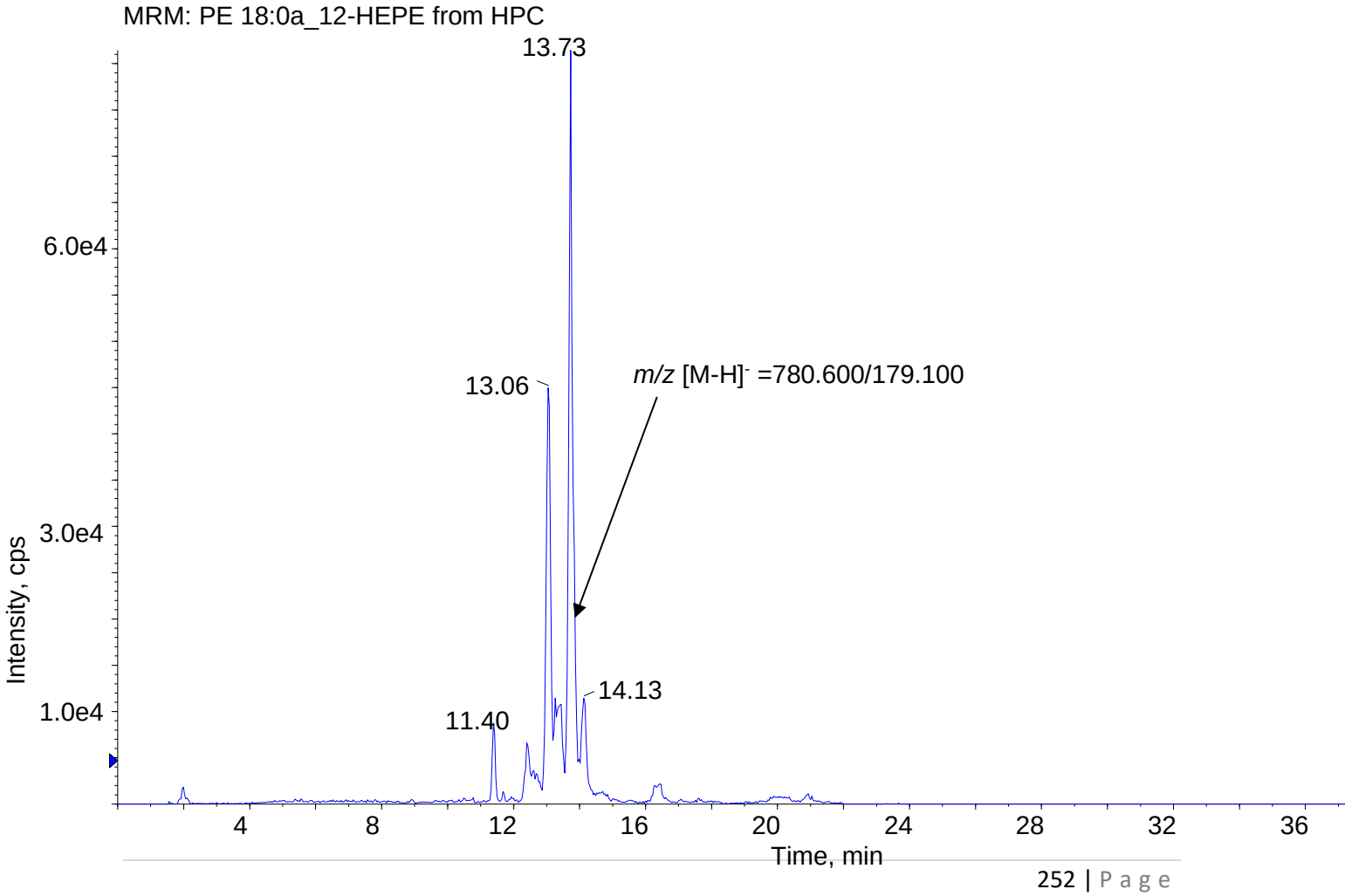
MRM: PE 18:0a_12-HEPE from HPC
13.73
6.0e4
13.06
m/z [M-H]- =780.600/179.100
3.0e4
Intensity, cps
14.13
1.0e4
11.40
4
8
12
16
20
24
28
32
36
Time, min

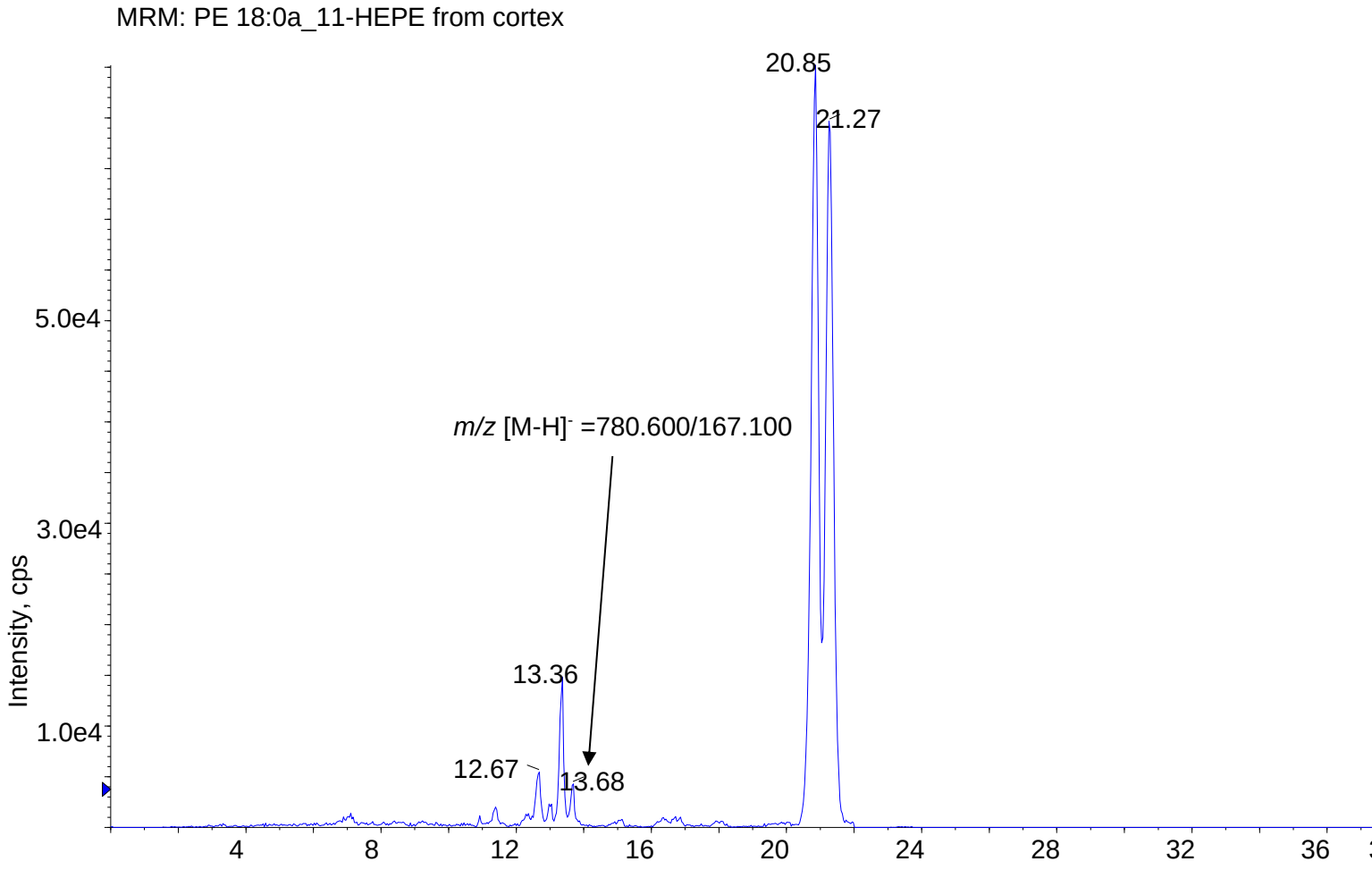
MRM: PE 18:0a_11-HEPE from cortex
20.85
21.27
5.0e4
m/z [M-H]- =780.600/167.100
3.0e4
Intensity, cps
13.36
1.0e4
12.67
13.68
4
8
12
16
20
24
28
32
36

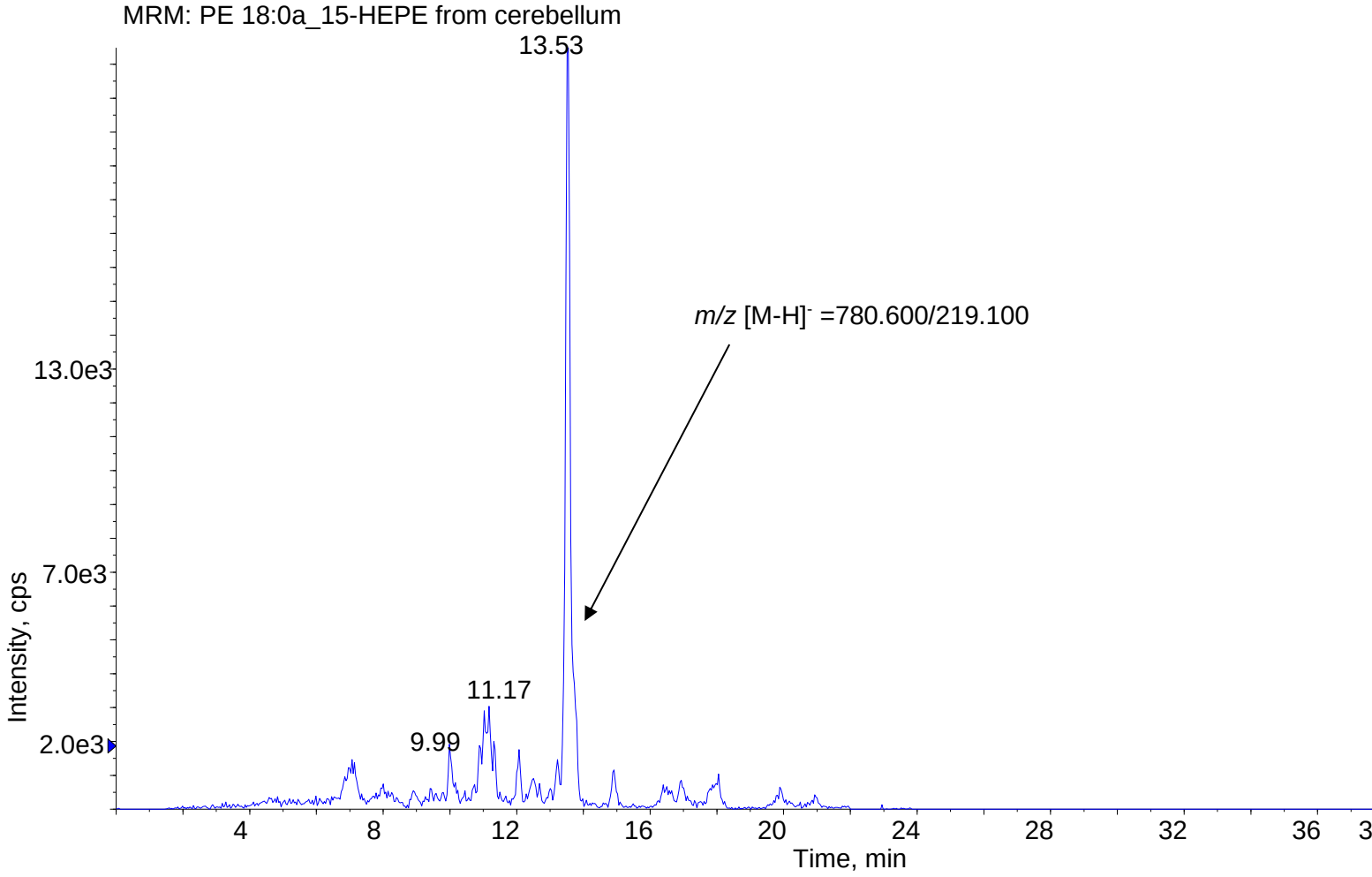
MRM: PE 18:0a_15-HEPE from cerebellum
13.53
m/z [M-H]- =780.600/219.100
13.0e3
7.0e3
Intensity, cps
11.17
9.99
2.0e3
4
8
12
16
20
24
28
32
36
Time, min

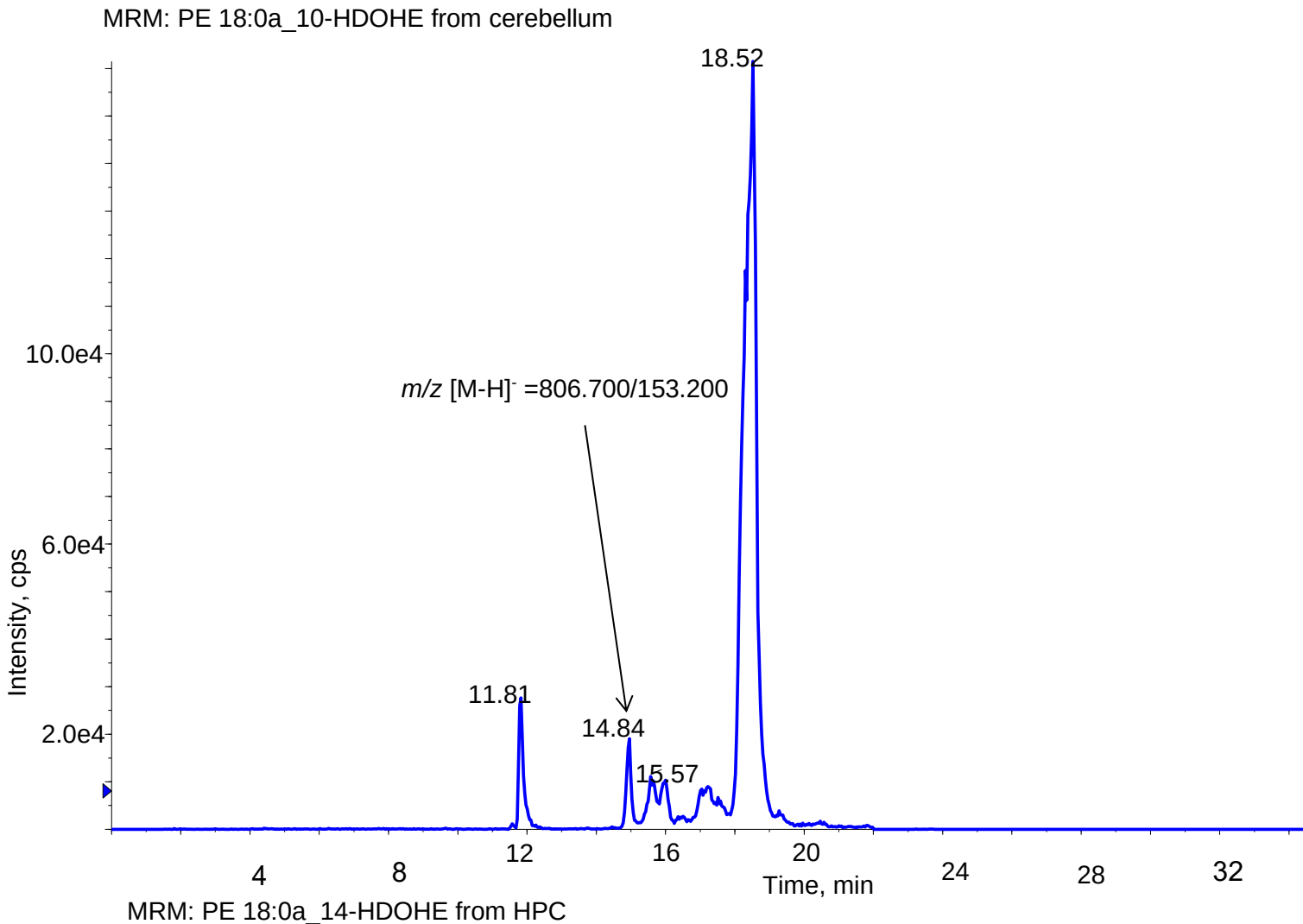
MRM: PE 18:0a_10-HDOHE from cerebellum
18.52
10.0e4
m/z [M-H]- =806.700/153.200
6.0e4
Intensity, cps
11.81
14.84
15.57
2.0e4
4
8
12
16
20
24
28
32
Time, min

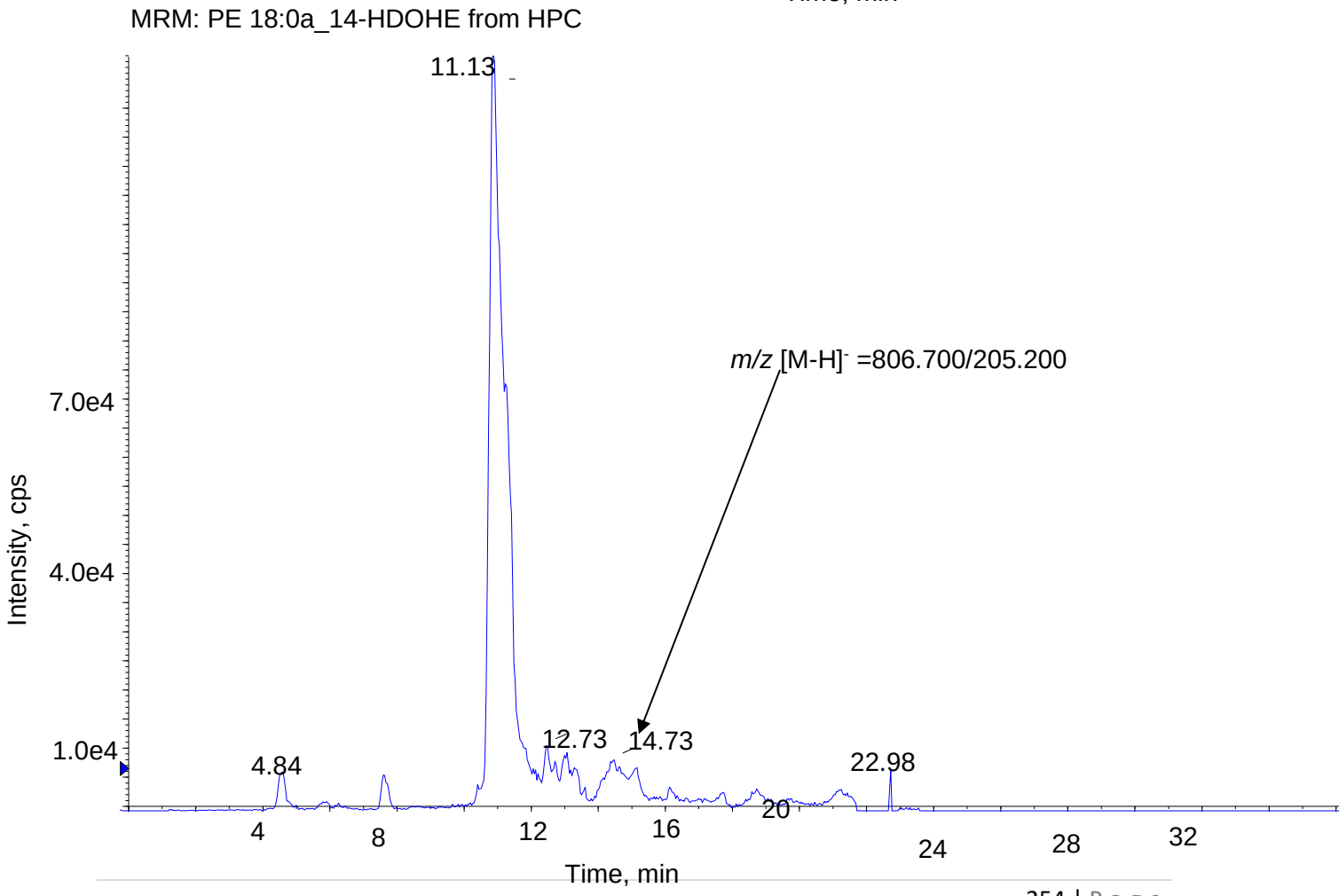
MRM: PE 18:0a_14-HDOHE from HPC
11.13
m/z [M-H]- =806.700/205.200
7.0e4
4.0e4
Intensity, cps
1.0e4
12.73
14.73
4.84
22.98
4
8
12
16
20
24
28
32
Time, min

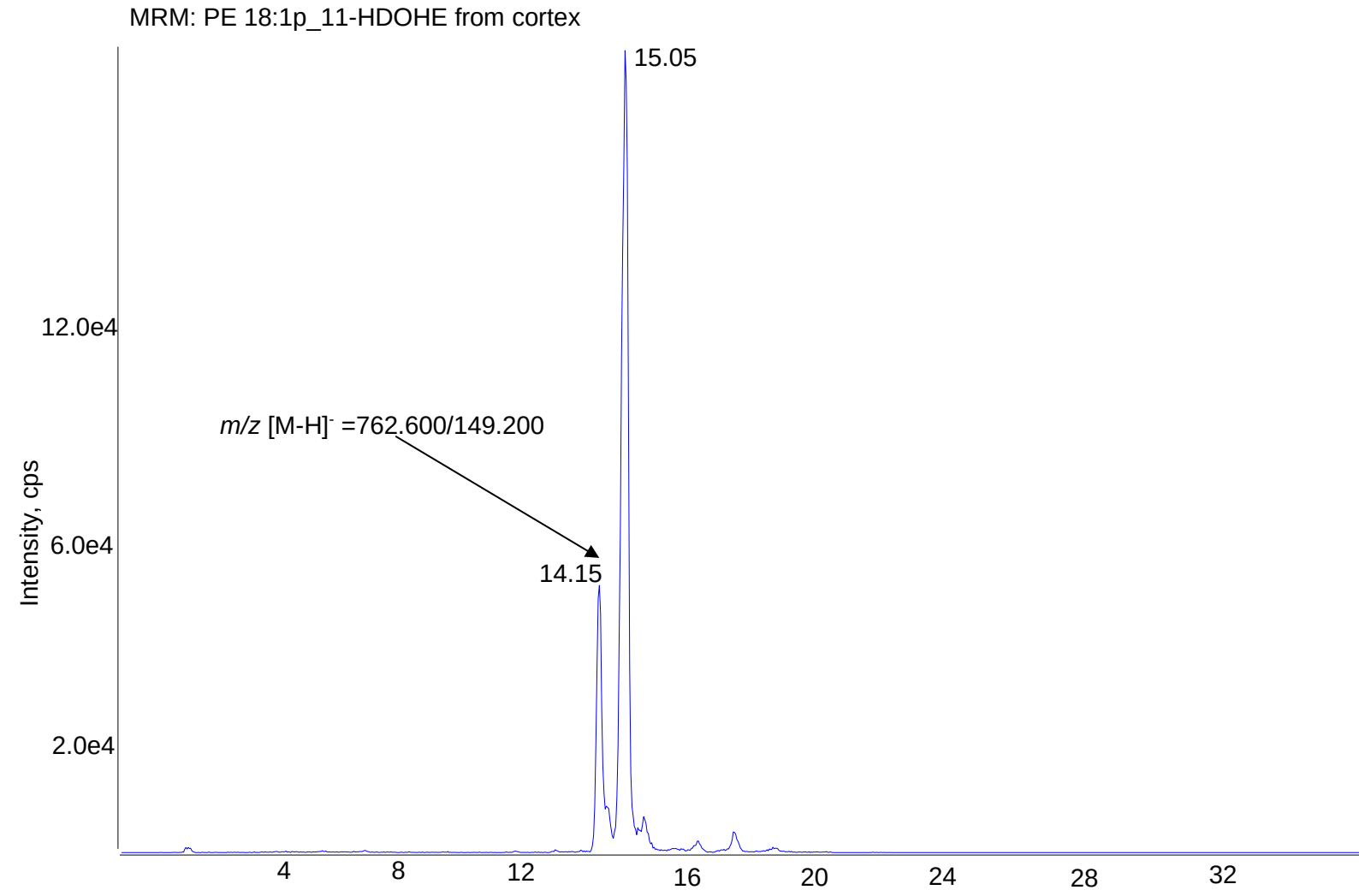
MRM: PE 18:1p_11-HDOHE from cortex
15.05
12.0e4
m/z [M-H]- =762.600/149.200
Intensity, cps
6.0e4
14.15
2.0e4
4
8
12
16
20
24
28
32

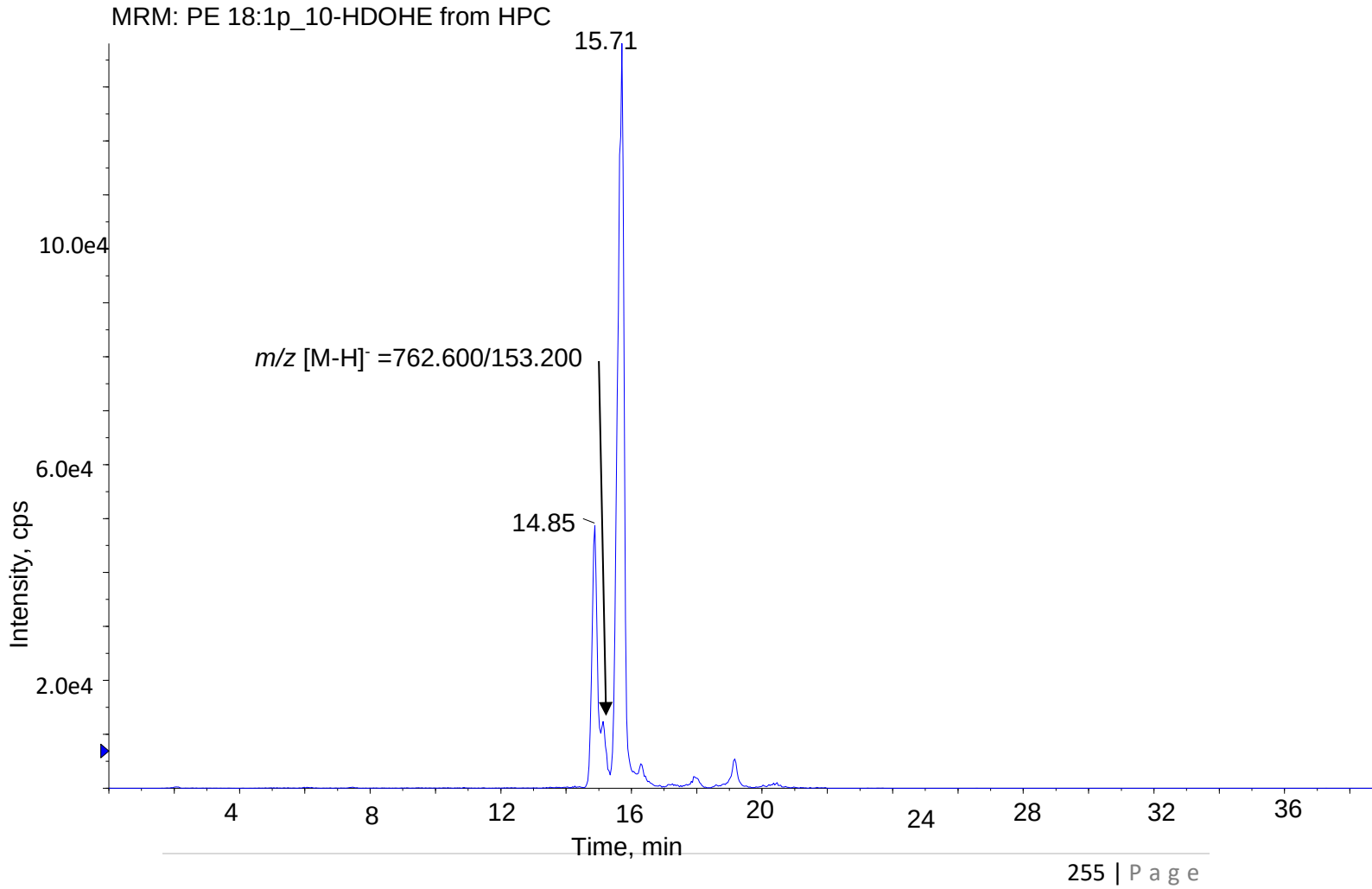
MRM: PE 18:1p_10-HDOHE from HPC
15.71
10.0e4
m/z [M-H]- =762.600/153.200
6.0e4
14.85
Intensity, cps
2.0e4
4
8
12
16
20
24
28
32
36
Time, min

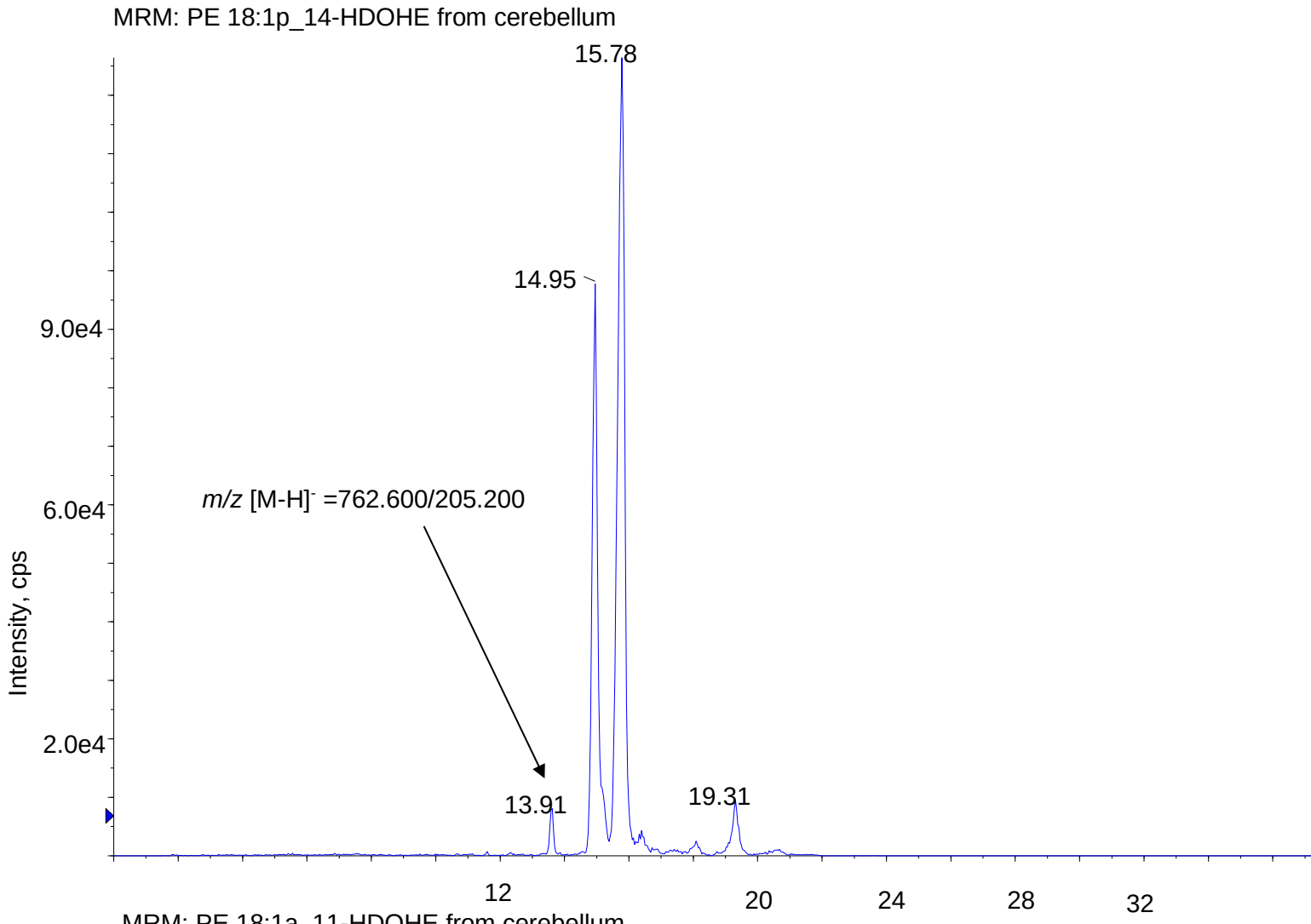
MRM: PE 18:1p_14-HDOHE from cerebellum
15.78
14.95
9.0e4
6.0e4
2.0e4
m/z [M-H]- =762.600/205.200
Intensity, cps
13.91
19.31
12
20
24
28
32

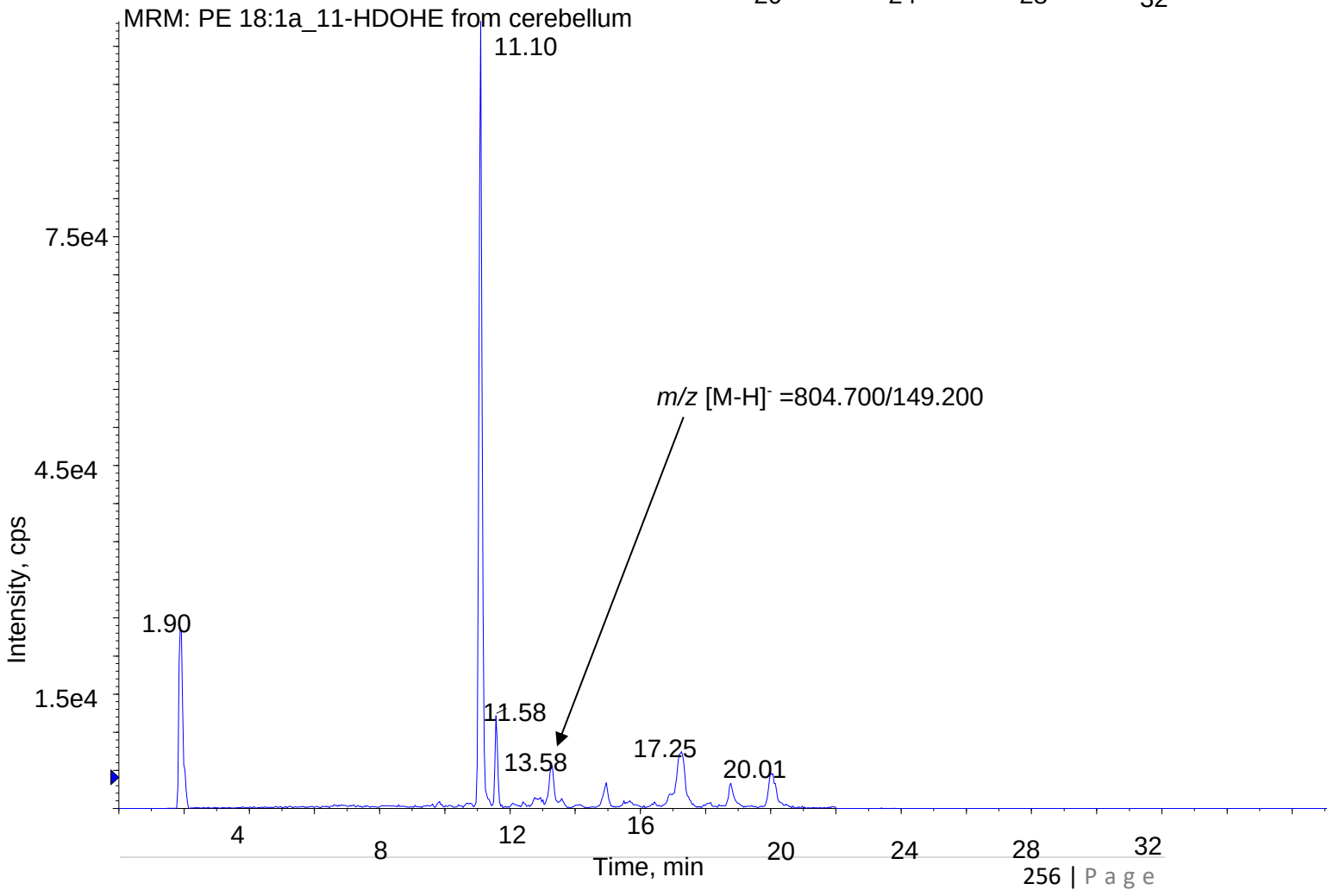
MRM: PE 18:1a_11-HDOHE from cerebellum
11.10
7.5e4
4.5e4
1.5e4
m/z [M-H]- =804.700/149.200
Intensity, cps
1.90
11.58
13.58
17.25
20.01
4
8
12
16
20
24
28
32
Time, min

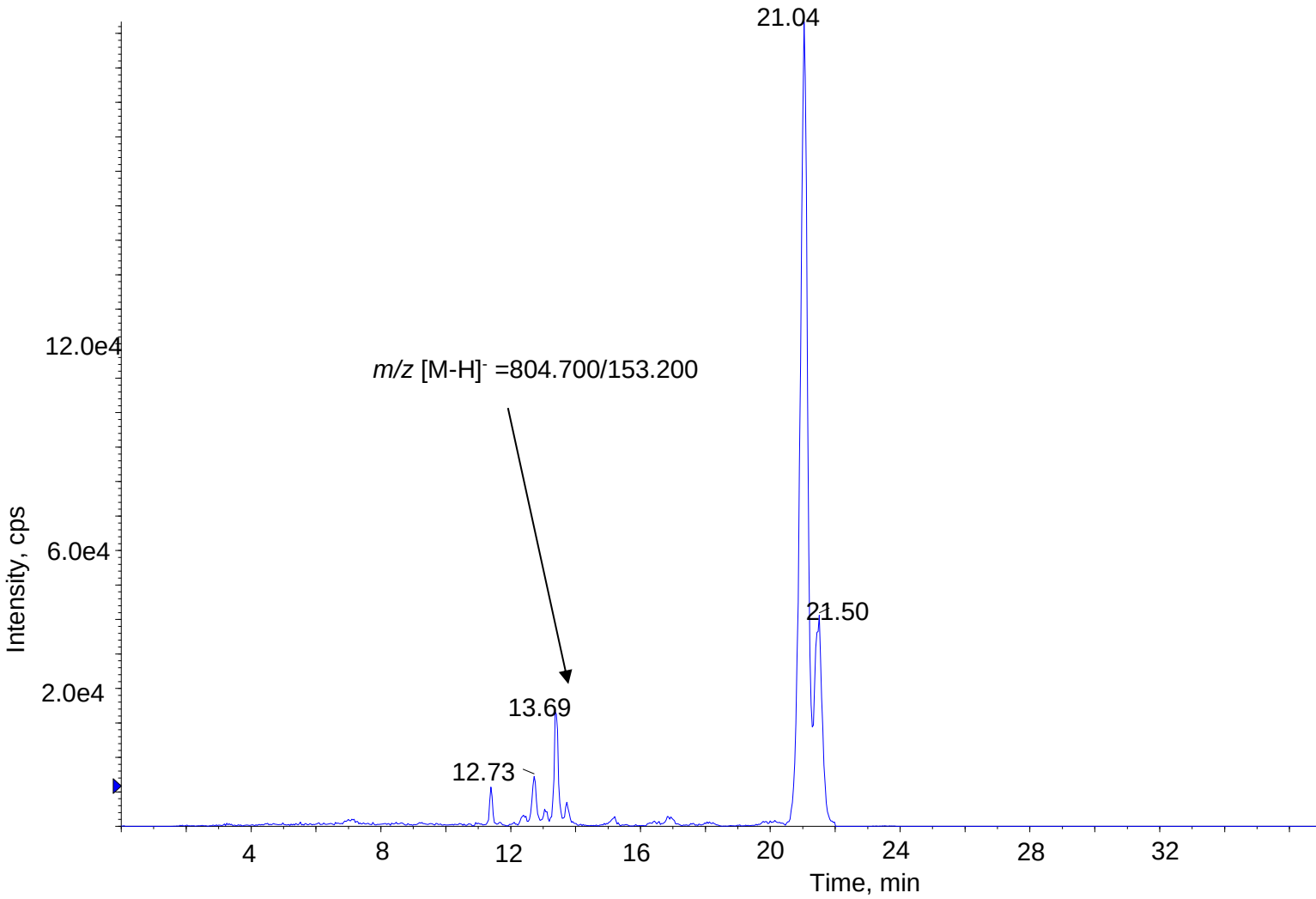

Figure 83. Representative MRM chromatograms in negative mode showing all negatively charged species with the retention times of sufficient peaks indicated in each individual eoxPL. Brain lipid extracts were separated as described in Material and Methods using reverse phase HPLC and analysed using LC/MS/MS**.**

7.6 Hierarchical clustering analysis indicates clustering by eoxPLs in *Alox15*$^{-/-}$ mice.

Using a targeted lipidomic approach, I measured 15 eoxPLs in the prefrontal cortex, HPC and cerebellum in 12 WT and 11 *Alox15*$^{-/-}$ male mice aged 15 months (Figure 9). In particular, the heatmap of the relative abundance was shown as log10 values for each lipid normalized to brain tissue weight (mg). The defined weight in each brain region was presented in Chapter 6. Hierarchical clustering was carried out to cluster oxidised phospholipids, showing clusters whereby different subclasses of lipids grouped exhibiting similar behaviour. The heatmap shows that eoxPLs' abundance was mainly different in the HPC compared to the other two brain regions between genotypes (Figure 84).

This heatmap shows two main clusters based on the levels of oxPEs. A closer examination revealed that PE 18:1p_11-HDOHE, PE 18:1p_14-HDOHE and PE 18:1p_10-HDOHE, which are the three molecular species containing plasmalogen, were grouped into cluster 1, showing a high abundance mainly in the cortex region. Similarly, the PE 18:1a_10-HDOHE and PE 18:1a_11-HDOHE were grouped into the same block in cluster 1, indicating moderate to high abundance. Also, PE 18:0a_5-HETE, PE 18:0a_11-HETE, PE 18:0a_15-HETE and PE 18:0a_12-HETE were grouped into cluster 2, demonstrating moderate quantity in the three brain regions. Conversely, PE 18:0a_11-HEPE, PE 18:0a_15-HEPE and PE 18:0a_12-HEPE were grouped, showing a very low abundance in the same block.

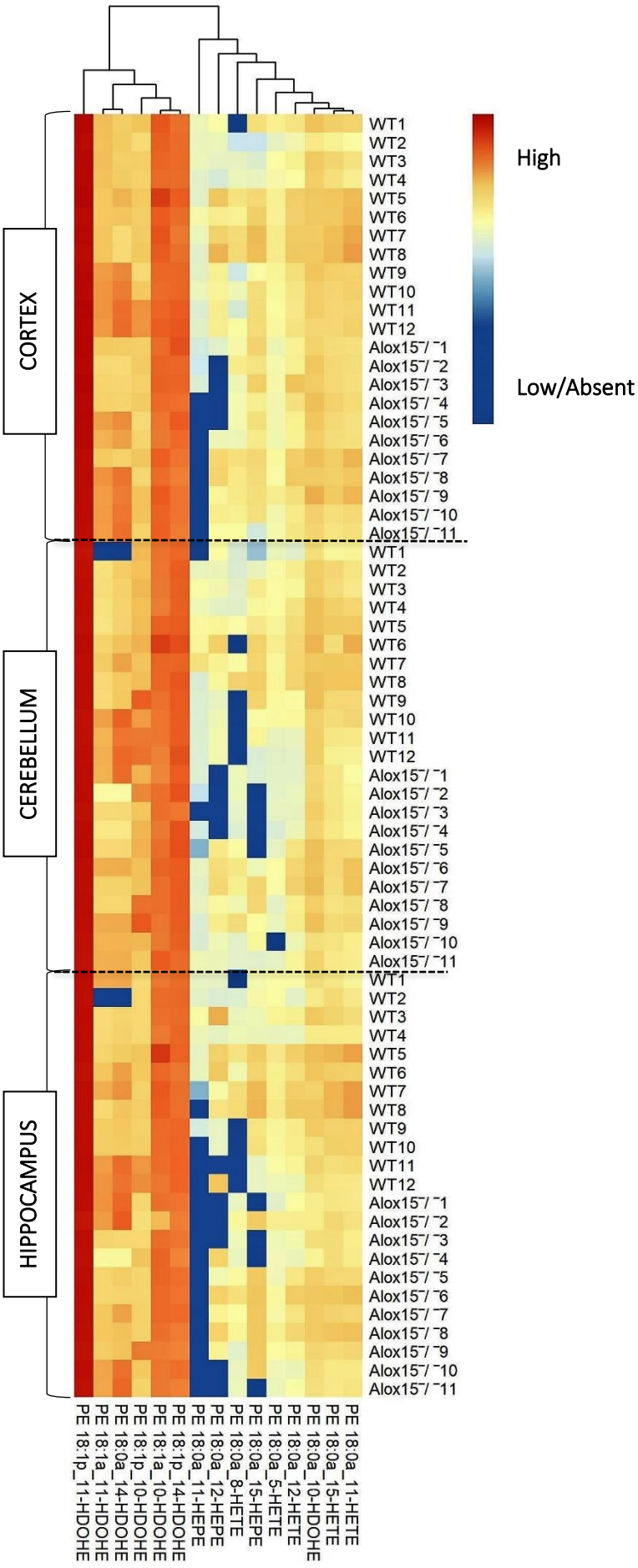
CORTEX
CEREBELLUM
HIPPOCAMPUS
WT1
WT2
WT3
WT4
WT5
WT6
WT7
WT8
WT9
WT10
WT11
WT12
Alox15-/-1
Alox15-/-2
Alox15-/-3
Alox15-/-4
Alox15-/-5
Alox15-/-6
Alox15-/-7
Alox15-/-8
Alox15-/-9
Alox15-/-10
Alox15-/-11
High
Low/Absent
PE 18:1p_11-HDOHE
PE 18:1a_11-HDOHE
PE 18:0a_14-HDOHE
PE 18:1p_10-HDOHE
PE 18:1a_10-HDOHE
PE 18:1p_14-HDOHE
PE 18:0a_11-HEPE
PE 18:0a_12-HEPE
PE 18:0a_8-HETE
PE 18:0a_15-HEPE
PE 18:0a_5-HETE
PE 18:0a_12-HETE
PE 18:0a_10-HDOHE
PE 18:0a_15-HETE
PE 18:0a_11-HETE

Figure 84. Hierarchical clustering heatmap analysis was performed for eoxPLs levels in the cortex, HPC, and cerebellum. Lipids were extracted from various brain regions as described in Materials and Methods and quantified by LC-MS/MS. The heatmap of the relative abundance was generated using 15 molecular species that differed among genotypes and was shown as log10 values for each lipid normalized to brain tissue weight (mg). log10 transformed and plotted as a heatmap with hierarchical clustering using the pheatmap R package. The columns in the heatmap represent lipids, and the rows display brain regions amongst genotypes. The heatmap colours indicate the abundance of lipids across various brain areas. Intensity levels were represented by a colour gradient, ranging from dark blue (low abundance) through white (moderate abundance) to dark red (high abundance of lipids). WT (n=12) and *Alox15*$^{-/-}$ (n=11).

7.7 LC/MS/MS analysis revealed significantly decreased PE 18:0a_15-HETE but unchanged diacyl PE 18:0a_12-HETE in *Alox15*$^{-/-}$ mice.

I next examined the detailed eoxPL lipid profiling on each individual group of lipids. Data in each brain region were analysed by Mann- Whitney non-parametric U test and Tukey box plots were generated for the genotype comparisons.

Alox15$^{-/-}$ mice showed significantly lower levels of PE 18:0a_5-HETE in the cortex, cerebellum and HPC than WT mice (P=0.0108, P=0.0221, P=0.014, respectively) (Figure 85). Similarly, a simple comparison revealed that PE 18:0a_11-HETE was reduced in the *Alox15*$^{-/-}$ HPC compared to WT mice (P=0.04820). Also, these lipids were lower in the cortex and cerebellum in *Alox15*$^{-/-}$ mice, but they didn't reach statistical significance (Figure 85). Next comparison demonstrated that PE 18:0a_15-HETE levels were significantly decreased in the cerebellum region of *Alox15*$^{-/-}$ mice compared to WT (P=0.0202). PE 18:0a_15-HETE was lower in the cortex and HPC of *Alox15*$^{-/-}$ mice than in WT mice, but this was not significant (Figure 85).

No significant differences were detected for PE 18:0a_12-HETE, which was detected at very low brain levels from both strains (Figure 86). No significant differences were observed for PE 18:0a_8-HETE between genotypes (Figure 86).

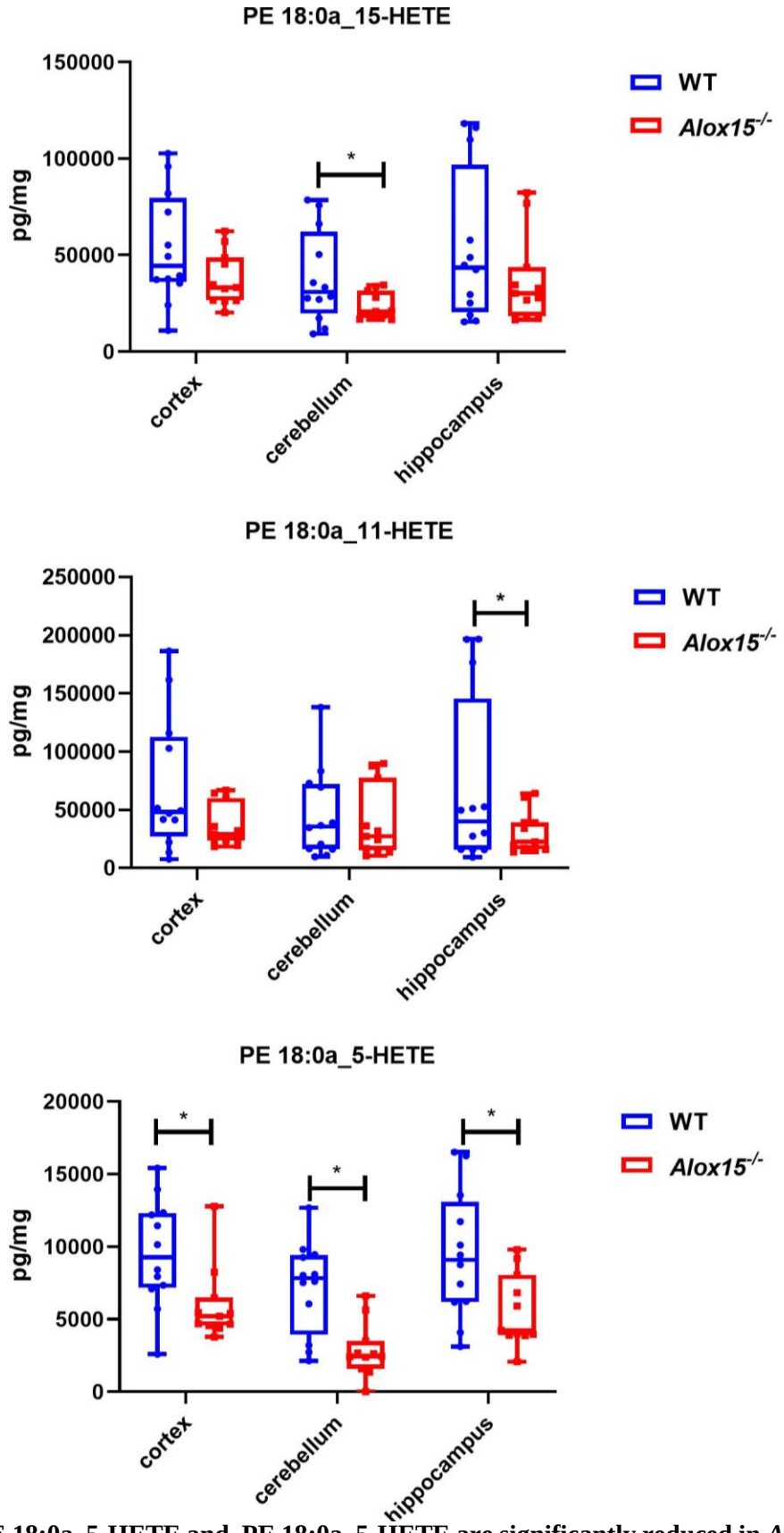

Figure 85. PE 18:0a_5-HETE and PE 18:0a_5-HETE are significantly reduced in *Alox15*$^{-/-}$ mice. Lipids were extracted from three brain regions as described in Materials and Methods. Data in each brain region were analysed using Mann- Whitney non-parametric U test and shown on Tukey box plots with mean ± S.E.M. WT (n=12) and *Alox15*$^{-/-}$ (n=11) *, **, *** and **** represent p≤0.05, p≤0.01, p≤0.001 and p≤0.0001 for genotype comparisons, respectively.

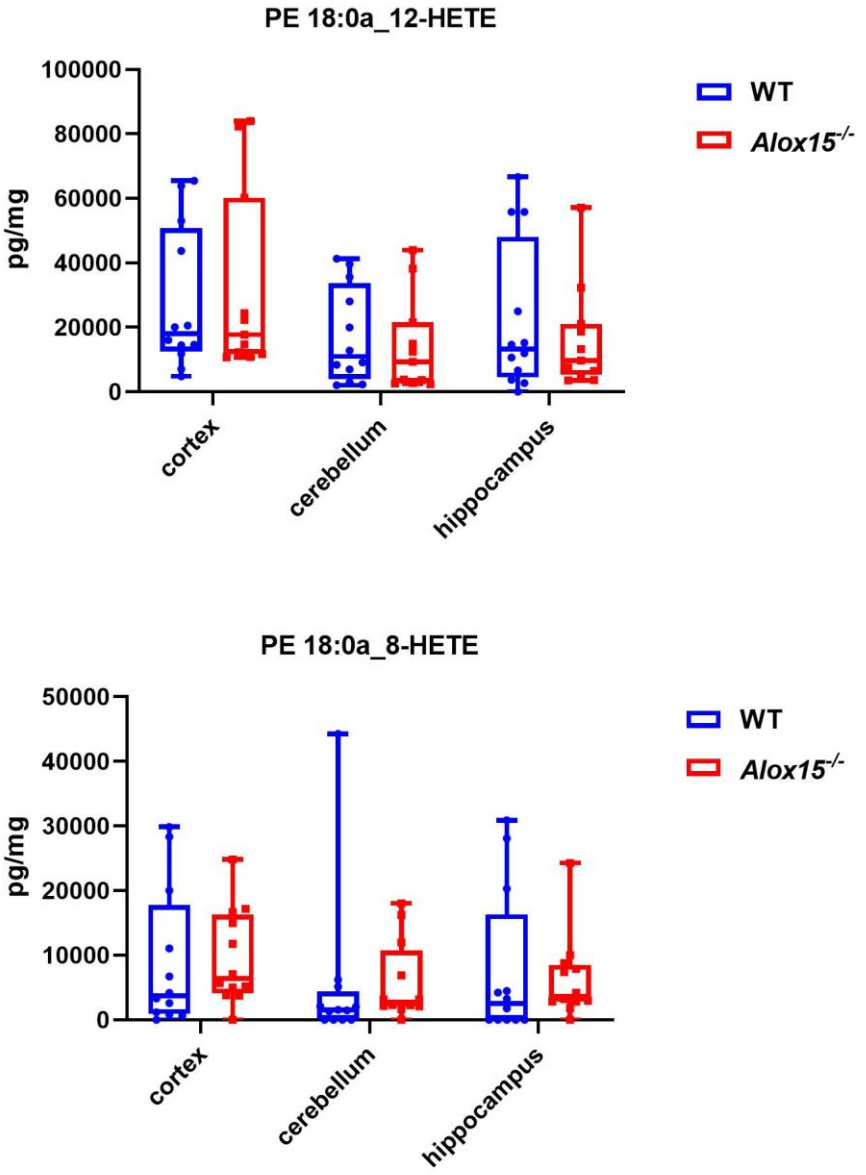

Figure 86. PE 18:0a_12-HETE and PE 18:0a_8-HETE remain unchanged in Alox15$^{-/-}$ mice. Lipids were extracted from three brain regions as described in Materials and Methods. Data in each brain region were analysed using Mann- Whitney non-parametric U test and shown on Tukey box plots with mean ± S.E.M WT (n=12) and Alox15$^{-/-}$ (n=11) *, **, *** and **** represent $p \leq 0.05$, $p \leq 0.01$, $p \leq 0.001$ and $p \leq 0.0001$ for genotype comparisons, respectively.

7.8 LC/MS/MS analysis showed unchanged acyl PE 18:0a_12-HEPE and PE 18:0a_15-HEPE in *Alox15*$^{-/-}$ mice.

MS/MS scanning of lipid extracts from various brain regions identified PE 18:0a_HEPEs synthesized from EPA oxidation, using precursor *m/z* 780.6 to product *m/z* 317.2 transitions (Figure 87). No significant differences were observed for PE 18:0a_11-HEPE in the three brain regions in both strains, and very low levels were detected. Similarly, PE 18:0a_12-HEPE and PE 18:0a_15-HEPE showed similar levels in the three brain regions of *Alox15*$^{-/-}$ and WT mice (Figure 87).

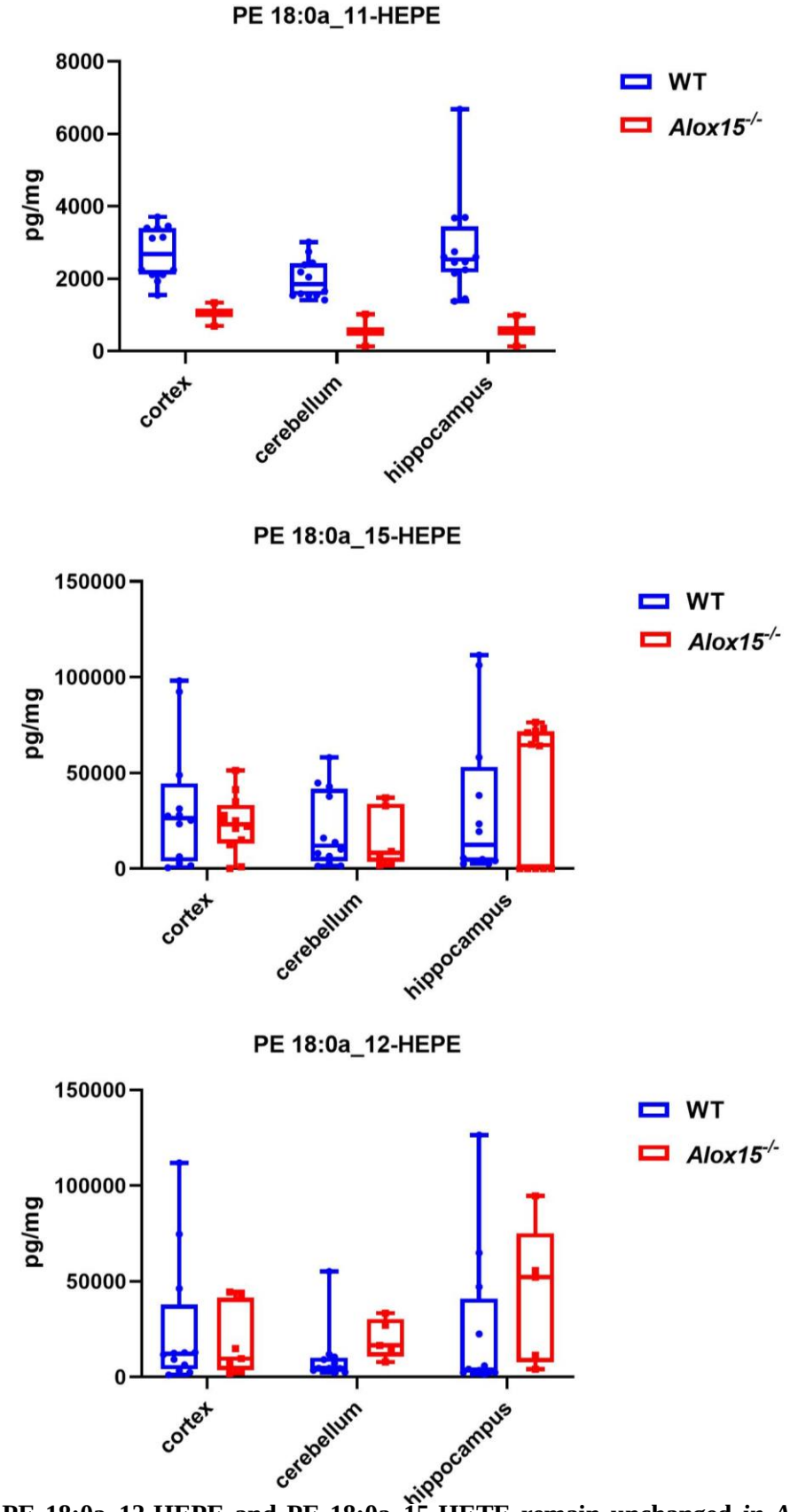

Figure 87. PE 18:0a_12-HEPE and PE 18:0a_15-HETE remain unchanged *in Alox15*$^{-/-}$ mice. Lipids were extracted from three brain regions as described in Materials and Methods. Data in each brain region were analysed using Mann- Whitney non-parametric U test and shown on Tukey box plots with mean ± S.E.M WT (n=12) and Alox15$^{-/-}$ (n=11) *, **, *** and **** represent $p \leq 0.05$, $p \leq 0.01$, $p \leq 0.001$ and $p \leq 0.0001$ for genotype comparisons, respectively.

7.9 LC/MS/MS analysis showed significantly decreased hippocampal PE 18:1a_10-HDOHE in *Alox15*$^{-/-}$ mice

LC/MS/MS analysis identified two diacyl PE 18:1a_HDOHEs containing oxygenated DHA, using precursor *m/z* 804.7 to product *m/z* 343.2 transition.

Mann-Whitney non-parametric U test was performed in the cortex, cerebellum and HPC revealing tha PE 18:1a_11-HDOHE was not altered between the genotypes (Figure 88). However, PE 18:1a_10-HDOHE levels were significantly decreased in the HPC of *Alox15*$^{-/-}$ mice compared to WT, but no alterations were observed in the cerebellum and cortex levels between the two strains (P=0.0351) (Figure 88).

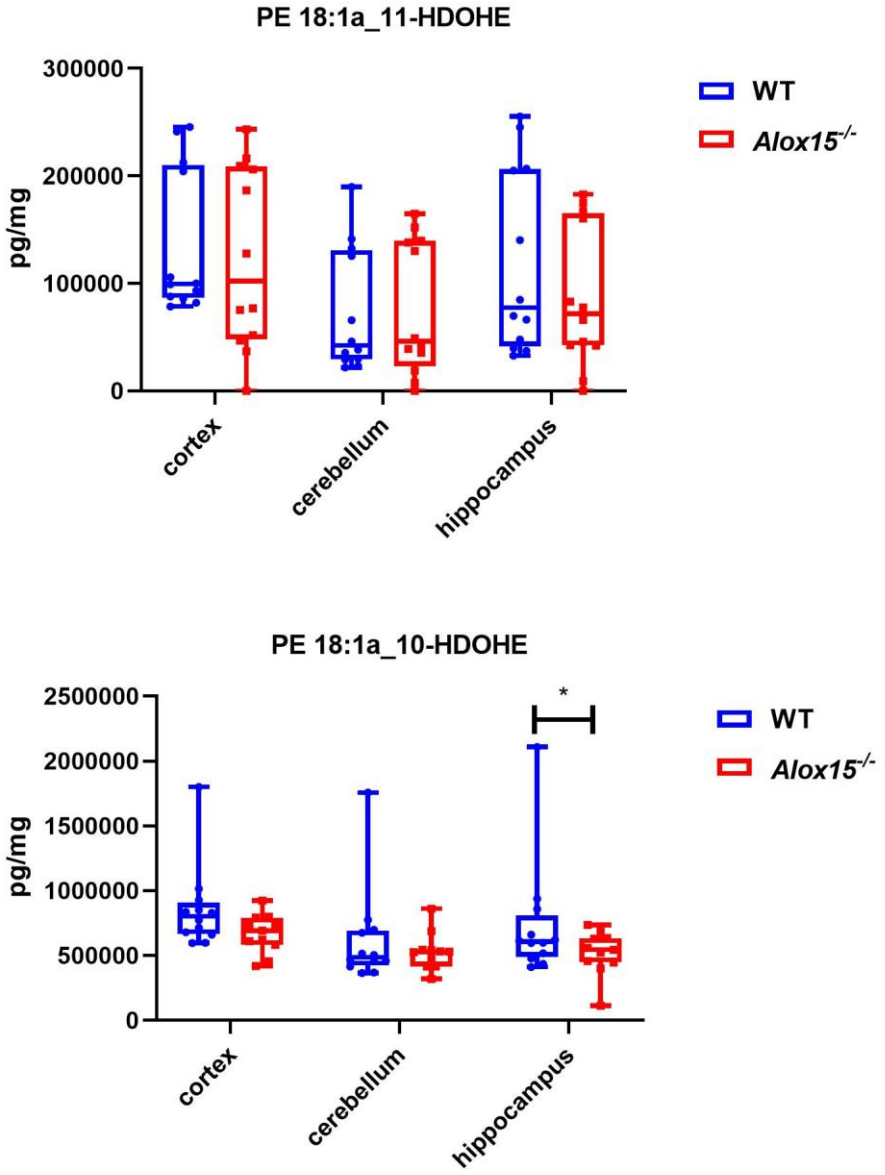

Figure 88. PE 18:1a_10-HDOHE is significantly decreased in the HPC in Alox15$^{-/-}$ mice. Lipids were extracted from three brain regions as described in Materials and Methods. Data in each brain region were analysed using Mann- Whitney non-parametric U test and shown on Tukey box plots with mean ± S.E.M. WT (n=12) and Alox15$^{-/-}$ (n=11) *, **, *** and **** represent p≤0.05, p≤0.01, p≤0.001 and p≤0.0001 for genotype comparisons, respectively.

7.10 LC/MS/MS analysis displayed unchanged PE 18:0a_HDOHE in *Alox15*$^{-/-}$ mice

MS/MS scanning reveals novel products, PE 18:0a_HDOHEs, using precursor *m/z* 806.7 to product *m/z* 343.2 transitions.

Figure 89 demonstrates that the PE 18:0a_14-HDOHE and PE 18:1a_10-HDOHE levels, arising from DHA oxidation by 12-LOX, remained unchanged in the three brain regions between *Alox15*$^{-/-}$ and WT mice.

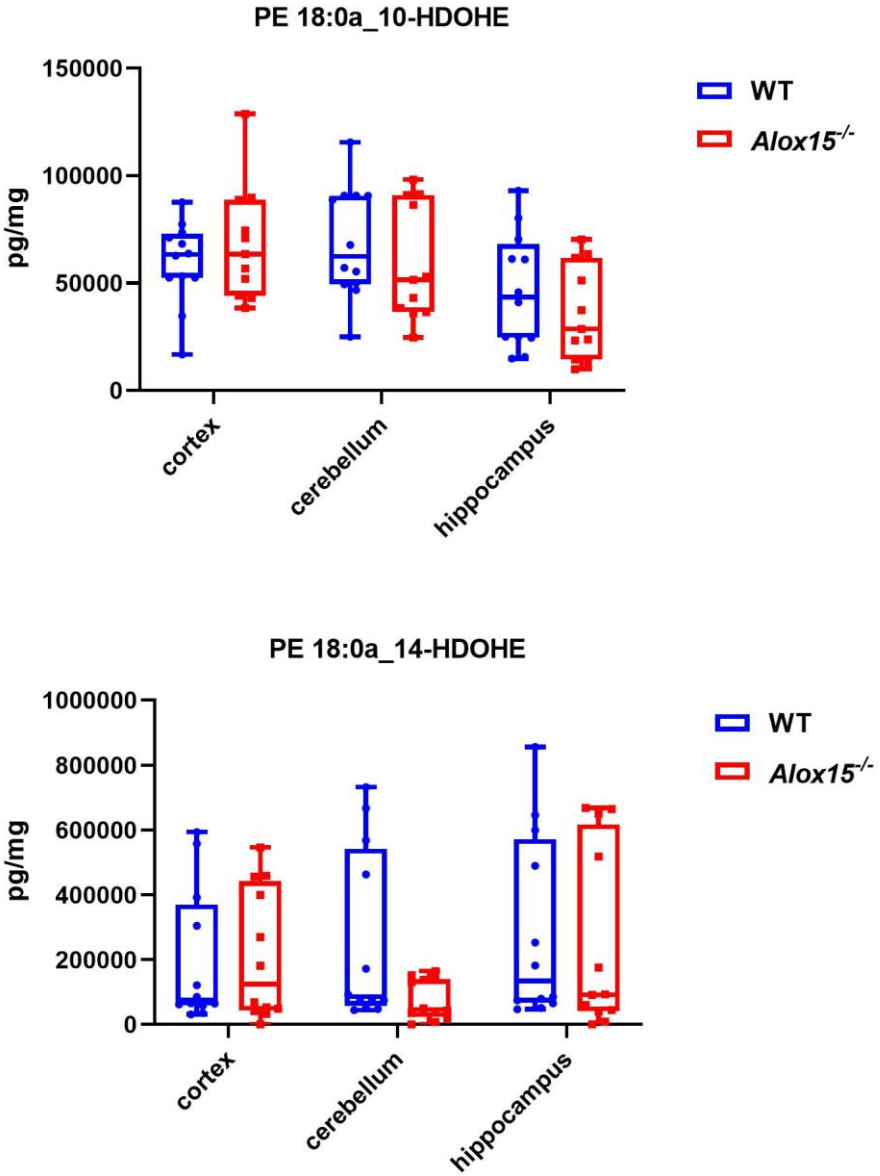

Figure 89. PE 18:0a_10-HDOHE and PE 18:0a_14-HDOHE remain unchanged in Alox15$^{-/-}$ mice. Lipids were extracted from three brain regions as described in Materials and Methods. Data in each brain region were analysed using Mann- Whitney non-parametric U test and shown on Tukey box plots with mean ± S.E.M. WT (n=12) and Alox15$^{-/-}$ (n=11) *, **, *** and **** represent p≤0.05, p≤0.01, p≤0.001 and p≤0.0001 for genotype comparisons, respectively.

7.11 LC/MS/MS analysis revealed significantly reduced hippocampal PE 18:1p_14-HDOHE in *Alox15*$^{-/-}$ mice

LC/MS/MS scanning suggested three plasmalogen PE 18:1p_HDOHEs, using precursor *m/z* 762.6 to product *m/z* 343.2 transitions.

Mann-Whitney non-parametric U test was performed in the HPC revealing tha PE 18:1p_14-HDOHE levels showed markedly decreased in the HPC in *Alox15*$^{-/-}$ mice compared to WT (P=0.0162) (Figure 90). Conversely, no differences between genotypes were observed in the cortex and cerebellum levels. Also, PE 18:1p_10-HDOHE showed very low levels in the three brain regions between *Alox15*$^{-/-}$ and WT mice, which was not significantly different.

Last, PE 18:1p_11-HDOHE levels were unchanged in the three brain regions between the two groups (Figure 90).

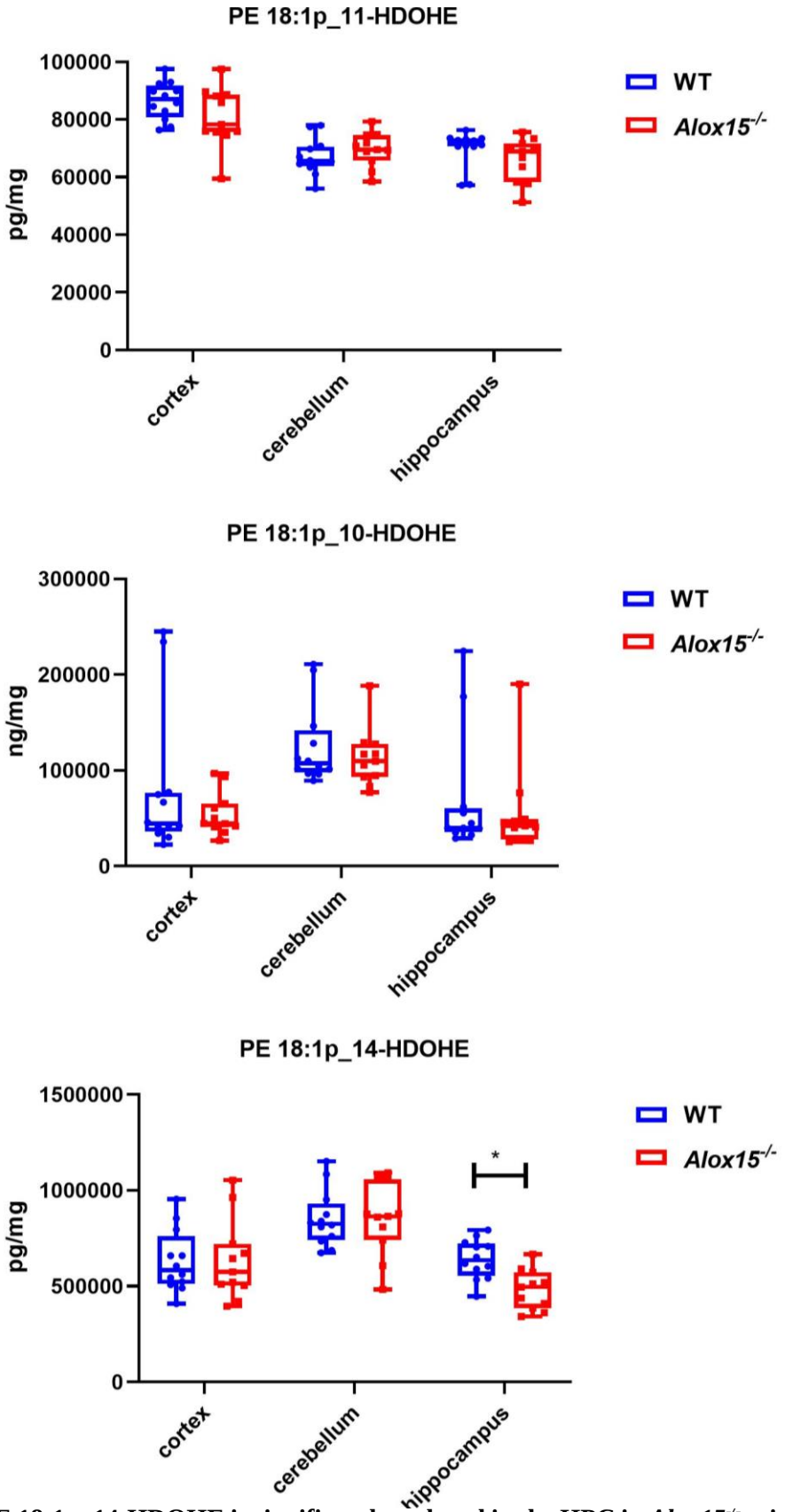

Figure 90. **PE 18:1p_14-HDOHE is significantly reduced in the HPC in *Alox15*$^{-/-}$ mice.** Lipids were extracted from three brain regions as described in Materials and Methods. Data in each brain region were analysed using Mann- Whitney non-parametric U test and shown on Tukey box plots with mean ± S.E.M WT (n=12) and *Alox15*$^{-/-}$ (n=11) *, **, *** and **** represent p≤0.05, p≤0.01, p≤0.001 and p≤0.0001 for genotype comparisons, respectively.

DISCUSSION

In the present study, a targeted LC-MS/MS approach in the negative ion mode was conducted on lipid extracts to identify families of oxidised phospholipids attached to PEs in multiple brain regions in WT control mice. Then their levels were assessed in mice genetically lacking *Alox15* gene. No previous studies have analysed eoxPLs in the WT mouse brain. Thus, several lipid *m/z* values were putatively generated by adding one oxygen onto native phospholipids from a previously published study (Bennett *et al.,* 2013). Of the 96 MRM transitions, 21 lipids were putatively validated in the WT brain lipidome, comprising PE with acyls- or plasmalogens (18:0a, 18:1a and 18:1p) at the *Sn1* position and 20:4(O),20:5(O), 22:6(O) at the *Sn2* position. Next, EPI spectra were acquired for each precursor ion. This demonstrated that five major ions predominate at *m/z* 782.6, *m/z* 780.6, *m/z* 804.7, *m/z* 762.6 and *m/z* 806.7. The main aim of this chapter was to determine whether eoxPLs, including HETE-PEs, HEPE-PEs and HDOHE-PEs were altered in *Alox15*$^{-/-}$. Having determined the eoxPLs in the WT mouse brain, the next question of this study was to examine any variations between genotypes and within the brain regions.

It is noteworthy that the signals and the relative abundance of the eoxPLs in the *Alox15*$^{-/-}$ brain regions and in the WT brain were weak and low. Notably, several chromatographic peaks detected by LC/MS/MS were weak and poorly resolved; thus, the data quality are not relatively high. Therefore, further work is required to determine the right peaks of eoxPLs on the chromatograms. However, despite this clear issue, there are some interesting findings.

The main finding of this study was that generation of PE 18:0a_12-HETE was not affected by genetic deletion of 12/15-LOX and was expressed in the brain in the *Alox15*$^{-/-}$. In particular, its levels were low in both groups of mice. This lipid could be generated non-enzymatically by ROS or can be formed via other LOXs, such as through the 12-LOX enzyme present in platelets. Conversely, an additional 12/15-LOX product, PE 18:0a_15-HETE, was also detected in the brain. This was significantly decreased in *Alox15*$^{-/-}$ mice compared to WT. Notably, PE 18:0a_15-HETE can be generated either from the COX pathway (15R-HETE-PE) or 12/15-LOX (15S-HETE-PE). Although in chapter 6, the oxylipin 5-HETE, the intact form, was significantly increased in *Alox15*$^{-/-}$ mice; however, in this chapter, PE 18:0a_5-HETE, generated from the oxidation of AA esterified into diacyl PE species, was significantly decreased in *Alox15*$^{-/-}$ mice than in WT mice. One potential reason for that could be the re-esterification part of 5-HETE back into the PL membrane to generate 5-HETE-PL resulting in changing their biophysical structure and modifying their action.

Also, PE 18:1p_14-HDOHE, which could be generated by 12/15-LOX, was significantly reduced in the HPC in *Alox15*$^{-/-}$ mice. This lipid can also be generated in platelets via 12-LOX. Conversely, PE 18:0a_14-HDOHE levels were similar between genotypes in the three brain regions. Thus, it was reported that the plasmalogens were detected, suggesting that distinct plasmalogen PE counterparts have intriguing properties and contributions to normal ageing. Plasmalogens have been shown to have a neuroprotective role in response to cellular oxidative stress, as their deficiency in the brain could occur via increased oxidative damage resulting in plasmalogen degradation by ROS species due to their vinyl ether linkage to the glycerol backbone (Braverman *et al.,* 2012; Messoas et al., 2018; Fitzner *et al.,* 2020). Due to the significant reduction of PE 18:1p_14-HDOHE in HPC, which is sensitive to cognitive decline due to healthy ageing, it is suggested that the aged *Alox15*$^{-/-}$ mice are correlated with increased lipid peroxidation, which has been related to the progression of many pathological states (Bannerman *et al.,* 2014; Karki *et al.,* 2020).

Apart from the detrimental functions of the generation of eoxPLs through the chemical modifications due to oxidation, enzymatically and non-enzymatically oxPL exert neuroprotective functions in limiting acute inflammation reactions via Toll-like receptors (TLR) by interacting with TLR4, mediating pro-inflammatory effects. (Imai, *et al.,* 2003; Greig, *et al.,* 2012).

A recent study by Narzt et al., 2022, showed that aged rats with spatial memory impairments had increased phospholipid hydroperoxides levels of the AA-derived molecular species in the prefrontal cortex compared to aged rats with no cognitive decline (Narzt et al., 2022).

Many biological functions have been ascribed to DHA, as it is the most abundant fatty acid in the *Sn*2 position in mouse PLs and is crucial for neuronal function. I propose that changes in DHA-containing PEs may be a general feature and biomarker of the ageing process (Little *et al*., 2007; Lin *et al.,* 2016). In addition to the prominent role of DHA, the substantial reduction in 14-HDOHE-PE might be important in the context of age-related cognitive changes in the *Alox15*$^{-/-}$ mice.

Additional future work could involve chiral chromatography of HETE-PLs, both PE 18:0a_15-HETE and PE 18:0a_12-HETE, to investigate whether they are enzymatically produced via other pathways independent of the *Alox15* pathway discussed in this chapter. Additionally, *Alox15*$^{-/-}$ female mice could be utilized to compare gender differences in their oxPLs profiling compared to control female WT mice.

Chapter 8:

General Discussion

8.1 Thesis Overview

The primary aims of this thesis were to examine the effect of *Alox15* gene deletion on neuronal function and lipid metabolism during ageing in mice. While studies have used animals genetically deficient in *Alox15* and showed its implication in various neuropathological conditions (Li *et al*., 1997; Yao, *et al.*, 2005; Yang *et al*., 2010; DeTure, *et al.*, 2019); in my study, the main focus was to investigate how the protein is involved in the brain regions and its impact in behaviour and lipid metabolism during brain health. The first aim involved the breeding and subsequent ageing of two cohorts of young to middle-aged and old mice with genetic deletion of *Alox15*. These mice were tested in a series of behavioural tests to evaluate the effects of deletion on behaviour during ageing, compared with similarly aged control WT mice. The lipid mediators generated via the 12/15-LOX during healthy brain ageing were also assessed across various brain regions. Below, to make the discussion more structured, I have summarised my key findings pointwise and discussed how they relate to the literature.

8.2 Summary of Findings

Age-related changes were observed in this study, such as significant alterations in mouse cognitive and emotional behaviours, body weight gain, food consumption, and lipid metabolism (Peters, 2006; Fantini *et al*., 2015; Castelli, *et al*., 2019). No studies to date have tested for a role for 12/15-LOX in the brain during normal ageing. To study normal brain function, various behavioural, neuroanatomical, and lipidomic analyses were conducted in 12/15-LOX deficient mice at five different age-points (4, 7, 10, 13, and 16 months). In particular, differences were reported from comparisons among young adults (4 months of age), middle-aged (7- 13 months of age) and aged (15 months of age) animals through behavioural tests (Shoji *et al.*, 2016). For the ageing phenotype, different aspects were considered:

8.2.1 Bodyweight increases significantly until middle age and then becomes steady in *Alox15*$^{-/-}$ *mice.*

In Chapter 3, findings from the physiological data with male and female *Alox15*$^{-/-}$ mice revealed that they were significantly heavier compared to age-matched control WT mice. These data suggested that *Alox15*$^{-/-}$ mice gradually display a significant age-related increase in body weight from 7 months of age, reaching a peak at 10 months of age, and then maintaining a stable level until the end point by 16 months of age compared to WT mice (Figure 18). This is suggestive of the rapid growth of mice until middle age, and then the weight gain continues at a much slower pace. Notably, no special diet, such as a high-fat diet, was provided to the

animals. This Chapter also showed no substantial differences in the total food intake observed during the 120 h period in aged 16 months *Alox15*$^{-/-}$ mice compared to WT mice for the remainder of the 5-day study period. The findings of this Chapter are generally consistent with previous reports in C57BL/6J mice from 2 to 18 months of age (Barreto *et al.*, 2010; Shoji, *et al*., 2019; Singhal, *et al.*, 2020; Yanai, *et al.*, 2021) who revealed that WT mice showed significantly increased effects of age on body weight. However, no metabolic phenotype has been reported previously for 12/15-LOX knockout mice, and Chapter 4 demonstrated that *Alox15*$^{-/-}$ mice behaved significantly different than WT mice. It is suggested that the genetic deletion of the *Alox15* likely modulates the body weight gain during normal ageing.

8.2.2 Spatial deficits, anxiety-like behaviour, and hippocampal protein markers

Chapter 4 evaluated the hypothesis that ageing may be associated with cognitive changes in male and female *Alox15*$^{-/-}$ mice. The main finding of this chapter was that genetic deletion of *Alox15* leads to a reproducible anxiety phenotype, as measured in the elevated plus maze, across the four different time points. Male and female *Alox15*$^{-/-}$ mice displayed significantly less exploration time in the open arms of the maze and a decreased number of open arm entries compared with age-matched WT mice, which was interpreted as an increase in anxiety-like behaviour (Figure 43 A). These data are consistent with previously published work showing that manipulation of *Alox15*, particularly overexpression of *Alox15*, resulted in increased anxiety-like behaviour in aged female mice (Joshi *et al*., 2014). Additionally, the same group found that deficiency of *Alox5* leads to an age-dependent increase in anxiety-like behaviour in female mice (Joshi *et al*., 2011). However, in 2021, an article published in "For Better Science" stated that Pratico, Joshi, and their colleagues' studies on AD appeared to be controversial*:* *https://forbetterscience.com/2020/10/22/the-pratfalls-of-domenico-pratico/*. The controversy was about identical WB results between mice across four different papers. Thus, previous work may need re-evaluation.

Chapter 4 also reported that *Alox15*$^{-/-}$ male and female mice showed a trend for an age-related decline in recognition memory compared to age-matched WT mice, but the differences did not reach statistical significance (Figure 30). Although there was a trend towards a decreased DR, both *Alox15*$^{-/-}$ male and female mice could discriminate between the objects at a rate significantly above chance, indicating no impact on their recognition memory processing. One explanation for these results could be that aged *Alox15*$^{-/-}$ mice had a weaker drive and preference to explore novelty than the WT mice during the TP. Another possibility is that the increased weight may have impacted their motivation to explore the whole arena.

Although object recognition appeared intact, *Alox15*$^{-/-}$ mice displayed spatial memory deficits, which may be linked to hippocampal deficits, in the OLT task. Specifically, *Alox15*$^{-/-}$ male and female mice demonstrated significantly reduced DR, as these mice spent significantly less time interacting with the object that moved into a new location than age-matched WT mice (Figure 37 A). There is considerable evidence that hippocampal lesions disrupt the performance of spatial memory tasks in C57BL/6J mice (Morris, *et al.,* 1990; Clark, *et al.,* 2007; Warburton, *et al*., 2010; Barker, *et al.,* 2011; Voikar, *et al.,* 2018). It was interesting to examine whether the findings of the OLT task, the spatial memory deficits at 15 months of age, were observed in other HPC-dependent behavioural studies, such as the spontaneous alternation T-maze paradigm. Specifically, the significantly reduced alternation performance on the T-maze task might be linked with hippocampal deficits (Rawlins, *et al.,* 1982). The results suggested that the genetic deletion of *Alox15* has detrimental effects on spatial learning and memory.

Over the past decade, there has been considerable evidence suggesting that spatial memory functions and anxiety-like behaviour are preferentially susceptible to dorsal hippocampal subregions as well as ventral hippocampal subregions, respectively, both in mice and humans (Burgess, *et al*., 2002; Pothuizen, *et al.,* 2004; Bast and Feldon. 2003; Fenselow and Dong, 2010; Bannerman, *et al*., 2014; Tu, *et al.,* 2014; Mei, *et al.,* 2020).

In Chapter 5, I, therefore, assessed whether the increased anxiety phenotype was connected to alterations in the expression levels of various protein markers, including parvalbumin, GABAergic, corticotrophin-releasing factor, and serotonergic receptors, as these have been implicated in increased anxiety-related behaviour in mice (Andrews, *et al.,* 1994; File, *et al*., 1996; Zou, *et al*., 2016; Page, *et al*., 2019; Sloviter, *et al.,* 1999; Schuler *et al.,* 2001; Pilc, *et al.,* 2005; Booker, *et al*., 2013; Giachino, *et al*., 2014). To this end, the analysis of the above target proteins were examined in the vHPC and dHPC of aged *Alox15*$^{-/-}$ mice. The main finding was that the anxiety-like behaviour was linked with significantly reduced numbers of PV-positive interneurons and $GABA_B$ receptor positive interneurons in hippocampal pyramidal and granule cells. These results are consistent with previous work that indicated that chronic stress-related anxiety is associated with decreased PV^+ interneurons in the vHPC and a reduced number of $GABA_B$ receptor-positive cells (Mombereau, *et al.,* 2004; Mombereau, *et al.,* 2005; Czeh *et al.,* 2005; Caballero, *et al.,* 2013; Godavarthi *et al*., 2014; Maier, *et al*., 2014; Giachino, *et al.,* 2014; Maie, *et al*., 2014; Song, *et al.,* 2021). In addition, the overexpression of the CRF_1 receptor was positively correlated with anxiety in the HPC in aged *Alox15*$^{-/-}$ mice compared to WT mice. Many animal studies demonstrated that the overexpression of the CRF_1 receptor was

particularly implicated in the early onset of significant anxiety disorders (Contarino, *et al.*, 1999; Bale, *et al.*, 2002; Van Gaalen, *et al.*, 2002). Last, deficiency of *Alox15* resulted in inconsistent results; the number of $5HT_{1A}$ receptor-positive cells was statistically increased in the vCA3 and the DG in *Alox15*$^{-/-}$ compared to WT mice, whereas the $5HT_{1A}$ receptor-positive cells in vCA1 subfield were significantly lower in *Alox15*$^{-/-}$ mice compared to WT mice. Together these data suggest that altered hippocampal expression levels of various proteins were correlated with anxiety-like behaviour in the *Alox15* pathway.

8.2.3 Locomotor activity reduces significantly at late-middle age in *Alox15*$^{-/-}$ mice.

In Chapter 4, I found that during normal ageing, there was a significant decrease in locomotor activity in *Alox15*$^{-/-}$ mice, from young to middle age and old age, concerning the distance that they moved and the speed at which they travelled during habituation compared to WT mice. The increased body weight with age may explain the significantly decreased locomotor activity in *Alox15*$^{-/-}$ mice. A study by Shoji has shown that no significant loss in locomotion function was reported from 2 to 7 months old C57BL/6J mice, but from 8 months of age and onwards, mice displayed decreased locomotor activity as well as increased body weight (Shoji, *et al.*, 2016; Singhal, *et al.*, 2020). Similarly, another study reported that older and heavier C57BL/6 mice showed reduced distance travelled compared to younger mice (Lalonde, *et al.*, 2009). These studies suggested an age-dependent decline in locomotor activity and an age-dependent increase in body weight. Herein, the reduction in activity may therefore be related to a natural age-related reduction in energy metabolism and/or physical deterioration, although this appears to be accelerated in *Alox15*$^{-/-}$.

8.2.4 Lipid metabolic profiling of *Alox15*$^{-/-}$ mice.

In Chapter 6, the generation of free eicosanoids in various brain regions, including the prefrontal cortex, HPC, and cerebellum, generated either enzymatically by LOXs, COXs, and CYPs pathways or non-enzymatically by reactive oxygen species was determined. The *Alox15*$^{-/-}$ mouse brain lipidome of a 24 oxylipin panel was described in Chapter 6, demonstrating lower levels of 12-HETE along with higher levels of 15-HETE compared with WT mice. *Alox12* encodes the platelet type 12-LOX in mice and generates 12-HETE; thus, the levels of 12-HETE in *Alox15*$^{-/-}$ mice may be made by *Alox12* as platelets cross the blood barrier during perfusion. Furthermore, the lipid profiling suggested that specific subsets of oxylipins produced significantly increased levels; the most notable were striking elevations in the relative abundance of prostaglandins derived from COX enzymes in *Alox15*$^{-/-}$ compared to WT mice. Taken together the abundant formation of 15-HETE and the increased expression of

prostaglandins, it is proposed that one of the COX isoforms may be induced, causing excessive production of prostaglandins and mediating inflammation.

12/15-LOX also generates oxidised phospholipids (eoxPLs) were characterised in Chapter 7, and the data revealed extremely low levels in both genotypes, suggesting that these lipids are not major products in the mouse brain. The deficiency of *Alox15* did not alter the levels of PE 18:0a_12-HETE between genotypes, suggesting that this lipid is likely by 12-LOX. Conversely, another product, PE 18:0a_15-HETE, demonstrated significantly reduced amounts in the *Alox15* mouse brain compared to WT mice. This lipid can be formed either by either 12/15-LOX or COX. This is the first lipidomic study investigating normal brain ageing via the *Alox15* pathway in mice. The aged brain is susceptible to oxidative stress as it contains high concentrations of fatty acids that are vulnerable to lipid peroxidation. Specifically, Chinnici *et al.* have shown that 12/15-LOX lipid products are associated with ageing-associated brain oxidative stress responses, damage and neuronal injury (Chinnici *et al*., 2005). They crossbred 12/15-LOX$^{-/-}$ mice with ApoE$^{-/-}$ and measured the levels of iPF$_{2a}$-VI, a marker of lipid peroxidation. They reported significantly elevated marker levels in the ApoE$^{-/-}$ mice expressing 12/15-LOX, suggesting that 12/15-LOX enzymatic activity is linked to mechanisms of oxidative stress responses in the brain.

8.3 Limitations

Here, I outline the limitations of the work presented in this thesis. Firstly, the global *Alox15* KO mouse models are obtained through the global elimination of the *Alox15* gene expression in multiple tissues within the body. The major downside to these mice is that they are technically complex to construct resulting in major deficiencies in *Alox15* expression and function, this results in redundancy within the *Alox15* metabolic pathway and also other lipid metabolic pathways. This may cause compensatory measures within the murine physiology to account for the biological changes which have not been investigated within this thesis.

In addition, *Alox15*$^{-/-}$ mice were subjected to a series of behavioural studies when compared with control C57BL/*6J* mice. The latter were brought in as group housed to the BSU unit in Cardiff University from Charles River UK at 12 weeks old and subjected to a 2-week period of acclimatization. A limitation of this study is the use of non-littermate control mice as the WT mice were reared separately from the KO mice, this key environmental difference could result in phenotypic changes that could have an additional effect to the phenotype observed when the *Alox15* gene is deleted.

The plethora of good-suited behavioural tasks available in the literature to assess cognitivefunction permits the use of alternative studies that would verify the deficits observed previously. In particular, the results from the OLT task in Chapter 4, showed that *Alox15*$^{-/-}$ mice displayed spatial learning and memory deficits, which represent some of the core elements *dependent on hippocampal function* (Bannerman, *et al.*, 2003). The most useful approach is to find an alternative behavioural task that would help to confirm these findings and obtain convincing results (Lewejohann, *et al.*, 2006). Many studies have extensively used the Morris water maze (MWM) test in mice as a task paradigm to assess the effect of age on this specific type of memory: for instance, they suggested that aged C57BL/6J mice displayed spatial memory deficits compared to young mice (Magnusson, *et al.*, 2003; Wong, *et al.*, 2007). Since the MWM task requires mice to have the ability and motivation to swim in a circular pool to find a camouflaged platform, an alternative hippocampal-dependent task was used in Chapter 4, to confirm whether the spatial deficits were extended to other behavioural tests, such as a spontaneous alternation T-maze paradigm (Klapdor, *et al.*, 1996). This task is generally less stressful than other memory tests, including the MWM (Harrison, *et al.*, 2009).

Furthermore, ageing is one of the critical factors influencing physiology and behaviours that should be carefully considered when designing behavioural tests and interpreting differences between genotypes. The behavioural data in Chapters 3 and 4 showed that ageing was associated with changes in cognitive function, locomotor activity, exploration time, and age-related physiological changes, including gradual increases in body weight. *Alox15*$^{-/-}$ mice showed deficits in spatial memory, which appeared to worsen with age. Given that only five-time points were tested in this study, these results captured only a snapshot of age-related changes in male and female *Alox15*$^{-/-}$ mice. However, more work is needed to determine: (i) the exact age at which the *Alox15*$^{-/-}$ mice developed spatial memory decline and anxiety-like behaviour relative to age-matched WT mice; (ii) whether the body weight declines in older *Alox15*$^{-/-}$ and (iii) whether the premature age-related memory decline in *Alox15*$^{-/-}$ males and females is related to the loss of gonadal hormones and circulating ovarian hormones, respectively. Recently, it has been reported that body weight declines in old mice, despite a decrease in energy expenditure and muscle mass (Del Campo, *et al*., 2018; Petr, *et al*., 2021).

Although the pattern of anxiety phenotype exhibited by *Alox15*$^{-/-}$ mice at the behavioural level was associated with ventral hippocampal-dependent dysfunction in Chapter 5, clinical imaging and post-mortem studies have also reported alterations of limbic brain regions in neural circuitry such as the medial prefrontal cortex and amygdala, which are critically involved in anxiety (Milad, *et al*., 2002; Bissonette, *et al*. 2014; Courtin, *et al*. 2014; Sparta, *et al*. 2014).

Therefore, an analysis of other (frontal) brain regions, including double staining related to the alterations in PV interneurons, GABAergic transmission, $5HT_{1A}$ receptor, and CRF_1 receptor expression, may add information to the network involved in the pathophysiology of anxiety disorders in the *Alox15* pathway. One possible explanation of the significant changes in the expression levels observed in Chapter 5 could result from direct actions of anxiety on the amygdala or mPFC dysfunction.

Lastly, the lipidomic data presented in Chapters 6 and 7 were in males; further experiments should be conducted in *Alox15*$^{-/-}$ female mice comparing gender differences in their lipid profiling of WT mice. Having profiled the eoxPLs in the *Alox15*$^{-/-}$ male mice, I would have quantified them to examine any differences in the exact concentrations in regard to WT mice.

8.4 Future Directions

8.4.1 Confirming the cellular origin of the *Alox15* lipid products in various brain regions

Future work could entail chiral analysis of 15-HETE to determine whether it originates from the COX pathway (15R-HETE) or *12/15-LOX* (15S-HETE). Notably, 12R-HETE and 12S-HETE, R and S stereochemistry were produced from 12-LOX and 12/15-LOX, respectively (Funk *et al.*, 2022; Ivanov, *et al.*, 2015). A further study to verify the cellular origin of the isomers and the increased lipid levels such as 5-LOX and COX-1 or -2 would involve measurement of protein levels as well as gene expression, utilising imaging in combination with immunohistochemistry imaging of brain tissue to localise products to their exact origin.

Further work could determine multiple immunofluorescence staining of the *Alox15* lipid products to evaluate their expression levels in neurons (NeuN), microglia (Iba-1), and astrocytes (GFAP) within distinct brain regions such as HPC, prefrontal cortex and cerebellum, which are the targeted brain regions from Chapter 6 and 7. These approaches could identify cell-type specific neurochemically/molecularly defined, including the entire population of neurons and particular types of glia such as astrocytes and microglia (Go, *et al.*, 2022).

8.4.2 Examination of the role of the cerebellum in cognition and behaviour

As illustrated in Chapter 6, most prostaglandins derived from COX enzymes, were signficantly elevated predominantly in the cerebellum in *Alox15*$^{-/-}$ mice. Future work could examine any impact of the cerebellum linked with the spatial deficits and Immunohistochemical GABA expression in Purkinje cells (PCs) of the cerebellar cortex (Wulff, *et al.*, 206; Husson, *et al.*, 201).

8.4.3 For further evaluation to crossbreed mice with *Alox15* deficiency with the Swedish mutation

So far, I have only looked at healthy mice, and the next step would be to extend these studies into neurodegenerative diseases. For this, I could backcross *Alox15*$^{-/-}$ mice with the targeted knock-in of a single London mutation in the *App* gene, a model of Alzheimer's disease. This shows mild cognitive impairment in an age-dependent manner without tau pathology and can allow the examination of possible correlations with either behaviour or targeted lipidomic analysis of brain regions within this study (Abe *et al.*, 2003).

Alternatively, I could backcross with the ApoE4-TR mice, the ε4 allele of apolipoprotein E, which is the strongest genetic risk factor for late-onset AD and also modulates oxidative stress responses (Huang *et al*., 2004; Yamazaki, *et al*., 2019), which results in a catastrophic increase of lipoprotein particles, to characterise the lipids generated via this pathway (Sheng, *et al.*, 1998). Also, it has been reported that *ApoE*$^{-/-}$ mice have reduced synapses, and memory and learning dysfunction, proposing a requirement for ApoE for healthy brain ageing (Masliah *et al.*, 1995; Lane-Donovan, *et al.*, 2016).

8.4.4 Investigating changes at the level of synapse in the brain of Alox15$^{-/-}$ mice

Future work could include evaluation of the expression of synaptophysin, post-synaptic density-95 (PSD-95) and microtubule-associated protein 2 (MAP2), both of which are indicative of pre-and post-synaptic density in the brain between genotypes. To this end, I would determine whether synapse density is correlated with changes in lipid metabolism in the brain regions in *Alox15*$^{-/-}$ mice.

8.4.5 Possible mechanisms are regulating the $GABA_B$ receptor, CRF_1 and $5\text{-}HT_{1A}$ receptors.

Further studies are required to determine the underlying mechanisms by which $GABA_B$, $5HT_{1A}$ and CRF_1 receptors alter anxiety-like behaviour in *Alox15*$^{-/-}$ mice and how receptor activation leads to activation of CREB (cAMP response element-binding protein). It is known that this transcription factor is involved in anxiety-like behaviour by regulating its phosphorylation state (Carlezon *et al.*, 2005). To this end, an investigation of the levels of CREB in the *Alox15*$^{-/-}$ mouse brain using Western Blotting could be undertaken. Furthermore, CREB activates many genes; CREB promotes its binding to the CRE site and leads to gene transcription regulating memory processing and formation (Marie, *et al.*, 2005; Kandel, *et al.*, 2012). Notably, I will apply CRISPR/Cas9 technology to target the role of the critical CREB-targeted genes that may facilitate mmemoryconsolidation and anxiety.

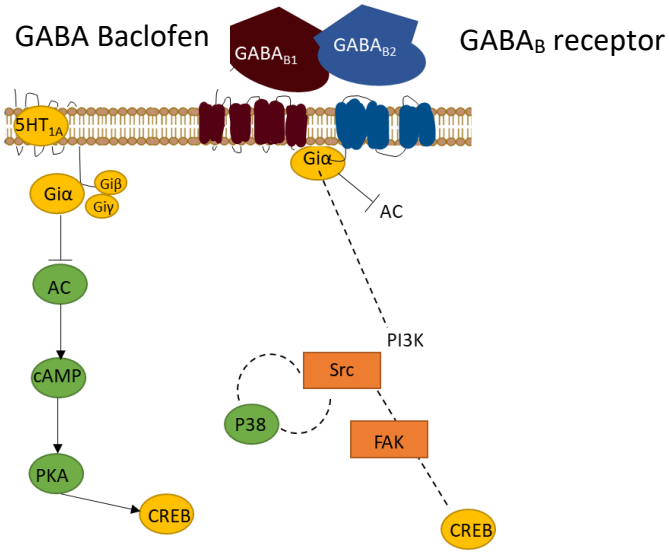

Figure 91. Schematic representation of the signalling pathway mediated by $GABA_B$ receptor and $5HT_{1A}$ receptor leading to CREB activation. Adapted from Serrano-Regal, *et al.*, 2020.

8.4.6 Possible mechanisms regulating the expression of PPAR-γ receptors

PPAR-γ (peroxisome proliferator-activated receptor-gamma), a subtype of PPARs, is most expressed in adipose tissue. PPAR-γ expression regulates genes whose activation exerts neuroprotective effects through anti-inflammatory properties and reduces oxidative stress (Chen et al., 2012; Zolezzi et al., 2013). 12/15-LOX has been shown to activate PPAR-γ by producing fatty acid metabolites, which act as PPAR-γ ligands (Sun *et al.*, 2015). Also, emerging data demonstrate that PPAR-γ expression increases in GABAergic positive neurons in the amygdala and the HPC (Domi *et al.*, 2016, 2019). To this end of how *Alox15* regulates all these findings and given the reduced numbers of $GABA_B$ positive interneurons in

hippocampal pyramidal and granule cells in *Alox15*$^{-/-}$ mice, it is proposed that the lack of PPAR-γ ligands in the *Alox15*$^{-/-}$ mice lead to reduced PPAR-γ ability to induce relevant proteins, which has to be elucidated further.

8.5 Conclusion

In conclusion, this thesis sets out different approaches to elucidate the role of *Alox15* in regulating normal brain function in mice. Behaviourally, there was a pattern of spatial deficits and anxiety phenotype exhibited by *Alox15*$^{-/-}$ mice which appeared to worsen with age. The spatial memory decline and increased anxiety were associated with dorsal and ventral hippocampal-dependent dysfunction. Ultimately, a better understanding of how brain lipid metabolism changes could deduce the mechanisms to indicate cognitive health in age GABAing populations and identify those who are at risk for the development of dementia. At the lipidomic level, the aim was to characterise the *Alox15*$^{-/-}$ mouse brain lipidome and examine whether it varied compared to control mice within various regions using LC-MS/MS. To this end, I found that the two lipid products of 12/15-LOX, 12-HETE and 15-HETE, are produced by the non-enzymatic oxidation of AA.

Chapter 9:

References

Abe, Y., Kouyama, K., Tomita, T., Tomita, Y., Ban, N., Nawa, M., Matsuoka, M., Niikura, T., Aiso, S., Kita, Y. and Iwatsubo, T., 2003. Analysis of neurons created from wild-type and Alzheimer's mutation knock-in embryonic stem cells by a highly efficient differentiation protocol. *Journal of Neuroscience*, *23*(24), pp.8513-8525.Zhang, W., Xu, C., Tu, H., Wang, Y., Sun, Q., Hu, P., Hu, Y., Rondard, P. and Liu, J., 2015. GABAB receptor upregulates fragile X mental retardation protein expression in neurons. *Scientific reports*, *5*(1), pp.1-13.

Adhikari, A., Topiwala, M.A. and Gordon, J.A., 2010. Synchronised activity between the ventral hippocampus and the medial prefrontal cortex during anxiety. *Neuron*, *65*(2), pp.257-269.

Aichler, M. and Walch, A., 2015. MALDI Imaging mass spectrometry: current frontiers and perspectives in pathology research and practice. *Laboratory investigation*, *95*(4), pp.422-431.

Aika, Y., Ren, J.Q., Kosaka, K. and Kosaka, T., 1994. Quantitative analysis of GABA-like-immunoreactive and parvalbumin-containing neurons in the CA1 region of the rat hippocampus using a stereological method, the disector. *Experimental brain research*, *99*(2), pp.267-276.

Akimova, E., Lanzenberger, R. and Kasper, S., 2009. The serotonin-1A receptor in anxiety disorders. Biological psychiatry, 66(7), pp.627-635.

Alashmali, S.M., Lin, L., Trépanier, M.O., Cisbani, G. and Bazinet, R.P., 2019. The effects of n-6 polyunsaturated fatty acid deprivation on the inflammatory gene response to lipopolysaccharide in the mouse hippocampus. Journal of neuroinflammation, 16(1), p.237.

Aldrovandi M, Hammond VJ, Podmore H, Hornshaw M, Clark SR, Marnett LJ, et al. Human platelets generate phospholipid-esterified prostaglandins via cyclooxygenase-1 that are inhibited by low-dose aspirin supplementation. *J Lipid Res* (2013) 54(11):3085–97.

Aldrovandi, M. and O'Donnell, V.B., 2013. Oxidized PLs and vascular inflammation. *Current atherosclerosis reports*, *15*(5), pp.1-8.

Andreou, A. and Feussner, I., 2009. Lipoxygenases–structure and reaction mechanism. Phytochemistry, 70(13-14), pp.1504-1510.

Aoyagi, R., Ikeda, K., Isobe, Y. and Arita, M., 2017. Comprehensive analyses of oxidized phospholipids using a measured MS/MS spectra library. *Journal of lipid research*, *58*(11), pp.2229-2237.

Ase, AR, Reader, TA, Hen, R., Riad, M. and Descarries, L., 2001. Regional changes in density of serotonin transporter in the brain of 5-HT1A and 5-HT1B knockout mice, and of serotonin innervation in the 5-HT1B knockout. Journal of neurochemistry, 78(3), pp.619-630.

Astarita, G., Kendall, A.C., Dennis, E.A. and Nicolaou, A., 2015. Targeted lipidomic strategies for oxygenated metabolites of polyunsaturated fatty acids. *Biochimica et Biophysica Acta (BBA)-Molecular and Cell Biology of Lipids*, *1851*(4), pp.456-468.

Astarita, G., McKenzie, J.H., Wang, B., Strassburg, K., Doneanu, A., Johnson, J., Baker, A., Hankemeier, T., Murphy, J., Vreeken, R.J. and Langridge, J., 2014. A protective lipidomic biosignature associated with a balanced omega-6/omega-3 ratio in fat-1 transgenic mice. *PloS one*, *9*(4), p.e96221.

Austin Pickens, C., Yin, Z., Sordillo, L.M. and Fenton, J.I., 2019. Arachidonic acid-derived hydroxyeicosatetraenoic acids are positively associated with colon polyps in adult males: a cross-sectional study. *Scientific Reports*, *9*(1), pp.1-10.

Aveldano, M.I. and Sprecher, H., 1983. Synthesis of hydroxy fatty acids from 4, 7, 10, 13, 16, 19-[1-14C] docosahexaenoic acid by human platelets. *Journal of Biological Chemistry*, *258*(15), pp.9339-9343.

Babaev, O., Chatain, C.P. and Krueger-Burg, D., 2018. Inhibition in the amygdala anxiety circuitry. Experimental & molecular medicine, 50(4), pp.1-16.

Baer, A.N., Costello, P.B. and Green, F.A., 1990. Free and esterified 13 (R, S)-hydroxyoctadecadienoic acids: principal oxygenase products in psoriatic skin scales. *Journal of Lipid Research*, *31*(1), pp.125-130.

Bailey, J.M., Bryant, R.W., Whiting, J. and Salata, K., 1983. Characterization of 11-HETE and 15-HETE, together with prostacyclin, as major products of the cyclooxygenase pathway in cultured rat aorta smooth muscle cells. *Journal of lipid research*, *24*(11), pp.1419-1428.

Bale, T.L., Contarino, A., Smith, G.W., Chan, R., Gold, L.H., Sawchenko, P.E., Koob, G.F., Vale, W.W. and Lee, K.F., 2000. Mice deficient for corticotropin-releasing hormone receptor-2 display anxiety-like behaviour and are hypersensitive to stress. Nature genetics, 24(4), pp.410-414.

Bannerman, D.M., Sprengel, R., Sanderson, D.J., McHugh, S.B., Rawlins, J.N.P., Monyer, H. and Seeburg, PH, 2014. Hippocampal synaptic plasticity, spatial memory and anxiety. Nature reviews neuroscience, 15(3), pp.181-192.

Bannerman, D.M., Yee, B.K., Good, M.A., Heupel, M.J., Iversen, S.D. and Rawlins, J.N.P., 1999. Double dissociation of function within the hippocampus: a comparison of dorsal, ventral, and complete hippocampal cytotoxic lesions. Behavioral neuroscience, 113(6), p.1170.

Barkus, C., McHugh, S.B., Sprengel, R., Seeburg, P.H., Rawlins, J.N.P. and Bannerman, D.M., 2010. Hippocampal NMDA receptors and anxiety: at the interface between cognition and emotion. European journal of pharmacology, 626(1), pp.49-56.

Barreiro-Iglesias, A., 2020. Role of cyclooxygenases and prostaglandins in adult brain neurogenesis. Prostaglandins & Other Lipid Mediators, p.106498

Barreto, G., Huang, T.T. and Giffard, R.G., 2010. Age-related defects in sensorimotor activity, spatial learning and memory in C57BL/6 mice. *Journal of neurosurgical anesthesiology*, *22*(3), p.214.

Bartholome, O., de la Brassinne Bonardeaux, O., Neirinckx, V. and Rogister, B., 2020. A Composite Sketch of Fast-Spiking Parvalbumin-Positive Neurons. *Cerebral Cortex Communications*, *1*(1), Bannerman, D.M., Grubb, M., Deacon, R.M.J., Yee, B.K., Feldon, J. and Rawlins, J.N.P., 2003. Ventral hippocampal lesions affect anxiety but not spatial learning. Behavioural brain research, 139(1-2), pp.197-213.

Basinger, H. and Hogg, J.P., 2019. Neuroanatomy, brainstem.

Bazinet, R.P. and Layé, S., 2014. Polyunsaturated fatty acids and their metabolites in brain function and disease. *Nature Reviews Neuroscience*, *15*(12), pp.771-785.

Beck, S.G., Choi, K.C. and List, T.J., 1992. Comparison of 5-hydroxytryptamine1A-mediated hyperpolarization in CA1 and CA3 hippocampal pyramidal cells. Journal of Pharmacology and Experimental Therapeutics, 263(1), pp.350-359.

Benardo, L.S., 1995. N-methyl-D-aspartate transmission modulates GABAB-mediated inhibition of rat hippocampal pyramidal neurons in vitro. *Neuroscience*, *68*(3), pp.637-643.

Benice, T.S., Rizk, A., Kohama, S., Pfankuch, T. and Raber, J., 2006. Sex-differences in age-related cognitive decline in C57BL/6J mice associated with increased brain microtubule-associated protein 2 and synaptophysin immunoreactivity. *Neuroscience*, *137*(2), pp.413-423.

Bennett, S.A., Valenzuela, N., Xu, H., Franko, B., Fai, S. and Figeys, D., 2013. Using neurolipidomics to identify phospholipid mediators of synaptic (dys) function in Alzheimer's Disease. *Frontiers in physiology*, *4*, p.168.

Berger, J., 2017. Introduction to the Nervous System. In *Case Closed! Neuroanatomy* (pp. 13-32). CRC Press.

Berger, M., Gray, J.A. and Roth, B.L., 2009. The expanded biology of serotonin. *Annual review of medicine*, *60*, pp.355-366.

Bettler, B., Kaupmann, K., Mosbacher, J. and Gassmann, M., 2004. Molecular structure and physiological functions of GABAB receptors. *Physiological reviews*, *84*(3), pp.835-867.

Bezaire, M.J. and Soltesz, I., 2013. Quantitative assessment of CA1 local circuits: knowledge base for interneuron-pyramidal cell connectivity. Hippocampus, 23(9), pp.751-785.

Bhat, R., Axtell, R., Mitra, A., Miranda, M., Lock, C., Tsien, R.W. and Steinman, L., 2010. Inhibitory role for GABA in autoimmune inflammation. *Proceedings of the National Academy of Sciences*, *107*(6), pp.2580-2585.

Blanco, A. and Blanco, G., 2017. *Medical biochemistry*. Academic Press.

Bligh, E.G. and Dyer, W.J., 1959. A rapid method of total lipid extraction and purification. *Canadian journal of biochemistry and physiology*, *37*(8), pp.911-917.

Blinkouskaya, Y., Caçoilo, A., Gollamudi, T., Jalalian, S. and Weickenmeier, J., 2021. Brain aging mechanisms with mechanical manifestations. *Mechanisms of ageing and development*, *200*, p.111575.

Booker, S.A., Gross, A., Althof, D., Shigemoto, R., Bettler, B., Frotscher, M., Hearing, M., Wickman, K., Watanabe, M., Kulik, Á. and Vida, I., 2013. Differential GABAB-receptor-mediated effects in perisomatic-and dendrite-targeting parvalbumin interneurons. *Journal of Neuroscience*, *33*(18), pp.7961-7974.

Booker, S.A., Harada, H., Elgueta, C., Bank, J., Bartos, M., Kulik, A. and Vida, I., 2020. Presynaptic GABAB receptors functionally uncouple somatostatin interneurons from the active hippocampal network. Elife, 9, p.e51156.

Bourin, M., 2015. Animal models for screening anxiolytic-like drugs: a perspective. *Dialogues in clinical neuroscience*, *17*(3), p.295.

Bowery, N., 1989. GABAB receptors and their significance in mammalian pharmacology. *Trends in Pharmacological Sciences*, *10*(10), pp.401-407.

Brambilla, P., Perez, J., Barale, F., Schettini, G. and Soares, J.C., 2003. GABAergic dysfunction in mood disorders. *Molecular psychiatry*, *8*(8), pp.721-737.

Braverman, N.E. and Moser, A.B., 2012. Functions of plasmalogen lipids in health and disease. *Biochimica et Biophysica Acta (BBA)-Molecular Basis of Disease*, *1822*(9), pp.1442-1452.

Brunson, K.L., Avishai-Eliner, S., Hatalski, C.G. and Baram, TZ, 2001. Neurobiology of the stress response early in life: evolution of a concept and the role of corticotropin releasing hormone. *Molecular psychiatry*, *6*(6), pp.647-656.

Brunson, K.L., Eghbal-Ahmadi, M., Bender, R., Chen, Y. and Baram, TZ, 2001. Long-term, progressive hippocampal cell loss and dysfunction induced by early-life administration of corticotropin-releasing hormone reproduce the effects of early-life stress. *Proceedings of the National Academy of Sciences*, *98*(15), pp.8856-8861.

Brunson, K.L., Grigoriadis, D.E., Lorang, M.T. and Baram, T.Z., 2002. Corticotropin-releasing hormone (CRH) downregulates the function of its receptor (CRF1) and induces CRF1

expression in hippocampal and cortical regions of the immature rat brain. *Experimental neurology*, *176*(1), pp.75-86.

Burgess, N., Maguire, E.A. and O'Keefe, J., 2002. The human hippocampus and spatial and episodic memory. *Neuron*, *35*(4), pp.625-641.

Caballero, A., Diah, K.C. and Tseng, K.Y., 2013. Region-specific upregulation of parvalbumin-, but not calretinin-positive cells in the ventral hippocampus during adolescence. *Hippocampus*, *23*(12), pp.1331-1336.

Cabungcal, J.H., Steullet, P., Kraftsik, R., Cuenod, M. and Do, K.Q., 2013. Early-life insults impair parvalbumin interneurons via oxidative stress: reversal by N-acetylcysteine. Biological psychiatry, 73(6), pp.574-582.

Caillard, O., Moreno, H., Schwaller, B., Llano, I., Celio, M.R. and Marty, A., 2000. Role of the calcium-binding protein parvalbumin in short-term synaptic plasticity. *Proceedings of the National Academy of Sciences*, *97*(24), pp.13372-13377.

Calder, P.C., 2006. n− 3 Polyunsaturated fatty acids, inflammation, and inflammatory diseases. *The American journal of clinical nutrition*, *83*(6), pp.1505S-1519S.

Canbay, H.S., 2017. Effectiveness of liquid-liquid extraction, solid phase extraction, and headspace technique for determination of some volatile water-soluble compounds of rose aromatic water. *International Journal of Analytical Chemistry*, *2017*.

Cannistraro, P.A. and Rauch, S.L., 2003. Neural circuitry of anxiety: evidence from structural and functional neuroimaging studies. *Psychopharmacology bulletin*, *37*(4), pp.8-25.

Cao, K., Shen, C., Yuan, Y., Bai, S., Yang, L., Guo, L., Zhang, R. and Shi, Y., 2019. SiNiSan ameliorates the depression-like behavior of rats that experienced maternal separation through 5-HT1A receptor/CREB/BDNF pathway. *Frontiers in psychiatry*, *10*, p.160.

Carlezon Jr, W.A., Duman, R.S. and Nestler, E.J., 2005. The many faces of CREB. *Trends in neurosciences*, *28*(8), pp.436-445.

Cater, R.J., Chua, G.L., Erramilli, S.K., Keener, J.E., Choy, B.C., Tokarz, P., Chin, C.F., Quek, D.Q., Kloss, B., Pepe, J.G. and Parisi, G., 2021. Structural basis of omega-3 fatty acid transport across the blood–brain barrier. *Nature*, *595*(7866), pp.315-319.

Cawello, W., Schweer, H., Dietrich, B., Seyberth, H.W., Albrecht, D., Fox, A. and Hohmuth, H., 1997. Pharmacokinetics of prostaglandin E1 and its main metabolites after intracavernous injection and short-term infusion of prostaglandin E1 in patients with erectile dysfunction. *The Journal of urology*, *158*(4), pp.1403-1407.

Chalifoux, J.R. and Carter, A.G., 2011. GABAB receptor modulation of synaptic function. *Current opinion in neurobiology*, *21*(2), pp.339-344.

Chan, R.B., Oliveira, T.G., Cortes, E.P., Honig, L.S., Duff, K.E., Small, S.A., Wenk, M.R., Shui, G. and Di Paolo, G., 2012. Comparative lipidomic analysis of mouse and human brain with Alzheimer disease. *Journal of Biological Chemistry*, *287*(4), pp.2678-2688.

Charles, K.J., Deuchars, J., Davies, C.H. and Pangalos, M.N., 2003. GABAB receptor subunit expression in glia. *Molecular and Cellular Neuroscience*, *24*(1), pp.214-223.

Chen, Y., Andres, A., Frotscher, M. and Baram, T.Z., 2012. Tuning synaptic transmission in the hippocampus by stress: the CRH system. Frontiers in cellular neuroscience, 6, p.13.

Chen, Y., Bender, R.A., Brunson, K.L., Pomper, J.K., Grigoriadis, D.E., Wurst, W. and Baram, T.Z., 2004. Modulation of dendritic differentiation by corticotropin-releasing factor in the developing hippocampus. *Proceedings of the National Academy of Sciences*, *101*(44), pp.15782-15787.

Chen, Y., Brunson, K.L., Müller, M.B., Cariaga, W. and Baram, T.Z., 2000. Immunocytochemical distribution of corticotropin-releasing hormone receptor type-1 (CRF1)-like immunoreactivity in the mouse brain: Light microscopy analysis using an antibody directed against the C-terminus. *Journal of Comparative Neurology*, *420*(3), pp.305-323.

Chen, Y., Dubé, C.M., Rice, C.J. and Baram, T.Z., 2008. Rapid loss of dendritic spines after stress involves derangement of spine dynamics by corticotropin-releasing hormone. Journal of Neuroscience, 28(11), pp.2903-2911.

Chinnici, C.M., Yao, Y. and Praticò, D., 2007. The 5-lipoxygenase enzymatic pathway in the mouse brain: young versus old. Neurobiology of aging, 28(9), pp.1457-1462.

Chiu, H.H. and Kuo, C.H., 2020. Gas chromatography-mass spectrometry-based analytical strategies for fatty acid analysis in biological samples. *Journal of food and drug analysis*, *28*(1), pp.60-73.

Choi, J., Yin, T., Shinozaki, K., Lampe, J.W., Stevens, J.F., Becker, L.B. and Kim, J., 2018. Comprehensive analysis of phospholipids in the brain, heart, kidney, and liver: brain phospholipids are least enriched with polyunsaturated fatty acids. *Molecular and cellular biochemistry*, *442*(1), pp.187-201.

Choi, S.H., Langenbach, R. and Bosetti, F., 2006. Cyclooxygenase-1 and-2 enzymes differentially regulate the brain upstream NF-κB pathway and downstream enzymes involved in prostaglandin biosynthesis. *Journal of neurochemistry*, *98*(3), pp.801-811.

Christie, W.W. and Harwood, J.L., 2020. Oxidation of polyunsaturated fatty acids to produce lipid mediators. Essays in Biochemistry, 64(3), pp.401-421.

Christoffel, D.J., Golden, S.A. and Russo, S.J., 2011. Structural and synaptic plasticity in stress-related disorders. Reviews in the Neurosciences, 22(5), pp.535-549.

Chu, J. and Praticò, D., 2012. Involvement of 5-lipoxygenase activating protein in the amyloidotic phenotype of an Alzheimer's disease mouse model. *Journal of Neuroinflammation*, *9*(1), pp.1-10.

Chu, J. and Praticò, D., 2016. The 5-Lipoxygenase as modulator of Alzheimer's γ-secretase and therapeutic target. Brain research bulletin, 126, pp.207-212.

Clark, S.R., Guy, C.J., Scurr, M.J., Taylor, P.R., Kift-Morgan, A.P., Hammond, V.J., Thomas, C.P., Coles, B., Roberts, G.W., Eberl, M. and Jones, S.A., 2011. Esterified eicosanoids are acutely generated by 5-lipoxygenase in primary human neutrophils and in human and murine infection. Blood, The Journal of the American Society of Hematology, 117(6), pp.2033-2043.

Coffa, G. and Brash, A.R., 2004. A single active site residue directs oxygenation stereospecificity in lipoxygenases: stereocontrol is linked to the position of oxygenation. Proceedings of the National Academy of Sciences, 101(44), pp.15579-15584.

Cole, J.H., Marioni, R.E., Harris, S.E. and Deary, I.J., 2019. Brain age and other bodily 'ages': implications for neuropsychiatry. *Molecular psychiatry*, *24*(2), pp.266-281.

Collin, T., Chat, M., Lucas, M.G., Moreno, H., Racay, P., Schwaller, B., Marty, A. and Llano, I., 2005. Developmental changes in parvalbumin regulate presynaptic Ca2+ signaling. *Journal of Neuroscience*, *25*(1), pp.96-107.

Combrinck, M., Williams, J., De Berardinis, M.A., Warden, D., Puopolo, M., Smith, A.D. and Minghetti, L., 2006. Levels of CSF prostaglandin E2, cognitive decline, and survival in Alzheimer's disease. *Journal of Neurology, Neurosurgery & Psychiatry*, *77*(1), pp.85-88.

Connor, W.E., 2000. Importance of n− 3 fatty acids in health and disease. *The American journal of clinical nutrition*, *71*(1), pp.171S-175S.

Contarino, A., Dellu, F., Koob, G.F., Smith, G.W., Lee, K.F., Vale, W. and Gold, LH, 1999. Reduced anxiety-like and cognitive performance in mice lacking the corticotropin-releasing factor receptor 1. Brain research, 835(1), pp.1-9.

Crankshaw, D.J. and Gaspar, V., 1995. Pharmacological characterization in vitro of prostanoid receptors in the myometrium of nonpregnant ewes. *Reproduction*, *103*(1), pp.55-61.

Crawley, J.N., 2008. Behavioral phenotyping strategies for mutant mice. *Neuron*, *57*(6), pp.809-818.

Cryan, J.F. and Holmes, A., 2005. The ascent of mouse: advances in modelling human depression and anxiety. Nature reviews Drug discovery, 4(9), pp.775-790.

Cryan, J.F., Kelly, P.H., Chaperon, F., Gentsch, C., Mombereau, C., Lingenhoehl, K., Froestl, W., Bettler, B., Kaupmann, K. and Spooren, W.P., 2004. Behavioral characterization of the novel GABAB receptor-positive modulator GS39783 (N, N′-dicyclopentyl-2-methylsulfanyl-

5-nitro-pyrimidine-4, 6-diamine): anxiolytic-like activity without side effects associated with baclofen or benzodiazepines. *Journal of Pharmacology and Experimental Therapeutics*, *310*(3), pp.952-963.

Czapski, G.A., Czubowicz, K., Strosznajder, J.B. and Strosznajder, R.P., 2016. The lipoxygenases: their regulation and implication in Alzheimer's disease. Neurochemical research, 41(1-2), pp.243-257.

Czéh, B., Pudovkina, O., van der Hart, M.G., Simon, M., Heilbronner, U., Michaelis, T., Watanabe, T., Frahm, J. and Fuchs, E., 2005. Examining SLV-323, a novel NK 1 receptor antagonist, in a chronic psychosocial stress model for depression. *Psychopharmacology*, *180*(3), pp.548-557.

Czeh, B., Simon, M., Van Der Hart, M.G., Schmelting, B., Hesselink, M.B. and Fuchs, E., 2005. Chronic stress decreases the number of parvalbumin-immunoreactive interneurons in the hippocampus: prevention by treatment with a substance P receptor (NK 1) antagonist. *Neuropsychopharmacology*, *30*(1), pp.67-79.

Czéh, B., Varga, Z.K.K., Henningsen, K., Kovács, G.L., Miseta, A. and Wiborg, O., 2015. Chronic stress reduces the number of GABAergic interneurons in the adult rat hippocampus, dorsal-ventral and region-specific differences. *Hippocampus*, *25*(3), pp.393-405.

Czesak, M., Le François, B., Millar, A.M., Deria, M., Daigle, M., Visvader, J.E., Anisman, H. and Albert, P.R., 2012. Increased serotonin-1A (5-HT1A) autoreceptor expression and reduced raphe serotonin levels in deformed epidermal autoregulatory factor-1 (Deaf-1) gene knock-out mice. Journal of Biological Chemistry, 287(9), pp.6615-6627.

Dandi, E., Kalamari, A., Touloumi, O., Lagoudaki, R., Nousiopoulou, E., Simeonidou, C., Spandou, E. and Tata, D.A., 2018. Beneficial effects of environmental enrichment on behavior, stress reactivity and synaptophysin/BDNF expression in hippocampus following early life stress. International Journal of Developmental Neuroscience, 67, pp.19-32.

Deacon, R.M., Bannerman, D.M. and Rawlins, J.N.P., 2002. Anxiolytic effects of cytotoxic hippocampal lesions in rats. *Behavioral neuroscience*, *116*(3), p.494.

Deary, I.J., Corley, J., Gow, A.J., Harris, S.E., Houlihan, L.M., Marioni, R.E., Penke, L., Rafnsson, S.B. and Starr, J.M., 2009. Age-associated cognitive decline. *British medical bulletin*, *92*(1), pp.135-152.

Degro, C.E., Kulik, A., Booker, S.A. and Vida, I., 2015. Compartmental distribution of GABAB receptor-mediated currents along the somatodendritic axis of hippocampal principal cells. *Frontiers in synaptic neuroscience*, *7*, p.6.

Del Campo, A., Contreras-Hernández, I., Castro-Sepúlveda, M., Campos, C.A., Figueroa, R., Tevy, M.F., Eisner, V., Casas, M. and Jaimovich, E., 2018. Muscle function decline and mitochondria changes in middle age precede sarcopenia in mice. *Aging (Albany NY)*, *10*(1), p.34.

Deng, X., Gu, L., Sui, N., Guo, J. and Liang, J., 2019. Parvalbumin interneuron in the ventral hippocampus functions as a discriminator in social memory. *Proceedings of the National Academy of Sciences*, *116*(33), pp.16583-16592.

Dennis, E.A., Cao, J., Hsu, Y.H., Magrioti, V. and Kokotos, G., 2011. Phospholipase A2 enzymes: physical structure, biological function, disease implication, chemical inhibition, and therapeutic intervention. Chemical reviews, 111(10), pp.6130-6185.

DeTure, M.A. and Dickson, D.W., 2019. The neuropathological diagnosis of Alzheimer's disease. *Molecular neurodegeneration*, *14*(1), pp.1-18.

Devassy, J.G., Leng, S., Gabbs, M., Monirujjaman, M. and Aukema, H.M., 2016. Omega-3 polyunsaturated fatty acids and oxylipins in neuroinflammation and management of Alzheimer disease. *Advances in Nutrition*, *7*(5), pp.905-916.

Dobrian, A.D., Morris, M.A., Taylor-Fishwick, D.A., Holman, T.R., Imai, Y., Mirmira, R.G. and Nadler, J.L., 2019. Role of the 12-lipoxygenase pathway in diabetes pathogenesis and complications. *Pharmacology & therapeutics*, *195*, pp.100-110.

Domi, E., Caputi, F.F., Romualdi, P., Domi, A., Scuppa, G., Candeletti, S., Atkins, A., Heilig, M., Demopulos, G., Gaitanaris, G. and Ciccocioppo, R., 2019. Activation of PPARγ attenuates the expression of physical and affective nicotine withdrawal symptoms through mechanisms involving amygdala and hippocampus neurotransmission. *Journal of Neuroscience*, *39*(49), pp.9864-9875.

Domi, E., Uhrig, S., Soverchia, L., Spanagel, R., Hansson, A.C., Barbier, E., Heilig, M., Ciccocioppo, R. and Ubaldi, M., 2016. Genetic deletion of neuronal PPARγ enhances the emotional response to acute stress and exacerbates anxiety: an effect reversed by rescue of amygdala PPARγ function. *Journal of Neuroscience*, *36*(50), pp.12611-12623.

Driscoll, I., Hamilton, D.A., Petropoulos, H., Yeo, R.A., Brooks, W.M., Baumgartner, R.N. and Sutherland, R.J., 2003. The aging hippocampus: cognitive, biochemical and structural findings. *Cerebral cortex*, *13*(12), pp.1344-1351.

Driscoll, I., Howard, S.R., Stone, J.C., Monfils, M.H., Tomanek, B., Brooks, W.M. and Sutherland, R.J., 2006. The aging hippocampus: a multi-level analysis in the rat. *Neuroscience*, *139*(4), pp.1173-1185.

Duman, R.S., 1998. Novel therapeutic approaches beyond the serotonin receptor. *Biological psychiatry*, *44*(5), pp.324-335.

Emre, C., Do, K.V., Jun, B., Hjorth, E., Alcalde, S.G., Kautzmann, M.A.I., Gordon, W.C., Nilsson, P., Bazan, N.G. and Schultzberg, M., 2021. Age-related changes in brain phospholipids and bioactive lipids in the APP knock-in mouse model of Alzheimer's disease. *Acta Neuropathologica Communications*, *9*(1), pp.1-26.

Emson, P.C., 2007. GABAB receptors: structure and function. *Progress in brain research*, *160*, pp.43-57.

Erickson, C.A. and Barnes, C.A., 2003. The neurobiology of memory changes in normal aging. *Experimental gerontology*, *38*(1-2), pp.61-69.

Fabre, V., Beaufour, C., Evrard, A., Rioux, A., Hanoun, N., Lesch, K.P., Murphy, D.L., Lanfumey, L., Hamon, M. and Martres, M.P., 2000. Altered expression and functions of serotonin 5-HT1A and 5-HT1B receptors in knock-out mice lacking the 5-HT transporter. European Journal of Neuroscience, 12(7), pp.2299-2310.

Fang, X., Xie, J., Chu, S., Jiang, Y., An, Y., Li, C., Gong, X., Zhai, R., Huang, Z., Qiu, C. and Dai, X., 2021. Quadrupole-linear ion trap tandem mass spectrometry system for clinical biomarker analysis. *Engineering*.

Farine, L., Niemann, M., Schneider, A. and Bütikofer, P., 2015. Phosphatidylethanolamine and phosphatidylcholine biosynthesis by the Kennedy pathway occurs at different sites in Trypanosoma brucei. Scientific reports, 5(1), pp.1-11.

Feingold, K.R. and Grunfeld, C., 2015. Introduction to lipids and lipoproteins.

Felice, D., O'Leary, O.F., Pizzo, R.C. and Cryan, J.F., 2012. Blockade of the GABAB receptor increases neurogenesis in the ventral but not dorsal adult hippocampus: relevance to antidepressant action. Neuropharmacology, 63(8), pp.1380-1388.

Ferguson, C.S. and Tyndale, R.F., 2011. Cytochrome P450 enzymes in the brain: emerging evidence of biological significance. Trends in pharmacological sciences, 32(12), pp.708-714.

Filice, F., Vörckel, K.J., Sungur, A.Ö., Wöhr, M. and Schwaller, B., 2016. Reduction in parvalbumin expression not loss of the parvalbumin-expressing GABA interneuron subpopulation in genetic parvalbumin and shank mouse models of autism. *Molecular brain*, *9*(1), pp.1-17.

Fitzner, D., Bader, J.M., Penkert, H., Bergner, C.G., Su, M., Weil, M.T., Surma, M.A., Mann, M., Klose, C. and Simons, M., 2020. Cell-type-and brain-region-resolved mouse brain lipidome. *Cell Reports*, *32*(11), p.108132.

Frick, K.M., Burlingame, L.A., Arters, J.A. and Berger-Sweeney, J., 1999. Reference memory, anxiety and estrous cyclicity in C57BL/6NIA mice are affected by age and sex. *Neuroscience*, *95*(1), pp.293-307.

Fuchs, E.C., Zivkovic, A.R., Cunningham, M.O., Middleton, S., LeBeau, F.E., Bannerman, D.M., Rozov, A., Whittington, M.A., Traub, R.D., Rawlins, J.N.P. and Monyer, H., 2007. Recruitment of parvalbumin-positive interneurons determines hippocampal function and associated behavior. *Neuron*, *53*(4), pp.591-604.

Funk, C.D., Chen, X.S., Johnson, E.N. and Zhao, L., 2002. Lipoxygenase genes and their targeted disruption. *Prostaglandins & other lipid mediators*, *68*, pp.303-312.

Gabbs, M., Leng, S., Devassy, J.G., Monirujjaman, M. and Aukema, H.M., 2015. Advances in our understanding of oxylipins derived from dietary PUFAs. Advances in nutrition, 6(5), pp.513-540.

Gabbs, M., Leng, S., Devassy, J.G., Monirujjaman, M. and Aukema, H.M., 2015. Advances in our understanding of oxylipins derived from dietary PUFAs. Advances in nutrition, 6(5), pp.513-540.

Gao, S., Zhou, L., Lu, J., Fang, Y., Wu, H., Xu, W., Pan, Y., Wang, J., Wang, X., Zhang, J. and Shao, A., 2022. Cepharanthine attenuates early brain injury after subarachnoid hemorrhage in mice via inhibiting 15-lipoxygenase-1-mediated microglia and endothelial cell ferroptosis. *Oxidative medicine and cellular longevity*, *2022*.

Garcia-Garcia, A.L., Newman-Tancredi, A. and Leonardo, E.D., 2014. P5-HT 1A receptors in mood and anxiety: recent insights into autoreceptor versus heteroreceptor function. *Psychopharmacology*, *231*(4), pp.623-636.

Gassmann, M. and Bettler, B., 2012. Regulation of neuronal GABA B receptor functions by subunit composition. *Nature Reviews Neuroscience*, *13*(6), pp.380-394.

Giachino, C., Barz, M., Tchorz, J.S., Tome, M., Gassmann, M., Bischofberger, J., Bettler, B. and Taylor, V., 2014. GABA suppresses neurogenesis in the adult hippocampus through GABAB receptors. *Development*, *141*(1), pp.83-90.

Giannopoulos, P.F., Chu, J., Joshi, Y.B., Sperow, M., Li, J.G., Kirby, L.G. and Praticò, D., 2013. 5-lipoxygenase activating protein reduction ameliorates cognitive deficit, synaptic dysfunction, and neuropathology in a mouse model of Alzheimer's disease. *Biological psychiatry*, *74*(5), pp.348-356. Hopfgartner, G., Varesio, E., Tschäppät, V., Grivet, C., Bourgogne, E. and Leuthold, L.A., 2004. Triple quadrupole linear ion trap mass spectrometer for the analysis of small molecules and macromolecules. *Journal of mass spectrometry*, *39*(8), pp.845-855.

Gijón, M.A., Riekhof, W.R., Zarini, S., Murphy, R.C. and Voelker, D.R., 2008. Lysophospholipid acyltransferases and arachidonate recycling in human neutrophils. *Journal of Biological Chemistry*, *283*(44), pp.30235-30245.

Gilroy, D.W., Colville-Nash, P.R., Willis, D., Chivers, J., Paul-Clark, M.J. and Willoughby, D.A., 1999. Inducible cyclooxygenase may have anti-inflammatory properties. Nature medicine, 5(6), pp.698-701.

Ginty, D.D., Bonni, A. and Greenberg, M.E., 1994. Nerve growth factor activates a Ras-dependent protein kinase that stimulates c-fos transcription via phosphorylation of CREB. Cell, 77(5), pp.713-725.

Glaser, P.E. and Gross, R.W., 1994. Plasmenylethanolamine facilitates rapid membrane fusion: a stopped-flow kinetic investigation correlating the propensity of a major plasma membrane constituent to adopt an HII phase with its ability to promote membrane fusion. *Biochemistry*, *33*(19), pp.5805-5812.

Godavarthi, S.K., Dey, P., Maheshwari, M. and Ranjan Jana, N., 2012. Defective glucocorticoid hormone receptor signaling leads to increased stress and anxiety in a mouse model of Angelman syndrome. *Human Molecular Genetics*, *21*(8), pp.1824-1834.

Godavarthi, S.K., Sharma, A. and Jana, N.R., 2014. Reversal of reduced parvalbumin neurons in hippocampus and amygdala of Angelman syndrome model mice by chronic treatment of fluoxetine. *Journal of neurochemistry*, *130*(3), pp.444-454. S.K., Sharma, A. and Jana, N.R., 2014. Reversal of reduced parvalbumin neurons in hippocampus and amygdala of Angelman syndrome model mice by chronic treatment of fluoxetine. *Journal of neurochemistry*, *130*(3), pp.444-454.

Goldberg, E.M., Clark, B.D., Zagha, E., Nahmani, M., Erisir, A. and Rudy, B., 2008. K+ channels at the axon initial segment dampen near-threshold excitability of neocortical fast-spiking GABAergic interneurons. *Neuron*, *58*(3), pp.387-400.

Gonzalez-Burgos, G., Fish, K.N. and Lewis, D.A., 2011. GABA neuron alterations, cortical circuit dysfunction and cognitive deficits in schizophrenia. *Neural plasticity*, *2011*..

Goodfellow, N.M., Bailey, C.D. and Lambe, E.K., 2012. The native serotonin 5-HT5A receptor: electrophysiological characterization in rodent cortex and 5-HT1A-mediated compensatory plasticity in the knock-out mouse. Journal of Neuroscience, 32(17), pp.5804-5809.

Goodfellow, N.M., Benekareddy, M., Vaidya, V.A. and Lambe, E.K., 2009. Layer II/III of the prefrontal cortex: inhibition by the serotonin 5-HT1A receptor in development and stress. Journal of Neuroscience, 29(32), pp.10094-10103.

Gorelick, P.B., Counts, S.E. and Nyenhuis, D., 2016. Vascular cognitive impairment and dementia. *Biochimica et Biophysica Acta (BBA)-Molecular Basis of Disease*, *1862*(5), pp.860-868.

Govindpani, K., Calvo-Flores Guzmán, B., Vinnakota, C., Waldvogel, H.J., Faull, R.L. and Kwakowsky, A., 2017. Towards a better understanding of GABAergic remodeling in Alzheimer's disease. *International journal of molecular sciences*, *18*(8), p.1813.

Greig FH, Kennedy S, Spickett CM. Physiological effects of oxidized phospholipids and their cellular signaling mechanisms in inflammation. Free Radic Biol Med. 2012 Jan 15;52(2):266-80. doi: 10.1016/j.freeradbiomed.2011.10.481. Epub 2011 Oct 31. PMID: 22080084.

Grone, B.P. and Maruska, K.P., 2016. Three distinct glutamate decarboxylase genes in vertebrates. *Scientific reports*, *6*(1), pp.1-9.

Gross, C., Santarelli, L., Brunner, D., Zhuang, X. and Hen, R., 2000. Altered fear circuits in 5-HT1A receptor KO mice. Biological psychiatry, 48(12), pp.1157-1163.

Gross, J.H., 2006. *Mass spectrometry: a textbook*. Springer Science & Business Media.

Guan, Z., Wang, Y., Cairns, N.J., Lantos, P.L., Dallner, G. and Sindelar, P.J., 1999. Decrease and structural modifications of phosphatidylethanolamine plasmalogen in the brain with Alzheimer disease. *Journal of neuropathology and experimental neurology*, *58*(7), pp.740-747.

Guido, D.M., McKenna, R. and Mathews, W.R., 1993. Quantitation of hydroperoxy-eicosatetraenoic acids and hydroxy-eicosatetraenoic acids as indicators of lipid peroxidation using gas chromatography-mass spectrometry. *Analytical biochemistry*, *209*(1), pp.123-129.

H Vinkers, C., F Cryan, J., Olivier, B. and Groenink, L., 2010. Elucidating GABAA and GABAB receptor functions in anxiety using the stress-induced hyperthermia paradigm: A review. *The Open Pharmacology Journal*, *4*(1).

Haddjeri, N., Blier, P. and de Montigny, C., 1998. Long-term antidepressant treatments result in a tonic activation of forebrain 5-HT1A receptors. *Journal of Neuroscience*, *18*(23), pp.10150-10156.

Hajeyah, A.A., Griffiths, W.J., Wang, Y., Finch, A.J. and O'Donnell, V.B., 2020. The biosynthesis of enzymatically oxidized lipids. Frontiers in Endocrinology, 11.

Halloran, B.P., Ferguson, V.L., Simske, S.J., Burghardt, A., Venton, LL and Majumdar, S., 2002. Changes in bone structure and mass with advancing age in the male C57BL/6J mouse. *Journal of bone and mineral research*, *17*(6), pp.1044-1050.

Hammond, V.J. and O'Donnell, V.B., 2012. Esterified eicosanoids: generation, characterization and function. Biochimica et Biophysica Acta (BBA)-Biomembranes, 1818(10), pp.2403-2412.

Hamon, M., 2000. The main features of central 5-HT 1A receptors. In Serotoninergic Neurons and 5-HT Receptors in the CNS (pp. 239-268). Springer, Berlin, Heidelberg.

Han, H.A., Cortez, M.A. and Snead III, O.C., 2012. GABAB receptor and absence epilepsy. *Jasper's Basic Mechanisms of the Epilepsies [Internet]. 4th edition*.

Han, X. and Gross, R.W., 2005. Shotgun lipidomics: electrospray ionization mass spectrometric analysis and quantitation of cellular lipidomes directly from crude extracts of biological samples. *Mass spectrometry reviews*, *24*(3), pp.367-412.

Han, X., Holtzman, D.M. and McKeel Jr, D.W., 2001. Plasmalogen deficiency in early Alzheimer's disease subjects and in animal models: molecular characterization using electrospray ionization mass spectrometry. *Journal of neurochemistry*, *77*(4), pp.1168-1180.

Hancock, S.E., Friedrich, M.G., Mitchell, T.W., Truscott, R.J. and Else, P.L., 2015. Decreases in phospholipids containing adrenic and arachidonic acids occur in the human hippocampus over the adult lifespan. *Lipids*, *50*(9), pp.861-872.

Hannon, J. and Hoyer, D., 2008. Molecular biology of 5-HT receptors. Behavioural brain research, 195(1), pp.198-213.

Harper, A., 2010. Mouse models of neurological disorders—A comparison of heritable and acquired traits. *Biochimica et Biophysica Acta (BBA)-Molecular Basis of Disease*, *1802*(10), pp.785-795.

Harrison, F.E., Hosseini, A.H. and McDonald, M.P., 2009. Endogenous anxiety and stress responses in water maze and Barnes maze spatial memory tasks. *Behavioural brain research*, *198*(1), pp.247-251.

Hashimoto, M., Hossain, S., Shimada, T., Sugioka, K., Yamasaki, H., Fujii, Y., Ishibashi, Y., Oka, J.I. and Shido, O., 2002. Docosahexaenoic acid provides protection from impairment of learning ability in Alzheimer's disease model rats. Journal of neurochemistry, 81(5), pp.1084-1091.

Hayakawa, M., Sugiyama, S., Takamura, T., Yokoo, K., Iwata, M., Suzuki, K., Taki, F., Takahashi, S. and Ozawa, T., 1986. Neutrophils biosynthesize leukotoxin, 9, 10-epoxy-12-octadecenoate. *Biochemical and biophysical research communications*, *137*(1), pp.424-430.

Heizmann, C.W., 1984. Parvalbumin, and intracellular calcium-binding protein; distribution, properties and possible roles in mammalian cells. *Experientia*, *40*(9), pp.910-921.

Hill, A.S., Sahay, A. and Hen, R., 2015. Increasing adult hippocampal neurogenesis is sufficient to reduce anxiety and depression-like behaviors. *Neuropsychopharmacology*, *40*(10), pp.2368-2378.

Hillhouse, E.W. and Grammatopoulos, D.K., 2006. The molecular mechanisms underlying the regulation of the biological activity of corticotropin-releasing hormone receptors: implications for physiology and pathophysiology. Endocrine reviews, 27(3), pp.260-286.

Hirai, H., Tanaka, K., Yoshie, O., Ogawa, K., Kenmotsu, K., Takamori, Y., Ichimasa, M., Sugamura, K., Nakamura, M., Takano, S. and Nagata, K., 2001. Prostaglandin D2 selectively induces chemotaxis in T helper type 2 cells, eosinophils, and basophils via seven-transmembrane receptor CRTH2. *The Journal of experimental medicine*, *193*(2), pp.255-262.

Ho, C.S., Lam, C.W.K., Chan, M.H.M., Cheung, R.C.K., Law, L.K., Lit, L.C.W., Ng, K.F., Suen, M.W.M. and Tai, H., 2003. Electrospray ionisation mass spectrometry: principles and clinical applications. *The Clinical Biochemist Reviews*, *24*(1), p.3.

Holmes, A. and Cryan, J.F., 2006. Modeling human anxiety and depression in mutant mice. In *Transgenic and knockout models of neuropsychiatric disorders* (pp. 237-263). Humana Press.

Hu, H., Gan, J. and Jonas, P., 2014. Fast-spiking, parvalbumin+ GABAergic interneurons: From cellular design to microcircuit function. Science, 345(6196).

Hussain, G., Schmitt, F., Loeffler, J.P. and Aguilar, J.L.G.D., 2013. Fatting the brain: a brief of recent research. *Frontiers in cellular neuroscience*, *7*, p.144.

Hussain, G., Wang, J., Rasul, A., Anwar, H., Imran, A., Qasim, M., Zafar, S., Kamran, S.K.S., Razzaq, A., Aziz, N. and Ahmad, W., 2019. Role of cholesterol and sphingolipids in brain development and neurological diseases. Lipids in health and disease, 18(1), pp.1-12.

Husson, Z., Rousseau, C.V., Broll, I., Zeilhofer, H.U. and Dieudonné, S., 2014. Differential GABAergic and glycinergic inputs of inhibitory interneurons and Purkinje cells to principal cells of the cerebellar nuclei. *Journal of Neuroscience*, *34*(28), pp.9418-9431.

Imai Y, Kuba K, Neely GG, Yaghubian-Malhami R, Perkmann T, van Loo G, Ermolaeva M, Veldhuizen R, Leung YH, Wang H, Liu H, Sun Y, Pasparakis M, Kopf M, Mech C, Bavari S, Peiris JS, Slutsky AS, Akira S, Hultqvist M, Holmdahl R, Nicholls J, Jiang C, Binder CJ, Penninger JM. Identification of oxidative stress and Toll-like receptor 4 signaling as a key pathway of acute lung injury. Cell. 2008 Apr 18;133(2):235-49. doi: 10.1016/j.cell.2008.02.043. PMID: 18423196; PMCID: PMC7112336.

Ivanov, I., Kuhn, H. and Heydeck, D., 2015. Structural and functional biology of arachidonic acid 15-lipoxygenase-1 (ALOX15). *Gene*, *573*(1), pp.1-32.

Jacobsen, K.X., Czesak, M., Deria, M., Le François, B. and Albert, P.R., 2011. Region-specific regulation of 5-HT1A receptor expression by Pet-1-dependent mechanisms in vivo. Journal of neurochemistry, 116(6), pp.1066-1076.

Janak, P.H. and Tye, K.M., 2015. From circuits to behaviour in the amygdala. *Nature*, *517*(7534), pp.284-292.

Jenkins, D.J., Sievenpiper, J.L., Pauly, D., Sumaila, U.R., Kendall, C.W. and Mowat, F.M., 2009. Are dietary recommendations for the use of fish oils sustainable?. *Cmaj*, *180*(6), pp.633-637.

Jimenez, J.C., Su, K., Goldberg, A.R., Luna, V.M., Biane, J.S., Ordek, G., Zhou, P., Ong, S.K., Wright, M.A., Zweifel, L. and Paninski, L., 2018. Anxiety cells in a hippocampal-hypothalamic circuit. Neuron, 97(3), pp.670-683.

Joels, M., 2001. Corticosteroid actions in the hippocampus. *Journal of neuroendocrinology*, *13*(8), pp.657-669.

Johnson, A.A. and Stolzing, A., 2019. The role of lipid metabolism in aging, lifespan regulation, and age-related disease. Aging cell, 18(6), p.e13048.

Joshi, Y.B., Di Meco, A. and Praticò, D., 2014. Overexpression of 12/15-lipoxygenase increases anxiety behavior in female mice. Neurobiology of Aging, 35(5), pp.1032-1036.

Jurado-Parras, M.T., Delgado-García, J.M., Sánchez-Campusano, R., Gassmann, M., Bettler, B. and Gruart, A., 2016. Presynaptic GABAB receptors regulate hippocampal synapses during associative learning in behaving mice. PloS one, 11(2), p.e0148800.

Kaczkurkin, A.N., Raznahan, A. and Satterthwaite, T.D., 2019. Sex differences in the developing brain: insights from multimodal neuroimaging. Neuropsychopharmacology, 44(1), pp.71-85.

Kageyama, K., Hanada, K., Moriyama, T., Imaizumi, T., Satoh, K. and Suda, T., 2007. Differential regulation of CREB and ERK phosphorylation through corticotropin-releasing factor receptors type 1 and 2 in AtT-20 and A7r5 cells. Molecular and cellular endocrinology, 263(1-2), pp.90-102.

Kandel, E.R., 2012. The molecular biology of memory: cAMP, PKA, CRE, CREB-1, CREB-2, and CPEB. *Molecular brain*, *5*(1), pp.1-12.

Karki, P. and Birukov, K.G., 2020. Oxidized phospholipids in healthy and diseased lung endothelium. *Cells*, *9*(4), p.981.

Kaufmann, W.E., Worley, P.F., Pegg, J., Bremer, M. and Isakson, P., 1996. COX-2, a synaptically induced enzyme, is expressed by excitatory neurons at postsynaptic sites in rat cerebral cortex. *Proceedings of the National Academy of Sciences*, *93*(6), pp.2317-2321.

Kawaguchi, Y., Katsumaru, H., Kosaka, T., Heizmann, C.W. and Hama, K., 1987. Fast spiking cells in rat hippocampus (CA1 region) contain the calcium-binding protein parvalbumin. *Brain research*, *416*(2), pp.369-374.

Kerr, D.I.B. and Ong, J., 1995. GABAB receptors. *Pharmacology & therapeutics*, *67*(2), pp.187-246.

Kim, J.J. and Diamond, D.M., 2002. The stressed hippocampus, synaptic plasticity and lost memories. *Nature Reviews Neuroscience*, *3*(6), pp.453-462.

Kim, S.N., Akindehin, S., Kwon, H.J., Son, Y.H., Saha, A., Jung, Y.S., Seong, J.K., Lim, K.M., Sung, J.H., Maddipati, K.R. and Lee, Y.H., 2018. Anti-inflammatory role of 15-lipoxygenase contributes to the maintenance of skin integrity in mice. *Scientific reports*, *8*(1), pp.1-11.

Kirkwood, L., Aldujaili, E. and Drummond, S., 2007. Effects of advice on dietary intake and/or physical activity on body composition, blood lipids and insulin resistance following a low-fat, sucrose-containing, high-carbohydrate, energy-restricted diet. International Journal of Food Sciences and Nutrition, 58(5), pp.383-397.

Kjelstrup, K.G., Tuvnes, F.A., Steffenach, H.A., Murison, R., Moser, E.I. and Moser, M.B., 2002. Reduced fear expression after lesions of the ventral hippocampus. *Proceedings of the National Academy of Sciences*, *99*(16), pp.10825-10830.

Klapdor, K. and Van der staay, F.J., 1996. The Morris water-escape task in mice: strain differences and effects of intra-maze contrast and brightness. *Physiology & behavior*, *60*(5), pp.1247-1254.

Klausberger, T. and Somogyi, P., 2008. Neuronal diversity and temporal dynamics: the unity of hippocampal circuit operations. *Science*, *321*(5885), pp.53-57.

Köfeler, H.C., Ahrends, R., Baker, E.S., Ekroos, K., Han, X., Hoffmann, N., Holčapek, M., Wenk, M.R. and Liebisch, G., 2021. Recommendations for good practice in MS-based lipidomics. *Journal of lipid research*, *62*.

Köfeler, H.C., Fauland, A., Rechberger, G.N. and Trötzmüller, M., 2012. Mass spectrometry based lipidomics: an overview of technological platforms. *Metabolites*, *2*(1), pp.19-38.

Konrad Lehmann, André Steinecke, Jürgen Bolz, "GABA through the Ages: Regulation of Cortical Function and Plasticity by Inhibitory Interneurons", Neural Plasticity, vol. 2012, Article ID 892784, 11 pages, 2012. https://doi.org/10.1155/2012/892784

Kosaka, T., Katsumaru, H., Hama, K., Wu, J.Y. and Heizmann, C.W., 1987. GABAergic neurons containing the Ca2+-binding protein parvalbumin in the rat hippocampus and dentate gyrus. Brain research, 419(1-2), pp.119-130.

Krabbe, S., Gründemann, J. and Lüthi, A., 2018. Amygdala inhibitory circuits regulate associative fear conditioning. Biological psychiatry, 83(10), pp.800-809.

Kriska, T., Cepura, C., Magier, D., Siangjong, L., Gauthier, K.M. and Campbell, W.B., 2012. Mice lacking macrophage 12/15-lipoxygenase are resistant to experimental hypertension. *American Journal of Physiology-Heart and Circulatory Physiology*, *302*(11), pp.H2428-H2438.

Krystal, J.H., Sanacora, G., Blumberg, H., Anand, A., Charney, D.S., Marek, G., Epperson, C.N., Goddard, A. and Mason, G.F., 2002. Glutamate and GABA systems as targets for novel antidepressant and mood-stabilizing treatments. *Molecular psychiatry*, *7*(1), pp.S71-S80.

Kühn, H. and O'Donnell, V.B., 2006. Inflammation and immune regulation by 12/15-lipoxygenases. Progress in lipid research, 45(4), pp.334-356.

Kuhn, H. and Thiele, B.J., 1999. The diversity of the lipoxygenase family: many sequence data but little information on biological significance. FEBS letters, 449(1), pp.7-11.

Kuhn, H., Gehring, T., Schröter, A. and Heydeck, D., 2016. Cytokine-dependent expression regulation of ALOX15. *J Cytokine Biol Kuhn*, *1*(2), p.106

Kuschner, C.E., Choi, J., Yin, T., Shinozaki, K., Becker, L.B., Lampe, J.W. and Kim, J., 2018. Comparing phospholipid profiles of mitochondria and whole tissue: Higher PUFA content in mitochondria is driven by increased phosphatidylcholine unsaturation. *Journal of Chromatography B*, *1093*, pp.147-157.

Lalonde, R. and Strazielle, C., 2009. Exploratory activity and motor coordination in old versus middle-aged C57BL/6J mice. *Archives of gerontology and geriatrics*, *49*(1), pp.39-42.

Lam, D.D., Garfield, A.S., Marston, O.J., Shaw, J. and Heisler, L.K., 2010. Brain serotonin system in the coordination of food intake and body weight. *Pharmacology Biochemistry and Behavior*, *97*(1), pp.84-91.

Lammers, C.H., Schweitzer, P., Facchinetti, P., Arrang, J.M., Madamba, S.G., Siggins, G.R. and Piomelli, D., 1996. Arachidonate 5-lipoxygenase and its activating protein: prominent hippocampal expression and role in somatostatin signaling. *Journal of neurochemistry*, *66*(1), pp.147-152.

Lane-Donovan, C., Wong, W.M., Durakoglugil, M.S., Wasser, C.R., Jiang, S., Xian, X. and Herz, J., 2016. Genetic restoration of plasma ApoE improves cognition and partially restores synaptic defects in ApoE-deficient mice. *Journal of Neuroscience*, *36*(39), pp.10141-10150.

Langfelder, P., Zhang, B. and Horvath, S., 2008. Defining clusters from a hierarchical cluster tree: the Dynamic Tree Cut package for R. *Bioinformatics*, *24*(5), pp.719-720.

Lawson, J.A., Patrono, C., Ciabattoni, G. and FitzGerald, G.A., 1986. Long-lived enzymatic metabolites of thromboxane B2 in the human circulation. *Analytical biochemistry*, *155*(1), pp.198-205.

Lee, J., Park, Y., Yang, W., Chung, H., Choi, W., Inoue, H., Kuwayama, K. and Park, J., 2012. Cross-examination of liquid–liquid extraction (LLE) and solid-phase microextraction (SPME) methods for impurity profiling of methamphetamine. *Forensic science international*, *215*(1-3), pp.175-178.

Lewejohann, L., Reinhard, C., Schrewe, A., Brandewiede, J., Haemisch, A., Görtz, N., Schachner, M. and Sachser, N., 2006. Environmental bias? Effects of housing conditions, laboratory environment and experimenter on behavioral tests. *Genes, Brain and Behavior*, *5*(1), pp.64-72.

Lewis, K., Li, C., Perrin, M.H., Blount, A., Kunitake, K., Donaldson, C., Vaughan, J., Reyes, T.M., Gulyas, J., Fischer, W. and Bilezikjian, L., 2001. Identification of urocortin III, an additional member of the corticotropin-releasing factor (CRF) family with high affinity for the CRF2 receptor. Proceedings of the National Academy of Sciences, 98(13), pp.7570-7575.

Lezak, K.R., Missig, G. and Carlezon Jr, W.A., 2017. Behavioral methods to study anxiety in rodents. *Dialogues in clinical neuroscience*, *19*(2), p.181.)

Li, P., Stewart, R., Butler, A., Gonzalez-Cota, A.L., Harmon, S. and Salkoff, L., 2017. GABA-B controls persistent Na+ current and coupled Na+-activated K+ current. Eneuro, 4(3).

Li, Y.E., Preissl, S., Hou, X., Zhang, Z., Zhang, K., Qiu, Y., Poirion, O.B., Li, B., Chiou, J., Liu, H. and Pinto-Duarte, A., 2021. An atlas of gene regulatory elements in adult mouse cerebrum. *Nature*, *598*(7879), pp.129-136.

Liebisch, G., Fahy, E., Aoki, J., Dennis, E.A., Durand, T., Ejsing, C.S., Fedorova, M., Feussner, I., Griffiths, W.J., Köfeler, H. and Merrill, A.H., 2020. Update on LIPID MAPS classification, nomenclature, and shorthand notation for MS-derived lipid structures. *Journal of lipid research*, *61*(12), pp.1539-1555.

Liebisch, G., Vizcaíno, J.A., Köfeler, H., Trötzmüller, M., Griffiths, W.J., Schmitz, G., Spener, F. and Wakelam, M.J., 2013. Shorthand notation for lipid structures derived from mass spectrometry. *Journal of lipid research*, *54*(6), pp.1523-1530.

Likhtik, E., Pelletier, J.G., Paz, R. and Paré, D., 2005. Prefrontal control of the amygdala. Journal of Neuroscience, 25(32), pp.7429-7437.

Lim, G.P., Calon, F., Morihara, T., Yang, F., Teter, B., Ubeda, O., Salem, N., Frautschy, S.A. and Cole, G.M., 2005. A diet enriched with the omega-3 fatty acid docosahexaenoic acid

reduces amyloid burden in an aged Alzheimer mouse model. *Journal of Neuroscience*, *25*(12), pp.3032-3040.

Lin, C.C. and Huang, T.L., 2017. Epigenetic biomarkers in neuropsychiatric disorders. In *Neuropsychiatric disorders and epigenetics* (pp. 35-66). Academic Press.

Lin, L., Cao, B., Xu, Z., Sui, Y., Chen, J., Luan, Q., Yang, R., Li, S. and Li, K.F., 2016. In vivo HMRS and lipidomic profiling reveals comprehensive changes of hippocampal metabolism during aging in mice. *Biochemical and biophysical research communications*, *470*(1), pp.9-14.

Lísa, M., Cífková, E., Khalikova, M., Ovčačíková, M. and Holčapek, M., 2017. Lipidomic analysis of biological samples: comparison of liquid chromatography, supercritical fluid chromatography and direct infusion mass spectrometry methods. *Journal of Chromatography A*, *1525*, pp.96-108.

Lisman, J., 2015. The challenge of understanding the brain: where we stand in 2015. *Neuron*, *86*(4), pp.864-882.

Little, S.J., Lynch, M.A., Manku, M. and Nicolaou, A., 2007. Docosahexaenoic acid-induced changes in phospholipids in cortex of young and aged rats: a lipidomic analysis. *Prostaglandins, leukotrienes and essential fatty acids*, *77*(3-4), pp.155-162.

Liu, G.Y., Moon, S.H., Jenkins, C.M., Sims, H.F., Guan, S. and Gross, R.W., 2019. Synthesis of oxidized phospholipids by sn-1 acyltransferase using 2–15-HETE lysophospholipids. *Journal of Biological Chemistry*, *294*(26), pp.10146-10159.

Lu, A., Steiner, M.A., Whittle, N., Vogl, A.M., Walser, S.M., Ableitner, M., Refojo, D., Ekker, M., Rubenstein, J.L., Stalla, G.K. and Singewald, N., 2008. Conditional mouse mutants highlight mechanisms of corticotropin-releasing hormone effects on stress-coping behavior. *Molecular psychiatry*, *13*(11), pp.1028-1042.

Lydiard, RB, 2003. The role of GABA in anxiety disorders. *Journal of Clinical Psychiatry*, *64*, pp.21-27.

Magnusson, K.R., Scruggs, B., Aniya, J., Wright, K.C., Ontl, T., Xing, Y. and Bai, L., 2003. Age-related deficits in mice performing working memory tasks in a water maze. *Behavioral neuroscience*, *117*(3), p.485.

Maier, Patrick J., Khaled Zemoura, Mario A. Acuña, Gonzalo E. Yévenes, Hanns Ulrich Zeilhofer, and Dietmar Benke. "Ischemia-like oxygen and glucose deprivation mediates down-regulation of cell surface γ-aminobutyric acidB receptors via the endoplasmic reticulum (ER) stress-induced transcription factor CCAAT/enhancer-binding protein (C/EBP)-homologous protein (CHOP)." *Journal of Biological Chemistry* 289, no. 18 (2014): 12896-12907.

Marie, H., Morishita, W., Yu, X., Calakos, N. and Malenka, R.C., 2005. Generation of silent synapses by acute in vivo expression of CaMKIV and CREB. *Neuron*, *45*(5), pp.741-752.

Marín, O., 2012. Interneuron dysfunction in psychiatric disorders. *Nature Reviews Neuroscience*, *13*(2), pp.107-120.

Martin, E.I., Ressler, K.J., Binder, E. and Nemeroff, C.B., 2009. The neurobiology of anxiety disorders: brain imaging, genetics, and psychoneuroendocrinology. *Psychiatric Clinics*, *32*(3), pp.549-575.

Maskrey, B.H. and O'Donnell, V.B., 2008. Analysis of eicosanoids and related lipid mediators using mass spectrometry. Biochemical Society Transactions, 36(5), pp.1055-1059.

Maskrey, B.H., Bermudez-Fajardo, A., Morgan, A.H., Stewart-Jones, E., Dioszeghy, V., Taylor, G.W., Baker, P.R., Coles, B., Coffey, M.J., Kühn, H. and O'Donnell, V.B., 2007. Activated platelets and monocytes generate four hydroxyphosphatidylethanolamines via lipoxygenase. *Journal of Biological Chemistry*, *282*(28), pp.20151-20163.

Maskrey, B.H., Megson, I.L., Rossi, A.G. and Whitfield, P.D., 2013. Emerging importance of omega-3 fatty acids in the innate immune response: Molecular mechanisms and lipidomic strategies for their analysis. *Molecular nutrition & food research*, *57*(8), pp.1390-1400.

McEwen, B.S. and Sapolsky, R.M., 1995. Stress and cognitive function. *Current opinion in neurobiology*, *5*(2), pp.205-216.

McEwen, B.S., 1999. Stress and hippocampal plasticity. Annual review of neuroscience, 22(1), pp.105-122.

McEwen, B.S., Eiland, L., Hunter, R.G. and Miller, M.M., 2012. Stress and anxiety: structural plasticity and epigenetic regulation as a consequence of stress. *Neuropharmacology*, *62*(1), pp.3-12.

McEwen, B.S., Nasca, C. and Gray, J.D., 2016. Stress effects on neuronal structure: hippocampus, amygdala, and prefrontal cortex. *Neuropsychopharmacology*, *41*(1), pp.3-23.

McHugh, S.B., Campbell, T.G., Taylor, A.M., Rawlins, J.N.P. and Bannerman, D.M., 2008. A role for dorsal and ventral hippocampus in inter-temporal choice cost-benefit decision making. Behavioral Neuroscience, 122(1), p.1.

McHugh, S.B., Deacon, R.M.J., Rawlins, J.N.P. and Bannerman, D.M., 2004. Amygdala and ventral hippocampus contribute differentially to mechanisms of fear and anxiety. *Behavioral neuroscience*, *118*(1), p.63.

McQuail, J.A., Frazier, C.J. and Bizon, J.L., 2015. Molecular aspects of age-related cognitive decline: the role of GABA signaling. *Trends in molecular medicine*, *21*(7), pp.450-460.

Mei, L., Zhou, Y., Sun, Y., Liu, H., Zhang, D., Liu, P. and Shu, H., 2020. Acetylcholine muscarinic receptors in ventral hippocampus modulate stress-induced anxiety-like behaviors in mice. *Frontiers in Molecular Neuroscience*, *13*, p.598811.

Messias, M.C.F., Mecatti, G.C., Priolli, D.G. and de Oliveira Carvalho, P., 2018. Plasmalogen lipids: functional mechanism and their involvement in gastrointestinal cancer. *Lipids in Health and Disease*, *17*(1), pp.1-12.

Misheva, M., Kotzamanis, K., Davies, L.C., Tyrrell, V.J., Rodrigues, P.R., Benavides, G.A., Hinz, C., Murphy, R.C., Kennedy, P., Taylor, P.R. and Rosas, M., 2022. Oxylipin metabolism is controlled by mitochondrial β-oxidation during bacterial inflammation. *Nature communications*, *13*(1), pp.1-20.

Miyata, J., Yokokura, Y., Moro, K., Arai, H., Fukunaga, K. and Arita, M., 2021. 12/15-Lipoxygenase regulates IL-33-induced eosinophilic airway inflammation in mice. *Frontiers in immunology*, *12*, p.687192.

Moran, J.H., Weise, R., Schnellmann, R.G., Freeman, J.P. and Grant, D.F., 1997. Cytotoxicity of linoleic acid diols to renal proximal tubular cells. *Toxicology and applied pharmacology*, *146*(1), pp.53-59.

Morgan, A.H., Dioszeghy, V., Maskrey, B.H., Thomas, C.P., Clark, S.R., Mathie, S.A., Lloyd, C.M., Kühn, H., Topley, N., Coles, B.C. and Taylor, P.R., 2009. Phosphatidylethanolamine-esterified eicosanoids in the mouse: tissue localization and inflammation-dependent formation in Th-2 disease. *Journal of Biological Chemistry*, *284*(32), pp.21185-21191.

Morgan, L.T., Thomas, C.P., Kühn, H. and O'Donnell, V.B., 2010. Thrombin-activated human platelets acutely generate oxidized docosahexaenoic-acid-containing phospholipids via 12-lipoxygenase. *Biochemical Journal*, *431*(1), pp.141-148.

Morris, R., 1984. Developments of a water-maze procedure for studying spatial learning in the rat. *Journal of neuroscience methods*, *11*(1), pp.47-60.

Morris, R.G.M., Schenk, F., Tweedie, F. and Jarrard, L.E., 1990. Ibotenate lesions of hippocampus and/or subiculum: dissociating components of allocentric spatial learning. *European Journal of Neuroscience*, *2*(12), pp.1016-1028.

Morrissette, D.A., Parachikova, A., Green, K.N. and LaFerla, F.M., 2009. Relevance of transgenic mouse models to human Alzheimer disease. *Journal of Biological Chemistry*, *284*(10), pp.6033-6037.

Mota, C., Taipa, R., das Neves, S.P., Monteiro-Martins, S., Monteiro, S., Palha, J.A., Sousa, N., Sousa, J.C. and Cerqueira, J.J., 2019. Structural and molecular correlates of cognitive aging in the rat. *Scientific reports*, *9*(1), pp.1-14.

Müller, M.B., Zimmermann, S., Sillaber, I., Hagemeyer, T.P., Deussing, J.M., Timpl, P., Kormann, M.S., Droste, S.K., Kühn, R., Reul, J.M. and Holsboer, F., 2003. Limbic corticotropin-releasing hormone receptor 1 mediates anxiety-related behavior and hormonal adaptation to stress. Nature neuroscience, 6(10), pp.1100-1107.

Murthy, S., Kane, G.A., Katchur, N.J., Mejia, P.S.L., Obiofuma, G., Buschman, T.J., McEwen, B.S. and Gould, E., 2019. Perineuronal nets, inhibitory interneurons, and anxiety-related ventral hippocampal neuronal oscillations are altered by early life adversity. *Biological psychiatry*, *85*(12), pp.1011-1020.

Narzt, M.S., Kremslehner, C., Golabi, B., Nagelreiter, I.M., Malikovic, J., Hussein, A.M., Plasenzotti, R., Korz, V., Lubec, G., Gruber, F. and Lubec, J., 2022. Molecular species of oxidized phospholipids in brain differentiate between learning-and memory impaired and unimpaired aged rats. *Amino Acids*, pp.1-16.

Newcomer, M.E. and Brash, A.R., 2015. The structural basis for specificity in lipoxygenase catalysis. Protein Science, 24(3), pp.298-309.

Nguyen, C.H., Stadler, S., Brenner, S., Huttary, N., Krieger, S., Jäger, W., Dolznig, H. and Krupitza, G., 2016. Cancer cell-derived 12 (S)-HETE signals via 12-HETE receptor, RHO, ROCK and MLC2 to induce lymph endothelial barrier breaching. *British journal of cancer*, *115*(3), pp.364-370.

Nie, Q. and Nie, S., 2019. High-performance liquid chromatography for food quality evaluation. In Evaluation Technologies for Food Quality (pp. 267-299). Woodhead Publishing.

Nieuwenhuys, R. and Puelles, L., 2015. *Towards a new neuromorphology*. Springer.

Norris, S.E., Friedrich, M.G., Mitchell, T.W., Truscott, R.J. and Else, P.L., 2015. Human prefrontal cortex phospholipids containing docosahexaenoic acid increase during normal adult aging, whereas those containing arachidonic acid decrease. *Neurobiology of aging*, *36*(4), pp.1659-1669.

O'Donnell, V.B. and Murphy, R.C., 2012. New families of bioactive oxidised phospholipids generated by immune cells: identification and signaling actions. Blood, The Journal of the American Society of Hematology, 120(10), pp.1985-1992.

O'Donnell, V.B., Maskrey, B. and Taylor, G.W., 2009. Eicosanoids: generation and detection in mammalian cells. In Lipid Signaling Protocols (pp. 1-19). Humana Press, Totowa, NJ.

O'Donnell, V.B., Rossjohn, J. and Wakelam, M.J., 2019. Phospholipid signaling in innate immune cells. The Journal of clinical investigation, 128(7), pp.2670-2679.

O'Donnell, V.B., 2011. Mass spectrometry analysis of oxidized phosphatidylcholine and phosphatidylethanolamine. *Biochimica et Biophysica Acta (BBA)-Molecular and Cell Biology of Lipids*, *1811*(11), pp.818-826.

O'Donnell, V.B., Maskrey, B. and Taylor, G.W., 2009. Eicosanoids: generation and detection in mammalian cells. In Lipid Signaling Protocols (pp. 1-19). Humana Press, Totowa, NJ.

Ögren, S.O., Eriksson, T.M., Elvander-Tottie, E., D'Addario, C., Ekström, J.C., Svenningsson, P., Meister, B., Kehr, J. and Stiedl, O., 2008. The role of 5-HT1A receptors in learning and memory. *Behavioural brain research*, *195*(1), pp.54-77.

Ojo, J.O., Algamal, M., Leary, P., Abdullah, L., Mouzon, B., Evans, J.E., Mullan, M. and Crawford, F., 2018. Disruption in brain phospholipid content in a humanized tau transgenic model following repetitive mild traumatic brain injury. *Frontiers in neuroscience*, p.893.

Orr, S.K., Palumbo, S., Bosetti, F., Mount, H.T., Kang, J.X., Carol, E., Ma, D.W., Serhan, C.N. and Bazinet, R.P., 2013. Unesterified docosahexaenoic acid is protective in neuroinflammation. *Journal of neurochemistry*, *127*(3), p.378.

Padgett, C.L. and Slesinger, P.A., 2010. GABAB receptor coupling to G-proteins and ion channels. Advances in pharmacology, 58, pp.123-147.

Palchaudhuri M, Flugge G (2005): 5-HT1A receptor expression in pyramidal neurons of cortical and limbic brain regions. *Cell Tissue Res* 321:159–172.

Parks, C.L., Robinson, P.S., Sibille, E., Shenk, T. and Toth, M., 1998. Increased anxiety of mice lacking the serotonin1A receptor. *Proceedings of the national academy of sciences*, *95*(18), pp.10734-10739.

Passingham, R.E., 1979. The hippocampus as a cognitive map| J. O'Keefe & L. Nadel, Oxford University Press, Oxford (1978). 570 pp.,£ 25.00.

Petr, M.A., Alfaras, I., Krawcyzk, M., Bair, W.N., Mitchell, S.J., Morrell, C.H., Studenski, S.A., Price, N.L., Fishbein, K.W., Spencer, R.G. and Scheibye-Knudsen, M., 2021. A cross-sectional study of functional and metabolic changes during aging through the lifespan in male mice. *Elife*, *10*, p.e62952.

Picq, M., Chen, P., Perez, M., Michaud, M., Véricel, E., Guichardant, M. and Lagarde, M., 2010. DHA metabolism: targeting the brain and lipoxygenation. *Molecular neurobiology*, *42*(1), pp.48-51.

Pompeiano, M., Palacios, J.M. and Mengod, G., 1992. Distribution and cellular localization of mRNA coding for 5-HT1A receptor in the rat brain: correlation with receptor binding. *Journal of Neuroscience*, *12*(2), pp.440-453.

Pothuizen, H.H., Zhang, W.N., Jongen-Rêlo, A.L., Feldon, J. and Yee, B.K., 2004. Dissociation of function between the dorsal and the ventral hippocampus in spatial learning abilities of the rat: a within-subject, within-task comparison of reference and working spatial memory. *European Journal of Neuroscience*, *19*(3), pp.705-712.

Powell, W.S. and Rokach, J., 2015. Biosynthesis, biological effects, and receptors of hydroxyeicosatetraenoic acids (HETEs) and oxoeicosatetraenoic acids (oxo-ETEs) derived from arachidonic acid. *Biochimica et Biophysica Acta (BBA)-Molecular and Cell Biology of Lipids*, *1851*(4), pp.340-355.

Powell, W.S., Gravelle, F. and Gravel, S., 1992. Metabolism of 5 (S)-hydroxy-6, 8, 11, 14-eicosatetraenoic acid and other 5 (S)-hydroxyeicosanoids by a specific dehydrogenase in human polymorphonuclear leukocytes. *Journal of Biological Chemistry*, *267*(27), pp.19233-19241.

Powell, W.S., Zhang, Y. and Gravel, S., 1994. Effects of phorbol myristate acetate on the synthesis of 5-oxo-6, 8, 11, 14-eicosatetraenoic acid by human polymorphonuclear leukocytes. *Biochemistry*, *33*(13), pp.3927-3933.

Pradas, I., Jové, M., Huynh, K., Puig, J., Inglés, M., Borrás, C., Viña, J., Meikle, P.J. and Pamplona, R., 2019. Exceptional human longevity is associated with a specific plasma phenotype of ether lipids. *Redox biology*, *21*, p.101127.

Puppolo, M., Varma, D. and Jansen, S.A., 2014. A review of analytical methods for eicosanoids in brain tissue. Journal of Chromatography B, 964, pp.50-64.

Qi, K., Hall, M. and Deckelbaum, R.J., 2002. Long-chain polyunsaturated fatty acid accretion in brain. *Current Opinion in Clinical Nutrition & Metabolic Care*, *5*(2), pp.133-138.

Ramboz, S. et al. Serotonin receptor 1A knockout: an animal model of anxiety-related disorder. *Proc. Natl Acad. Sci. USA* **95**, 14476–14481 (1998).

Rapp, P.R., Stack, E.C. and Gallagher, M., 1999. Morphometric studies of the aged hippocampus: I. Volumetric analysis in behaviorally characterized rats. *Journal of Comparative Neurology*, *403*(4), pp.459-470.

Rawlins, J.N.P. and Olton, D.S., 1982. The septo-hippocampal system and cognitive mapping. Behavioural brain research, 5(4), pp.331-358.

reil, C., Abert Vian, M., Zemb, T., Kunz, W. and Chemat, F., 2017. "Bligh and Dyer" and Folch methods for solid–liquid–liquid extraction of lipids from microorganisms. Comprehension of solvatation mechanisms and towards substitution with alternative solvents. International journal of molecular sciences, 18(4), p.708.

Reis, J.P., Macera, C.A., Araneta, M.R., Lindsay, S.P., Marshall, S.J. and Wingard, D.L., 2009. Comparison of overall obesity and body fat distribution in predicting risk of mortality. Obesity, 17(6), pp.1232-1239.

Reisz, J.A., Zheng, C., D'Alessandro, A. and Nemkov, T., 2019. Untargeted and semi-targeted lipid analysis of biological samples using mass spectrometry-based metabolomics. *High-Throughput Metabolomics: Methods and Protocols*, pp.121-135.

Reynaud, D., Thickitt, C.P. and Paceasciak, C.R., 1993. Facile preparation and structural determination of monohydroxy derivatives of docosahexaenoic acid (HDoHE) by α-tocopherol-directed autoxidation. *Analytical biochemistry*, *214*(1), pp.165-170.

Riad, M., Garcia, S., Watkins, K.C., Jodoin, N., Doucet, É., Langlois, X., El Mestikawy, S., Hamon, M. and Descarries, L., 2000. Somatodendritic localization of 5-HT1A and preterminal axonal localization of 5-HT1B serotonin receptors in adult rat brain. *Journal of Comparative Neurology*, *417*(2), pp.181-194.

Ricciotti, E. and FitzGerald, G.A., 2011. Prostaglandins and inflammation. *Arteriosclerosis, thrombosis, and vascular biology*, *31*(5), pp.986-1000.

Ridgway, N.D., 2021. Phospholipid synthesis in mammalian cells. In *Biochemistry of lipids, lipoproteins and membranes* (pp. 227-258). Elsevier.

Roberts 2nd, L.J., Brash, A.R. and Oates, J.A., 1982. Metabolic fate of thromboxane A2 and prostacyclin. Advances in prostaglandin, thromboxane, and leukotriene research, 10, pp.211-225.

Rothwell, J. and Kofler, M., 2012. Neurophysiology of the brainstem-structure and function of brainstem circuits. *Clinical Neurophysiology*, *1*(123), pp.2-3

Rubin, P. and Mollison, K.W., 2007. Pharmacotherapy of diseases mediated by 5-lipoxygenase pathway eicosanoids. *Prostaglandins & other lipid mediators*, *83*(3), pp.188-197.

Ryan, V.H., Primiani, C.T., Rao, J.S., Ahn, K., Rapoport, S.I. and Blanchard, H., 2014. Coordination of gene expression of arachidonic and docosahexaenoic acid cascade enzymes during human brain development and aging. PloS one, 9(6), p.e100858.

Salmon, J.A. and Higgs, G.A., 1987. Prostaglandins and leukotrienes as inflammatory mediators. *British medical bulletin*, *43*(2), pp.285-296.

Salomon, R.G., Miller, D.B., Raychaudhuri, S.R., Avasthi, K., Lal, K. and Levison, B.S., 1984. Prostaglandin endoperoxides. 15. Asymmetric total synthesis of levuglandin E2. *Journal of the American Chemical Society*, *106*(26), pp.8296-8298.

Santana, N., Bortolozzi, A., Serrats, J., Mengod, G. and Artigas, F., 2004. Expression of serotonin1A and serotonin2A receptors in pyramidal and GABAergic neurons of the rat prefrontal cortex. *Cerebral cortex*, *14*(10), pp.1100-1109.

Santarelli, L., Saxe, M., Gross, C., Surget, A., Battaglia, F., Dulawa, S., Weisstaub, N., Lee, J., Duman, R., Arancio, O. and Belzung, C., 2003. Requirement of hippocampal neurogenesis for the behavioral effects of antidepressants. *science*, *301*(5634), pp.805-809.

Schebb, N.H., Ostermann, A.I., Yang, J., Hammock, B.D., Hahn, A. and Schuchardt, J.P., 2014. Comparison of the effects of long-chain omega-3 fatty acid supplementation on plasma levels of free and esterified oxylipins. *Prostaglandins & other lipid mediators*, *113*, pp.21-29.

Schmouth, J.F., Bonaguro, R.J., Corso-Diaz, X. and Simpson, E.M., 2012. Modelling human regulatory variation in mouse: finding the function in genome-wide association studies and whole-genome sequencing. *PLoS genetics*, *8*(3), p.e1002544.

Serhan, C.N., Hong, S., Gronert, K., Colgan, S.P., Devchand, P.R., Mirick, G. and Moussignac, R.L., 2002. Resolvins: a family of bioactive products of omega-3 fatty acid transformation circuits initiated by aspirin treatment that counter proinflammation signals. *The Journal of experimental medicine*, *196*(8), pp.1025-1037.

Serrano-Regal, M.P., Bayón-Cordero, L., Ordaz, R.P., Garay, E., Limon, A., Arellano, R.O., Matute, C. and Sánchez-Gómez, M.V., 2020. Expression and function of GABA receptors in myelinating cells. *Frontiers in cellular neuroscience*, *14*, p.256.

Shalini, S.M., Ho, C.F.Y., Ng, Y.K., Tong, J.X., Ong, E.S., Herr, D.R., Dawe, G.S. and Ong, W.Y., 2018. Distribution of Alox15 in the rat brain and its role in prefrontal cortical resolvin D1 formation and spatial working memory. *Molecular Neurobiology*, *55*(2), pp.1537-1550.

Sheng, H., Laskowitz, D.T., Bennett, E., Schmechel, D.E., Bart, R.D., Saunders, A.M., Pearlstein, R.D., Roses, A.D. and Warner, D.S., 1998. Apolipoprotein E isoform-specific differences in outcome from focal ischemia in transgenic mice. *Journal of Cerebral Blood Flow & Metabolism*, *18*(4), pp.361-366.

Shoji, H. and Miyakawa, T., 2019. Age-related behavioral changes from young to old age in male mice of a C57 BL/6J strain maintained under a genetic stability program. *Neuropsychopharmacology reports*, *39*(2), pp.100-118.

Shoji, H., Takao, K., Hattori, S. and Miyakawa, T., 2016. Age-related changes in behavior in C57BL/6J mice from young adulthood to middle age. *Molecular brain*, *9*(1), pp.1-18.

Singh, N.K. and Rao, G.N., 2019. Emerging role of 12/15-Lipoxygenase (ALOX15) in human pathologies. Progress in lipid research, 73, pp.28-45.

Singhal, G., Morgan, J., Jawahar, M.C., Corrigan, F., Jaehne, E.J., Toben, C., Breen, J., Pederson, S.M., Manavis, J., Hannan, A.J. and Baune, B.T., 2020. Effects of aging on the motor, cognitive and affective behaviors, neuroimmune responses and hippocampal gene expression. *Behavioural Brain Research*, *383*, p.112501.

Skowronska-Krawczyk, D. and Budin, I., 2020. Aging membranes: Unexplored functions for lipids in the lifespan of the central nervous system. *Experimental gerontology*, *131*, p.110817.

Smith, W.L., Urade, Y. and Jakobsson, P.J., 2011. Enzymes of the cyclooxygenase pathways of prostanoid biosynthesis. *Chemical reviews*, *111*(10), pp.5821-5865.

Söderberg, M., Edlund, C., Kristensson, K. and Dallner, G., 1990. Lipid compositions of different regions of the human brain during aging. *Journal of neurochemistry*, *54*(2), pp.415-423.

Sonnweber, T., Pizzini, A., Nairz, M., Weiss, G. and Tancevski, I., 2018. Arachidonic acid metabolites in cardiovascular and metabolic diseases. International journal of molecular sciences, 19(11), p.3285.

Sparvero, L.J., Amoscato, A.A., Kochanek, P.M., Pitt, B.R., Kagan, V.E. and Bayır, H., 2010. Mass-spectrometry based oxidative lipidomics and lipid imaging: applications in traumatic brain injury. Journal of neurochemistry, 115(6), pp.1322-1336.

Spector, A.A., 2009. Arachidonic acid cytochrome P450 epoxygenase pathway. Journal of lipid research, 50, pp.S52-S56.

Stephenson, D.J., MacKnight, H.P., Hoeferlin, L.A., Park, M.A., Allegood, J.C., Cardona, C.L. and Chalfant, C.E., 2019. A rapid and adaptable lipidomics method for quantitative UPLC-mass spectrometric analysis of phosphatidylethanolamine and phosphatidylcholine in vitro, and in cells. *Analytical Methods*, *11*(13), pp.1765-1776.

Steullet, P., Cabungcal, J.H., Coyle, J., Didriksen, M., Gill, K., Grace, A.A., Hensch, T.K., LaMantia, A.S., Lindemann, L., Maynard, T.M. and Meyer, U., 2017. Oxidative stress-driven parvalbumin interneuron impairment as a common mechanism in models of schizophrenia. *Molecular psychiatry*, *22*(7), pp.936-943.

Su, H.M., 2010. Mechanisms of n-3 fatty acid-mediated development and maintenance of learning memory performance. *The Journal of nutritional biochemistry*, *21*(5), pp.364-373.

Sun, D. and Funk, C.D., 1996. Disruption of 12/15-lipoxygenase expression in peritoneal macrophages: enhanced utilization of the 5-lipoxygenase pathway and diminished oxidation of low density lipoprotein. *Journal of Biological Chemistry*, *271*(39), pp.24055-24062.

Sun, L., Xu, Y.W., Han, J., Liang, H., Wang, N. and Cheng, Y., 2015. 12/15-Lipoxygenase metabolites of arachidonic acid activate PPARγ: a possible neuroprotective effect in ischemic brain. *Journal of lipid research*, *56*(3), pp.502-514.

Suzuki, H., Park, S.J., Tamura, M. and Ando, S., 1998. Effect of the long-term feeding of dietary lipids on the learning ability, fatty acid composition of brain stem phospholipids and synaptic membrane fluidity in adult mice: a comparison of sardine oil diet with palm oil diet. *Mechanisms of ageing and development*, *101*(1-2), pp.119-128.

Swardfager, W., Hennebelle, M., Yu, D., Hammock, B.D., Levitt, A.J., Hashimoto, K. and Taha, A.Y., 2018. Metabolic/inflammatory/vascular comorbidity in psychiatric disorders; soluble epoxide hydrolase (sEH) as a possible new target. Neuroscience & Biobehavioral Reviews, 87, pp.56-66.

Szczuko, M., Kotlęga, D., Palma, J., Zembroń-Łacny, A., Tylutka, A., Gołąb-Janowska, M. and Drozd, A., 2020. Lipoxins, RevD1 and 9, 13 HODE as the most important derivatives after an early incident of ischemic stroke. *Scientific reports*, *10*(1), pp.1-13.

Team, R.C., 2013. R: A language and environment for statistical computing. R Foundation for Statistical Computing, Vienna, Austria. *http://www. R-project. org/*.

Teunissen, S.F. and Eberlin, M.N., 2017. Transferring ions from solution to the gas phase: the two basic principles. *Journal of The American Society for Mass Spectrometry*, *28*(11), pp.2255-2261.

Thomas CP, Morgan LT, Maskrey BH, Murphy RC, Kuhn H, Hazen SL, et al. Phospholipid esterified eicosanoids are generated in agonist-activated human platelets and enhance tissue factor-dependent thrombin generation. *J Biol Chem* (2010) 285(10):6891–903

Tu, W., Cook, A., Scholl, J.L., Mears, M., Watt, M.J., Renner, K.J. and Forster, G.L., 2014. Serotonin in the ventral hippocampus modulates anxiety-like behavior during amphetamine withdrawal. *Neuroscience*, *281*, pp.35-43.

Urban, P.L., 2016. Quantitative mass spectrometry: an overview. *Philosophical Transactions of the Royal Society A: Mathematical, Physical and Engineering Sciences*, *374*(2079), p.20150382.

van Leyen, K., Kim, H.Y., Lee, S.R., Jin, G., Arai, K. and Lo, E.H., 2006. Baicalein and 12/15-lipoxygenase in the ischemic brain. Stroke, 37(12), pp.3014-3018.

Van Meer, G., Voelker, D.R. and Feigenson, G.W., 2008. Membrane lipids: where they are and how they behave. *Nature reviews Molecular cell biology*, *9*(2), pp.112-124.

van Tol, M.J., van der Wee, N.J., van den Heuvel, O.A., Nielen, M.M., Demenescu, L.R., Aleman, A., Renken, R., van Buchem, M.A., Zitman, F.G. and Veltman, D.J., 2010. Regional

brain volume in depression and anxiety disorders. *Archives of general psychiatry*, *67*(10), pp.1002-1011.

Vangaveti, V., Baune, B.T. and Kennedy, R.L., 2010. Hydroxyoctadecadienoic acids: novel regulators of macrophage differentiation and atherogenesis. *Therapeutic advances in endocrinology and metabolism*, *1*(2), pp.51-60.

VanRollins, M. and Murphy, R.C., 1984. Autooxidation of docosahexaenoic acid: analysis of ten isomers of hydroxydocosahexaenoate. *Journal of lipid research*, *25*(5), pp.507-517.

VanRollins, M., Baker, R.C., Sprecher, H.W. and Murphy, R.C., 1984. Oxidation of docosahexaenoic acid by rat liver microsomes. *Journal of Biological Chemistry*, *259*(9), pp.5776-5783.

Varnas K, Halldin C, Hall H (2004): Autoradiographic distribution of serotonin transporters and receptor subtypes in human brain. Hum Brain Mapp 22:246 –260.

Voikar, V., Krackow, S., Lipp, H.P., Rau, A., Colacicco, G. and Wolfer, D.P., 2018. Automated dissection of permanent effects of hippocampal or prefrontal lesions on performance at spatial, working memory and circadian timing tasks of C57BL/6 mice in IntelliCage. *Behavioural brain research*, *352*, pp.8-22.

Westlund, P., Kumlin, M., Nordenström, A. and Granström, E., 1986. Circulating and urinary thromboxane B2 metabolites in the rabbit: 11-dehydro-thromboxane B2 as parameter of thromboxane production. *Prostaglandins*, *31*(3), pp.413-443.

Wong, A.A. and Brown, R.E., 2007. Age-related changes in visual acuity, learning and memory in C57BL/6J and DBA/2J mice. *Neurobiology of aging*, *28*(10), pp.1577-1593.

Wong, M.W., Braidy, N., Poljak, A., Pickford, R., Thambisetty, M. and Sachdev, P.S., 2017. Dysregulation of lipids in Alzheimer's disease and their role as potential biomarkers. *Alzheimer's & Dementia*, *13*(7), pp.810-827.

Wu, C.Y., Lerner, F.M., e Silva, A.C., Possoit, H.E., Hsieh, T.H., Neumann, J.T., Minagar, A., Lin, H.W. and Lee, R.H., 2018. Utilizing the modified T-maze to assess functional memory outcomes after cardiac arrest. *JoVE (Journal of Visualized Experiments)*, (131), p.e56694.

Wu, Z., Shon, J.C. and Liu, K.H., 2014. Mass spectrometry-based lipidomics and its application to biomedical research. *Journal of lifestyle medicine*, *4*(1), p.17.

Wulff, P., Schonewille, M., Renzi, M., Viltono, L., Sassoè-Pognetto, M., Badura, A., Gao, Z., Hoebeek, F.E., Van Dorp, S., Wisden, W. and Farrant, M., 2009. Synaptic inhibition of Purkinje cells mediates consolidation of vestibulo-cerebellar motor learning. *Nature neuroscience*, *12*(8), pp.1042-1049.

Xiao, G., Tsai, A.L., Palmer, G., Boyar, W.C., Marshall, P.J. and Kulmacz, R.J., 1997. Analysis of hydroperoxide-induced tyrosyl radicals and lipoxygenase activity in aspirin-treated human prostaglandin H synthase-2. *Biochemistry*, *36*(7), pp.1836-1845.

Xu, X., Roby, K.D. and Callaway, E.M., 2010. Immunochemical characterization of inhibitory mouse cortical neurons: three chemically distinct classes of inhibitory cells. *Journal of Comparative Neurology*, *518*(3), pp.389-404.

Yamagata, K., Andreasson, K.I., Kaufmann, W.E., Barnes, C.A. and Worley, P.F., 1993. Expression of a mitogen-inducible cyclooxygenase in brain neurons: regulation by synaptic activity and glucocorticoids. *Neuron*, *11*(2), pp.371-386.

Yamashita, A., Hayashi, Y., Nemoto-Sasaki, Y., Ito, M., Oka, S., Tanikawa, T., Waku, K. and Sugiura, T., 2014. Acyltransferases and transacylases that determine the fatty acid composition of glycerolipids and the metabolism of bioactive lipid mediators in mammalian cells and model organisms. *Progress in lipid research*, *53*, pp.18-81.

Yanai, S. and Endo, S., 2021. Functional aging in male C57BL/6J mice across the life-span: a systematic behavioral analysis of motor, emotional, and memory function to define an aging phenotype. *Frontiers in Aging Neuroscience*, p.457.

Yang, J., Schmelzer, K., Georgi, K. and Hammock, B.D., 2009. Quantitative profiling method for oxylipin metabolome by liquid chromatography electrospray ionization tandem mass spectrometry. *Analytical chemistry*, *81*(19), pp.8085-8093.

Yuan, Z.X., Majchrzak-Hong, S., Keyes, G.S., Iadarola, M.J., Mannes, A.J. and Ramsden, C.E., 2018. Lipidomic profiling of targeted oxylipins with ultra-performance liquid chromatography-tandem mass spectrometry. *Analytical and bioanalytical chemistry*, *410*(23), pp.6009-6029.

Zanger, U.M. and Schwab, M., 2013. Cytochrome P450 enzymes in drug metabolism: regulation of gene expression, enzyme activities, and impact of genetic variation. Pharmacology & therapeutics, 138(1), pp.103-141.

Zivkovic, A.M., Yang, J., Georgi, K., Hegedus, C., Nording, M.L., O'Sullivan, A., German, J.B., Hogg, R.J., Weiss, R.H., Bay, C. and Hammock, B.D., 2012. Serum oxylipin profiles in IgA nephropathy patients reflect kidney functional alterations. *Metabolomics*, *8*(6), pp.1102-1113